

Renu Sharma · Manohar Mishra ·
Janmenjoy Nayak · Bighnaraj Naik ·
Danilo Pelusi *Editors*

Innovation in Electrical Power Engineering, Communication, and Computing Technology

Proceedings of IEPCCT 2019

Lecture Notes in Electrical Engineering

Volume 630

Series Editors

Leopoldo Angrisani, Department of Electrical and Information Technologies Engineering, University of Napoli Federico II, Naples, Italy

Marco Arteaga, Departament de Control y Robótica, Universidad Nacional Autónoma de México, Coyoacán, Mexico

Bijaya Ketan Panigrahi, Electrical Engineering, Indian Institute of Technology Delhi, New Delhi, Delhi, India
Samarjit Chakraborty, Fakultät für Elektrotechnik und Informationstechnik, TU München, Munich, Germany

Jiming Chen, Zhejiang University, Hangzhou, Zhejiang, China

Shanben Chen, Materials Science and Engineering, Shanghai Jiao Tong University, Shanghai, China

Tan Kay Chen, Department of Electrical and Computer Engineering, National University of Singapore, Singapore, Singapore

Rüdiger Dillmann, Humanoids and Intelligent Systems Laboratory, Karlsruhe Institute for Technology, Karlsruhe, Germany

Haibin Duan, Beijing University of Aeronautics and Astronautics, Beijing, China

Gianluigi Ferrari, Università di Parma, Parma, Italy

Manuel Ferre, Centre for Automation and Robotics CAR (UPM-CSIC), Universidad Politécnica de Madrid, Madrid, Spain

Sandra Hirche, Department of Electrical Engineering and Information Science, Technische Universität München, Munich, Germany

Faryar Jabbari, Department of Mechanical and Aerospace Engineering, University of California, Irvine, CA, USA

Limin Jia, State Key Laboratory of Rail Traffic Control and Safety, Beijing Jiaotong University, Beijing, China

Janusz Kacprzyk, Systems Research Institute, Polish Academy of Sciences, Warsaw, Poland

Alaa Khamis, German University in Egypt El Tagamoa El Khames, New Cairo City, Egypt

Torsten Kroeger, Stanford University, Stanford, CA, USA

Qilian Liang, Department of Electrical Engineering, University of Texas at Arlington, Arlington, TX, USA

Ferran Martín, Departament d'Enginyeria Electrònica, Universitat Autònoma de Barcelona, Bellaterra, Barcelona, Spain

Tan Cher Ming, College of Engineering, Nanyang Technological University, Singapore, Singapore

Wolfgang Minker, Institute of Information Technology, University of Ulm, Ulm, Germany

Pradeep Misra, Department of Electrical Engineering, Wright State University, Dayton, OH, USA

Sebastian Möller, Quality and Usability Laboratory, TU Berlin, Berlin, Germany

Subhas Mukhopadhyay, School of Engineering & Advanced Technology, Massey University, Palmerston North, Manawatu-Wanganui, New Zealand

Cun-Zheng Ning, Electrical Engineering, Arizona State University, Tempe, AZ, USA

Toyoaki Nishida, Graduate School of Informatics, Kyoto University, Kyoto, Japan

Federica Pascucci, Dipartimento di Ingegneria, Università degli Studi "Roma Tre", Rome, Italy

Yong Qin, State Key Laboratory of Rail Traffic Control and Safety, Beijing Jiaotong University, Beijing, China

Gan Woon Seng, School of Electrical & Electronic Engineering, Nanyang Technological University, Singapore, Singapore

Joachim Speidel, Institute of Telecommunications, Universität Stuttgart, Stuttgart, Germany

Germano Veiga, Campus da FEUP, INESC Porto, Porto, Portugal

Haitao Wu, Academy of Opto-electronics, Chinese Academy of Sciences, Beijing, China

Junjie James Zhang, Charlotte, NC, USA

The book series *Lecture Notes in Electrical Engineering* (LNEE) publishes the latest developments in Electrical Engineering - quickly, informally and in high quality. While original research reported in proceedings and monographs has traditionally formed the core of LNEE, we also encourage authors to submit books devoted to supporting student education and professional training in the various fields and applications areas of electrical engineering. The series cover classical and emerging topics concerning:

- Communication Engineering, Information Theory and Networks
- Electronics Engineering and Microelectronics
- Signal, Image and Speech Processing
- Wireless and Mobile Communication
- Circuits and Systems
- Energy Systems, Power Electronics and Electrical Machines
- Electro-optical Engineering
- Instrumentation Engineering
- Avionics Engineering
- Control Systems
- Internet-of-Things and Cybersecurity
- Biomedical Devices, MEMS and NEMS

For general information about this book series, comments or suggestions, please contact leontina.dicecco@springer.com.

To submit a proposal or request further information, please contact the Publishing Editor in your country:

China

Jasmine Dou, Associate Editor (jasmine.dou@springer.com)

India, Japan, Rest of Asia

Swati Meherishi, Executive Editor (Swati.Meherishi@springer.com)

Southeast Asia, Australia, New Zealand

Ramesh Nath Premnath, Editor (ramesh.premnath@springernature.com)

USA, Canada:

Michael Luby, Senior Editor (michael.luby@springer.com)

All other Countries:

Leontina Di Cecco, Senior Editor (leontina.dicecco@springer.com)

**** Indexing: The books of this series are submitted to ISI Proceedings, EI-Compendex, SCOPUS, MetaPress, Web of Science and Springerlink ****

More information about this series at <http://www.springer.com/series/7818>

Renu Sharma · Manohar Mishra ·
Janmenjoy Nayak · Bighnaraj Naik ·
Danilo Pelusi
Editors

Innovation in Electrical Power Engineering, Communication, and Computing Technology

Proceedings of IEPCCT 2019

 Springer

Editors

Renu Sharma
Department of Electrical Engineering
Institute of Technical Education
and Research
Siksha 'O' Anusandhan
(Deemed to be University)
Bhubaneswar, Odisha, India

Manohar Mishra
Department of Electrical and Electronics
Engineering, Institute of Technical
Education and Research
Siksha 'O' Anusandhan
(Deemed to be University)
Bhubaneswar, Odisha, India

Janmenjoy Nayak
Department of Computer Science
and Engineering
Aditya Institute of Technology
and Management (AITAM), Tekkali
Kotturu, Andhra Pradesh, India

Bighnaraj Naik
Department of Computer Application
Veer Surendra Sai University of Technology
Burla, Sambalpur, Odisha, India

Danilo Pelusi
Faculty of Communication Sciences
University of Teramo
(Coste Sant'agostino Campus)
Teramo, Italy

ISSN 1876-1100

ISSN 1876-1119 (electronic)

Lecture Notes in Electrical Engineering

ISBN 978-981-15-2304-5

ISBN 978-981-15-2305-2 (eBook)

<https://doi.org/10.1007/978-981-15-2305-2>

© Springer Nature Singapore Pte Ltd. 2020

This work is subject to copyright. All rights are reserved by the Publisher, whether the whole or part of the material is concerned, specifically the rights of translation, reprinting, reuse of illustrations, recitation, broadcasting, reproduction on microfilms or in any other physical way, and transmission or information storage and retrieval, electronic adaptation, computer software, or by similar or dissimilar methodology now known or hereafter developed.

The use of general descriptive names, registered names, trademarks, service marks, etc. in this publication does not imply, even in the absence of a specific statement, that such names are exempt from the relevant protective laws and regulations and therefore free for general use.

The publisher, the authors and the editors are safe to assume that the advice and information in this book are believed to be true and accurate at the date of publication. Neither the publisher nor the authors or the editors give a warranty, expressed or implied, with respect to the material contained herein or for any errors or omissions that may have been made. The publisher remains neutral with regard to jurisdictional claims in published maps and institutional affiliations.

This Springer imprint is published by the registered company Springer Nature Singapore Pte Ltd. The registered company address is: 152 Beach Road, #21-01/04 Gateway East, Singapore 189721, Singapore

Committees

Chief Patron

Prof. Manoj Ranjan Nayak, President, Siksha ‘O’ Anusandhan (Deemed to be University), Bhubaneswar, Odisha, India

Patron

Prof. Amit Banerjee, Vice-Chancellor, Siksha ‘O’ Anusandhan (Deemed to be University), Bhubaneswar, Odisha, India

Honorary General Chair

Prof. Pradipta Kishore Dash, Director, Multi-disciplinary research center (MDRC), Siksha ‘O’ Anusandhan (Deemed to be University), Bhubaneswar, Odisha, India

General Chairs

Prof. Bijaya Ketan Panigrahi, Professor, Department of Electrical Engineering, IIT Delhi, India

Prof. Pradipta Kumar Nanda, Dean (Research), Siksha ‘O’ Anusandhan (Deemed to be University), Bhubaneswar, Odisha, India

Prof. Renu Sharma, Professor, Department of Electrical Engineering, Siksha ‘O’ Anusandhan (Deemed to be University), Bhubaneswar, Odisha, India

General Co-chairs

Prof. Sanjeeb Kumar Kar, Professor, Department of Electrical Engineering, Siksha 'O' Anusandhan (Deemed to be University), Bhubaneswar, Odisha, India

Prof. Pravat Kumar Rout, Professor, Department of Electrical and Electronics Engineering, Siksha 'O' Anusandhan (Deemed to be University), Bhubaneswar, Odisha, India

Prof. Niranjana Nayak, Associate Professor, Department of Electrical and Electronics Engineering, Siksha 'O' Anusandhan (Deemed to be University), Bhubaneswar, Odisha, India

Program Chairs

Prof. Janmenjoy Nayak, Associate Professor, Department of Computer Science and Engineering, Aditya Institute of Technology and Management, Andhra Pradesh, India.

Prof. Bighnaraj Naik, Assistant Professor, Department of Computer Application, Veer Surendra Sai University of Technology, Burla, Odisha, India

Prof. Manoj Kumar Debnath, Assistant Professor, Department of Electrical Engineering, Siksha 'O' Anusandhan (Deemed to be University), Bhubaneswar, Odisha, India

Organizing Chairs

Prof. Manohar Mishra, Associate Professor, Department of Electrical and Electronics Engineering, Siksha 'O' Anusandhan (Deemed to be University), Bhubaneswar, Odisha, India

Prof. Binod Kumar Sahu, Associate Professor, Department of Electrical Engineering, Siksha 'O' Anusandhan (Deemed to be University), Bhubaneswar, Odisha, India

International Advisory Committee

Prof. Damodar Acharya (Chair), Siksha 'O' Anusandhan (Deemed to be University), Bhubaneswar, Odisha, India

Prof. Sanjib Kumar Panda, NUS, Singapore

Prof. Bayoumi, Ehab H.E., Abu Dhabi Men's College, UAE

Prof. A. Abraham, Machine Intelligence Research Labs, USA

Prof. Sanjeevikumar Padmanaban, Aalborg University, Denmark

Dr. Baharat Joyti Ranjan Sahu, Sungkyunkwan University, South Korea
Prof. Akshay Kumar Rathore, Concordia University, Chicago
Prof. Ramazan Bayindir, Gazi University, Turkey
Dr. Danilo Pelusi, University of Teramo, Italy
Prof. Akhtar Kalam, Melbourne Australia
Prof. Prasanta Mohapatra, University of California
Dr. Ahamed Zobaa, Brunel University, UK

National Advisory Committee

Prof. Damodar Acharya (Chair), Siksha 'O' Anusandhan (Deemed to be University), Bhubaneswar, Odisha, India
Prof. Bidyadhar Subudhi, IIT Goa, India
Prof. S. R. Samantray, IIT Bhubaneswar, India
Prof. S. K. Kulkarni, AGU, Shimla, India
Prof. Niva Das, Siksha 'O' Anusandhan (Deemed to be University), Bhubaneswar, Odisha, India
Dr. Swagatam Das, Indian Statistical Institute, Kolkata, India
Prof. Trilochan Panigrahi, NIT Goa, India
Prof. C. N. Bhende, IIT Bhubaneswar, India
Prof. S. K. Bharadwaj, MNNIT, Madhya Pradesh, India
Prof. Srikanta Pattnaik, Siksha 'O' Anusandhan (Deemed to be University), Bhubaneswar, Odisha, India
Prof. P. K. Sahu, Siksha 'O' Anusandhan (Deemed to be University), Bhubaneswar, Odisha, India

Technical Committee

Dr. Danilo Pelusi, University of Teramo, Italy
Dr. Sazia Hasan, BITS Pilani, Dubai Campus
Dr. Abhisek Rajan, NIT Sikkim
Dr. Mohit Ranjan Panda, CVRCE, Bhubaneswar
Dr. Shahed Mohammadi, Ayandegan University, Tonekabon, Iran
Dr. Sukanta Kishore Bisoyi, CVRCE, Bhubaneswar
Dr. G. T. Chandrasekhar, SSCE, Andhra Pradesh
Dr. Soumya Ranjan Mishra, MVJ College of Engineering, Bangalore
Dr. Prakash Kumar Ray, CET, BPUT, Bhubaneswar, India
Dr. Malaya Kumar Nath, NIT Puducherry
Prof. Sumit Kushwaha, Kamla Nehru Institute of Technology, UP
Dr. Trupti Swanakar, SOA, Bhubaneswar

Prof. Jyotir Moy Chatterjee, Asia Pacific University of Technology and Innovation, Nepal

Dr. Joymala Moirangthen, NUS, Singapore

Dr. K. R. Krishnanand, NUS, Singapore

Dr. Sidhartha Panda, VSSUT Engineering College, Burla

Dr. N. P. Padhy, IIT Roorkee

Prof. M. Nageswara Rao, K L University, Vijayawada

Prof. P. S. Kulkarni, VNIT, Nagpur

Dr. Ahmed Faheem Zobaa, BU, UK

Dr. Akhtar Kalam, VU, Australia

Dr. Rajesh Kumar Patnaik, GMR, AP

Dr. Krushna Keshab Mohapatra, SOA, Bhubaneswar

Dr. Kolla Bhanu Prakash, K L University, Vijayawada

Publicity Chairs

Prof. Amar Bijaya Nanda, Siksha 'O' Anusandhan, Bhubaneswar, India

Dr. Basanta Kumar Panigrahi, Siksha 'O' Anusandhan, Bhubaneswar, India

Mr. Tapas Kumar Mohapatra, Siksha 'O' Anusandhan, Bhubaneswar, India

Mr. Tanmoya Parida, Siksha 'O' Anusandhan, Bhubaneswar, India

Website Chairs

Dr. Nakul Charan Sahu, Siksha 'O' Anusandhan, Bhubaneswar, India

Mr. P. Suresh Kumar, DLBCE, Visakhapatnam

Dr. Shubhranshu Mohan Parida, Siksha 'O' Anusandhan, Bhubaneswar, India

Registration Chairs

Prof. Pradeep Kumar Mohanty, Siksha 'O' Anusandhan, Bhubaneswar, India

Mr. Satish Choudhury, Siksha 'O' Anusandhan, Bhubaneswar, India

Mr. Amiya Kumar Naik, Siksha 'O' Anusandhan, Bhubaneswar, India

Mr. Rasmi Ranjan Panigrahi, GEC, Bhubaneswar, India

Publication Chairs

Dr. Binod Kumar Sahu, Siksha 'O' Anusandhan, Bhubaneswar, India

Dr. Manohar Mishra, Siksha 'O' Anusandhan, Bhubaneswar, India

Prof. Renu Sharma, Siksha 'O' Anusandhan, Bhubaneswar, India

Finance Chairs

Prof. Manas Kumar Malik, Siksha 'O' Anusandhan, Bhubaneswar, India

Dr. Priyabrata Pattanaik, Siksha 'O' Anusandhan, Bhubaneswar, India

Sponsorship Chairs

Prof. Ranjan Kumar Mallick, Siksha 'O' Anusandhan, Bhubaneswar, India

Dr. Sujit Kumar Dash, Siksha 'O' Anusandhan, Bhubaneswar, India

Dr. Subhendu Pati, Siksha 'O' Anusandhan, Bhubaneswar, India

IEPCCT Reviewers

Dr. Santosh Ku Sahoo, CVR College of Engineering, Hyderabad, India

Dr. Kola Bhanu Prakash, K L University, Vijayawada

Dr. Sarat Ch. Nayak, CMR College of Engineering & Technology (Autonomous), Hyderabad, India

Dr. G. T. Chandra Sekhar, SSCE, Srikakulam

Mr. Ch. Jagan Mohan Rao, Veer Surendra Sai University of Technology, Burla, Odisha

Dr. Swagat Kumar pati, SOA, Bhubaneswar

Dr. Pradeep Kumar Mohanty, SOA, Bhubaneswar

Dr. Kaushik Paul, NIT Jamshedpur

Dr. Yogendra Arya, MSIT, Delhi

Dr. Puja Dash, GVPCE, Visakhapatnam, Andhra Pradesh

Mrs. Sarita Samal, KIIT, Bhubaneswar

Mr. Prasant Barik, OUAT, Bhubaneswar

Mr. Nimai Patel, Government College of Engineering, Keonjhar

Mr. Preeti Ranjan Sahu, VSSUT, Burla

Dr. Bhagyalaxmi Jena, SOA, Bhubaneswar

Ms. Kumari kasturi, SOA, Bhubaneswar

Mr. Basanta Panigrahi, SOA, Bhubaneswar

Mr. Tapas Mohapatra, SOA, Bhubaneswar
 Mr. Abhisek Parida, NIT Rourkela
 Mr. Arun Aggrawal, SOA, Bhubaneswar
 Dr. Sangram Kumar Mohapatra, Government College of Engineering, Keonjhar
 Dr. Banishree Mishra, KIIT
 Dr. Prakash Chandra Sahoo, SIT, Sambalpur
 Mr. Shiba Ranjan Paital, IIIT Bhubaneswar
 Mr. Bibhuti Sahu, VSSUT, Burla
 Dr. Pratap Ranjan Mohanty, SOA, Bhubaneswar
 Dr. P. Vittal, AITAM, AP
 Mr. P. Suresh Kumar, Dr. Lankapalli Bullayya College
 Dr. Ram Chandra Barik, Vikash Enggineering College, Odisha
 Dr. P. Pradeepa, School of Engineering and Technology, Jain University, Bangalore
 Dr. R. Arulmurugan, Associate Professor, Department of EEE, S R Engineering College, Warangal
 Mr. Suresh Chandra Moharana, Kalinga Institute of Industrial Technology (KIIT), Bhubaneswar
 Dr. P. M. K. Prasad, Associate Professor, ECE Department, G.V.P College of Engineering for Women Visakhapatnam, Andhra Pradesh, India
 Mr. Debasis Mohapatra, PMEC, Berhampur
 Dr. M. Marimuthu, Assistant Professor, Department of Computing, Coimbatore Institute of Technology, Coimbatore—641014
 Ms. Santwana Sagnika, KIIT Deemed to be University, Odisha
 Dr. Nageswara Rao, Velagapudi Ramakrishna Siddhartha Engineering College
 Dr. S. Albert Alexander, Kongu Engineering College
 Dr. A. Abdul Rasheed, CMR Institute of Technology, Bangalore
 Dr. B. Satyanarayana, CMR Institute of Technology, Bangalore
 Dr. Rajesh Kumar, JNTU Hyderabad
 P. Raman, GMR Institute of Technology, Andhra Pradesh
 Dr. Soumi Dutta, Institute of Engineering and Management, Kolkata
 Dr. Ramesh Prusty, VSSUT, Burla
 Dr. B. Naik, VSSUT, Burla
 Dr. Janmenjoy Nayak, Aditya Institute of Technology And Management, Tekkali, Srikakulam
 Dr. Manoj Kumar Ghosal, Department of Farm Machinery and Power, CAET, OUAT
 Dr. Nallapaneni Sahoo, School of Energy and Environment, City University of Hong Kong, Kowloon, Hong Kong
 Dr. Ajay Kumar Dash, Department of Farm Machinery and Power, CAET, OUAT
 Dr. Abhisek Rajan, NIT Sikkim
 Dr. Bharat J. R. Sahoo, KNU, South Korea
 Dr. Malaya Nath, NIT Tiruchirappalli
 Dr. Asish Ranjan dash, CUTM, Paralakhemundi
 Dr. Sukant Bisoye, CVRCE, Bhubaneswar

Dr. Jyotir Moy Chatterjee, Asia Pacific University of Technology and Innovation, Kathmandu, Nepal
Dr. Sumit Kushwah, Kamla Nehru Institute of Technology, Uttar Pradesh
Dr. B. Surendiran, Associate Dean (Academic), Department of CSE, NIT Puducherry
Dr. Renu Sharma, ITER, SOA, Bhubaneswar
Dr. Sonali Goel, ITER, SOA, Bhubaneswar
Dr. Shakti Prakash Jena, Mechanical Engineering Department, ITER, SOA Deemed to be University.
Dr. Debabrata Singh, ITER, SOA, Bhubaneswar
Mr. Sayantan Sinha, ITER, SOA, Bhubaneswar
Dr. Debadatta Amaresh Gadanayak, ITER, SOA, Bhubaneswar
Dr. Manoj Kumar Debnath, ITER, SOA, Bhubaneswar
Dr. Binod Kumar Sahu, ITER, SOA, Bhubaneswar
Dr. Sanjeeb Kumar Kar, ITER, SOA, Bhubaneswar
Mr. Priya Ranjan Satpathy, ITER, SOA, Bhubaneswar
Miss. Sasmita.jena, ITER, SOA, Bhubaneswar
Mr. Rasmi Ranjan Panigrahi, ITER, SOA, Bhubaneswar
Mr. Satish Choudhury, ITER, SOA, Bhubaneswar
Ms. Subhadra Sahoo, ITER, SOA, Bhubaneswar
Dr. Mukesh Kumar Das, University of Manitoba, Canada
Dr. Kundan Kumar, ITER, SOA, Bhubaneswar
Dr. Narayan Nahak, ITER, SOA, Bhubaneswar
Dr. R. C. Agrawal, ITER, SOA, Bhubaneswar
Mr. Debasish Sitikantha, ITER, SOA, Bhubaneswar
Mr. A. B. Nanda, ITER, SOA, Bhubaneswar
Dr. P. K. Rout, ITER, SOA, Bhubaneswar
Dr. S. Dher, ITER, SOA, Bhubaneswar
Dr. S. Kar, ITER, SOA, Bhubaneswar
Dr. Shubhranshu Mohan Parida, ITER, SOA, Bhubaneswar
Dr. Rajesh Kumar Patnaik, GMR Institute of Technology, Rajam, under Jawaharlal Nehru Technical University, Kakinada (JNTUK)
Dr. Sthita Prajna Mishra, GMR Institute of Technology, Rajam, Srikakulam, Andhra Pradesh
Dr. N. D. Kausika, IIT Delhi
Mr. Byomokesh Dash, SOA, Bhubaneswar
Dr. Niva das, SOA, Bhubaneswar
Dr. Satyanarayanbhuyan, SOA, Bhubaneswar
Dr. Soumya Ranjan Mohanty, IIT BHU
Dr. Monalisa Pattnaik, NIT RKL
Dr. Asim Naskar, NIT RKL
Dr. MadhabTripathy, CET BBSR
Prof. S. S. Dash, GEC Keonjhor

Preface

The development and modernization of society are directly related to the innovative inventions and advancements of the present technology. The innovation in any technology and their approach of application in diverse domain can make the system become smarter; for example, the home became smart home, the present city became smart city, and the society became smart society. The innovation in engineering domains (such as electrical, electronics, mechanical, computer, and robotics) always plays a direct role in the present and future development of our society. However, the innovation in electrical, communication, and computing technology is always interrelated to each other. Though the innovation in one domain will definitely solve the problem associated with the particular problem, it may also help additionally to minimize the problem or may assist in a new innovation belonging to other domains. Therefore, continuous research in all these domains as well as proper disseminating the work is highly important for the development of the global society.

The first international conference entitled ‘Innovation in Electrical Power Engineering, Communication, and Computing Technology’ (IEPCCT-2019) is organized by the Department of Electrical Engineering, Institute of Technical Education and Research, Siksha ‘O’ Anusandhan (Deemed to be University), Bhubaneswar, Odisha, India, on December 13 and 14, 2019. The conference is focused on the direction of numerous advanced concepts or cutting-edge tools applied for electrical, electronics, and computer science domains. More than 150 articles have been received through online related to the scope of the conference area. Out of these submissions, we have chosen only 58 high-quality articles after a thorough rigorous peer-review process. In the peer-review process, several highly knowledgeable researchers/professors with expertise in single-/multi-domain have assisted us in unbiased decision making of the acceptance of the selected articles. Moreover, valuable suggestions of the advisory, program, and technical committees have also helped us for smoothing the peer-review process. The complete review process is based on several criteria, such as major contribution, technicality, clarity, and originality of some latest findings. The whole process starting from initial submission to the acceptance notification to authors is done electronically.

The first international conference ‘IEPCCT-2019’ is focused on sharing research and ideas among different academicians, researches, and scientists from throughout the world with an intention to global development. Therefore, the conference includes various keynote addresses particular to the scope of IEPCCT research topics. The sessions including presentation of the author’s contribution and key-notes address are principally organized in accordance with the significance and interdependency of the articles with reference to the basic concept and motivation of the conference.

The accepted manuscripts (original research and survey articles) have been well organized to emphasize the cutting-edge technologies applied in electrical, electronics, and computer science domains. We appreciate the authors’ contribution and value the choice that is ‘IEPCCT’ for disseminating the output of their research findings. We are also grateful for the help received from each individual reviewer and the Program Committee members regarding peer-review process.

Bhubaneswar, India
Bhubaneswar, India
Kotturu, India
Burla, India
Teramo, Italy

Renu Sharma
Manohar Mishra
Janmenjoy Nayak
Bighnaraj Naik
Danilo Pelusi

Acknowledgements

We are opportune to put forward key proposal and significance of IEPCCCT conference. This conference has attracted more than 200 academicians, professionals, and researchers all over the globe. The conference showed the gamut of original research findings. We could able to have communes in diversified fields of electrical, electronics, and computation engineering.

We would like to thank all the authors for their contributions. We sincerely show our gratitude to the authors who contributed their time and expertise.

We would like to convey my heartfelt thanks to National Advisory Committee and International Advisory Committee to be supportive and guiding us throughout the pre- and post-conference. We have been opportune to have strong eminent reviewers team who holistically did the reviewing and suggested the critical and strong remarks on the manuscripts.

We profusely thank the Organizing Committee who has shown the level of eagerness by well organizing and managing throughout the conference.

Our profound and authentic gratitude to the editorial members of Springer Publishing team. The proceedings sees the day of light in the graceful, innovative, and intelligent way. The IEPCCCT conference and proceedings ensured the acknowledgments to a huge congregation of people.

We are highly thankful to the management of SOA (Deemed to be University) and each faculty member of the Department of Electrical Engineering, ITER, for their constant support and motivation for making the conference successful. We would also like to thank Springer Editorial Members for their constant support for publishing the proceedings in 'Lecture Notes in Electrical Engineering' series.

About the Conference

The conference **First International Conference on Innovation in Electrical Power Engineering, Communication, and Computing Technology (IEPCCT-2019)** is focused on the direction of numerous advanced concepts or cutting-edge tools applied for electrical, electronics, and computer science domains. IEPCCT is a multi-disciplinary conference organized with an intention of sharing knowledge and views among each other by the different backgrounds of people, such as academicians, scientists, research scholars, and students working in the areas of electrical, electronics, advanced computing, and intelligent engineering. By this process, the authors/listeners (national or international levels) have got an opportunity to collaborate their thoughts in the direction of global development. The major objective of IEPCCT is to provide a useful platform for the global researchers to present their recent inventions in front of well-known professors and researchers working in similar research fields. It also helps to create awareness of the status of basic scientific study compared to current developments in distinct research domain.

The conference IEPCCT-2019 is directed in the direction of the knowledge and structure of positive research in different applications of electrical power engineering, communication, and computing technology which are leading and governing the technological domain. The proceedings of IEPCCT-2019 will be aiming the postgraduate students and researchers working in the discipline of electrical, electronics and computer science. Nowadays, the multi-disciplinary researches have gained a huge attention to fulfill the necessities of smart cities/countries. Therefore, this book may assist the future developments/researches by providing several recent innovations on electrical, computing, and communication engineering.

Contents

Solar-Fed Single-Input Three-Output DC–DC Converters for Low-Power Applications	1
P. Akhil Raj and Sabha Raj Arya	
Blind Feature-Based Steganalysis with and Without Cross Validation on Calibrated JPEG Images Using Support Vector Machine	17
Deepa D. Shankar and Adresya Suresh Azhakath	
Demand Side Management in Smart Grid	29
M. Ganesh and R. K. Patnaik	
Improvement of the Current Profile in Grid-Tied Hybrid Energy System by Three-Phase Shunt Active Filter	45
Rudranarayan Senapati, Sthita Prajna Mishra, Vamsiram Illa and Rajendra Narayan Senapati	
Novel Bludgeon-Shaped Microstrip Antenna with DGS for UWB Applications with Notch Band Characteristics	61
B. Ramesh, K. P. Vinay, Lal BabuPrasad, K. S. Ravi Kumar and D. V. Rama Koti Reddy	
Modeling, Simulation and Validation of 1200 kV UHV Autotransformer	71
Satyadharma Bharti and Satya Prakash Dubey	
Harmonics and Voltage Sag Compensation of a Solar PV-Based Distributed Generation Using MSRF-Based UPQC	87
Sarita Samal, Akansha Hota, Prakash Kumar Hota and Prasanta Kumar Barik	
Load Balancing in Cloud Computing: Survey	99
Arabinda Pradhan, Sukant Kishoro Bisoy and Pradeep Kumar Mallick	

Participation of Geothermal and Dish-Stirling Solar Power Plant for LFC Analysis Using Fractional-Order Controller	113
Priyambada Satapathy, Manoj Kumar Debnath, Pradeep Kumar Mohanty and Binod Kumar Sahu	
Use of Teaching Learning Based Optimization for Data Clustering	123
Anima Naik	
Studies on Off-Grid Solar Photovoltaic-Powered Micro-Irrigation System in Aerobic Rice Cultivation for Sustainable Agriculture and Mitigating Greenhouse Gas Emission	135
M. K. Ghosal, N. Sahoo and Sonali Goel	
Application of IoT in Predictive Maintenance Using Long-Range Communication (LoRa)	147
Siddharth Bhattar, Akash Verma and Sayantan Sinha	
PID-Based Electronic Load Controller for Three-Phase Synchronous Generator	157
Kamran Alam and Namarta Chopra	
Survey of Sentiment Analysis of Political Content on Twitter	169
Siddhesh Pai, Vaibhav Bagri, Shivani Butala and Pramod Bide	
Load Frequency Control Incorporating Electric Vehicles Using FOPID Controller with HVDC Link	181
Sunita Pahadasingh, Chitralkha Jena and Chinmoy Ku Panigrahi	
Automatic Generation Control in Deregulated Power Market Using Sunflower Optimization Algorithm	205
Abhilipsa Sahoo, Prakash Kumar Hota and B. Mohanty	
Implementation of Monte Carlo Simulation to the Distribution Network for Its Reliability Assessment	219
Ajaya Kumar Pradhan, Sanjeeb Kumar Kar, Pradeep Kumar shill and Pujashree Dash	
Retinal Image Segmentation Using Gabor Transform with Preprocessing and Hysteresis Thresholding	229
Sakambhari Mahapatra, U. R. Jena and Sonali Dash	
Multi-level Asymmetrical Inverters Using Two DC Ports with Less Number of Switches and Conversion Stages	241
Suraj Kumar Dash and Prakash Kumar Hota	
Fuzzy Granular Computing-Based Controller Design for Inverted Pendulum System with Delay	255
Srikanth Kavirayani	

Electrical Faults in Photovoltaic Modules: Analysis, Characterization and Detection	265
Priya Ranjan Satpathy, Sasmita Jena, Sobhit Panda and Renu Sharma	
Detection and Classification of Voltage Sag Causes Based on S-Transform and Extreme Learning Machine	277
Bhaskar Patnaik, Rasmi Ranjan Panigrahi, Manohar Mishra, Ranjan Kumar Jena and Manoj kumar Swain	
Accelerated Deep Learning in Proteomics—A Review	291
Deeba Khan and Seema Shedole	
DSTATCOM Using Limit Cycle Oscillator FLL with Optimized Gains of Voltage Error Controllers	301
Jayadeep Srikakolapu, Sabha Raj Arya and Rakesh Maurya	
Global Horizontal Irradiance Prediction Using Deep Neural Network Framework	317
Sambit Dash, Priya Ranjan Satpathy, Sobhit Panda and Renu Sharma	
A Hybrid Approach for Path Planning of Multiple AUVs	327
Madhusmita Panda, Bikramaditya Das and Bibhuti Bhusan Pati	
A Hybrid Framework for Fault Classification and Location in Power Distribution System Using Wavelet and Support Vector Machine	339
Satyajit Panigrahy and A. K. Chandel	
Effect of Soiling on Power Output of a Photovoltaic System	351
Sonali Goel, Sobhit Panda, Nallapaneni Manoj Kumar and Renu Sharma	
Ant Colony Optimization in Data Mining: Critical Perspective from 2015 to 2020	361
Janmenjoy Nayak, Kanithi Vakula, Paidi Dinesh, Bighnaraj Naik and Manohar Mishra	
Linear Quadratic Regulator Design for Stabilizing and Trajectory Tracking of Inverted Pendulum	375
Akshaya Kumar Patra, Alok Kumar Mishra, Anuja Nanda, Ramachandra Agrawal, Abhishek Patra and Shekharesh Barik	
Real-Time Position Estimation of Mobile Platform in Indoor and GPS-Denied Environments	389
Sagar Dhatrak and Damayanti Gharpure	
Steady Model for Classification of Handwritten Digit Recognition	401
Anujay Ghosh, Aruna Pavate, Vidit Gholam, Gauri Shenoy and Shefali Mahadik	

Optimal TCSC Location for Reactive Power Optimization Using Oppositional Salp Swarm Algorithm	413
Sheila Mahapatra, Saurav Raj and S. Mohan Krishna	
THD Reduction of On-Grid Solar Photovoltaic System Employing SPWM Technique	425
Suraj Kumar Panigrahi, Renu Sharma and Satyanarayan Bhuyan	
Estimation of Simple, Energy and Carbon Payback Periods of a 1 MWp Ground-Mounted Solar PV Plant at Tirupati Airport: A Case Study	439
S. Mohan Krishna, Sheila Mahapatra, Saurav Raj and J. L. Febin Daya	
Average Current-Controlled SEPIC Converter with High Power Factor Correction	451
Alok Kumar Mishra, Akshaya Kumar Patra, Ramachandra Agrawal, Lalit Mohan Satapathy, Anuja Nanda, Samarjeet Satapathy and Jnana Ranjan Swain	
Smartgrids/Microgrids in India: A Review on Relevance, Initiatives, Policies, Projects and Challenges	465
Ashutosh Nayan Dey, Basanta K. Panigrahi and Sanjeeb Kumar Kar	
LFC Analysis in PV-Thermal System Using Non-integer Controller	475
Jyoti Ranjan Padhi, Manoj Kumar Debnath, Sanjeeb Kumar Kar and Binod Kumar Sahu	
Power Generation from Various Interconnecting Solar PV Networks for an Electrically Coupled Solar PV-TEG System Under Healthy and Partly Cloudy Condition	485
Sasmita Jena, Shalini Patro, Subham Subrajeet Barik, Sambit Tripathy, Keshav Krishna, Priya Ranjan Satpathy and Sanjeeb Kumar Kar	
Constraint Based Design of Multi-stage Core Type Multipole Field Electromagnetic Launching System (CMFELS) and Its Possible Use in the Catapult System	499
Srichandan Kondamudi and Sandhya Thotakura	
Performance Analysis of Fractional-Order High-Pass Filter	511
Kumar Biswal, Madhab Chandra and Sanjeeb Kumar Kar	
Application of 2DOF and 3DOF Controller for LFC Analysis in Multi-generation System	521
Gayatri Mohapatra, Manoj Kumar Debnath and Krushna Keshab Mohapatra	

Automatic Recognition of the Early Stage of Alzheimer’s Disease Based on Discrete Wavelet Transform and Reduced Deep Convolutional Neural Network 531
 Bhanja Kishor Swain, Mrutyunjaya Sahani and Renu Sharma

Employing Thermoelectric Coupled Solar PV Hybrid System in Non-conventional Distribution Generation 543
 Sasmita Jena, Keshav Krishna, Sambit Tripathy, Subham Subrajeet Barik, Shalini Patro, Priya Ranjan Satpathy and Sanjeeb Kumar Kar

Design of Artificial Pancreas Based on Fuzzy Logic Control in Type-I Diabetes Patient 557
 Akshaya Kumar Patra, Anuja Nanda, Shantisudha Panigrahi and Alok Kumar Mishra

Comparative Analysis of LMS-Based Control Algorithms for Grid Integrated PV System 571
 Satish Choudhury, Byomakesh Dash, Bidyadhar Subudhi and Renu Sharma

Comparative Analysis of Adaptive Filtration Techniques Using DSTATCOM for Distribution System 583
 Byomakesh Dash, Satish Choudhury, Bidyadhar Subudhi and Renu Sharma

Fractional Order PID Controller Design for Stabilizing and Trajectory Tracking of Vehicle System 595
 Akshaya Kumar Patra, Alok Kumar Mishra and Ramachandra Agrawal

Optimum Design of PV-Battery-Based Microgrid with Mutation Volatilization-Dependent Water Cycle Algorithm 609
 Shaktinarayana Mishra, Saumya Ranjan Lenka, Prachitara Satapathy and Pravati Nayak

New Modified Water Cycle Optimized Fuzzy PI Controller for Improved Stability of Photovoltaic-Based Distributed Generation Towards Microgrid Integration 623
 M. Mohamed Hamad Adam, Naeem M. S. Hannon and Snehamoy Dhar

Voltage Stabilization in a Single-Phase SEIG System with Electronic Load Controller 637
 Subhendu Khatua, Abhijeet Choudhury, Swagat Pati, Sanjeeb Kumar Kar and Renu Sharma

EV Battery Charging with Input Power Factor Correction Using a Buck–Boost Converter 647
 Prateek Kumar Sahoo, Sagar Kumar Champati, Ashish Pattanaik and Tapas Kumar Mohapatra

IoT Based Real-Time Water Quality Monitoring and Classification . . . 661
Sujaya Das Gupta, M. S. Zambare, N. M. Kulkarni and A. D. Shaligram

**Motion Control of an IPMSM Drive System Using Sliding Mode
Controller 671**
A. K. Naik, A. K. Panda, Sanjeeb Kumar Kar and M. Sahoo

**Performance of Second-Order Generalized Integrator Based Adaptive
Filter Under Adverse Grid Conditions 685**
Banishree Misra, Arkadip Majumdar and Sudhananda Pal

**Stability Improvement in Power System Integrated with WECS
Using Dolphin Echolocation Optimized Hybrid PID Plus
FLC-Based PSS 697**
Prakash K. Ray, Shiba R. Paital, Lalit Kumar, Bhola Jha, Sanjay Gairola
and Manoj Kumar Panda

**Economic Operation of Diesel Generator in an Isolated Hybrid System
with Pumped Hydro Storage 709**
Subrat Bhol, Nakul Charan Sahu and AmarBijay Nanda

**SHO Algorithm-Based Fuzzy-Aided PID Controller
for AGC Study 721**
S. Sahoo, N. K. Jena, D. P. Das, Binod Kumar Sahu
and Manoj Kumar Debnath

About the Editors

Dr. Renu Sharma is working as a Professor and Head of the Department of Electrical Engineering under the Faculty of Engineering & Technology, Siksha 'O' Anusandhan University, Bhubaneswar. She received her Ph.D. in Electrical Engineering from Siksha 'O' Anusandhan University, Bhubaneswar, in 2014 and M.Tech in Electrical Engineering from Jadavpur University in 2006. At present, she has more than twenty years of teaching experience in the field of Electrical Engineering. She is a life member IE (India), member IET, member IEEE, life member ISTE, life member ISSE. Her research areas are smart grid, soft computing, solar photovoltaic systems, power system scheduling, evolutionary algorithms, and wireless sensor networks. She has published more than 40 research papers in various reputed peer-reviewed international journals, conferences, and book chapters. She has served as reviewers from various reputed journal publishers such as Springer, IEEE, Elsevier, and Inderscience. She is currently guiding eight Ph.D. scholars and one postdoctoral fellow. She has organized several FDP and workshops sponsored by Typhoon HIL, AICTE, DST, etc.

Dr. Manohar Mishra is an Associate Professor in the Department of Electronics & Electrical Engineering, under the Faculty of Engineering & Technology, Siksha 'O' Anusandhan University, Bhubaneswar. He received his Ph.D. in Electrical Engineering, M.Tech. in Power Electronics and Drives, and B.Tech. in Electrical Engineering in 2017, 2012, and 2008, respectively. He has published more than 22 research papers in various reputed peer-reviewed international journals, conferences, and book chapters. He has served as reviewers for various reputed journal publishers such as Springer, IEEE, Elsevier, and Inderscience. At present, he has more than eight years of teaching experience in the field of Electrical Engineering. He is a member of IEEE. He is currently guiding two Ph.D. and Master scholars. His area of interest includes power system analysis, power system protection, signal processing, power quality, distribution generation system, and micro-grid.

Dr. Janmenjoy Nayak is working as an Associate Professor, Department of Computer Science and Engineering, Aditya Institute of Technology and Management (AITAM), Tekkali, K Kotturu, AP- 532201, India. He has published more than 80 research papers in various reputed peer-reviewed referred journals, international conferences, and book chapters. He is the recipient of Best Researcher Award from Jawaharlal Nehru University of Technology, Kakinada, Andhra Pradesh for the AY: 2018–2019, Young Faculty in Engineering-2017 Award by Venus International Foundation, Chennai and Best Young Researcher in Computer Science Engineering, by Institute of Technical and Scientific Research, ITRS Foundation Award-2017, Jaipur, Rajasthan. Moreover, he is the recipient of Outstanding Reviewer for the journal “Engineering Applications of Artificial Intelligence” for 2017, by Elsevier Publications. His area of interest includes data mining, nature inspired algorithms, and soft computing. He is the regular member of IEEE and life member of some of the reputed societies like CSI India, etc. He has edited four books from various publishers such as Elsevier, Springer, and IGI Global. He has been serving as Guest Editor of various journal special issues from Elsevier, Springer, and Inderscience. He has served as Volume Editor of International Conference on Computational Intelligence in Data Mining (ICCIDM-2017, ICCIDM-2018), International Conference on Computational Intelligence in Pattern Recognition(CIPR-2019), International Conference on Application of Robotics in Industry using Advanced Mechanisms (ARIAM-2019), and International Conference on “Soft Computing in Data Analytics (SCDA-2018).

Dr. Bighnaraj Naik is an Assistant Professor in the Department of Computer Application, Veer Surendra Sai University of Technology (Formerly UCE Burla), Odisha, India. He received his Ph.D. in Computer Science and Engineering, M.Tech. in Computer Science and Engineering, and B.E. in Information Technology in 2016, 2009, and 2006, respectively. He has published more than 70 research papers in various reputed peer-reviewed international journals, conferences, and book chapters. He has edited four books from various publishers such as Elsevier, Springer, and IGI Global. At present, he has more than ten years of teaching experience in the field of Computer Science and IT. He is a member of IEEE. His area of interest includes data mining, computational intelligence, soft computing, and its applications. He has been serving as Guest Editor of various journal special issues from Elsevier, Springer, and Inderscience. He has served as Convener & Volume Editor of International Conference on Computational Intelligence in Data Mining (ICCIDM-2017, ICCIDM-2018) and International Conference on Computational Intelligence in Pattern Recognition—2019, IEST, Shibpur, West Bengal.

Dr. Danilo Pelusi has received the Ph.D. degree in Computational Astrophysics from the University of Teramo, Italy. Presently, he is holding the position of Associate Professor at the Faculty of Communication Sciences, University of Teramo. Associate Editor of IEEE Transactions on Emerging Topics in Computational Intelligence, IEEE Access, International Journal of Machine

Learning and Cybernetics (Springer) and Array (Elsevier), he served as Guest Editor for Elsevier, Springer, and Inderscience journals, as program member of many conferences, and as editorial board member of many journals. Reviewer of reputed journals such as IEEE Transactions on Fuzzy Systems and IEEE Transactions on Neural Networks and Machine Learning, his research interests include fuzzy logic, neural networks, information theory, and evolutionary algorithms.

Solar-Fed Single-Input Three-Output DC–DC Converters for Low-Power Applications



P. Akhil Raj and Sabha Raj Arya

Abstract Due to two significant benefits such as less voltage and high density of energy, the DC-to-DC converter has become very common today in the world's electronic sector. The production of the DC-to-DC converter is therefore comparatively larger than that of normal AC-DC converters. The studies are developing multi-output DC-to-DC converters in latest years. These investigations focus on isolated as well as non-isolated DC-to-DC converters. A small input and output ripple sides, a minimum amount of switches, elevated voltage increase and lighter weight are the primary benefits of this type of converters. A single-input three-output SEPIC-Cuk-boost combination converter is analysed. It is working, and modelling and applications are also discussed. The solar panel used for the analysis is modelled by using its mathematical equations. Comparative studies of incremental conductance (IC) and Extended Perturb-Perturb (EPP) MPPT techniques are discussed for extracting highest power from the solar panel. The proposed solar-fed model is simulated by using MATLAB software. The experimental set-up of single-input to three-output SEPIC-Cuk-boost converter is developed, and the performance is compared with the simulated results. This proposed converter is able to generate two DC bipolar and one boosted DC output voltages.

Keywords Bipolar · MPPT · DC/DC converters · Duty cycle · Efficiency

1 Introduction

Renewable energy sources will provide better efficiency and clean energy. However, compared with other sources of renewable energy, solar power generation is readily accessible [1]. The solar-powered energy sources are commonly used for battery charging, lighting, solar pumping, etc. A pollution-free solution for the existing power crisis is overcome by using solar energy with maximum power extraction [2]. The proposed solar systems in this paper successively are applied in thermal power

P. A. Raj · S. R. Arya (✉)

Department of Electrical Engineering, Sardar Vallabhbhai National Institute of Technology, Surat 395007, India

© Springer Nature Singapore Pte Ltd. 2020

R. Sharma et al. (eds.), *Innovation in Electrical Power Engineering, Communication, and Computing Technology*, Lecture Notes in Electrical Engineering 630,

https://doi.org/10.1007/978-981-15-2305-2_1

plants, hydroelectric power stations, wind energy stations, etc. The low efficiency and loss of energy are the main problems with the solar-based system. Gil-Antonio et al. [3] in this, the peak energy monitoring algorithm for reducing the disadvantage of the solar PV system was discussed. Incremental conductance, neural network, fuzzy logic and ripple MPPT methods are evaluated to obtain highest energy from the solar panel. For extracting maximum power, a high-efficiency-type buck converter with a microcontroller-based control algorithm is explained in the literature [4]. This method is applied in the wind energy generation, and it is able to get 11–15% increment in the efficiency compared to the normal conversion techniques. For the laboratory purposes, modelling of a PV panel is a very challenging area because while modelling the panel, it is necessary to consider the change in solar irradiation, change in voltages and change in currents. A detailed mathematical modelling of the solar panel is explained in the literature [5]. In this paper, the panel model is verified by varying the insolation and temperature of the PV panel. It is also explained the different stages of the modelling with single diode, by considering the series and parallel resistances, etc. In [6], the mathematical analysis of the photovoltaic module is explained. The proposed analysis provides accurate and reliable responses for the different atmospheric conditions. The applications of a PV array can be classified into two categories where first is home applications and second is business applications. The major use of the home application is battery charging and lighting systems. Design of a solar-powered battery charging application is given in [7, 8]. The proposed topology in these papers contains a solar panel, an optimal controller to obtain the maximum efficiency and a battery. This type of configurations can be used in the field of electric vehicles. To achieve maximum effectiveness, an optimal control technique is discussed. Various energy monitoring techniques such as P and O MPPT, IC MPPT and constant voltage MPPT are efficient for achieving peak energy [9]. Among those methods, the perturb and observation method is the best cost-effective method due to only voltage is sensing [10]. But in the case of incremental conductance method, both voltage and current are sensing, and circuitry becomes more complex. That is why P and O method is more cost-effective. While designing a solar panel for small power applications, the protection also should be considered as discussed in the literature [11]. For battery charging applications, the solar panel's output terminal voltage always must be higher than that of the battery voltage. Also in order to avoid the reverse flow of current to the panel, a diode should be connected at the terminals of the panel.

The single-input three-output converters are also discussed in this paper. In the literature [12], a single-input three-output buck converter is explained. In this chapter, a DC-to-DC buck converter for dual applications controlled by normal PWM controller is discussed. It can adjust the voltage output with an error of less than 2%. Detailed design and study of low-level three-output voltage implemented with soft switching technology are discussed in the literature [13]. By implementing the converter, it is possible to get 5% more efficient than that of the normal converter without the soft switching technique and also able to work under closed-loop operation. In this, zero current switching is used, and efficiently, it can also obtain the inverted output. In any power supply applications, a constant/regulated DC voltage is required.

To retain a controlled potential at the output terminals of any converter, a feedback controller is required. In [14], a study of closed-loop one-input more-output DC-to-DC converter is explained. The suggested converter topology can be worked under renewable energy sources with varying supply voltage, and the converter closed-loop operation is efficiently tracking the required reference voltage level. The effectiveness of such converters can be improved by the coupled inductors, and it is explained in [15]. Through this proposal, the converter can improve the efficiency of more than 95% which is only 91% for the normal converter. These types of converters are useful where common ground is required. The coupled inductor-based converters can improve the overall voltage gain of the system and improve efficiency. The concept of a coupled inductor with a boost converter is explained in [16]. The efficiency of any converter can be enhanced by implementing soft switching rather than hard switching. This soft switching method discusses a new idea of the modified many-output DC–DC converter [17]. This modified converter can deliver efficiency higher than that of normal converters and high step-up ratio. The converters with zero present switches, and zero voltage switches are described in [18]. The topology suggested is appropriate for low-voltage applications also. And a comparative study in terms of efficiency of this proposed topology and converters without the soft switching is also discussed in this literature. In this chapter, they proposed an interleaved technology which will reduce the ripple input and output voltage. For pulse generation, a PIC microcontroller is used. Due to these features, the converter can easily operate under light load conditions. In paper [19], a one-input many-output DC-to-DC converter based on a diode-clamped converter and its applications are discussed. The main advantage of a more-output DC–DC converter is that its cross-regulation property. This means there is no separate closed loop which is required for the individual output. Only one sensitive output is controlled, and automatically, the remaining output stages will be regulated. This is explained in the literature [20, 21].

In this work, a single-input three-output SEPIC-Cuk-boost combination converter is discussed. The SEPIC and Cuk are dual converter, and these converters can produce a bipolar DC voltage output. The boost converter will generate a voltage higher than the supply voltage. Only one switch controls the entire system. The gate pulses are produced by the microcontroller STM32F4. The microcontroller generates the pulses according to the solar irradiation and the MPPT. In this work, two MPPT methods are discussed such as IC and EPP. The comparative study of IC and EPP shows that IC algorithm is more stable than that of EPP and gives the high effectiveness. Therefore, the proposed converter with IC algorithm is subjected to dynamic insolation condition, and its performances are also analysed. This type of converter is useful as a DC supply source for sensors, telecom sector and seashore for indicators, etc.

2 Solar-Fed SEPIC-Cuk-Boost Combination Converter

From the mixture of SEPIC, Cuk and boost converters, a SEPIC-Cuk-boost combination converter is modelled. This mixed topology will offer a bipolar DC voltage and one voltage greater than the supply voltage. The circuit diagram of a solar-fed SEPIC-Cuk-boost combination DC–DC converter is given in Fig. 1a. It contains only one switch connected parallel to the supply side and two coupling capacitors C_1 and C_2 , and they are used to isolate two parts of the circuits which will allow the flow of power from the input side to the output side. This converter configuration has three outputs, two bipolar DC voltages and one voltage having magnitude greater than the input voltage [18]. The supplied energy source will be stored in inductors L_1 , L_2 and L_3 whenever the switch S is turned ON. The power will also be stored owing to the discharge of the C_1 and C_2 coupling capacitors. The diodes D_1 , D_2 and D_3 are in reverse bias during this turn ON interval. This interval is termed as mode 1 of operation, and it is shown in Fig. 1b. During this interval, the output capacitors C_{O1} , C_{O2} and C_{O3} provide energy to the loads.

As soon as the switch S gets turned OFF, the inductors will recharge condensers through the forward-biased freewheeling diodes D_1 , D_2 and D_3 , which is shown as mode 2 of operation in Fig. 1c.

3 Control Schemes

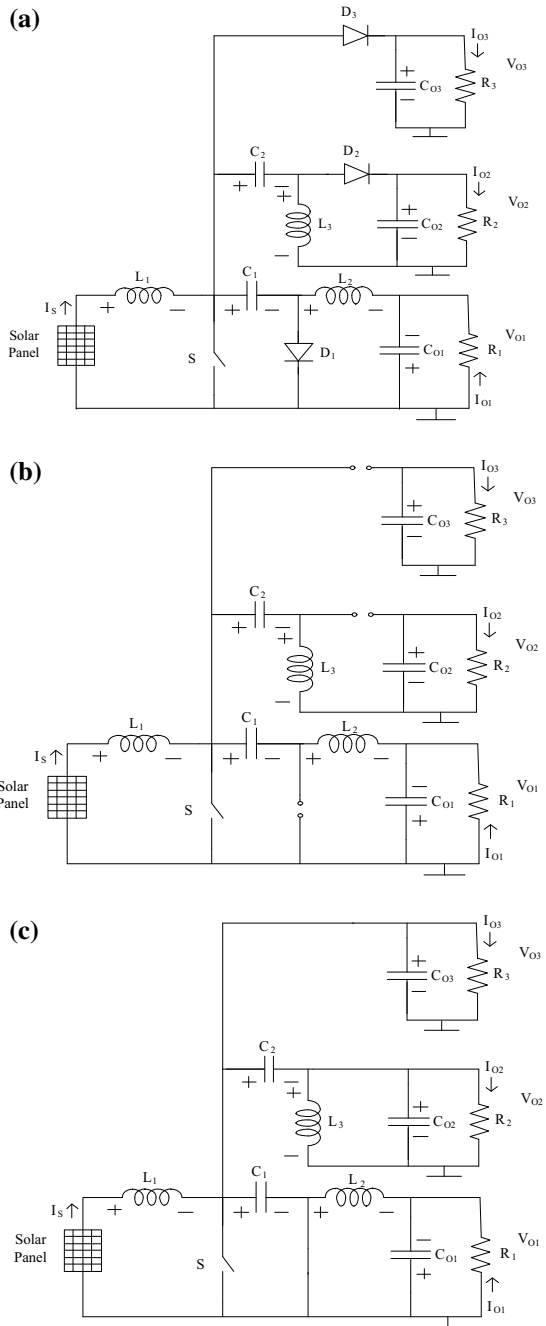
To obtain maximum effectiveness from the solar panel, the solar panel must be driven at its highest level of power. The highest power points of any solar panel will change according to the change in the solar irradiation. Therefore, the control scheme which is used to get highest effectiveness from the solar panel is MPPT techniques. The pulses produced by the MPPT will compare with the switching frequency of the converter and produce a corresponding duty ratio to control the switch. The common only used MPPT techniques are P and O, IC, APO, EPP, etc. Among these methods, the IC and EPP method are discussed in this paper.

3.1 Incremental Conductance (IC) Method [9]

IC MPPT is designed to overcome the disadvantages of P and O MPPT. The IC technique calculates the highest power point by incremental conductivity comparison with immediate solar PV conductivity. i.e.

$$\frac{I_{PV}}{V_{PV}} = \frac{dI_{PV}}{dV_{PV}} \quad (1)$$

Fig. 1 a Circuit diagram of solar-fed SEPIC-Cuk-boost combination converter, **b** mode 1 (during turn-ON) operation of solar-fed SEPIC-Cuk-boost combination converter and **c** mode 2 (during turn-OFF) operation of solar-fed SEPIC-Cuk-boost combination converter



where $\frac{I_{PV}}{V_{PV}} =$ Instantaneous conductance and $\frac{dI_{PV}}{dV_{PV}} =$ Incremental conductance.

The controller keeps this voltage to change the irradiation and repeat the process. The IC method is based on the study of the highest power point. The highest power point can be obtained if the energy shift ratio to the voltage change is zero.

3.2 *Estimate-Perturb-Perturb (EPP) MPPT Technique*

The technique of EPP is an expanded method of P and O. This method has one estimate mode between each two types of disturbance. The disturbance method performs the search for the highly nonlinear PV trait, and the estimation method compensates for irradiance-changing circumstances for the disturbance process. The EPP technique, which utilizes one estimate mode for both disturbance modes, considerably improves the tracking velocity of the MPPT control without reducing the precision of monitoring [9].

4 Simulation Performance

MATLAB software is used to perform the simulation-based job. The full configuration is executed with a sample rate of 5 μ S in a discrete mode. The advanced converter's switch frequency is regarded to be 10 kHz. The solar module is designed for normal test circumstances like 1000 W/m² and 25 °C. It observes the converter's static and dynamic output. The converters are operated, and the outcomes are also contrasted under incremental conductance MPPT and Estimate-Perturb-Perturb MPPT control systems. From these MPPT techniques, it is found that the IC MPPT method is more effective than that of EPP method. All the designed parameters are written in Appendix.

4.1 *Performance of Solar-Fed SEPIC-Cuk-Boost Combination Converter with Incremental Conductance (IC) MPPT*

The performance of a SEPIC-Cuk-boost combination converter controlled by incremental conductance (IC) MPPT technique is shown in Fig. 2. The waveforms shown in these are gate pulses (G), voltage obtained from the solar panel (V_{PV}), panel current (I_{PV}), output voltage of SEPIC, Cuk and boost converter (V_{O1} , V_{O2} and V_{O3}) and output currents of SEPIC, Cuk and boost (I_{O1} , I_{O2} and I_{O3}). The solar panel input current is in essence constant and pulsating. The solar panel can function at full energy stage, thus maintaining the panel's voltage and current throughout the

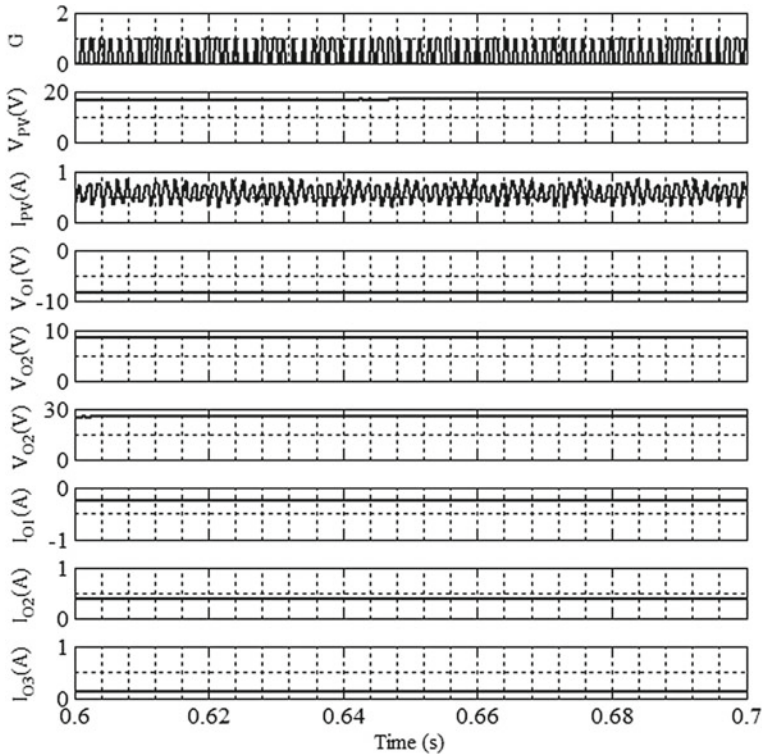


Fig. 2 Analysis of solar supplied SEPIC-Cuk-boost combination converter under incremental conductance (IC) MPPT technique

operation. The output voltages and currents obtained from the converter are shown in Table 1. From Table 1, it is observed that there are only 0.95 W losses during energy conversion. Therefore, the obtained efficiency is 90.36%. Here, the Cuk and SEPIC converters produce DC bipolar outputs, and boost produces a voltage higher than the input voltage.

4.2 Performance of Solar-Fed SEPIC-Cuk-Boost Combination Converter with Estimate-Perturb-Perturb (EPP) MPPT

The performance of a SEPIC-Cuk-boost combination converter controlled by Estimate-Perturb-Perturb (EPP) MPPT technique is shown in Fig. 3. This MPPT technique is an extended perturb and observe MPPT technique. The EPP technique, which utilizes one estimate mode for both disturbance modes, considerably improves

Table 1 Solar-fed SEPIC-CUK-boost converter at solar insolation of 1000 W/M²

Converters	V_{PV} (V)	I_{PV} (A)	P_{in} (W)	P_{O1} (W)	P_{O2} (W)	P_{O3} (W)	P_{out} (W)	Losses (W)	Efficiency (%)
<i>IC MPPT</i>									
SEPIC-Cuk-boost	17.07	0.58	9.90	2.61	3.27	3.05	8.94	0.95	90.36
<i>EPP MPPT</i>									
SEPIC-Cuk-boost	17.68	0.56	10.07	2.48	3.23	3.05	8.76	1.30	87.05

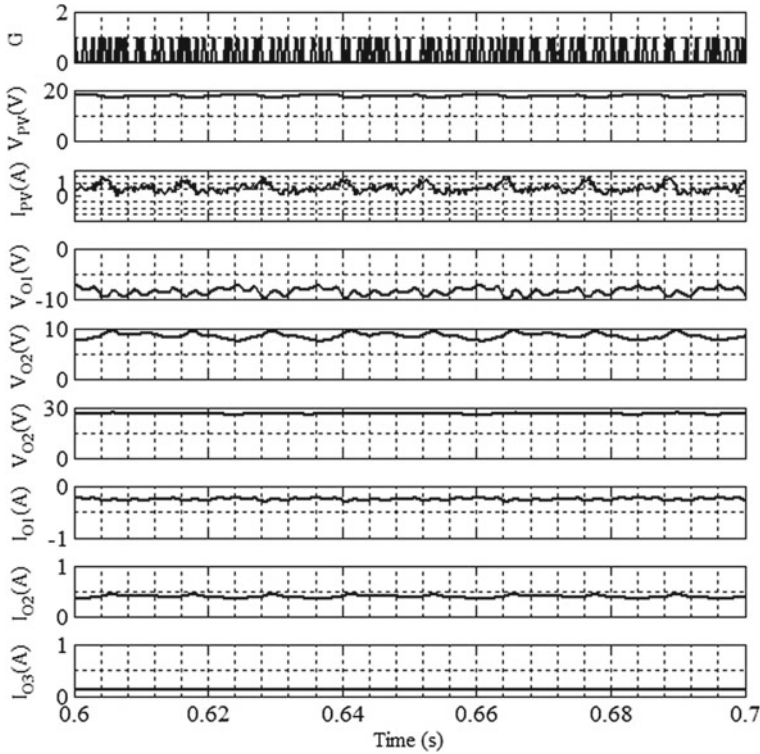


Fig. 3 Analysis of solar supplied SEPIC-Cuk-boost combination converter under Estimate-Perturb-Perturb (EPP) MPPT technique

the tracking velocity of the MPPT control without reducing the precision of monitoring. The waveforms shown in these are gate pulses (G), voltage obtained from the solar panel (V_{PV}), panel current (I_{PV}), output voltage of SEPIC, Cuk and boost converter (V_{O1} , V_{O2} and V_{O3}) and output currents of SEPIC, Cuk and boost (I_{O1} , I_{O2} and I_{O3}). The solar panel input current is constant and pulsating in nature.

The solar panel can function at the highest power point, and the panel's voltage and current are therefore preserved by V_{mp} and I_{mp} throughout the procedure. From Table 1, it is observed that by comparing the two MPPT methods, the incremental conductance technique gives the higher converter efficiency. Both the techniques are proficient of operating the solar panel at the highest power point. Therefore, the dynamic is analysed for the converter with IC MPPT technique, and it is explained below.

4.3 Dynamic Performance of Solar-Fed SEPIC-Cuk-Boost Combination Converter with Incremental Conductance (IC) MPPT

From the above analysis, it is observed that converters with incremental conductance (IC) MPPT algorithm have higher efficiency than that of Estimate-Perturb-Perturb (EPP) MPPT algorithm. Therefore, the varying solar irradiation is applied only for IC MPPT, and it is shown in Fig. 4. The output voltage from the PV panel is increased, while the insolation varies from 1000 to 2000 W/m². This has also improved the production of the converter. For this purpose, the simulation runs at 1000 W/m² till 0.65 s and is increased from 0.65 s till it is 2000 W/m². The solar panel can also operate on its largest power point condition under these variable circumstances.

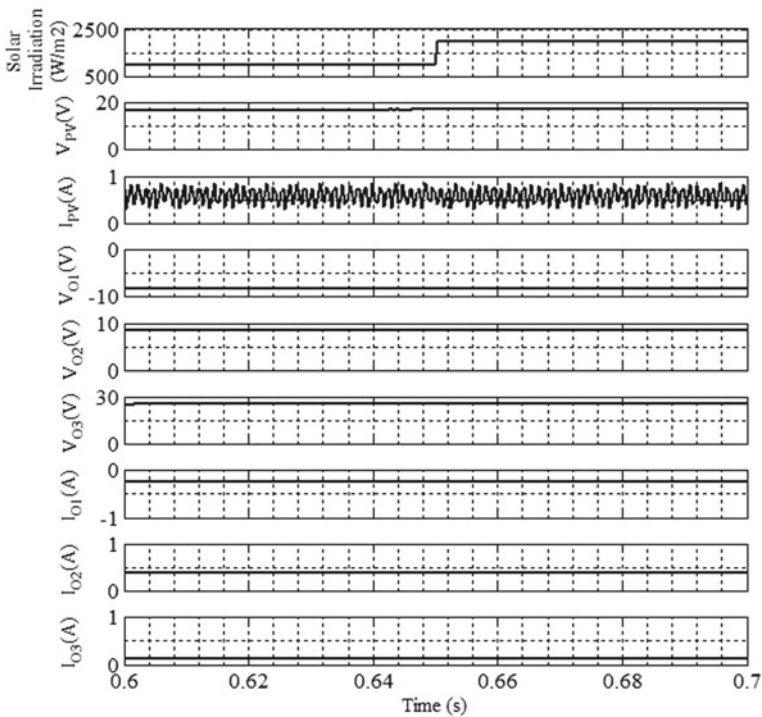


Fig. 4 Dynamic performance analysis of solar supplied SEPIC-Cuk-boost combination converter under incremental conductance (IC) MPPT technique

5 Experimental Performance of the SEPIC-CUK-Boost Combination Converter

The experimental set-up of SEPIC-Cuk-boost combination converter is displayed in Fig. 5. The solar panel used for the experiment is shown in Fig. 6. The converter is analysed with both constant DC supply and solar supply. It is observed that the SEPIC-Cuk-boost converter is working properly, and it gives the exact output according to the conversion formula. The gate pulses are created through the STM32F4 microcontroller kit interfaced with the MATLAB software. The waveforms are obtained in the DSO is analysed and compared. The converter operation with both these supplies is discussed in below sections.

Here, a solar panel of 10 W capacity is used as a supply source which is displayed in Fig. 6. This solar panel will come under PM-10 series. It is a mono-crystalline structure with 36 cells which is connected in a series manner.

Fig. 5 Experimental set-ups of the SEPIC-Cuk-boost combination converter

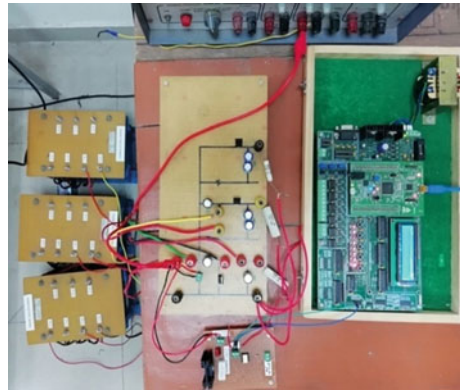
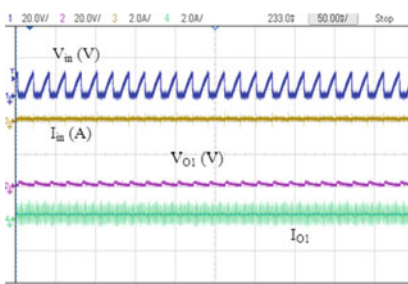


Fig. 6 Solar panel used for the experiment (PM-10 series, 12 V/10 W)

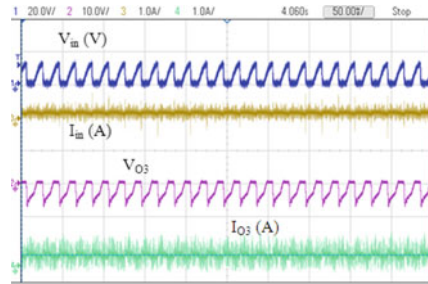


5.1 Experimental Result of SEPIC-Cuk-Boost Combination Converter with Solar Supply

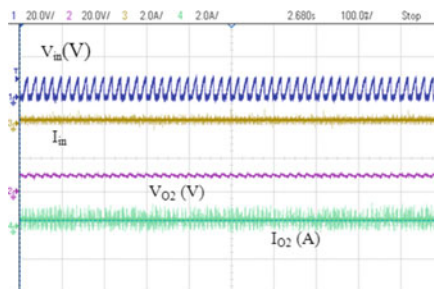
The developed SEPIC-Cuk-boost converter is tested with the solar power input. The entire set-up is run in an open-loop configuration. The solar panel has developed a voltage of 4 V at its terminals, and it is observed that the SEPIC-Cuk-boost converter is working properly and giving an output voltage according to the conversion formula. Figure 7 shows the output voltage and current waveforms of the combination converter. Figure 7a shows the results obtained from the SEPIC converter. The converter's input voltage is 4 V, and according to the input-output relationship, it can generate a voltage of 3 V at its terminals. The current developed is 0.1A. From the analysis, it is found that the current drawing from the supply, and output current is also constant in nature. Figure 7b shows the performance analysis of the Cuk converter. The Cuk converter is dual of SEPIC converter. Therefore, it produces the same magnitude of voltage like SEPIC with opposite polarity. Current magnitude



(a) In y-axis: CH1-20V/div, CH2-20V/div, CH3-2A/div and CH4-2A/div; In x-axis:50ms/div



(b) In y-axis: CH1-20V/div, CH2-10V/div, CH3-1A/div and CH4-1A/div; In x-axis:50ms/div



(c) In y-axis: CH1-20V/div, CH2-20V/div, CH3-2A/div and CH4-2A/div; In x-axis: 50ms/div

Fig. 7 Analysis of SEPIC-Cuk-boost combination converter with solar as input **a** SEPIC converter, **b** Cuk converter and **c** boost converter

Table 2 Analysis of solar-fed SEPIC-CUK-boost combination converter

V_{in} (V)	I_{in} (A)	SEPIC		Boost		Cuk	
		V_{O1} (V)	I_{O1} (A)	V_{O2} (V)	I_{O2} (A)	V_{O3} (V)	I_{O3} (A)
4	0.58	3.52	0.088	9	0.039	-3.51	-0.087

is also the same. In the DSO, channel-1 and channel-2 show the input and output voltages, and channel-3 and 4 show the input and output currents.

Figure 7c shows the results obtained from the boost converter. According to the relation, it is able to produce a voltage 9 V at its terminals. Here, channel-1, 2, 3 and 4 show the input voltage, output voltage, input current and output current, respectively. All the results obtained from the solar-fed SEPIC-Cuk-boost combination converter are summarized in Table 2. The solar panel used for the experiment is PM-10 series, and its rating is 10 W/12 V. The entire experiment is done in open loop. Therefore, the solar panel is not able to deliver its highest power. From the experiment, it is analysed that the conversion operation is efficiently achieved. The SEPIC-Cuk-boost converter is working as per the simulation.

6 Conclusion

The single-input three-output SEPIC-Cuk-boost combination converter is implemented with incremental conductance (IC) and Extended-Perturb-Perturb (EPP) MPPT methods. From the obtained results, it is understood that the IC MPPT gives more efficiency than that of EPP MPPT. The IC MPPT algorithm always gives a stable duty ratio which corresponds to the maximum power, whereas EPP is varying in nature. An improvement in the efficiency of 3.31% is achieved in the proposed converter with IC MPPT. The solar panel produces exact characteristics curves given in the datasheet. One of the disadvantages found out while designing the converters is that the set-up will become bulkier due to more number of components. To reduce the spark on the switch, its terminals are connected to ground during the implementation. The developed converter is able to produce a DC bipolar output and one boosted output. This type of converters can be used in the field of telecom applications where different voltage levels are required. The entire set-up is developed for a small range of voltages such as +3.51 V, -3.51 V and 9 V from a solar panel voltage of 4 V.

Appendix

Solar Panel Parameters

Open circuit voltage (V_{oc}) = 21.6 V, short circuit current (I_{sc}) = 0.68 A, maximum power (P_{mp}) = 10 W, maximum voltage (V_{mp}) = 17 V, maximum current (I_{mp}) = 0.58 A, number of linked module sequence (N_s) = 36, number of linked module parallel cells (N_p) = 1.

System Parameters for SEPIC-Cuk-Boost Combination Converter

PV voltage of 17 V and current of 0.58 A, linear load with $R_1, R_2 = 40 \Omega$, $R_3 = 230 \Omega$, $L_1, L_2, L_3 = 4$ mH, ESR of $L_1, L_2, L_3 = 83$ m Ω , $C_1, C_2 = 220$ μ F, $C_{O1}, C_{O2}, C_{O3} = 1000$ μ F, ESR of $C_1, C_2, C_{O1}, C_{O2}, C_{O3} = 5$ m Ω , ON resistance of MOSFET is 1.2 m Ω , internal diode resistance of MOSFET is 0.01 Ω , switching frequency (f_s) = 10 kHz.

References

1. Suresh H, Baskaran A, Sudarshan K et al (2007) Efficient charging of battery and production of power from solar energy. In: International conference on embedded systems, Las Vegas, pp 1–6
2. Nikolova S, Causevski A, Al-Salaymeh A (2013) Optimal operation of conventional power plants in power system with integrated renewable energy sources. *Energy Convers Manag* 65:697–703. <https://doi.org/10.1016/j.enconman.2011.11.035>
3. Gil Antonio L, Belem Saldivar M, Rodríguez P (2016) Maximum power point tracking techniques in photo voltaic systems: a brief review. *Int Conf Power Electron* 317–322
4. Koutroulis E, Kalaitzakis K (2006) Design of a maximum power tracking system for wind-energy-conversion applications. *IEEE Trans Industr Electron* 53:486–494. <https://doi.org/10.1109/tie.2006.870658>
5. Bellia H, Youcef R, Fatima M (2014) A detailed modeling of photovoltaic module using MATLAB. *NRIAG J Astron Geophys* 3:53–61. <https://doi.org/10.1016/j.nrjag.2014.04.001>
6. Nguyen X, Nguyen M (2015) Mathematical modeling of photovoltaic cell/module/arrays with tags in Matlab/Simulink. *Environ Syst Res*. <https://doi.org/10.1186/s40068-015-0047-9>
7. Liu K, Makaran J (2009) Design of a solar powered battery charger. In: IEEE electrical power and energy conference, Canada, pp 546–552
8. Suresh H, Baskaran A, Sudarshan K et al (2014) Efficient charging of battery and production of power from solar energy. In: International conference on embedded systems, Las Vegas, pp 231–237
9. Solanki C (2009) *Solar photovoltaics: fundamentals, technologies and applications*. PHI Publishers, New Delhi

10. Salami S, Huang C, Balagopal B, Chow M (2018) Experimental battery monitoring system design for electric vehicle applications. In: IEEE international conference on industrial electronics for sustainable systems (IESES). pp 38–43
11. Moeini A, Iman-Eini H, Bakhshizadeh M (2014) Selective harmonic mitigation-pulse-width modulation technique with variable DC-link voltages in single and three-phase cascaded H-bridge inverters. *IET Power Electron* 7:924–932. <https://doi.org/10.1049/iet-pel.2013.0315>
12. Lingeswaran G, Rajasekaran R (2013) Single input three output DC-DC buck converter. *Int J Technol Eng Syst (IJTES)* 45–50
13. Karthik S, Jegan C and Ilango R (2014) Design of single input multiple output dc-dc Converter. *Int J Eng Manage Res*
14. Maheswara Rao B, Nagalingachari K, Sri Ram L (2015) Closed-loop control of single-input multiple-output DC-DC Converter. *Int Res J Eng Technol (IRJET)* 782–788
15. Wai R, Jheng K (2013) High-efficiency single-input multiple-output DC–DC converter. *IEEE Trans Power Electron* 28:886–898. <https://doi.org/10.1109/tpe.2012.2205272>
16. Wai R, Duan R (2005) High step-up converter with coupled-inductor. *IEEE Trans Power Electron* 20:1025–1035. <https://doi.org/10.1109/tpe.2005.854023>
17. Kumar SA (2014) Modified single input multiple outputs DC-DC converter. *Int Conf Eng Technol Sci (ICETS'14)* 815–820
18. Kavitha HS (2016) High-efficiency single input multiple output DC-DC converters. *Int J Inf Futuristic Res* 3:659–1668
19. Nami A, Zare F, Ghosh A, Blaabjerg F (2010) Multi-output DC–DC converters based on diode-clamped converters configuration: topology and control strategy. *IET Power Electron* 3:197–208. <https://doi.org/10.1049/iet-pel.2008.0341>
20. Lijun Hang, Siran Wang, YileiGu et al (2011) High cross-regulation multioutput \$LLC\$ series resonant converter with magamp post regulator. *IEEE Trans Ind Electron* 58:3905–3913. <https://doi.org/10.1109/tie.2010.2098374>
21. Cho S, Kim C, Han S (2012) High-efficiency and low-cost tightly regulated dual-output \$LLC\$ resonant converter. *IEEE Trans Industr Electron* 59:2982–2991. <https://doi.org/10.1109/tie.2011.2170391>

Blind Feature-Based Steganalysis with and Without Cross Validation on Calibrated JPEG Images Using Support Vector Machine



Deepa D. Shankar  and Adresya Suresh Azhakath

Abstract The paper presents the comparative result analysis of calibrated JPEG images with and without cross-validation technique. Pixel-value differencing, LSB replacement, F5 and LSB Matching are used as steganographic algorithms. 25% of embedding is considered for the analysis. The images are calibrated before they are considered for analysis and relevant features are extracted. The classifier used is SVM with six various kernels and four types of sampling methods. The sampling methods are linear, shuffle, stratified and automatic. Radial, dot, Epanechnikov, multi-quadratic, polynomial and ANOVA kernels are taken into consideration in this paper.

Keywords Steganalysis · Cross validation · Sampling · Kernel · Calibration · Feature extraction

1 Introduction

Steganography is the way of furtive communiqué [1]. The paper proposes a comparative analysis of how well the analysis of the presence of a medium is recognized. The payload used is a text message and the medium used are images in JPEG format. The JPEG format was chosen since it is the most preferred medium of Internet transmission [2, 3]. Steganalysis can be commonly allocated into two. Targeted steganalysis is intended for a certain procedure and is, therefore, very tough for that algorithm. On the contrary, blind steganalysis can recognize anonymous stego systems. Since the steganographic algorithms are not known, statistical analysis has been taken into consideration for blind steganalysis. Machine-learning techniques are incorporated and classifiers are used to check whether the given image contains a message or

D. D. Shankar (✉)
Banasthali Vidyapith, Jaipur, Rajasthan, India
e-mail: deepadayashankar@gmail.com

A. S. Azhakath
BITS Pilani, Dubai, UAE
e-mail: sudee99@gmail.com

not. The use of statistics can give rise to false positives and false negatives. These errors need to be reduced to get a good detection rate. The paper considers four steganographic algorithms. LSB replacement is the simplest steganographic system [4, 5]. The LSB matching algorithm works by modifying the individual coefficients. The modification is done by randomly increasing or decreasing the bits. Due to this arrangement, LSB modification is difficult to detect than LSB replacement. Both LSB modification and LSB replacement embedding are done in spatial domain, whereas pixel-value differencing (PVD) and F5 embedding are done in transform domain [6]. F5 works under the principle of matrix embedding. The matrix embedding lowers the number of changes in embedding, when it is a small payload. This is the reason for F5 to be considered for analysis. PVD [7] works under transform domain and also make use of PRNG to achieve confidentiality just as F5 does. Two domains can be considered for steganalysis—spatial and transform. In spatial domain, the pixel values are considered directly, whereas in transform domain, the pixels undergo a transformation before the values are considered. The frequency of coefficients is used to create a histogram [3]. Different features had been considered in previous research [8–11]. The paper deals with images that are changed to transform domain. The transformation is discrete cosine transform (DCT). The DCT uses the concept of block dependency along with the concept of calibration in images to extract the features [13]. The technique of calibration is shown in Fig. 1. In calibration, the DCT-transformed image is converted into the spatial domain. Four pixels each from both horizontal and vertical side of the image are cropped. This is because the JPEG property states that any changes incorporated in the spatial image of a JPEG image will erase any existing embeddings. The changes can be either cropping, rotating or skewing.

Images that undergo calibration will have the similar features as the cover image. After calibration, the relevant features are mined from both images. Previous literature had discussed several features [8, 9, 11]. For analysis, this paper makes use of an arrangement of initial orders [12] and Markov features [10]. The characteristics are removed and served in a classification method to sense the incidence of a communication. Using the features, the cover and stego images are classified by the classifier. This paper makes use of support vector machine (SVM) as classifier. The consideration was due to the fact that the previous literature stated SVM to be an exceptional tool for presumptions in wide real-life scenarios. SVM is also the most prevalent classifier to decide the existence of payload [13].

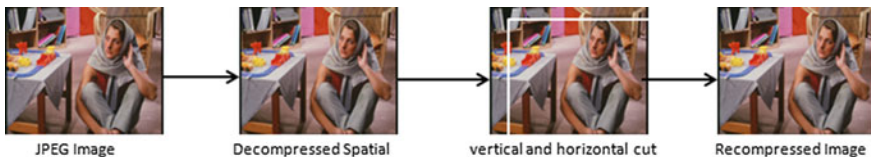


Fig. 1 Technique of calibration

2 Implementation

The work flow for the steganalytic scheme is given in Fig. 2.

2.1 Extraction of Features

The objective of the paper is a reasonable work with and without cross validation on calibrated images to achieve a decent classification for image with an embedding percentage of 25. The system emphasize upon removing the relevant features which will reach a totality of 274 features. The original DCT characteristics are 23 functionals [8]. The extraction is carried out and can be symbolized as:

$$F = |f(Si) - f(Ci)| \quad (1)$$

The initial values can be stretched to 193 functionals that are interblock dependencies [10]. The features of Markov are the dependencies of the intra block. The paper, therefore, takes into account the dependencies based on interblock and intrablock, to eliminate the shortcomings triggered by each of them. DCT coefficient array $d_{i(a,b)}$ defines a stego image, where i is the block and a and b are coefficients [9]. The dual histogram is signified by

$$g_{ab}^d = \sum_{i=1}^n x(d, d_{i(a,b)}) \quad (2)$$

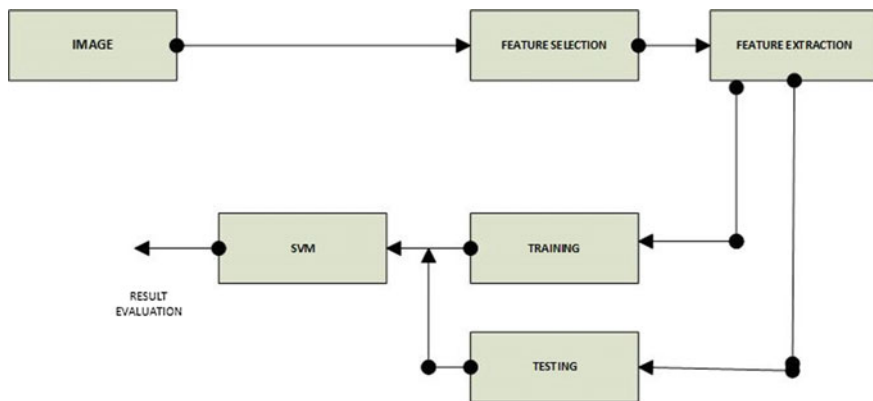


Fig. 2 Workflow diagram of steganalytic system

where g is the maximum block number and d is the value of the coefficient. Variance is epitomized as

$$V = \sum_{a,b=1}^8 \sum_{i=1}^{|I_{\text{row}}|-1} |d_{I_{\text{row}}(i)(a,b)} - d_{I_{\text{row}}(i+1)(a,b)}| + \sum_{a,b=1}^8 \sum_{i=1}^{|I_{\text{col}}|-1} |d_{I_{\text{col}}(i)(a,b)} - d_{I_{\text{col}}(i+1)(a,b)}| \quad (3)$$

where I_{row} and I_{col} are vectors of block indices [11, 14].

Blockiness is denoted as

$$B_{\alpha} = \frac{\sum_{a=1}^{\lfloor(A-1)/8\rfloor} \sum_{b=1}^B |x_{(8a,b)} - x_{(8a+1,b)}|^n + \sum_{a=1}^{\lfloor(B-1)/8\rfloor} \sum_{b=1}^A |x_{(8a,b)} - x_{(8a+1,b)}|^n}{B\lfloor(A-1)/8\rfloor + A\lfloor(B-1)/8\rfloor} \quad (4)$$

where A and B are the image dimensions. The sharing of probabilities of neighbouring DCT coefficient pairs is known as a co-occurrence. It is denoted as

$$C_{st} = \frac{\sum_{i=1}^{|I_{\text{row}}|-1} \sum_{a,b=1}^8 \delta(s, d_{a,(i)}(i, j)) \delta(t, d_{a,(i+1)}(a, b)) + \sum_{i=1}^{|I_{\text{col}}|-1} \sum_{a,b=1}^8 \delta(s, d_{a,(i)}(a, b)) \delta(t, d_{a,(i+1)}(a, b))}{|I_{\text{row}}| + |I_{\text{col}}|} \quad (5)$$

The Markov feature has four different arrays in horizontal, vertical and two diagonal directions.

2.2 Cross Validation

Usually, an image server is split into a variety of training and testing. This is achieved by assigning the image at random, thereby eliminating any bias. No rules are in place to verify that the testing and training set have to be identical. Training and testing are executed k times to avoid performance dissimilarity, known as k -fold validation. In this paper, the definition of cross validation is 10 for the value of k [12]. Here, the training and testing are done 10 times. The value of k can be changed.

2.3 SVM Classification

The classification phase is performed after feature extraction. The SVM gives an optimal hyperplane with the training dataset to classify the hyperplane [13] as shown in Fig. 3. This gives the minimum distance to sustain the vector, which is called the margin.

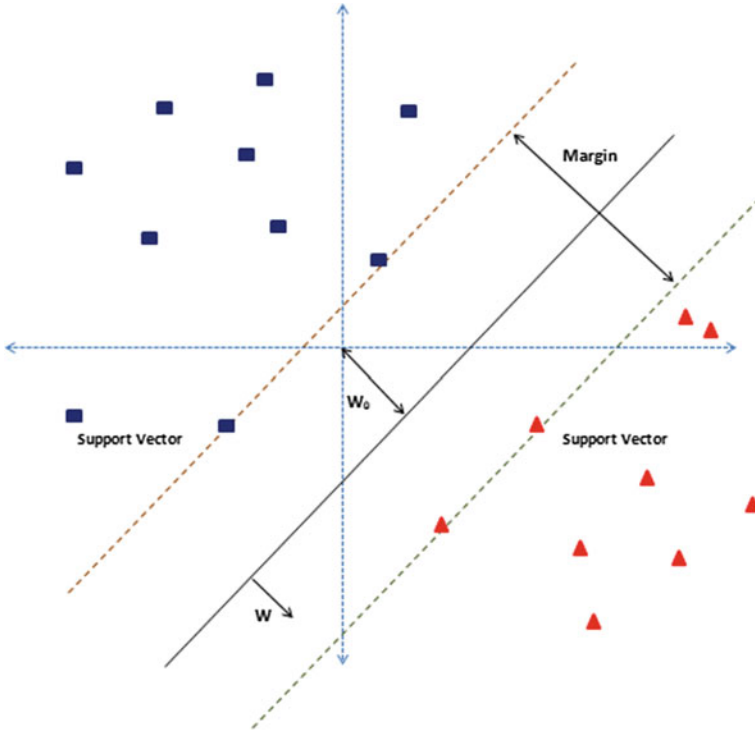


Fig. 3 Classification using support vector machine

The choice of SVM is because of its efficiency to work well with high-dimensional features and the flexibility to choose a greater number of kernels.

The following Eq. (6) characterizes the radial kernel

$$e^{(-g\|a-b\|^2)} \quad (6)$$

where g is the gamma parameter. The dot kernel is characterized by

$$k(a, b) = a * b \quad (7)$$

The Eq. (7) represents the polynomial kernel

$$k(a, b) = (a * b + 1)^v \quad (8)$$

v is known as the degree of the kernel.

The ANOVA kernel is said as

$$e^{(-g(a-b))} \quad (9)$$

The Epanechnikov kernel is shown by the function

$$(3/4)(1 - n^2) \quad (10)$$

for n between -1 and 1 and zero for n outside that range. Equation (11) describes multiquadratic kernel

$$\sqrt{\|a - b\|^2 + c^2} \quad (11)$$

3 Experimental Results

The experimental results of the works are explained as below:

3.1 Database of Images

The performance of a research depends on the quality of the database used for it. This paper uses a collection of 2300 images each of JPEG format. The image is compressed to 256×256 in size. UCID standard dataset [15] of 1500 JPEG images is used as the training dataset and the standard INRIA image dataset [16] of 800 images are taken as the test dataset. The images are calibrated and the relevant features are selected and extracted for classification. The selection of features is based on their sensitivity towards embedding changes.

3.2 Feature Extraction

The features adapted in this paper are 274 comprising of first order, second order, extended DCT and Markovian features. All features are normalized before any analysis is done.

3.3 Training Phase

The dataset of 1,500 images each with 274 characteristics is used during the training stage. The characteristics are fed into the classifier after being either marked as stego or cover, thus decreasing the amount of false positives and false negatives.

3.4 Testing Phase

The phase comes after the classifier is trained. 800 images are used for testing and features are extracted. In order to avoid overfitting, it is highly recommended to have the test dataset to be different from training dataset. Moreover, this concept is correct for the scenario because the analysis is always performed with real-time information.

4 Analysis of Results

In this paper, only calibrated images are used for classification. SVMs are generally flexible for various sampling and diverse kernels and, therefore, reflected for classification in this paper.

4.1 Results with No Cross Validation

The results with no cross validation done with four steganographic schemes is as explained below (Tables 1 and 2).

From the above results, multiquadratic kernel, radial kernel and Epanechnikov kernel give lower results than the other mentioned kernels. ANOVA, polynomial and dot kernel offer improved result with stratified sampling.

Table 1 Results on LSB replacement

	Linear	Shuffle	Stratified	Automatic
Dot	55.13	73.29	72.85	72.85
Radial	42.89	42.24	42.7	42.7
Polynomial	56.2	72.3	55.12	55.12
Multiquadratic	42.9	48.16	50	50
Epanechnikov	43.78	44.46	44.79	44.79
ANOVA	57.12	72.52	73.3	73.3

Table 2 Results on LSB matching

	Linear	Shuffle	Stratified	Automatic
Dot	53.4	73.3	72.4	72.4
Radial	44.8	46.03	45.7	45.7
Polynomial	53.07	73.28	72.6	72.6
Multiquadratic	45.91	52.57	53.23	53.23
Epanechnikov	53.11	48.4	48.93	48.93
ANOVA	54.6	59.73	72.45	72.45

From the above results, radial, multiquadratic and Epanechnikov kernels provide a lower result rate than the other kernel functions. The above results give good results with ANOVA, polynomial and dot kernel with stratified sampling (Tables 3 and 4).

The worthy results are obtained with ANOVA, polynomial and dot kernel with stratified sampling.

The above results give good results with ANOVA, polynomial and dot kernel with stratified sampling.

Table 3 Results on pixel-value differencing

	Linear	Shuffle	Stratified	Automatic
Dot	42.78	53.1	51.83	51.83
Radial	42.89	31.73	31.90	31.90
Polynomial	41.98	53.21	51.21	51.21
Multiquadratic	42.67	48.13	50	50
Epanechnikov	42.78	36.33	37.34	37.34
ANOVA	42.89	50.41	51.12	51.12

Table 4 Results on F5

	Linear	Shuffle	Stratified	Automatic
Dot	55.10	75.89	74.83	74.83
Radial	42.67	53.2	53.72	53.72
Polynomial	51.12	72.34	71.82	71.82
Multiquadratic	40.52	48.17	50	50
Epanechnikov	54.24	54.13	56.34	56.34
ANOVA	56.13	76.27	84.78	84.78

4.2 Results with Cross Validation

The results with no cross validation done with four steganographic schemes are as explained below (Table 5):

The above findings indicate that with stratified sampling, the ANOVA gives a better outcome (Table 6).

In the above result, the stratified sampling gives a better result with polynomial kernel (Table 7).

Similar to other kernels, the dot kernel gives a better result with stratified sampling (Table 8).

From the consequence, it can be understood that with stratified sampling, the ANOVA gives the highest outcome.

Table 5 Results on LSB replacement

	Linear	Shuffle	Stratified	Automatic
Dot	69.51	74.66	74.66	74.66
Radial	43.88	56.78	67.95	67.95
Polynomial	71.3	73.62	73.62	73.62
Multiquadratic	43.78	49.73	50.03	50.03
Epanechnikov	43.88	48.2	47.07	47.07
ANOVA	64.98	74.32	74.32	74.32

Table 6 Results on LSB matching

	Linear	Shuffle	Stratified	Automatic
Dot	65.96	73.46	73.49	73.49
Radial	48.38	49.72	50.2	50.2
Polynomial	68.83	72.4	77.58	77.58
Multiquadratic	52.32	52.29	52.29	52.29
Epanechnikov	56.23	48.16	48.14	48.14
ANOVA	61.7	73.27	73.2	73.2

Table 7 Results on F5

	Linear	Shuffle	Stratified	Automatic
Dot	92.74	97.35	97.26	97.26
Radial	50.26	56.12	57.53	57.53
Polynomial	90.35	94.82	94.69	94.69
Multiquadratic	50.02	47.74	49.96	49.96
Epanechnikov	62.26	56.12	57.53	57.53
ANOVA	91.24	93.56	94.65	94.65

Table 8 Results on pixel-value differencing

	Linear	Shuffle	Stratified	Automatic
Dot	5.68	54.31	54.31	54.31
Radial	6.4	40.21	40.78	40.78
Polynomial	43.87	53.82	53.18	53.18
Multiquadratic	49.6	57.63	58.35	58.35
Epanechnikov	52.06	47.31	48.25	48.25
ANOVA	52.94	63.88	71.75	71.75

5 Conclusion

The payload was embedded using four different steganographic algorithms. The embedding rate used here is 25. The dataset used for analysis is calibrated to have an estimate of cover image. SVM is the classifier used for the dataset. The findings were obtained from multiple kernels and sampling techniques. The final review suggests that the cross-validation outcome is better than the result without cross validation. For LSB replacement, the polynomial kernel gives better result with cross validation than without it. In LSB matching, both dot and polynomial give good result with cross validation. PVD gives better result with ANOVA and stratified sampling. F5 gives the best classification rate with ANOVA, cross validation and stratified sampling.

References

1. Kumar BR, Murti PR (2011) Data security and authentication using steganography. *Int J Comput Sci Inf Technol* 2(4):1453–1456
2. Sherif M, Badr M, Salim I (2014) A review on steganalysis techniques: from image format point of view. *Int J Comput Appl* 1:0975–8887
3. Shankar DD, Upadhyay P (2016) Performance analysis of various feature sets in calibrated blind steganalysis. *Int J Comput Sci Netw Secur* 16:29
4. Goljan M, Fridrich J, Soukal T (2003) Higher-order statistical steganalysis of palette images. *Proc SPIE* 5020:178–190
5. Ker AD (2005) A general framework for the structural analysis of LSB replacement. In: *Proceedings of the 7th information hiding workshop*, pp 296–311
6. Westfeld A (2001) F5—a steganographic algorithm. In: *Information hiding: 4th international workshop*, pp 289–302
7. Wu D-C, Tsai W-H (2003) A steganographic method of images by pixel-value differencing. *Patt Recogn Lett* 24:1613
8. Attaby AA, Alsammak AK, Mursi Ahmed MFM (2018) Data hiding inside JPEG images with high resistance to steganalysis using a novel technique. *DCT-M3 Ain Shams Eng J* 9(4):46–50
9. Zeng J, Li B, Huang J, Tan S (2017) Large scale JPEG image steganalysis using hybrid deep learning framework. *IEEE Trans Inf Forens Secur* 1–14:1200
10. Pevny T, Fridrich J, Merging Markov (2007) DCT features for multiclass JPEG steganalysis. In: *SPIE proceedings, electronic imaging, security, steganography and watermarking of multimedia contents*, vol IX, pp 301–314

11. Ashu A, Chhikara R (2014) Performance evaluation of first and second order features for steganalysis. *Int J Comput Appl* 92:17–22
12. Kokkinos Y, Margaritis KG (2018) Managing the computational cost of model selection and cross-validation in extreme learning machines via Cholesky, SVD, QR and eigen decompositions. *Neurocomputing* 21:29–45
13. Liu P, Yang C, Liu F, Song X (2015) Improving steganalysis by fusing SVM classifiers for JPEG images. In: *International conference on computer science and mechanical automation (CSMA)*, pp 185–190
14. Kodovsky J, Fridrich J (2009) Calibrated revisited. In: *The workshop in ACM multimedia and security*, pp 63–74
15. Schaefer G, Stich M (2004) UCID-an uncompressed colour image database. In: *SPIE conference storage and retrieval methods and applications for multimedia*
16. Jegou H, Schmid C (2008) Hamming embedding and weak geometric consistency for large scale image search. In: *European conference computer vision*

Demand Side Management in Smart Grid



M. Ganesh and R. K. Patnaik

Abstract Smart grid is a bidirectional electric and communication network which includes various energy and operational devices including smart accessories, smart meters, nonconventional energy resources and energy-saving devices. Through two-way digital communication, it is used to supply electricity to consumers and domestic purposes. Smart grid technologies are enforced in India in order to reduce transmission and distribution losses. Demand side management is an important function of a smart grid and it helps to deduce the utilization costs of electricity. It allows energy suppliers to reduce peak load demand. The method which is proposed composed of modern system identification and it enables the user to schedule their loads. This potentially balances both supply side and demand side in order to make the system more efficient. However, due to lack of proper coordination among the agents, it may cause significant peaks in demand, which will in turn reduce efficiency of overall system. In order to correlate the agents in a decentralized manner, we are introducing a mechanism of decentralized demand side management (DDSM) in smart grid. Peak demand of domestic customers in the grid can be reduced through proper coordination among customers.

Keywords Demand side management · Decentralized demand side management (DDSM) · Non-conventional energy resources · Smart grid · Smart meters · Two-way digital communication

M. Ganesh · R. K. Patnaik (✉)

GMR Institute of Technology, GMR Nagar, Rajam, Srikakulam, Andhra Pradesh 532127, India
e-mail: rajehkumar.p@gmrit.edu.in

M. Ganesh

e-mail: gmeesala1@gmail.com

© Springer Nature Singapore Pte Ltd. 2020

R. Sharma et al. (eds.), *Innovation in Electrical Power Engineering, Communication, and Computing Technology*, Lecture Notes in Electrical Engineering 630,
https://doi.org/10.1007/978-981-15-2305-2_3

1 Introduction

To reduce the ever-increasing demand supply gap, present Indian electricity sector is facing many problems. In India's transmission and distribution sector, energy losses are exceeding 30% which is undesirable. Smart grid technologies are implemented in India in order to reduce transmission and distribution losses.

1.1 Introduction to Smart Grid

Through two-way digital communication, smart grid is used to supply electricity to consumers and domestic purposes [1]. Whenever any equipment fails or any outage occur, because of two-way communication, smart grid will automatically reroute and self-heal the fault before they became large-scale blackouts [2]. Smart grid is able to increase efficiency and reduce the energy cost through real-time monitoring and customer load scheduling [3].

1.2 Literature Survey

The grid is a combined network of energy providers and energy suppliers synchronized together with transmission and distribution systems, and it can be operated from different control centers [1]. Smart grid is an evolved grid system which manages electrical demand in a reliable, sustainable and in an economic manner. And, it is built on advanced infrastructure and it is tuned to facilitate the integration of all renewable energy resources [4]. Smart grid uses the latest advanced technologies in order to optimize the use of assets. By continuously sensing and rating their capacities, assets are allowed to be greater loads, and it automatically reschedules the load [5]. Whenever any equipment fails or any outage occur, because of two-way communication, smart grid isolates the fault before they became large scale blackouts [6]. Demand side management plays a key role in energy management of the smart grid, and it provides support toward various areas like decentralized energy resource management, electricity market control and management. By reducing or deferring loads, most DSM approaches advice a group of consumers to reduce their ongoing demand [7].

1.3 Demand Side Management

Demand side management is an important function of smart grid, which helps the energy suppliers to decrease the peak load demand and it allows reduction in electricity bills by shifting loads from peak hours to non-peak hours [8]. Demand side management is the blueprint, accomplishment and supervision of customer activities in order to schedule the usage of power. Demand side management increases the share of renewable energy resources to manage the peak demand [9].

1.4 Main Purpose of Demand Side Management

In order to flatten the load demand curve, demand side management enforces the consumers to utilize minimum power during peak hours and it shifts energy usage from peak hours to non-peak hours. DSM has the ability to control consumption according to generation [10]. And, it can increase the integration of large-scale renewable energy sources in order to reduce operation and maintenance costs for devices and through proper user load scheduling and real-time monitoring, and electricity costs for users are ultimately minimized [9].

2 Basic Load Shaping Techniques

Demand side management is a tool for different load objectives such as

2.1 Peak Clipping

Peak clipping is the reduction of load on the grid predominantly during the period of high peak demand.

2.2 Valley Filing

Load factors of system can be improved by raising the load during off-peak times. This technique is usually called valley filling. By using this technique, load curve can be flattened, and thus, perfect balance is established between supply and loads which will, in turn, increase the system efficiency [11].

2.3 Load Shifting

Raising the load on the grid during off-peak times and reducing the load on the grid during high peak times, in order to flatten the load curve, is called load shifting.

2.4 Strategic Conservation

Strategic conservation is reduction of load in a whole day by using energy-saving devices or smart appliances or by decreasing overall utilization.

2.5 Strategic Load Growth

Strategic load growth defines that sales of electricity can be increased gradually, which affects spontaneously on growth of economy.

2.6 Flexible Load Shape

Flexible load shaping provides a chance to consumers to buy some amount of electricity at reliability, which is less than normal quality of power.

The above-discussed load objectives are shown in Fig. 1.

The way electricity sold now does not say about real-time costs nor cannot estimate cost at peak hours. When electricity generation is scarce, prices will rise up, and supplier wants to sell more but, on the other side, consumers will decrease their consumption due to high price. In this way, by using DSM technique, perfect balance

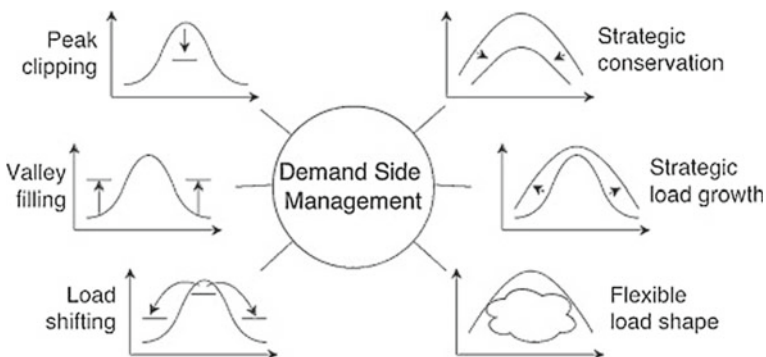


Fig. 1 Basic load shaping techniques

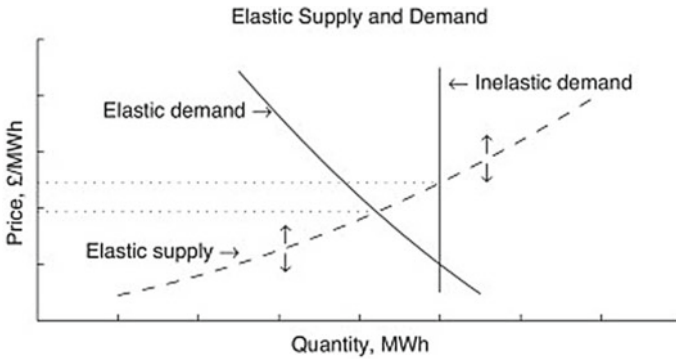


Fig. 2 Elastic supply and demand

is achieved between elastic supply and demand as shown in Fig. 2. [12]. Thus, DSM plays a key role in increasing the system efficiency.

If real-time price was brought into picture, then the price must be flexible on receiving end side in opposition to fixed electricity price [1]. During some times when renewable energy is less in amount, then price would increase for equal amount of energy, which will shift the demand curve up.

3 DSM Techniques, Proposed Strategies and Methods

DSM strategies are based on heuristic optimization problem. Proposed optimization problem tends to optimize the demand curve as close as possible to favorable demand curve [1]. Figure 3 illustrates system block diagram and various components involved in it.

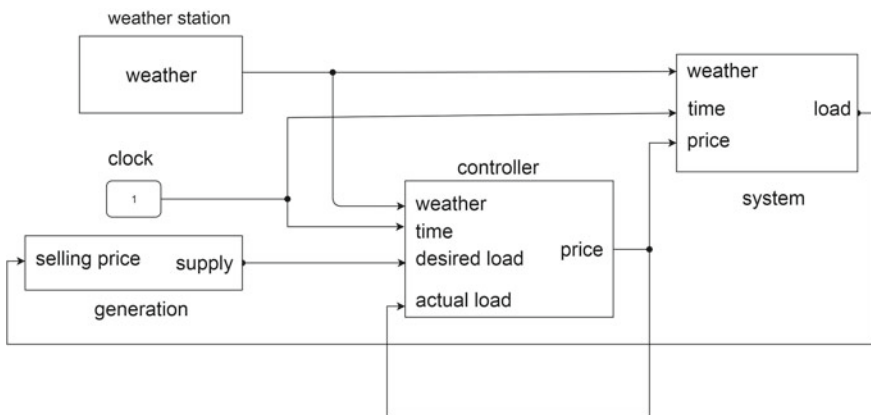


Fig. 3 System block diagram

3.1 Components of Block Diagram

There are various components in block diagram and each of it is explained below in detail.

3.1.1 System

Here, block diagram system includes climate, time information and price as inputs and predicted demand as output [1]. In order to reduce the high peaks in demand curve, it is important to design an accurate system model.

3.1.2 Generation

Information about the desired load can be supplied from generation side and it is nothing but sum of all generator outputs which are connected to the network. Using feedback, real-time price can be calculated and depends on it, generators will connect and disconnect from the network [1]. If the price is more, more generators are connected to the grid to sell the electricity, but, due to high price, customers will shut down their loads. Thus, balance is achieved between supply and demand which increases overall efficiency [6].

3.1.3 Climate and Time Information

Many external factors like time information and weather influence the behavior of the system [13]. Approximate price signal is generated by processing the weather and time information in a controller.

3.1.4 Model Predictive Controller

In order to match desired generation and the illustrative demand, the controller optimizes the upcoming price signal. Right price for a total load is computed by a controller which is close to expected load from side of generation [14]. For this application, the most suitable controller is a model predictive controller (MPC) as shown in Fig. 4, because inputs can be controlled, measured disturbances and time constants are large enough for (MPC) [1].

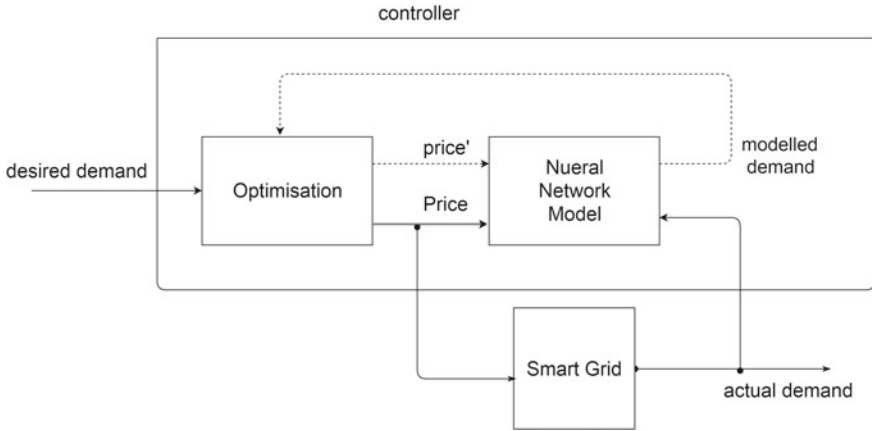


Fig. 4 Neural network predictive controller

4 Decentralized Demand Side Management

Most DSM approaches advise a group of users to decrease their present demand, which can be achieved by deferring their loads. First, we justify the user to optimize their price signal by deferring their loads [15]. The adaptive and autonomous behavior of agents plays a major role in achieving performance benefits of smart grid. In this way, we proposed the mechanism of DDSM.

4.1 Deferrable Loads

They usually inculcate time periods in which they can be switched on or off either by consumer or by the controlling devices [7]. Depending on the usage and temperature of home, loads are classified as: water heating and space heating devices and cold devices. Depending on various external factors, their behavior can be varied beyond the control of user [16]. Different loads based on precise running times and running periods are called shiftable static loads (SSLs). The loads which depend on temperature are called as thermal loads.

4.2 Shiftable Static Loads

Let $l \in L$ denotes the setoff SSLs and time slots for device to be turned on by the consumer are denoted by $O_l \in T$. Let the time at which user wants to turn on the device is $O_l \in T$. For example, (one person wants to switch on the device when he is

away) if any deferment from the predetermined time, then consumer will to loss of comfort [17]. Let deferment of the device is denoted by $d_l \in \{-24, -23, \dots, 23, 24\}$ and power rating of the device is denoted by $r_1 \in R^+$ in kw [16]. From a uniform distribution $U(v_{min}^1, v_{max}^1)$ where $v_{min}^1, v_{max}^1 \in T$ the duration v^1 (in time slots) of each device is calculated, and it depends on type of device used. For example, a washing machine typically operates for 1 and 3 h [18]. Let $c_1 \in R^+$ is the marginal cost associated with deferment of the device to differentiate from preset time. Then overall comfort cost becomes as $c_1 = \Delta c_1 |d_1|$. This leads to more deviation in smart meters, which will cause more discomfort to consumer [19]. The main function in the optimization model is effective d_i and it tells about the price paid by the consumer. Let the price $\forall t \in T$, now the aim is then to minimize the comfort cost and marginal cost is given in Eqs. 1 and 2. [15].

$$\min_{d_i, \forall l \in L} \sum \sigma c_l + \sum_{t \in T} \sum_{t \in T} \gamma^l r_l p_t v^l o \quad (1)$$

Such that,

$$\gamma_t^l = \begin{cases} 1, & t = t' + d_t \\ 0, & \text{otherwise} \end{cases} \quad (2)$$

where $t' \in o_l$

Based on deferment factor d_l , device turn on times factor $o_l, \gamma_t^l \in \{0, 1\}$ determines when the device need to be turned on or turned off. The number of time slots for which device 1 has to be turned on is denoted by v^1 and scaling factor is denoted by $\sigma \in [0, 1]$ determines importance among the comfort and price.

4.3 Thermal Loads

Standard adaptive thermostats can be used to warm up the home to the required level of temperature exactly during the presence of user [15]. The thermostats ensure that the home is always maintained warm, by properly turning on the thermostats before the presence of consumer and according to his requirement [20]. In order to guarantee the required temperature to be reached during presence of user, intelligent adaptive thermostats always aim to optimize the heating or cooling profile [7]. And by doing so, costs are minimized. The heater we choose to develop is a heat injector; it will extract heat from one place and transfer it to some other place.

4.4 Home and Heater Properties

Let us model and simulate the thermal properties of the home and the heater. Let the rate of thermal leakage o the home is denoted by $\phi \in R^+$ and measured in w/k. Let $T_{\text{in}}^t \in R^+$ be the internal temperature of the home and $T_{\text{ext}}^t \in R^+$ be the external temperature at time t . $T_{\text{opt}}^t \in R^+$ be the desired temperature at which user is more comfortable, for example typically 22.5 °C. $a_{\text{hc}} \in R^+$ in (j/kg/k) be the heat capacity in the home, total mass of air in the home is denoted as $a_{\text{mass}} \in R^+$ in (kg). The power rating of the heater is $r_h \in R^+$ in kW [21]. $o_h \in T$ be time slots at which the heat pump is turned on. Given this, we have also defined the variable $h_{\text{on}}^t \in \{0, 1\}$ for $t \in T$, where $h_{\text{on}}^t = 1$, if $t < o_h$ and 0 otherwise. Therefore, the total heat input in the system is given in Eq. 3.

$$n_l^t = h_{\text{on}}^{t-1} - \phi(T_{\text{in}}^{t-1} - T_{\text{ext}}^{t-1}) \quad (3)$$

The relationship between internal temperature and amount of heat injected into the home at the time is given in Eqs. 4 and 5

$$T_{\text{in}}^t = T_{\text{in}}^{t-1} + \frac{kn_i^t}{a_{\text{hc}} a_{\text{mass}}} \quad (4)$$

where

$$k = \frac{24 * 3600}{t} \quad (5)$$

K is heater turn-on time in seconds. Let $c_{\text{on}}^t \in \{0, 1\}$ be the comfort at every time slot $t \in T$ such that $c_{\text{on}}^t = 1$ if the consumer wants comfort and otherwise $c_{\text{on}}^t = 0$. We calculate the instantaneous comfort cost during every time slot, as $c_h^t \in R^+$ such that

$$\Delta c_h^t = \begin{cases} c_{\text{on}}^t \omega_1 (T_{\text{in}}^t - T_{\text{opt}})^2, & T_{\text{in}}^t \geq T_{\text{opt}} \\ c_{\text{on}}^t \omega_2 (T_{\text{in}}^t - T_{\text{opt}})^2, & T_{\text{in}}^t < T_{\text{opt}} \end{cases} \quad (6)$$

Here in Eq. 6, $\omega_1, \omega_2 \in [0, 1]$ are constants which determine the effect of a difference in temperature [16]. The combination of present instantaneous comfort cost at time $t - 1$ is total comfort cost at time t and it is given by Eq. 7.

$$c_h^t = \Delta c_h^t + \gamma c_h^{t-1} \quad (7)$$

Here, $\gamma \in [0, 1]$ scales the effect of previous time slot on current one.

4.5 Pricing Mechanism

The pricing mechanism that we propose estimates the cost of generating electricity to the consumers. Generally, in the time of use pricing mechanism, consumers are allowed to pay fixed price of electricity by their suppliers. Time of use (TOU) pricing mechanism simply hides the real-time pricing of bill, which fluctuates depend on the type of alternators used [3]. Specifically, the price signal for every 30-min time period can be offered by real-time pricing mechanism (RTP) [15]. RTP mechanism is much beneficial than time of use (TOU) mechanism, by allowing customers to flexibly manage their load demand to mitigate peaks when the price of power is more expensive [16].

Demand curve cannot be made flattened, only by applying RTP mechanism. This is because, for example, if all agents are provided a poor price of electricity for the next 30 min period, all agents will turn on their loads for next 30 min which leads to generate peaks in demand [22]. Figure 5 shows a comparison between RTP and TOU pricing mechanisms.

To overcome this problem, we proposed a technique to ensure adaptive behavior for users, which is based on real-time pricing mechanism (RTP).

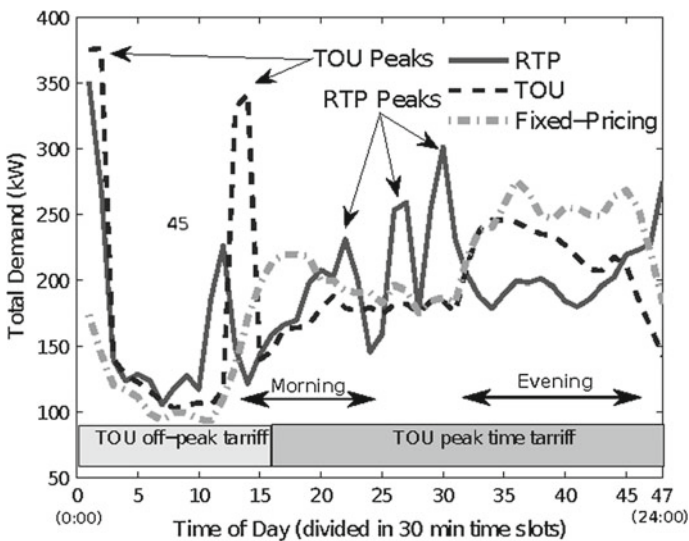


Fig. 5 Comparison between RTP and TOU pricing mechanisms

4.6 The Adaptive Mechanism

Our adaptive mechanism for DDSM determines how to reschedule the deferrable loads present in the home (i.e., thermal and shiftable static loads).

Specifically an agent I gradually adopts its deferment parameter d_1^{i*} .

$$d_1^i(t+1) = d_1^i(t) + \beta^i(d_1^{i*} - d_1^i(t)) \quad (8)$$

Fastness of user reacting to changing conditions is denoted by $\beta^i \in (0, 1]$ as taken in Eq. 8. Specifically, it reoptimizes the load profile with a probability of $\alpha \in (0, 1)$, on any particular day. It checks the probability of α based on estimated prices p_t . Let N^* be the number of users that will reoptimize on any specific day, where n is number of users [11]. While doing so, we instigate some inertia to optimization, in order to ensure that all DSM enabled users do not reoptimize at the identical time. For sufficiently small values of α and β , a stable and desirable output is achieved, where grid demand curve gets leveled. Although users are not directly communicated with DSM, our methodology enables implicit togetherness among users [8].

4.7 Performance of Adaptive Mechanism

Primarily, we can assess the performance of an adaptive mechanism, by differentiating the grid efficiency, while using our decentralized demand side management technique with overall information against a favorable behavior of system [12]. For a given system, favorable solution can be achieved with a load factor of 0.76. Faster consolidation to optimal solution can be achieved with higher values of α , but it does allow the system to get a response closer to favorable solution [18]. For larger values of α , there will be no concurrency, such that peaks are simply shifted instead of leveling, because so many users are reoptimizing their loads in an identical time. Thus, we can say that system converges to optimal behavior when α is reasonably smaller.

4.8 Emergent Behavior of Adaptive Mechanism

The load factor of domestic customers will tend to optimum load factor of 0.76 through the adaptive mechanism, and also the carbon reduction percentage increases up to 6% as shown in Fig. 6.

Now, we analyze the smart home by using the load duration curves (LDC). The LDC is used to explain the correlation between capacity requirements of generation and capacity of utilization.

Figure 7 shows that the LDC of the system, from 100 to 80% of peak demand

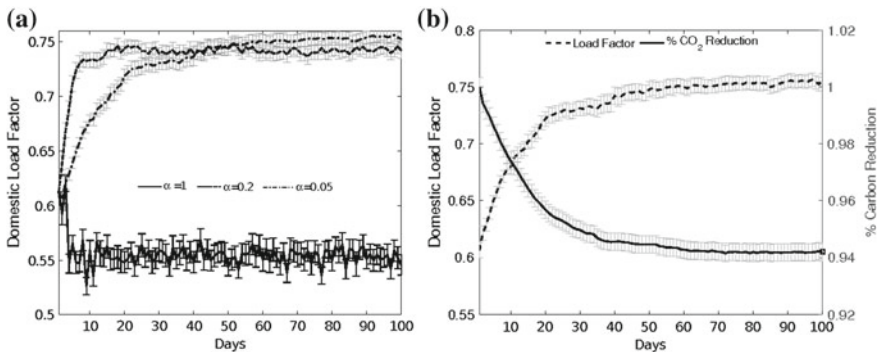
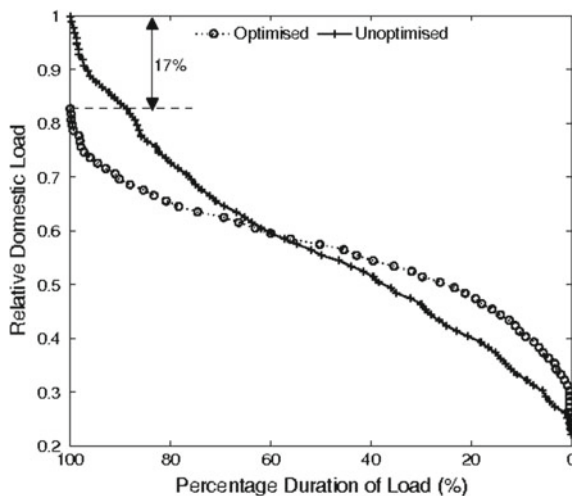


Fig. 6 Simulated DDSM with respect to, **a** different probabilities, **b** load factor and carbon emissions

Fig. 7 Duration of load curve for consumers at 7% of electrification



region the demand curve gets flattened, which means flattening of peak demands. Let $x_r \in (0, 1)$ is a probability that they have DDSM capability where $r \in s$. We have to analyze how x_r will change as the payoff of the agent's changes with and without DDSM. Aiming to analyze how the proportion of population adapting smart meters and DDSM by using following Eq. 9.

$$\begin{aligned} \dot{x} &= [u(e^r, x) - u(x, x)]x_r \\ u(x, x) &= \sum_{r \in s} u(e^r, x)x_r \end{aligned} \quad (9)$$

The expected payoff of an agent is denoted by $u(x, x)$; the payoff an agent with DDSM is denoted by $u(e^x, x)$.

From Fig. 7 in optimized curve, the domestic load reduces by 17 at 100% peak load, while compared with unoptimized curve. This means that all agents will willingly adopt smart meters and DDSM [19]. Figure 8 shows the payoffs of an agent with and without DSM.

Various comparisons between different techniques like load shifting technique and decentralized demand side management are noted in Table 1.

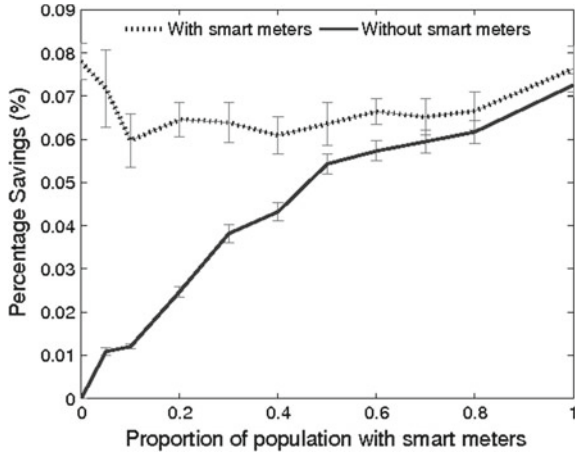


Fig. 8 For different proportions of the population, savings of agents with and without DDSM and by using smart meters

Table 1 Performance analysis

Load shifting technique	User-defined control for decentralized demand side management
1. The method which is proposed composed of modern system identification and it enables the user to schedule their loads	1. We introduced this technique (DDSM) which permits the users to defer their loads according to grid prices
2. The main objective of this technique is to reduce peak loads and it provides facility to influence the utilization of electricity	2. Moreover, this technique says that “simply leaving the smart meters to react to price or frequency fluctuations can cause all devices to respond at the same time which leads to generate peak demand [23]”
3. To decrease utilization of energy, energy management units like smart meters are used to communicate with local area networks (LAN) and home area networks (HAN)	3. In order to overcome this problem, some control strategies are implemented which allows proper coordination among smart meters
4. Strategy for load shifting in demand side management is based on heuristic optimization	4. The above technique of user-defined approach will represent many individuals’ smart homes and in meanwhile large number of such smart homes are simulated

5 Conclusions

In the above-proposed techniques, there are many features that can be improved but our concentration is mainly fascinated on distribution side demand side management. By using above-proposed techniques, it is possible to improve efficiency of the grid, capacity of grid, quality of power supply and sustainability and it is possible to reduce carbon footprints by using proposed technologies and by accomplishing advanced technologies [16].

All the above-discussed DSM techniques are used to flatten the load curve and in order to reach desired demand. And also in this paper, we introduced a smart home model and presented our decentralized demand side management (DDSM) technique through which all agents can coordinate in decentralize manner. Overshoots can be reduced up to 17% and carbon emissions can be reduced up to 6% and performance of the grid can be increased by implementing the mechanism of DDSM. We have proven that, because of increased electrification, our decentralized demand side management will mitigate the respective peaks in load demand curve.

6 Future Scope

Effective future work is to incorporate both climate and price forecasting in order to prolong all the above mechanisms toward effective commercial, industrial and domestic consumers in the society. And to examine our proposed techniques in situations where some of the buildings are not involved with agents by which energy providers has to optimize their behavior.

References

1. Balakumar P, Sathiya S (2017) Demand side management in smart grid using load shifting technique. In: Electrical, instrumentation and communication engineering (ICEICE), 2017 ieece international conference on 2017 Apr 27, pp 1–6, IEEE
2. Gelazankas L, Gamage KA (2014) Demand side management in smart grid: a review and proposal for future direction. *Sustain Cities Soc* 11:22–30
3. Ahmad W et al (2019) Pro utility pro consumer comfort demand side management in smart grid. In: Workshops of the international conference on advanced information networking and applications. Springer, Cham
4. U.S. Department of Energy (2006) Benefits of demand response in electricity markets and recommendations for achieving them
5. Shuja SM et al (2019) Towards efficient scheduling of smart appliances for energy management by candidate solution updation algorithm in smart grid. In: International conference on advanced information networking and applications, Springer, Cham
6. Kothari DP, Nagrath IJ (2009) *Modern power systems*, 3rd edn. McGraw-Hill, New Delhi
7. Albadi MH, E-Saadany EF (2007) Demand response in electricity markets: an overview. In: IEEE power engineering society general meeting

8. Palensky P, Dietrich D (2011) Demand side management: demand response, intelligent energy systems, and smart loads. *Ind Inf* 7(3):381–388
9. Charles River Associates (2005) Premier on demand side management with an emphasis on price-responsive programs
10. Tiptapakorn S, Lee W (2007) A residential consumer-centered load control strategy in real time electricity pricing environment. In: *Proceedings of north American 39th IEEE power symposium (NAPS-2007)*, pp 505–510
11. Cheng Y (2012) Architecture and principles of smart grid for distribution power generation and demand side management. In: *Proceedings of the 1st international conference on smart grids and green IT systems (SMARTGREENS 2012)*, pp 5–13
12. European Commission (2006) *European smart grids technology platform: vision and strategy for Europe's electricity networks of the future*. Luxembourg: Office for Official publication of the European communities. Eur 22040
13. Mohammad N, Yateendra M (2019) *Demand side management and demand response for smart grid. Smart grids and their communication systems*, Springer, Singapore, pp 197–231
14. Fuller JC, Schneifer KP, Chassin D (2011) Analysis of residential demand response and double action markets. In: *IEEE power and energy society general meeting*
15. Ramchurn SD, Vytelingum P, Rogers A, Jennings NR (2011) Agent based control for decentralized demand side management in the smart grid. In: *Proceedings of the 10th international conference on autonomous agents and multi agent systems (AAMAS 2011)*, pp 5–12
16. Gellings CW, Chamberlin JH *Demand side management: concept and methods*
17. Gellings CW (1985) The concept of demand side management for electric utilities. *Proceedings of the IEEE* 73(10):1468–1470
18. Gellingd CW, Chamberlin J (1988) *Demand side management: concepts and methods*. The Fairmont press Inc., Lelburn
19. Schuler RE (2004) Self-regulating markets for electricity: Letting customers into the game. In: *Proceedings of IEEE power systems conference and exposition 3*, pp 1524–1528
20. Global Smart Energy (2008) *The electricity economy: new opportunities from the transformation of the electric power sector*
21. Zhuo M, Goa Y, Li G (2008) Study on improvement of available transfer capability by demand side management. *Electric Utility Deregul Restruct Power Tech* 2008:545–550
22. Longathiran T, Srinivasan D (2011) Demand side management in smart grid using heuristic optimization. *IEEE Trans Smart Grid* 3(3):1244–1252
23. Strbac G (2008) Demand side management: benefits and challenges. *Energy Policy* 36(12):4419–4426

Improvement of the Current Profile in Grid-Tied Hybrid Energy System by Three-Phase Shunt Active Filter



Rudranarayan Senapati, Sthita Prajna Mishra, Vamsiram Illa and Rajendra Narayan Senapati

Abstract This is all about harmonic the current mitigation (as one of the major power quality issues) through the imaginary power owing to their precise and audacious action by shunt active filter (ShAF) build on sinusoidal current control strategy (SCCS) in a grid-tied PV system. The SCCS is employed to liberate sinusoidal current commenced from the supply additionally with a burly synchronizing (phase-locked loop) circuit, concise the controller for ShAF. Explicitly by a sinusoidal current control based controller, ShAF acts as a harmonic isolator amidst with load and supply. The performance of the said technique is evaluated using MATLAB R2016a under passive load (nonlinear load), and the observations are discussed. The efficacy of the ShAF in harmonics mitigation is validated through the proposed simulation. The total harmonic distortion (THD) of current and voltage ascertains controller's practicability for the ShAF delivering harmonic separation of passive loads in the grid-tied hybrid energy system.

Keywords Power quality · Shunt active power filter · Sinusoidal current control strategy · Custom power devices · Total harmonic distortion

R. Senapati · V. Illa

School of Electrical Engineering, KIIT Deemed to be University, Bhubaneswar, Odisha 751024, India

e-mail: rsenapatifel@kiit.ac.in

V. Illa

e-mail: vamsiram.illa@gmail.com

S. P. Mishra (✉)

Department of EEE, GMR Institute of Technology, Rajam, Andhra Pradesh 532127, India

e-mail: sthitaprajna.m@gmrit.edu.in

R. N. Senapati

Bhubaneswar, Odisha 751002, India

e-mail: rajendra0507@gmail.com

© Springer Nature Singapore Pte Ltd. 2020

R. Sharma et al. (eds.), *Innovation in Electrical Power Engineering, Communication, and Computing Technology*, Lecture Notes in Electrical Engineering 630,

https://doi.org/10.1007/978-981-15-2305-2_4

1 Introduction

There is an overwhelming advance of electrical power in the preceding years because of the progress in scientific know-how to satisfy the growing expectations of consumer as well as fiscal gain. The current research reveals the steady advancement in scientific way to tap energy from renewable energy sources (RES) instead of relying over the widespread energy sources that are not much trustworthy and impose adverse effect on the environment. Power generation through RES prospers in accomplishing a viable energy world. Power quality (PQ) is a vital factor of the distribution system that confirms obtaining disturbance free and stable power. Poor supply quality might harm the operation of the connected loads and additionally results with trigger frequency imbalances. Also, the lifespan of the equipment will be afflicted. The large penetration of RE is a bonus for the top need but might result in problematic high PQ issues. DG integration inside a circulation network creates wavering of voltage and voltage unbalance founded on its irregular nature. Voltage enhancement inside a distribution network is responsive to short-term changes that might end in unusual operation associated with the voltage regulation products deployed within the network. The existing quality dilemmas are developed with all their variation into the irradiance that might maintain for a smaller or longer passage of time period alongside PV-integrated system. The voltage difference impacts the voltage at the point of common coupling (PCC). Hence, aiding with the DG associated systems, the PQ dilemmas are generally governed by voltage rise, imbalance and flicker within the working system. Admit of power electronics devices develops a compact and reliable system additionally responsible for the introduction of harmonics in the system. Harmonics issue might be important in the near foreseeable future as the integration of hybrid energy system (photovoltaic, wind, tidal, etc.) is growing day by day. Harmonics, in particular, are induced through DG inverters in the distribution system. The voltage harmonics could have reduced with their durable big-scale PV cluster connection point, but the impact of current harmonics might exist at higher-order frequencies.

Primarily, harmonics are incorporated due to the presence of nonlinear loads in the electrical network bringing abundant shortcomings in the network. The sarcastic current disturbs the origin of accessibility equipped enough to amend the distortion (the harmonic and the reactive part of load parameter), i.e. current [1]. Hence, it is essential to contemplate and amend the PQ issues and confine the THD within recommendation of IEEE standards. Therefore, for elimination of harmonics, the introduction of custom power devices (CPDs) in the grid system (specifically power filters) is vital [2]. Aiming on the various CPDs, specifically PFs, and the ShAF is a convincing alternate for minimization of harmonic as appeared due to nonlinear loads. To accomplish compensation, reference signal generation is considerable with an objective of design and control of active power filters (APF). Custom of APFs safeguards electrical appliances which are overstated by impoverished the PQ and evade the diffusion of causes in stabilities of the power systems.

2 Shunt Active Filter

Nowadays, ShAF is regularly used in commercial process around the globe. Controller of ShAF is discriminating and adaptive in nature. In other contest, it compensates the harmonic current component of particular nonlinear load, as well as records the fluctuation in harmonics at ease [3].

2.1 Configuration of ShAF

The schematic diagram of ShAF is shown in Fig. 1 which consists of two components, i.e. PWM converter (PWMC) and active filter controller (AFC).

A PWMC is liable to deal with power and incorporates the compensating current to be depleted from the system. The AFC is responsible to handle the signal and determines the actual time contemporary compensating current, passing continuously to PWMC. Mostly, ShAF works in a closed-loop method. It anticipates the current flowing through the load and estimates the instantaneous compensating/shunt reference current i_c^* for the PWMC. The ShAF uses either the voltage source converter (VSC) or the current source converter (CSC). CSC is used due to its firmness. These days, commercially used ShAF employs VSC owed to higher efficiency, the low preliminary cost as compared to CSC and reduced physical dimensions. It must be distinguished that no supply is given to the converter; rather an energy storing element (capacitor particularly for voltage-fed converter or inductor for current-fed converter) is connected at DC end of the converters as ShAF needs to act like a compensator. In supplement, there should be zero average energy exchange between the PFs and the power system [4].

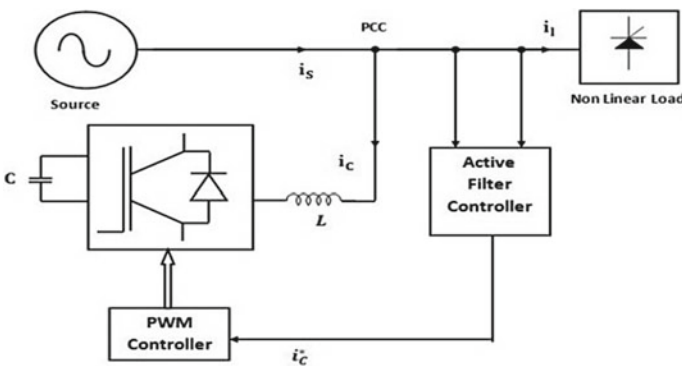


Fig. 1 Schematic diagram of ShAF

3 Control Strategy

Several methods are there for the design of a control algorithm towards active filtering. Among all of the active filters, the pq —theory is found to be an absolutely efficient fundamental for designing of controllers. The control strategies for active filters based on pq —theory are conferred here. The normal interpretation of the pq —theory illustrates that it is absurd to compensate the load current as well as compel the compensated source current to entertain ensuing optimum compensation attributes *concurrently* due to voltage harmonics in power system as well as imbalances in supply frequency: (1) a steady instantaneous source active power, (2) a sinusoidal source current and (3) the minimum supply RMS current which transfers energy to load with less loss in the transmission line. It is feasible to appease the above-mentioned three attributes simultaneously for 3- φ balanced sinusoidal voltages. But, for non-sinusoidal as well as irregular supply voltages, compensation of load current is carried by the ShAF assuring for a single optimal compensation only.

4 Sinusoidal Current Control Strategy

The sinusoidal current control strategy (SCCS) is based on instantaneous power theory, which in turn based on the transformation from abc —frame to $\alpha\beta 0$ —frame. But, the reason for not adopting control in abc —reference frame is that in a 3- φ system the three phases are mutually dependent on each other, so independent control of the quantities is difficult. To make the control simple, 3- φ quantities are converted into 2- φ mutually independent quantities, so that easier control is possible in pq —domain, which is a stationary reference frame. The purpose of choosing this control strategy is its simplicity in implementation. So far, several applications of this strategy have been seen in different kinds of literature. For a system with multiple renewable energy systems integrated, implementing a robust control becomes cumbersome, as the control of renewable itself requires a lot of complexities [5]. The control involves 3- φ quantities first converted into 2- φ quantities. Then, these three-phase quantities are used to evaluate the instantaneous powers in a time domain; both instantaneous active as well as reactive power can be estimated. By using low-pass filter, the harmonic power can be extracted, which can be used to set up the compensating current once the zero sequence power is known. The neutral point clamped capacitor voltage can be used to evaluate the zero sequence power. Hence, the above-mentioned method is termed as SCCS as the compensating current is sinusoidal in nature. Advantages of pq —theory over all other compensating theories are it can be valid for both steady state and transient state. Instantaneous power can be defined on $\alpha\beta 0$ —frame, i.e. in three-phase form. abc —frame to $\alpha\beta 0$ —frame transformation is also known as Clarke transformation. There is an obvious question raised for selection of the ShAF, and numerous reasons can be cited.

Here \bar{p}_0 is unidirectional energy flow as conventional active power representing \tilde{p}_0 as the oscillating component whose average value is zero. Interestingly, zero sequence power \bar{p}_0 cannot be obtained alone without \tilde{p}_0 , the oscillating component. Hence, the total zero sequence components always associated with both the average and oscillating component. The instantaneous zero sequence power components in the fundamental voltage and current or in harmonics do not add any impact on instantaneous real power and imaginary power. The total instantaneous active power is always same as the addition of instantaneous true power and instantaneous zero sequence power which includes both average and oscillating components. The instantaneous reactive power reveals the energy exchanged between system even in the harmonic and unbalance condition. Figure 3 shows the total instantaneous active power flow and instantaneous reactive power flow in between the two systems.

$p + p_0 \rightarrow$ Total instantaneous power flow in unit time.

$q \rightarrow$ Power exchange between three phases without any transfer of energy

The active and reactive current components derived from the instantaneous abc voltages and currents are given in Eq. (2):

$$\begin{bmatrix} i_\alpha \\ i_\beta \end{bmatrix} = \underbrace{\frac{1}{v_\alpha^2 + v_\beta^2} \begin{bmatrix} v_\alpha & v_\beta \\ v_\beta & -v_\alpha \end{bmatrix} \begin{bmatrix} p \\ 0 \end{bmatrix}}_{\text{Active Part}} + \underbrace{\frac{1}{v_\alpha^2 + v_\beta^2} \begin{bmatrix} v_\alpha & v_\beta \\ v_\beta & -v_\alpha \end{bmatrix} \begin{bmatrix} 0 \\ q \end{bmatrix}}_{\text{Reactive Part}} \quad (2)$$

With the use of inverse Clarke transformation, abc real and imaginary current may be obtained as follows:

$$\begin{bmatrix} i_{a(p)} \\ i_{b(p)} \\ i_{c(p)} \end{bmatrix} = \sqrt{\frac{2}{3}} \begin{bmatrix} 1 & 0 \\ -\frac{1}{2} & \frac{\sqrt{3}}{2} \\ -\frac{1}{2} & -\frac{\sqrt{3}}{2} \end{bmatrix} \left(\frac{v_\alpha i_\alpha + v_\beta i_\beta}{v_\alpha^2 + v_\beta^2} \right) \begin{bmatrix} v_\alpha \\ v_\beta \end{bmatrix} \quad (3)$$

and

$$\begin{bmatrix} i_{a(q)} \\ i_{b(q)} \\ i_{c(q)} \end{bmatrix} = \left(\frac{v_{ab}i_c + v_{bc}i_a + v_{ca}i_b}{v_{ab}^2 + v_{bc}^2 + v_{ca}^2} \right) \begin{bmatrix} v_{bc} \\ v_{ca} \\ v_{ab} \end{bmatrix} \quad (4)$$

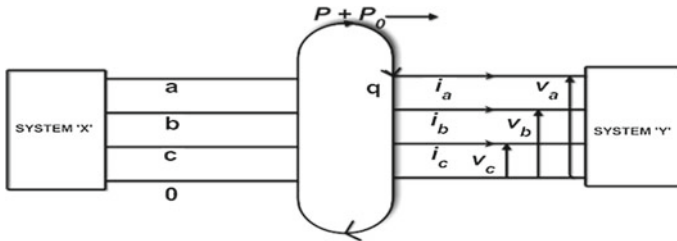


Fig. 3 Physical significance of instantaneous power in $\alpha\beta 0$ —frame

where v_{ab}, v_{bc}, v_{ca} are the line voltages, $i_{a(p)}, i_{b(p)}, i_{c(p)}$ and $i_{a(q)}, i_{b(q)}, i_{c(q)}$ are the real and imaginary current components generating real and imaginary power, respectively. The line voltage does not contain any zero sequence components as represented in Eq. (5).

$$v_{ab} + v_{bc} + v_{ca} = 0 \tag{5}$$

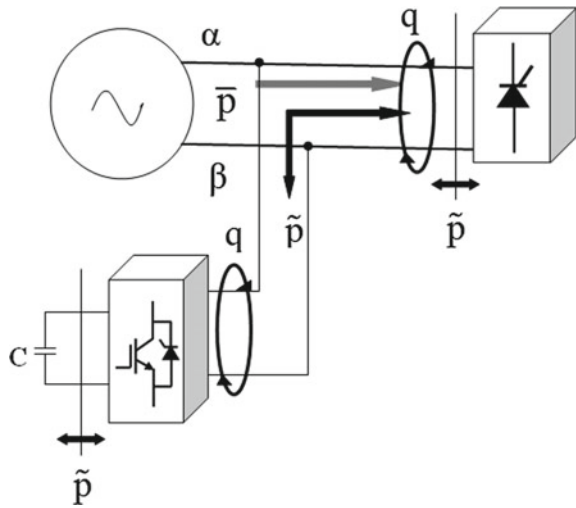
Hence, Eqs. (3) and (4) can be rewritten as expressed in Eq. (6)

$$\begin{bmatrix} i_a \\ i_b \\ i_c \end{bmatrix} = \begin{bmatrix} i_0 \\ i_0 \\ i_0 \end{bmatrix} + \begin{bmatrix} i_{a(p)} \\ i_{b(p)} \\ i_{c(p)} \end{bmatrix} + \begin{bmatrix} i_{a(q)} \\ i_{b(q)} \\ i_{c(q)} \end{bmatrix} \tag{6}$$

The basic block diagram revealing the performance of ShAF is shown in Fig. 4, illustrating different powers like fundamental active power and reactive power, harmonic active power, etc.

From Fig. 4, it is clear that the ShAF compensates the harmonic active power (\tilde{p}), power loss \tilde{p}_{loss} and reactive power q as well. Hence, it is able to maintain the power factor and THD as well. Certainly, the instantaneous power theory exercises explicitly for the design of regulators (controller) for the APFs [7].

Fig. 4 Optimal power flow provided by shunt current compensation



4.1 Control Block Diagram

Figure 5 exemplifies the control block of SCC technique with 3- ϕ ShAF. The control block of the AFC for SCC includes positive voltage detector that includes phase-lock loop (PLL) circuit, DC voltage regulator, instantaneous power calculation block, compensating power selection block and compensating reference current calculation block. The 3- ϕ voltage can be transformed into 2- ϕ voltage with the help of Clarke transformation by the Eq. (7) which further participates in power calculation module to ascertain both watt power and reactive power besides 2- ϕ current i_α and i_β .

$$\begin{bmatrix} v_0 \\ v_\alpha \\ v_\beta \end{bmatrix} = \sqrt{\frac{2}{3}} \begin{bmatrix} \frac{1}{\sqrt{2}} & \frac{1}{\sqrt{2}} & \frac{1}{\sqrt{2}} \\ 1 & -\frac{1}{2} & -\frac{1}{2} \\ 0 & \frac{\sqrt{3}}{2} & \frac{\sqrt{3}}{2} \end{bmatrix} \begin{bmatrix} v'_a \\ v'_b \\ v'_c \end{bmatrix} \tag{7}$$

Similarly, three-phase line current can be converted into 2- ϕ by using Clarke transformation as given in Eq. (8) which helps in calculating true and imaginary power including 2- ϕ voltage (v'_α and v'_β).

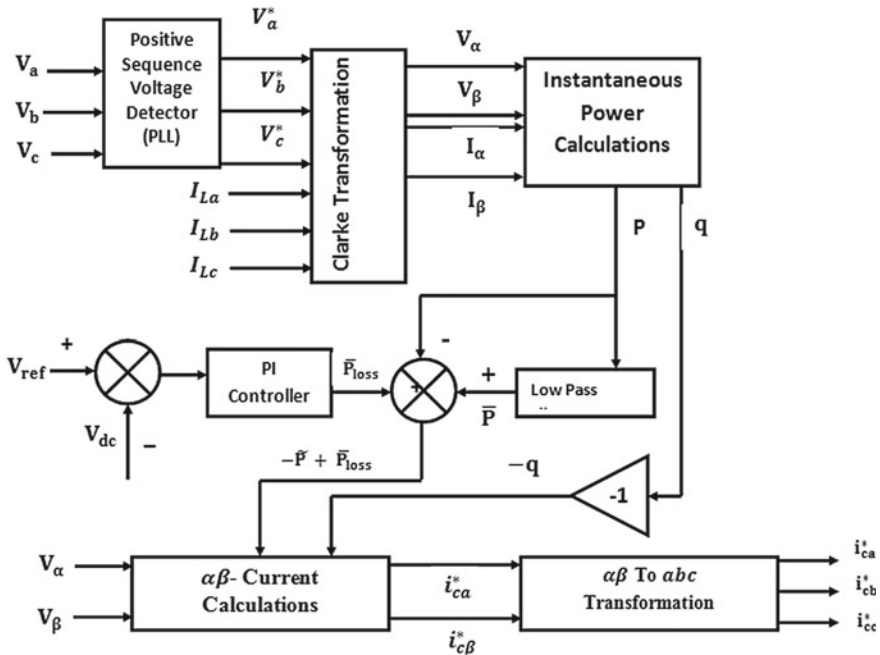


Fig. 5 Block diagram of a sinusoidal current control strategy

$$\begin{bmatrix} i_0 \\ i_\alpha \\ i_\beta \end{bmatrix} = \sqrt{\frac{2}{3}} \begin{bmatrix} \frac{1}{\sqrt{2}} & \frac{1}{\sqrt{2}} & \frac{1}{\sqrt{2}} \\ 1 & -\frac{1}{2} & -\frac{1}{2} \\ 0 & \frac{\sqrt{3}}{2} & \frac{\sqrt{3}}{2} \end{bmatrix} \begin{bmatrix} i_a \\ i_b \\ i_c \end{bmatrix} \quad (8)$$

The benefit of implementing the Clarke transformation is to convert 3- ϕ system into the 2- ϕ and allows independent control in two phases. Three instant powers, zero sequence component, active component p and reactive component q with instant phase voltages and line currents, are expressed in Eq. (9):

$$\begin{bmatrix} p_0 \\ p \\ q \end{bmatrix} = \begin{bmatrix} v_0 & 0 & 0 \\ 0 & v'_\alpha & v_\beta \\ 0 & v_\beta & -v'_\alpha \end{bmatrix} \begin{bmatrix} i_0 \\ i_\alpha \\ i_\beta \end{bmatrix} \quad (9)$$

The expression for watt and VAR power is bestowed in Eqs. (10) and (11) respectively.

$$p = v'_\alpha \cdot i_\alpha + v'_\beta \cdot i_\beta \quad (10)$$

$$q = v'_\beta \cdot i_\alpha + v'_\alpha \cdot i_\beta \quad (11)$$

The SCCS optimizes the entire algorithm of the controller for 3P3W ShAF compensating the oscillating watt and VAR power of the load (constant instantaneous power control strategy).

5 Results and Simulation Analysis

The analysis of ShAF is performed in two different environments as given below:

- A. Behavioural study of ShAF for 3P3W system with passive nonlinear load.
- B. Behavioural study of ShAF for a hybrid system of PV-grid with constant irradiance condition.

The nonlinear load parameters for ShAF are given in Table 1.

Table 1 Load parameter

Item	Value	
	Case—A	Case—B
Resistance	60 Ω	10 Ω
Inductance	0.15 mH	–
Grid voltage	2 kV	230 V (RMS)
DC link capacitance	10,000 μ F	200 μ F
PV voltage	–	104 V

5.1 ShAF for a 3- ϕ 3-Wire (3P3W) System with Nonlinear Load Condition

The simulation results so obtained are discussed as follows.

Figure 6a represents the performance of source voltage considering the ShAF resulting source voltage characteristic in phase with the Fig. 6b presenting the performance of the source current of a 3 ϕ 3W system. Because of nonlinear load (i.e. RL rectifier circuit), the load voltage and load current are distorted and unbalanced in the absence of compensation, but applying SCCS, characteristics of both load voltage and current become balanced and smooth as in Fig. 6a and b. The circuit breakers (CB) were given a time delay of 0.1 s to see the actual performance before the inception of the ShAF into the circuit. The nonlinear behaviour of the load giving rise to distortions can be seen during the first 0.1 s. After this, due to the effect of ShAF on the system, the balanced and distortion-free current can be observed. With the

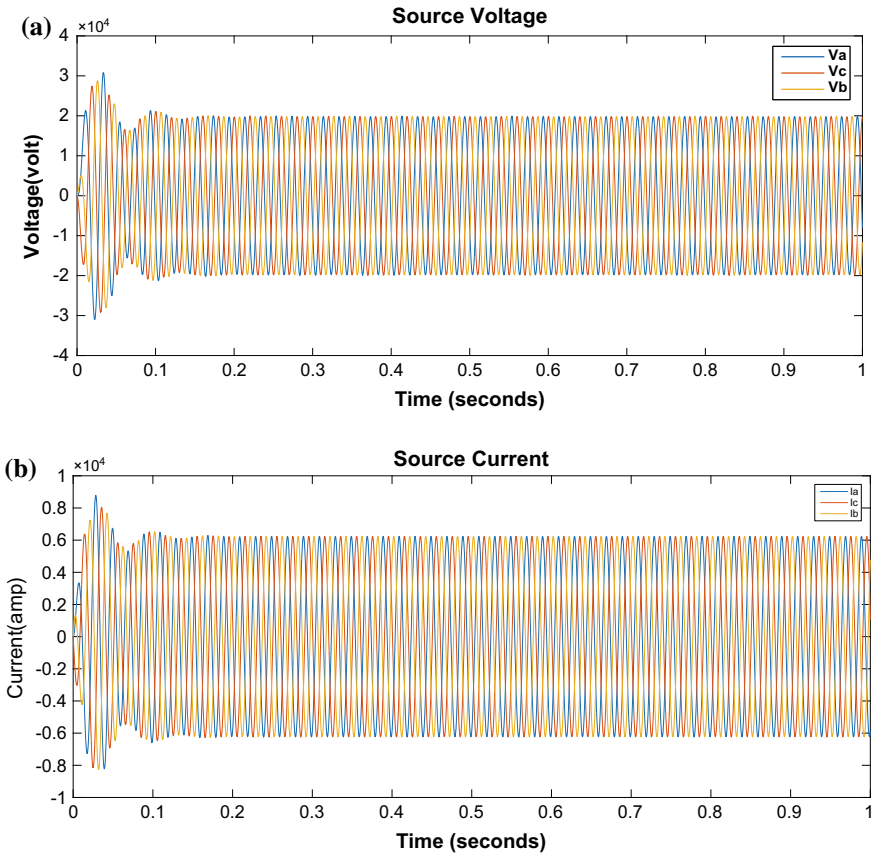


Fig. 6 a Source voltages. b Source currents

introduction of ShAF, the source current waveform is obtained with peak amplitude 600A. These waveforms disclose the compensation of ShAF for the disturbances at the source end. Figure 7a and b represent load end voltage and current, respectively. Figure 8 represents compensating waveforms of ShAF. The initial distortion observed in Fig. 8a and b for the first 0.1 s is due to the operation of CB as discussed earlier. The load is found to have sinusoidal terminal voltage. It draws a non-sinusoidal current making the source current to distort. The harmonic in source current has been eliminated using ShAF. The initial transients observed in Fig. 8a and b and subsequent figures for the first 0.1 s are due to the operation of CB which has already been discussed. The FFT analysis of the source current is shown in Fig. 9. It is observed that besides fundamental, fifth, seventh, ninth harmonics exist, but these harmonics are quite suppressed. The fifth harmonic percentage is little higher than 0.02%, while that of the 7th harmonic is less than 0.01%. The resultant THD of source current is 0.03% because of the ShAF compensation process.

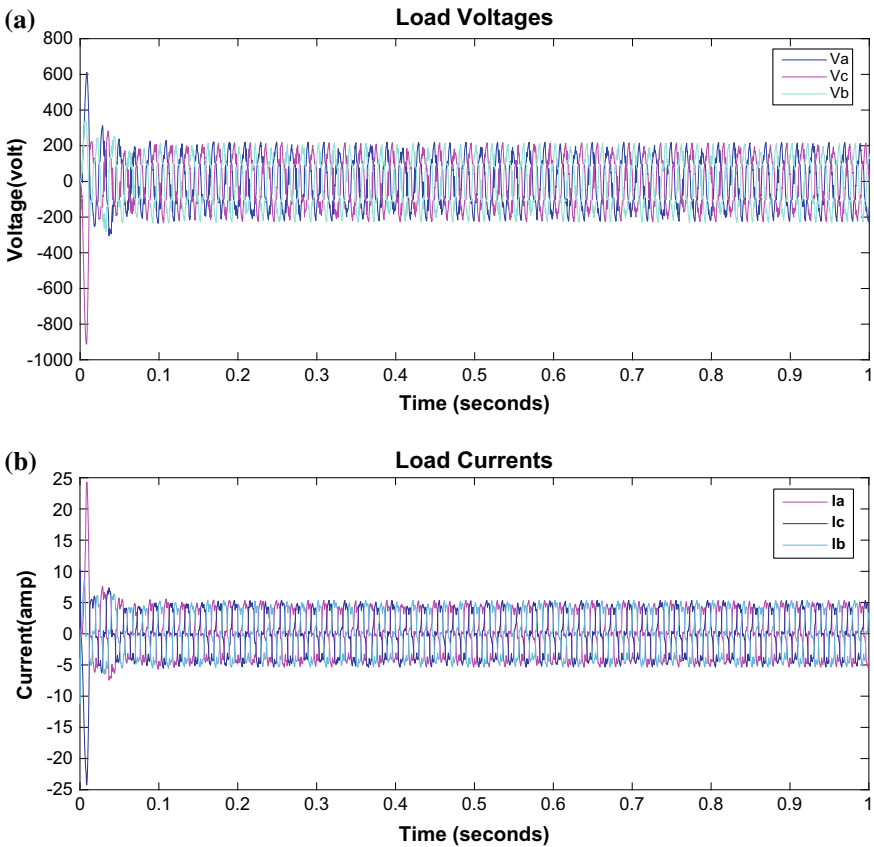


Fig. 7 a Load end voltage. b Load end current

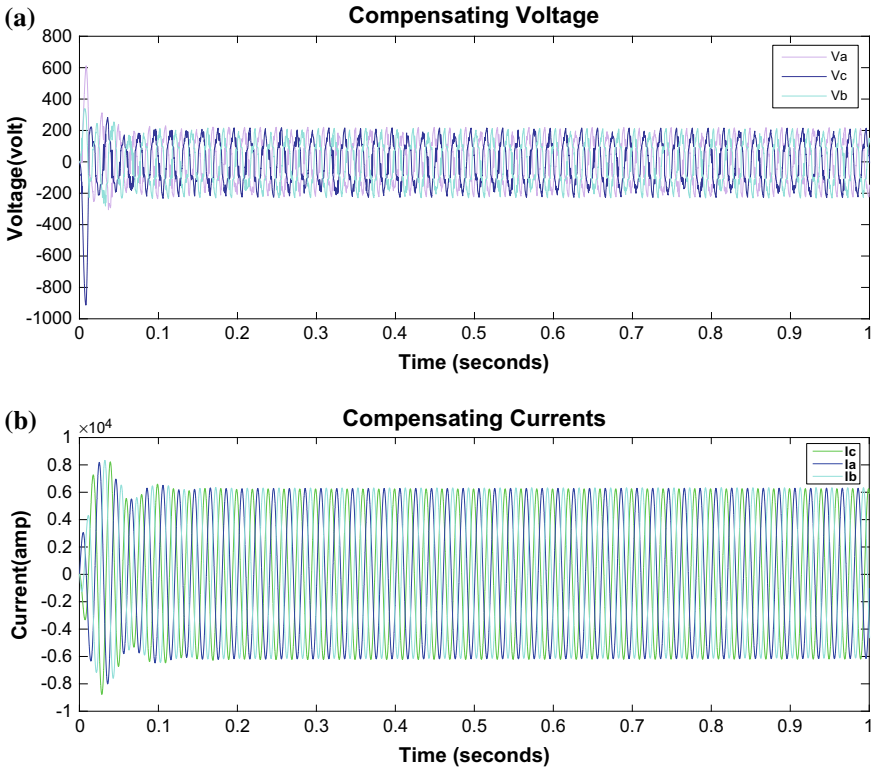


Fig. 8 a Compensating waveforms of ShAF: shunt voltage. b Compensating waveforms of ShAF: shunt current

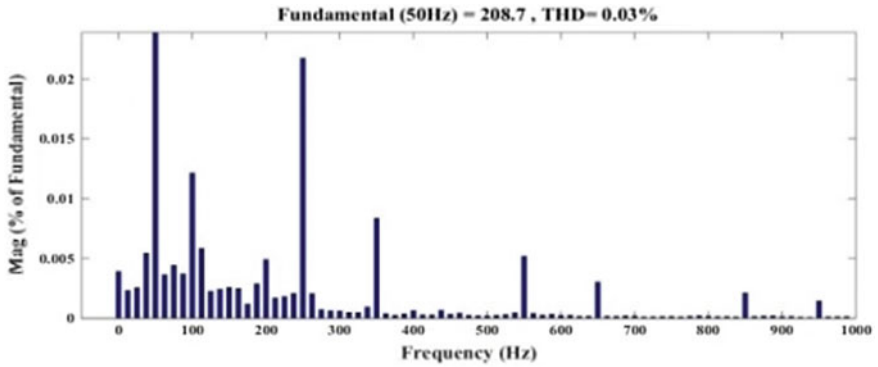


Fig. 9 FFT analysis of source current

5.2 For a PV-Grid System (Constant Irradiance Condition)

Figure 10 presents the current injection by the ShAF. The waveforms so associated disclose about the compensation of the abnormalities by the ShAF at the source end. Additionally, the current THD of grid-injected voltage end is obtained as 1.40% because of the compensation of ShAF. Similarly, Fig. 11 presents grid-injected voltage (230 V) and current with RMS value of 1.782A. From the FFT analysis of grid-injected current in Fig. 12, the THD in grid-injected current is 1.4%. The smoothness of the voltage and the current was due to the action of ShAF. The grid-injected voltage and current are almost sinusoids and do not have a significant content of dominant harmonics. It is observed that more of the current is diverted through the filter. So, it can be inferred that the shunt component must have high current carrying capacity. Figure 13a and b show the PV output voltage and the current waveform. The fuel cell and battery voltage are fed to common DC link to obtain similar waveform like PV output voltage. The DC Link voltage does not fluctuate much. Its fluctuation is around 1.25 V, which is within a limit of 5%. The THD of grid-injected current waveform is 1.4%. There exists only one dominant harmonics, i.e. fifth harmonics, which has been suppressed significantly. Its value is of the order of 0.1%. Some of the inter-harmonics of the very low magnitude were found to be present. Although these inter-harmonics are not of concern, these are still can be eliminated by the passive filter. The above analysis infers the injected current waveform of the ShAF that is alternating which indicates the achievement on the basis of the SCCS. Besides, it furnishes effective injection of power to the grid in the interconnected mode as enviable.

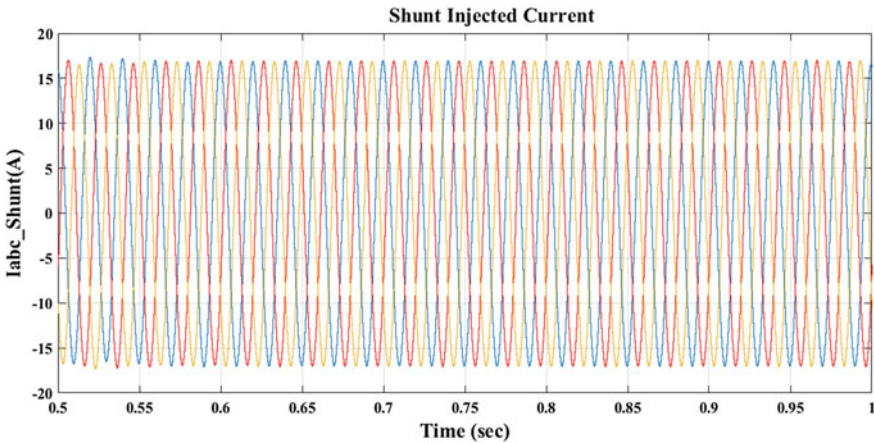


Fig. 10 Injected current by shunt compensator of a hybrid network of PV-grid system

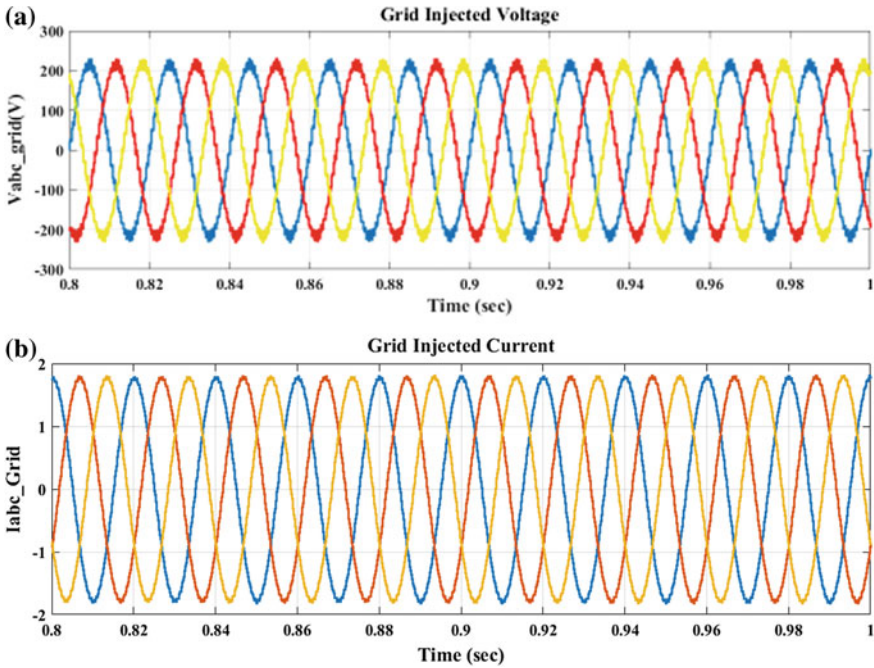


Fig. 11 a PV-grid network: grid-injected voltage. b PV-grid network: grid-injected current

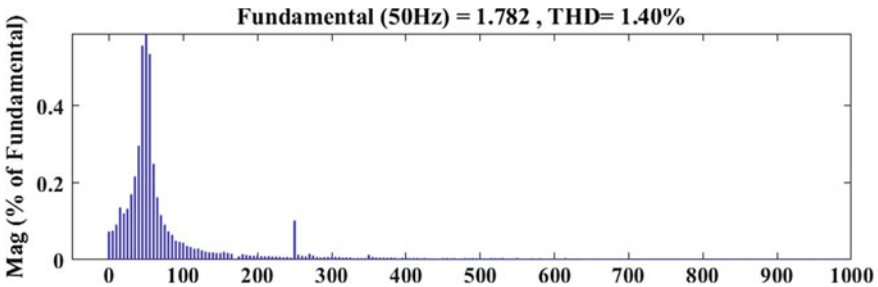


Fig. 12 Harmonic analysis of grid-injected current waveform

6 Conclusion

The ShAF based on SCCS offers assurance against the current harmonics as well as improves the power factor. The grid-injected current in case of ShAF under the PV-integrated condition is found to be 1.4%. The efficacy of the proposed methodology for ShAF can be validated by comparing the performance of some other techniques proposed by other authors as discussed in Table 2.

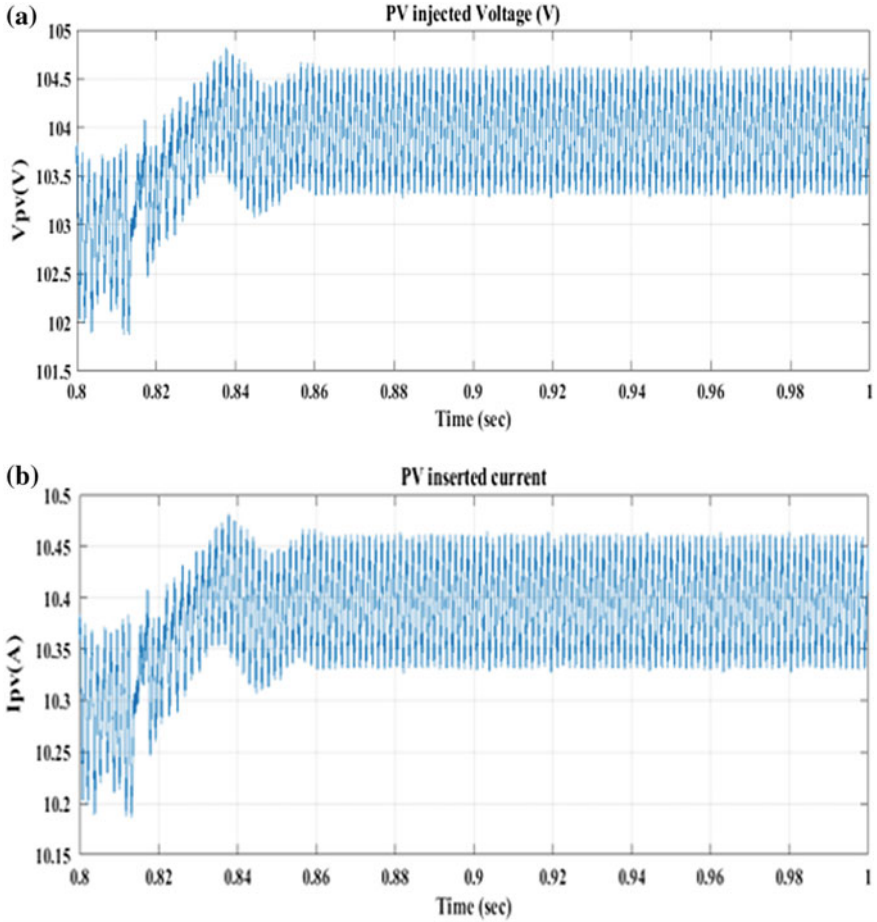


Fig. 13 a PV output voltage. b PV output current

Table 2 Validation for shunt active filter

Author	Proposed methodology	Grid Current THD (%)
Jain et al. [8]	Fuzzy logic controller	1.42
Tang et al. [9]	ShAPF with LCL filter	3.49
Proposed sinusoidal current control strategy	SCCS applied to 3P3W strategy	1.40

References

1. Aredes M, Hafner J, Heumann K (1997) Three-phase fourwire shunt active filter control strategies. *IEEE Trans Power Electron* 12(2):311–318
2. Senthilkumar A, Poongothai K, Selvakumar S, Silambarasan M, Raj PADV (2015) Mitigation of harmonic distortion in microgrid system using adaptive neural learning algorithm based shunt active power filter. *Procedia Technol* 21:147–154
3. Akagi H, Watanabe EH, Aredes M (2007) *Instantaneous power theory and applications to power conditioning*, vol 31. Wiley
4. Senapati R, Sahoo RK, Senapati RN, Panda PC (2016) Performance evaluation of sinusoidal current control strategy unified power quality conditioner. In: *International conference on electrical, electronics, and optimization techniques (ICEEOT)*, pp 1404–1408. IEEE
5. Senapati R, Sahoo RK, Pradhan S, Senapati RN (2017, August). Sinusoidal current control strategy for 3-phase shunt active filter in grid-tied PV system. In: *2017 International conference on energy, communication, data analytics and soft computing (ICECDS)*, pp 1272–1277. IEEE
6. Senapati R (2018) Study and analysis of performance of 3-phase shunt active filter in grid-tied PV-fuel cell system employing sinusoidal current control strategy. *Int J Renew Energy Res (IJRER)* 8(1):67–81
7. Senapati R, Senapati RN, Behera P, Moharana MK (2016, October) Performance analysis of unified power quality conditioner in a grid connected PV system. In: *2016 International conference on signal processing, communication, power and embedded system (SCOPEs)*, pp 416–420. IEEE
8. Jain SK, Agrawal P, Gupta HO (2002) Fuzzy logic controlled shunt active power filter for power quality improvement. *IEE Proc-Electr Power Appl* 149(5):317–328
9. Tang Y, Loh PC, Wang P, Choo FH, Gao F, Blaabjerg F (2012) Generalized design of high performance shunt active power filter with output LCL filter. *IEEE Trans Ind Electron* 59(3):1443–1452

Novel Bludgeon-Shaped Microstrip Antenna with DGS for UWB Applications with Notch Band Characteristics



**B. Ramesh, K. P. Vinay, Lal BabuPrasad, K. S. Ravi Kumar
and D. V. Rama Koti Reddy**

Abstract In this work, a novel bludgeon-shaped microstrip patch antenna with defected ground structure (DGS) is recommended for UltraWide Band (UWB) i.e., (3.1–10.6 GHz) applications with band notch characteristics. The encouraged antenna is simulated and fabricated using RT DURIOD 5880 substrate with epsilon value of 2.2 having the scale of $60 \times 60 \times 1.6 \text{ mm}^3$. The circular-shaped patch is chosen with radius of 14 mm and 50Ω microstrip line feeding technique is used for the simplicity of the design. The circular slots and circular-shaped patch are delivered to improve the radiation traits and overall performance of the recommended antenna. To acquire the UWB frequency of operation, rectangular defected ground structure (RDGS) is implemented in the ground plane. Further, three rectangular slots of different dimensions are etched to accomplish the band notch configuration. The recommended antenna is simulated using 3D electromagnetic simulation tool CST MICROWAVE STUDIO Version 16. The evolved antenna is tested using MS46122B 20 GHz vector network analyzer. The effectiveness of the antenna is proven the usage of the specifications like return loss (S_{11}), VSWR, and simulated radiation patterns.

Keywords Defected ground structure (DGS) · UltraWide band (UWB) · Notch band · Microstrip line feed · CSTMWS and vector network analyzer

B. Ramesh · K. P. Vinay · L. BabuPrasad · K. S. Ravi Kumar (✉)
Department of ECE, Raghu Engineering College, Visakhapatnam 531162, India
e-mail: srinivas.ravikumar260@gmail.com

B. Ramesh
e-mail: rameshboddu11@gmail.com

K. P. Vinay
e-mail: phanikvinay@gmail.com

L. BabuPrasad
e-mail: gulablal@gmail.com

D. V. Rama Koti Reddy
Department of Instrumentation, Andhra University, Visakhapatnam 530003, India
e-mail: rkreddy_67@yahoo.co.in

© Springer Nature Singapore Pte Ltd. 2020
R. Sharma et al. (eds.), *Innovation in Electrical Power Engineering, Communication, and Computing Technology*, Lecture Notes in Electrical Engineering 630,
https://doi.org/10.1007/978-981-15-2305-2_5

1 Introduction

The range of frequencies from 3.1 to 10.6 GHz is declared for commercial operations of UWB by federal communication commission (FCC) [1]. Nowadays the design and the development of UltraWide band systems have gathered attention of many researchers in the communication system because of its inevitable advantages like low cost, high data rate, simple hardware configuration and low power consumption in real applications. Moreover, there exist some interference in the UWB systems due to the presence of some narrowband communication systems such as WLAN (5.15–5.825 GHz), Wi-max (3.3–3.6 GHz), European C-band (3.8–4.2 GHz), and X-band satellite communication systems (7.25–8.4 GHz). Hence, it is far vital to implement notched UWB antennas to avoid the interference from the present slender band communication systems. To conquer this trouble, numerous designs are applied inside the literature like single notch and multi band notch UWB antennas. One of the simplest methods of obtaining notch band characteristics is by introducing different shapes of slots in the radiating patch of UltraWide band antennas.

Recently, double notch characteristics are created by embedding H-shaped slots [2], U-shaped slots [3], T-shaped slots [4], elliptical-shaped slot [5], C-shaped slot along pair of U-shaped parasitic resonators [6], modified I-shaped slot along capacitive loading [7], two quasi-square radiating patches, split ring resonators (SRRs) [8], CSRRs [9, 10], and inserting parasitic elements of different shapes [11–14].

A miniaturized bludgeon shaped with DGS for twin band-notched UWB antenna is carried out on this letter. The bludgeon formed radiating patch is used to reduce the mutual coupling and to get most field strength in the specified direction. The rectangular fashioned DGS is used to reap UWB operation. The slots at the DGS are etched to get notch band traits. The proposed antenna is suitable for surveillance systems, wireless body area networks (WBANs), sensing and portable Internet of things (IoT) applications in the UWB region. The simulated outcomes are furnished and compared with measured values.

2 Antenna Design

The geometry of the completed antenna is illustrated in Fig. 1 together with the design parameters. The technical specifications of the designed antenna are shown in Table 1.

The recommended antenna is engraved on a RT 5880 substrate having a dielectric constant (ϵ_r) = 2.2 and tangent loss of 0.078 with thickness of $h = 1.6$ mm. By using FR-4 substrate with $\epsilon_r = 4.3$, the desired notch band characteristics are not achieved, so the proposed antenna is designed using RT 5880 substrate. The recommended antenna is designed in the following steps. In step 1, a circular patch of radius 14 mm is designed along with a $60 * 60$ mm² ground plane. The radius of the radiating patch was evaluated using Eq. 1:

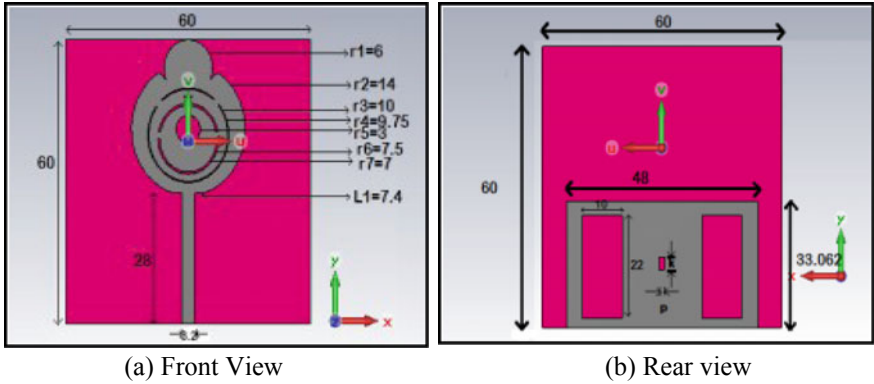


Fig. 1 Prototype of the implemented antenna

Table 1 Specifications of the designed antenna

Patch							
Parameter	r_1	r_2	r_3	r_4	r_5	r_6	r_7
Dimensions (in mm)	6	14	10	9.75	3	7.5	7
Substrate							
Parameters	l		b		H		
Dimensions (in mm)	60		60		1.6		
Ground plane							
Parameters	L		B		k		P
Dimensions (in mm)	48		33		1.79		1.3

$$\text{radius of the circular patch } a = (87.94/f_r\sqrt{\epsilon_r})\text{mm} \tag{1}$$

In step 2, the DGS is implemented on the ground plane and reduced from $60 * 60 * 0.2 \text{ mm}^3$ to $48 * 33 * 0.2 \text{ mm}^3$. In step 3, the DGS has been further optimized by etching two rectangular slots of dimensions $10 * 22 \text{ mm}^2$ which are mirror images, and another rectangular slot of dimensions $1.3 * 1.7 \text{ mm}^2$ has been etched at the center of the DGS. In step 4, a circular slot of radius 3 mm is taken out from the circular patch; a segment of radius 14.21 mm is removed from the top of the circular patch; and a circular-shaped ring of outer and inner radii of 7.5 mm and 7 mm, respectively, is removed from the circular patch as a next step of optimization. Further, the circular-shaped conducting material with a radius of 6 mm is integrated with the circular patch along two slots of dimensions $1.6 * 1.2 \text{ mm}^2$ which are implanted on the patch to join the circular ring and the circular patch and another circular ring of radii 10 and 9.75 mm is removed from the patch. Mutual coupling is reduced by choosing the ratio of the radius of the circular patch to the width of the feed far greater than 1. By reducing mutual coupling, the excitation energy is entirely

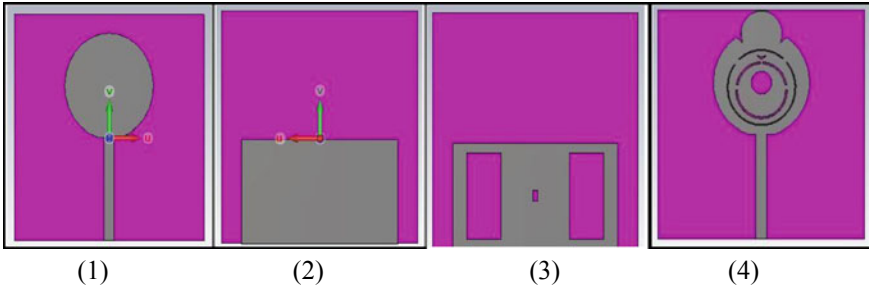


Fig. 2 Stepwise optimization figures of the implemented antenna

transferred to the circular radiating patch and optimizing the patch and DGS, the most field strength is radiated into free space. Figure 2 shows the stepwise optimizations of the recommended antenna.

3 Simulation and Measurement

The simulated return loss plot of optimization step-1 of the endorsed antenna with $60\text{ mm} \times 60\text{ mm}$ ground plane is proven in Fig. 3. The return loss of -21.49 dB is achieved at 15.05 GHz frequency with bandwidth of 30 MHz .

To improve the operating frequency of the recommended antenna, the DGS with dimensions $48 \times 33 \times 0.2\text{ mm}^3$ is implemented in step 2. Figure 4 depicts the return loss plot of optimization step 2 with rectangular DGS where the minimum return

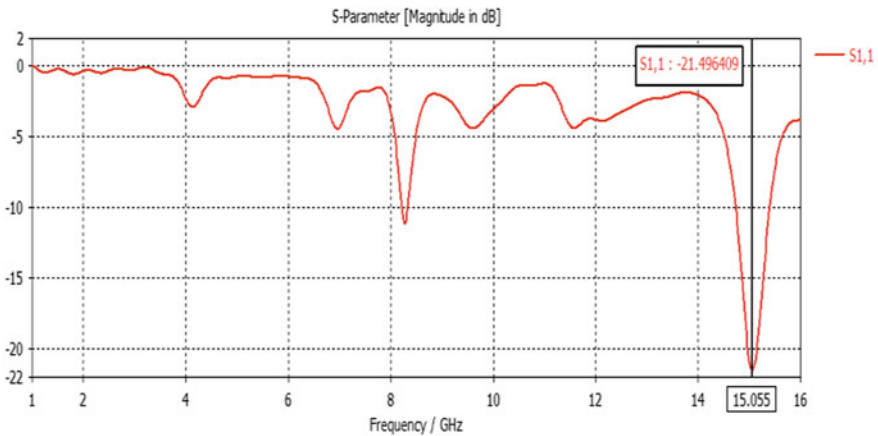


Fig. 3 S₁₁ plot for the optimization step 1

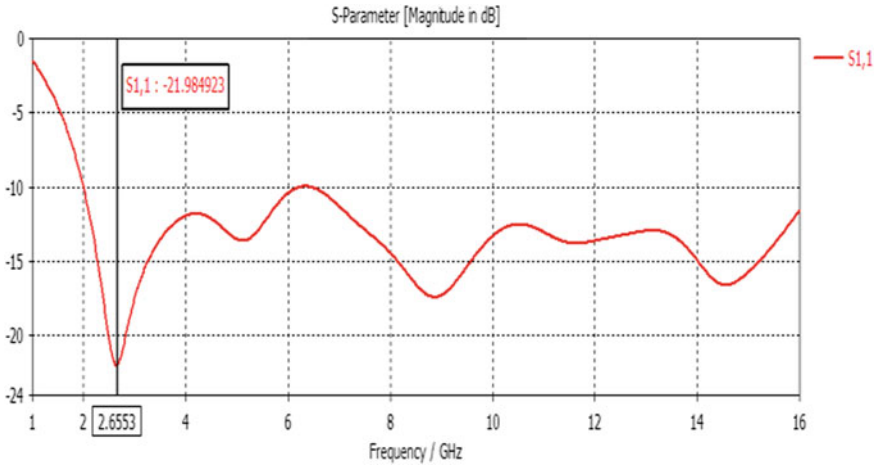


Fig. 4 S₁₁ plot for the optimization step 2

loss is -21.98 dB at a resonating frequency of 2.655 GHz and the total operating frequency is from 2 to 16 GHz, and the bandwidth is nearly 14 GHz.

In the third step, two rectangular shape slots are perforated on the partial ground plane to obtain the band notch characteristics. Because of these two rectangular slots, dual band notch characteristics are achieved from 3.87 to 4.13 GHz and 4.9 – 5.25 GHz. The simulated return loss plot of optimization step-3 is depicted in Fig. 5.

Further, a small rectangular slot is etched on the DGS and two more rejection bands are achieved at 5.43 – 5.61 GHz and $5.856.92$ GHz, respectively. The simulated return loss plot with three rectangular slots on the DGS is depicted in Fig. 6.

In the fourth step of optimization, the circular-shaped patch is optimized to get the bludgeon shape, and the performance of the antenna is improved in such way that the DGS may cause the reduction of the directivity and gain over the entire bandwidth. To the uniform gain and directivity, the patch is optimized into bludgeon shape. The DGS cause the reduction of gain from 6.2 to 2.574 dBi. The 3D-radiation pattern

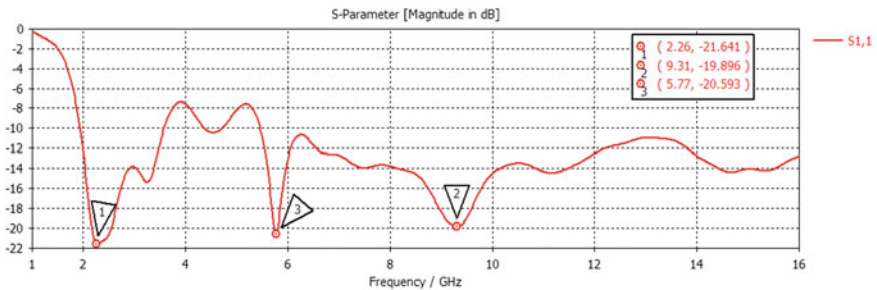


Fig. 5 S₁₁ plot for the optimization step 3

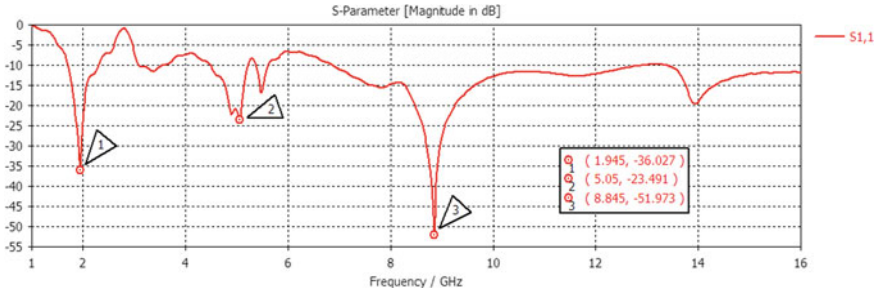


Fig. 6 S₁₁ plot for the optimization step 3

with DGS is shown in Fig. 7. The improved directivity of 5.023 dBi with bludgeon shape is depicted in Fig. 8.

To validate the simulated antenna results, the antenna is fabricated using the usage of RT DURIOD 5880 with epsilon of 2.2 and tested using the usage of MS46122B 20 GHz vector network analyzer. The fabricated antenna is depicted in Fig. 9.

The dimension setup of the fabricated antenna arrangement with vector network analyzer is proven in Fig. 10. The agreement between the simulated results and fabricated results is fairly right over the frequency band of interest. The return loss plot of fabricated antenna is shown in Fig. 11. The comparisons between simulated and measured are shown in desk-2 (Table 2).

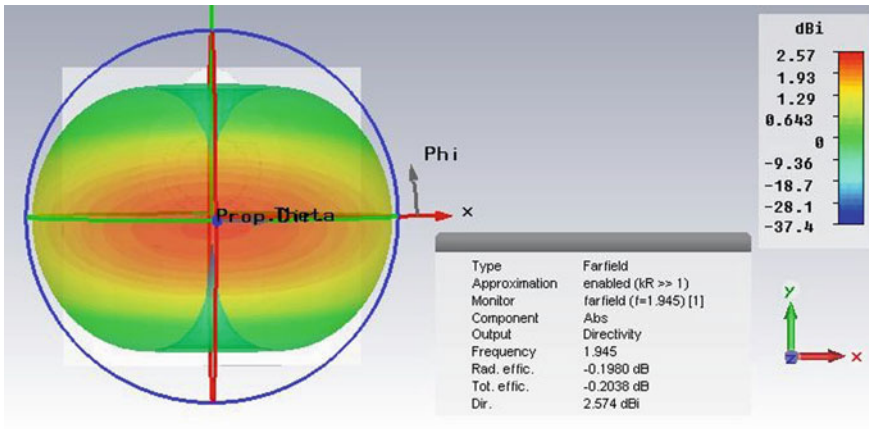


Fig. 7 Radiation pattern of the designed antenna with DGS without bludgeon shape

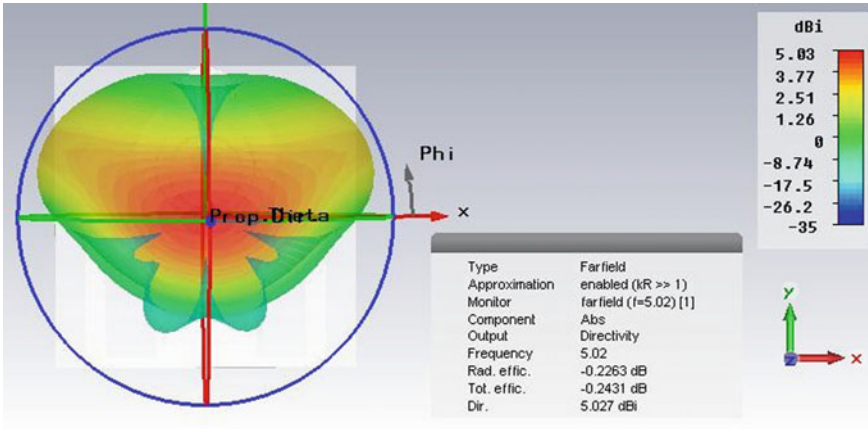


Fig. 8 Radiation pattern of the designed antenna with DGS with bludgeon shape

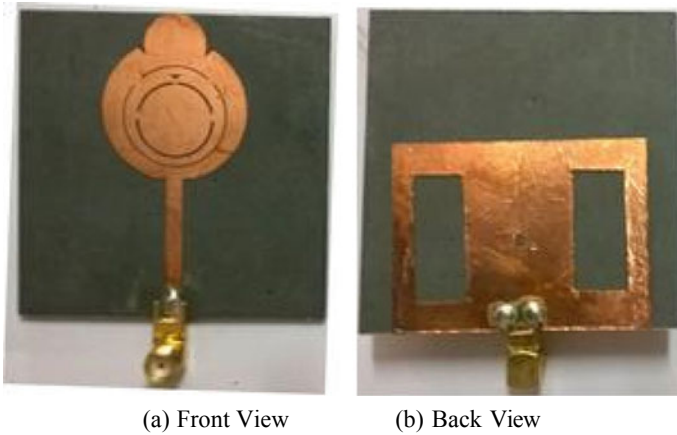


Fig. 9 Fabricated bludgeon-shaped antenna

4 Conclusion

In this letter, a novel bludgeon-shaped microstrip antenna is developed for UWB notch band applications like satellite communication, amateur radio communication, and radar applications. This band-notched nature is very much useful to reduce the mutual coupling between the nearby frequency wireless operating systems. A simple circular patch gives return loss of -21.49 dB at 15 GHz with operating bandwidth of 30 MHz which is enhanced by introducing rectangular slotted DGS in the ground plane to UWB frequency range with notch band operation. A novel modified circular ring slots called bludgeon shape is introduced in the radiating patch to improve the

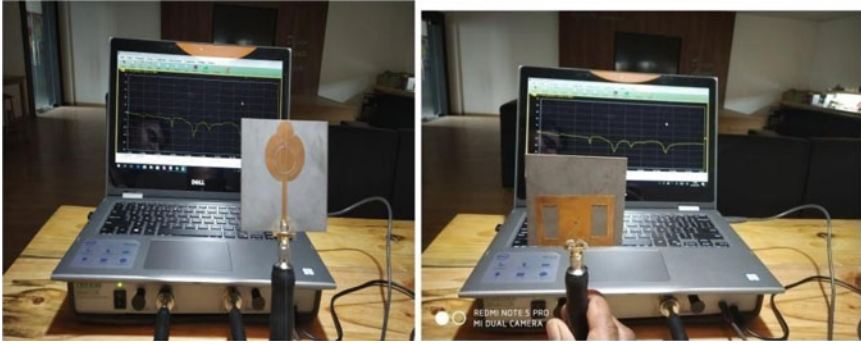


Fig. 10 Measurement setup of the fabricated antenna with network analyzer

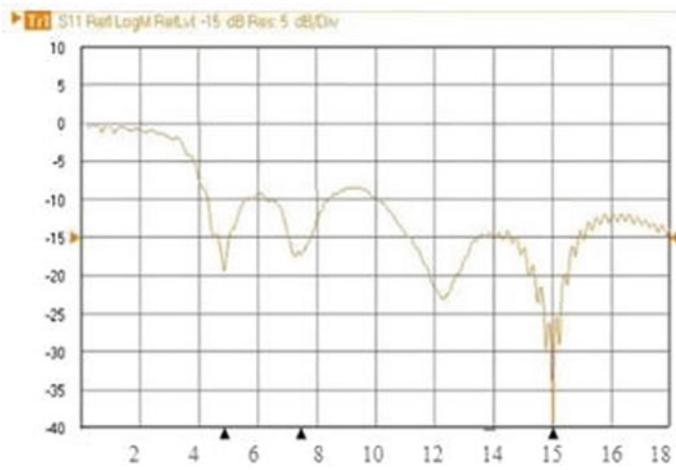


Fig. 11 S_{11} plot of the fabricated antenna

Table 2 Depicts the comparison between the simulated antenna results and fabricated antenna measured results

Antenna	Frequency (in GHz)	S_{11} (in dB)
Simulated antenna	1.945	-36.03
	5.02	-23.49
	8.845	-51.97
Fabricated antenna	5.13	-19.74
	3.71	-17.12
	8.05	-40.0

radiation characteristics i.e., 5.027 dBi. The measured results show that there is very good agreement with simulated results. The simulated results are estimated by using CSTMWS.

References

1. Federal Communications Commission. Revision of Part 15 of the commission's rules regarding ultra-wideband transmission systems. First report and order. ET Docket 98–153, FCC 02–48,2002.1–118
2. Jaglan N, SD Gupta, Kanaujia BK, Srivastava S (2017, May) Design and development of efficient EBG structures-based band notched UWB circular monopole antenna. *Wirel Pers Commun* 1–27 (Springer)
3. Beigi P, Nourinia J, Mohammadi B, Valizade A (2015) Bandwidth enhancement of small square monopole antenna with dual band notch characteristics using U-shaped slot and butterfly shape parasitic element on backplane for UWB applications. *Appl Comput Electromagn* 30:78
4. Gao G, He L, Hu B, Cong X (2015) Novel dual band-notched UWB antenna with t-shaped slot and CSRR structure. *Microw Opt Technol Lett* 57:1584
5. Majeed H, Sayidmarie KH (2019) UWB elliptical patch monopole antenna with dual-band notched characteristics. *Int J Electr Comput Eng (IJECE)* 9(5):3591–3598
6. Habash Mahmoud F, Tantawy Anour S, Atallah Hany A, Abdel-Rahman Adel B (2018) Compact size triple notched-bands UWB antenna with sharp band-rejection characteristics at WiMAX and WLAN bands. *Adv Electromagn* 7(3):99–103
7. Rahman MU, NagshvarianJahromi M, Mirjavadi SS, Hamouda AM (2019) Compact UWB band-notched antenna with integrated bluetooth for personal wireless communication and UWB applications. *Electronics* 8:158
8. Ding J, Lin Z, Ying Z, He S (2007) A compact ultra-wideband slot antenna with multiple notch frequency bands. *Microw Opt Technol Lett* 49(12):3056–3060
9. Tang Z, Lian R, Yin Y (2015) Differential-fed UWB patch antenna with triple band-notched characteristics. *Electron Lett* 51:1728–1730
10. Vendik IB, Rusakov A, Kanjanasit K (2017) Ultra wide band (UWB) planar antenna with single-, dual-, and triple-band notched characteristic based on electric ring resonator. *IEEE Antennas Wirel Propag Lett* 16:1597–1600
11. Badamchi Z, Zehforoosh Y (2015) Switchable single/dual band filtering UWB antenna using parasitic element and t-shaped stub wave cancellers. *Microw Opt Technol Lett* 57:2946
12. Zehforoosh Y, Sedgi T (2016) An Improved CPW-fed printed UWB antenna with controllable band-notched functions. *J Comm Eng* 5:38
13. Kim KH, SO Park (2006) Analysis of the small band rejected antenna with the parasitic strip for UWB. *IEEE Trans Antenna Propag* 54(6):1688–1692
14. Rafique U, Ali SA (2014) Ultra-wideband patch antenna for K-band applications. *TELKOMNIKA Indonesian J Electr Eng* 12(12)

Modeling, Simulation and Validation of 1200 kV UHV Autotransformer



Satyadharma Bharti and Satya Prakash Dubey

Abstract At present, work on the 1200 kV transmission system is in progress in India. Research work is going on at National Test Station, Bina, where 1200 kV setup with single-circuit and double-circuit line is installed. In order to investigate the performance of ultra-high voltage (UHV) system, the design modifications and other technical studies related to the transmission system, its simulation study is required. A UHV autotransformer is the main part of any UHV transmission system. Early research suggested the use of single-phase three-winding transformer model of PSCAD software (4.2 version) to model an ultra-high voltage autotransformer. The novel method uses a bank of three ‘single-phase three-winding autotransformers’ and a three-phase star-star autotransformer with tertiary (with provision of a Star or delta connection of tertiary winding and choice of delta lag or lead) model of PSCAD 4.6 version. This paper presents the modeling and simulation and validation of 1200 kV UHV autotransformer using these models. The simulation results are validated and verified through the actual field test results, and it is found that the autotransformer module of PSCAD 4.6 software is suitable for simulation study of the UHV installation.

Keywords Autotransformer · Ultra-high voltage transmission · PSCAD

Abbreviations

EMTDC Electromagnetic Transients including DC
HV High Voltage
IV Intermediate Voltage

S. Bharti (✉)

Electrical Engineering Department, Rungta College of Engineering and Technology, Bhilai, India
e-mail: s.bharti@rungta.ac.in

S. P. Dubey

Central Research Committee, Rungta College of Engineering and Technology, Bhilai, India
e-mail: dr.sp.dubey@rungta.ac.in

© Springer Nature Singapore Pte Ltd. 2020

R. Sharma et al. (eds.), *Innovation in Electrical Power Engineering, Communication, and Computing Technology*, Lecture Notes in Electrical Engineering 630,
https://doi.org/10.1007/978-981-15-2305-2_6

LV	Low Voltage
NTS	National Test Station
PGCIL	Powergrid Corporation of India Limited
PSCAD	Power System Computer-Aided Design
UHV	Ultra-High Voltage

1 Introduction

The need for simulation is always experienced prior to design and model any real system. For simulation study of power system-related problems, PSCAD software provides a good solution. The earlier version of PSCAD 4.2 introduced many elements in its library, namely rotating machines, transformers, transmission lines, switchgears and accessories of power system; however, the facility of modeling of an autotransformer was not made available in the PSCAD 4.2 version. The conventional two-winding transformer of the PSCAD 4.2 library can be used to model an autotransformer as shown in Fig. 1.

This illustrates the equivalent model of a single-phase autotransformer of PSCAD, in which classical single-phase transformer component with the provision of a tap changer at the secondary winding is used [1].

This non-availability of an autotransformer model is removed in the PSCAD 4.6 version, and the user can pick up the single- or three-phase autotransformer with the provision of tertiary winding for simulation purpose. The validity of any software can be proven only when its results are matched with the actual tests conducted on the real system; the present work is a novel attempt of validating the software performance at the level of ultra-high voltage transmission with the help

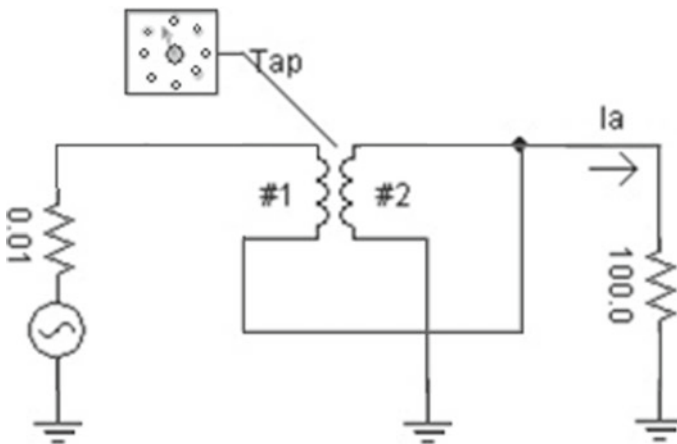


Fig. 1 Autotransformer equivalent model in PSCAD



Fig. 2 A 1200 kV autotransformer manufactured by Crompton Greaves Ltd. [2]

of an actual system installed at National Test Station (NTS), Bina, Madhya Pradesh, India, under the control of Powergrid Corporation of India Limited (PGCIL). Apart from 1200 kV autotransformer, other major equipment installed at NTS Bina are capacitive voltage transformer, circuit breaker, surge arrester, bus post insulator, etc. This work is successfully accomplished by a consortium of 35 Indian manufacturers who have manufactured the equipment, accessories and apparatus indigenously as per the guidelines of the PGCIL. The autotransformers of this system were manufactured by Bharat Heavy Electricals Ltd., Crompton Greaves Ltd. and Vijai Electricals Ltd. [2–5]. Technical brochures [6–8] are already released with the parameters and other details of the Indian 1200 kV UHVAC system. Figure 2 shows a photograph of transportation of one such 1200 kV autotransformer, manufactured and tested by Crompton Greaves Ltd.

The autotransformer is one of the main and most critical equipment of UHVAC system; the success of the UHVAC system depends mainly on the performance of autotransformer. As the various steps of design, manufacturing, factory-testing, transporting, commissioning and on-site testing of a reliable 1200 kV autotransformer pose severe challenges to the designers, the conventional design techniques of 400–765 kV autotransformer cannot be simply scaled up for UHV technology. Higher voltage level demands unique design features and considerations for insulation content, and the manufacturing and testing process becomes more challenging [9]. In this paper, simulation study of the bank of three ‘single-phase, three-winding autotransformers’ and a three-phase star-star autotransformer with tertiary is carried out with the help of PSCAD 4.6, and the results are compared with the system installed at Bina.

2 History of Major UHV Transformers

Research on ultra-high voltage transmission systems in different parts of the world started in 1970s and 1980s and experimental lines UHV test stations were built in few countries like USA, USSR, Italy, Japan and China [5, 10].

2.1 3000 MVA Transformer Bank in Japan

The basic parameters of 1100 kV, 3000 MVA transformer bank of Tokyo Electric Power Company (TEPCO), Japan, are given in Table 1.

Due to transport constraints, the single phase of the transformer is designed to be composed of two units as shown in Fig. 3. Each unit is transported separately to the substation site and assembled there [11].

2.2 200 MVA Autotransformers for Italy

Basic specifications of Italy project UHV autotransformer are listed in Table 2.

2.3 USSR's Commercial Line

The transformer specifications for the 1150 kV Ekibastuz–Kokchotav–Kustanai transmission system commissioned in 1985 are given in Table 3.

Table 1 Specifications of transformer bank of TEPCO

Parameter	Specifications
Rated power	3000/3 MVA, single-phase
Voltage ratio	$1050/\sqrt{3}$, $525/\sqrt{3}$, 147 kV
Rated frequency	50 Hz
Tertiary power	1200/3 MVA
On-load tapings at neutral point	+7% to -7%, 27 taps for voltage range $1133.6/\sqrt{3}$ – $986.5/\sqrt{3}$ kV
Impedance	18%
Method of cooling	Oil-directed air-forced (ODAF)
BIL-LI (kV peak)	HV 1950, IV 1300, LV 750
PD	$1.5 U_m/\sqrt{3}$ $U_m = 1100$ kVp

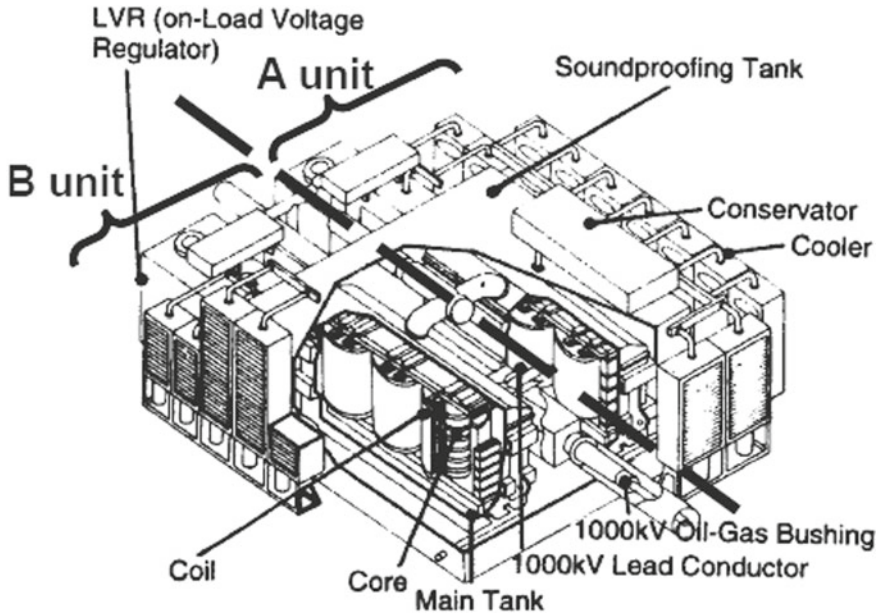


Fig. 3 TEPCO transformer (single-phase) [11]

Table 2 Specifications of transformer for Italy project

Parameter	Specifications
Rated power	400/400/50 MVA, single phase
Voltage ratio	$1000/\sqrt{3}$, $400/\sqrt{3}$, 122 kV
Rated frequency	50 Hz
% Impedance	15
Cooling method	ODAF
BIL (kV peak)-LI	HV 2400 kV, IV 1300 kV, LV 125 kV
SIL	HV 1950 kV
PD	$1.5 U_m/\sqrt{3}$ ($U_m = 1050$ kV)

Table 3 Specifications of USSR project

Parameter	Specifications
Rated power	667 MVA, single phase
Voltage ratio	$1150/\sqrt{3}$, $500\sqrt{3}$ kV
Rated frequency	50 Hz, single phase
% Impedance	13
BIL (kV peak)-LI	HV 2550 kV FW, 2800 kV CW
SI	IV 1800 kV, FW, 1950 kV CW HV 2100 kV

2.4 Autotransformer at China UHV Project

The parameters of 1000 kV autotransformer of China Jindongnan–Nanyang–Jingmen UHVAC Demonstration Project are given in Table 4.

2.5 333 MVA Autotransformers at India

Basic specifications of 1200 kV autotransformer, installed at National Test Station, Bina (MP), are given in Table 5.

Status of Indian research and development carried out by Powergrid Corporation of India toward UHV AC transmission is explained and updated [12]. It also describes

Table 4 Specifications of China UHV project

Parameter	Specifications
Rated power HV/IV/LV	1000/1000/334 MVA
Rated, no-load voltage (kV)	$[1050/\sqrt{3}]/[525/\sqrt{3}] \pm 5\%/[110]$
Rated frequency & phase	50 Hz, 1-phase
% Impedance HV-IV	$18\% \pm 7.5\%$ tol.
Insulation levels	
(i) Full-wave lightning impulse withstand voltage	2250 kV (Peak)
(ii) Chopped-wave lightning impulse withstand voltage	2400 kV (Peak)
(iii) Switching impulse withstand voltage	1800 kV (Peak)
(iv) Power frequency withstand voltage (RMS), kV	1100 (5 min)

Table 5 Transformer specifications for Indian project [5]

Parameter	Specifications
Rated power HV/IV/LV	333/333/111 MVA (single phase)
Rated no-load voltage (kV) HV/IV/LV	$[1150/\sqrt{3}]/[400/\sqrt{3}]/[33]$
Rated frequency & phase	50 Hz, 1-phase
% Impedance HV-IV, HV-LV and IV-LV	$18\% \pm 10\%$ tol., 40 and 20% (MIN.)
Insulation levels	2250/1300/250/95
(i) Full-wave lightning impulse voltage (kV peak) HV/IV/LV/neutral	1800 1.5 PU (1.0 PU = $1200/\sqrt{3}$)
(ii) Switching impulse voltage (kV peak) HV	
(iii) ACLD PD level	
Type of cooling, cooling equipment coolers	OFAF/ODAF, $4 \times 33.3\%$ OFAF
Temp. rises top oil/winding by resistance °C	40 °C: Top Oil/45 °C: winding

future planning of UHVAC development in India; a 1,200 kV single-circuit transmission line from Wardha to Aurangabad, which is located in the western part of the country, is currently under construction. Initially, the line will operate at 400 kV; at a later date, this line will be upgraded to 1,200 kV. Additional 1,200 kV transmission lines are in the planning stage [12].

3 Autotransformer Modeling and Simulation

Sun Shu-bo et al. describe the importance of autotransformer as a main and crucial one, and highlight the significance of the quality for successful operation of UHV project [13]. The necessity of modeling UHV power transformer and electromagnetic simulation study with the help of EMTDC software is highlighted. The method of using three-winding transformer with the help of ‘unified magnetic equivalent circuit’ (UMEC) transformer model for modeling of autotransformer is suggested by Zeng et al. [14]. Bathini et al. also confirm the non-availability of built-in model for three-phase autotransformer with tertiary in an older version. Accordingly, three single-phase, three-winding transformers are used to represent three-phase autotransformer with tertiary [15].

The actual autotransformer for 1200 kV UHVAC system is shown in Fig. 4. This is installed at National Test Station, Bina, and no-load testing was carried out after charging [16].

Present work is a novel attempt of analyzing the performance of the newly introduced model of the autotransformer available in PSCAD library of the new version at UHV level. The standard parameters are used for the modeling of autotransformer, as indicated in Table 5, and the performance of the simulation model is analyzed and compared with the results of actual autotransformer. Various essential tests like essential routine tests, type tests and special tests as per Indian and International Electro-technical Standard, IEC 60076 [18], are conducted on the simulation model of the autotransformer of PSCAD 4.6 and compared with the result of actual autotransformer made and tested by M/s Vijai Electricals Ltd., at their Hyderabad-based ultra-high voltage laboratory [4]. Various computer simulation and smart computing techniques lead to improvement in product design and result in cost optimization of 1200 kV autotransformer [19].

The classical approach of transformer modeling in PSCAD software [1] is based on the theory of mutual coupling between two windings having self-inductance of first and second winding as L_{11} and L_{22} with value of mutual inductance between windings 1 and 2 equal to L_{12} . With these notations, the relation between voltage and current of first and second winding V_1 , V_2 and I_1 , I_2 (respectively) is given in Eq. (1):

$$\begin{bmatrix} V_1 \\ V_2 \end{bmatrix} = \begin{bmatrix} L_{11} & L_{12} \\ L_{12} & L_{22} \end{bmatrix} \cdot \frac{d}{dt} \begin{bmatrix} I_1 \\ I_2 \end{bmatrix} \quad (1)$$

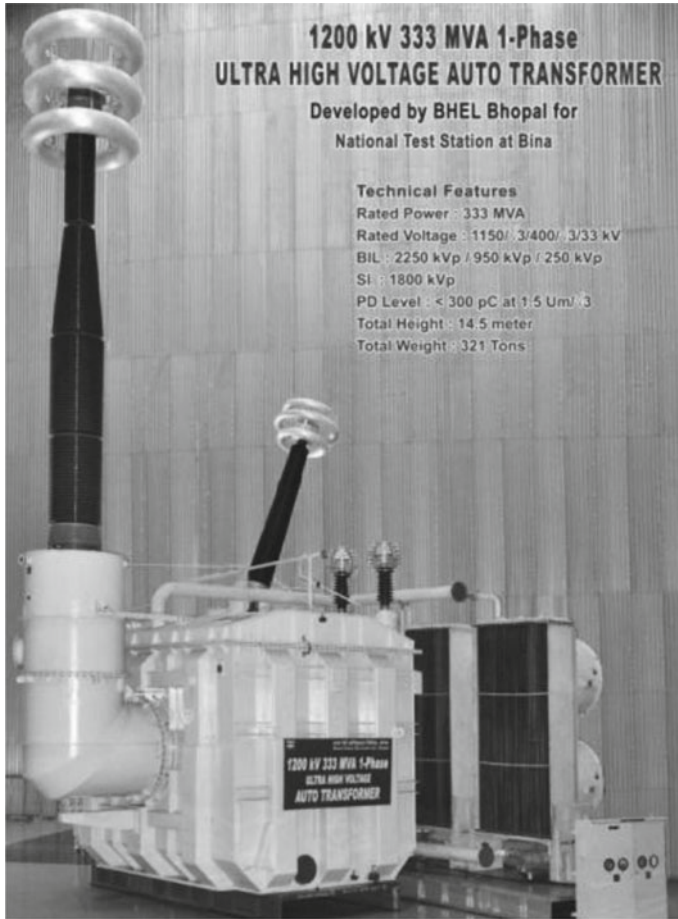


Fig. 4 1200 kV autotransformer developed by BHEL [17]

The current in the windings can be solved using Eq. (2).

$$\frac{d}{dt} \begin{bmatrix} I_1 \\ I_2 \end{bmatrix} = \frac{1}{L_{11}L_{22}(1 - K_{12}^2)} \cdot \begin{bmatrix} L_{22} & -L_{21} \\ -L_{12} & L_{11} \end{bmatrix} \cdot \begin{bmatrix} V_1 \\ V_2 \end{bmatrix} \quad (2)$$

where $K_{12} = \frac{L_{12}}{\sqrt{L_{11} \cdot L_{22}}}$ is the coupling coefficient.

In an ideal transformer with tightly coupled windings on the same leg of the core, the turn ratio $a = E_1/E_2$ Eq. (1) is expressed by Eq. (3).

$$\begin{bmatrix} V_1 \\ a \cdot V_2 \end{bmatrix} = \begin{bmatrix} L_{11} & a \cdot L_{12} \\ a \cdot L_{12} & a^2 \cdot L_{22} \end{bmatrix} \cdot \frac{d}{dt} \begin{bmatrix} I_1 \\ I_2/a \end{bmatrix} \quad (3)$$

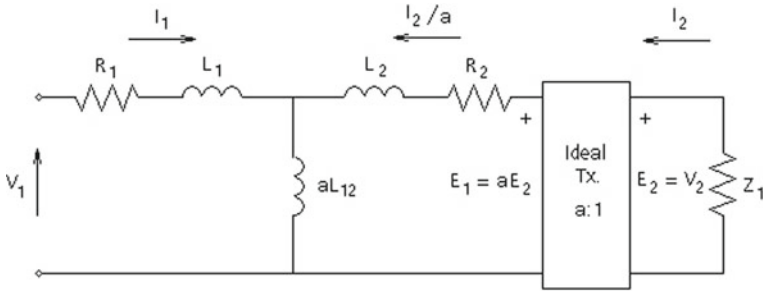


Fig. 5 Equivalent circuit of two mutually coupled coils

Figure 5 gives the equivalent circuit of two mutually coupled windings where

$$L_1 = L_{11} - a \cdot L_{12} \quad (4)$$

$$L_2 = a^2 \cdot L_{22} - a \cdot L_{12} \quad (5)$$

Thus, for two windings coupled on the same transformer core, relation can be obtained for derivatives of transformer currents in terms of the voltage, using Eqs. (6), (7), (8). For an ideal transformer:

$$\frac{d}{dt} \begin{bmatrix} I_1 \\ I_2 \end{bmatrix} = \frac{1}{L} \cdot \begin{bmatrix} 1 & -a \\ -a & a^2 \end{bmatrix} \cdot \begin{bmatrix} V_1 \\ V_2 \end{bmatrix} \quad (6)$$

where leakage inductance between first and second winding, as measured from the terminals of first winding, refer Eqs. (4) and (5)

$$L = L_1 + a^2 \cdot L_2 \quad (7)$$

and turns ratio

$$a = \frac{V_1}{V_2} = \sqrt{\frac{L_{11}}{L_{22}}} \quad (8)$$

For an ideal three-winding transformer, the inverted inductance matrix is expressed by Eq. (9) [1]:

$$\begin{bmatrix} L_{11} & L_{12} & L_{13} \\ L_{21} & L_{22} & L_{23} \\ L_{31} & L_{32} & L_{33} \end{bmatrix} = \frac{1}{LL} \cdot \begin{bmatrix} L_2 + L_3 & -a_{12} \cdot L_3 & -a_{13} \cdot L_2 \\ -a_{12} \cdot L_3 & a_{22}(L_1 + L_3) & -a_{23} \cdot L_1 \\ -a_{13} \cdot L_2 & -a_{23} \cdot L_1 & a_{33}(L_1 + L_2) \end{bmatrix} \quad (9)$$

where

$$a_{12} = \frac{V_1}{V_2}; a_{22} = \left(\frac{V_1}{V_2}\right)^2; a_{13} = \frac{V_1}{V_3}; a_{23} = \frac{V_1^2}{V_2 \cdot V_3}$$

$$a_{33} = \left(\frac{V_1}{V_3}\right)^2; LL = L_1 \cdot L_2 + L_2 \cdot L_3 + L_3 \cdot L_1$$

V_1 = RMS single-phase voltage rating of HV winding.

V_2 = RMS single-phase voltage rating of IV winding.

V_3 = RMS single-phase voltage rating of LV winding.

4 Result and Discussion

This section presents the results of voltage ratio, polarity test, no-load loss and no-load current measurement, at rated frequency. It also covers studies on three-phase transformer bank followed by a case study.

4.1 Measurement of Voltage Ratio

At the outset, measurement of voltage ratio is performed on the simulation model of autotransformer using PSCAD 4.6. The measured simulation results are shown in Fig. 6, and the results are compiled in Table 6. Their deviation with the specified voltage ratio is also tabulated. The specified voltage ratios for various combinations are found to be:

- i. High voltage and intermediate voltage winding,
i.e., HV/IV ratio = $(1150/\sqrt{3})/(400/\sqrt{3}) = 2.875$;
- ii. High voltage and low voltage winding,
i.e., HV/LV ratio = $(1150/\sqrt{3})/(33) = 20.12$; and
- iii. Intermediate voltage and low voltage winding IV/LV = $(400/\sqrt{3})/(33) = 6.998$.

All measured values are within $\pm 5\%$ tolerance of the specified values, and hence, the results are found to be satisfactory. Actual autotransformers of 1200 kV UHVAC are successfully commissioned at National Test Station, Bina [20], and have exhibited similar results.

4.2 Check for Polarity

The connection diagram for polarity testing is given in Fig. 7.

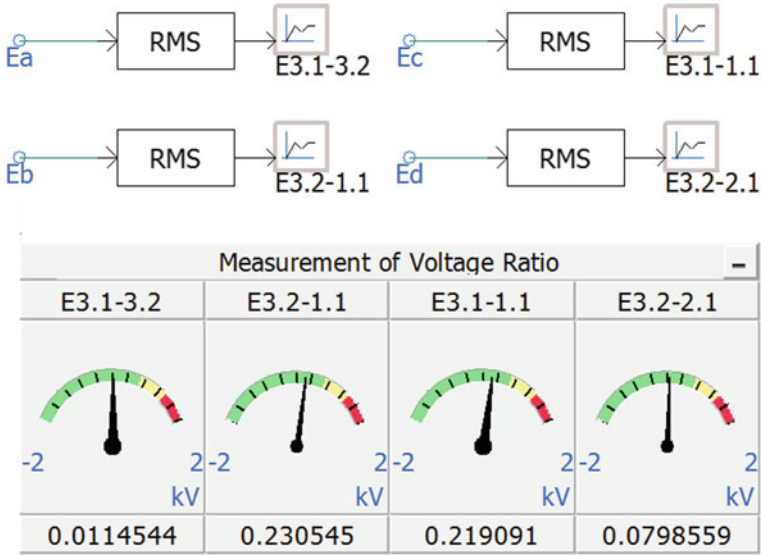


Fig. 6 Measurement of voltage ratio and polarity

Table 6 Measurement of voltage ratio of windings

Winding under test	Specified ratio	Measured ratio	Deviation (%)
HV/IV	2.875	2.887	-0.41%
HV/LV	20.120	20.127	-0.03%
IV/LV	6.998	6.9716	0.37%

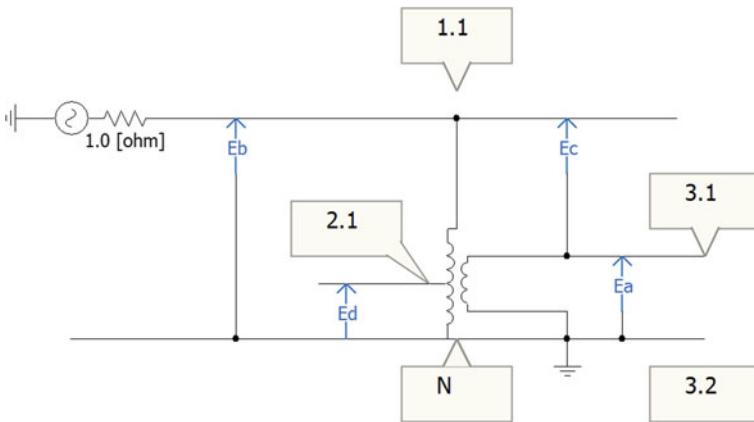


Fig. 7 Schematic diagram of the polarity testing of autotransformer

For the verification of the polarity, terminals N and 3.2 were shorted, supply was given between 1.1 and N , and the voltage between 3.1–3.2 and 1.1–3.1 was recorded. The calculation confirms the nature of polarity.

Supply given between 1.1 and N 230.545 V
 Measured voltage between 3.1 and 3.2 11.4544 V
 Measured voltage between 1.1 and 3.1 219.091 V
 Hence as $V(1.1-N) - V(3.1-3.2)$ 219.0906 $\approx V(1.1-3.1)$

The polarity proved to be subtractive in nature.

4.3 No-Load Loss and No-Load Current Measurement, at Rated Frequency

The no-load loss and current at 90, 100 and 110% excitation are measured with the help of the simulation model of the autotransformer of PSCAD 4.6. For the computer simulation, the RMS value and the mean value of the voltage are taken as same for the calculation of the corrected no-load loss as per IEC guidelines. A voltage of 29.77 kV, 33.07 kV and 36.33 kV is applied to the LV winding of the autotransformer to obtain 90%, 100% and 110% excitation, respectively. The simulation results are tabulated in Table 7. Here, corrected and measured no-load losses are same because of the unity ratio on RMS voltage to the mean voltage. Under this test condition:

The autotransformer is energized from LV side
 Base kV @ 100% no-load current 33 kV
 Base MVA for % no-load current 111 MVA.

The result obtained from no-load test on the actual transformer manufactured by M/s Vijai Electricals Ltd. for 100% rated voltage is found to be 141.32 kW [4], which is very close to the simulation model result of 146.723 kW.

Table 7 No-load test on the transformer

% Rated voltage	Voltage to be applied (kV)	Measured applied voltage (RMS)	No-load current (Amp)	No-load current in terms of % full load current	Measured no-load loss (kW)	Corrected no-load loss, P_c (kW)
90%	29.70	29.77	19.2	0.57%	118.885	118.885
100%	33.00	33.07	21.38	0.63%	146.723	146.723
110%	36.3	36.33	23.48	0.69%	176.006	176.006

4.4 Studies on Three-Phase Transformer Bank

Figure 8a gives the schematic diagram for the simulation model for a three-phase autotransformer, which can be used for on-load studies. Figure 8b indicates the method suggested by early researchers, who have used older version of PSCAD software [15], whereas the simulation shown in Fig. 8c gives schematic diagram of an autotransformer model of PSCAD 4.6 that uses built-in model of autotransformer to make the bank.

Due to several critical issues related to the transformer design and manufacturing, special care is required at UHV level [9]. As such, the present validity testing confirms the use of simulation model of the autotransformer available in the PSCAD library for the modeling and simulation of UHV autotransformer. It also eliminates the problem of inaccuracy with the use of single-phase two-winding autotransformer model [21–23].

4.5 Case Study on PSCAD Autotransformer

I. S. Jha et al. in their paper ‘Operational Experience in 1200 kV National Test Station (UHVAC), India’ [24] describe a fault experienced at National Test Station, Bina.

Waveforms of the disturbance recorder were studied to investigate the nature of the fault. A simulation model of the test station was prepared (see Fig. 9), and a single line to ground fault was confirmed after 50–60 ms of charging the line [24]. It is found that the use of PSCAD simulation has proved it as an effective tool for study and analysis.

5 Conclusion

The simulation study of the UHV autotransformer is carried out using the PSCAD 4.6 software model of single-phase three-winding transformer model as well as a three-phase star-star autotransformer with tertiary model. The study gave satisfactory results for voltage ratio, polarity, no-load test, etc., when compared with the actual autotransformer operating at 1200 kV voltage level. The PSCAD model was also found to be an effective and validated tool to simulate and analyze the fault condition. This validation will prove a milestone for future researchers and academicians. The 333 MVA 1200 kV autotransformers have been successfully commissioned at National Test Station, Bina. The simulation study of 1200 kV UHVAC transformer will be highly beneficial for the study of 1200 kV transmission system.

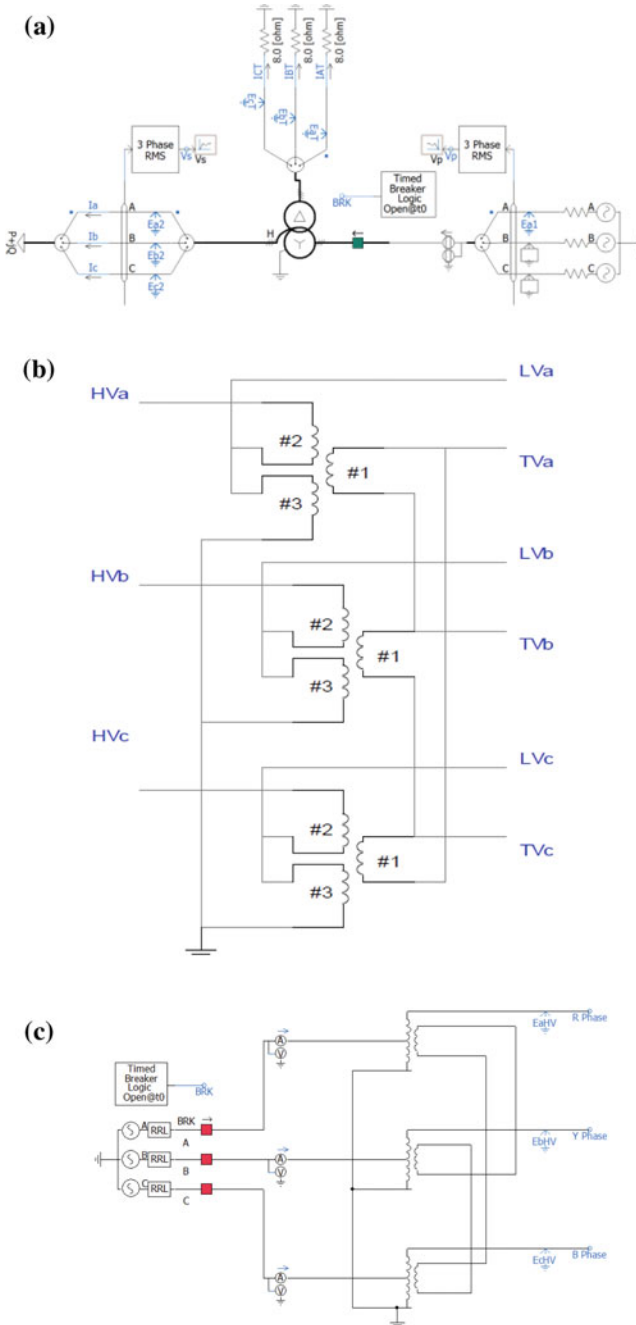


Fig. 8 a Simulation model for three-phase autotransformer b Schematic diagram of autotransformer on the older version of PSCAD software [15] c The use of built-in model of autotransformer to make the bank

10. Huang D et al (2009) Ultra high voltage transmission in China: developments, current status and future prospects. *Proc IEEE* 97.3:555–583
11. Nakamura A, Taniguchi H, Yokoyama A (2007) 1100 kV AC Transmission Project in Japan. IEC/CIGRE UHV symposium, Beijing 18021
12. Jha IS, Agrawal et al (2013) India's Powergrid R&D Efforts. *Transm Distrib World*
13. Sun S-b, Fang M, Zhong J-t (2007) Development and design of 1000 kV autotransformer. *Electr Equip* 8.4:6–10
14. Zeng L-j et al (2010) Modeling and electromagnetic transient simulation of UHV autotransformer. *Proceedings of the CSEE*1:91–97
15. Bathini V et al (2010) Surge transfer study for power transformer using EMTDC/PSCAD. In: 16th National power systems conference
16. Bharti S, Dubey SP (2016) No-load performance study of 1200 kV Indian UHVAC transmission system. *High Voltage* 1.3:130–137
17. Profile of Bharat Heavy Electricals Ltd. Bhopal. <https://www.bhelpl.co.in/pnpr-new/pnprmain/bhelproductprofile.pdf>. Accessed 21 Jan 2019
18. IEC 60076-3 (2000) (Second edition—2000) 'Power Transformer' Part 3: Insulation levels, dielectric tests and external clearances in air © International Electrotechnical Commission
19. Bharti S, Dubey SP (2018) Application of smart computing techniques in cost optimization of 1200 kV autotransformer. *J Inf Optim Sci* 39.1:249–262. <https://doi.org/10.1080/02522667.2017.1374727>
20. Nayak RN, Bhatnagar MC, De Bhowmick BN (2009) 1200 kV Transmission system and status of development of substation equipment/transmission line material in India. *Water Energy Int* 66(4):70–77
21. Hao Y, Yonghai X, Yingying L et al (2009) Simulation and harmonic analysis on ultra high voltage ac transmission system. In: *Energy and environment technology, ICEET'09, IEEE international conference*, vol 2, pp 283–286
22. Salimi M, Gole AM, Jayasinghe RP (2013) Improvement of transformer saturation modeling for electromagnetic transient programs. IPST, Vancouver
23. Brandwajn V, Donnel HW, Dommel II (1982) Matrix representation of three-phase n-winding transformers for steady-state and transient studies. *IEEE Trans Power Apparatus Syst* (6):1369–78
24. Jha IS, De Bhowmick BN, Rao SB et al (2017) Operational experience in 1200 kV national test station (UHVAC), India. *CIGRE India J* 6(1):15–28

Harmonics and Voltage Sag Compensation of a Solar PV-Based Distributed Generation Using MSRF-Based UPQC



Sarita Samal, Akansha Hota, Prakash Kumar Hota
and Prasanta Kumar Barik

Abstract This paper deals with source current harmonics and voltage sag compensation of a solar photovoltaic (PV)-based distributed generation (DG) system using unified power quality conditioner (UPQC). Despite the several benefits of DG like excellent energy supply, reducing expansion of power distribution system, environmental friendly and so on, there are several challenges existing due to the integration of DG with the grid or operating it in stand-alone mode. Power quality (PQ) issue is one of the main technical challenges in DG power system. In order to provide improved PQ of energy supply, it is necessary to analyze the harmonics distortion of the system as well as the voltage sag and swell. The UPQC has been widely useful, and it is confirmed to be the best solution to diminish this PQ issue. This paper explores the detail of PQ impacts in a DG (comprising of solar PV) system operates in stand-alone mode. The voltage sag compensation with voltage and current harmonics is estimated under varying load situation with a control scheme like modified synchronous reference frame technique. The proposed model is developed in MATLAB/SIMULINK^R, and the result obtained validates the superiority of proposed technique over others in terms of harmonics elimination and sag compensation.

Keywords Distributed generation · Power quality · Harmonics · Sag · MSRF

S. Samal

School of EE, KIIT Deemed to be University, Bhubaneswar, Odisha, India
e-mail: saritaruchy@gmail.com

A. Hota · P. K. Hota

Department of EE, VSSUT, Burla, India
e-mail: 1997.akansha@gmail.com

P. K. Hota

e-mail: p_hota@rediffmail.com

P. K. Barik (✉)

Department of MEE, CAET, OUAT, Bhubaneswar, India
e-mail: prasantbarik05@gmail.com

© Springer Nature Singapore Pte Ltd. 2020

R. Sharma et al. (eds.), *Innovation in Electrical Power Engineering, Communication, and Computing Technology*, Lecture Notes in Electrical Engineering 630,
https://doi.org/10.1007/978-981-15-2305-2_7

1 Introduction

Distributed generation (DG) can be represented as a small-scale power system that contains loads, energy sources, energy storage units and control and protection systems [1]. Using DG is more attractive as it improves the system quality, decreases the carbon emission and reduces the losses in transmission and distribution systems [2]. When DG is connected to utility grid, the control systems required to maintain the active and reactive power output from the energy sources connected to DG are simple. However, under autonomous operation, the DG is disconnected from the utility grid and operates in islanded condition. Usually, a stand-alone DG system is used to supply power to isolated areas or places interconnected to a weak grid. The application of above DG on the other hand reduces the probability of energy supply scarcity. The proposed DG consists of renewable energy sources (RES)-based power sources (i.e., solar PV) and storage device such as battery along with controllable loads [3, 4]. The solar PV is depended upon the climatic condition, and hence, to get uninterrupted power supply at any time and maintaining the continuity of load current, one of the most developed energy sources like fuel cell is combined with these RES [5]. The increase of power electronics-based equipment in household appliances and industries is the main cause of pollution of power system [6]. The research in the area of power electronics makes sure that unified power quality conditioner (UPQC) plays a vital role in achieving superior power quality levels.

In the present scenario, the series active power filters (APFs) and shunt APF normally termed as SAPF alone do not meet the requirement for compensating the PQ distortions. A UPQC consists of two inverters integrated with the DC-link capacitor where the series APF is integrated through a series transformer and the shunt is through interfacing inductor. The series inverter acts as a voltage source, whereas the shunt one acts as a current source. Simultaneous compensation of voltage- and current-related PQ distortions using UPQC is achieved by proper controlling of series APF and shunt APF [7]. The shunt APF is employed for providing compensating currents to PCC for generation/absorption of reactive power and harmonics suppression. Moreover, the operation of SAPF is depended upon three main parts which are momentous in its design: control method used for the generation of reference current, technique used for switching pulses generation for the inverter and the controller used for DC-link capacitor voltage regulation. Different control strategy explained in literature is as follows. The use of SAPFs for current harmonic compensation typically in domestic, commercial and industrial applications has explained by Montero et al. [8]. The experimental study and simulation design of a SAPF for harmonics and reactive power compensation are explained by Jain et al. [9]. The power balance theory for active and reactive power compensation has developed by Singh et al. [10]. The instantaneous reactive power techniques of three-phase shunt active filter for compensation of source current harmonics have been explained by Akagi et al. [11]. Sag is the most significant PQ problem faced by lots of industrial consumers. The control for such a case can be analyzed by protecting sensitive loads in order to preserve a load voltage without sudden phase shift. Different control strategies for

series APF are analyzed by Benachaiba et al. [12] with importance on the reimbursement of voltage sags with phase jump. Different control techniques to reimburse voltage sags with phase jump are also projected and compared by Jowder et al. [13]. To ensure stable operation and improve the system performance of DG in island mode, a comparative study of two different control techniques is used in UPQC. The control technique for reference current generation, i.e., synchronous reference frame (SRF) method and modified synchronous reference frame (MSRF) method in conjunction with pulse width modulation-based hysteresis band controller, is proposed in this paper by using MATLAB simulation software. The PQ issues like voltage sag compensation, current and voltage harmonics were analyzed at both linear and nonlinear loads.

2 Proposed System

The projected DG system (comprising of solar and storage device) is shown in Fig. 1 where DG system generates DC power to the DC bus, and by using a power inverter, this DC power is converted into AC. The AC bus delivers the power to the load which may be a linear or nonlinear. The UPQC is located in between the DG and nonlinear load which manages the power quality of the system by using different control techniques.

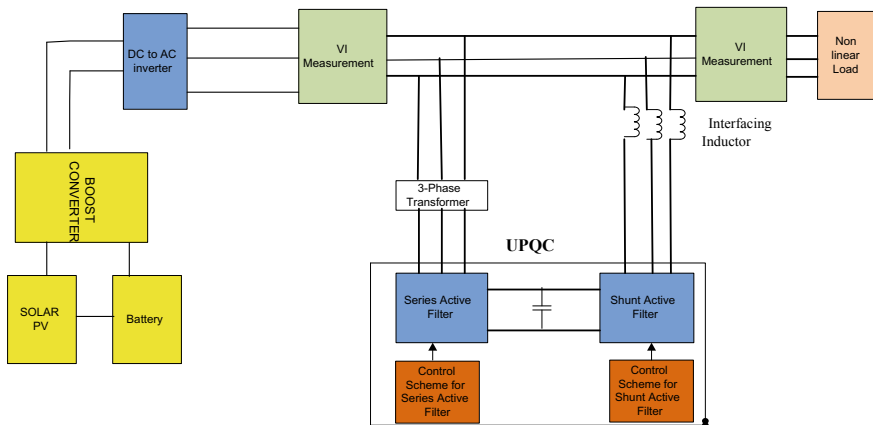


Fig. 1 Basic block diagram of DG with UPQC

2.1 Modeling of Solar PV

A single diode model-based PV cell is used for design of DG in the proposed work. Figure 2 represents the single diode equivalent model of solar PV system. The basic equation for design of PV system is presented in (1) [14, 15].

$$I_{PV} = N_P \times I_{PH} - N_P \times I_O \left[\exp \left\{ \frac{q \times V_{PV} + I_{PV} \times R_{se}}{N_s \times AkT} \right\} - 1 \right] \quad (1)$$

Figure 3 shows the MATLAB simulation of PV with MPPT and boost converter, and Fig. 4 shows its corresponding output voltage where the required voltage of 230 V is achieved. The parameters required for design of solar PV system are illustrated in Table 1 [16, 17].

2.2 Modeling of UPQC

This chapter begins with system configuration and detailed description of UPQC. The basic structure of UPQC is shown in Fig. 5, which consists of two inverters

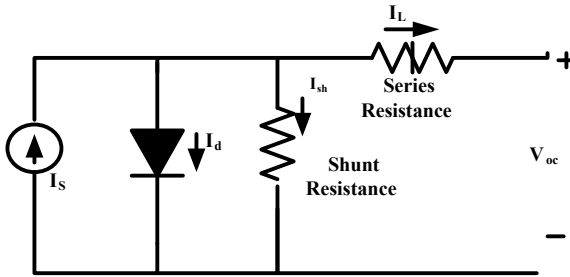


Fig. 2 Solar cell single diode model

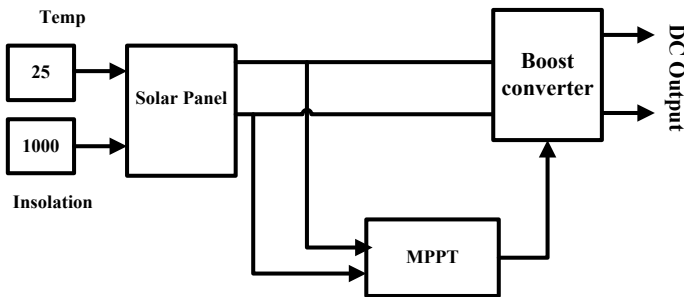


Fig. 3 Simulation of solar PV with MPPT and boost converter

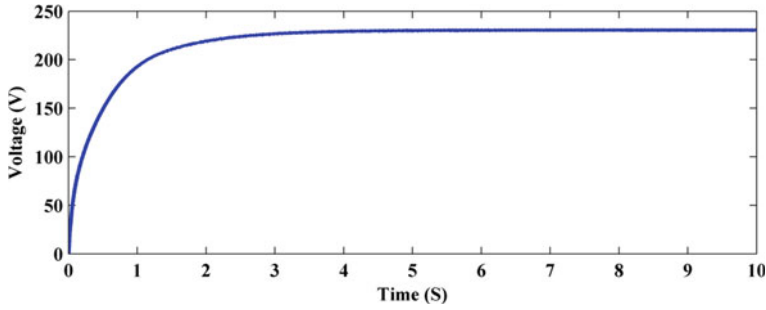


Fig. 4 Output voltage of boost converter

Table 1 Different parameters and their ratings to carry out the simulation work of solar PV

Different parameters	Ratings
No. of cells in series (N_p)	72
Cells in parallel (N_s)	01
Short circuit current (I_{sc})	10.2 A
Open circuit voltage (V_{oc})	90.5 V
Voltage at maximum power (V_{mp})	81.5 V
Current at maximum power (I_{mp})	8.6 A
Output voltage	230 V

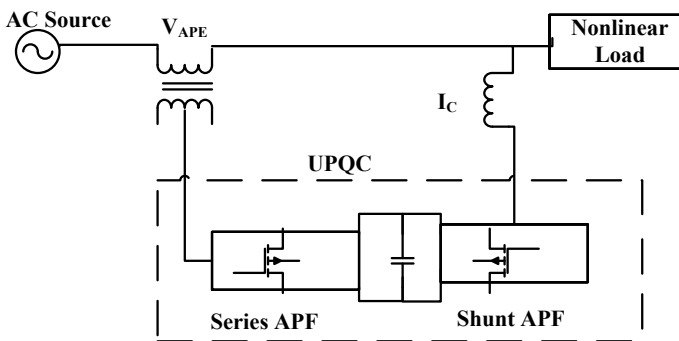


Fig. 5 Basic UPQC system block diagram

connected to a common DC-link capacitor. The series inverter is connected through a series transformer, and the shunt inverter is connected in parallel with the point of common coupling. The series inverter acts as a voltage source, whereas the shunt one acts as a current source. The main function of UPQC is to control the power flow and reduce the harmonics distortion in both voltage and current waveforms.

The series APF topology is shown in Fig. 6. The series APF protects load from

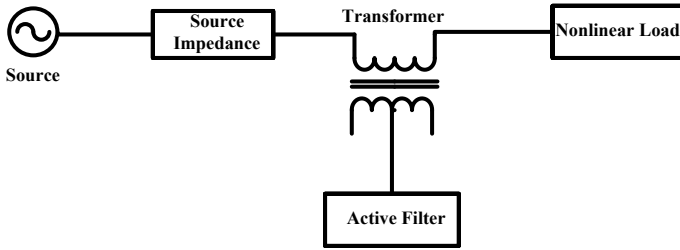


Fig. 6 Block diagram of series active filter

the utility side disturbances. In case of series APF, Park’s transformation method is used for generation of unit vector signal. A PWM generator, generating synchronized switching pulses, is given to the six switches of the series converter.

Figure 7 shows the basic structure of shunt active filter. The shunt active power filter injects compensating current to the PCC such that the load current becomes harmonics-free. The SAPF generates compensating current, which is in opposition to the harmonic current generated by nonlinear load. This compensating current cancels out the current harmonics caused and makes the load current sinusoidal. So, the SAPF is used to eradicate current harmonics and reimburse reactive power at the source side so as to make load current harmonics-free.

Equations 2 and 3 show instantaneous current and the source voltage.

$$I_s(t) = I_L(t) - I_C(t) \tag{2}$$

$$V_s(t) = V_m \sin \omega t \tag{3}$$

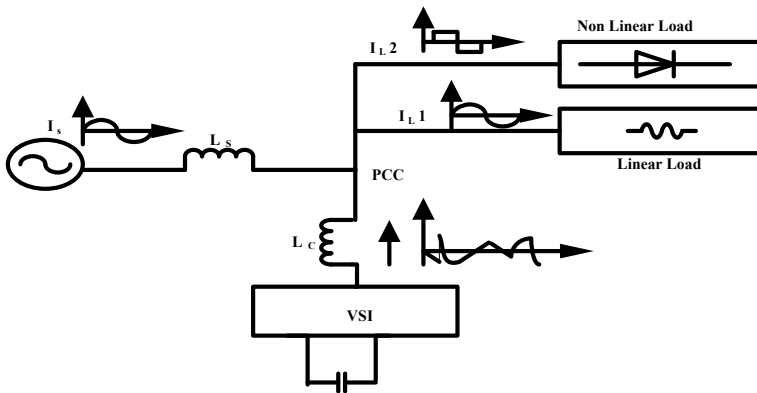


Fig. 7 Block diagram of shunt active filter

Fourier series method is used for expressing the nonlinear load current as shown in Eq. 4.

$$I_s(t) = I_1 \sin(\omega t + \Phi_1) + \sum_{n=2}^{\varepsilon} I_n \sin(n\omega t + \Phi_n) \quad (4)$$

The compensation current of the active filter should be expressed by

$$I_c(t) = I_L(t) - I_s(t) \quad (5)$$

Hence, for the exact compensation of reactive power and harmonics, it is essential to determine $I_s(t)$. The instantaneous value of source, load and compensation current can be expressed by $I_s(t)$, $I_L(t)$ & $I_C(t)$, where $V_s(t)$ and V_m correspond to instantaneous value and peak value of source voltage.

2.3 Control Scheme of UPQC

The MSRF controller scheme works in steady state as well as in dynamic condition exquisitely to manage the active and reactive power and reduce the harmonics in load current. The literature in review reveals that MSRF technique has much more advantages as compared to SRF scheme, so the authors have selected this control scheme for UPQC operation. The control scheme does not use the PLL circuit as used by SRF scheme, which makes the system more compatible and may be operated in load changing condition. The MSRF scheme with its control algorithm is given below.

2.3.1 Modified Synchronous Reference Frame (MSRF) Method

Figure 8 shows the block diagram of modified SRF method. The unit vector is generated by vector orientation method not by PLL. Figure 9 shows the block diagram to generate unit vector by sensing the supply voltage. The unit vector generation is described by using Eqs. (6) and (7).

$$\cos\theta = \frac{V_\alpha}{\sqrt{(V_{s\alpha}^2) + (V_{s\beta}^2)}} \quad (6)$$

$$\sin\theta = \frac{V_\beta}{\sqrt{(V_{s\alpha}^2) + (V_{s\beta}^2)}} \quad (7)$$

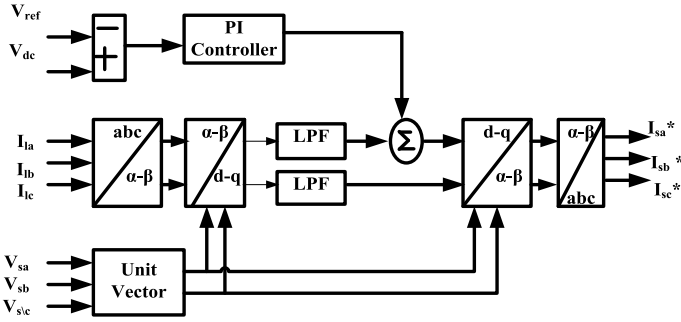


Fig. 8 Block diagram of modified SRF method

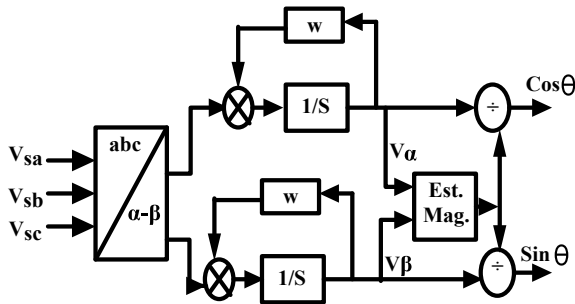


Fig. 9 Unit vector generation block diagram

2.3.2 Hysteresis Band Current Controller

Figure 10 shows the block diagram of hysteresis current regulator which generates the required pulses for inverter. In the current regulator, the error signal is generated by comparing the reference current I_{sa}^* and actual current I_{sa} .

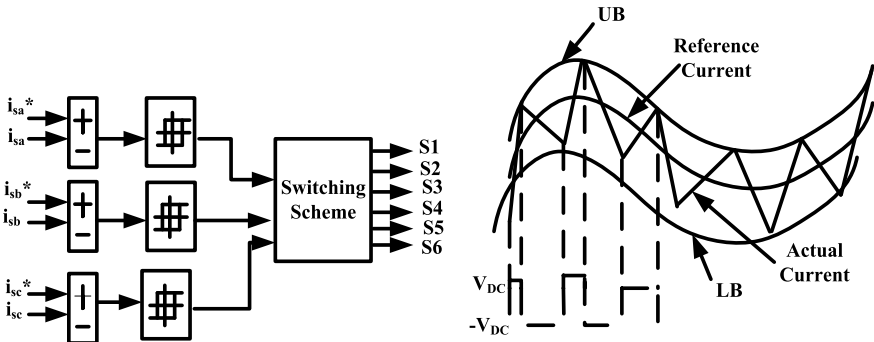


Fig. 10 Hysteresis current controller scheme

The switching pulses required for the inverter are designed in such a way that when the error signal goes beyond the upper band of hysteresis loop, the lower switches of inverter are ON and upper switches are OFF, and similarly, the upper switches are ON and lower switches are OFF when the error signal exceeds the lower band. So, the actual current is always tracked with respect to reference current inside the hysteresis band.

3 Simulation Results and Discussion

In this case, the system performance is analyzed by connecting nonlinear load with the DG system first without UPQC and then with MSRF-based UPQC. The performance of series APF can be evaluated by introducing voltage sag into the system. The profile of load voltage shown in Fig. 11a conforms that voltage sag is introduced from 0.1 to 0.3 s of the load voltage waveform. For sag condition, the series APF detects the voltage drop and injects the required voltage through the series coupling transformer. It maintains the rated voltage across the load terminal. In order to compensate the load voltage sag, UPQC (employing MSRF scheme) is turned on, which injects compensating voltage at the PCC as displayed in Fig. 11b; as a result, the load voltage is same as that of source voltage. The load voltage after compensation is shown in Fig. 11c. In general, the operation of the series part of the UPQC can be described as rapid detection of voltage variations at source, and it injects the compensation voltage which maintains rated voltage across the load terminal.

The shunt VSI in the UPQC is realized as shunt APF and is applied to solve the current-related PQ distortions, current harmonic distortion, reactive power demand, etc. In order to investigate the performance of shunt APF, a rectifier-based nonlinear load is introduced into the system and the level of harmonics is checked. It is observed from Fig. 12a that the source current waveform has a total harmonic distortion (THD) of 16.60% as per the FFT analysis of the source current shown in Fig. 12b. In order to make source current to be sinusoidal, the shunt APF of the UPQC with conventional MSRF technique is turned on, at $t = 0.1$ s which injects compensating current as displayed in Fig. 12c. Hence, the THD level comes down to 2.54% as shown in Fig. 12d.

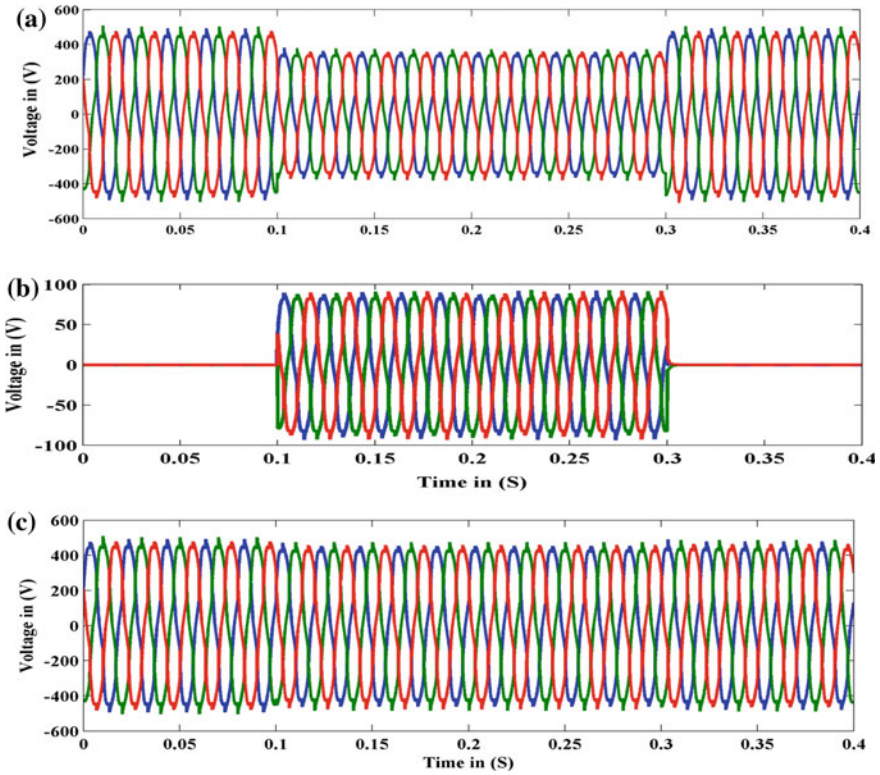


Fig. 11 Profile obtained under (sag compensation) **a** Load voltage before compensation. **b** Compensating voltage injected by UPQC. **c** Load voltage after compensation

4 Conclusion

The research reveals that MSRF technique of UPQC makes possible for improving the power quality of a solar PV-based DG system connected with nonlinear load. The advantage of MSRF technique is that instead of using PLL circuit it uses a basic unit vector generation scheme for the production of sine and cosine angles. The suggested method delivers superior output than the existing method in terms of harmonic mitigation and compensation of active and reactive power. In the future, the work may be extended by integrating different control approach for reference current generation of UPQC, and DC-link voltage control algorithm may be implemented for better PQ mitigation purpose.

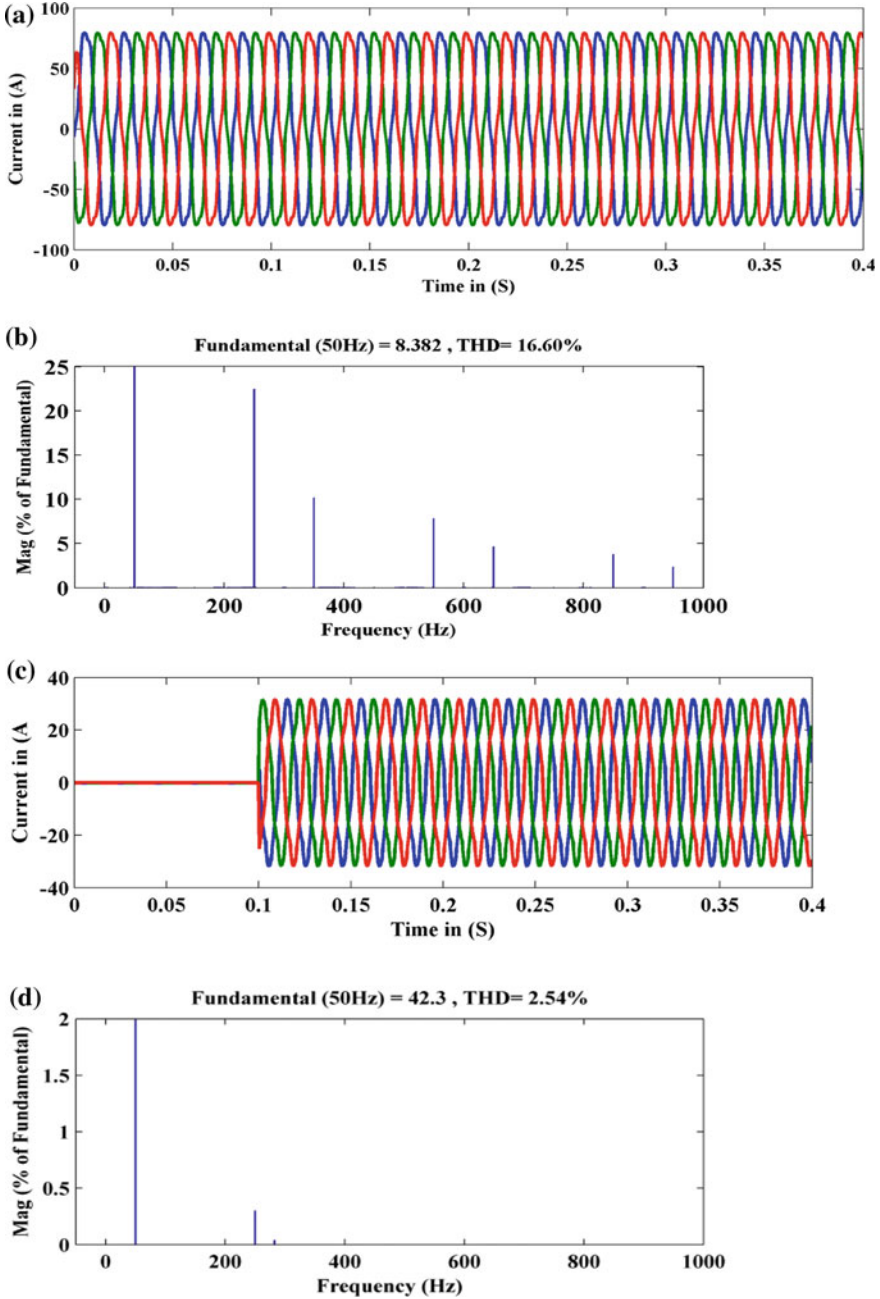


Fig. 12 Profile obtained under (harmonics mitigation) a Source current before compensation. b Harmonics content before compensation. c Compensating current injected by UPQC. d Harmonics content after compensation

References

1. Badoni M, Singh B, Singh A (2017) Implementation of echo-state network-based control for power quality improvement. *IEEE Trans Ind Electron* 64(7):5576–5584
2. Mahmoud MS, Rahman MSU, Fouad MS (2015) Review of microgrid architectures—a system of systems perspective. *IET Renew Power Gener* 9(8):1064–1078
3. Samal S, Hota PK (2017) Design and analysis of solar PV-fuel cell and wind energy based microgrid system for power quality improvement. *Cogent Eng* 4(1):1402453
4. Suresh M, Patnaik SS, Suresh Y, Panda AK (2011) Comparison of two compensation control strategies for shunt active power filter in three-phase four-wire system. In: *Innovative smart grid technologies (ISGT), IEEE PES*, pp 1–6
5. Tang Y, Loh PC, Wang P, Choo FH, Gao F, Blaabjerg F (2012) Generalized design of high performance shunt active power filter with output LCL filter. *IEEE Trans Ind Electron* 59(3):1443–1452
6. Hosseinpour M, Yazdian A, Mohamadian M, Kazempour J (2008) Design and simulation of UPQC to improve power quality and transfer wind energy to grid. *J Appl Sci* 8(21):3770–3782
7. Xu Q, Hu X, Wang P, Xiao J, Tu P, Wen C, Lee MY (2017) A decentralized dynamic power sharing strategy for hybrid energy storage system in autonomous DC microgrid. *IEEE Trans Ind Electron* 64(7):5930–5941
8. Montero MIM, Cadaval ER, Gonzalez FB (2007) Comparison of control strategies for shunt active power filters in three-phase four-wire systems. *IEEE Trans Power Electron* 22(1):229–236
9. Samal S, Hota PK (2017) Power quality improvement by solar photo-voltaic/fuel cell integrated system using unified power quality conditioner. *Int J Renew Energy Res (IJRER)* 7(4):2075–2084
10. Singh BN, Singh B, Chandra A, Al-Haddad K (2005) Design and digital implementation of active filter with power balance theory. In: *IEEE Proceedings-electrical power application*, vol 152(5), pp 1149–1160
11. Akagi H, Kanazawa Y, Nabae A (1984) Instantaneous reactive power compensators comprising switching devices without energy storage components. *IEEE Trans Ind Electron Appl* 20(3):625–630
12. Samal S, Hota PK (2017) Power quality improvement by solar photo-voltaic/wind energy integrated system using unified power quality conditioner. *Int J Power Electron Drive Syst* 8(3):14–24
13. Jowder FAL (2009) Design and analysis of dynamic voltage restorer for deep voltage sag and harmonic compensation. *IET Gener Transm Distrib* 3(6):547–560
14. Altas IH, Sharaf AM () A photovoltaic array simulation model for Matlab-Simulink GUI environment. In: *Clean Electrical Power, ICCEP'07*, pp 341–345
15. Femia N, Petrone G, Spagnuolo G, Vitelli M (2007) Optimization of perturb and observe maximum power point tracking method. *IEEE Trans Power Electron* 20(4):963–973
16. Viinamäki J, Jokipii J, Messo T, Suntio T, Sitbon M, Kuperman A (2014) Comprehensive dynamic analysis of photovoltaic generator interfacing DC–DC boost power stage. *IET Renew Power Gener* 9(4):306–314
17. Kalirasa A, Dash SS (2010) Simulation of closed loop controlled boost converter for solar installation. *Serb J Electr Eng* 7(1):121–130

Load Balancing in Cloud Computing: Survey



Arabinda Pradhan, Sukant Kishoro Bisoy and Pradeep Kumar Mallick

Abstract Today cloud computing is the most rising innovation due to its groundbreaking and significant power. It is a type of Internet-based computing which enables to provide various services in cost-effective manner on user's demand. Virtualization, grid technique and utility computing are the most popular emerged technologies, which are used in cloud computing and make it most powerful. But still cloud computing has number of critical issues, such as security, load adjusting, adaptation to non-critical failure and so forth. The gigantic development of cloud computing will cause the overburden on the server. In this way, it will lead to degrade the performance of networks. A decent load balancing adjusting can make cloud computing increasingly productive and improves execution of client fulfilment. This paper exhibits the far-reaching survey of cloud computing and load balancing techniques.

Keywords Cloud computing · Load balancing · Virtual machine

1 Introduction

Cloud computing provides web-based services with a user's information, computation and software as shown in Fig. 1. It also provides on-demand access to sharing resources like servers, storage, networks, applications and services [1].

Cloud provides a good platform and infrastructure to its end user. Every one of the administrations offered by servers to customers are given by cloud service provider (CSP) which is on a very basic level equivalent to filling in as the Internet service provider (ISP) in the electronic registering. Figure 2 shows the virtualization concept

A. Pradhan (✉) · S. K. Bisoy
Department of CSE, CVRCE, Bhubaneswar, Odisha, India
e-mail: arabindapradhan1@gmail.com

S. K. Bisoy
e-mail: sukantabisoyi@yahoo.com

P. K. Mallick
Department of CSE, KIIT, Bhubaneswar, Odisha, India
e-mail: pradeepmallick84@gmail.com

© Springer Nature Singapore Pte Ltd. 2020
R. Sharma et al. (eds.), *Innovation in Electrical Power Engineering, Communication, and Computing Technology*, Lecture Notes in Electrical Engineering 630,
https://doi.org/10.1007/978-981-15-2305-2_8

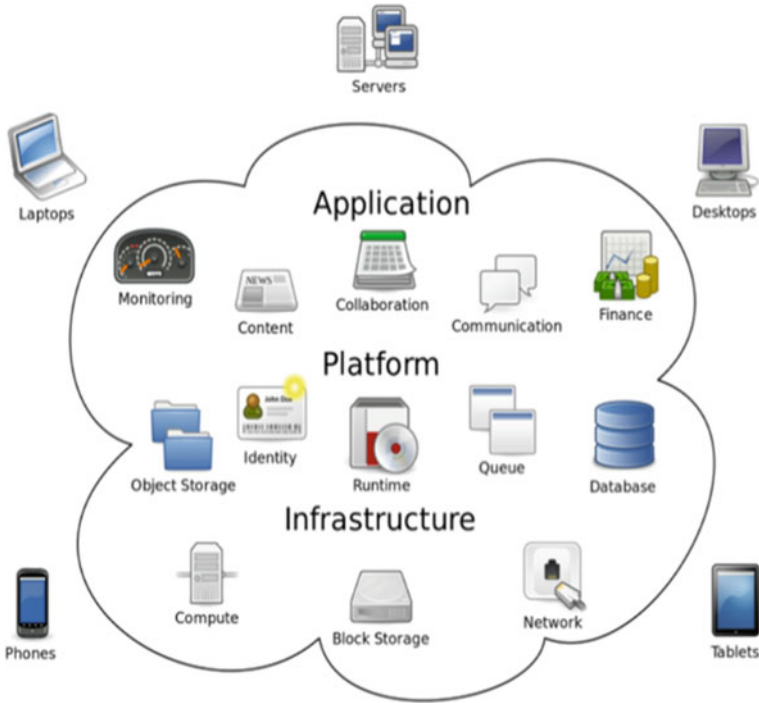


Fig. 1 Cloud computing [1]

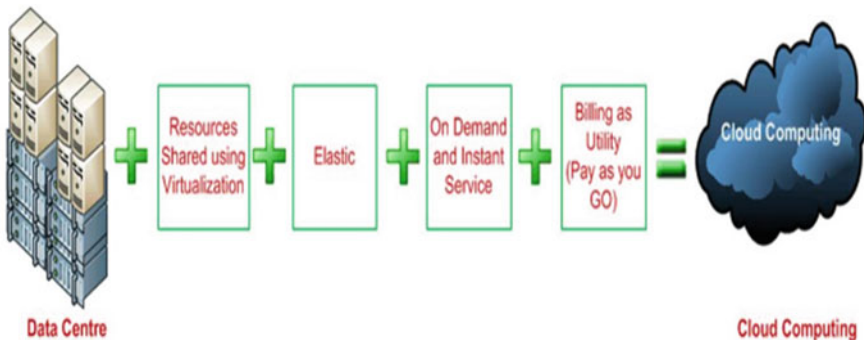


Fig. 2 Schematic diagram of cloud computing [2]

where user can access all the resources with a high-speed network which includes low cost. This innovation is planned with the new thought of organizations provisioning to customers without procuring these organizations and set away on their local memory [12]. Virtualization technology in cloud computing helps enterprises or an



Fig. 3 Three level of cloud computing [3]

organization to lease registering power as virtual machines to the clients. The clients may use number of virtual machines [13].

Through cloud network, end users and organization share, process and store their needed information in third-party data centres [2]. It depends on sharing of resources through virtualization technique. Through virtualized memory stockpiling system, the memory interface for a visitor OS is virtualized and provides high storage capacity [14]. Cloud computing involves three levels: cloud customer or client or user, cloud service provider (CSP) and cloud network (transmission media or path of the cloud) as illustrated in Fig. 3 [3].

In this paper, Sect. 2 contains features and characteristics, and then following sections are as follows: deployment model, service model, various research area, load balancing concept, architecture, entities, classification, advantage and CloudSim simulation tool.

2 Features [4] and Characteristics [2]

Features and characteristics of cloud computing are written as below:

- Mobility and wide network access: all required services are available anywhere in the globe.
- Saves time: users are accessing and view their needed information.
- Popular: most of people are using cloud computing to get their services.
- Cost: due to pay as use, it is very cost-effective.
- Maintenance: maintenance is easy in cloud computing.
- Throughput: cloud computing gives a good effective result because many users can work simultaneously on same data.
- Reliability: cloud computing is reliable in nature.
- Elasticity: resources and data are pooled on demand.
- Security: information is secure.
- Scalable: scale of cloud computing is increased.
- On-demand self-service: in cloud computing, client can persistently watch the server time, capacities and designated organize capacity.
- Resources pooling: resources are being used by user as on demand.

- Rapid elasticity: a wide range of services just as assets are accessible to its end client.
- Measure services: every asset that is utilized can be assessed, controlled and declared for both the provider and purchaser. IT administrations are charged as pay per use.

3 Cloud Deployment Model

There are four sorts of cloud deployment models [5]:

- Private cloud: this cloud computing is overseen by single association or by a specialist organization [7], and also its infrastructure is used by this organization.
- Community cloud: this cloud is overseen by a few associations and supports a particular network and has shared the applications or services.
- Public cloud: this model possesses and overseen by a huge cloud service provider (CSP). All customers who need to use resources on a participation premise or on a membership premise [7].
- Hybrid cloud: it is the combination of at least two of the above models, i.e. public, private and community model [7].

4 Service Model

There are different types of service architecture in Fig. 4 as follows [3]:

- Software as a Service (SaaS),
- Platform as a Service (PaaS),
- Infrastructure as a Service (IaaS).

4.1 Software as a Service (SaaS) [1]

It provides software licensing on subscription and then implements as on demand. All required software is remotely available, so no extra hardware is required. There is no need for organization to maintain set-up or installation.

The SaaS can be categorized as [1]:

- Business utility SaaS: some applications are used by business and individuals for organization to store and process the data, for example use of customer relationship management (CRM).

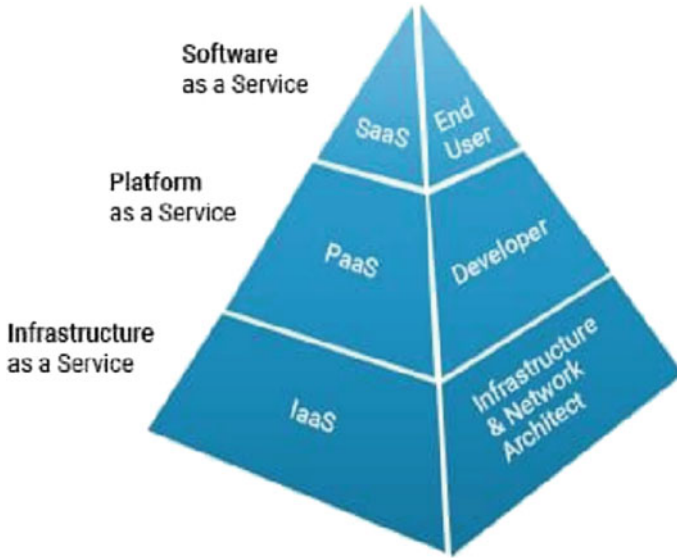


Fig. 4 Service model of cloud computing [6]

- Social networking SaaS: Nowadays social media is spread over. Some applications like Facebook, Twitter, Instagram, etc. are used by individuals for sharing information or data, videos and networking.

4.2 Platform as a Service (PaaS) [1]

This model conveys different applications over the Internet. PaaS provides various tools for software and hardware which are needed for various application developments. Resources are provided by PaaS and maintain by IT team. A PaaS provider supports all software users to sign in and begin utilizing the stage through a web program interface. By the help of PaaS, users manage, develop, deploy, configure and maintain various applications that developed over the cloud.

The PaaS can be categorized as:

- Computing platforms: it provides various platforms such as Amazon, Snapdeal and other web services. It provides processing, storage place and available bandwidth for services. User can upload their software to run various applications on their infrastructure.
- Business application platforms: it provides various application platforms that are suitable for all type of business application. It will provide to its users that high flexibility with less technical efforts and easily maintain.

- Social application platforms: it will provide platform to various social platforms such as Twitter and Facebook, and others provide API, where developers required writing new application.

4.3 *Infrastructure as a Service (IaaS)*

It is a model that gives virtualized figuring asset idea over the web, where a cloud provider has the foundation segments customarily that is available in an on-premises server farm or data centre. The cloud provider additionally gives charging, observing, sign in, security, load adjusting and bunching [8]. IaaS provides online services for underlying network infrastructure like physical computing resources, location, scaling, security, backup, etc. This shows an advantage for both whom providing the infrastructure and who use it. In particular, IaaS provides a good marketing that runs their business on web. Infrastructure such as hardware, data centre, host, server space.

5 Research Areas in Cloud Computing

As cloud administrations have various spaces, issues, organization models and particular algorithmic methodologies, there is an immense degree for research. The accompanying subjects offer a great deal of degree for research researchers in the cloud framework area. Various research areas are shown in Table 1.

Table 1 Various research field in cloud computing

1. Load balancing	2. Cloud access control
3. Security	4. Energy improvement
5. Virtualization	6. Information isolation security
7. Data isolation and recuperation	8. Verifiable calculation
9. Scheduling for asset improvement	10. Failure discovery and forecast
11. Cloud cryptography	12. Task scheduling

6 Load Balancing Concept

Load balancing is based upon the distributing of workloads in cloud computing environment. It balances all workload requests by various resources among different PCs, frameworks or servers. The basic goals of utilizing load balancing are:

- To keep up framework solidness.
- To improve framework execution.

7 Load Balancing Architecture [17]

Load balancing mentioned in Fig. 5 comprises of four principles, for example client, data centre controller, load balancer and the calculation to be utilized.

Following steps are utilized for the execution of a solicitation by the client.

- I. Every demand from client lands at data centre controller.
- II. Data centre controller lines all the approaching solicitations and questions the central load balancer for assignment of solicitations.
- III. Central load balancer includes a database that holds tables which are parsed following the computation to be used finds the most sensible virtual machine and returns the ID of the picked VM to the data centre controller.
- IV. At long last, data centre controller assigns the solicitation to VM whose ID is given by central load balancer.

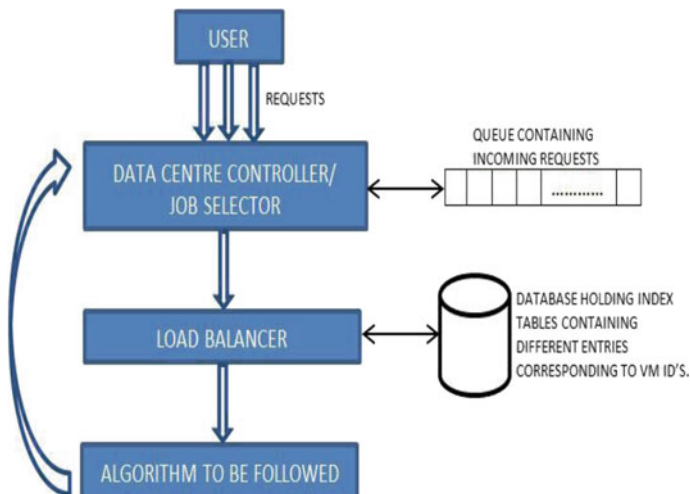


Fig. 5 Load balancing architecture [17]

8 Load Balancing Entities [15]

There are five entities involves in CloudSim simulation for load balancing such as data centre, data centre broker, host, virtual machine (VM) and cloudlet (task).

From Fig. 6, two VMs are present within physical machine host. Data centre is register inside CIS and all the information or characteristics about data centre is goes into broker.

8.1 Data Centre

It is the core model of infrastructure services that create data centre classes in CloudSim that classes are used in load balancing method. It is composed set of host which is in charge of overseeing virtual machines during their life cycle. Data centre is very similar to IaaS provider from input task with regard to VMs through data centre broker [15].

8.2 Data Centre Broker

It is a data centre broker class, which is responsible to submit the task to data centre. Initially, it communicates to cloud information service (CIS, it is an entity that contains the available resources on cloud) to retrieve the resources from CIS. It has the details of characteristics of what the data centre has. It is used for submitting VM provisioning requests to be able data centre and submit the task to VMs [15].

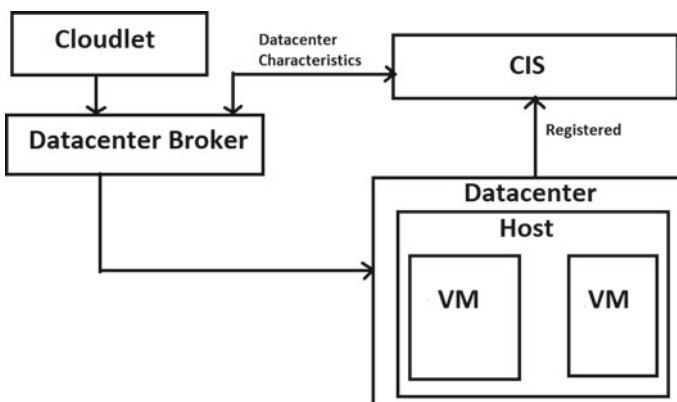


Fig. 6 CloudSim entities of load balancing

8.3 Host

It is the physical machine in a cloud. It is appointed a pre-designed handling ability, memory, stockpiling, data transmission and booking arrangement for designating preparing centres to VM [15]. Actually, this physical host is virtualized into number of VMs for allocating the processor according to request from users or organizations.

8.4 Virtual Machine

It is a logical machine in cloud that is virtualized on number of VM. Host has number of VM and allocating core or processor based on sharing policy, i.e. space shared and time shared. Each VM is handling each request from user [15].

8.5 Cloudlets

It is also known as task that is handled by VM in CloudSim framework. It will be submitted in broker, and broker has information about data centre. So, broker assigns the cloudlet to some VM that is within host [15].

9 Load Balancing Classification [10]

This is divided into two categories: static load balancing and dynamic load balancing.

9.1 Static Load Balancing

This type of load balancing is used only in homogeneous environments and not flexible that means it cannot change its attribute. All the entities are fixed in nature. This algorithm will not check the incoming requests and state of node [10]. Some static algorithms are as follows:

- Round robin load balancing algorithm (RR),
- Load balancing min-min algorithm (LB Min-Min),
- Load balancing min-max algorithm (LB Min-Max).

9.1.1 RR Algorithm

In this calculation, fixed quantum time is given to the task or assignment. It assigns jobs to all hubs in a roundabout manner. Processors are allocated in a roundabout request. This computation gives faster response by virtue of proportional remaining task at hand appropriation among procedures. Regardless, a couple of centres or hubs may be over stacked while others remain latent and under-utilized.

9.1.2 LB Min-Min

A rundown of jobs is kept up, and least fulfilment time is determined for all the available hubs. Job with least fulfilment time is appointed to the machine. It gives great outcomes when little undertaking is more.

9.1.3 LB Min-Max

A rundown of jobs is kept up, and least fulfilment time is determined for all the available hubs. Job with most extreme finishing time is consigned to the machine.

9.2 Dynamic Load Balancing

This strategy utilizes past and current state of hub to distribute the load. The user requirements and resources can be changed at run time. They are suited in homogeneous as well as heterogeneous environments. Dynamic load balancing is two types.

9.2.1 Distributed

This type of load balancing adjusts the calculation of load that is executed by all data centre and sharing the load among these data centre.

9.2.2 Centralized

In this type, a central hub is in charge of load balancing of the entire framework. Different hubs communicate with this focal hub [10].

Some common dynamic algorithms are as follows:

- Throttled load balancing algorithm,
- Equally spread current execution (ESCE) load balancing algorithm,

- Modified throttled load balancing algorithm,
- Throttled modified algorithm (TMA),
- Throttled load balancing algorithm [10, 12, 16–18].

This method is used for distribution of load that completely deploy on VMs. At the point when the customer sends the solicitation, the load balancer quickly gets caution and scans for the gathering which can oversee effectively and allocates that request.

- ESCE [10]

This algorithm keeps up the rundown of whole virtual machines and tasks. At the point when this algorithm gets a solicitation, it filters the rundown of VMs. On the off chance that a VM is discovered which can deal with the customer's solicitation, at that point the solicitation is assigned to that specific VM. This calculation disseminates the equivalent burden among all VMs.

- Modified throttled load balancing algorithm [16, 17]

In this algorithm, the load balancer keeps up a file table of virtual machines containing the province of VMs. The calculation utilizes a technique for choosing a VM for handling customer's solicitation where the most readily accessible VM is chosen. If the machine is free, then it is doled out with the solicitation and ID of VM is come back to data centre controller; otherwise, (-1) is returned. At the point when the following solicitation shows up, the list table is filtered from record alongside effectively allocated VM and in like manner next VM is picked relying upon the province of VM.

- Throttled modified algorithm (TMA) [16]

The TMA load balancer performs burden adjusting by refreshing and keeping up two record tables. Accessible index: status of VMs is accessible '0'. Busy index: status of VMs is not accessible '1'. It provides a better performance than other load balancing algorithm.

10 Advantage of Load Balancing [9, 11]

Various advantages of load balancing are described as below:

- Throughput: it improves the result or throughput.
- Fault tolerance: system must be free from failure.
- Migration: resources are moved from hub to hub to improve performance.
- Response time: measuring to take the resources for service.
- Scalability: improve the system scale and performance.
- Cost-effective: system improves their performance with lower cost.

11 CloudSim [15]

CloudSim is an efficient simulation tool which can be used to creating a good infrastructure of cloud. All proposed algorithm is run under this tool. It also is used for assigning each client request to available VMs. Those VMs are present in host and managed by data centres. Version name is CloudSim 3.0.3.

12 Conclusion and Future Work

Cloud provides a good platform and infrastructure to its end user. Every one of the administrations offered by servers to clients is given by CSP which is on a very basic level equivalent to filling in as the ISP in the electronic registering. Load balancing helps appropriate use of resources and improves the presentation of the framework. It balances all workload requests by various resources among different PCs, frameworks or servers. Many research fields are available in load balancing as mentioned in Table 1. The basic goals are to keep up framework solidness and to improve framework execution. We have summarized the basic concepts of load balancing with hot research area. In future, we would develop a heuristic-based load balancing algorithm to optimize different parameters.

References

1. Samreen SN, Valmik NK, Salve SM, Khan PN (2018) Introduction to cloud computing. IRJET 05(02)
2. Diaby T, Rad BB (2017) Cloud computing: a review of the concepts and deployment models. I.J. Inf Technol Comput Sci 6:50–58
3. Chary CN, Ashok D, Dilip P (2017) Advantages and solutions in cloud computing. Int J Innovative Comput Sci Eng (IJEACSE) 4(3):149–152
4. Fatima N, Parveen Z (2017) Cloud computing issues and countermeasures. Int J Eng Appl Comp Sci (IJEACS) 02(02)
5. Trilochan, Verma A (2017) Cloud computing: evolution and challenges. IJESC 7(4)
6. Paul V, Pandita S, Randiva M (2018) Cloud computing review. Int Res J Eng Technol (IRJET) 05(03)
7. Aathishvar M, Kumar NM, Ganesh K (2018) Study on cloud computing. Int J Contemp Res Comput Sci Technol (IJCRCST) 4(1)
8. Sindhu S, Sindhu D (2017) Cloud computing models and security challenges. IJESC 7(4)
9. Narayanan SS, Ramakrishnan M (2016) A comprehensive study on load balancing algorithms in cloud computing environments. Res J Appl Sci Eng Technol 13(10):794–799
10. Sajjan RS, Yashwantro BR (2017) Load balancing and its algorithms in cloud computing: a survey. IJCSE 5(1):95–100
11. Amandeep, Yadav V, Mohammad F (2014) Different strategies for load balancing in cloud computing environment: a critical study. IJSRET 3(1):85–90
12. Choudhary R, Kothari A (2018) A novel technique for load balancing in cloud computing environment. iJ: Int J Softw Hardw Res Eng 6. ISSN-2347-4890

13. Dhari A, Khaldun IA (2017) An efficient load balancing scheme for cloud computing. *Indian J Sci Technol* 10(11). <https://doi.org/10.17485/ijst/2017/v10i11/110107>
14. Carlos BW, Yong WL, Duncan B, Olmsted A, Vassilakopoulos M, Lambrinouidakis C (2017) Cloud computing 2017. The eighth international conference on Cloud Computing, GRIDs, and Virtualization, Athens, Greece. ISBN: 978-1-61208-529-6
15. Patel S, Bhatt M (2017) Implementation of load balancing in cloud computing thorough Round Robin & Priority using CloudSim. *Int J Rapid Res Eng Technol Appl Sci* 3(11)
16. Phi1 NX, Tin CT, Thu LNK, Hung TC (2018) Proposed load balancing algorithm to reduce response time and processing time on cloud computing. *Int J Comput Netw Commun (IJCNC)* 10(3)
17. Bhagyalakshmi, Malhotra D (2018) Review paper on Throttled Load balancing algorithm in cloud computing environment. *IJSRSET* 4(2). Print ISSN: 2395-1990
18. Panchal B, Parida S (2018) A review: different improvised Throttled load balancing algorithms in cloud computing environment. 5(7). ISSN 2349-4476. www.ijetmas.com, July 2017

Participation of Geothermal and Dish-Stirling Solar Power Plant for LFC Analysis Using Fractional-Order Controller



Priyambada Satapathy, Manoj Kumar Debnath, Pradeep Kumar Mohanty and Binod Kumar Sahu

Abstract In this article, a novel heuristic moth flame optimization (MFO) technique has been suggested to optimize the gains of fractional-order proportional–integral–derivative (FOPID) controller and PID controller over a hybrid source power plant to analyze the load frequency control (LFC). Each area comprises dish-stirling solar thermal system (DSTS), conventional steam power plant (SPP), and a geothermal power plant (GTPP) to scrutinize the vigorous performance of power system for load frequency control. For more analysis, governor dead-band (GDB) and generation rate constraint (GRC) of the SPP have been considered as 0.036 and 0.003, respectively. The dynamic responses of two equal area systems are observed by implementing FOPID and PID controllers independently. The investigation exposes the dominance of FOPID controller over PID controller.

Keywords Load frequency control · Moth flame optimization · Fractional-order PID controller

1 Introduction

National geographic estimated that 320 billion kilowatt-hours of energy every day is required to meet the never-ending struggle of human race in order to enhance the standard of living. Although in present scenario the massive requirement is fulfilled by burning of fossil fuels, it is also non-renewable and rapidly reducing. These

P. Satapathy · M. K. Debnath (✉) · P. K. Mohanty · B. K. Sahu
Siksha 'O' Anusandhan Deemed to be University, Bhubaneswar, Odisha 751030, India
e-mail: mkd.odisha@gmail.com

P. Satapathy
e-mail: lirasatapathy@gmail.com

P. K. Mohanty
e-mail: pradipmohanty@soa.ac.in

B. K. Sahu
e-mail: binoditer@gmail.com

© Springer Nature Singapore Pte Ltd. 2020
R. Sharma et al. (eds.), *Innovation in Electrical Power Engineering, Communication, and Computing Technology*, Lecture Notes in Electrical Engineering 630,
https://doi.org/10.1007/978-981-15-2305-2_9

fuel sources have also contributed greatly to global warming and pollution. A few promising alternatives like atomic energy, solar energy, geothermal energy, energy from wind, ocean energy, and bio-fuels are explored just for a cleaner and greener future. An interconnected system comprises several control areas to produce power to meet the customer demand as well as the requirement of constant frequency, and constant tie-line power exchange is also required for the steady operation. Thus, load frequency controller is deliberated to uphold equilibrium within the power generation and load demand in each area in order to enrich the quality of delivered power [1, 2].

For LFC analysis, researchers employed ant lion optimizer algorithm-based PID plus second-order derivative controller in a hybrid power system [3]. The technique of controller is established in a hydro-generating unit for AGC [4]. Further, addition of two degrees of freedom fractional-order controller along with PID controller enriches the beauty of AGC [5]. A new innovative grasshopper optimization algorithm is suggested to tune the fractional-order PID controller in order to get better dynamic responses for AGC [6]. In 2019, a fuzzy logic-based FOPI-FOPD controller is employed by author for better frequency regulation [7]. In [8], a brief discussion has been given about adaptive neuro-fuzzy inference system over AGC. The logic of superconducting magnetic energy storage unit added with thyristor controlled series compensator is implemented to face all the challenges regarding LFC issues [9]. Moth flame optimization technique is inspired by the navigation method of moths in nature known as transverse orientation. The MFO algorithm provides very promising and competitive responses for real engineering complications. In 2018, authors employed MFO tuning method in a multi-area network to solve AGC issues [10]. The application of MFO technique is implemented by using cascaded controller [11] and fuzzy logic-based PID controller [12] to analyze the LFC problems. Literature study exposes that authors suggested MFO method to tune PIDF controller in a photovoltaic incorporated power system for frequency regulation [13]. Few years back, authors gave a brief description about transfer function of AGC along with governor dead-band [14]. Again in 2013, authors researched about two degrees of freedom PID controller along with governor dead-band nonlinearity tuned by differential evolution technique for LFC scrutiny [15]. A modified gray wolf optimization (GWO) technique is employed to tune hybrid PID-fuzzy-PID controller for research analysis on LFC [16]. In 2019, authors introduced an innovative 2-DOF-PID controller along with GWO technique over a multi-source system [17]. In [18], gravitational search algorithm (GSA) is employed to tune the fuzzy-PID controller over hybrid system. A novel profound PD-fuzzy-PID cascaded controller is implemented to regulate the oscillations on frequency during disturbances [19].

A detailed research analysis implies that PID controller is employed in most of the cases due to its simplicity, but PID controllers are not capable to perform well in the combined mode in many control processes. So an innovative fractional-order PID controller tuned with MFO is deliberated in this article to solve the numerous AGC issues. The salient points of the research work in this article are as follows:

- i. To construct a two equal area multi-source (GTPP, DSTS, and SPP) power system model in MATLAB/Simulink environment.

- ii. Governor dead-band (GDB) and generation rate constraint (GRC) have been considered for more analysis of SPP for AGC.
- iii. Modeling and enactment a novel MFO-tuned FOPID controller for LFC.
- iv. To estimate and compare the performance of the FOPID controller approach with PID controller to face LFC problems.

2 System Investigated

Figure 1 deliberates the transfer function model of examined two equal area power systems interconnected by a tie-line. Both the areas comprise a geothermal power plant (GTPP), a dish-stirling solar thermal system (DSTS), and a steam power plant (SPP) as a source of generating power. The reheat turbine of solar power plant is considered along with governor dead-band (0.036) and generation rate constraint (3%). The values of different constraints of this scrutinized system are given in appendix. The parameters of FOPID and PID controller are tuned by employing

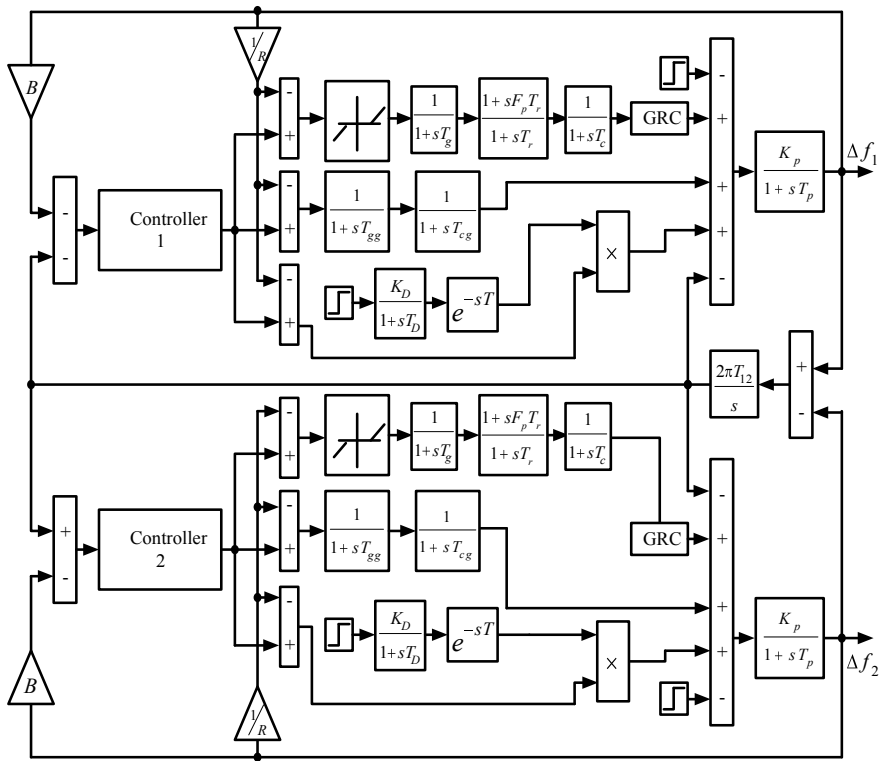


Fig. 1 Transfer function model of the power system under study

MFO technique. Area control error (ACE) works as input to the controller of each area, and the expression of ACE for the two area systems is represented below

$$ACE_1 = \Delta P_{12} + B_1 \Delta \omega_1 \quad (1)$$

$$ACE_2 = \Delta P_{21} + B_2 \Delta \omega_2 \quad (2)$$

To achieve the desired responses of moth flame optimization technique, integral time absolute error has been considered as cost function. Equation (3) signifies the expression for ITAE objective function.

$$ITAE = \int_0^t (|\Delta f_1| + |\Delta f_2| + |\Delta P_{tie}|) \times t dt \quad (3)$$

3 Controller Structures and Their Optimal Design

PID Controller

Proportional–integral–derivative (PID) controller is still deliberated as the utmost demandable controller for its simple construction and reliable nature. The parallel connection of proportional, integral, and derivative controller leads to the fruitful operation of PID controller. The transfer function of output and input of the controller in terms of time domain is described in Eqs. (4) and (5), respectively

$$u(t) = K_p e(t) + K_i \int_0^t e(t) dt + K_d \frac{de(t)}{dt} \quad (4)$$

$$G(s) = K_p + \frac{K_i}{s} + K_d s \quad (5)$$

where K_p , K_i , and K_d signify the proportional, integral, and derivative gains, respectively.

FOPID Controller

Fractional calculus is the simplification process of normal calculus. The differential equation is working along with fractional calculus for the fruitful operation of fractional-order controller. Infinite number of poles and zeros are needed to accomplish the transfer function of fractional-order controller. The below Eq. (6) represents the transfer function of fractional-order controller.

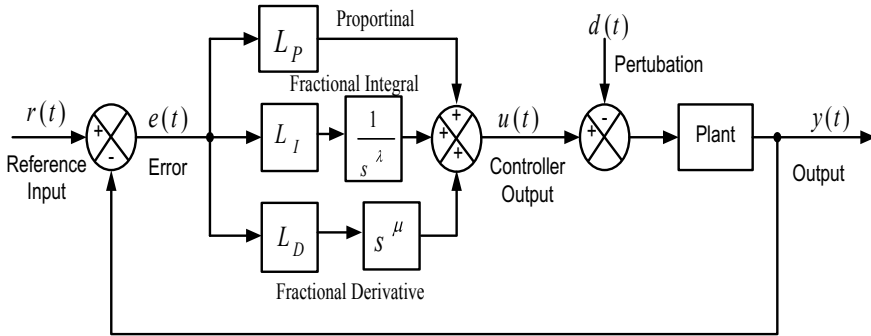


Fig. 2 Structure of FOPID controller

$$G_C(s) = K_p + \frac{K_i}{s^\lambda} + K_d s^\mu \tag{6}$$

In this above-described equation, λ and μ signify the fractional order of derivative and integral controller. The minimal value of λ and μ can be any real number within 0–1. The FOPID can be performed as a PI, PD, and PID controllers depending on the significance of λ and μ . The significance of both λ and μ must be kept as 1 to perform like a PID controller. To execute like a PI and PD controller, the significance of λ and μ for a FOPID controller must be kept in (1,0) and (0,1), respectively. The internal structure of FOPID controller is portrayed in Fig. 2.

4 Optimization Technique: Moth Flame Optimization (MFO)

In nature, larvae and adult are two main stages of insect in their lifetime. Generally, the conversion of larvae into moth occurs inside the cocoons. Moths travel by using transverse orientation for navigation method in night. Transverse orientation method is very helpful to walk in a straight path during long-distance journey. Similarly, by using this navigation technique, moth flies by sustaining a fixed angle with respect to the moonlight. The gain of the suggested PID and FOPID controller is updated by using the mathematical model of the navigation technique. The following steps are to be followed for the successful execution of MFO technique.

- i. Initialize the population of moths by knowing their strength. At initial condition, mention the higher band, lower band, and the dimensions of moths.
- ii. Update the location of moths with their previous location to get the best position.
- iii. Calculate the objective function values of MFO technique by employing the below equation

$$M(i, j) = (ub(i) - lb(i)) * rand + lb(i) \tag{7}$$

Here i and j signify the number of moth and flame, respectively. $ub(i)$ and $lb(i)$ are the upper band and lower band of the i th variable.

- iv. Finally, each moth updates their location to get the best position by employing the fitness value.
- v. Logarithm spiral mechanism is executed in order to execute the best fitness value and described in below equation.

$$S(M_i, F_j) = D_i \cdot e^{bt} \cdot \cos(2\pi t) + F_j \tag{8}$$

Here D_i is the distance between the moth and flame, and it is find out by $D_i = |F_j - M_i|$.

- vi. If $gen < max^m$, then update the generation by repeating the steps (ii)–(v) or else stop the program and find out the best fitness and best position.

5 Results and Discussion

Simulation of two equal areas of power system has been done by using MATLAB/Simulink circumstances. Simulink model is called through MFO program to optimally design the controllers by minimizing the cost function, i.e., ITAE. The efficacy and sturdiness of this designed hybrid system along with PID and FOPID controller are perceived from the dynamic responses. The analysis of this recommended controller has been done by subjecting 0.01 p.u SLP for both conventional PID and FOPID controller in area 1 separately. The instabilities of frequency of area 1 and area 2 and deviation interline power are represented in Figs. (3, 4, and 5) by tuning the gains of PID and FOPID controllers with moth flame optimization technique, respectively. Table 1 signifies the gains of suggested controllers as well as the time constant of geothermal power system. The transient response analysis on the basis of maximum overshoot, undershoot, and settling time of all deviations are

Fig. 3 Frequency deviation in area 1 due to SLP in area 1

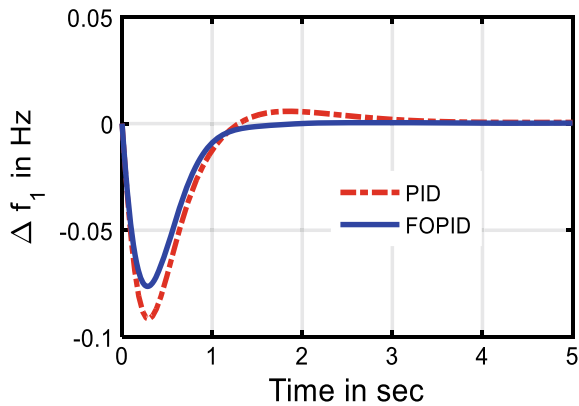


Fig. 4 Frequency deviation in area 2 due to SLP in area 1

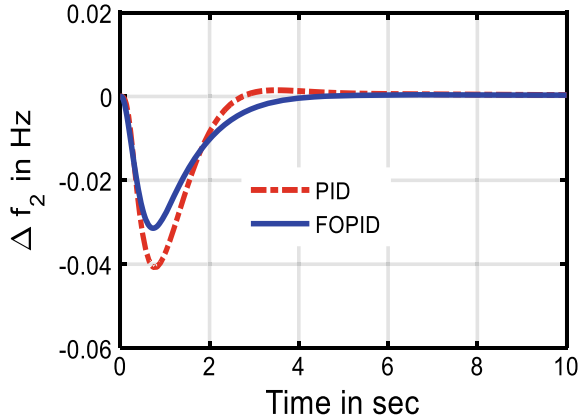
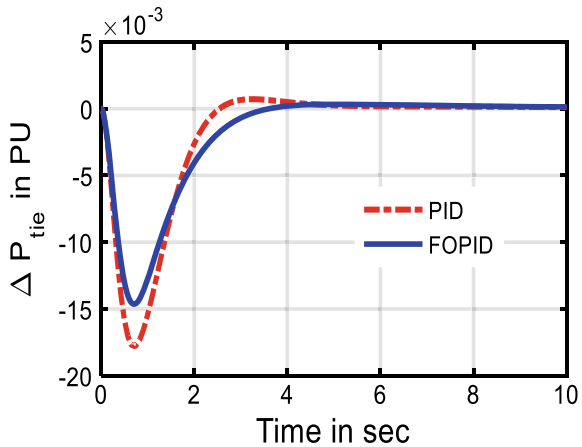


Fig. 5 Tie-line power deviation due to SLP in area 1



listed in Table 2. From the responses (Figs. 3, 4, and 5) and Table 2, it is proved that the offered technique provides more stability in the scrutinized system for AGC.

6 Conclusion

The objective of the current study is to analyze a PID controller and FOPID controller to regulate the frequency in a hybrid power system. An equal two area systems (GPP, DSTS, and SPP) comprises six units observed by employing ITAE as cost function. A SLP of 0.01 p.u is offered to confirm the efficacy of the employed FOPID controller which is introduced over a multi-source hybrid scrutinized system. The performance of the recommended controller is observed in terms of settling time, undershoot, and

Table 1 FOPID/PID controller constraints tuned by MFO technique

Controller	Control area 1					Control area 2				
	λ	μ	L_P	L_I	L_D	λ	μ	L_P	L_I	L_D
PID	NA	NA	0.7175	2.0000	0.2860	NA	NA	0.7709	0.4236	0.8805
FOPID	0.95	0.89	1.1482	2.0000	0.1838	0.97	0.87	0.1386	0.0899	2.0000

Table 2 Time-based response factors of PID and FOPID controllers over a hybrid multi-source system

Observation	Time domain evaluative indices of response	PID controller	FOPID controller
ΔP_{tie}	T_s in sec (0.05% band)	3.9715	3.1179
	Undershoots (Hz)	-0.0178	-0.0146
	Overshoots (Hz)	0.0007	0.000336
Δf_1	T_s in sec (0.05% band)	6.6962	1.7640
	Undershoots (Hz)	-0.0915	-0.0763
	Overshoots (Hz)	0.0058	0.000487
Δf_2	T_s in sec (0.05% band)	7.0940	3.8999
	Undershoots (PU)	-0.0407	-0.0314
	Overshoots (PU)	0.0015	0.000378

overshoot, and it helps to reduce the oscillation in the dynamic responses of system during perturbation.

Appendix

$T_p = 20, K_p = 120, T_c = 0.3, T_g = 0.08, F_p = 0.5, T_r = 10, B = 0.425, R = 2.4, T_{12} = 0.086, T_d = 5, K_d = 1, T_{gg} = 0.08, T_{cg} = 0.1.$

References

1. Johansson TB et al (1993) Renewable energy: sources for fuels and electricity.
2. Nanda J, Kaul BL (1978) Automatic generation control of an interconnected power system. In: Proceedings of the institution of electrical engineers, vol 125(5). IET Digital Library
3. Saikia LC, Sinha N (2016) Automatic generation control of a multi-area system using ant lion optimizer algorithm based PID plus second order controller. Int J Electr Power Energy Syst 80:52–63
4. Khodabakhshian A, Hooshmand R (2010) A new PID controller design for automatic generation control of hydro power systems. Int J Electr Power Energy Syst 32(5):375–382
5. Debbarma S, Lalit CS, Sinha N (2014) Automatic generation control using two degree of freedom fractional order PID controller. Int J Electr Power Energy Syst 58:120–129
6. Guha D, Roy PK, Banerjee S (2019) Grasshopper optimization algorithm-scaled fractional-order PI-D controller applied to reduced-order model of load frequency control system. Int J Model Simul:1–26
7. Arya Y (2019) A new optimized fuzzy FOPI-FOPD controller for automatic generation control of electric power systems. J Franklin Inst
8. Hosseini SH, Etemadi AH (2008) Adaptive neuro-fuzzy inference system based automatic generation control. Electr Power Syst Res 78(7):1230–1239

9. Padhan, S, Sahu RK, Panda S (2014) Automatic generation control with thyristor controlled series compensator including superconducting magnetic energy storage units. *Ain Shams Eng J* 5.3:759–774
10. Barisal AK, Lal DK (2018) Application of moth flame optimization algorithm for AGC of multi-area interconnected power systems. *Int J Energy Optim Eng (IJEEOE)* 7.1:22–49
11. Saikia LC, Saha D (2016) Automatic generation control in competitive market conditions with moth-flame optimization based cascade controller. 2016 IEEE Region 10 conference (TENCON). IEEE
12. Sahu PC, Prusty RC, Panda S (2017) MFO algorithm based fuzzy-PID controller in automatic generation control of multi-area system. In: 2017 International conference on circuit, power and computing technologies (ICCPCT). IEEE
13. Sharma M et al (2018) Frequency regulation in PV integrated power system using MFO tuned PIDF controller. In: 2018 IEEE 8th Power India international conference (PIICON). IEEE
14. Wu FF, Dea VS (1978) Describing-function analysis of automatic generation control system with governor deadband. *Electr Power Syst Res* 1.2:113–116
15. Sahu RK, Panda S, Rout UK (2013) DE optimized parallel 2-DOF PID controller for load frequency control of power system with governor dead-band nonlinearity. *Int J Electr Power Energy Syst* 49:19–33
16. Debnath MK, Jena T, Sanyal SK (2019) Frequency control analysis with PID-fuzzy-PID hybrid controller tuned by modified GWO technique. *Int Trans Electric Energy Syst*:e12074
17. Debnath MK, Singh MB, Mallick RK (2016) Design of optimal 2-DOF PID controller using GWO technique for automatic generation control of a multisource power system. 2016 IEEE Uttar Pradesh section international conference on electrical, computer and electronics engineering (UPCON). IEEE
18. Debnath MK et al (2016) Gravitational search algorithm (GSA) optimized fuzzy-PID controller design for load frequency control of an interconnected multi-area power system. In: 2016 International conference on circuit, power and computing technologies (ICCPCT). IEEE
19. Debnath MK, Jena T, Mallick RK (2017) Optimal design of PD-Fuzzy-PID cascaded controller for automatic generation control. *Cogent Eng* 4.1:1416535

Use of Teaching Learning Based Optimization for Data Clustering



Anima Naik

Abstract In the literature, there are hundreds of population-based optimization algorithms, which are inspired by nature. These algorithms have been proposed to solve different problems of different research area. Among them, teaching-learning-based optimization (TLBO) algorithm is one, which is based on learner's behavior in the classroom. For improvement of performance of this algorithm, number of variants of TLBO algorithms already have been proposed. This paper compares the performance of these variants of TLBO in terms of clustering of unlabeled data sets. Here, it has been shown how different variants of TLBO can be used to find the clusters of a user-specified cluster numbers. These algorithms are evaluated by using some real-life datasets and compared their performances by some statistical tests.

Keywords Teaching-learning-based optimization · Data clustering · Quantization error

Abbreviations

ESS	Extremely statistical significant
VSS	Very statistical significant
NSS	Not statistical significant
SS	Statistical significant
CTLBO	CoTLBO
PID	Pima Indian diabetes
HS	Haberman's survival
HR	Hayes Roth
EDM	Euclidean distance measure
UTT	Unpaired <i>t</i> -test
SE	Standard error

A. Naik (✉)
KL University, Hyderabad 500075, India
e-mail: animanaik@klh.edu.in

© Springer Nature Singapore Pte Ltd. 2020
R. Sharma et al. (eds.), *Innovation in Electrical Power Engineering, Communication, and Computing Technology*, Lecture Notes in Electrical Engineering 630,
https://doi.org/10.1007/978-981-15-2305-2_10

1 Introduction

In cluster analysis, data is partitioned into groups based on some measure of similarity. Clusters are formed so that objects in the same cluster are very similar and objects in different clusters are distinct. Hard clustering and soft clustering are two broad categories of clustering. “*In hard clustering each data point belongs to only one cluster whereas in soft clustering each data point can belong to more than one cluster*”. Here, we have concentrated only on hard clustering. Many hard clustering methods can be from literature, such as k-mean, iterative self-organizing data (ISODATA), and learning vector quantizers (LVQ).

We can see from literature that there are number of population-based optimization techniques that have been used for data clustering. PSO, DE, ABC, ACO, TLBO etc. are commonly used algorithm for data clustering. Among them, TLBO is algorithm-specific parameter-free algorithm [1]. Hence, there is no risk on tuning parameters in terms of decreasing performance of algorithm. Already this algorithm has been successfully applied by various researchers to solve different problems of different research areas [2–9]. They have supported that the TLBO algorithm is an effective optimization algorithm and involves comparatively less computational effort. So the effectiveness and the computational effort requirement of TLBO may be considered. The concept of elitism is utilized in most of the evolutionary and population-based optimization algorithm. Based on this elitism concept, the number of problems has been solved using TLBO [10]. Similarly, researchers have done different modification on TLBO for improvement of convergence characteristic of TLBO algorithm [11–16]. So that variants of TLBO algorithm has been evolved. As TLBO algorithm can be used for data clustering [3], effectiveness and performance of variants of TLBO algorithms have been checked while clustering some real-life datasets.

The remaining of paper has been arranged in the form of Sect. 2 which describes TLBO and variants of TLBO algorithms in brief. Section 3 describes the implementation of variants of TLBO algorithm for data clustering problems and compares their performance. The paper concludes with Sect. 4.

2 TLBO Algorithm

TLBO algorithm is based on learners’ output that is influenced by teacher as well as other learners from classroom. This optimization algorithm goes through two phases. The first phase is “Teacher Phase” where learner learns from the teacher and the second phase is “Learner Phase” where learner learns through the interaction between learners. For details of TLBO, go through [1] and for mTLBO, WTLBO, OTLBO, ITLBO, CoTLBO, and elitist TLBO (ETLBO) go through papers [10–16], respectively. Table 1 describes the concepts and parameters on TLBO as well as variants of TLBO in short.

Table 1 Concepts and parameters of TLBO and variants of TLBO algorithms

Algorithm	TLBO	mTLBO	WTLBO	OTLBO	ITLBO	CoTLBO	ETLBO
Concept on algorithm	Original TLBO	Based on tutorial concept an extra term is added in Learner phase	Based on weight factor w new learner is calculated from its previous value	Based on orthogonal design concept	Vary random vector in range (0.5, 1)	Based on cooperation for improve performance	Worst solution replaced with elite solution
Parameter	No parameters	No parameter	$W_{\min} = 0.1$ $W_{\max} = 0.9$	Level $Q = 6$	No parameters	No parameters	No parameters

3 Data Clustering with Variant of TLBO

In the frame of reference of clustering, a learner vector of algorithm can be constructed such that it contains N_c number of cluster centroid vectors. So that each learner vector X_i can be represented as

$$X_i = (M_{i,1}, M_{i,2}, \dots, M_{i,j} \dots M_{i,N_c}) \quad (1)$$

where $M_{i,j}$ is j -th cluster centroid vector of the i -th learner vector in cluster C_{ij} . Therefore, a swarm or a group of learner vectors represent a number of candidate clustering for the current data vectors Z_p . The fitness of learner vectors can be measured using quantization error

$$J_e = \frac{\sum_j^{N_c} \left[\sum_{\forall Z_p \in C_{ij}} \text{dist}(Z_p, M_j) / |C_{ij}| \right]}{N_c} \quad (2)$$

Where dist represents the EDM and $|C_{ij}|$ is the cardinality of data vectors in cluster C_{ij} .

3.1 TLBO Clustering Algorithm

The data vectors can be clustered using the concept of TLBO algorithm as:

1. Initialize learner vector of TLBO algorithm for clustering such that each learner vector contains NUM randomly selected cluster centroids.
2. For iteration $iter = 1$ to $iter_{max}$ do
 - (a) For each learner vector i do
 - (b) For each data vector Z_p
 - I. Calculate the EDM $\text{dist}(Z_p, M_{ij})$ to all cluster centroids C_{ij} .
 - II. Assign Z_p to cluster C_{ij} such that $(Z_p, M_{ij}) = \forall c = 1, 2, \dots, N_c^{\text{dist}(Z_p, M_{ic})}$.
 - III. Find the fitness using Eq. (2).
 - (c) Update the cluster centroids using equations of teacher phase and learner phase of respective algorithm.

Where $iter_{max}$ is maximum number of iteration.

3.2 Simulation Result

This section compares the results of TLBO, elitist TLBO, and TLBO variants clustering algorithms on 12 datasets. The quality of respective clustering is measured according to the quantization error as defined in Eq. (2).

As the algorithms are stochastic in nature and the results of two successive runs usually not match all the results are recorded over 40 simulations. All algorithms used 10 particles and run for 3000 function evaluations. *“For all algorithms, cluster centroids are randomly initialized. The cluster centroids are also randomly fixed between X_{max} and X_{min} , which denote the maximum and minimum numerical values of any feature of the data set under test, respectively”* [11].

“For comparing the performance of algorithms, we focus on computational time required to find the solution. For comparing the speed of the algorithms, we choose the number of fitness function evaluations (FEs) as a measure of computation time instead of generations or iterations [11].”

Finally, we would like to say that all the experiment codes are implemented using MATLAB software on a Pentium 4, 2 GB memory laptop in Windows 7 environment.

Table 2 summarizes the results obtained from TLBO variants, classical TLBO and elitist TLBO clustering algorithms on 12 real-life datasets over 40 simulations in terms of mean and standard deviation.

From Table 2, it is shown that CoTLBO algorithm is keeping first position in clustering the dataset in comparison to other algorithms in all twelve datasets except seeds dataset. In seeds dataset, mTLBO algorithm is keeping the first position.

Average ranking on optimization algorithms obtained by Friedman’s test based on the performance from Table 2 is shown in Table 3. From Table 3, it is clear that CoTLBO algorithm keeps first position for data clustering. mTLBO, classical TLBO, ITLBO, ETLBO, OTLBO, and WTLBO keep second, third, fourth, fifth, sixth, and seventh position, respectively, for data clustering.

From Table 3, it is clear that the CoTLBO algorithm is ranked first. So unpaired t -tests (UTT) have been used to compare the means of the results produced by CoTLBO algorithm and other six algorithms. *“The unpaired t -test assumes that the data have been sampled from a normally distributed population. From the concepts of the central limit theorem, one may note that as sample sizes increase, the sampling distribution of the mean approaches a normal distribution regardless of the shape of the original population. A sample size around 40 allows the normality assumptions conducive for performing the unpaired t -tests* [17].”

The t -test results between CoTLBO and TLBO, CoTLBO and mTLBO, CoTLBO and ITLBO, CoTLBO and OTLBO, CoTLBO and WTLBO, and CoTLBO and ETLBO are given in Tables 4, 5, 6, 7, 8, and 9, respectively.

From Tables 2 and 4, it is clear that CoTLBO algorithm is statistically significant than classical TLBO algorithm in all dataset except for seeds data. In this dataset, classical TLBO algorithm provides nearly solution with CoTLBO algorithm. So in 11 cases CoTLBO algorithm gives significant solution than classical TLBO.

Table 2 Quantization error-based fitness function value in term of mean and standard deviation

Algorithm dataset	Iris dataset	Glass dataset	Wine dataset	Balance scale
TLBO	$0.2800 \pm 4.89e-4$	$0.0399 \pm 8.92e-4$	337.6825 ± 0.0596	0.4735 ± 0.0050
mTLBO	$0.2800 \pm 6.73e-6$	0.0390 ± 0.0012	337.6723 ± 0.0628	0.4820 ± 0.0220
ITLBO	0.2800 ± 0.0010	0.0406 ± 0.0011	337.8922 ± 0.3097	0.4673 ± 0.0080
OTLBO	0.2857 ± 0.0023	0.0449 ± 0.0026	339.2163 ± 0.6613	0.4990 ± 0.0172
wTLBO	0.2854 ± 0.0025	0.0424 ± 0.0011	338.6509 ± 0.6643	0.5210 ± 0.0120
CTLBO	$0.2789 \pm 7.90e-4$	0.0376 ± 0.0012	337.6299 ± 0.0004	$0.4444 \pm 8.68e-13$
E TLBO	0.2812 ± 0.0011	0.0402 ± 0.0019	338.1145 ± 0.0349	0.4890 ± 0.0148
	<i>PID dataset</i>	<i>Ecoli dataset</i>	<i>HR dataset</i>	<i>HS dataset</i>
TLBO	14.4565 ± 0.0037	$0.0591 \pm 7.21e-4$	0.2192 ± 0.0055	5.0498 ± 0.0518
mTLBO	14.4572 ± 0.0033	0.0582 ± 0.0016	0.2184 ± 0.0052	4.9852 ± 0.0149
ITLBO	14.4556 ± 0.0026	0.0600 ± 0.0019	0.2224 ± 0.0098	$4.9697 \pm 2.26e-4$
OTLBO	14.4825 ± 0.0127	0.0619 ± 0.0024	0.2422 ± 0.0214	5.0308 ± 0.0349
wTLBO	14.4846 ± 0.2100	0.0594 ± 0.0014	0.2498 ± 0.0129	5.2477 ± 0.1545
CTLBO	14.4545 ± 0.0029	0.0525 ± 0.0045	$0.2093 \pm 1.06e-14$	4.9618 ± 0.0052
ETLBO	14.4819 ± 0.0019	0.0590 ± 0.0023	0.2491 ± 0.0289	5.2511 ± 0.0071
	<i>Zoo dataset</i>	<i>Seeds dataset</i>	<i>Fertility dataset</i>	<i>Vowel dataset</i>
TLBO	$0.0076 \pm 4.13e-4$	$0.3181 \pm 6.24e-4$	$0.2187 \pm 8.48e-5$	33.8605 ± 1.4882
mTLBO	$0.0075 \pm 4.30e-4$	$0.3176 \pm 6.13e-4$	$0.2186 \pm 2.28e-5$	33.0568 ± 1.4302
ITLBO	$0.0088 \pm 7.85e-5$	0.3187 ± 0.0019	$0.2186 \pm 5.27e-6$	34.1437 ± 2.0720
OTLBO	0.0057 ± 0.0040	0.3206 ± 0.0022	$0.2212 \pm 7.94e-4$	35.1256 ± 1.9962
wTLBO	$0.0029 \pm 6.89e-4$	0.3257 ± 0.0019	0.2197 ± 0.0012	39.8829 ± 1.6963
CTLBO	0.0024 ± 0.0012	0.3186 ± 0.0025	0.2186 ± 0	25.6672 ± 1.0023
E TLBO	0.0069 ± 0.0031	0.3180 ± 2.0032	$0.2187 \pm 8.56e-05$	33.2903 ± 1.1023

Table 3 Average ranking of optimization algorithms using Table 2

Algorithm	TLBO	mTLBO	ITLBO	OTLBO	WTLBO	CoTLBO	ETLBO
Ranking	3.5833	2.6667	4.0	5.8333	5.9167	1.25	4.5833

Similarly, in Table 5 we see that in all cases except fertility dataset the results are statistical significant. Hence, from Tables 2 and 5 it is clear that CoTLBO algorithm is statistical significant than mTLBO algorithm in 10 cases, whereas mTLBO is statistical significant than CoTLBO in 1 case, and in 1 case, mTLBO shows nearly solution with CoTLBO.

From Table 6, we see that in all cases except seed and fertility dataset the results are statistical significant. Hence, from Tables 2 and 6 it is clear that CoTLBO algorithm is statistical significant than ITLBO algorithm in 10 cases, whereas ITLBO shows nearly solution with CoTLBO in 2 cases.

Table 4 UTT between the CoTLBO and TLBO on datasets of Table 2

Dataset	SE	<i>t</i>	Two-tailed <i>P</i>	Significance
Iris dataset	0.000	7.4873	<0.0001	ESS
Glass dataset	9.7299	9.7299	<0.0001	ESS
Wine dataset	0.009	5.5816	<0.0001	ESS
Balance scale	0.001	36.8089	<0.0001	ESS
PID dataset	0.001	2.6907	=0.0087	VSS
HS dataset	0.008	10.6907	<0.0001	ESS
HR dataset	0.001	11.3842	<0.0001	ESS
Ecoli dataset	0.001	9.1591	<0.0001	ESS
Zoo dataset	0.000	25.9163	<0.0001	ESS
Vowel dataset	0.284	28.8805	<0.0001	ESS
Seeds dataset	0.000	1.2273	=0.2234	NSS
Fertility dataset	0.000	7.4629	<0.0001	ESS

Table 5 UTT between the CoTLBO and mTLBO on datasets of Table 2

Dataset	SE	<i>t</i>	Two-tailed <i>P</i>	Significance
Iris dataset	0.000	8.8054	<0.0001	ESS
Glass dataset	0.000	5.2175	<0.0001	ESS
Wine dataset	0.010	4.2700	<0.0001	ESS
Balance scale	0.003	10.8092	<0.0001	ESS
PID dataset	0.001	0.2879	=0.0002	ESS
HS dataset	0.001	3.8870	<0.0001	ESS
HR dataset	0.001	11.0680	<0.0001	ESS
Ecoli dataset	0.001	7.5482	<0.0001	ESS
Zoo dataset	0.000	25.3011	<0.0001	ESS
Vowel dataset	0.276	26.7606	<0.0001	ESS
Seeds dataset	0.000	2.4570	=0.0162	SS
Fertility dataset	0.000	0.0000	=0.0001	NSS

From Table 7, we see that in all cases the results are statistical significant. So from Tables 2 and 7, it is clear that CoTLBO algorithm is statistical significant than OTLBO algorithm in all 12 cases.

From Table 8, we see that in all cases except Pima Indian diabetes dataset the results are statistical significant. Hence, from Tables 2 and 8 it is clear that CoTLBO algorithm is statistical significant than WTLBO algorithm in 11 cases, and in 1 case, WTLBO shows nearly solution with CoTLBO.

From Table 9, we see that in all cases except seed dataset the results are statistical significant. Hence, from Tables 2 and 9 it is clear that CoTLBO algorithm is statistical

Table 6 UTT between the CoTLBO and ITLBO on datasets of Table 2

Dataset	SE	t	Two-tailed P	Significance
Iris dataset	0.000	5.4589	<0.0001	ESS
Glass dataset	0.000	11.6554	<0.0001	ESS
Wine dataset	0.049	5.3566	<0.0001	ESS
Balance scale	0.001	18.1040	<0.0001	ESS
PID dataset	0.002	13.5940	<0.0001	ESS
HS dataset	0.001	9.5994	<0.0001	ESS
HR dataset	0.002	8.4543	<0.0001	ESS
Ecoli dataset	0.001	9.7108	<0.0001	ESS
Zoo dataset	0.000	33.6590	<0.0001	ESS
Vowel dataset	0.364	23.2916	<0.0001	ESS
Seeds dataset	0.000	0.2014	=0.8409	NSS
Fertility dataset	0.000	0.000	=0.0001	NSS

Table 7 UTT between the CoTLBO and OTLBO on datasets of Table 2

Dataset	SE	t	Two-tailed P	Significance
Iris dataset	0.000	17.6844	<0.0001	ESS
Glass dataset	0.000	16.1230	<0.0001	ESS
Wine dataset	0.105	15.1720	<0.0001	ESS
Balance scale	0.003	20.0768	<0.0001	ESS
PID dataset	0.002	9.2460	<0.0001	ESS
HS dataset	0.006	12.0629	<0.0001	ESS
HR dataset	0.003	12.3676	<0.0001	ESS
Ecoli dataset	0.003	2.7186	=0.0081	VSS
Zoo dataset	0.001	4.9977	<0.0001	ESS
Vowel dataset	0.353	26.7807	<0.0001	ESS
Seeds dataset	0.001	3.7983	=0.0003	ESS
Fertility dataset	0.000	20.7091	<0.0001	ESS

significant than elitist TLBO algorithm in 11 cases, whereas in 1 case elitist TLBO shows nearly solution with CoTLBO.

Due to shortage of space, only one dataset that is iris dataset has been considered to show the “*effect of varying number of clusters versus quantization error*” [11]. It is shown that an increase in clusters number expected quantization error goes down. It shows clearly in Fig. 1.

Due to shortage of space, only two results have been considered. Figs. 2 and 3 illustrate convergence behavior of TLBO, ETLBO and five variants of TLBO algorithms on Hayes Roth and fertility dataset, respectively.

Table 8 UTT between the CoTLBO and WTLBO on datasets of Table 2

Dataset	SE	<i>t</i>	Two-tailed <i>P</i>	Significance
Iris dataset	0.000	15.6795	≪0.0001	ESS
Glass dataset	0.000	18.6487	<0.0001	ESS
Wine dataset	0.105	9.7206	<0.0001	ESS
Balance scale	0.002	40.3717	<0.0001	ESS
PID dataset	0.033	0.9064	=0.3675	NSS
HS Dataset	0.024	11.6969	<0.0001	ESS
HR dataset	0.002	19.8562	<0.0001	ESS
Ecoli dataset	0.001	9.2599	<0.0001	VSS
Zoo dataset	0.000	2.2851	=0.0250	ESS
Vowel dataset	0.312	45.6319	<0.0001	ESS
Seeds dataset	0.000	14.3005	<0.0001	ESS
Fertility dataset	0.000	5.7975	<0.0001	ESS

Table 9 UTT between the CoTLBO and ETLBO on datasets of Table 2

Dataset	SE	<i>t</i>	Two- tailed <i>P</i>	Significance
Iris dataset	0.000	10.7408	<0.0001	ESS
Glass dataset	0.000	7.3174	<0.0001	ESS
Wine dataset	0.006	87.8137	<0.0001	ESS
Balance scale	0.002	19.0591	<0.0001	ESS
PID dataset	0.001	49.9837	<0.0001	ESS
HS dataset	0.001	207.9063	<0.0001	ESS
HR dataset	0.005	8.7099	<0.0001	ESS
Ecoli dataset	0.001	8.1345	<0.0001	VSS
Zoo dataset	0.001	8.5617	=0.0250	ESS
Vowel dataset	0.236	32.3607	<0.0001	ESS
Seeds dataset	3.163	0.0002	=9998	NSS
Fertility dataset	0.000	7.3856	<0.0001	ESS

4 Conclusion

This paper investigates the effectiveness on variants TLBO, elitist TLBO and classical TLBO on clustering 12 real-life datasets. It has been shown that in 11 cases CoTLBO and in 1 case mTLBO show their superiority than other algorithms. From Figures it illustrates that the convergence behavior of most of the algorithms exhibited a faster, but premature convergence to a large quantization error, while the CoTLBO algorithms had slower convergence, but to lower quantization errors with stable convergence. It is concluded that CoTLBO performs better while clustering unlabeled

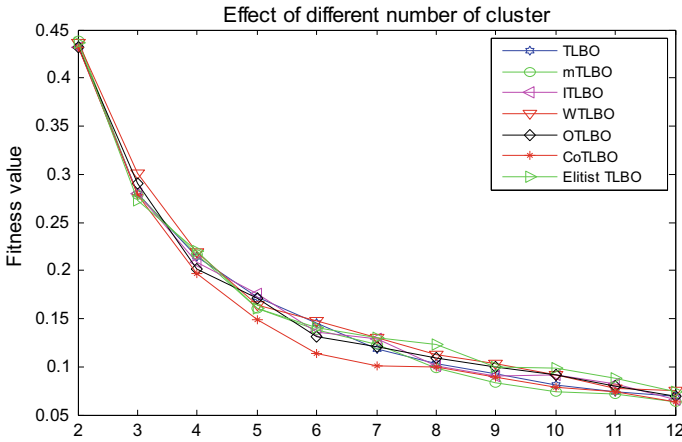


Fig. 1 Effect of different number of clusters on iris dataset

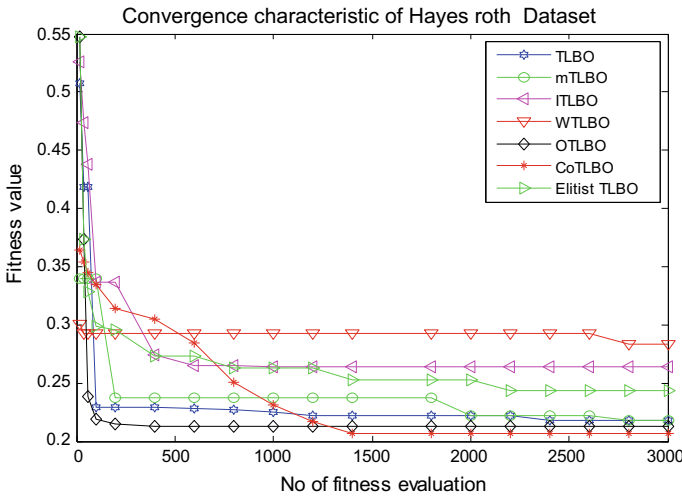


Fig. 2 Convergence characteristic of Hayes Roth dataset

datasets. As further study, we check the performance of these algorithms while clustering complex and high dimensional datasets as well as on solving constrained as well as unconstrained optimization problems.

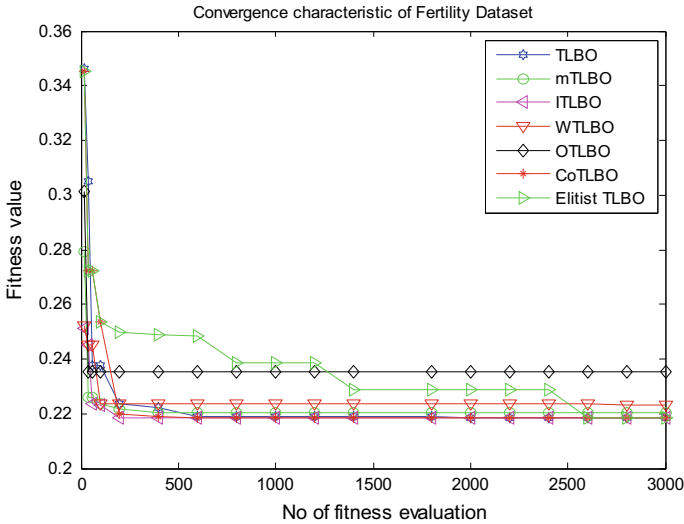


Fig. 3 Convergence characteristic of fertility dataset

References

- Rao RV, Savsani VJ, Vakharia DP (2011) Teaching–learning-based optimization: a novel method for constrained mechanical design optimization problems. *Comput Aided Des* 43:303–315
- Niknam T, Azizpanah-Abarghoee R, Marimani MR (2012) A new multiobjective approach based on TLBO for location of automatic voltage regulators in distribution systems. *Eng Appl Artif Intell*. <http://dx.doi.org/10.1016/j.engappai.2012.07.004>
- Satapathy SC, Naik A (2011) Data clustering based on teaching–learning-based optimization. *Swarm, Evolutionary, and Memetic Computing, Lecture Notes in Computer Science*, vol 7077. Springer-Verlag, Berlin, pp 148–156
- Satapathy SC, Naik A, Parvathi K (2012) High dimensional real parameter optimization with teaching learning based optimization. *Int J Ind Eng Comput*. <https://doi.org/10.5267/j.ijiec.2012.06.001>
- Toğan V (2012) Design of planar steel frames using teaching–learning based optimization. *Eng Struct* 34:225–232
- Satapathy SC, Naik A, Parvathi K (2012) Teaching learning based optimization for neural networks learning enhancement. *LNCS*, vol 7677. Springer-Verlag Berlin Heidelberg, pp. 761–769
- Satapathy SC, Naik A, Parvathi K (2012) 0–1 Integer programming for generation maintenance scheduling in power systems based on teaching learning based optimization (TLBO), *CCIS*, vol 306. Springer-Verlag Berlin Heidelberg, pp 53–63
- Satapathy SC, Naik A, Parvathi K (2012) Improvement of initial cluster center of c-means using teaching learning based optimization. *Procedia Technol* 6:428–435 (Elsevier)
- Naik A, Parvathi K, Satapathy SC, Nayak R, Panda BS (2012) QoS multicast routing using teaching learning based optimization. Springer-Verlag Berlin Heidelberg, pp 49–55
- Rao RV, Patel V (2012) An elitist teaching–learning-based optimization algorithm for solving complex constrained optimization problems. *Int J Ind Eng Comput* 3:535–560
- Satapathy SC, Naik A (2014) Modified teaching -learning-based optimization algorithm for global numerical optimization—a comparative study. *Swarm Evol Comput* 16:28–37

12. Satapathy SC, Naik A (2013) A modified teaching learning based optimization (mTLBO) for global search. *Recent Patent Comput Sci* 6(1):60–72
13. Satapathy SC, Naik A (2012) Improved teaching learning based optimization for global function optimization. *Decis Sci Lett* 2(1):23–34
14. Satapathy SC, Naik A, Parvathi K (2013) Weighted teaching learning based optimization for global function optimization. *Appl Math* 4:429–439
15. Satapathy SC, Naik A, Parvathi K (2013) A teaching learning based optimization based on orthogonal design for solving global optimization problems. *SpringerPlus* 2(1), 130
16. Satapathy SC, Naik A (2013) Cooperative teaching–learning based optimisation for global function optimization. *Int J Appl Res Inf Technol Comput (IJARITAC)*
17. Flury B (1997) *A first course in multivariate statistics*. Springer-Verlag, Berlin, Germany, 28

Studies on Off-Grid Solar Photovoltaic-Powered Micro-Irrigation System in Aerobic Rice Cultivation for Sustainable Agriculture and Mitigating Greenhouse Gas Emission



M. K. Ghosal, N. Sahoo and Sonali Goel

Abstract Aerobic rice cultivation is nowadays gaining importance due to the constraints in the availability of required amount of water for traditional rice growing system. An attempt has therefore been made to develop a portable solar photovoltaic-powered (off-grid) drip irrigation system for aerobic rice cultivation, which is a water-saving and less-water-consuming rice production system without any compromise with decline in yield. It is suitable mostly in the water-deficient, non-irrigated, and off-grid areas. There may be the saving of 40–45% of water for irrigation purpose compared to the conventional method, mitigation of 0.55 million tons of CO₂ with the replacement of existing diesel and electric pump sets and 0.2 million tons of CH₄ from 4.0 million hectares of rice fields in the state of Odisha, India, through the system, developed by adopting aerobic rice cultivation. The pay-back period of the setup is estimated to be 4 years and total annual saving of Rs. 675 crores due to reduction in the use of electrical energy and petroleum fuels through the existing pump sets in Odisha. Monthly income of Rs. 4000/– throughout the year was achieved by adopting aerobic rice cultivation in 1 acre (0.4 ha) of land.

Keywords Off-grid power system · Solar photovoltaic system · Micro-irrigation · Water use efficiency · Aerobic rice cultivation · Greenhouse gases mitigation

M. K. Ghosal (✉) · N. Sahoo
College of Agricultural Engineering and Technology, Odisha University of Agriculture and Technology, Bhubaneswar 751003, Odisha, India
e-mail: mkgghosal1@rediffmail.com

N. Sahoo
e-mail: narayan_swce@yahoo.co.in

S. Goel
Department of Electrical Engineering, ITER, Siksha 'O' Anusandhan Deemed to be University, Bhubaneswar 751030, Odisha, India
e-mail: sonali19881@gmail.com

© Springer Nature Singapore Pte Ltd. 2020
R. Sharma et al. (eds.), *Innovation in Electrical Power Engineering, Communication, and Computing Technology*, Lecture Notes in Electrical Engineering 630,
https://doi.org/10.1007/978-981-15-2305-2_11

1 Introduction

Sustainability of rice production in the present context of fast-growing population is a big challenge before all of us with respect to achieving food security and controlling over the increased concerns of water scarcity, energy crisis, and global warming due to the emission of greenhouse gases through anthropogenic activities particularly in the agricultural sector [1, 2]. In order to attain self-sufficiency in food grain, the production and productivity of rice crop alone play a crucial role not only for our state Odisha but also for India, Asia, and the world as well, as rice is the principal food of more than 60% of the world's population and around 90% of the rice area worldwide is in Asia and low land rice fields produce about 75% of the world's rice supply [3]. Agriculture too in Odisha to a considerable extent means growing rice. It is the staple food for almost the entire population of Odisha, and therefore, the state economy is directly linked with the improvements in production and productivity of rice [4]. Rice production practices mostly followed in the state are through wet and low land cultivation, covering about 80% of the total rice area, and the methods of cultivation are usually transplanting of seedlings and broadcasting of sprouted seeds in the puddled soil. In the above method of cultivation, the field remains either in fully or partially flooded condition most of the time of the growing season, creating favorable environment for emission of methane, which is one of the principal and potent greenhouse gases relative to global warming potential of 25 times higher than that of CO₂ and accounts for one-third of the current global warming phenomenon [5]. Rice cultivation is a major source of atmospheric CH₄ and contributes about 10–20% of total methane emission to the atmosphere [6]. The environmental experts have now recognized and expressed in intergovernmental panel on climate change (IPCC 2010) that the submerged rice fields are the most significant contributors of atmospheric methane [7]. According to the current estimate, the production of rice needs to be enhanced by around 70% to meet the demands for ever-increasing population by 2030, thus making rice cultivation a potential major cause of growing atmospheric methane [8].

Aerobic rice cultivation where fields remain unsaturated or nearer to saturation throughout the season like an upland crop offers an opportunity to produce rice with less water [9]. Aerobic and upland rice are both grown under aerobic condition; however, the former is under controlled water management system but latter is not [10]. Aerobic rice is a new cropping system in which specially developed varieties are directly seeded in well-drained, un-puddled, and unsaturated soil conditions for most of the crop-growing period. The rice is grown like an upland crop with adequate inputs and supplementary irrigation when rainfall is insufficient. Aerobic rice varieties are bred by combining the draft resistance of upland varieties with high yielding characteristics of low land cultivars. Some of the suitable varieties like CRDhan-200 (pyari), Naveen, and Annada are also available in our state Odisha. Aerobic rice is therefore grown with the use of external inputs such as supplementary irrigation and fertilizers with an aim to maintain the productivity at par with the traditional production system without compromise with yield decline. The micro-irrigation in

general and drip irrigation in particular have received considerable attention from researchers, policy makers, economists, etc., for its perceived ability to contribute significantly to groundwater resources development, agricultural productivity, economic growth, and environmental sustainability [8, 11, 12, 13, 14]. Currently, our state has around 1.38 lakhs (35%) grid-based (electric) and 2.47 lakhs (65%) diesel irrigation pump sets. However, erratic grid supply of electricity and high cost of diesel pumping continue to remain as a big problem for the farmers. The rising cost of using diesel for powering irrigation pump sets is often beyond the means of small and marginal farmers. Consequently, the lack of required amount of water often leads to poor growth of plants, thereby reducing yields and income. Hence, use of conventional diesel/gasoline-powered pumping systems poses an economic risk to the farmers. Scientific studies reveal that timely and required amount of water availability for the crop favors the increase in the yield by 10–15% [15]. The burning of petroleum fuels also creates threats by polluting environment and causing global warming by releasing a considerable amount of CO₂ into the atmosphere. The continuous exhaustion of limited stocks of conventional energy sources and their environmental impacts have, therefore, forced researchers, planners, and policy makers to search for the reliable, environment-friendly, and cost-effective energy resources to power water pumping system in a sustainable manner [16]. Hence, to keep pace with the growing demands of energy and acute shortage of water, solar photovoltaic water pumping device may be integrated with drip irrigation system for rice cultivation in addressing the issues of food security under climate change scenario [17]. Thus, an integrated approach of water-saving technology and reliable source of energy along with the reduced greenhouse gas emissions from the conventional method of rice cultivation has been thought up in the proposed study to achieve food security of the nation. An attempt is therefore made to study the feasibility and performance of solar photovoltaic-powered drip irrigation system in aerobic rice cultivation.

2 Materials and Methods

Design and development of solar photovoltaic (SPV) drip irrigation system (Fig. 1) have been made for cultivating paddy in 1 acre (0.4 ha) of land to achieve secured irrigation and to improve water use efficiency mostly in aerobic method of cultivation. The details of the design and developments are mentioned below. The experiments were carried out during the year 2017–18 in OUAT farm, Bhubaneswar, Odisha, which lies at the latitude of 20° 15' N and longitude of 85° 52' E and coming under warm and humid climatic condition. Paddy was cultivated in rabi and summer seasons. The soil type of the experimental site is sandy loam, and the climate of the study area is humid and subtropical in nature.

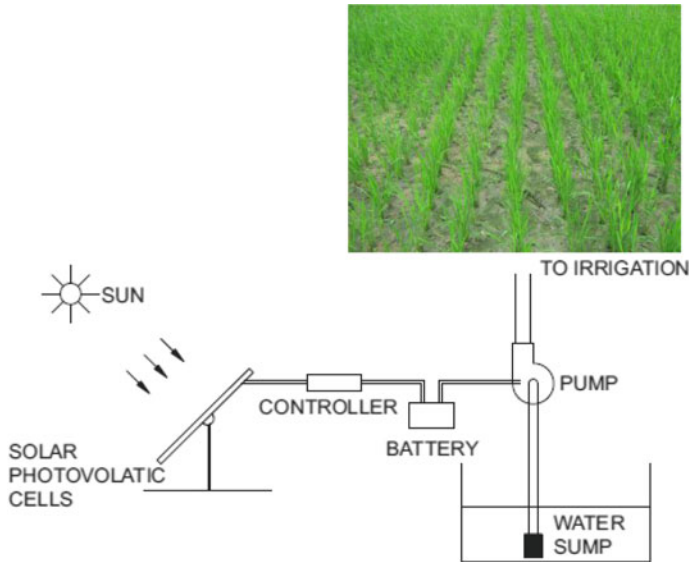


Fig. 1 Experimental setup for solar water pumping-based drip irrigation in aerobic rice

2.1 The Cost Estimate for Solar Photovoltaic-Powered Drip Irrigation System

- i. Solar PV module of 1000 W @ Rs. 50 per Wp = Rs. 50,000
- ii. 1 hp DC motor with pump set = Rs. 80,000
- iii. Mounting structure = Rs. 15,000
- iv. Civil works/balance of system = Rs. 20,000
- v. Drip setup for 1 acre land = Rs. 35,000

Total = Rs. 2, 00,000.

2.2 Economics of Using Various Water Pumping Devices

Information for cost analysis

- i. Cost of 1 hp electric pump set = Rs. 7,000
- ii. Cost of 1 hp diesel pump set = Rs. 10,000
- iii. Cost of 1 hp PV-powered pump set = Rs. 1,00,000
- iv. Prevailing interest rate may be taken as 10%
- v. Efficiencies of motor vary from 70 to 80% (70% taken)
- vi. Efficiencies of pump vary from 70 to 80% (70% taken)
- vii. Efficiencies of diesel engine vary from 30 to 40% (40% taken)

- viii. Useful life of PV panel vary from 20 to 25 years (can be taken 22 years)
- ix. Useful life of diesel engine pump set = 8 years
- x. Useful life of electric pump set = 8 years
- xi. Maintenance cost of PV system with drip as 0.5% of total capital cost per year
- xii. Maintenance cost of diesel engine pump set as 10% of total capital cost per year
- xiii. Maintenance cost of electric pump set as 10% of total capital cost per year
- xiv. Annual working hours of diesel, electric pump sets, and PV system be 500 h
- xv. One hp engine consumes about 250 ml. diesel per hour (present cost of diesel Rs. 60/l)
- xvi. One unit of electric energy (1 kWh) = Rs. 5.00
- xvii. Salvage value of diesel pump set be taken as 20% of capital cost
- xviii. Salvage value of electric pump set be taken as 20% of capital cost
- xix. Salvage value of PV-powered pump set be taken as 5% of capital cost
- xx. Operator's time spent in the proposed system be 1 h/day (labor charge Rs. 250/day)
- xxi. Energy consumption (kWh) of electric pump set = $(\text{BHP})/(\text{motor efficiency} \times \text{pump efficiency}) \times 0.746 \times 1 \text{ h}$
- xxii. Cost per hour of operation of diesel pump set = $(\text{BHP})/(\text{motor efficiency} \times \text{pump efficiency}) \times \text{fuel consumed in liters/hour/BHP} \times \text{cost of fuel/lit.}$

(i) Hourly operating cost of PV-powered water pumping device with drip system

Fixed Cost

- (i) Depreciation

$D = (C - S)/(L \times H)$ where C = capital cost; S = Salvage Value;
 L = Useful life of device; H = Annual working hour
 Putting the values of all necessary data, $D = \text{Rs. } 17.27/\text{h}$

- (ii) Interest $(I) = (C + S)/(2) \times (\text{Interest rate}/100) \times (1/H) = \text{Rs. } 21/\text{h}$
 Insurance and taxes and housing are not applicable
 Total fixed cost = $17.27 + 21 = \text{Rs. } 38.27/\text{h}$.

Variable Cost

- (i) Fuel cost = Nil
- (ii) Lubricants = Nil
- (iii) Repair and maintenance = $(C) \times (0.5/100) \times (1/H) = \text{Rs. } 2/\text{h}$
- (iv) Operator's wages $\text{Rs. } 250/8 = \text{Rs. } 31.25/\text{h}$

Total variable cost = $2 + 31.25 = \text{Rs. } 33.25/\text{h}$

Total operation cost per hour = Total fixed cost/hour + Total variable cost/hour = **Rs. 71/h.**

(ii) Hourly operating cost of diesel pump set**Fixed Cost****(i) Depreciation**

$D = (C - S)/(L \times H)$ where C = capital cost; S = Salvage Value;

L = Useful life of device; H = Annual working hour

Putting the values of all necessary data, $D = \text{Rs. } 2.0/\text{h}$

(ii) Interest (I) = $(C + S)/(2) \times (\text{Interest rate}/100) \times (1/H) = \text{Rs. } 1.2/\text{h}$

Insurance and taxes and housing are not applicable

Total fixed cost = $2.0 + 1.2 = \text{Rs. } 3.20/\text{h}$.

Variable Cost

(i) Fuel cost = $(1)/(0.4 \times 0.7) \times 0.25 \times 60 = \text{Rs. } 53.57/\text{h}$

(ii) Lubricants = 20% of cost of fuel = $\text{Rs. } 10.71/\text{h}$

(iii) Repair and maintenance = $(C) \times (10/100) \times (1/H) = \text{Rs. } 2.0/\text{h}$

(iv) Operator's wages $\text{Rs. } 250/8 = \text{Rs. } 31.25/\text{h}$

Total variable cost = $53.57 + 10.71 + 2.0 + 31.25 = \text{Rs. } 97.53/\text{h}$

Total operation cost per hour = Total fixed cost/hour + Total variable cost/hour = **Rs. 100/h.**

(iii) Hourly operating cost of electric pump set**Fixed Cost****(i) Depreciation**

$D = (C - S)/(L \times H)$ where C = capital cost; S = Salvage Value; L = Useful life of device; H = Annual working hour

Putting the values of all necessary data, $D = \text{Rs. } 1.4/\text{h}$

(ii) Interest (I) = $(C + S)/(2) \times (\text{Interest rate}/100) \times (1/H) = \text{Rs. } 0.84/\text{h}$

Insurance and taxes and housing are not applicable

Total fixed cost = $1.4 + 0.84 = \text{Rs. } 2.24/\text{h}$.

Variable Cost

(i) Energy consumption (kWh) = $(1)/(0.7 \times 0.7) \times 0.746 = 1.52 \text{ kWh}$

(ii) Electric energy cost = $1.52 \times 5 = \text{Rs. } 7.6/\text{h}$

(iii) Lubricants = 20% of cost of fuel = $\text{Rs. } 1.52/\text{h}$

(iv) Repair and maintenance = $(C) \times (10/100) \times (1/H) = \text{Rs. } 1.4/\text{h}$

(v) Operator's wages $\text{Rs. } 250/8 = \text{Rs. } 31.25/\text{h}$

Total variable cost = $7.6 + 1.52 + 1.4 + 31.25 = \text{Rs. } 41.77/\text{h}$

Total operation cost per hour = Total fixed cost/hour + Total variable cost/hour = **Rs. 44/h.**

3 Results and Discussion

The results of the experiment conducted during the course of the study are presented in this section. Rice is one of the most important and major crops in Odisha and is grown in an area of 40 lakh ha in kharif season and only 2.5 lakh ha in rabi season [4]. Kharif rice is entirely monsoon-fed. The area for rice cultivation during rabi season has not been covered widely due to lack of assured irrigation causing most of the cultivable land to remain unutilized. The yield of rice from the areas during rabi season is not satisfactory due to erratic supply of grid electricity for operating irrigation pumps. Farmers are also not interested to use diesel pump sets due to frequent rise in the cost of diesel fuel. Hence, captive power and water source along with water-saving technology for rice cultivation are the only alternative for the resource-poor farmers of the state. The harnessing of solar energy for electricity generation through PV system is a viable option in the state due to abundant availability of solar radiation in about 300 days in a year. The variety chosen for the study was CR Dhan-200 (Pyari). This variety of rice was cultivated for the present study in order to evaluate the effectiveness of the developed solar PV drip irrigation device with respect to production and productivity, without depending upon conventional source of energy and flooded system of watering practice. The cost of cultivating rice in 1 acre of land has been mentioned (Table 1) in order to know the annual profits out of it and its payback period. Similarly, the mitigation of greenhouse gases with the use of the developed setup has been estimated compared with traditional diesel and electric pump sets for its contribution in combating global warming and climate change, thus achieving sustainable agriculture.

(i) **Cost of Cultivation in 1.0 Acre Land**

(ii) **Benefit**

Yield of paddy in aerobic rice practice = 2.5 tones/acre;

By-product yield = 1.5 tones/acre; Returns from paddy @ Rs. 1350/quintals = 33,750;

Returns from by-product @ Rs. 250/quintal = 3,750;

Total returns = 33,750 + 3,750 = Rs. 37,500;

Net gain = Rs. 37,500 – Rs. 13,500 = Rs. 24,000 (kharif);

Net gain = Rs. 37,500 – Rs. 13,500 = Rs. 24,000 (rabi);

Total gain from 1 acre of aerobic rice cultivation in a year = Rs. 48,000; Monthly income from aerobic rice cultivation with assured water supply = Rs. 48,000/12 = Rs. 4000 per month

Simple payback period = (Initial investment cost)/(Net annual gain) = 2,00,000/48,000 = 4.1 years \approx 4 years.

Table 1 Cost-benefit calculation of aerobic rice cultivation in 1 Acre (0.4 ha) land

S. No.	Name of operation	Implements used	No. of operation	Man-h/Acre	Operation cost (Rs.)	Input (kg)	Cost of input (Rs.)	Total cost (Rs.)
1	Tillage	Tractor drawn rotavator	1	2	1200	-	-	1200
2	Seed					20 kg		500
3	Direct line sowing (by rope method)		1	8	31.25/h			250
4	Manures and fertilizer	FYM	Once			1 tractor load	1500	1500
		Gromer	Twice			100 kg	1000	1000
		Potash	Twice			100 kg	1000	1000
5	Interculture (cono weeder)	Manual	Thrice	16	31.25/h			1500
6	Plant protection	Knapsack sprayer	Thrice	2	31.25/h	Pesticides	2000	2062
7	Irrigation	Solar PV-powered drip system	45 (2 days interval)	1	Rs. 51/h			2295
8	Harvesting	Hired reaper	Once	1				750
9	Threshing	Pedal thresher	Once	50-60 kg/h	Six man days			1500
Total cost								13,557 \approx 13,500

3.1 Estimation for Mitigation of CO₂ Emission by Use of Solar Photovoltaic-Powered Water Pumping System

The existing diesel and electric pump sets in our state is 2.47 lakhs and 1.38 lakhs, respectively, in the power rating range of 1–5 hp. Taking the average power rating of both diesel and electric pump sets as 3 hp, the amount of emissions of CO₂ are as follows;

1. One hp engine consumes about 250 ml of diesel per hour.
2. Burning of 1 liter of diesel releases 3 kg of CO₂ to the atmosphere.
3. The average carbon dioxide emission for electricity generation from coal-based thermal power plant is approximately 1.58 kg of CO₂ per kWh at the source.
4. Annual working hours of diesel and electric pump sets can be taken 500 h.
5. Annual CO₂ emissions from 2.47 lakhs diesel pump set to be 30 crores kg in our state.
6. Annual CO₂ emissions from 1.38 lakhs electric pump set to be 25 crores kg in our state.
7. Total annual electrical energy consumption from 1.38 lakhs electric pump sets can be saved in the tune of 15×10^7 kWh (saving around 15 crore units of electricity costing about Rs. 75 crores/annum).
8. Total annual diesel consumption from 2.47 lakhs diesel pump sets can be saved in the tune of 10×10^7 liters of diesel (saving around Rs. 600 crores/annum).

3.2 Estimation for Mitigation of CH₄ Emission by Shifting from Anaerobic to Aerobic Rice Cultivation

Rice fields have been identified as a major source of atmospheric methane. The global methane emission rate from rice fields was recently estimated to be 40 Tg/year (1 Tg = 10^{12} g) which accounts for about 8% of the total methane emission. The reduction in the amount of methane emission from the conventional method of rice cultivation is estimated as follows;

- 1 On an average, 50 kg methane is emitted from 1 ha of transplanted rice crops in one crop-growing season.
- 2 Annual area under rice cultivation in the state Odisha is 4.0 million hectares (both kharif and rabi).
- 3 Annual area under rice cultivation in India is 43.0 million hectares (both kharif and rabi).
- 4 Mitigation of CH₄ emissions through aerobic rice cultivation is 0.2 million tons and 2.15 million tons per annum in Odisha and India, respectively.

4 Conclusion

A portable solar photovoltaic-powered drip irrigation system for aerobic rice cultivation in warm and humid climate of Odisha appears to be a viable proposition looking into the present day's concerns of water scarcity and energy crisis in agricultural sector. The following conclusions may be drawn from the study.

- i. Monthly income of Rs. 4000/- throughout the year may be possible by adopting aerobic rice cultivation in 1 acre of land both during rabi and summer seasons.
- ii. The small and marginal farmers of the state may be attracted to adopt off-grid solar photovoltaic-powered water pumping system as the hourly operating cost is Rs. 71/h and Rs. 44/h for electric pump set and Rs. 100/h for diesel pump set.
- iii. Payback period of the proposed setup is 4 years, due to which, it may be easily accepted by the small and marginal farmers of the state in spite of its high initial cost.
- iv. Total annual CO₂ emissions can be mitigated by 0.55 million tons with the replacement of existing diesel and electric pump sets in our state by the adoption of a reliable off-grid solar photovoltaic-powered system in irrigation sector.
- v. Total annual CH₄ emissions can be mitigated by 0.2 million tons from 4.0 million hectares rice fields in Odisha.
- vi. Total annual electrical energy consumption from 1.38 lakhs electric pump sets can be saved in the tune of 15×10^7 kWh (saving around 15 crores units of electricity costing about Rs. 75 crores/annum).
- vii. Total annual diesel consumption from 2.47 lakhs diesel pump sets can be saved in the tune of 10×10^7 liters of diesel (saving around Rs. 600 crores/annum).

References

1. Hossain MA, Hassan MS, Mottalib MA, Ahmmed S (2015) Techno-economic feasibility of solar pump irrigations for eco-friendly environment. *Proced Eng* 105:670–678
2. Nazmul KM (2016) Municipal solid waste to energy generation in Bangladesh: possible scenarios to generate renewable electricity in Dhaka and Chittagong city. *J Renew Energy* 2016, ID 1712370
3. Singh JS (2010) Capping methane emission. *Science reporter*, September, 2010, pp 29–30
4. Anonymous (2017) *Agricultural statistics 2017*, Govt. of Odisha
5. Garg Amit, Kankal Bhushan, Shukla PR (2011) Methane emissions in India: Sub-regional and sectoral trends. *Atmos Environ* 45(2011):4922–4929
6. Pathak H, Aggarwal PK (2012) Low carbon technologies for agriculture: a study on rice and wheat systems in Indo-Gangetic plains. Division of Environmental Science, IARI, New Delhi
7. Jain N, Pathak H, Mitra S, Bhatia A (2004) Emission of methane from rice fields—a review. *J Sci Ind Res* 63:101–115
8. Singh R, Kundu DK, Bandyopadhyaya KK (2010) Enhancing agricultural productivity through enhanced water use efficiency. *J Agric Phys* 10:1–15
9. Patel DP, Das A, Munda GC, Ghosh PK, Bordoloi JS, Kumar M (2010) Evaluation of yield and physiological attributes of high-yielding rice varieties under aerobic and flood-irrigated management practices in mid-hills ecosystem. *Agric Water Manag* 97(2010):1269–1276

10. Parthasarathi T, Vanitha K, Lakshmanakumar P, Kalaiyarasi D (2012) Aerobic rice-mitigating water stress for the future climate change. *Int J Agron Plant Prod* 3(7):241–254
11. Kashiv A, Bilala A, Shirazi N, Dwivedi A, Joshi R (2016) Solar drip irrigation system. *Int J Emerg Technol Adv Eng* 6(4)
12. Hoque N, Roy A, Beg RAB, Das BK (2016) Techno-economic evaluation of solar irrigation plants installed in Bangladesh. *Int J Renew Energy Dev* 5(1):73–78
13. Campana PE, Li H, Zhang J, Yan J (2015) Economic optimization of photovoltaic water pumping systems for irrigation. *Energy Conserv Manag*
14. Shinde VB, Wandre SS (2015) Solar photovoltaic water pumping system for irrigation: a review. *Afr J Agric Res* 10(2):2267–2273
15. Narale PD, Rathore NS, Kothari S (2013) Study of solar PV water pumping system for irrigation of horticulture crops. *Int J Eng Sci Invent* 2(12):54–60
16. Pradhan A, Ali SM (2016) Analysis of solar performance with change in temperature. *Int J Appl Eng Res* 11:5225–5227
17. Gopal C, Mohanraj M, Chandra Mohan P, Chandrasekhar P (2013) Renewable energy source water pumping systems—a literature reviews. *Renew Sustain Energy Rev* 25(2013):351–370

Application of IoT in Predictive Maintenance Using Long-Range Communication (LoRa)



Siddharth Bhattar, Akash Verma and Sayantan Sinha 

Abstract The traditional Internet has been subjected to revolutionary change by the concept of Internet of Things (IoT) and has added new dimensions in the world of human-centric services. This concept basically indicates the ability of different devices to connect with each other and communicate effectively. But this revolution comes at the cost of increased demand in the number of sensor nodes that needs to be assimilated in a network. This problem is also followed by the presence of an effective network solution that has the ability to contain these requirements consequently. The wireless sensor network generally includes energy-limited devices, so energy-saving technologies are of growing concern. Latency, range coverage and bandwidth are among other issues in this IoT. LoRa emerged as the emerging solution to the above problems which has the main intention to save energy. This provides long-range, low-power data transmission rate and provides higher efficiency in wireless data communication. LoRa turns out to be the potential device to realize a large number of Internet of Things applications. A large number of papers have reported the performance and efficiency of LoRa-based wireless area network (LoRaWAN) in the fields of outdoor and radio communication, but the maximum of its potential is still unexplored. This paper effectively tries to put down some of the applications of LoRa in the field of predictive maintenance. The detailed hardware specifications and the experimental results are furnished to establish the supremacy of LoRa over other network devices in predictive maintenance.

Keywords LoRa · Long range · IoT · Wireless area network · Predictive maintenance

S. Bhattar · A. Verma
Karkhana Makerspace, Bhubaneswar, Odisha 751030, India
e-mail: gkbhattar@gmail.com

A. Verma
e-mail: avkbond007@gmail.com

S. Sinha (✉)
Siksha 'O' Anusandhan Deemed to be University, Odisha 751030, India
e-mail: sayantansinha51@gmail.com

© Springer Nature Singapore Pte Ltd. 2020
R. Sharma et al. (eds.), *Innovation in Electrical Power Engineering, Communication, and Computing Technology*, Lecture Notes in Electrical Engineering 630,
https://doi.org/10.1007/978-981-15-2305-2_12

1 Introduction

The revolutionary paradigm named Internet of Things (IoT) has defined itself the future of Internet. This aims at giving each and every thing around us the capability to communicate with one another. Extensive research has been done for the past recent years to explore the possibilities of IoT and also focus on its development under various categories based on various projects taken for consideration. Paper [1] and paper [2] focus on various instances like smart homes, smart cities where the various possibilities of IoT are explored. Till date, there has been no specific model so far according to which an IoT model can be implemented and the deployment mainly depends on applications. It may happen that one way of application of IoT to a particular problem might act as the best way of deployment to some another IoT problem. This diversified nature of IoT has made experts predict more than 50 billion connections with things possible by 2020 [3].

The rapid development of IoT over the recent years brought to light a large number of issues regarding the energy restrictions of wireless sensor nodes. Studies conducted all over the world proposed many techniques for optimizing the transmission power required for each nodes. Research has revealed that [4] some work has been done to ensure network connectivity keeping in mind minimum wastage of power and maximizing its lifetime. Research proposal by Aziz et al. [5] has proposed topology modifications to ensure energy optimization in wireless sensor nodes. To address new challenges in effective communication, heterogeneity in IoT is considered as a viable alternative solution to minimize energy issues in WSN [6]. The same heterogeneity concept is also applied in gateway level which is elaborated in [7]. Latency, range coverage and bandwidth are some of the important concerns when massive nodes are connected to the Internet. Hence, LoRa mainly recognizes gadgets that possess limited energy and transfers few bytes in every time scale [8].

LoRa among all the other different technologies has emerged as the rising star of the recent generations. With recent CSS (chirp spread spectrum) modulation, LoRa module provides signals with improved resilience and provides strong resistance to interference, Doppler's effect and multipath effect. LoRa functions basically through a two-layer approach: (a) a physical layer mainly governed by radio modulation technique identified as CSS (chirp spread spectrum) and (b) the presence of LoRaWAN, basically a MAC layer protocol designed to provide access to LoRa architecture. This paper provides a detailed description regarding an overview to LoRa technology followed by its application in predictive maintenance.

2 Lora Architecture

The LoRa (long range) device is the new dawn of a bright future in the field of smart communication techniques. The LoRa system can be divided into three divisions in an attempt to study its architecture.

- (a) LoRa end devices: These basically include the sensors and the actuators that are connected by any kind of interfaces to various gateways fitted for LoRa communication.
- (b) LoRa gateways: These act as the main point of connection between the end devices and the main network system. The main network acts as the prima facie for the architecture.
- (c) LoRa net server: This portion can be interpreted as the brain of the entire architecture. This mainly handles the entire performance and controls the entire process of resource management and also deals with security maintenance.

The basic layout of LoRa architecture is displayed in Fig. 1. The architecture is mainly a star topology-based architecture where all the end devices are connected to a LoRa communication gateway which in turn connects it to a common network server. This communication is done via standard Internet topologies. Various protocol architectures that the gateways implement to transfer the data from the end devices to the network server are depicted in Fig. 2. The gateways have the function of decoding all the messages that are forwarded to them by various end devices connected to them. The gateways then add some extra piece of information to the decoded messages which defines the quality of the reception and then forwards it to the network server.

Application		
LoRa MAC		
MAC Options		
Class A	Class B	Class C
LoRa Modulation		
Regional ISM Band		

Fig. 1 LoRa architecture

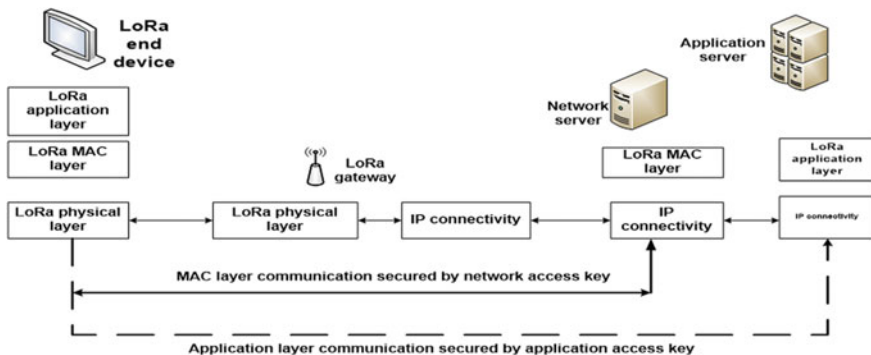


Fig. 2 Connection protocols between LoRa and end devices

The network server replies to all the messages from the end devices and chooses a particular gateway based on some criterions like stable communication connectivity and many more. Thus, a total transparency is maintained between the gateways and the end devices. The gateways make the end devices logically connected to the network server.

The LoRa network basically acts as an input or a central point for three basic types of end devices. They are Class A which includes all possible end devices that communicate with the net server via gateways. Class B is specifically for beacons, and Class C is for continuously listening mode. Each of these devices and their operating modes are elaborately discussed in [9]. Class A basically includes the default functional mode of the Lora network and is to be supported by all LoRa devices. In Class A, the end devices are responsible for the starting of any transmission to the server via the gateways. These transmissions occur in complete asynchronous nature. At the end of each transmission uplink, the portal to the end devices is kept open for at least two times. The first instance of opening is when the devices are waiting for any information that will be sent to them by the network devices. The second instance of opening is when the gateways occur on different sub-bands all together which test the resiliency of the signal transmission subject to channel fluctuations. The Class A devices are mainly used for monitoring purposes, and the data that are generated by the end devices are coordinated and guided centrally by a control station. Class B devices basically synchronize with the network server and is mainly introduced to control the uplink and the downlink transmission. The synchronization is done with the help of specific packets of information sent by the beacons and is transmitted via the Class B gateways. This makes it possible for the Class B end devices to receive packets of information in a synchronized manner irrespective of the uplink traffic. They are mainly dedicated to provide user support according to its needs.

Class C end devices are mainly meant for end devices that do not have any strict energy limitations and can always keep the receiver window open for exchange of information. This class of end devices are still in the draft form, and research is been done all over the world to provide a better insight if it's functioning and implementations. Figure 3 depicts the various class categories for LoRa devices.

3 LoRa Gateways

LG02 and OLG02 are termed as the two common open-source gateways for LoRa communication. It basically acts as a bridge for LoRa end devices to communicate with the network server via Wi-fi or mobile communication network. These gateways allow user to send data at extremely low rates and also ensures long-range data transmission along with immunity against interferences. Incorporated with rich Internet connections, these gateways allow flexible communication of users with the sensor devices via Internet. They are designed to support LoRa protocol in a single frequency range and ensure duplex communication which enhances communication

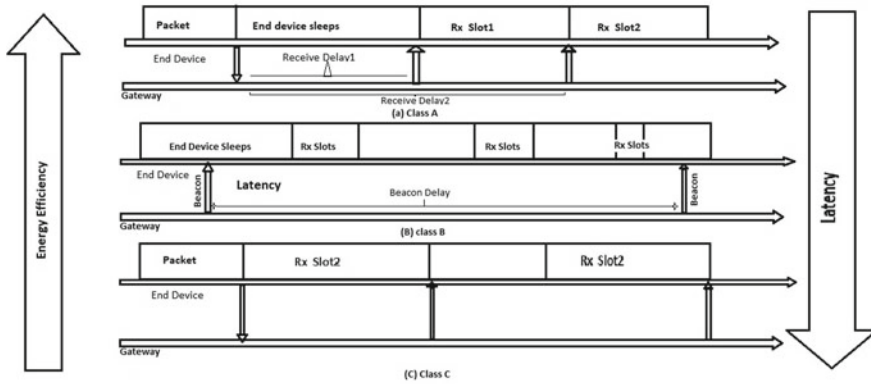


Fig. 3 Various connections between Classes A, B and C devices

efficiency. It provides low-cost IoT support to nearly about 50 to 300 sensor nodes. Figure 4 gives us a brief insight about the LG02 gateway configuration.

The hardware specifications of LG02 gateway is as follows:

Hardware requirements:

- (a) 400 MHz ar9331 processor
- (b) 64 MB RAM
- (c) 16 MB flash memory

Interface specifications:

- (a) 10 M/100 M RJ45 Ports × 2
- (b) Wi-fi: 802.11 b/g/n
- (c) LoRa wireless

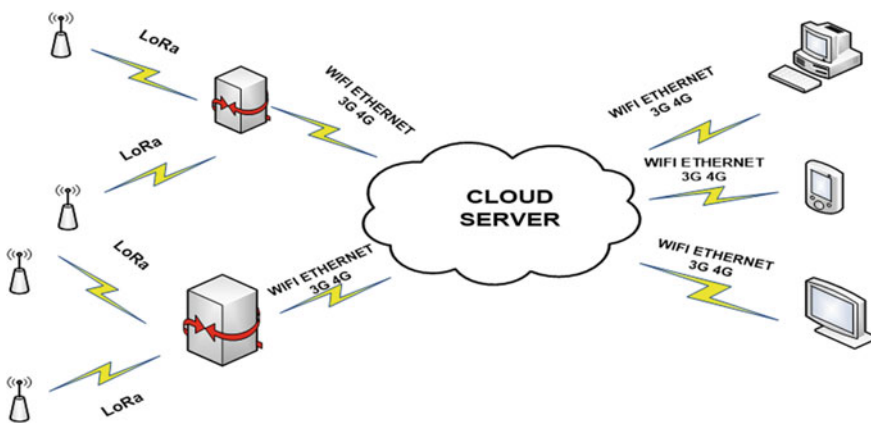


Fig. 4 A brief insight about the LG02 gateway configuration

- (d) Power input: 12 V DC
- (e) USB 2.0 host connector \times 1
- (f) USB 2.0 host internal interface \times 1
- (g) 2 \times LoRa Interfaces

Wi-fi specifications:

- (a) IEEE 802.11b/g/n
- (b) Frequency band: 2.4–2.462 GHz
- (c) Tx power:
- (d) 11n tx power: mcs7/15: 11 db mcs0: 17 db
- (e) 11b tx power: 18 db
- (f) 11g 54M tx power: 12 db
- (g) 11g 6M tx power: 18 db

Wi-fi sensitivity

- (a) 11g 54M: -71 dbm
- (b) 11n 20M: -67 dbm

The LG02 and OLG02 have the same firmware and work the same on the software side. The only difference is that LG02 works as an indoor LoRa module with or without Wi-fi connectivity, whereas OLG02 is just an outdoor version of a LoRa module with duplex communication strategy.

4 Transceiver Module

As already discussed, LoRa module supports duplex communication, so there must be a device capable of transmitting as well as receiving packets of information. The RFM module which comes in various versions, namely RFM95/96/97/98, has the special feature of transmitting and receiving data utilizing minimal amount of energy. The main benefits of this module are that it is capable of transmitting data over a very long range and also provides resistance to high interference conditions. This module is being patented by Hope and has an ability to achieve a high sensitivity of nearly 148 dBm in very low-cost expenses. It has proved to be very effective in blocking undesired interference and shows a high degree of selectivity over conventional modulation techniques.

5 Experimental Setup

The following experimental setup was done for executing predictive maintenance view of LoRa communication using IoT. The entire PCB model of the proposed experimental setup is given in Fig. 5:

The apparatus needed for the setup is listed below:

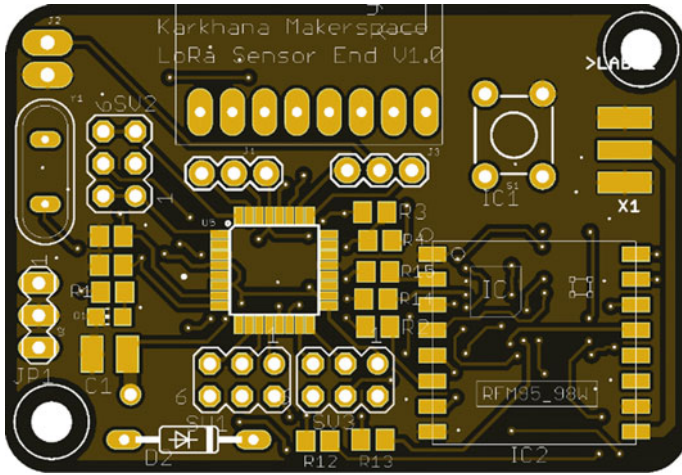


Fig. 5 PCB layout of the proposed experimental setup

- (a) Accelerometer: The accelerometer module MPU 6050 is being used as the sensor devices.
- (b) Arduino: The Arduino Uno powered by AtMega 328p microcontroller is basically used for initiating communication with the LoRa module. The LoRa communication module used is SX1276 which basically is a radio frequency transceiver rated at an operating frequency of 868 MHz. The entire setup is then configured in Indian frequency.
- (c) Glass-encapsulated temperature sensor which acts as a second sensor device is elaborated in Fig. (6).
- (d) A LoRa gateway preferable LG02 dragino.

Fig. 6 Developed prototype model used for predictive maintenance



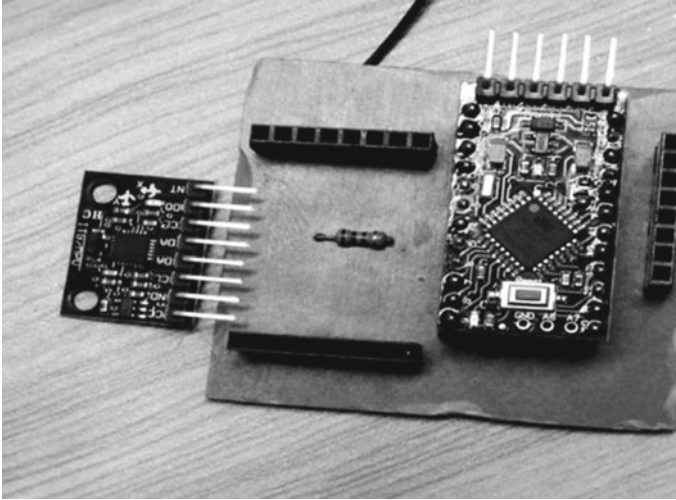


Fig. 7 Final prototype in hardware form

The accelerometer and the glass-encapsulated temperature sensor module are used as the sensor devices in this experiment. The data from both the sensors are sent to the Arduino Uno. As both the data are in analog form, they had to be converted to digital using a ADC which is a 10-bit analog to digital converter present on board of Arduino UNO. The data are then converted to digital values and are sent to the LoRa module via LG02 dragino gateway. These data from the LoRa module are uploaded to the Thingspeak cloud and are stored there. These data can be accessed by a machine learning prediction module and reverted back via the same route in case of any abnormal observations. This method can be used to ensure when the machine is in a faulty state or normal state. The glass-encapsulated temperature sensor and the accelerometer module can be fitted to any motor part and their temperature and their spinning coordinated can be sent to the cloud via LoRa technology. These data can be accessed, and in case of any abnormalities sensed in the data, a prediction technique powered by machine learning can be used to find out the state of the machine. The final prototype is illustrated in Fig. (7).

6 Conclusion

The sensor mainly the accelerometers and the glass-encapsulated temperature sensor sends the values to the LoRa gateways with the help of Arduino interface. The entire communication is done on the basis of I2C protocol. These data are then uploaded to the cloud and can be monitored from remote distances. Any discrepancies and these

data can be downstreamed and are then put through a prediction technique powered by machine learning which helps us to identify the faulty state of the machines. Thus, the machine can be maintained even from remote locations with the help of LoRa communication gateway powered by IoT.

References

1. Abu-Mahfouz AM et al (2015) Toward developing a distributed autonomous energy management system (DAEMS). AFRICON 2015. IEEE
2. Abu-Mahfouz AM et al (2016) Real-time dynamic hydraulic model for potable water loss reduction. *Proced Eng* 154:99–106
3. Want R, Schilit BN, Jenson S (2015) Enabling the internet of things. *Computer* 1:28–35
4. Asorey-Cacheda R et al (2013) On maximizing the lifetime of wireless sensor networks by optimally assigning energy supplies. *Sensors* 13(8):10219–10244
5. Akyildiz IF et al (2002) Wireless sensor networks: a survey. *Comput Netw* 38(4):393–422
6. Surligas M, Makrogiannakis A, Papadakis S (2015) Empowering the IoT heterogeneous wireless networking with software defined radio. In: 2015 IEEE 81st vehicular technology conference (VTC Spring). IEEE
7. Gioia E, Passaro P, Petracca M (2016) AMBER: An advanced gateway solution to support heterogeneous IoT technologies. In: 2016 24th international conference on software, telecommunications and computer networks (SoftCOM). IEEE
8. Alliance LR (2015) White paper: a technical overview of LoRa and LoRaWAN. The LoRa Alliance: San Ramon, CA, USA, pp 7–11
9. Sinha RS, Wei Y, Hwang SH (2017) A survey on LPWA technology: LoRa and NB-IoT. *Ict Expr* 3(1):14–21

PID-Based Electronic Load Controller for Three-Phase Synchronous Generator



Kamran Alam and Namarta Chopra

Abstract This paper presents a project based on Proportional–Integral–Derivative (PID) for the implementation of load controller for three-phase synchronous generator. Electronic load controller is a device which is related to power electronics method of controlling, managing and monitoring frequency of a system. Mostly, in rural areas, we do not have access to grid for power. There pico- and micro-hydropower can be implemented to provide power. For persistent operation and control of a three-phase synchronous generator, an electronic load controller has been implemented rather than using speed controller governor which is much more expensive. With the help of the proposed device, load output can be controlled, and thus, frequency can be maintained constant which again reduces worst case of overloading on generator. Therefore, with the help of the proposed scheme, protection of both generator and user's load can be maintained. The proposed system can play a vital role in run-off-river type hydropower station because there is no point of saving water. Thus, the proposed system can be used to minimize the overall cost of installation of the hydropower plant up to a large extent in rural areas where we do not have access to grid connection for electricity.

Keywords PID controller · Power system · Frequency sensor · Current sensor · Electronic load controller

1 Introduction

Electronic load controller is the concept of embedded system in power electronics which is used to maintain constant frequency on generator. In context of generator, the change in user's load is proportional to the increase or decrease in frequency. In steady state, power generated is given by Eq. 1.

K. Alam (✉) · N. Chopra
Amritsar College of Engineering and Technology, Amritsar, India
e-mail: kamrannt@gmail.com

N. Chopra
e-mail: kadnamarta@yahoo.co.in

© Springer Nature Singapore Pte Ltd. 2020
R. Sharma et al. (eds.), *Innovation in Electrical Power Engineering, Communication, and Computing Technology*, Lecture Notes in Electrical Engineering 630,
https://doi.org/10.1007/978-981-15-2305-2_13

$$\text{Generator power} = \text{power consumed by user} + \text{losses} \quad (1)$$

The main aim of electronic load controller is to reduce the cost of hydropower installation by replacing speed-controlled mechanical governor system. A mechanical governor maintains constant frequency on generator by controlling the flow of water. Mostly, two things were required for the installation of this device.

- Abundant runoff water.
- Suitable resistive load to dissipate excess energy.

Hydropower uses renewable energy which is used to generate power by the water stored in a dam, which is in the form of potential energy and is converted into kinetic energy so that work is said to be done in a turbine.

The typical large hydropower plant might suffer with long gestation period, ecological changes, loss due to long transmission lines, submergence of forest and underground mineral resources. The re-habitation of large population may require from the area to be submerged. Due to all mentioned factors above, large hydropower plants are not feasible. On the other hand, micro-, pico- and mini-hydropower plant can perform efficiently because they are free from those aspects. In most of the countries, hydropower plant having capacity upto 100 kW is regarded as micro-hydropower plant [1]. In micro-, pico- and mini-hydropower plants, run-of-river is used because there is no point to store water. The flow of water is fixed to the turbine; hence, it gives constant output power, but the consumer's load changes rapidly with time. Therefore, the speed of generator is altered due to the change in consumer's load, so frequency of the generator is also disturbed. The change in consumer's load is proportional to the change in frequency; i.e., if load on generator increases, frequency decreases, and reversely, when load on generator decreases, frequency increases [2–4]. Whenever there is variation in consumer's load, it is balanced with the help of electronic load controller. The major function of electronic load controller is to dissipate extra amount of energy to the dummy load. ELC maintains constant frequency and regulates the voltage of the generator by continuously monitoring consumer's load and dissipating excess amount of energy to the dummy load in order to gain constant frequency [5–9].

The function of the proposed system is to assure the safety of generator's winding by turning it off when it is overloaded. It will maintain the frequency and stability, despite the change in electric load.

2 Literature Review

In this section, various works performed by different authors are presented. Shailendra Kumar Rai et al. have proposed the simulation on pulse width modulation-based ELC. There are several components to sense voltage, current and frequency. Whenever there is change or fluctuation in the user's load, the blast load is triggered

which helps to calculate the pulse width modulation. Also, the driver circuit dissipates excessive power in order to gain steady state. In this system, DC-based control switching is used [1].

Nan Win Aung and Aung Ze Ya have proposed an ELC which is based on binary load action. In this concept, many dummy loads are connected with different power ratings of various electric loads. Whenever there is a change in an electric load, frequency will be varied, and at a time, microcontroller will calculate the required amount of power which is necessary to maintain the stability of the system. So, with the help of switching devices, dummy loads are triggered [10].

Binary load regulation is a technique where dummy load is made up of several series and parallel combinations of resistive loads arranged in a binary pattern. Whenever there is a change in customer's load, there is a proportional change in frequency of the power system, and microcontroller calculates the required combination of blast load required to make system's frequency constant. Therefore, switching operation is followed during transient period only. In stable condition, switch is in "OFF" state, so full voltage is applied to the new combination of blast load. In this proposed system, harmonics are not introduced in the steady-state condition [11].

3 Hardware Description of Proposed System

In order to design the proposed scheme, the following list of hardware and software is required.

Hardware required:

- Rectifier
- Driver circuit (thyristor is used)
- Frequency sensing circuit
- Notch detection circuit
- Current sensing circuit
- Microcontroller board.

Software required:

- PROTEUS
- ARDUINO
- ISIS 7 PROFESSIONAL.

3.1 Notch Detection Circuit

Zero crossing detector circuit can be designed by the use of operational amplifiers like LM324, LM741, refer Figs. 1 and 2. It is also known as sine wave to square wave converter as referred in Fig. 3. There are two terminals where the voltage is

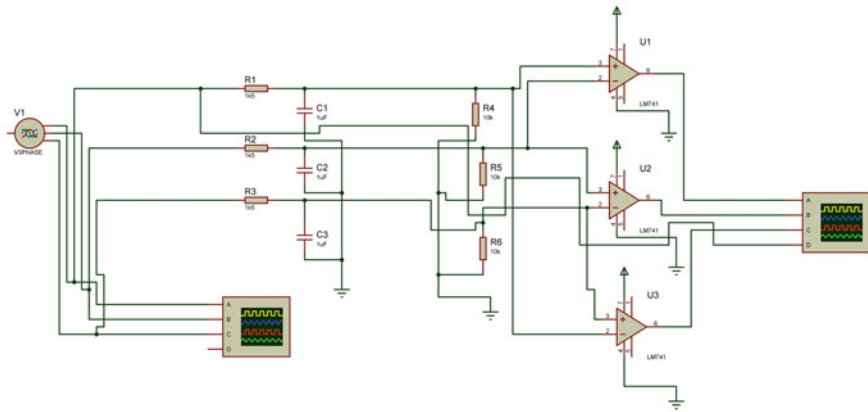


Fig. 1 Notch detection circuit

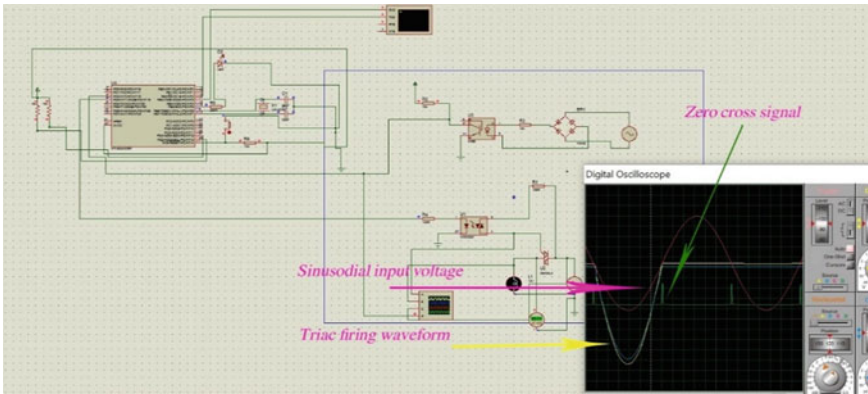


Fig. 2 TRIAC firing and zero cross

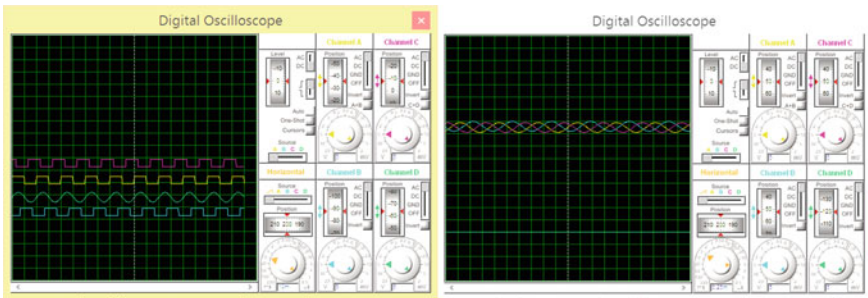


Fig. 3 Input/output waveform from notch circuit

compared, and when the waveform crosses to the zero, the output voltage is equal to reference voltage.

Function of this circuit is to detect zero crossing of waveform; whenever there is a zero cross, it gives high output. This circuit has huge importance to calculate the exact timing for firing angle of thyristor.

3.2 Current Sensor

A current sensor is an electronic circuit which is used to detect the current flowing through a circuit as referred in Fig. 4. It generates a signal which is proportional to the current flowing through a wire. But for practical implementation of current sensor, Hall effect sensor-based ACS712 is used, refer Fig. 5. LM741 chip is an 8-pin IC. Pins 1 and 5 are offset nulls, which we do not connect in our circuit. To power up the IC, we connect positive DC voltage at pin 7 and ground at pin 4. Pin 2 is inverting terminal of Op-amp LM741, and pin 3 is non-inverting terminal. Current transformer is connected to the main supply, and shunt resistance is connected in parallel to CT.

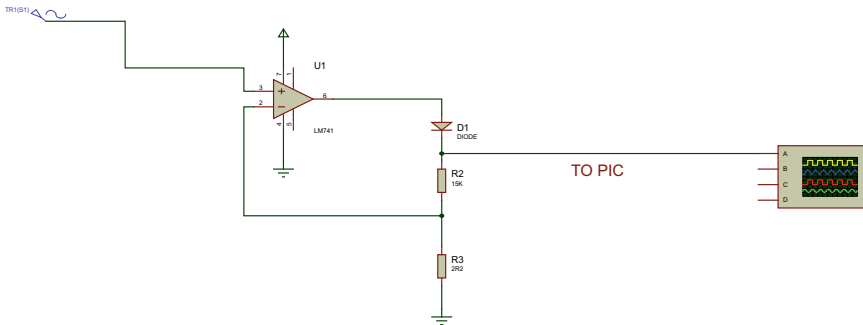
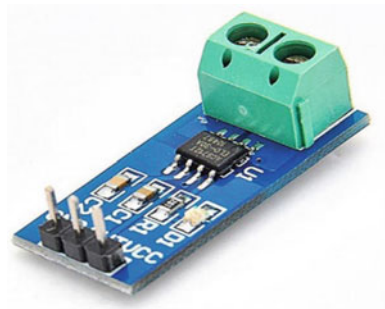


Fig. 4 Current sensor circuit

Fig. 5 Acs712 Hall effect current sensor



But in the proposed scheme, we have used ACS712 current sensor module for accuracy and fast response functionality because it works on the principle of Hall effect.

Current transformer is connected to the main supply, and shunt resistance is connected in parallel to CT, refer Fig. 3.

We have selected V_{CC} as 10 V. Therefore, the resistance is so selected; if it is 10 V, it should give 10 mA. Calculation of resistance is done by applying Ohm's law refer Eq. 2.

$$\begin{aligned} V_S &= I \times R \\ 10 &= 10 \text{ mA} \times R \end{aligned} \quad (2)$$

Therefore, R we get is 1 k Ω .

Therefore, the threshold value of current that we can measure is 10 mA. The output voltage across R2 can be given by voltage divider formula, refer Eq. 3.

$$V_{\text{out}} = V_S \left(1 + \frac{R2}{R3} \right) \quad (3)$$

Atmega328p contains 10-bit analog to digital converter, which means that we can map input voltage from 0 to operating voltages, either 3.3 or 5 into integer value from 0 to 1024.

3.3 Frequency Sensor

In this proposed system, frequency sensor has been used for the real-time measurement of frequency variation. For this circuit, a step-down transformer is used for the conversion of high voltage into low voltage. Also, a transistor is used to convert sine wave into square wave, refer Fig. 6. A frequency has been calculated with the following set of code.

```
duration1= pulseIn(freqpin, HIGH); // when the wave has
on waveform
duration2= pulseIn(freqpin, LOW); //when the wave has
low or off waveform
sum=duration1+duration2; //sum of both the duration for
one complete cycle
freq=(1/sum*1000000); //time is being converted into
second so that we can get frequency
Frequency (f) = 1/time
```

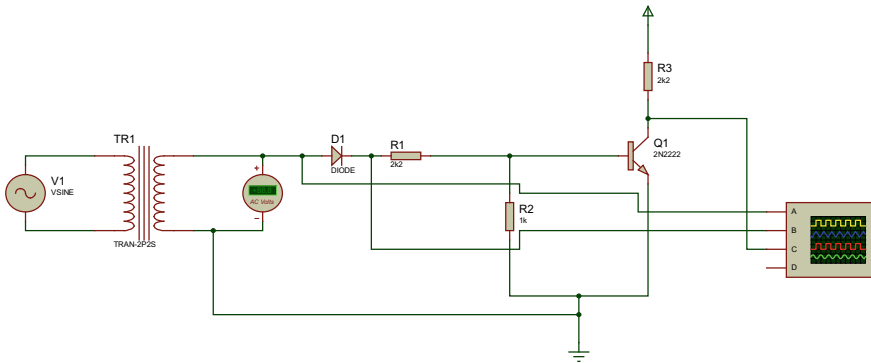


Fig. 6 Frequency sensor circuit

3.4 Dummy Load

Dummy load is used to consume an excess amount of power generated in the circuit to maintain an effective system performance. It helps to protect the entire circuit from damage, and due to the resistive nature of dummy load, lead and lag condition of phase angle will not be encountered.

3.5 Energy Dissipation Circuit

Energy dissipation circuit is used to dissipate the required amount of power needed for stability. If heavy load from generator is removed suddenly, then excess amount of power is sent to dummy load through given circuit in Fig. 7 to balance load and frequency. For the implementation of this mechanism, a gate-controlled circuit is provided with TRIAC (BTA 41 600b).

4 Methodology

In order to achieve the stated objective, the following methodologies were adopted:

- Step 1 Study of various types of existing electronic load controllers
- Step 2 Prepare a simulation model of the proposed scheme on proteus
- Step 3 Prepare a hardware design in ISIS 7 professional
- Step 4 Hardware assembling and testing the parts of designed hardware
- Step 5 Tuning of PID
- Step 6 Testing the functioning of the proposed ELC scheme in a generator.

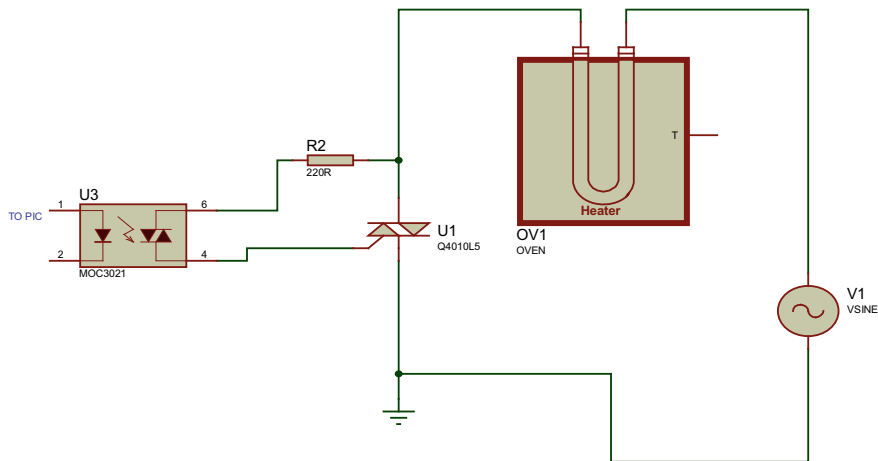


Fig. 7 Gate driver circuit

5 Proposed System

Figure 8 shows the proposed scheme of electronic load controller. The main function of the proposed scheme is that it has the ability to draw different currents from different phases of the generator terminals which allow it to compensate for the unbalanced consumer current. Therefore, the frequency of the system is balanced. This feature results in generator currents being balanced even when consumer loads are unbalanced. Thus, overloading of generator is also reduced. The proposed system is embedded with variety of sensors like zero cross detector, TRIAC gate driver circuit, frequency sensor, current sensor, notch detection sensor. The function of frequency sensor is to sense the change in frequency at any instance of time. Current sensor is used to calculate the current in each phase. Zero cross circuit is used to detect correct timing for firing of TRIAC at certain delay or firing angle. Notch detecting circuit is used to calculate waveform's ON and OFF time period to calculate exact firing delay.

6 Results

The proposed scheme is tested for various conditions, refer Fig. 8, and the output is noted as mentioned above, refer Table 1.

In the first condition, we did not apply any consumer's load; therefore, all power is drained to the blast load. The microcontroller detects no load, and hence, frequency is increased. Microcontroller calculates the required amount of firing angle and fires TRIAC. The total power of the generator was drained to the dummy load in the first condition. In the second condition, consumer's current was 4.6Amp, but the generator

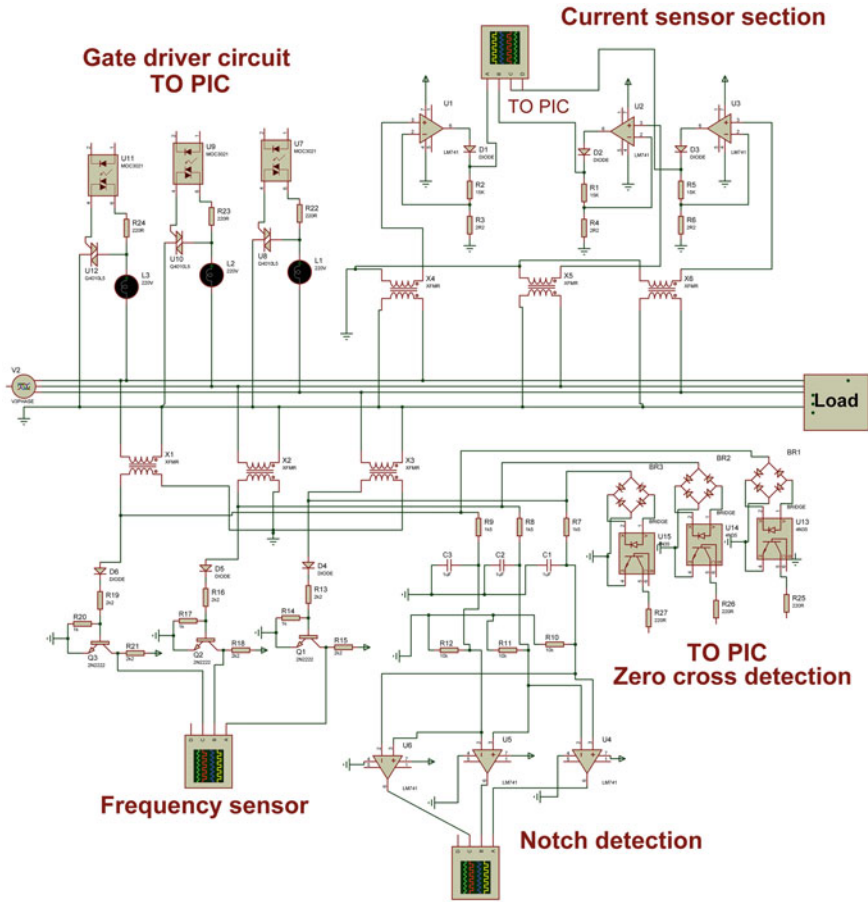


Fig. 8 Proposed proteus schematic circuit diagram

Table 1 Gate driver circuit

Current RMS value	Condition 1	Condition 2	Condition 3	Condition 4
Consumer's current (A)	0	4.6	7.2	7.5
Blast current (A)	7.2	2.6	0	0
Frequency (Hz)	50.07	50.06	50	48 (Auto Shutdown)

was rated as 7.2 A. Therefore, the required amount of firing angle is calculated by microcontroller, and dummy current was 2.6 A.

For hardware implementation and oscilloscope output of TRIAC firing refer Fig. 9. The proposed scheme is implemented on Hardware and is tested for all possible outcomes.

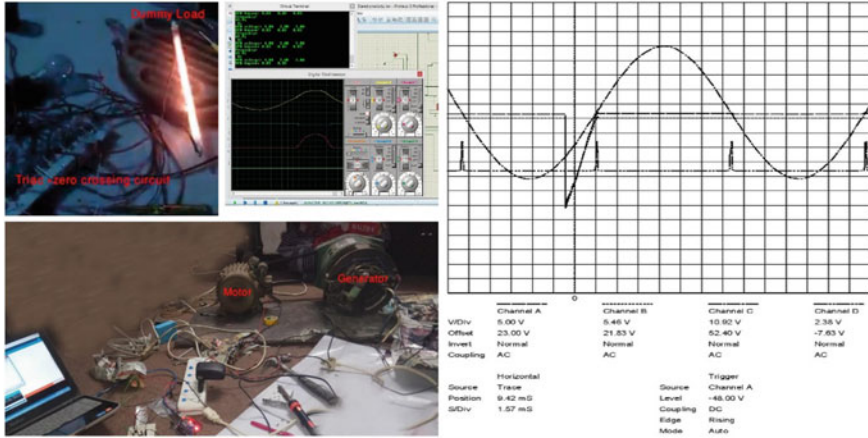


Fig. 9 Oscilloscope reading and practical implementation circuit

Thus, the generated current and consumer’s current are balanced by the application of the proposed scheme. Therefore, frequency of the system is remained constant.

In third condition, consumer’s current was 7.2 A. Therefore, the generated current and consumer’s current are equal, so there is no firing of TRIAC. In the fourth condition, consumer’s current is more than generated current which is the main cause of overloading of generator; therefore, the system is shutdown to prevent damage to the power system.

Firing angle calculation

One complete cycle = 50 Hz (Asia region)

Time taken to complete once complete cycle = 1/(Frequency)

One full 50 Hz wave is equal to 1/50=20 ms

Every zero crossing thus can be represented as: (50 Hz) → 10 ms (1/2 Cycle) or 10 ms=10,000 μs.

Therefore at 0 μs, the firing is full, and at 10,000 μs, TRIAC is completely OFF.

7 Conclusion with Future Work

By the use of PID-based electronic load controller, we can easily control and monitor frequency of the generator. We can reduce worst case of overloading on generator. Therefore, there is a very less risk of damage of generator which is very costly. Thus, frequency can be maintained constant with least error.

Since this is an era of science and technology, we will make better monitoring and controlling by the implementation of IOT. So that people from another location can control, manage and update the system. We can also utilize excess power to be drained, to charge up street light batteries. We will be able to protect the generator

from abnormal frequency, over excitation and over voltage, unbalanced load, over-speed protection by the implementation of advanced transducers and programming logics.

Acknowledgements The author delightedly acknowledges the I.K.G Punjab Technical University, Kapurthala, to carry out research work based on the proposed scheme.

The author would like to express sincere gratitude to Amritsar group of colleges and Professor Dr. Narinder Sharma and HOD Gurjeet Singh for their guidance, support and valuable suggestions to proceed on the project during research. He also wants to thank his guider Lochan Basyal for his support and help.

I want to express my appreciation to my wonderful parents. My parents deserve special thanks for giving me the very best that they could. Thanks to my father Er. Aftabalam and brother irfanalam for all the interest they have shown in my education ever since I was a child. Thanks to my mother and sister for their affection and gentleness toward me.

References

1. Rai SK, Rahi OP, Kumar S (2015) Implementation of electronic load controller for control of micro hydro power plant. IEEE 2015
2. Singh B, Murthy SS, Goel M, Tandon AK (2006) A steady state analysis on voltage and frequency control of self-excited induction generator in micro-hydro system. In: International conference on power electronics, drives and energy systems, pp 1–6
3. Rahi OP, Chandel AK, Sharma MG (2012) Simulation studies for refurbishment and uprating of hydro power plants. *Int J Adv Eng Sci Technol (IJAEST)* 1(2):200–208
4. Rahi OP, Chandel AK, Sharma MG (2011) Fuzzy logic based approach for condition monitoring of hydro generator. *Int J Soft Comput* 6(41):85–90
5. Singh B, Murthy SS, Gupta S (2006) Analysis and design of electronic load controller for self-excited induction generators. *IEEE Trans Energy Convers* 21:285–293
6. Kapoor P, Phunchock L, Kumar S, Rahi OP (2012) Frequency control of micro hydro power plant using electronic load controller. *Int J Eng Res Appl (IJERA)* 2(4):733–737
7. Rahi OP, Gagrai SK, Rawat SK (2013) Simulation of turbine governing in hydro power plants. In: International conference on future trends in electronics and electrical engineering (FTEE–2013) Bangkok, Thailand, 13–14 July 2013, pp 34–37
8. Rahi OP, Chandel AK, Sharma MG (2014) Investigations into the design of a hydro power plants. *Indian J Power River Valley Dev*, pp 132–144
9. Rahi OP, Kumar G (2014) Simulation studies for refurbishment and uprating of hydro power plants. *IEEE Power and Energy Society General Meeting 2014 at the Gaylord National Resort and Convention Center located in National Harbor, Washington, DC, 27–31 July 2014*, pp 1–5
10. Aung NW, Ya AZ (2015) Microcontroller based electrical parameter monitoring system of electronic load controller used in micro hydro power plant. *J Electr Electron Eng* 3(5):97–109
11. Henderson D (1998) An advanced electronic load governor for control of micro hydroelectric generation. *IEEE Trans Energy Convers* 13(3):300–304

Survey of Sentiment Analysis of Political Content on Twitter



Siddhesh Pai, Vaibhav Bagri, Shivani Butala and Pramod Bide

Abstract Social media usage has seen a dramatic rise in the recent years. With the use of just 140 characters on Twitter, people can voice their opinion on any subject. Various techniques have come up to identify the sentiment of these tweets so as to reach appropriate conclusions. Sentiment analysis of tweets related to politics is theorized to be able to identify public sentiment toward candidates and predict election results. The methodologies have been broadly classified into lexicon-based approaches and machine learning-based approaches. Algorithms like Naive Bayes (NB), support vector machine (SVM) and neural networks are used in machine learning-based approaches. Owing to their greater flexibility, they are more useful than lexicon-based approaches when it comes to political tweet analysis. A survey of all these approaches reveals that SVM provides accuracy over 70%, making it the most efficient algorithm for political sentiment analysis of tweets.

Keywords Social media analysis · Opinion mining · Politics

1 Introduction

The ease of availability of the Internet and rise in the usage of smartphones has led to a drastic increase in the use of social media. Social media is not only used to update people about their personal lives, but also to express opinions nowadays. If anyone feels indignant, they simply log on to Twitter, Facebook or Instagram and post a

S. Pai (✉) · V. Bagri · S. Butala · P. Bide
Computer Engineering Department, Sardar Patel Institute of Technology, Andheri (West),
Mumbai 400059, India
e-mail: siddhesh.pai@spit.ac.in

V. Bagri
e-mail: vaibhav.bagri@spit.ac.in

S. Butala
e-mail: shivani.butala@spit.ac.in

P. Bide
e-mail: pramod_bide@spit.ac.in

© Springer Nature Singapore Pte Ltd. 2020
R. Sharma et al. (eds.), *Innovation in Electrical Power Engineering, Communication, and Computing Technology*, Lecture Notes in Electrical Engineering 630,
https://doi.org/10.1007/978-981-15-2305-2_14

complaint. It spreads through social media like wildfire, with people supporting the claim one after the other and eventually it even spreads to people who you do not know.

Similarly, people express their opinions regarding political parties on their social media feeds, be it in support of the party, or against the party. Twitter is one of the most commonly used platforms in such cases, since tweets are available to view for everyone. These tweets can be analyzed to identify the sentiment being portrayed by the person. This can be used to predict the person’s opinion regarding the particular political party and who would he/she vote for in an election.

There has been a lot of work previously to identify the sentiment of a particular tweet. There are two main approaches for this—lexicon-based and machine learning-based. Lexicon-based approaches use pre-classified sentiments for certain lexicons. After dividing a tweet into separate words, the sentiment is identified based on these lexicons. Machine learning approaches provide various algorithms for sentiment analysis—namely Naive Bayes (NB), support vector machines (SVM) and neural network models. The accuracy of each approach differs on the basis of dataset used and preprocessing performed on the data. Figure 1 shows all the different methods that can be employed.

This paper extensively surveys the existing methodologies and techniques for performing political sentiment analysis of tweets. Various parameters are determined to compare the performance of the existing approaches and determine which might be the best fit approach to use in future. The organization of the paper first introduces and explains the existing technologies, followed by a comparison table of the same. Following that, the results of the survey are discussed, and a conclusion is drawn regarding which algorithm is best suited for this work.

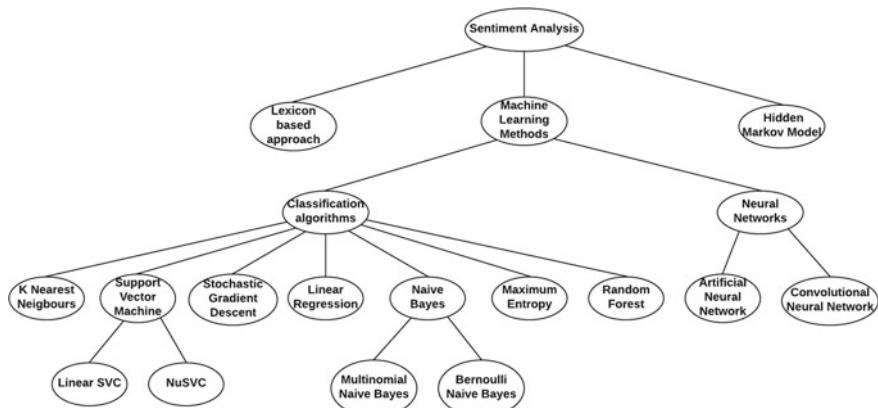


Fig. 1 Methods for sentiment analysis

2 Literature Survey

While it is possible to carry out sentiment analysis of tweets, the first major question arises regarding extraction of tweets. Thus, a Twitter API is used for data collection purposes using Python libraries like Tweepy and Twython [1–4]. Tools like Rapid-Miner are also used to extract data from tweets or statutes using search queries [5]. Crawling method is also used for the process of obtaining data from social media tweets [6].

The text obtained in each tweet is up to 140 characters long. However, tweets contain certain unnecessary terms which can be removed during preprocessing to reduce the size of overall input dataset. Preprocessing was performed for removal of white spaces, different URLs or hyperlinks along with the retweets and emojis [3, 7–10]. The different stop words, that is the words which often occur in sentences but contribute little to the meaning of the sentence were also eliminated [1, 5, 6]. Expansion of various emoticons and abbreviations was done for better accuracy [1, 10]. Chamansingh et al. [3] even classified the emoticons, i.e., If ‘:)’ then it gave label as positive and for ‘:(’ it gave the label negative. Special characters like hashtags were sometimes stored separately [7, 11] or were completely removed in certain cases [5, 6, 8, 10].

The sentiment of the tweets obtained can be analyzed via two possible approaches—lexicon-based and machine learning-based.

One of the most common ways to identify the sentiment of tweets is by using the lexicon-based approach. The lexicon-based approach looks up all the words in the tweet itself and then assigns a polarity to each word on the basis of a predefined score. The overall score is then aggregated in order to obtain a collective score for the tweet and ultimately classifying it as positive, negative or neutral.

There are multiple approaches which build on this basic lexicon-based approach by tweaking the approach in order to increase the accuracy. Since this approach is unsupervised, a rich lexical resource is needed in order to power this approach like SentiWordNet [12, 13], HindiWordNet [8], AFINN-11 [14]. The tweets are split into subtweets on the basis of conjunctions since there might be multiple entities being referred to in one single tweet. Each subtweet is then assigned a polarity instead of the whole tweet in order to achieve better results [15]. The lexicon-based approach can also be powered by the subjectivity lexicon developed by Wiebe and colleagues which harnesses the presence of 8222 words along with their POS tag in order to classify a tweet [11]. A simple technique which makes the lexicon-based approach more powerful is flipping the polarity of the words on the basis of negation words like not, however, although, etc. [8, 11, 12]. ‘Hashtagged’-based LBA considers the hashtags mentioned in a tweet in order to determine the sentiment of tweets. Hashtags are manually classified as positive, negative or neutral for a particular entity and then these hashtags are searched for within tweets in order to generate concrete evidence of polarity for that entity [11].

Neutral tweets for a particular entity give us significant insight into the popularity of that entity among other entities [9]. Words that are not present in the dictionary

are not allotted a score at first but after an initial iteration, the presence of the new words is detected across all the tweets. The average sentiment score of the tweets containing the new word is calculated and this score is then assigned to that new word and added to the dictionary [14].

Machine learning-based methods include a number of different possible algorithms like Naive Bayes, SVM, Maximum entropy, Neural Networks, etc. A training dataset needs to be provided to the model before it can be used for actual sentiment analysis which can be obtained from movie reviews from NLTK Python library [10] or from Sentiment140 [1]. Manual labeling of tweets can be done to identify the positive, negative and neutral words along with the different features [7, 8]. A load dictionary was used consisting of different positive, negative and neutral words and word weighing was done for each tweet. Positive words were assigned a score of +1, whereas negative words were assigned -1 and 0 for neutral tweets [6].

Naive Bayes is the basic classification process which follows the Bayes Theorem. It assumes that all the features are autonomous [3]. The formula for assigning labels is as follows:

$$P(\text{label features}) = P(\text{label}) * P(\text{features label})$$

The labels signify the various sentiments, i.e., positive, neutral and negative, and the input features are the words obtained from the tweets and P stands for the various probabilities which need to be trained.

SVM on the other hand makes use of decision planes to classify the different data. It is used when the data available is smaller in size than the various attributes. SVM is a type of supervised learning model which involves training a sentiment classifier using the count of the occurrence of the various words. The input numerical data is used in the testing phase to generate patterns and the labels for the classes [3].

Chamansingh et al. [3] proposed a model using SVM, maximum entropy along with Chi-square feature selection to assign word score for every word and then compare on the basis of on runtime, file size and accuracy. The Chi-square test is used for the same to determine statistically if two events are independent or not. The goal is to choose the features with the highest Chi-square scores so that they are more dependent on each other.

Neural networks are another potential way of assigning sentiment to the tweets. The network can be given a training set of vocabulary with the associated emotion. Learning on the basis of that, test data can be correspondingly assigned a sentiment (positive, negative and neutral). The advantage of this over other methods is that it considers the order in which the words appear and does not simply break the sentence into a bag of words. Thus, if any positive statement is preceded by a negation or vice versa, the network can successfully identify and take appropriate action.

Neural networks itself is a vast field and there are multiple approaches toward sentiment analysis within it as well. Tweets consist of sentences. Since multiple tweets are taken as input and each word is considered a feature, the number of words is very large. It is computationally very difficult to handle those numbers of features. Hence convolutional neural networks are used to convert the data into a form that is

easier to process. Pota et al. [16] introduced a method of depicting the text of tweets in the form of vectors comprising of subword information. This is given as input to a pretrained convolutional neural network model to identify the sentiment of the particular tweet.

Recurrent neural networks (RNN) can also be used in a similar manner for sentiment analysis. The problem with RNN is that while training, if the gradient is too small, then the model trains very slowly. Also, the gradient values keep decreasing, making the training of the model very difficult. Long short-term memory (LSTM) is used to overcome this problem. When a preprocessed set of tweets are given as input to this model, the polarity regarding the sentiment can be identified [17].

To handle the negation and double negation aspect of a sentence, the previous state of the word read in the sentence is needed. Hence, if a 'not' is read, then the state must be shifted to identify the next sentiment as opposite of what it usually means. Sentiment analysis using the Hidden Markov Model helps in this as it takes into consideration the states proceeding as well as following the current state [13].

3 Discussion

Table 1 provides a comparison of the various methodologies adopted in the existing approaches. The parameters of comparison are the dataset used, accuracy obtained, results, and limitations of the particular approach.

4 Performance Analysis

The lexicon-based approach employed across the papers yields highly inconsistent and fairly inaccurate results in this domain. Most papers yield an accuracy of less than 50% which is significantly less than other sophisticated methods. The base of the problem for a lexicon-based approach is the lexical resource itself. The presence of multiple, subjective and limited lexical resources significantly impact the output of the results produced by the lexicon-based approach.

Since our survey of sentiment analysis is in the political domain, the content to be analyzed calls for a lexical resource created toward some sort of political analysis. One of the methods employs a subjective lexical resource with POS tagging but it results in an accuracy dip which is counterintuitive. Also, the language to be analyzed is again restricted to the language of words in the lexical resource itself. Although there are resources coming up in multiple languages, the use of these resources is still limited at this point of time.

The lexicon-based approach is a completely unsupervised method relying on the lexical resource itself which we have established has no context to the political domain. Analysis of content relating to the political domain needs some context of this domain in order to achieve better results. Hence, all in all, the results and

Table 1 Discussion

Methodology	Dataset	Accuracy	Research results	Limitations and gaps
Removes non-authentic tweets and applies LBA to the subtweets which are created after breaking down of the authentic tweet [15]	Twitter streaming API collected 10 million tweets in the campaign period	Manual evaluation of a 100 tweets shows an average accuracy of 83.3%	Mean absolute error was calculated between the actual election result and the compiled result which showed a difference of 0.61% for a 60-day time frame	The fixation of time frame as 60 days is a drawback along with the dubious method to remove the non-authentic tweets
A subjectivity lexicon was used in the LBA where a score and the POS tag are used to evaluate the word present in the tweet. The hashtag also determines the polarity of the tweet [11]	NodeXL was used to extract 600,000 tweets mentioning the candidates	An accuracy of 45% was achieved using the hashtag-based approach	The results were correlated with the actual election outcome which stood true for the Republicans but not for the democrats	Considering the POS tag actually leads in a dip in accuracy
Keywords were identified which classified a tweet as positive, negative or neutral for a particular candidate [9]	Twitter API was used to fetch tweets based on keywords related to the French election	The first method differed from the actual result by 2% and the second method by 38%	The two methods employed predict the winner of the actual election wrongly	The method does not make use of a proper lexical resource and the selection of keywords are highly subjective
The polarity and subjectivity, both are calculated using LBA for a given tweet in order to perform prediction [2]	Twython API is used to fetch tweets for three candidates	Not addressed	The results propose a maximum negative sentiment toward Trump which actually contradicts the actual election result	Uses a very naive approach and cannot support multiple languages

(continued)

Table 1 (continued)

Methodology	Dataset	Accuracy	Research results	Limitations and gaps
Standard LBA is taken using AFINN-111 dictionary. Words not present in the dictionary are handled using a new algorithm [14]	Twitter API is used to fetch tweets for Narendra Modi, count not mentioned	Not addressed	The result states that overall sentiment toward Narendra Modi increases after his foreign visit	The approach is very basic and the scope of the paper is limited only to one political figure at one point of time
Opinion-Lexicon approach was taken in order to assign polarity to the tweets. Made use of a dictionary provided on GitHub [4]	Twitter search API fetches 1500 tweets each for Arvind Kejriwal and Modi	Not addressed	Results show Narendra Modi has a more positive perception and is more influential than Arvind Kejriwal on the Twitter platform	The source of the lexical resource calls for speculation on the classification of tweets
Manually labeled 3600 tweets after preprocessing and used NB, KNN, Prind, RF, NBMIN, SVM classifiers [7]	Extraction of 612,802 tweets from Twitter API in JSON format	Average accuracy of classification is 70% for positive and negative tweets whereas inclusion of neutral tweets lead to an accuracy of 50%	Identified the user participation during elections province wise and the top 5 political parties in Pakistan and compared the results to the actual votes	Accuracy dips significantly when neutral tweet classification is added
Manually Labeled 36 k tweets and used NB and SVM classifiers [8]	Hindi tweet corpus from Twitter archiver. Hindi SentiWordNet for dictionary-based approach	Naive Bayes—62.1% SVM—78.4% dictionary-based—34%	The SVM algorithm has the highest accuracy. BJP had a better chance of winning according to the predictions which matched the actual results	Dictionary-based approach yielded poor results. Emoticons were not considered. Limited dataset was used

(continued)

Table 1 (continued)

Methodology	Dataset	Accuracy	Research results	Limitations and gaps
Used diffusion estimation model to predict sentiment of next tweet of a user and made use of support vector classifier [18]	Rensselaer Polytechnic Institute dataset. Twitter Indian election network (TIEN) was built	Pearson correlation coefficient obtained was between 0.83 and 0.986	Predicted Narendra Modi will win the election. Identified the individuals on social media who are the most influential on any topic	Limited resources, extensive data are needed to predict coalitions between political parties. Earlier time frame should be considered for better accuracy of results
Manually labeled 3600 tweets after preprocessing and used NB, KNN, RF, NBMIN, SVM classifiers [7]	Extraction of 612,802 tweets from Twitter API in JSON format	Average accuracy of classification is 70% for positive and negative tweets whereas inclusion of neutral tweets lead to an accuracy of 50%	Identified the user participation during elections province wise and the top 5 political parties in Pakistan and compared the results to the actual votes	Accuracy dips significantly when neutral tweet classification is added
Manually labeled 36 k tweets and used NB and SVM classifiers [8]	Hindi tweet corpus from Twitter archiver. Hindi SentiWordNet for dictionary-based approach	Naive Bayes—62.1% SVM—78.4% dictionary-based—34%	The SVM algorithm has the highest accuracy. BJP had a better chance of winning according to the predictions which matched the actual results	Dictionary-based approach yielded poor results. Emoticons were not considered. Limited dataset was used
Used diffusion estimation model to predict sentiment of next tweet of a user and made use of support vector classifier [18]	Rensselaer polytechnic Institute dataset. Twitter Indian election network (TIEN) was built	Pearson correlation coefficient obtained was between 0.83 and 0.986	Predicted Narendra Modi will win the election. Identified the individuals on social media who are the most influential on any topic	Limited resources, extensive data is needed to predict coalitions between political parties. Earlier time frame should be considered for better accuracy of results

(continued)

Table 1 (continued)

Methodology	Dataset	Accuracy	Research results	Limitations and gaps
Classification algorithms like NB, NBMN, Bernoulli NB linear regression, SGDC, linear SVC, SVC for sentiment analysis [10]	Twitter API using python library Tweepy. The training data obtained from movie reviews from NLTK python library	The average accuracies for the three parties are 59.69%, 78.66%, 73.33%, 70.25%, 72.66%, 70.33% and 72%, respectively	Multinomial Naive Bayes gives the most accurate results of around 78%. Also showed that BJP is likely to win the elections based on public opinion	Not addressed
Binary Multinomial Naive Bayes (learning-based approach) [1]	Twitter API, SentiWordNet used with 10,000 positive data points and 10,000 negative points and 181 positive data points and 177 negative data as test data	The positive and negative accuracies were 0.689944 and 0.689944 respectively	Prediction results show that Hillary Clinton will win the election using electoral college	Does not take into consideration emoticons and slangs, might consider more than 1 vote per user if the user tweeted more than once
A clustering algorithm, i.e., K-means with $2 \leq k \leq 30$ was used to cluster the words with similar sentiments [5]	Rapid miner used to extract data from tweets or statuses using search queries	Not addressed	Results show the percentage of positive, negative and neutral tweets (8.57%, 34.29%, 57.14% respectively) about Donald Trump	Due to lack of experimentation, the results achieved were not up to the mark
Naive Bayes, SVM and maximum entropy algorithms were used as classifiers and compared for tweets [3]	The dataset was obtained the Twitter search API and it constrained about 1.6 million tweets	SVM classifier—78.14% maximum entropy—78.07% Naive Bayes—77.06%	Comparison on the basis of accuracy, classification runtime and file size, and max entropy used to obtain best result	Domain-specific tweets can yield better results

inferences achieved from the lexicon-based approach call for a supervised and more sophisticated approach.

Coming to supervised approaches, we first consider approaches using neural networks. CNN gave an accuracy of approximately 61%, while ANN provided up to 71% accuracy for their particular datasets. These models derive the important features for sentiment analysis using various linear combinations of input data. The output is provided as a nonlinear function of these features. Since the model is learning from an input data of political tweets, the sentiment is analyzed keeping the political scenario in mind.

One major drawback though is the lack of training data available. For this reason, some models had to be trained with a movie review dataset, as political tweets with their sentiments identified are not readily available. Another factor is that these models are trained using gradient descent methods, which does not always lead to a global optimal solution. The additional computational cost of using a separate model to solve the vanishing gradient problem adds to the difficulties faced in this approach. This prompted the use of certain other classification algorithms.

The classification algorithms for prediction of sentiments give more accurate results as compared to the lexicon-based approach and neural networks. These methods do not require a dictionary or dataset of words along with the classes (positive, negative and neutral). They are supervised methods which make use of training data with no manual labeling and thus are faster and better than the dictionary-based approach.

The use of various classifiers like Naive Bayes, support vector machine, linear regression, maximum entropy model, random forest, etc. in identifying the positive and negative sentiments result in an average accuracy of greater than 70% whereas the inclusion of neutral sentiments brings down the accuracy to about 50%. The performance of the classification algorithms can also be compared on the basis of the file size of the features as well as the classification runtime. Support vector machine and Multinomial Naive Bayes have the highest accuracy rate among all the classifiers (80%). However, accuracy is largely dependent on the quality of the training data and can be further improved by making use of a balanced dataset for training purposes. Figure 2 shows a comparison between average accuracies of all the methods.

Sarcasm detection and prediction of sentiments for emoticons can further enhance the results for supervised as well as unsupervised approaches. A hybrid approach must be developed so that the drawbacks of these individual methods can be overcome and the sentiment classification process can be further enhanced.

5 Conclusion

Tweets are an effective way for people to express their opinion and this fact can be exploited to analyze the different sentiments of public in various spheres of society such as the political field. In this paper, we conducted a survey regarding the different

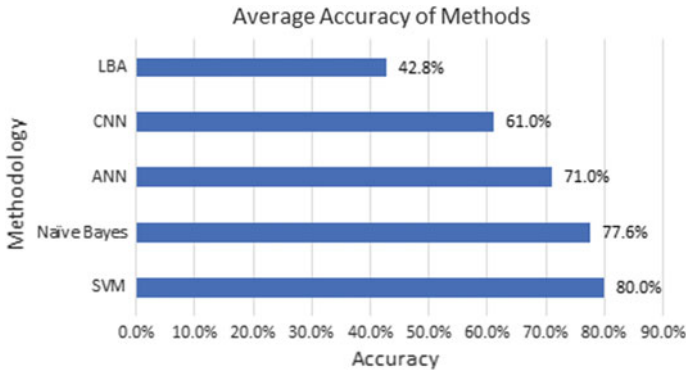


Fig. 2 Accuracy of various methodologies

approaches for sentiment analysis of political tweets. The tweets are classified as positive, negative and neutral, and based on this classification, the political party with the highest ratio of positive tweets is predicted to win the election. The different methods for sentiment analysis such as the lexicon-based approach and the machine learning methods consisting of neural networks and classification algorithms were compared in terms of their accuracy and limitations. From this survey, it can be concluded that the classification algorithms, more specifically the support vector machine and the Multinomial Naive Bayes classifiers have the highest accuracy of about 80%. However, hybrid algorithms must be developed which overcome the various drawbacks of the individual methods. Further research is required to improve the accuracy of sentiment prediction by considering sarcasm and even emoticons.

References

1. Wicaksono AJ, Suyoto, Pranowo (2016) A proposed method for predicting us presidential election by analyzing sentiment in social media. In: 2016 2nd international conference on science in information technology (ICSITech), Oct 2016, pp 276–280
2. Nausheen F, Begum SH (2018) Sentiment analysis to predict election results using python. In: 2018 2nd international conference on inventive systems and control (ICISC), Jan 2018, pp 1259–1262
3. Chamansingh N, Hosein P (2016) Efficient sentiment classification of twitter feeds. In: 2016 IEEE international conference on knowledge engineering and applications (ICKEA), Sep 2016, pp 78–82
4. Dubey G, Chawla S, Kaur K (2017) Social media opinion analysis for indian political diplomats. In: 2017 7th international conference on cloud computing, data science engineering—confluence, Jan 2017, pp 681–686
5. Iija M, Uni E, Onko D (2018) Collection and sentiment analysis of twitter data on the political atmosphere. In: 2018 14th symposium on neural networks and applications (NEUREL), Nov 2018, pp 1–5
6. Buntoro G (2019) Sentiments analysis for prediction the governor of east java 2018 in twitter. *Int J Artif Intell Inform* 1:03

7. Razzaq MA, Qamar AM, Bilal HS (2014) Prediction and analysis of Pakistan election 2013 based on sentiment analysis. In: 2014 IEEE/ACM International Conference on Advances in Social Networks Analysis and Mining (ASONAM 2014), Aug 2014, 700–703
8. Sharma P, Moh T (2016) Prediction of Indian election using sentiment analysis on hindi twitter. In: 2016 IEEE international conference on big data (big data), Dec 2016, pp 1966–1971
9. Wang L, Gan JQ (2017) Prediction of the 2017 French election based on twitter data analysis. In: 2017 9th computer science and electronic engineering (CEECE), Sep 2017, pp 89–93
10. Juneja P, Ojha U (2017) Casting online votes: to predict offline results using sentiment analysis by machine learning classifiers. In: 2017 8th International Conference on Computing, Communication and Networking Technologies (ICCCNT), July 2017, pp 1–6
11. Rezapour R, Wang L, Abdar O, Diesner J (2017) Identifying the overlap between election result and candidates ranking based on hashtag-enhanced, lexicon-based sentiment analysis. In: 2017 IEEE 11th International Conference on Semantic Computing (ICSC), Jan 2017, pp 93–96
12. Teratipally V, Gunda A (2016) Sentiment analysis of political news articles and the effect of negation scope. *Int Res J Eng Technol (IRJET)* 03:1104–1109
13. Jose R, Chooralil VS (2016) Prediction of election result by enhanced sentiment analysis on twitter data using classifier ensemble approach. In: 2016 international conference on data mining and advanced computing (SAPIENCE), Mar 2016, pp 64–67
14. Malik A, Kapoor D, Singh A (2016) Sentiment analysis on political tweets. In: International symposium on fusion of science technology (ISFT), Jan 2016, pp 359–361
15. Ibrahim M, Abdillah O, Wicaksono AF, Adriani M (2015) Buzzer detection and sentiment analysis for predicting presidential election results in a twitter nation. In: 2015 IEEE international conference on data mining workshop (ICDMW), Nov 2015, pp 1348–1353
16. Pota M, Esposito M, Palomino MA, Masala GL (2018) A subword-based deep learning approach for sentiment analysis of political tweets. In: 2018 32nd international conference on advanced information networking and applications work-shops (WAINA), May 2018, pp 651–656
17. Dorle S, Pise DN (2018) Political sentiment analysis through social media. In: 2018 second international conference on computing methodologies and communication (ICCMC), Feb 2018, pp 869–873
18. Kagan V, Stevens A, Subrahmanian VS (2015) Using twitter sentiment to forecast the 2013 Pakistani election and the 2014 Indian election. *IEEE Intell Syst* 30(1):2–5

Load Frequency Control Incorporating Electric Vehicles Using FOPID Controller with HVDC Link



Sunita Pahadasingh, Chitralkha Jena and Chinmoy Ku Panigrahi

Abstract This study reveals the load frequency control of an unequal four-area thermal system with HVDC link considering suitable generation rate constraint. Performances of controllers such as proportional–integral–derivative (PID) and fractional-order PID (FOPID) are separately evaluated in the system. At first, plug-in electric vehicle (PEV) is applied to the thermal unit system to provide the stability for fluctuated load demand, which is widely expected from customer side as a spinning reserve. For the better quality of solution and improvement of convergence property, a hybrid differential evolution particle swarm optimization (DEPSO) technique is used here. DC tie-line is introduced here which improves the stability of system as compared to AC link. Comparison of dynamic responses corresponding to above controllers reveals that FOPID outperforms better than conventional PID controller. Also, a comparison has performed with and without PEV applied to four-area systems. The simulation is carried out by using MATLAB/SIMULINK software with step load perturbation (SLP).

Keywords Load frequency control (LFC) · Vehicle to grid (V2G) · Plug-in electric vehicle (PEV) · High-voltage DC transmission (HVDC)

S. Pahadasingh (✉)

Research Scholar, School of Electrical Engineering, KIIT University, Bhubaneswar, Odisha 751024, India

e-mail: spahadasingh@gmail.com

C. Jena · C. K. Panigrahi

School of Electrical Engineering, KIIT University, Bhubaneswar, Odisha 751024, India

e-mail: chitralkha.jenafel@kiit.ac.in

C. K. Panigrahi

e-mail: panigrahichinmoy@gmail.com

© Springer Nature Singapore Pte Ltd. 2020

R. Sharma et al. (eds.), *Innovation in Electrical Power Engineering, Communication, and Computing Technology*, Lecture Notes in Electrical Engineering 630,

https://doi.org/10.1007/978-981-15-2305-2_15

1 Introduction

The electrical energy produced basically depends on generating units and load demands. For an interconnected power system, a proper balance between real power and load should be maintained. Hence, the frequency and tie-line power attained their nominal values. This disturbance is overcome by close control of real power. The literature survey reveals that the research in the field of load frequency control is started by Concordia [1]. In past literatures, many researchers stated the better performance of LFC for isolated as well as interconnected multi-area systems. Few of these are related with the system nonlinearities considering suitable GRC [2, 3] to the proposed system.

Several controller and optimization techniques such as PSO [4], DE [5], bacterial foraging optimization (BFO) technique [6], and biogeography-based optimization (BBO) [7] have been implemented for LFC system. This proposed system is applied on four-area system with simultaneous appearance of GRC with electric vehicle. Many researchers have used EV aggregator model [8–11] in LFC system for spinning reserve for smart power system. Area control error implemented in system can be overcome with the help of vehicle to grid control and controller parameters proposed for each control area which were separately evaluated. Conventional controllers are generally considered to mitigate the oscillation in single area as well as multi-area. Various researchers have already discussed about these secondary controllers such as classical [3], optimal [12], fuzzy logic, and ANN [13]. But there are many physical systems which are realized by fractional-order differential equations [14]. Hence, the main objective of this study is designing the FOPID controller with the electric vehicle aggregator. FOPID could satisfy at most 5 robustness criteria ($K_p, K_I, K_D, \lambda, \mu$) as compared to the conventional PID controller which has three parameters to be tuned. A proper objective function is choosing for performance of optimization technique. Time-domain objective functions are integral square error (ISE), integral absolute error (IAE), and integral time absolute error (ITAE). ITAE criterion generally produces smaller overshoots and oscillation than all. Introduction of HVDC link has a greater approach towards multi-area power system than AC link only [15, 16].

In this era of computational revolution, more and more heuristic methods for optimization are evolving. Various fields of studies have been explored with these types of optimization techniques. Here, a hybrid DEPSO optimization technique is used which has faster convergence characteristic as compared to PSO and DE.

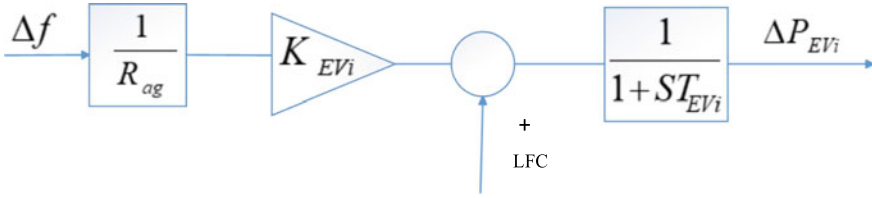


Fig. 1 Basic structure of EVs model

2 Methodology

2.1 Proposed Model

At first, the proposed system comprises an interconnected four-area unequal thermal power generation with reheat-type turbine using FOPID controller with a SLP (step load perturbation) applied to control area 1. Then, the system model using FOPID controller with electric vehicle is introduced. The general expression of area control error (ACE) is expressed in Eq. 1 [17].

$$ACE_i = \sum_{j=1}^N \Delta P_{ij} + B_i \Delta f_i \quad i = 1 \dots 4 \tag{1}$$

B_1 and B_2 are the frequency bias factor of i th area, and Δf is the frequency for i th area.

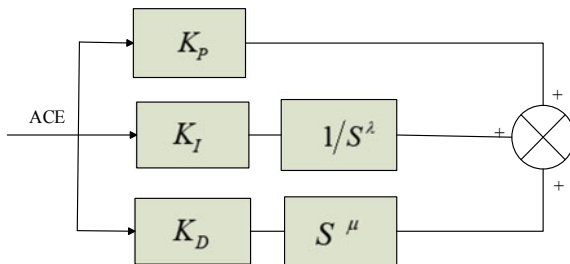
Discharged EVs are applied to each area to reduce the unbalance between generation and demand. EV structure model is shown in Fig. 1 [10]. Fast response characteristics of EVs battery make EV fleet efficiently to stabilise the frequency fluctuations. In this model, R_{ag} is the droop coefficient same as to thermal unit and ΔP_{EV_i} is the incremental change in i th generation. K_{EV_i} is the gain of EV, and T_{EV_i} is the time constant of EV battery.

2.2 Gain Scheduling Control

Concept of FOPID controller is proposed by Podlubny. Referring to the Caputo’s fractional differ-integration, at zero initial condition the fractional-order transfer function can be derived from ordinary differential equation. Fractional-order derivative can be expressed as in Eq. 2. [10]

$${}_c D_t^\alpha f(t) = \frac{1}{\Gamma(n - \alpha)} \frac{d^n}{dt^n} \int_c^t (t - \tau)^{n-\alpha-1} f(\tau) d\tau \tag{2}$$

Fig. 2 Model structure of FOPID controller



where ${}^c_0D_t^{-\alpha}$ is the fractional operator $n - 1 \leq \alpha \leq n$, n is an integer, and $\gamma(\cdot)$ is the Euler's gamma function. Fractional-order integral is given by Eq. 3. [10]. General transfer function equation for FOPID controller is given in Eq. 4. [10]

$${}^c_0D_t^{-\alpha} f(t) = \frac{1}{\gamma(\alpha)} \int_c^t (t - \tau)^{\alpha-1} f(\tau) d\tau \tag{3}$$

$$G_c(s) = K_p + K_i/S^{\lambda} + K_d S^{\mu} \tag{4}$$

Schematic representation of the FOPID controller is shown in Fig. 2 [14]. This structure has basically five tuning parameters that are three controller gains $\{K_p, K_i, K_d\}$ and two fractional-order integra-differential operators $\{\lambda, \mu\}$. Classical PID controller can be formed from this controller structure for $\lambda = 1$ and $\mu = 1$. In Fig. 3 [7], transfer function of EV model is shown. Similarly using the tie-line power, four-area systems are designed with the help of SIMULINK.

2.3 Concept of HVDC

In this paper, a concept of HVDC link is utilized to enhance the transient stability of system. If the control area is interconnected by parallel AC lines, then either one area has not sufficient reserve capacity to enhance the power required in either case.

HVDC transmission line in parallel with existing AC line has enough frequency capability to compensate the demand in area 1.

For an interconnected power system, DC link not only improves the stability but also stabilizes the frequency oscillations due to gradual change of load in case of weak AC tie-line.

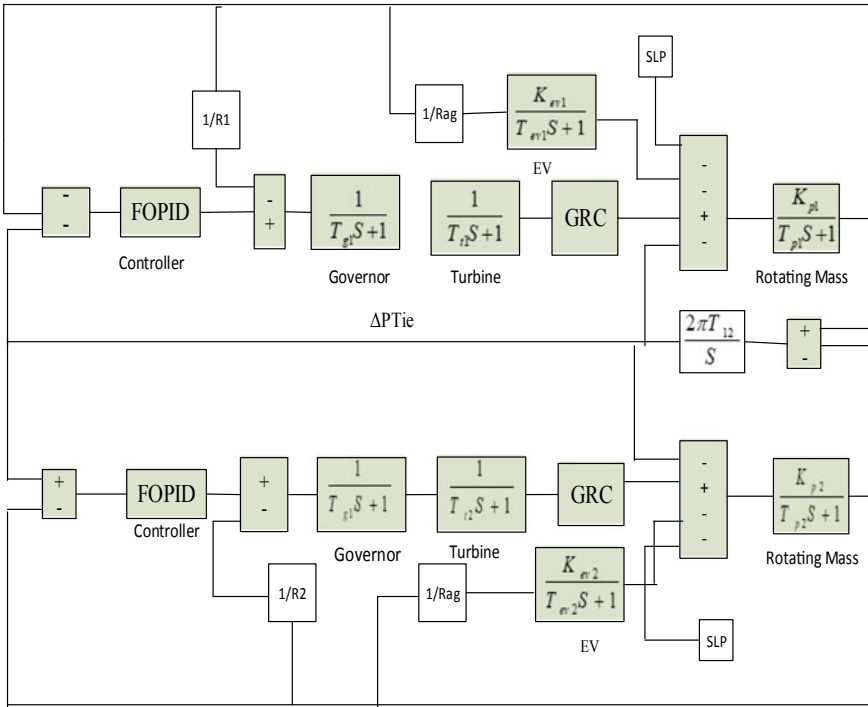


Fig. 3 Transfer function model for two-area thermal system using FOPID controller with EV

2.4 Optimization Technique

Though particle swarm optimization (PSO) is easy to implement, it suffers from prematurity problem. Though DE is very useful for optimizing nonlinear, non-differentiable operations, it does not meet the expectation for higher-dimensional searching problems. Also in DE, the candidate solution moves very fast initially, but at later stages, it does not perform satisfactorily at the time of fine-tuning operation. Due to these, a hybrid technique combining PSO with DE, referred to as DEPSO, has employed for LFC problems. The combined effect of both improves the convergence characteristics as compared to individual. It also increases the system stability due to proper balance between exploration and exploitation. In DEPSO, particles might not experience an unexpected loss of diversity, because the current location and p_{best} have less chance to close with g_{best} . The basic steps for DEPSO algorithm are

- Initialize the population randomly with size N_p . Giving D is the dimension of particle to be optimized.
- Randomly initialize the velocity for each particle to be used in PSO algorithm.
- DE operation starts for mutation, crossover, and selection process.

- i) Generate mutant vector V_i using scaling factor F and three distinct integers r_1 , r_2 , and r_3 in size $[1, N_p]$.

$$V_i = X_{i,r1} + F(X_{i,r2} - X_{i,r3})$$

- ii) For crossover operation, U_i vector is generated using crossover rate (CR)

$$U_i = \begin{cases} V_i, & r \text{ and } (D, 1) \leq CR \\ X_i, & \text{otherwise} \end{cases}$$

- iii) For selection process, the target vector X_i is generated to minimize the function f

$$\begin{aligned} X_i &= U_i & \text{if } f(U_i) \leq f(X_i) \\ X_i &= X_i & \text{if } f(X_i) \leq f(U_i) \end{aligned}$$

- iv) Determine the P_{best} and G_{best} for each solution

- From DE operation obtained value of X_i is taken as initial for PSO.
- The velocity and position of each swarm are updated, and the fitness of objective function is evaluated.
- To select best solutions for the next iteration, compare the fitness value and the iteration count is updated.
- The steps are continued until to achieve the meeting criterion.

3 Simulation Results

In this paper, simulation has done using MATLAB/SIMULINK software. Here, thermal units are considered with generation rate constraints for four-area system. At first, PID controller is applied to this proposed system. Then, a FOPID controller is applied to each area. A SLP of 1% is considered for area 1. The five controller parameters are optimized for FOPID controller for each area. HVDC link is connected to each area. Then, simulations have done for FOPID controller considering PEV which has seven controller parameters to be optimized for each area. Then, a comparison is made between the FOPID controller with and without PEV.

3.1 Comparison Result Between FOPID Controller and PID Controller

Fig. 4 Frequency variation in area 1

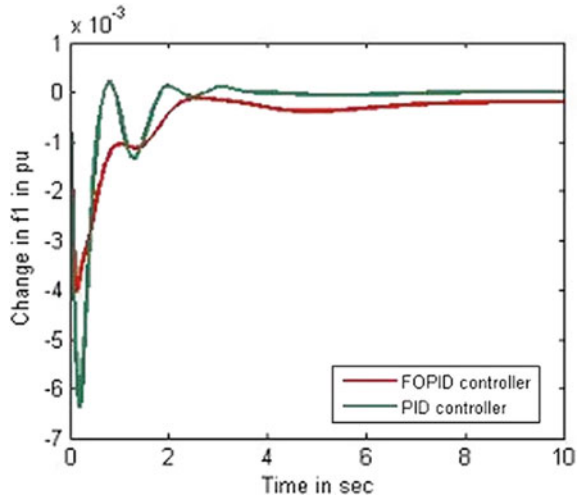


Fig. 5 Frequency variation in area 2

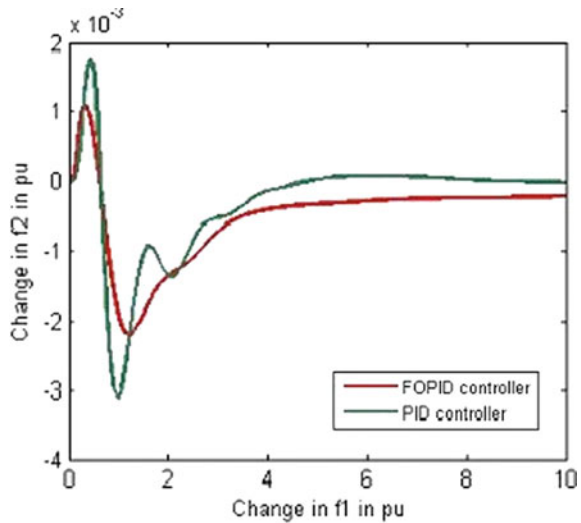


Fig. 6 Frequency variation in area 3

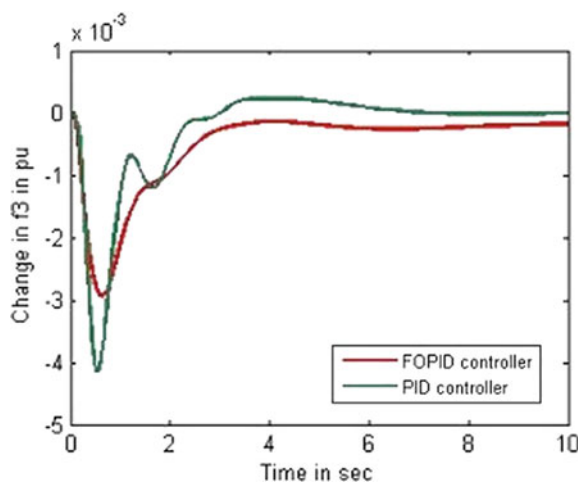


Fig. 7 Frequency variation in area 4

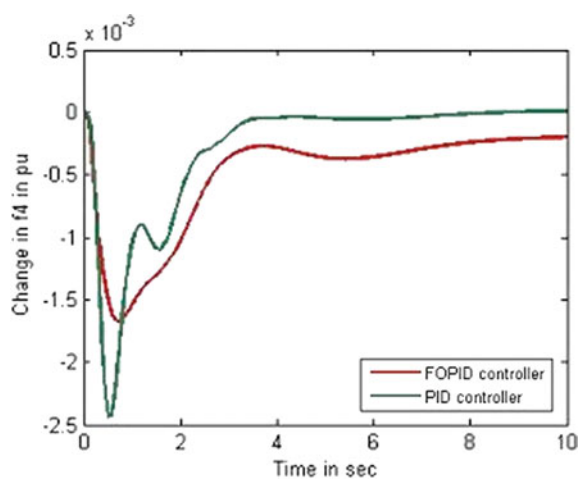


Fig. 8 Tie-line power deviation in area 1

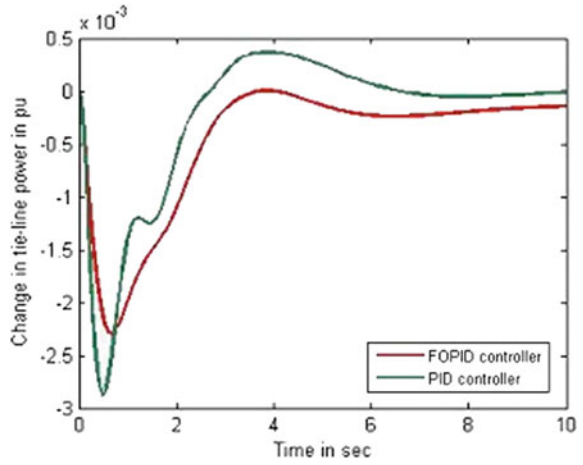


Fig. 9 Tie-line power deviation in area 2

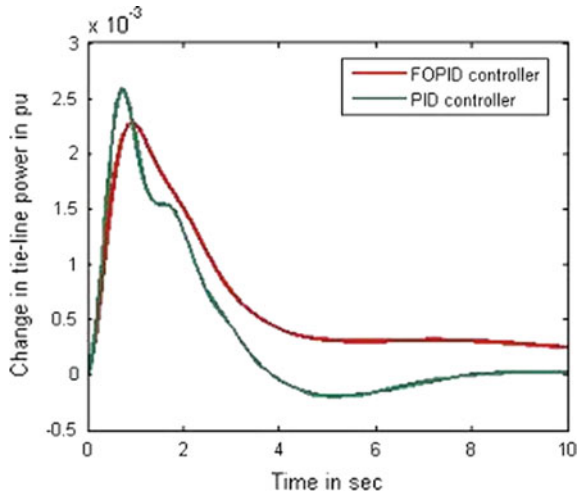


Fig. 10 Tie-line power deviation in area 2

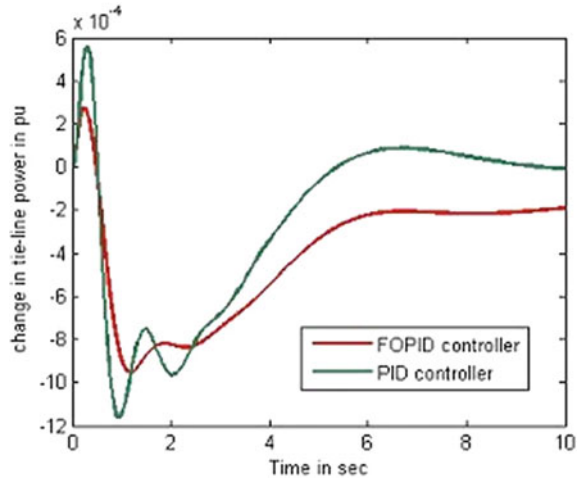
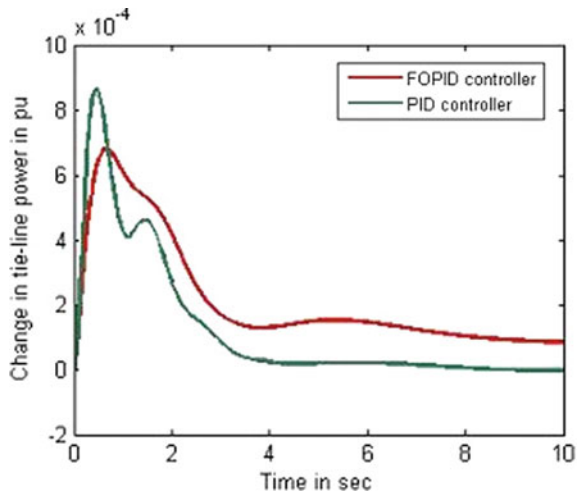


Fig. 11 Tie-line power deviation in area 2



3.2 Comparison Result Between FOPID Controller with EV and Without EV

Fig. 12 Frequency variation in area 1

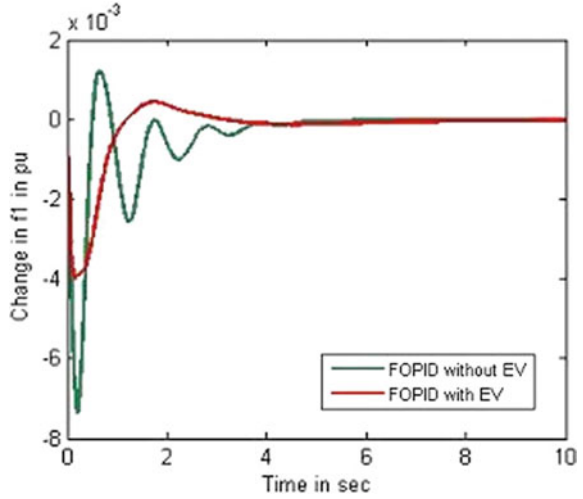


Fig. 13 Frequency variation in area 2

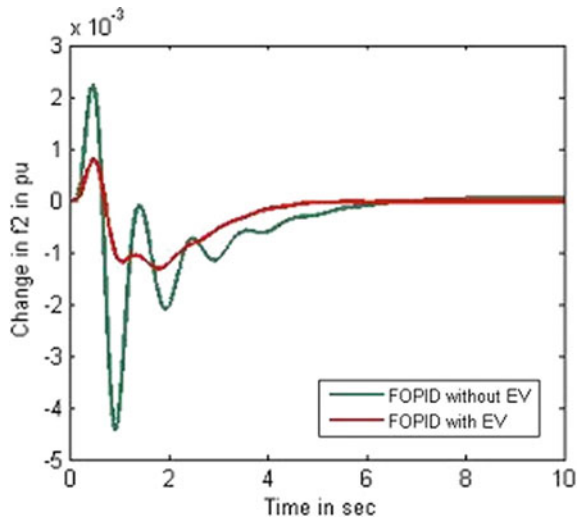


Fig. 14 Frequency variation in area 3

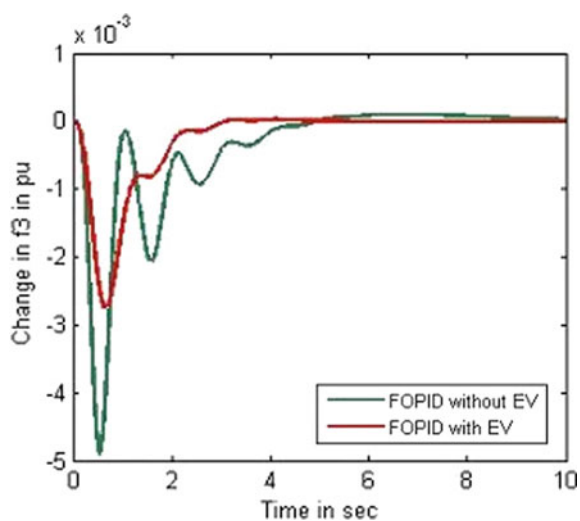


Fig. 15 Frequency variation in area 4

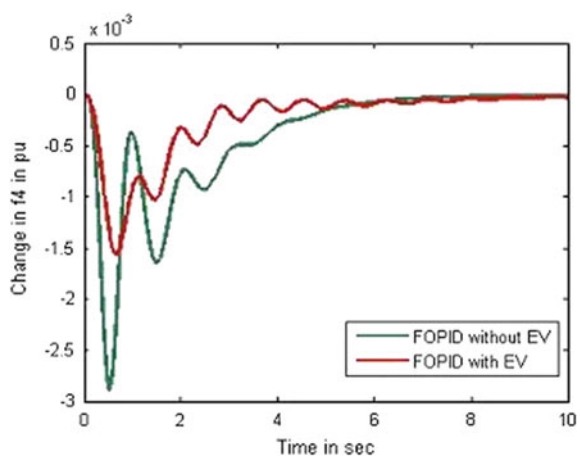


Fig. 16 Tie-line power deviation in area 1

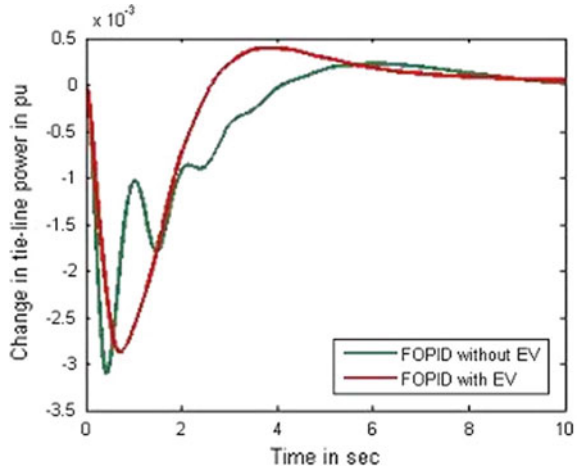


Fig. 17 Tie-line power deviation in area 2

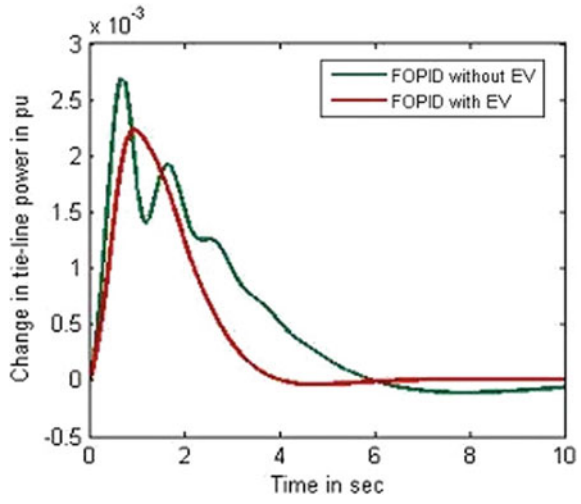


Fig. 18 Tie-line power deviation in area 3

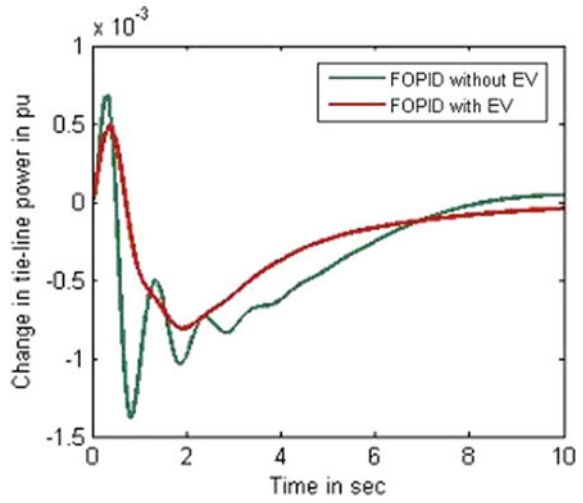


Fig. 19 Tie-line power deviation in area 4

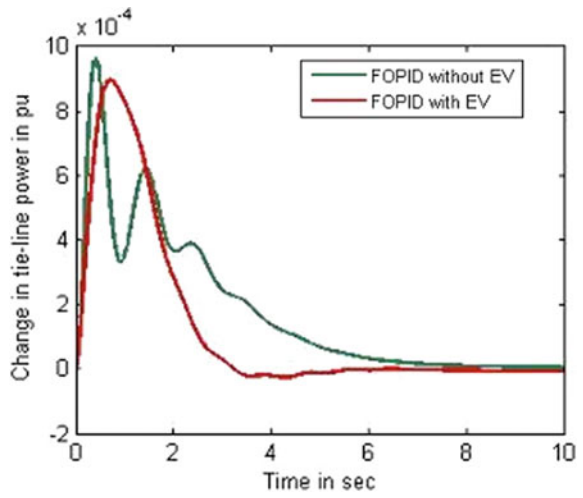


Fig. 20 Frequency variation in area 1

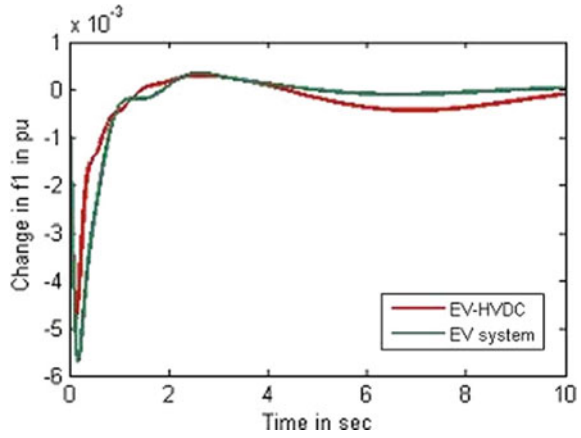
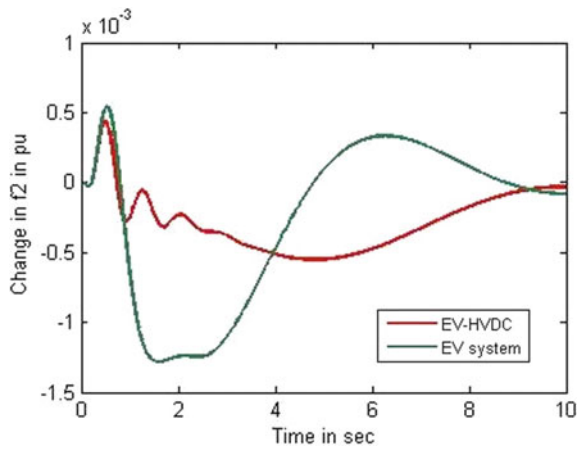


Fig. 21 Frequency variation in area 2



3.3 Comparison Results Between FOPID Controller with EV and EV with HVDC Link

Fig. 22 Frequency variation in area 3

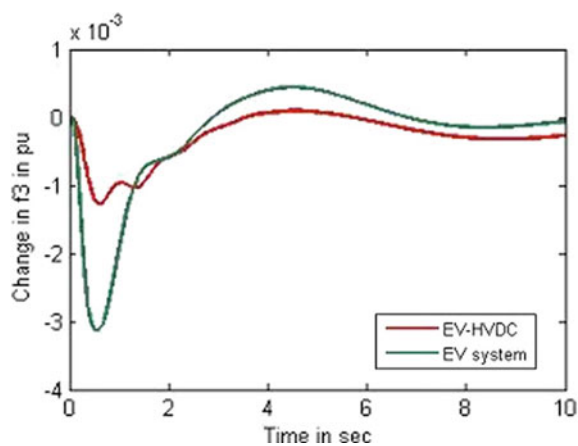


Fig. 23 Frequency variation in area 4

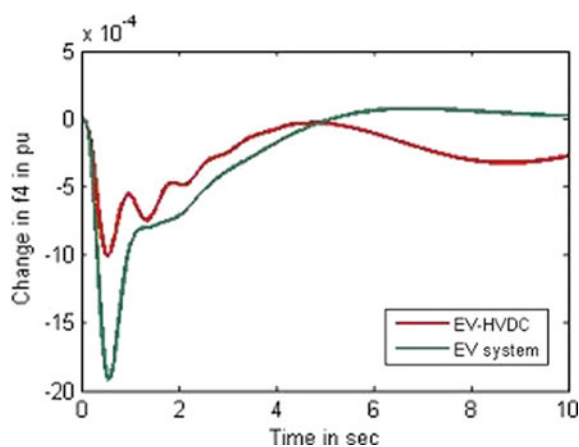


Fig. 24 Tie-line power deviation in area 1

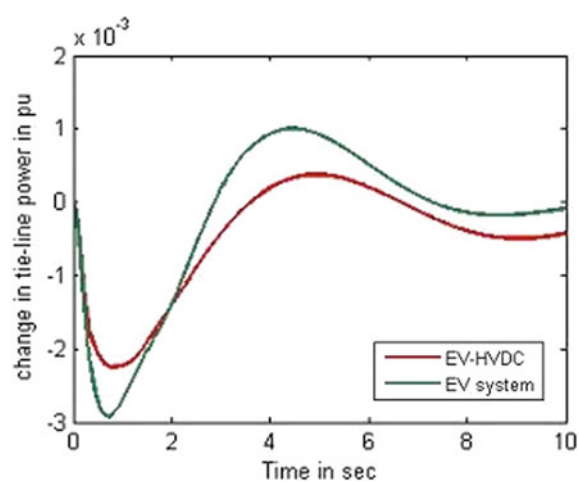


Fig. 25 Tie-line power deviation in area 2

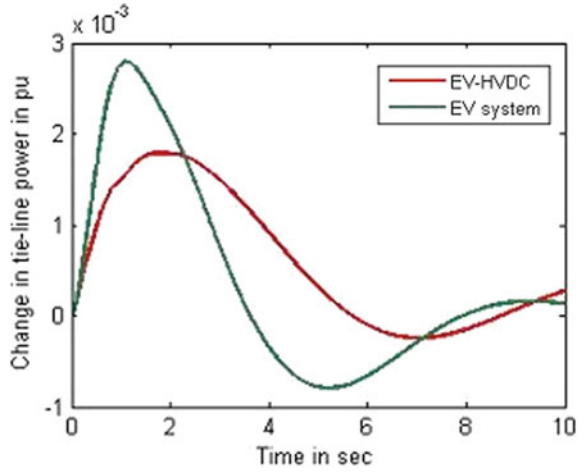


Fig. 26 Tie-line power deviation in area 3

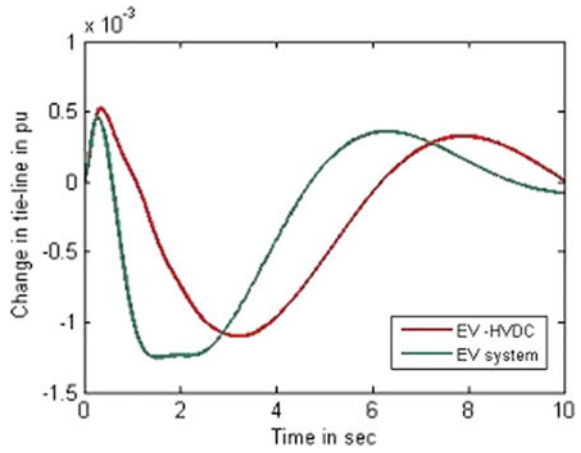
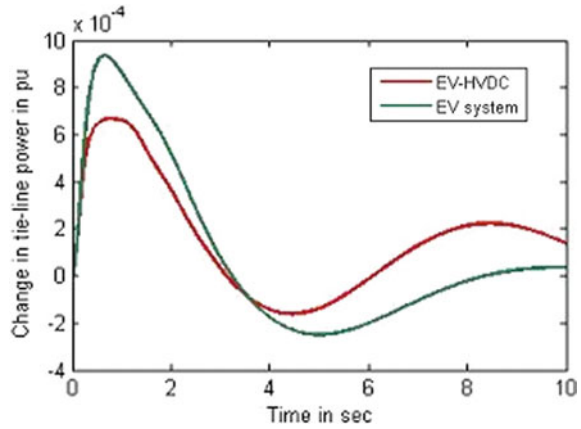


Fig. 27 Tie-line power deviation in area 3



4 Results and Discussions

In this study, LFC is applied to four-area system with the effect of electric vehicle and HVDC link optimized by DEPSO algorithm. At first, a PID controller is tuned by DEPSO algorithm, then with FOPID controller. With this, a comparison is made between these controllers by numerous simulation results. From the simulation results, it is clearly visible in Figs. 4, 5, 6, 7, 8, 9, 10, and 11 that FOPID controller has better dynamic performance as compared to PID controller. After that, tuning of LFC by FOPID controller in addition to EV system has been considered and comparison is taken between effect of EV with and without EV to that system. In Figs. 12, 13, 14, 15, 16, 17, 18, and 19, the comparison simulation results of EV system are shown. Then, comparison is made between EV system and effect of HVDC link with this through numerous simulations and that is shown in Figs. 20, 21, 22, 23, 24, 25, 26, and 27. From this observation table, it is cleared that addition of HVDC link to this existing AC line has better performance characteristics. FOPID and PID controller gain parameter values are notified in Table 4. Objective function values of performance indexes are mentioned in Table 1.

4.1 Observation

The objective function of different performance indexes is compared and notified in Table 1. From the simulation results, the dynamic responses of PID and FOPID are observed and mentioned in Table 2. Table 3 indicates the performance responses of EV system, and Table 4 notifies the performance nature of HCDC link of the

Table 1 Performance index values for 10 numbers of iteration

Specification	Performance index		
	ITAE	IAE	ISE $\times 10^{-4}$
Fitness value	0.1564	0.0375	0.8831
	0.1564	0.0376	0.9252
	0.0531	0.0330	0.7428
	0.0985	0.0325	0.6741
	0.1196	0.0325	0.6612
	0.1366	0.0331	0.9215
	0.1441	0.0358	0.7420
	0.0876	0.0415	0.7502
	0.1628	0.0495	0.9388
	0.2455	0.0490	0.5166
Maximum value	5.919	0.2793	1.5901

Table 2 Undershoot (min), overshoot (max), and settling time (Ts) values for frequency and tie-line power deviation

Model	Min	f1	f2	f3	f4	tie1	tie2	tie3	tie4
FOPID controller		-4.0431	-2.1849	-2.9373	-1.6741	-2.2947	-0	-0.9533	-0
	Max	<i>f1</i>	<i>f2</i>	<i>f3</i>	<i>f4</i>	<i>tie1</i>	<i>tie2</i>	<i>tie3</i>	<i>tie4</i>
		0	1.1063	0.0000	0.0000	0.0047	2.2802	0.2753	0.6827
		<i>Settling time in s</i>							
PID controller		4.76	5.82	6.20	6.43	6.91	7.14	7.84	8.05
	Min	<i>f1</i>	<i>f2</i>	<i>f3</i>	<i>f4</i>	<i>tie1</i>	<i>tie2</i>	<i>tie3</i>	<i>tie4</i>
		-6.3847	-3.0967	-4.1331	-2.4324	-2.8701	-0.1927	-1.1611	-0.0034
	Max	<i>f1</i>	<i>f2</i>	<i>f3</i>	<i>f4</i>	<i>tie1</i>	<i>tie2</i>	<i>tie3</i>	<i>tie4</i>
		0.2093	1.7759	0.2245	0.0082	0.3646	2.5818	0.5568	0.8660
	<i>Settling time in s</i>								
	5.13	5.43	6.43	6.79	7.31	7.80	8.15	8.36	

Table 3 Undershoot (min), overshoot (max), and settling time (Ts) values for frequency and tie-line power deviation

Model	Min	f1	f2	f3	f4	tie1	tie2	tie3	tie4
FOPID with EV		-3.9931	-1.3162	-2.7509	-1.5611	-2.8760	-0.0382	-0.8115	-0.0266
	<i>Max</i>	<i>f1</i>	<i>f2</i>	<i>f3</i>	<i>f4</i>	<i>tie1</i>	<i>tie2</i>	<i>tie3</i>	<i>tie4</i>
		0.4382	0.7857	0.0218	0.0000	0.3899	2.2342	0.4797	0.8966
<i>Settling time in s</i>									
FOPID without EV		5.49	6.92	7.06	7.43	8.28	9.07	9.28	9.76
	<i>Min</i>	<i>f1</i>	<i>f2</i>	<i>f3</i>	<i>f4</i>	<i>tie1</i>	<i>tie2</i>	<i>tie3</i>	<i>tie4</i>
		-7.3772	-4.4311	-4.9020	-2.8821	-3.1123	-0.1096	-1.3813	-0.0000
<i>Max</i>	<i>f1</i>	<i>f2</i>	<i>f3</i>	<i>f4</i>	<i>tie1</i>	<i>tie2</i>	<i>tie3</i>	<i>tie4</i>	
	1.4187	2.2314	0.6954	0.0012	0.2226	2.6965	0.6818	0.9662	
<i>Settling time in s</i>									
	5.92	7.45	7.63	8.24	8.66	9.17	9.49	10.02	

Table 4 Undershoot (min), overshoot (max), and settling time (Ts) values for frequency and tie-line power deviation

Model	Min	f1	f2	f3	f4	tie1	tie2	tie3	tie4
FOPID with EV		-5.7087	-1.2820	-3.1307	-1.9232	-2.9251	-0.7928	-1.2520	-0.2495
	Max	f1	f2	f3	f4	tie1	tie2	tie3	tie4
		0.3406	0.5463	0.4440	0.0748	1.0021	2.7911	0.4631	0.9365
	Settling time (Ts) in s								
FOPID-EV with HVDC		5.49	6.92	7.06	7.43	8.28	9.07	9.28	9.76
	Min	f1	f2	f3	f4	tie1	tie2	tie3	tie4
		-4.7657	-0.5503	-1.2743	-1.0055	-2.2528	-0.2424	-1.1013	-0.1612
Max	f1	f2	f3	f4	tie1	tie2	tie3	tie4	
		0.2735	0.4430	0.0988	0.0000	0.3746	1.7867	0.5246	0.6677
	Settling time (Ts) in s								
	4.05	5.64	6.08	6.58	6.90	7.84	8.03	8.48	

Table 5 Values of controller gain parameters optimized by DEPSO technique

Gain parameters	FOPID-EV-HVDC	FOPID-EV	PID
K_1	1.9818	0.867	1.7713
K_2	1.7501	1.6730	2.0000
K_3	1.2606	1.2783	1.1734
λ_1	0.8171	1.0553	–
μ_1	1.1038	1.0700	–
K_{ev1}	1.1505	1.0604	–
T_{ev1}	1.0047	1.2509	–
K_4	0.8085	0.4257	2.0000
K_5	1.4691	1.4379	0.0100
K_6	0.6796	1.7221	0.4893
λ_2	1.1906	0.1648	–
μ_2	0.7643	0.4176	–
K_{ev2}	2.0000	1.5845	–
T_{ev2}	1.0557	0.0100	–
K_7	1.2000	1.8611	1.3058
K_8	1.2512	1.7677	0.0100
K_9	0.0247	1.5838	2.0000
λ_3	0.4665	0.6489	–
μ_3	1.5933	1.2443	–
K_{ev3}	2.0000	0.8596	–
T_{ev2}	1.8069	0.4807	–
K_{10}	1.0910	1.1025	0.0100
K_{11}	1.7911	1.7535	2.0000
K_{12}	0.5485	1.0937	1.5204
λ_4	1.0454	1.1131	–
μ_4	0.5850	0.8264	–
K_{ev4}	1.7003	1.5684	–
T_{ev4}	1.7661	0.7025	–

proposed FOPID_EV model. The gain parameters of controller optimized by DEPSO are mentioned in Table 5.

5 Conclusion

The application of hybrid DEPSO technique to optimize various parameters such as K_p , K_I , K_D , μ and λ for FOPID controller on an unequal four-area thermal LFC

system is found to be successful. Considering system nonlinearity, GRC in this multi-area AGC system, the proposed FOPID controller provides impressive dynamic response. Again, FOPID controller with electric vehicle has better dynamic responses as compared to FOPID alone in terms of overshoot and undershoot. EV with DC link has improved stability as compared to existing AC tie-line. Controller parameters are tuned by hybrid DEPSO conducting a balance between exploration and exploitation.

References

1. Concordia C, Kirchmayer LK (1954) Tie-line power and frequency: part II. *AISE Trans*, III-A 73:133–146
2. Elgerd OI, Fosha C (1970) Optimum megawatt frequency control of multi-area electric energy systems. *IEEE Trans Power Appar Syst PAS* 89(4):556–563
3. Saikia LC, Nanda J, Mishra S (2011) Performance comparison of several classical controllers in AGC for multi-area interconnected thermal system. *Int J Electr Power Energy Syst* 33:394–401
4. Ahuja A, Aggarwal SK (2014) Robust fractional order PID controller for LFC using particle swarm optimization. *IEEE Trans* 978-1-4799-6042-2/14
5. Mohanty B, Panda S, Hota PK (2014) Controller parameters tuning of differential evolution algorithm and its application to load frequency control of multi source power system. *Electr Power Energy Syst* 54:77–85
6. Ali ES, Abd-Elazim SM (2011) Bacteria foraging optimization algorithm based load-frequency controller for interconnected power system. *Int J Electr Power Energy Syst* 33:633–638
7. Rahman A, Saikia LC, Sinha N (2016) AGC of an unequal four-area thermal system using biogeography based optimised 3DOF-PID controller. *IET Renew Power Gener* (2016)
8. Izadkhast S, Garcia-Gonzalez P, Frías P (2015) An aggregate model of plug-in electric vehicles for primary frequency control. *IEEE Trans Power Syst* 30(2):1475–1482
9. Pham TN, Trinh H, Hien LV (2016) Load frequency control of power systems with electric vehicles and diverse transmission links using distributed functional observers. *IEEE Trans Smart Grid* 7(1):238–252
10. Debbarma S, Dutta A (2017) Utilizing electric vehicles for LFC in restructured power systems using fractional order controller. *IEEE Trans Smart Grid* 8(6):2554–2564
11. Debbarma S, Dutta A (2018) Frequency regulation in deregulated market using vehicle-to-grid services in residential distribution network. *IEEE system journal* 12(3):2812–2820
12. Yamashita K, Taniguchi T (1986) Optimal observer design for load frequency control. *Int J Electr Power Energy Syst* 8:93–100; Golpira H, Bevrani H, Golpira H (2011) Application of GA optimization for automatic generation control design in an interconnected power system. *Energy Convers Manage* 52:2247–2255
13. Demiroren A, Zeynelgil HL, Sengor NS (2004) Automatic generation control using ANN technique for multi-area power system with SMES units. *Electr Power Compon Syst* 32:193–213
14. Debbarma S, Saikia LC, Sinha N (2014) Automatic generation control using two degree of freedom fractional order PID controller. *Int J Electr Power Energy Syst* 58:120–129
15. Arya Y, Kumar N (2016) AGC of a multi-area multi-source hydrothermal power system interconnected via AC/DC parallel links under deregulated environment. *Int J Electr Power Energy Syst* 75:127–138
16. Ibraheem N, Bhatti TS (2014) AGC of two area power system interconnected by AC/DC links with diverse sources in each area. *Electr Power Energy Syst* 55:297–304
17. Saadat H (2002) *Power system analysis*. Mc Graw-Hill, New Delhi

Automatic Generation Control in Deregulated Power Market Using Sunflower Optimization Algorithm



Abhilipsa Sahoo, Prakash Kumar Hota and B. Mohanty

Abstract The restructuring of electrical power industries creates competitiveness among the market players, due to which the complexity of load frequency issues is gradually increasing in nature. So for mitigating these load frequency issues controllers are used. This chapter proposes automatic generation control (AGC) for two interconnected control areas, each consisting of two power generation sources, i.e. reheat steam turbine in conjunction with nonlinear generation rate constraint and gas turbine generation in a restructured market environment. Sunflower optimization (SFO) algorithm is used for optimal tuning of proportional, integral and derivative (PID) controller considering the integral square error as the objective function. For analysing the market dynamics, the concept of area participation matrix (APM) and DISCO participation matrix (DPM) has been simulated. The effectiveness of this two-area system has been tested with various market scenarios like poolco trading, bilateral trading and contract violation. The yield of the proposed algorithm shows better performance in contrast to the other methods used for tuning the PID controller.

Keywords AGC · DISCO participation matrix · Sunflower optimization algorithm · Deregulated power market

1 Introduction

Nowadays deregulated market operations were adopted by the different market players worldwide because of the restructuring of vertically integrated utilities (VIU). In VIU, a single utility does the complete operation of the power system, whereas

A. Sahoo (✉) · P. K. Hota · B. Mohanty
Veer Surendra Sai University of Technology (VSSUT), Burla, Odisha, India
e-mail: abhilipsa.sahoo@gmail.com

P. K. Hota
e-mail: p_hota@rediffmail.com

B. Mohanty
e-mail: banaja_m@yahoo.com

© Springer Nature Singapore Pte Ltd. 2020
R. Sharma et al. (eds.), *Innovation in Electrical Power Engineering, Communication, and Computing Technology*, Lecture Notes in Electrical Engineering 630,
https://doi.org/10.1007/978-981-15-2305-2_16

in deregulation, many utilities dose the operation of power system. This restructured system comprises of three companies, namely power-generating companies (GENCOS), power-distributing companies (DISCOS) and power-transmitting companies (TRANSCOS). Apart from this, one system is also there to operate named as independent system operator (ISO). As we know that an electrical power system has been growing immensely vast in size and altering constructions, it has become a vital matter to operate and control the system. To achieve stable condition in an electrical system, the power generation by the system must be match to the losses and the load demanded by the system. In power system while carrying out operation, there are many times we can incur random variations in load, which leads to immediate consequence of mismatch in generation load. This mismatch of power results in variation in system frequency. In order to obtain a stable state between generation and variations in load, a controller is primitively required. Proper modulation between the demand of system and generator output is coordinated by the automatic generation control using sunflower optimization algorithm.

Considering reheat type turbine with generation rate constraint (GRC) in thermal power plant for the analysis of AGC in restructured power system by bacteria foraging optimization algorithm was analysed by Nanda [1]. Number of areas can be studied for analysis of AGC. In [2], Saikia LC provides AGC for two equal area and unequal areas having 3% GRC and single reheat turbine along with IDD controller. The transient performance of AGC for an interconnected control area with hydro-thermal-diesel mixed generating sources was analysed by Bhatt in [3]. The restructured power market comprises many GENCOS and DISCOS. Each of GENCOS and DISCOS makes deal with each other for transaction of power, which is explained in [4]. For trading of power, DISCO can contract with GENCOS of other control area by the process of bilateral trading. DPM reflects the relationship between GENCOS and DISCO and used for assessment of bilateral trading in the competitive power market. Donde [5] proposes the concept of DPM. The paper [6] explained the application of flexible neural networks, as a feasible solution, to automatic generation control problem for the competitive power market environment. Optimized gain controller and bias factor is used in AGC after restructuring the power system for bilateral transaction of power among GENCOS and DISCOS using participation matrix in [7]. Debbarma [8] investigated the performance of FOPID and IO controller and its sensitivity analysis in AGC for contract violation case in deregulated power system. Optimal transient response with increment of load for interconnected generating system by applying GA provided by Ghoshal [9]. Tyagi [10] provides the design scheme of decentralized AGC for various types of power transaction in competitive electricity market. In [11], the authors worked in two areas under restructured power market for the thermal and gas model by optimizing the controller using DE and GA. Guilherme Ferreira Gomes proposed a nature-inspired heuristic global optimization algorithm known as sunflower optimization algorithm in [12]. The authors analyse the various control strategies for designing the AGC model considering multiple sources under different market situation in deregulated environment in [13]. In [14], the author designs PID controller using the concept of fuzzy logic and DE optimization technique for modelling AGC in restructured market. The authors Ravi Shankar et al.

[15] consider multiple interconnected areas for designing AGC and used AC/DC link and UPFC for mitigating the variations which occur in system response in deregulated competitive market.

From the literature survey, it is perceived that several optimization techniques have been suggested for AGC by obtaining acceptable steadiness among transient fluctuations and frequency variations through zero steady-state error. In the view of present power scenario, the authors have made an endeavour for analysing AGC, which consists of two equal control areas in deregulated scenario. Here, each control area comprises thermal–gas generation sources. The parameters for the two-area system are taken from [11]. To study automatic generation control, conventional proportional-integral-derivative controller is deliberated to disclose the performance. The controller’s gain is tuned by using SFO algorithm. The effectiveness of this two-area system has tested with various market scenarios like unilateral, bilateral and contract violation market trading to study dynamics of the system. The yield of the proposed algorithm is compared with others, for proposed restructured power market.

2 Deregulated Power System Under Study

In a deregulated environment, the analysis of AGC is implemented in an identical two-control area system, in which each part comprises thermal and gas producing sources. Both the areas consist of two numbers of generating and distributing companies. A reheat type turbine having a constraint of 3% generation rate per min is present in the thermal unit, and a gas turbine is present in the gas-generating unit [11]. Figures 1 and 2 depict two different diagrams named as the schematic representation and model of transfer function, respectively, for the two-area system under study.

2.1 DISCO Participation Matrix

For trading of power, DISCO can contract with GENCO or number of GENCOs. Since in a deregulated power market more number of generating and distributing

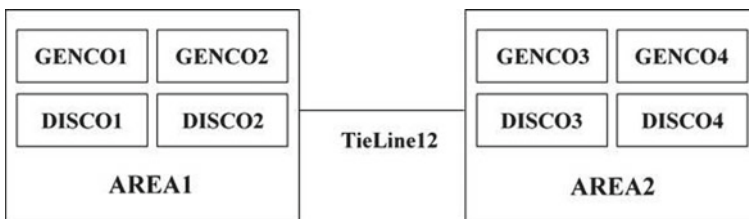


Fig. 1 Schematic representation of two-area system

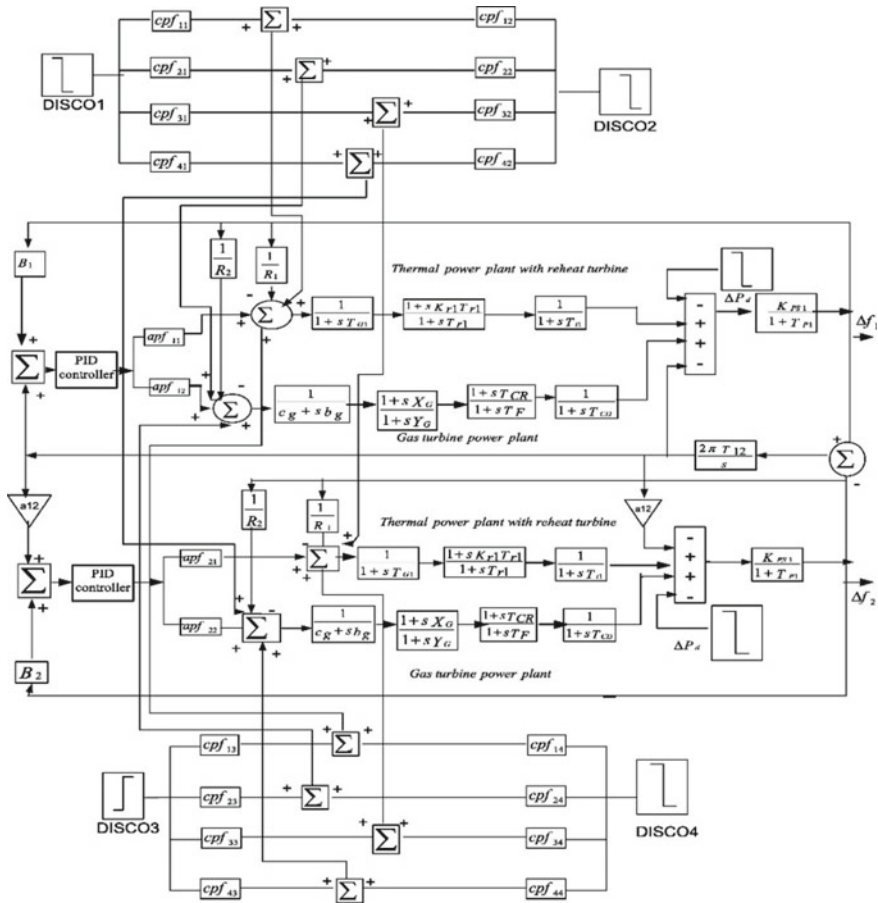


Fig. 2 Transfer function model of two-area system

companies are present, so a DISCO can make deal with GENCOs of own area or with other control areas for trading of power freely. Since the load demanded by a DISCO must be fulfilled by GENCO, so it is require sending the information regarding the load demand by DISCO to GENCO. This information can be achieved by using the conception of DISCO participation matrix (DPM). It is a matrix where the number of rows and column shows GENCOs and DISCOs taking part in power trading, respectively. All element of DPM represents contract participate factor (cpf), which is given by the ratio of particular DISCO’s power contract from a particular GENCO to the total power contracted by that particular DISCO. The DPM for previously mentioned two-control area system is expressed in matrix form as follows:

$$\text{DPM} = \begin{bmatrix} \text{cpf}_{11} & \text{cpf}_{12} & \text{cpf}_{13} & \text{cpf}_{14} \\ \text{cpf}_{21} & \text{cpf}_{22} & \text{cpf}_{23} & \text{cpf}_{24} \\ \text{cpf}_{31} & \text{cpf}_{32} & \text{cpf}_{33} & \text{cpf}_{34} \\ \text{cpf}_{41} & \text{cpf}_{42} & \text{cpf}_{43} & \text{cpf}_{44} \end{bmatrix} \quad (1)$$

where cpf_{xy} = part of full load power dealt by y th DISCO from x th GENCO.

The summation of each elements of y th column of the DPM must be satisfied to unity represented by Eq. (2)

$$\sum_{x=1}^n \text{cpf}_{xy} = 1 \quad \forall y = 1, 2, \dots, m \quad (2)$$

where n = quantity of GENCO and m = quantity of DISCO.

2.2 Area Participation Matrix

Since it is not possible by DISCOS in every time to maintain the contract for allocation of power from GENCOS, so uncontracted power demand arises as it violates the contracts at some times. Therefore, GENCOS must be allocated these uncontracted power demands to the DISCOS of same area. Therefore, it is important to consider the uncontracted power demand allocation for developing the dynamic model. Area participation matrix (APM) is used for this allocation of uncontracted power demand based on area participation factor (apf). In APM, the rows represent the number of GENCOS of the corresponding areas, and the columns represent the number of areas. The APM for previously mentioned two-control area system is expressed in matrix form as follows:

$$\text{APM} = \begin{bmatrix} \text{apf}_1 & 0 \\ \text{apf}_2 & 0 \\ 0 & \text{apf}_3 \\ 0 & \text{apf}_4 \end{bmatrix} \quad (3)$$

3 Problem Formulation

The expression for the scheduled power flow in the tie line under steady state is

$$\begin{aligned} \Delta P_{\text{tie line}12}^{\text{sch}} = & (\text{demand of DISCOs available in AREA2 from GENCOS of AREA1}) \\ & - (\text{demand of DISCOs available in AREA1 from GENCOS of AREA2}) \end{aligned} \quad (4)$$

The error present in tie line power at any instant of time is expressed as

$$\Delta P_{\text{tieline12}}^{\text{error}} = \Delta P_{\text{tieline12}}^{\text{act}} - \Delta P_{\text{tieline12}}^{\text{sch}} \quad (5)$$

where,

$$\Delta P_{\text{tieline12}}^{\text{act}} = \frac{2\pi * T_{12}}{S} (\Delta F_1 - \Delta F_2) \quad (6)$$

The error in tie line power will be zero only when the actual and scheduled power becomes same, and this happens in steady-state condition. According to this tie line error, an area control error (ACE) signal is generated for each part of the area, which is given as follows,

$$\text{ACE}_n = B_n \Delta F_n + \Delta P_{\text{tieline12}}^{\text{error}} \quad (7)$$

Three parameters, i.e. gains of proportional (k_p), integral (k_i) and derivative (k_d) controller, are essential for designing the controller. Here, two different gain values are chosen for two areas. The objective function is defined based on integral criterion, i.e. ISE known as integral square error. Mathematically, it is described as:

$$J = \int_0^t ((\Delta F_1)^2 + (\Delta F_2)^2 + (\Delta P_{\text{tieline12}}^2)) \cdot dt \quad (8)$$

Thus, the optimization problem becomes,

$$\min \cdot J \quad (9)$$

$$\text{Subject to, } k_{p_{\min}} \leq k_p \leq k_{p_{\max}}, k_{i_{\min}}, k_{d_{\min}} \leq k_d \leq k_{d_{\max}} \quad (10)$$

where $k_{p_{\min}}, k_{i_{\min}}, k_{d_{\min}}$ are lower bounds, and $k_{p_{\max}}, k_{i_{\max}}, k_{d_{\max}}$ are upper bounds. The range of the parameter k is chosen between 0 and 8.

4 Sunflower Optimization Algorithm

SFO algorithm is one of the optimization methods based on the instinctive nature of sunflower. This method is explained taking the concept of motion of the sunflowers. The suggested SFO method is used for problems based on multimodals [12]. It is a heuristic large-scale optimization technique based on population. SFO algorithm imparts robustness because of its pollination and root velocity in comparison with other algorithms. Everyday a sunflower completes its cycle of activities, which can be observed very apparently. Their activities include: everyday, they wake up as sun

risers in the east and move in the direction of sun from sunrise in east to sunset in west alike the needles of a clock. After sunset, they again move to the opposite direction, i.e. from west to east by its own to begin their day-to-day cycle from the next morning. Another important factor of this optimization technique is inverse square law radiation. According to this law, radiation intensity is proportional to 1/square of the distance. Thus, each plant receives the radiation of heat is given by:

$$Q_n = \frac{P}{4\pi r_n^2} \quad (11)$$

where Q_n = heat intensity, P = source power, r_n = the distance from the plant n to the current best.

Direction of sunflower with respect to the sun is derived by the equation as given below:

$$\vec{S}_n = \frac{x^* - x_n}{x^* - x'_n} \quad n = 1, 2, \dots, i \quad (12)$$

Based on direction of \vec{S} , the step for the sunflowers is calculated by:

$$d_n = \lambda \times P_n(\|x_n + x_{n-1}\|) \times \|x_n + x_{n-1}\| \quad (13)$$

where λ is taken as constant which explains the plants inertial displacement. $P_n(\|x_n + x_{n-1}\|)$ is the pollination likelihood, i.e. the sunflower (i) fertilizes with its adjacent flower ($i - 1$) to generate a fresh inhabitant in a new position which varies in accordance with every distance among the flowers. This can be inferred that those individuals who are nearer to the sun will take comparatively small moves seeking a local elegance, whereas the individuals who are far away from sun will move normally. Besides, it is quite essential to confine the maximum steps moved by each individual, so as to avoid omitting areas prone to be global minimum candidates. Equation given below explains the maximum step as:

$$d_{\max} = \frac{x_{\max} - x_{\min}}{2 \times N_p} \quad (14)$$

where x_{\max} is the upper bound, x_{\min} is the lower bound and N_p is the quantity of plants of whole population. The fresh plantation becomes:

$$\vec{x}_{n+1} = \vec{x}_n + d_i \times \vec{s}_i \quad (15)$$

The pseudo-code for SFO algorithm is shown below,

```

Initialization of inhabitants of sunflowers
Find the best position (sun) and fitness function
Towards sun, orientate the flowers
While (i<maxiter)

```

Find the direction vector for all inhabitants using (12)
Eradicate $m(\%)$ sunflowers which is farther away from sun
Determine step for each sunflower using (14)
Best n sunflower will pollinate closer to sun
Evaluate the fresh objects
If the fresh object is overall best, then update sun
End while
Obtain best position

5 Implementation of SFO for AGC

Sunflower optimization manifests to be the most efficient technique for determining the gains of controller and minimizing the integral square error. Figure 3 represents the implementing flow chart of the suggested SFO algorithm.

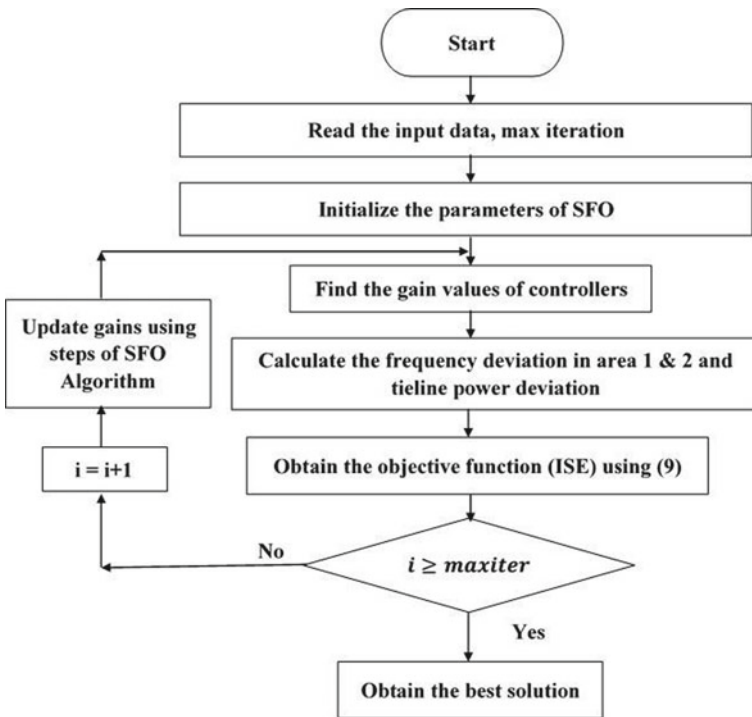


Fig. 3 Flow chart of proposed SFO algorithm

6 Case Study

The execution of the proposed algorithm is performed under different market scenario like unilateral, bilateral and contract violation correspondingly. The complete simulation is done in MATLAB R2018a software. The outcomes obtained thereof are summarized in Tables 1 and 2 for the above market transaction which is compared with DE and GA simulations [11].

Unilateral Trading

Table 1 Comparison of peak overshoot, undershoot, settling time and ISE under unilateral, bilateral case

		Unilateral			Bilateral		
		GA	DE	SFO	GA	DE	SFO
Peak OS	ΔF_1	0.1503	0.9409	0.0355	0.1478	0.0988	0.0286
	ΔF_2	0.0138	0.012	0.0094	0.1036	0.0683	0.0196
	ΔP_{tie}	0.0096	0.0057	0.0037	0.0812	0.0514	0.0151
Peak US	ΔF_1	-0.2916	-0.2574	-0.1501	-0.3949	-0.3664	-0.1930
	ΔF_2	-0.1191	-0.0946	-0.0392	-0.2976	-0.2158	-0.1411
	ΔP_{tie}	-0.0327	-0.0215	-0.0127	-0.0279	-0.0186	-0.0056
Ts	ΔF_1	6.11	5.52	3.2900	12.5	10.87	6.0600
	ΔF_2	6.79	4.51	4.0800	12.64	11.47	6.6800
	ΔP_{tie}	2.4	1.88	1.2400	3.2	3.08	1.9900
ISE	0.0935	0.0548	0.0088	0.7348	0.4945	0.0177	

Table 2 Comparison of peak overshoot, undershoot, settling time and ISE under contract violation case

		Contract violation		
		GA	DE	SFO
Peak OS	ΔF_1	0.1177	0.1093	0.0279
	ΔF_2	0.0474	0.0641	0.0188
	ΔP_{tie}	0.01	0.0095	0.0015
Peak US	ΔF_1	-0.5742	-0.3921	-0.2327
	ΔF_2	-0.3856	-0.2089	-0.1284
	ΔP_{tie}	-0.0449	-0.0221	-0.0112
Ts	ΔF_1	17.19	11.71	5.6500
	ΔF_2	17.43	12.49	5.5800
	ΔP_{tie}	4.25	3.47	1.9000
ISE		1.2967	0.7605	0.0271

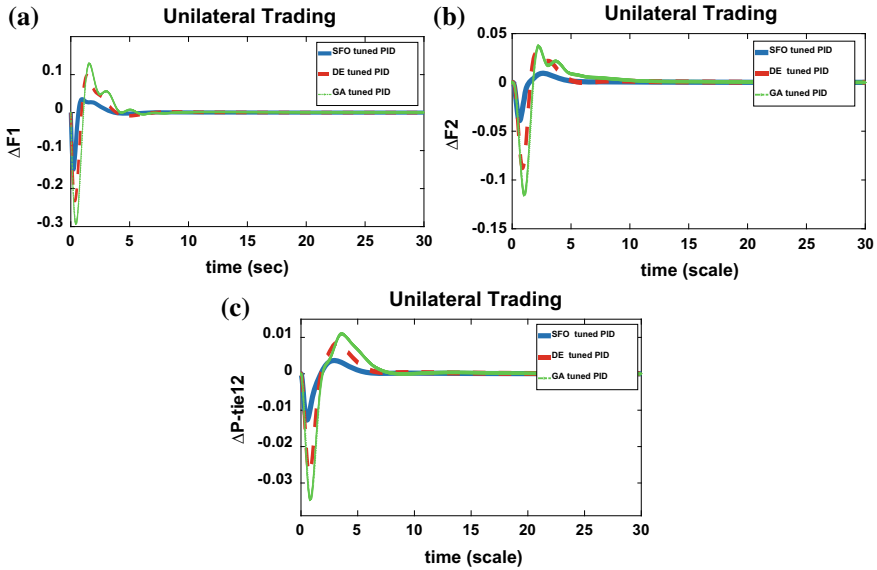


Fig. 4 **a** Change in frequency in area1. **b** Change in frequency in area2. **c** Tie line power deviation

For this case, GENCOS of each area and DISCOS of one area were taken part in trading. So its apf is $apf_1 = apf_2 = apf_3 = apf_4 = 0.5$. Let the change in load happen in area 1 by DISCO1 and DISCO2. So its DPM becomes DPM_1 . The simulation results are shown in Fig. 4a–c which gives the dynamic performance of the system. From these figures, it is obtained that the settling times are improved by 40.3%, 9.5% and 34.04% in area 1, 2 and tie line12, respectively, from DE algorithm, which shows the dynamic performance of the system. All the analyses were also compared with GA algorithm.

$$DPM_1 = \begin{bmatrix} 0.5 & 0.5 & 0 & 0 \\ 0.5 & 0.5 & 0 & 0 \\ 0 & 0 & 0 & 0 \\ 0 & 0 & 0 & 0 \end{bmatrix} \quad DPM_2 = \begin{bmatrix} 0.5 & 0.25 & 0 & 0.3 \\ 0.2 & 0.25 & 0 & 0 \\ 0 & 0.25 & 1 & 0.7 \\ 0.3 & 0.25 & 0 & 0 \end{bmatrix}$$

Bilateral Trading

For this case, each DISCO makes deal with all GENCOS for power trading. Let its apf is assumed as $apf_1 = 0.75$, $apf_2 = 0.25$, $apf_3 = 0.5$, $apf_4 = 0.5$. For this trading, the demand required by each DISCO is 0.1pu from GENCOS as per DPM. So its DPM represented by DPM_2 . The simulation results are shown in Fig. 5a–c. From these figures, it is obtained that the overshoot and settling time are improved by 71.05% and 44.25%, respectively, in area1 from DE algorithm. Likewise, 71.3% and 41.76%, respectively, are in area2 and 70% and 35.38%, respectively, are in tie line12. All the analyses were also compared with GA algorithm.

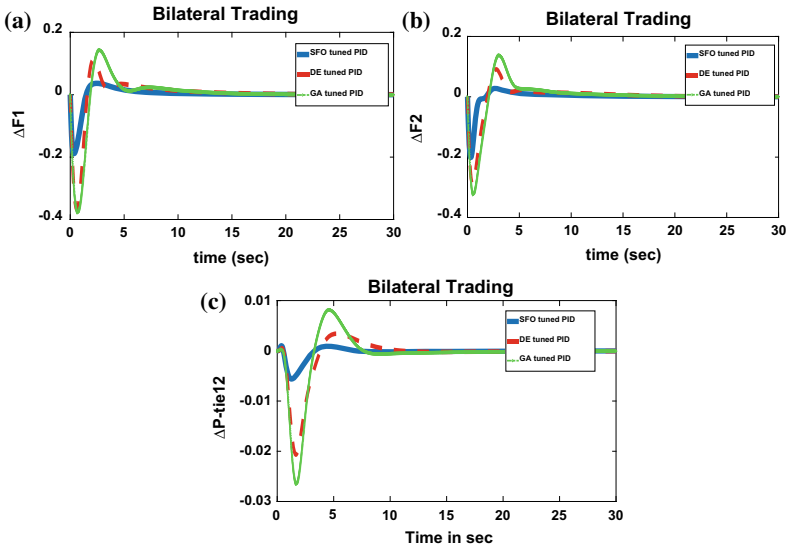


Fig. 5 **a** Change in frequency in area1. **b** Change in frequency in area2. **c** Tie line power deviation

Contract Violation

This case arises only when DISCO demands more than the specified demand. This extra demand must be fulfilled by GENCOS of the same area. Let DISCO2 of area1 violate contract by demanding extra 0.1pu power. Then, the total load of areal becomes,

$$\Delta P_{Load1} = \text{load of (DISCO1 + DISCO2) + extra load} = (0.1 + 0.1) + 0.1 = 0.3\text{pu}$$

The total load of area2 and DPM is the same as of case2. The simulation results are shown in Fig. 6a–c. From these figures, it is obtained that the overshoot and settling time are improved by 74.4% and 51.75%, respectively, in area1 from DE algorithm. Likewise, 70.6% and 55.32%, respectively, are in area2 and 70% and 45.245% are in tie line12, respectively. All the analyses were also compared with GA algorithm.

7 Conclusion

This chapter renders the relevant execution of SFO technique for determining the gains of controller for the AGC of two equal control areas in deregulated power system. The performance of the suggested technique is done considering different market scenarios like unilateral, bilateral and contract violation. From the comparison, it is perceived that the results are better by minimizing the integral error, which indicates the technique is more effective. The outcomes from the SFO provide high

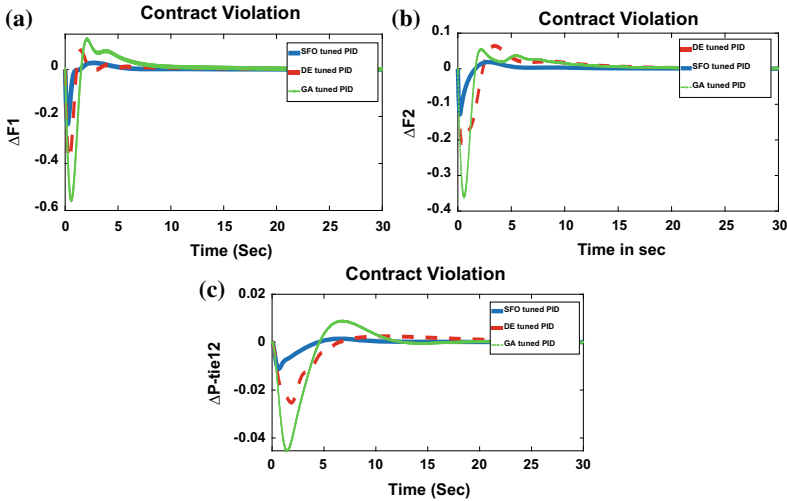


Fig. 6 **a** Change in frequency in area1. **b** Change in frequency in area2. **c** Tie line power deviation

improvement in overshoot, undershoot and settling time by tuning the controller optimally for different deregulated market scenarios as compared to DE and GA.

References

1. Nanda J, Mishra S, Saikia LC (2009) Maiden application of bacterial foraging based optimization technique in multiarea automatic generation control. *IEEE Trans Power Syst* 24(2):602–609
2. Saikia LC, Nanda J, Mishra S (2011) Performance comparison of several classical controllers in AGC for multi area interconnected thermal system. *Int J Electr Power Energy Syst* 33(3):394–401
3. Bhatt P, Roy R, Ghoshal SP (2010) GA/Particle swarm intelligence based optimization of two specific varieties of controller devices applied to two area multi-units automatic generation control. *Int J Electr Power Energy Syst* 32(4):299–310
4. Fathima AP, Khan MA (2008) Design of a new market structure and robust controller for frequency regulation services in the deregulated power system. *Electr Power Compon Syst* 36(8):864–883
5. Donde V, Pai MA, Hiskens IA (2001) Simulation and optimization in an AGC system after deregulation. *IEEE Trans Power Syst* 16(3):481–489
6. Bevrani H, Teshnehlab M, Bevrani H (2000) Load frequency controller design in a deregulated environment using flexible neural networks. In: *Proceedings of 15th international power system conference*, pp 1–6
7. Demiroren A, Zeynelgil HL (2007) GA application to optimization of AGC in three area power system after deregulation. *Electr Power Energy Syst* 29:230–240
8. Debbarma S, Saikia LC, Sinha N (2013) AGC of a multi-area thermal system under deregulated environment using a non-integer controller. *Electr Power Syst Res* 95:175–183
9. Ghoshal SP (2004) Application of GA/GA-SA based fuzzy automatic generation control of a multi-area thermal generating system. *Electr Power Syst Res* 70:115–127

10. Tyagi B, Srivastava SC (2006) A decentralized automatic generation control scheme for competitive electricity markets. *IEEE Trans Power Syst* 21:312–319
11. Hota PK, Mohanty B (2016) Automatic generation control of multi source power generation under deregulated environment. *Int J Electr Power Energy Syst*, 205–214
12. Gomes GF, daCunha SS, Anceletti AC (2018) A sunflower optimization (SFO) algorithm applied to damage identification on laminated composite plates. *Eng Comput*
13. Daraz A, Malik SA, ul Haq A (2018) Review of automatic generation control for multi-source interconnected power system under deregulated environment. In: 2018 international conference on power generation systems and renewable energy technologies (PGSRET), pp 1–5, IEEE
14. Ajithapriyadarsini S, Mary PM, Iruthayarajan MW (2019) Automatic generation control of a multi-area power system with renewable energy source under deregulated environment: adaptive fuzzy logic-based differential evolution (DE) algorithm. *Soft Comput*, 1–15
15. Shankar R, Kumar A, Raj U, Chatterjee K (2019) Fruit fly algorithm-based automatic generation control of multiarea interconnected power system with FACTS and AC/DC links in deregulated power environment. *Int Trans Electr Energy Syst Wiley* 29(1):e2690

Implementation of Monte Carlo Simulation to the Distribution Network for Its Reliability Assessment



Ajoya Kumar Pradhan, Sanjeeb Kumar Kar, Pradeep Kumar shill and Pujashree Dash

Abstract Nowadays, there is increased interest toward the use of renewable energy resources for electricity generation in developing nations. The properties like increased reliability, good power quality and eco-friendly operation of the resources force the mankind for greater acceptance. The solar photovoltaic cell of silicon material is the main source of power generation due to social, economical and environmental benefits with public support and government incentives. Both the analytical and simulation methodologies are used for evaluation process of reliability. The randomness of PV can be covered by the implementation of Monte Carlo simulation methodology. The reliability of the distribution system can be evaluated by using time sequential Monte Carlo simulation method. At each load point of IEEE 33-bus system, the failure rate and repair time are calculated. Reliability indices like SAIFI, SAIDI and CAIDI are evaluated at constant output of rooftop PVs at each load point.

Keywords Reliability · Simulation · Monte Carlo simulation · Renewable energy sources · Solar photovoltaic cell

A. K. Pradhan (✉)

Department of Electrical & Electronics Engineering, GITAM, Bhubaneswar 752054, India
e-mail: ajoya.p@gmail.com

S. K. Kar

Department of Electrical Engineering, SOA Deemed to be University, Bhubaneswar 751030, India
e-mail: sanjeebkar@soa.ac.in

P. K. shill

Department of Electrical Engineering, GITAM, Bhubaneswar 752054, India
e-mail: pkshill92@gmail.com

P. Dash

Department of Electrical Engineering, VSSUT, Burla, India
e-mail: pujashree.keepsake@gmail.com

© Springer Nature Singapore Pte Ltd. 2020

R. Sharma et al. (eds.), *Innovation in Electrical Power Engineering, Communication, and Computing Technology*, Lecture Notes in Electrical Engineering 630,
https://doi.org/10.1007/978-981-15-2305-2_17

1 Introduction

The renewable energy resources such as wind, solar, hydro, biomass, geothermal and tidal are very much accepted worldwide. The utilization of these sources creates no environmental pollution with GHG gases or any climatic change. The distribution system is in an important transition phase in which it is changing from unidirectional power flow of passive distribution systems to bidirectional flow of active distribution networks including small-scale generators. On the other hand, there is an increasing interest to install distribution generators for backup generation, peak shaving, net metering, voltage support, reduction of energy-loss, release of system capacity and reliability improvement. Among the renewable energy resources which are advancing very fast toward grid parity, there is no doubt about solar energy being the frontrunner. With the advance technologies, the improved solar efficiency, the distribution system reliability can be improvised. Reliability assessment of entire system is the focusing area in increasing power demand scenario. Probability concept methodology can be very valuable for the assessment of power system performance [1]. Monte Carlo simulation (MCS) tools [2, 3] have proven exceptionally functional for reliability assessment problems and also provide an extensive series of reliability evaluation, mostly for huge and complex distribution systems. Reliability assessments and statistical performance records of the distribution system are to be maintained on the basis of number of outages, their frequency, their time duration and the number of affected customers [4]. The analytical approach to study the impact of DG on reliability indices was presented [5]. The reliability evaluation using the event count indices SAIFI and SAIDI is proposed. The effect on inserting distributed generation in radial distribution system is studied in this paper. For one-year analytical period, the Averaged Interruption Frequency (AIF) and the Average Interruption Duration (AID) are evaluated before calculation of customer-oriented indices. Reliability evaluation of distribution system containing renewable distribution generations is proposed in this paper [6]. Simulation-based technique that is Monte Carlo simulation is proposed. Stochastic model of PV and wind system is used to simulate their output values. Stochastic model is the simulation-oriented method to explain the non-deterministic performance and arbitrariness of the system. Data of weight factor is used to construct the load model. MCS assessment methodology [7, 8] can be divided into non-sequential and sequential methods. Reliability assessment using MCS and cross-entropy methods [7] considers the Markov model and load state transitions. Model impact of distribution generation to distribution system reliability [9] using comprehensive and sequential MCS model is another field of consideration. The technical approach toward the reliability of networked distribution system [10] is a novel idea for the evaluation process of reliability of future power distribution systems. The proposed Encoded Markov cutest (EMCS) algorithm is based upon identification of circuit minimal tie sets by means of the idea of Petri nets and increases the efficiency of evaluation. Monte Carlo simulation is also used for the assessment of a system with renewable DG units [11] during different operational modes. The generalized systematic approach is to assess the reliability of distribution

system with renewable distribution generators and micro-grids [12] which proposes the method of assessment of distribution system in island mode. The islanded mode operation of micro-grids is also helpful to enhance the reliability of system. The micro-grids are consisting of conventional and renewable DGs. A new analytical technique which considers load curtailment as well as load shedding is proposed here. The adequacy evaluation of PV at distribution load point requires the evaluation of TTF and TTR of each component of system along with the PV connected to the load point of the distribution system. The system's overall failure rate and repair time is the combination of TTF and TTR of each component at that load point and PV generating system. The consideration of insolation and weather effect leads to three state models rather than two-state model of PV generating system. The basic objective of this research work to obtain the behavior of distribution system including solar DG units. Here, the Monte Carlo-based method for the adequacy assessment of distribution system with solar DGs is adopted. Reliability evaluation is done using even count indices SAIDI, SAIFI, CAIDI and ASAI.

2 Basic Methods of Reliability Assessment

Various methods are used to calculate power system reliability indices. The basic approach is analytical and simulation. In analytical techniques, the system is represented by mathematical models, and by using numerical solutions, reliability indices are evaluated. They give expected indices in relatively short computing time. The complex systems and complex operating procedures require frequent assumptions during modeling with loss of some real significance. Analytical techniques have been sufficient enough to provide the results for making objective decision.

Simulation methods simulate the actual process and random behavior of the system to estimate the reliability indices. The method treats the problem as a sequence of real experiments. The techniques can consider virtually all aspects and contingencies inherent in power system planning, operation and design. These comprise random events such as outages and repairs of elements represented by general probability distributions, dependent events and component behavior, queuing of failed components, load variations, input energy variation, as well as other operating policies. Simulation technique is divided into two categories:

- (a) Random: The interval of time of simulation period is chosen randomly. The random approach is the history, which has no effect.
- (b) Sequential: The basic interval of time of simulated period is in sequential order. If there is any effect of history on present conditions, then the sequential approach is used.

3 Reliability Indices

Reliability indices indicate the performance capacity, which is used for the assessment of distribution system performance and competence. In addition to that, they are statistical aggregation of reliability data for a well-defined set of loads, components or customers. For a whole system, operating region, substation service territory or feeder, the reliability indices are average values of particular reliability characteristics. In this research, the distribution system reliability indices are categorized as: load point indices and customer-oriented indices.

3.1 Load Point Indices

There are three basic reliability parameters, i.e., average failure rate (λ_s), average outage time (r_s), average annual outage time (U_s) as mentioned in Eqs. (1–3). For calculation purpose of these indices, failure rate (λ_i) and repair rate (r_i) of every element ‘ i ’ in the system are necessary.

$$\lambda_s = \sum_i \lambda_i \quad (\text{Failure/Year}) \quad (1)$$

$$U_s = \sum_i \lambda_i r_i \quad (\text{Hours/Year}) \quad (2)$$

$$r_s = \frac{U_s}{\lambda_s} = \frac{\sum_i \lambda_i r_i}{\sum_i \lambda_i} \quad (\text{Hours/interruption}) \quad (3)$$

3.2 Customer-Oriented Indices

The load point indices that are the primary indices are primarily important; they do not always give a complete representation of system behavior and response. Thus, customer-oriented indices are considered as the cumulative measure of reliability test and are very often utilized as reliability benchmarks and targets of improvement. For reliability studies, the sustained interruption indices are as follows:

System Average Interruption Frequency Index (SAIFI)

SAIFI is a measure of number of sustained interruptions an average customer will experience for an interval of a year. It can be expressed as in Eq. (4). The only way to improve SAIFI for affixed number of customers is to reduce the number of sustained interruptions experienced by customers.

$$\text{SAIFI} = \frac{\sum_s \lambda_s N_s}{\sum_s N_s} \quad (\text{Interruption/year}) \quad (4)$$

System Average Interruption Duration Index (SAIDI)

SAIDI is the measure of number of interruption hours an average customer will experience in one year. It can be expressed as in Eq. (5). SAIDI may be enhanced with the help of decreasing the total number of interrupted periods or by decreasing the interrupted durations for a predetermined number of customers; thus, reliability can be enhanced by reducing SAIDI.

$$\text{SAIDI} = \frac{\sum_s U_s N_s}{\sum_s N_s} \quad (\text{Hours/Year}) \quad (5)$$

Customer Average Interruption Duration Index (CAIDI)

CAIDI is the average time period of interruption for customers in one year. It can be expressed as in Eq. (6). It signifies how long an average interruption sustains and depends upon the utility response time to contingencies of the system. By decreasing the length of interrupted time period or by raising the number of short interruptions, CAIDI can be improved.

$$\text{CAIDI} = \frac{\sum_s U_s N_s}{\sum_s \lambda_s N_s} = \frac{\text{SAIDI}}{\text{SAIFI}} \quad (\text{hours}) \quad (6)$$

Average Service Availability Index (ASAI)

ASAI is the measure of availability of consumer service during the total consumer demand. It can be expressed as in Eq. (7). This is defined as the ratio of customer hours of service availability to demanded customer hours. It is the customer-weighted accessibility of distributed system which gives the similar information as SAIDI. Greater the ASAI values, greater is the levels of reliability of the system. Consequently, the majority of US utilities are having ASAI values more than 0.999.

$$\text{ASAI} = \frac{8760 - \text{SAIDI}}{8760} \quad (7)$$

4 Monte Carlo Simulation

In this study, the distribution system consists of renewable energy sources like solar photovoltaic (PV). The solar irradiance is intermittent in nature. So, the outcome of PV system is not deterministic in nature. The Distribution system should be capable enough to handle the sudden power drops, as the photovoltaic (PV) generator's output power is variable in nature. Because of the unpredictability of PV characteristic, Monte Carlo simulation method is appropriate one. So for complex nonlinear distribution systems, MCS-based reliability evaluation is very useful. As compared to analytical method, MCS provides maximum data regarding the load point and the system reliability indices. Due to the random nature of power systems failures, MCS can be an option for the simulation of these system failures. MCS is a probabilistic methodology which may be utilized as to forecast the characteristics of the system mechanism. When the system behavior does not depend on the past events, one of the MCS types of simulation, i.e., random simulation is used. The artificial history is desirable in chronological simulation method and can be found out by means of arbitrarily generated up and down times for the apparatus of the system. Time to failure (TTF) is the time period required for the failure of the component. This time for each component is chosen arbitrarily by using equation Eq. (8).

$$\text{TTF} = -\frac{1}{\lambda_i} \ln(n) \quad (8)$$

where λ is system failure rate of element, and n is an arbitrary number (ranging 0 to 1)

Time to repair (TTR) or time to replace (TTR) is the time needed to repair or replace a failed component. Also, this time period is forecasted at random by the equation Eq. (9).

$$\text{TTR} = -\frac{1}{\mu_i} \ln(n) \quad (9)$$

Here, r is repair rate of system component.

The exponential distribution is followed by both TTF and TTR. Artificial history of distribution system mechanism may be predicted by generating TTF and TTR for covering simulation times (e.g., 1 year) in sequential order. MCS are performed under a large number of scenarios for obtaining an accurate result depending on the case study. The simulation time can be extended for very long duration. Then, the average is calculated. In the research work, the simulation is performed for one-year duration.

5 Simulation Procedure

STEP 1 (Algorithm for DG location)

When a component fails due to a sustained fault, a portion of system will be out of service, and the customers will experience an interruption.

- a. Find the fault location.
- b. Isolate the faulted component by the closest switching device by performing the upstream search. We assume all switches are automatic.
- c. Downstream restoration is performed by connecting the alternate source (PV) which was connected to the faulted location through a normally open switch (NOS) in normal operating condition.
- d. Find the failure time and repair time of the faulted failed component.

STEP 2 (Algorithm for MCS considering reconfiguration)

The process of Monte Carlo simulation can be briefly decided as follows

- a. Begin with first sample year.
- b. At time zero, identify the zones of fault.
- c. Apply the STEP 1 to identify the interrupted customers.
- d. Generate the failure and restoration hourly history for PV by drawing sample values of TTF and TTR.
- e. Obtain the overall system hourly operating condition by combining the operating cycle of all components and PV.
- f. Determine customer-oriented indices in both analytical and MCS method.
- g. Repeat steps from c–f for all load points and for one simulation year. Otherwise go to step h.
- h. Obtain the overall system reliability indices during the total simulation time.

6 Test System and Results

IEEE 33-bus radial distribution system [13] is studied in this research work as shown in Fig. 1. The network has one main feeder, three laterals and 32 number of load points. The total number of customers for this system is 3200 with 100 numbers of customers at each load point, and total load is 3.75 MW. The test system is shown in Fig. 1. The bus-1 stands for conventional source of electrical power generator, the only source of energy to whole system. Bus-2 to bus-33 are considered as load points. Each branch in system is numbered basing on its in-bus number. Therefore, there are 32 numbers of branches with numbering from branch-1 to branch-32. As the test system is suitably small, it permits the execution of reliability calculations within reasonable computation time. Here in this case, the distribution system is highly automated, and this automatic switching will significantly reduce the interruption

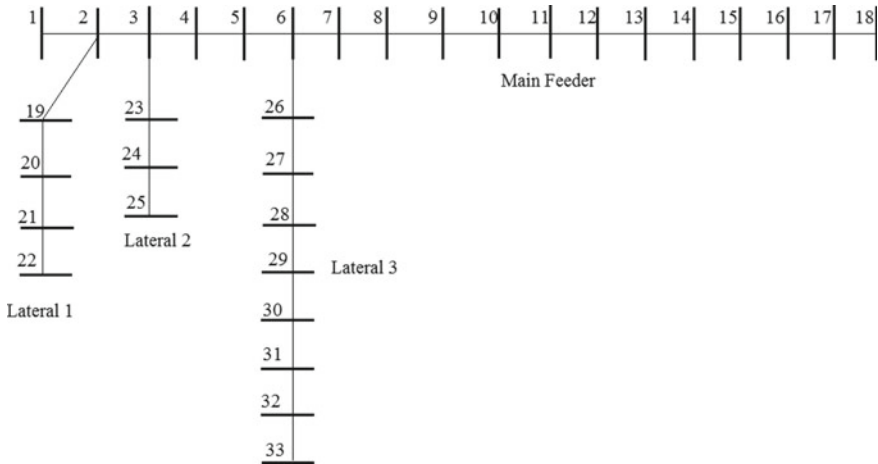


Fig. 1 IEEE 33-bus test system

time. Thus, switching time n-fault detection times are neglected. Each load point can be connected with total 1.5 MW PV system. The whole system is divided into three subgroups in which bus 2, 3 and lateral 1, lateral 2 are in subgroup 1; bus 4, 5, 6 and lateral 3 are in subgroup 2; and finally, bus 7 to bus 18 of main feeder come under subgroup 3. Each subgroup is supplied with PV system with maximum operating condition of 1.5 MW power. During fault, they are operated to supply the faulted load point of its subgroup. The average rate of failure and time of repair of photovoltaic system are 0.12 f/yr and 60 h. It is supposed that fuses and sub-breakers are operated perfectly. The assumption is made that there is no effect of weather change and constant insolation condition. The failure rate and repair time at each load point are shown in Fig. 2. The rate of failure is the function of length and distance from the main source. Load point distant from the supply source has more failure rate that the load points closer to the supply source. The failure rate of generator is very low because of AGC system.

Average time of interruption is a function of failure rate and mean time of restoration of network components. Hence, all the feeders in IEEE 33-bus system are connected to adjacent photovoltaic system via a normal operating point (means in normal condition, the breakers are open) that allow network operator to shift the load in case of main feeder failure. Load transfer during failure would result in less mean time of interruption. The system is considered as the fully automated. Thus, the switching time and fault detection time are neglected.

The failure time and the repair time are the random parameters to be considered in MCS technique. Here, we are considering the exponential distribution.

The customer-oriented reliability indices are calculated under two cases that are with PV and without PV at faulted load point. The reliability indices SAIFI, SAIDI, CAIDI and ASAI are considered, and the results are shown in Table 1.

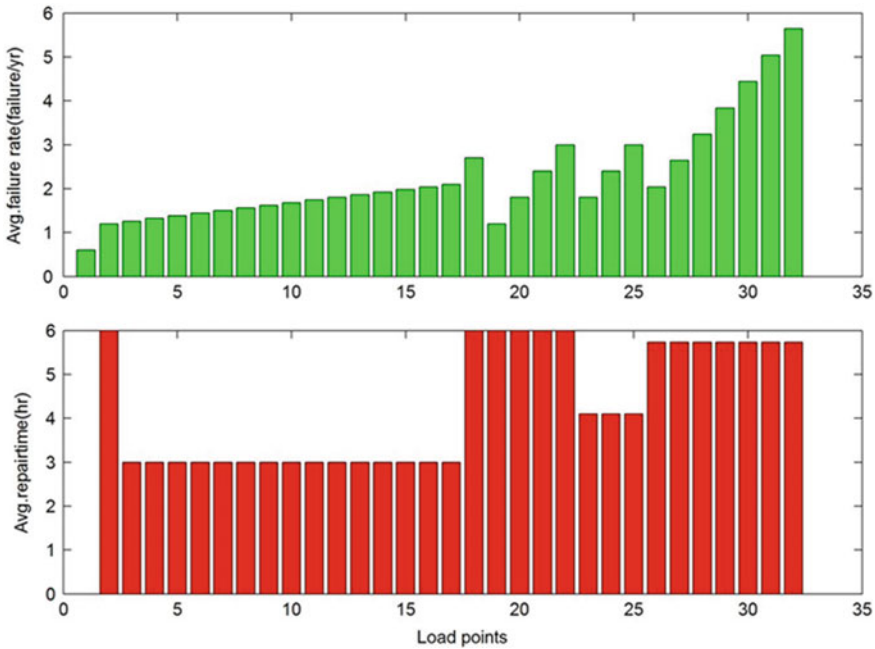


Fig. 2 Failure rate and repair time at each load point

Table 1 Reliability indices

	SAIFI	SAIDI	CAIDI	ASAI
Without DG	2.2556	10.4022	4.6117	0.9988
With DG	2.3758	10.7622	4.3787	0.9988

7 Conclusions

In this paper, reliability indices of distribution system using Monte Carlo simulation are presented. Here the DGs are used as backup generation. This approach takes into consideration PV characteristic in two-state models. The test system is IEEE 33-bus radial system. The system indices such as SAIFI, SAIDI, CAIDI and ASAI are computed using developed program in MATLAB. The random Monte Carlo simulation is used. The reliability assessment in this work is checked by implementing PV at each load point which is connected to respective load point with automated switches. The reliability analysis shows that using of PV as backup source causes deterioration in reliability of system. This is due to the failure of PV. PV without any storage and other backup DG (conventional, non-conventional) are not reliable for system. Therefore, the combinations like PV-wind, PV-battery storage, PV-wind-storage, PV-wind-diesel, etc. are implemented for the improvement of reliability of

distribution system at load side. Monte Carlo simulation method is most suitable technique for reliability assessment in case of renewable DGs because it is considered the randomness of the renewable sources. Analytical method is appropriate for system with sufficient data and having DGs with constant output.

References

1. Billinton R, Allan RN (2006) Reliability evaluation of power systems, 2nd edn. Plenum Press, New York
2. Billinton R, Allan RN (1992) Reliability evaluation of engineering systems concepts and techniques, 2nd edn. Business Media, New York
3. Billinton R, Li W (1994) Reliability assessment of electric power system using monte carlo methods. Plenum Press
4. Ringlee RJ (1966) Steps in measuring service continuity. *Distribution* 28:14–18
5. Al-Muhaini M, Heydt GT, Huynh A (2010) The reliability of power distribution systems as calculated using system theoretic concepts. In: IEEE conference on power and energy society general meeting, Minneapolis, MN, pp 1–8, July 2010
6. Abdulaziz A, Raghavan AS, Chowdhury BH (2012) Reliability evaluation of distribution systems containing renewable distributed generations. In: IEEE conference (North American power symposium), Champaign, IL, pp 1–6, Sept 2012
7. da Silva AML, Farnandez RAG, Singh C (2010) Generating capacity reliability evaluation based on monte-carlo simulation and cross-entropy methods. *IEEE Trans Power Syst* 25(1)
8. Conti S, Rizzo SA (2015) Monte carlo simulation by using a systematic approach to assess distribution system reliability considering international islanding. *IEEE Trans. Power Deliv* 30(1)
9. Li F, Sabir N (2008) Monte carlo simulation to evaluate the reliability improvement with DG connected to distribution system. In: International conference on electrical power system, high voltages, electric machines (power 08)
10. Al-Muhaini M, Heydt GT (2013) Novel method for evaluating future power distribution system reliability. *IEEE Trans Power Syst* 28(3)
11. Youli S, Nagasaka K (2010) Monte carlo simulation method used in reliability evaluation of a laboratory-based micro grid. In: International multi conference of engineers and computer scientists, vol 2, Mar 2010
12. Contour S, Nicolosi R, Rizzo SA (2012) Generalized systematic approach to distribution system reliability with renewable distributed generators and microgrids. *IEEE Trans Power Deliv* 27(1)
13. Raoofat M (2011) Simultaneous allocation of DGs and remote controllable switches in distribution networks considering multilevel load model. *Int J Electr Power Energy Syst* 33:1429–1436

Retinal Image Segmentation Using Gabor Transform with Preprocessing and Hysteresis Thresholding



Sakambhari Mahapatra, U. R. Jena and Sonali Dash

Abstract Scientific study revealed that eyes are the best indicators of many diseases like glaucoma, diabetic retinopathy, hypertension, and stroke. By examining the segmented retinal blood vessel network, ophthalmologist can get the information regarding the abnormality. The objective of this research is to provide reliable segmented retinal blood vessel to assist the ophthalmologists to figure out the abnormality precisely. In this work, enhanced Gabor filter in multiple orientation is employed for the retinal blood vessel extraction. The suggested method combines sharpening operation and median filtering with Gabor transform to get enhanced Gabor transformed images. Finally, to get the segmented output hysteresis thresholding is applied on the enhanced Gabor transformed images. As hysteresis thresholding takes into consideration the connectedness between neighboring pixels, it performs better in segmenting the vessels. The suggested integrated approach has improved the accuracy and specificity. Experiment on 20 retinal images of DRIVE database indicated 95.06% accuracy and 98.83% specificity.

Keywords Retinal blood vessel segmentation · Gabor filter · Hysteresis threshold · Image sharpening

S. Mahapatra (✉) · U. R. Jena
Department of Electronics and Telecommunication, Veer Surendra Sai University of Technology,
Burla 768018, India
e-mail: mahapatra.shakambhari@gmail.com

U. R. Jena
e-mail: urjena@rediffmail.com

S. Dash
Department of Electronics and Communication Engineering, Raghu Institute of Technology,
Vishakhapatnam, India
e-mail: sonali.isan@gmail.com

© Springer Nature Singapore Pte Ltd. 2020
R. Sharma et al. (eds.), *Innovation in Electrical Power Engineering, Communication, and Computing Technology*, Lecture Notes in Electrical Engineering 630,
https://doi.org/10.1007/978-981-15-2305-2_18

229

1 Introduction

Glaucoma, diabetic retinopathy, cataract, and macular degeneration are few among the diseases which can lead to blindness. Scientific study revealed that these cases can be prevented if detected in early stage. Retinal blood vessel plays important role in identifying these cases. Regular monitoring and diagnosis of several other diseases like hypertension, stroke, and cardiovascular disease can also be done from retinal blood vessels. Though manual extraction of retinal blood vessel is possible, it is time consuming and tedious, requiring skilled technicians. Thus, a large number of researches are going on recently for automatic segmentation of blood vessels.

Several methods have been proposed for blood vessel segmentation with different databases. Ali et al. [1] applied Gabor filter for enhancement and Otsu method, ISODATA, and K-mean clustering method for segmentation for binarization. Biran et al. [2] applied local entropy thresholding and sequential filtering on Gabor filtered image for vessel extraction. Nandy et al. [3] proposed an optimal Gabor filter bank based on entropy measure and used artificial neural network for classifying normal and abnormal retinal fundus images. Gabor Filters are directionally sensitive filters with tunable scale and elongation parameters are applied for vessel extraction by Rangayyan et al. [4]. Osareh et al. [5] combined Gabor filter with Gaussian mixture model and discriminative support vector machine classifiers for fundus vessel segmentation. Curvelet transform [6] and Rizlet transform [7] have also been applied for blood vessel extraction by various researchers. Chaudhuri applied match filter [8] for vessel segmentation. Various optimization techniques [9] are also proposed recently to improve the segmentation result. Aguirre et al. [10] have filtered the noise using low-pass radius filter and further applied Gabor filter and Gaussian fractional derivative to improve the contour of vessel. Although various methods are proposed for segmentation of retinal blood vessel, still accurate blood vessel extraction is a challenging task due to vessel width variation and low-quality retinal image. We have applied image sharpening and median filter to retinal image before Gabor filtration, which improved the accuracy when segmented. The rest of the paper is organized as follows. Section 2 describes the preliminaries of various methods used in our approach. The proposed method is described in detail in Sect. 3. The experimental results and evaluation are illustrated in Sect. 4. Section 5 concludes the work described in this paper.

2 Preliminaries

2.1 Image Sharpening

Image sharpening technique is used to enhance and highlight the edges and boosts the fine details of an image. It is done to refine the contrast between the foreground and the background. Image sharpening is mostly done by Laplacian operator. Laplacian

operator on image ‘ I ’ is defined by Eq. (1), where $I(x, y)$ is the pixel being processed, at coordinate (x, y) .

$$\begin{aligned} \nabla^2 I = & [I(x - 1, y - 1) + I(x - 1, y) + I(x - 1, y + 1) + I(x + 1, y - 1) \\ & + I(x + 1, y) + I(x + 1, y + 1) \\ & + I(x, y - 1) + I(x, y + 1) - 8I(x, y)] \end{aligned} \quad (1)$$

Here the intensity of all the eight pixels (except the center pixel) in 3×3 neighborhood of the processing pixels is added, and eight times of the center pixel value $I(x, y)$ is subtracted from the sum. This process is repeated for each and every pixel in the image to get the sharpened image.

2.2 Median Filtering

Median filtering generally eliminates salt-and-pepper noise as well as smoothen the image. It also removes the malformation due to Laplacian operation. The algorithm for median filtering is as follows. A 2D window of size 3×3 taking the processing pixel $I(x, y)$ at center is used. In the selected window, the pixel values are arranged in ascending order. From the arranged pixels, the median value I_{med} is picked and the processing pixel $I(x, y)$ is replaced by I_{med} . Similarly, this replacement is done for every pixel in the retinal image to get the median filtered image.

2.3 Gabor Transform

Gabor transform is implemented through Gabor filter defined as Eq. (2).

$$g(x, y) = \frac{1}{2\pi\sigma_x\sigma_y} \exp\left[-\frac{1}{2}\left(\frac{x^2}{\sigma_x^2} + \frac{y^2}{\sigma_y^2}\right)\right] \cos(2\pi f_0 x) \quad (2)$$

where σ_x and σ_y are the standard deviation values in the x - and y -directions, and f_0 is the frequency of the modulating sinusoid. These filters are directionally selective band-pass filters and are used as line detectors. Many researchers have applied Gabor filter to retinal image since it is an excellent edge detector. A Gabor filter as defined above in Eq. (2) is the product of a Gaussian envelope, which has optimal localization in frequency as well as in spatial domain, with a sine function.

2.4 Morphological Operation

Morphological operations are effective when shape of the element to be extracted is known priori. The vessels are piecewise linear so morphological operation is suitable for extracting them. Erosion, dilation, opening, and closing are few among the morphological operations. In morphological operation, a structuring element (SE) is used. The shape and size of the SE is dependent on the feature to be extracted or modified in the image. So selection of an appropriate SE is an important step in morphological operation. The main advantage of morphological operation is less computational complexity and less time and is also resistant to noise. The dilation and erosion are the basic morphological operations. The dilation of an image 'A' by a SE 'B' is denoted by $(A \oplus B)$. The SE 'B' is positioned with its origin at a pixel (x, y) , and the new pixel value at that location is calculated as:

$$g(x, y) = \begin{cases} 1 & \text{'B' hits 'A'} \\ 0 & \text{otherwise} \end{cases} \quad (3)$$

Similarly, erosion of image 'A' by SE 'B' is denoted as $(A \ominus B)$ and is defined as:

$$g(x, y) = \begin{cases} 1 & \text{'B' fits 'A'} \\ 0 & \text{otherwise} \end{cases} \quad (4)$$

2.5 Hysteresis Thresholding

Thresholding technique segments the image into multiple regions of interest. Blood vessel segmentation is a bilevel thresholding where the region of interest is vessel and background. For bilevel thresholding generally every pixel value is compared with the threshold and if the value of the pixel is greater than threshold, then it is replaced by 1, else it is replaced by '0'. In hysteresis thresholding, two threshold values are chosen, t_{LOW} and t_{HIGH} . Pixels whose values are higher than t_{HIGH} are replaced by '1' and whose values are lower than t_{LOW} are replaced by '0'. Pixels whose values are higher than t_{LOW} and is connected to pixel with value greater than or equal to t_{HIGH} in its eight neighborhoods that pixel is also replaced by '1'. Since the connectedness between the pixels is taken into consideration, hysteresis thresholding performs better for extraction of vessels.

3 Proposed Method

This approach of retinal blood vessel segmentation consists of three phases, namely image enhancement, segmentation, and post-processing. In this approach, inverted green channel is used since green channel exhibits higher contrast between the vessel and background as compared to the other two channels. Figure 1 shows the red, green, and blue components of retinal image.

3.1 Image Preprocessing

Because of non-uniform illumination and inferior contrast, image enhancement becomes elementary step before segmentation. The preprocessing stage enhances the image. It comprises four steps—image sharpening, median filtering, Gabor transform, and adaptive histogram equalization. Image sharpening improves the edges of the vessel and hence vessels appear clearer. Median filtering smooths the image as well reduces the distortion introduced by sharpening operation. The image sharpening and median filtering operations before the Gabor transform are the key modification in the proposed method, which improve the accuracy and specificity of result. The result of image sharpening and median filtering on inverted green channel is shown in Fig. 3. A Gabor filter bank with eight different orientations and $\sigma_x = 1.09$, $\sigma_y = 1.09$ is generated, as shown in Fig. 3c. The median filtered image is convolved with all the filters of the Gabor filter bank, and in each case, the maximum response is recorded. It enhances the image in different orientation while preserving the edges. The final stage of enhancement is adaptive histogram equalization (AHE) [11] operation, which improves the contrast between foreground and background. In AHE, image is divided into small tiles, and every pixel in the tile is transformed through a transformation function, which depends upon the neighborhood of the region. So the contrast in each tile is enhanced, and the overall histogram of the output image looks similar to a specified histogram. Then, bilinear interpolation is applied to combine the tiles. The objective of AHE is to find the histogram in local window and recombine all the local windows histogram to get the overall histogram distribution. Figure 4b shows result of AHE.

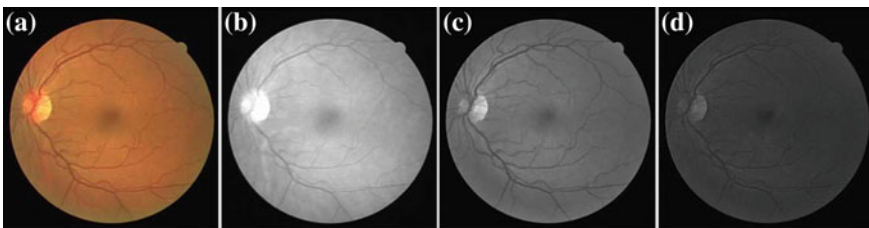
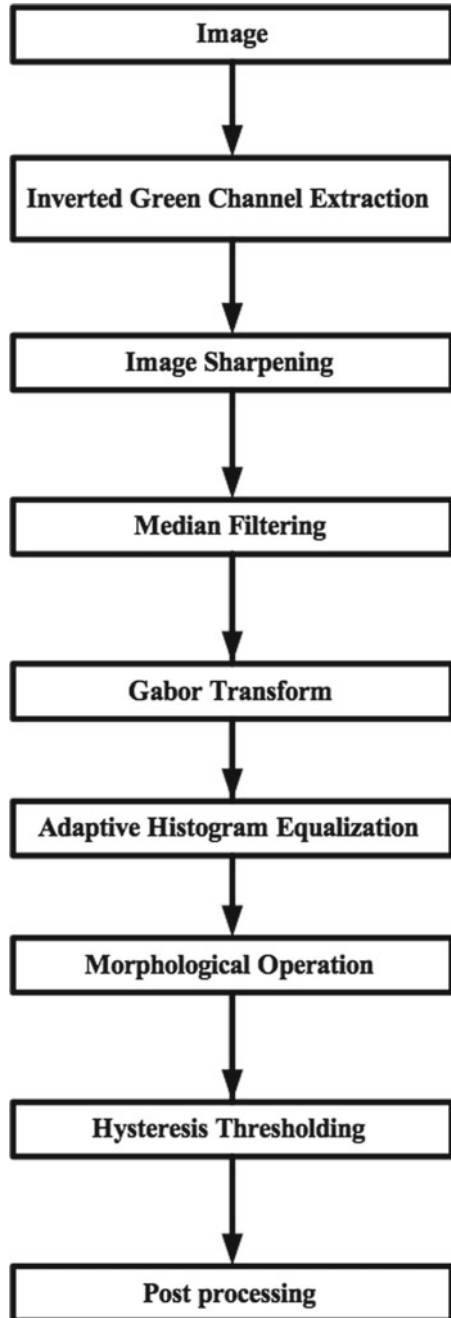


Fig. 1 a Color image, b red channel, c green channel, and d blue channel

Fig. 2 Block diagram of the proposed method



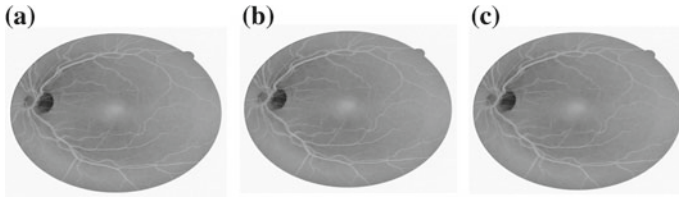


Fig. 3 **a** Inverted green channel, **b** sharpened image, and **c** median filtered image

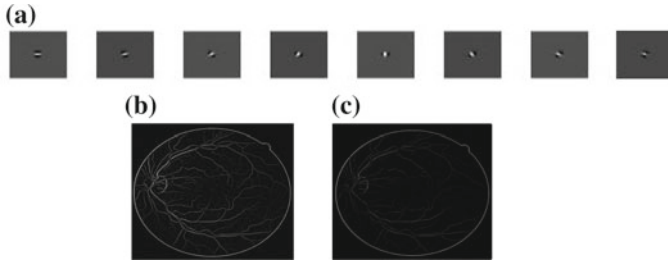


Fig. 4 **a** Gabor filter bank, **b** AHE image, and **c** image convolved with Gabor filters

3.2 Segmentation Using Morphological Operation and Hysteresis Thresholding

The optic disk needs to be removed before segmentation otherwise the algorithm may treat it as vessel; otherwise, performance of the method may degrade. Since the shape of the structure is known, so morphological operation can be preferred to extract it. So in the proposed method, a disk-shape structuring element with 8 pixel size is used. Morphological opening operation with the above SE removes the optic disk. The morphological opening operation of image ‘A’ by SE ‘B’ is simple erosion followed by dilation operation and is defined as follows:

$$A \circ B = (A \ominus B) \oplus B \tag{5}$$

The vessel segmentation process divides the image into background and vessel (foreground). Since the vessels are connected with each other, hysteresis thresholding is suitable for segmentation. By varying t_{HIGH} and t_{LOW} , within 50–200, we found the accuracy to be higher for $t_{HIGH} = 150$ and $t_{LOW} = 50$. The final segmented output is as illustrated in Fig. 5d.

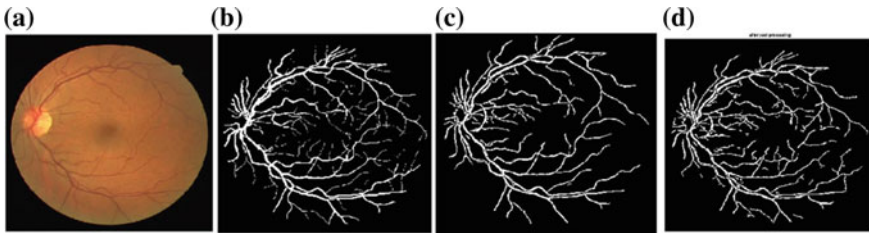


Fig. 5 **a** Original image, **b** manual segmentation result, **c** traditional Gabor filter segmentation, and **d** segmentation by Gabor combined with sharpening and median filtering

3.3 Post-processing

After applying thresholding, some undesirable pixels forming dots and very thin lines emerged as noise which is referred as false positive in the produced binary image, so in order to remove these undesirable pixels, some further processing has to be performed for improving the image [7]. To accomplish this task, an image opening (morphological operation) is used to eliminate the undesired pixels that are limited to or less than 30 pixels. Figure 5d shows the results of post-processing.

4 Results and Discussion

To appraise the proposed method, we have implemented the algorithm on digital retinal images for vessel extraction (DRIVE) database. DRIVE database consists of two parts—one training database set and testing database set. Each dataset contains 20 color retinal images, along with corresponding mask and ground truth images. Since the proposed method is an unsupervised method, we have used only the testing dataset. Accuracy and specificity are few performance measures to quantify the efficiency of the proposed method.

True positive (TP) = number of times a pixel is correctly identified as a vessel.

False positive (FP) = number of times a pixel is incorrectly identified as vessel.

True negative (TN) = number of times a pixel is correctly identified as background.

False negative (FN) = number of times a pixel is incorrectly identified as background.

For quantitative analysis value, true positive (TP), true negative (TN), false positive (FP), and false negative (FN) pixels are estimated, and on that basis, accuracy and specificity are calculated by Eq. (6).

$$\text{accuracy} = \frac{\text{TP} + \text{TN}}{\text{TP} + \text{TN} + \text{FP} + \text{FN}}, \text{Specificity} = \frac{\text{TN}}{\text{TN} + \text{FN}} \quad (6)$$

Table 1 illustrates the accuracy and specificity measure, when traditional Gabor

Table 1 Performance measure with traditional Gabor filter and hysteresis

Images	Accuracy	Specificity
1	95.3288	98.5808
2	94.9936	98.8851
3	94.3760	98.6377
4	94.8630	98.8735
5	95.0461	99.3473
6	94.5939	99.3889
7	95.0436	99.1254
8	94.2990	98.5496
9	95.0624	99.5314
10	95.5901	98.8593
11	95.1558	98.8546
12	95.0364	98.7422
13	94.7078	99.0642
14	95.6089	98.8278
15	95.3352	97.4715
16	94.6551	99.0722
17	94.5036	99.2112
18	95.3897	98.8822
19	95.9819	98.2709
20	95.5649	98.4481

transform is applied on 20 test images of DRIVE database. The maximum accuracy and specificity are found to be 95.9819 and 99.5314, respectively. The average value of accuracy and specificity is 95.02 and 98.46. Table 2 shows the accuracy and specificity parameters of the suggested method on DRIVE database. By sharpening the image and median filtering, it before applying Gabor transform enhanced the average accuracy to 95.06 and average specificity to 98.83. The average accuracy and average specificity of few other methods and the proposed method are shown in Table 3. Ali et al. [1] applied Gabor transform for image enhancement and segmented it by using three different methods, K-mean, ISODATA, and Otsu method. The average accuracy and specificity for the above methods are given in Table 3. The accuracy value was obtained by Katz [9] for enhancing the image by match filter and segmenting it using local entropy thresholding is 94.59. Sreejini and Govindan [12] improved the average accuracy to 95 by incorporating optimization technique in match filter.

Table 2 Performance measure of the suggested method

Images	Accuracy	Specificity
1	95.3594	98.2214
2	94.8970	98.4874
3	94.0756	97.9355
4	94.8603	98.6733
5	95.0676	98.9998
6	94.5463	99.0599
7	95.0061	98.6588
8	94.3842	98.2870
9	95.1524	99.3480
10	95.5983	98.4218
11	95.0067	98.5534
12	95.2028	98.5428
13	94.7500	98.7115
14	95.5631	98.3893
15	94.3890	96.3809
16	94.9209	98.8940
17	94.7078	99.0924
18	95.4564	98.4342
19	95.9644	97.9646
20	95.5613	98.1092

Table 3 Performance comparison on DRIVE database

Suggested method	Avg. accuracy	Avg. specificity
Gabor filter + K-means [1]	94.25	97.57
Gabor filter + ISODATA [1]	94.48	97.57
Gabor filter + Otsu [1]	94.53	97.85
Match filter + local entropy thresholding [9]	94.59	97.21
Match filter + PSO [12]	95.00	96.87
Gabor filter + hysteresis thresholding	95.02	98.46
Laplacian + median filtering + Gabor filter + hysteresis thresholding	95.06	98.83

5 Conclusion

In this paper, we presented an automatic retinal blood vessel segmentation technique based on Gabor transform in combination with hysteresis thresholding. To further improve the accuracy and specificity of the proposed method, image is sharpened

by Laplacian operator and median filtering is applied. From the results, it is clear that the simple image sharpening and median filtering operation added novelty to the algorithm as well as improved the accuracy and specificity parameters. The suggested method is implemented on DRIVE database, and average value of accuracy and specificity are found to be 95.06 and 98.83, respectively. Further, the method can be modified to improve the precision and sensitivity parameters also. Since the proposed method is an unsupervised method, it can even be applied to databases where training dataset is not available. In future, optimized Gabor filter [13, 14] can be applied to improve the results further. The suggested method can further be expanded to classify healthy and diseased cases of vessel network.

References

1. Ali A, Hussain A, Zaki WMDW (2018) Segmenting retinal blood vessels with Gabor filter and automatic binarization. *Int J Eng Technol (UAE)* 7(4):163–167
2. Biran A, Bidari PS, Almazroa A, Lakshminarayanan V, Raahemifar K (2016) Blood vessels extraction from retinal images using combined 2D Gabor wavelet transform with local entropy thresholding and alternative sequential filter. In: 2016 IEEE Canadian conference on electrical and computer engineering (CCECE), pp. 1–5, IEEE
3. Nandy M, Banerjee M (2012) Retinal vessel segmentation using Gabor filter and artificial neural network. In: Third international conference on emerging applications of information technology, 157–160
4. Rangayyan RM, Ayres FJ, Oloumi F, Oloumi F, Eshghzadeh-Zanjani P (2008) Detection of blood vessels in the retina with multiscale Gabor filters. *J Electr Imaging* 17(2):023018
5. Osareh A, Shadgar B (2008) Retinal vessel extraction using Gabor filters and support vector machines. In: Computer Society of Iran computer conference. Springer, Berlin, Heidelberg, pp 356–363
6. Kar SS, Maity SP (2014) Extraction of retinal blood vessel using curvelet transform and fuzzy c-means. In: 2014 22nd international conference on pattern recognition, IEEE, 3392–3397
7. Hassan G, El-Bendary N, Hassanien AE, Fahmy A, Snasel V (2015) Retinal blood vessel segmentation approach based on mathematical morphology. *Procedia Comput. Sci.* 65:612–622
8. Katz NORMAN, Nelson MARK, Goldbaum M, Chaudhuri S, Chatterjee S (1989) Detection of blood vessels in retinal images using two-dimensional matched filters. *IEEE Trans Med Imaging* 8(3):263–269
9. Qi C (2014) Maximum entropy for image segmentation based on an adaptive particle swarm optimization. *Appl Math Inf Sci* 8(6):3129
10. Aguirre-Ramos H et al (2018) Blood vessel segmentation in retinal fundus images using Gabor filters, fractional derivatives, and expectation maximization. *Appl Math Comput* 339:568–587
11. Mapayi T, Viriri S, Tapamo JR (2015) Adaptive thresholding technique for retinal vessel segmentation based on GLCM-energy information. *Comput Math Methods Med*
12. Sreejini KS, Govindan VK (2015) Improved multiscale matched filter for retina vessel segmentation using PSO algorithm. *Egypt Inform J* 16(3):253–260
13. Dora L et al (2019) A novel optimal Gabor algorithm for face classification. In: Soft computing for problem solving. Springer, Singapore, pp 821–832
14. Farnaz F et al (2017) Automatic parameters selection of Gabor filters with the imperialism competitive algorithm with application to retinal vessel segmentation. *Biocybern Biomed Eng* 37(1):246–254
15. Roychowdhury S, Koozekanani DD, Parhi KK (2015) Iterative vessel segmentation of fundus images. *IEEE Trans Biomed Eng* 62(7):1738–1749

16. Dash J, Bhoi N (2017) A thresholding based technique to extract retinal blood vessels from fundus images. *Future Comput Inform J* 2(2):103–109
17. Kar SS, Maity SP (2017) Detection of neovascularization in retinal images using mutual information maximization. *Comput Electr Eng* 62:194–208

Multi-level Asymmetrical Inverters Using Two DC Ports with Less Number of Switches and Conversion Stages



Suraj Kumar Dash and Prakash Kumar Hota

Abstract In recent years, many industrial applications need higher-powered appliances. It is difficult for a single semiconductor switch to connect directly for medium-voltage appliances. In high-power and medium-voltage circumstances, a multi-level power inverter design was provided as an alternative. A multi-level inverter is flexible to use in renewable source, and high-power rating is achieved. Multi-level inverters are categorized into two parts, (1) multi-level symmetrical inverters and (2) multi-level asymmetrical inverters. Here, the asymmetric multi-level inverter is called a dual-DC-port asymmetric multi-level inverter (DP-AMI) that uses only one topology to interface a low/high-voltage DC port and an AC port at the same time. DC source having low voltage like the battery or photovoltaic (PV) modules can provide power directly to the load within a single power conversion stage. It can improve the overall conversion efficiency of the system. The derivation scheme for DP-AMIs topology is given. The principle of operation, schemes used for modulation, and features of DP-AMIs are studied. This inverter's working principle was evaluated, and the expression of output voltage was obtained. Furthermore, the inverter is integrated with the photovoltaic cell, and its maximum power point is tracked. Finally, the outcome of the DP-AMI is compared to the cascaded H-bridge multi-level inverter. After the simulation, it has been found satisfactory results.

Keywords Asymmetrical multi-level inverter · High efficiency · Inverter · Single-stage conversion · Photo voltaic module

S. K. Dash (✉) · P. K. Hota
Veer Surendra Sai University of Technology, Burla, India
e-mail: surajdash555@gmail.com

P. K. Hota
e-mail: p_hota@rediffmail.com

© Springer Nature Singapore Pte Ltd. 2020
R. Sharma et al. (eds.), *Innovation in Electrical Power Engineering, Communication, and Computing Technology*, Lecture Notes in Electrical Engineering 630,
https://doi.org/10.1007/978-981-15-2305-2_19

1 Introduction

Most of our loads are AC; this load required constant voltage at the input. If these loads are connected to inverters, the inverter output voltage must be too controlled to meet the AC loads. There are many methods to control the output voltage. The supreme convenient controlling method for the output voltage is to use pulse width modulation (PWM) control in the inverters.

1.1 Multi-level Inverter

DC-to-AC power conversion can be done by using multi-level inverter in the PV system. There are three important multi-level inverters used in an industrial application known as (1) cascaded H-bridge (CHB-MLI) with separate DC sources [1], (2) the diode clamped (DC-MLI) [2], and (3) flying capacitor (FC-MLI) [3].

Three types of multi-level inverter are presented in Fig. 1, such as (a) three-level DC-MLI, (b) three-level FC-MLI, and (c) three-level CHB-MLI. The advantage of a MLI is that generated staircase waveform is closed to a sinusoidal waveform; therefore, it generates small harmonic distortion of output voltage and low switching stress. Also the input current drawn by multi-level inverter has less distortion. But the disadvantages of multi-level converters are that more number of power semiconductor switches needed and costly because of complicated modulation circuit [1–3].

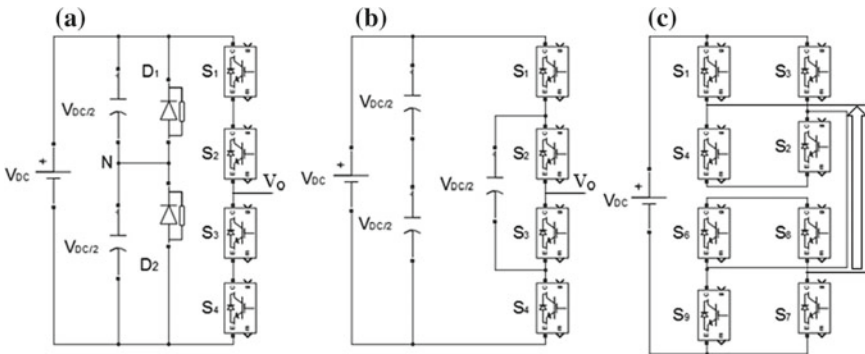


Fig. 1 Types of multi-level inverter

1.2 Asymmetrical Multi-level Inverter

Inverter is a static power electronic circuit which is used to connect several DC power sources like renewable energy sources, DC voltage buses, and storage batteries to the AC load. The three categories of inverter are buck type, boost type, and buck–boost type. In inverter of buck type, the supply DC voltage must be higher than the peak value of AC output voltage. Taking an example, the supply DC voltage of buck-type inverter is in the range of 380–400 V for the 220 V AC applications. So the inverter of boost type is used. It is used only when the DC input voltage cannot meet the requirement of AC load. So the input power which passes through two cascaded-connected power conversion systems creates switching loss, conduction loss, and reduced overall conversion efficiency. The DC-to-AC power conversion for two stages is shown in Fig. 2.

Actually, the inverter output voltage is varying with respect to time; it means the instantaneous value of output voltage is not all time greater than the DC source of low voltage. This gives a clue that if the AC voltage's instant value is lesser than the low-voltage DC source is directly give power to the inverter without passing through font DC–DC converter stage. Hence the part of the input power obtained from low voltage source passes through only one power conversion stage that is DC to AC instead of two power conversion stage, so conduction loss switching loss and voltage/current stress decreases and it lead to increases total DC to AC power conversion efficiency. The single phase DP-AMI is developed by three level inverter [4]. The DP-AMI connects both low/high voltage DC port and AC port simultaneously using one topology. This DP-AMI has several advantages since part of the input power directly supplies to the inverter without passing through DC–DC converter, so the power conversion stages, voltage stress of switch, switching losses, and conduction losses are reduced [1, 4, 5]. Based on the operation, the DP-AMI generated three voltage levels in the +ve half-cycle of voltage output, and the voltage stress of S_{L1} is V_L , but S_1 is $(V_H - V_L)$ instead of V_H when switched at high frequency. Therefore, the voltage stress and switching loss are reduced [6–8]. The DP-AMI-based DC/AC power conversion system is shown in Fig. 3.

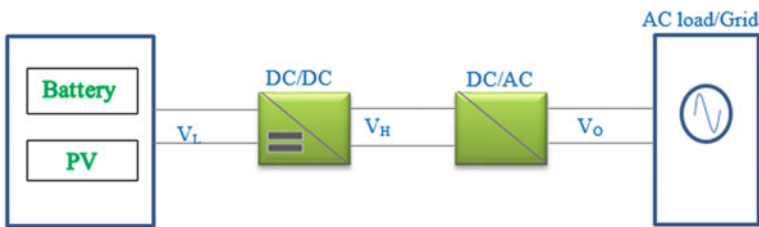


Fig. 2 Two-stage configuration of DC/AC power conversion system

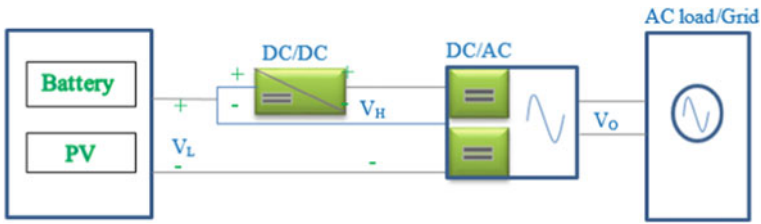


Fig. 3 DP-AMI-based configuration of DC/AC power conversion system

2 Operations and Modulation of the DP-AMI

Figure 4 represents the simplification diagram of DP-AMI. The operation principles and control of the DP-AMI are analyzed. Low- and high-voltage DC ports are used, and these voltage ports provide voltage level of the inverter [4, 9, 10].

2.1 Operation Principle

The output voltage of the positive half-cycle is studied in this section. In this modulation, two triangular carrier waves are used for the positive half-cycle; these two carriers are compared with the desired sin-wave signal at the output to generate the driving signals to the DP-AMI. The modulation strategy of the DP-AMI is described briefly in Table-1.

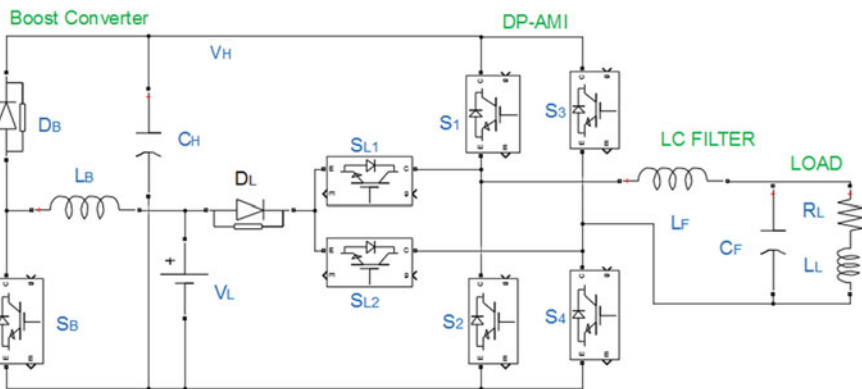


Fig. 4 Three-level T-type DP-AMI model

Table 1 Modulation of DP-AMI

State No.	Input voltage	Switches on state	Switches off state	Midpoint voltage V_{AB}
1	$V_L > V_o$	S_{L1} and S_4	$S_{L2}, S_1, S_2,$ and S_3	V_L
2	$V_L > V_o$	S_2 and S_4	$S_{L2}, S_1, S_2,$ and S_3	0
3	$V_L \leq V_o$	S_{L1}, S_1 and S_4	$S_{L2}, S_1, S_2,$ and S_3	V_H
4	$V_L \leq V_o$	S_{L1} and S_4	$S_{L2}, S_1, S_2,$ and S_3	V_L

2.2 Control Voltage Capability of DP-AMI

This DP-AMI interface with a renewable energy sources like photovoltaic energy system. Two DC ports are used, namely high-voltage DC source (V_H) and low-voltage DC source (V_L). The closed-loop control block diagram of the DP-AMI as shown in Fig. 5 is used to regulate the voltage of both V_o and V_H . The voltage V_H is controlled by the boost converter, the voltage V_o is controlled by the DP-AMI by using SPWM, and the voltage V_L is constant value [5, 9, 11, 12].

3 The MATLAB/Simulink Block Diagram of the DP-AMI

The model parameters of DC/AC system shown in Fig. 6 are: $V_L = 190$ V, $V_H = 380$ V, and $V_o = 380 \sin(100\pi t)$ V. The DP-AMI switches like $S_1, S_2, S_3, S_4, S_{L1}, S_{L2}$ are getting the modulated signal from SPWM. The boost converter parameters are $L_H = 5$ mH and $C_H = 300$ μ F. Finally, the DP-AMI generating voltage is passed through the LCL filter of parameters which are $L_{F1} = 3.6$ mH, $C_F = 2.54$ μ f, and $L_{F2} = 760$ mH for obtaining pure sinusoidal voltage. Here the load is RL load of values $R_L = 55$ Ω and $L = 2$ mH.

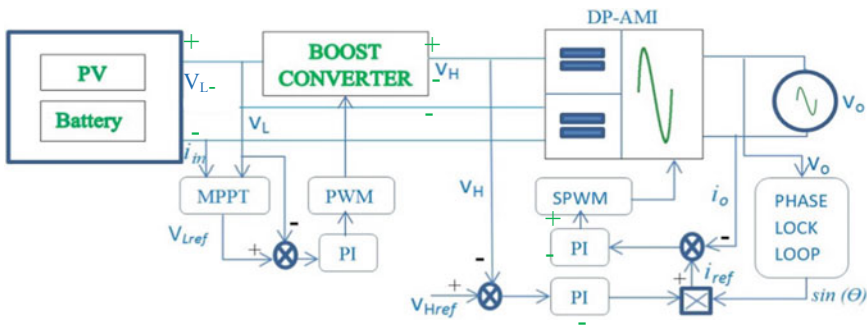


Fig. 5 Control block diagram of DP-AMI

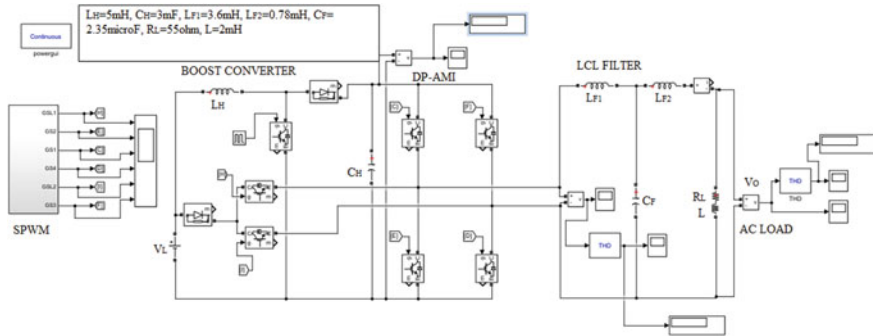


Fig. 6 MATLAB/Simulink block diagram of DP-AMI with LCL filter

Table 2 Operation of DP-AMI with different duty ratio of boost converter

Duty ratio	V_L (V)	V_H (V)	THD of V_{AB} (%)	THD of filtered V_o (%)
0.2	190	229.35	31.2	16.4
0.3	190	269.66	29.53	12.13
0.5	190	378.9	29.2	0.94
0.6	190	468.5	33.9	17.96

Table 2 represents the harmonic contents of DP-AMI with various duty ratios of the boost converter; it is found that at 0.5 duty ratio, harmonic contents in the output voltage are less, i.e., THD = 0.94%.

Here we generate pulse by using SPWM as shown in Fig. 7. In this modulation, triangular wave of high frequency is compared with sin wave of low frequency to generate pulse based on the desired sinusoidal output voltage.

3.1 The Schematic Control Block Diagram of the DP-AMI

This DP-AMI interface with a renewable energy sources like photovoltaic energy system is as shown in Fig. 8. Two DC ports are used, namely high-voltage DC source (V_H) and low-voltage DC source (V_L). The closed-loop control block diagram of the DP-AMI is used to control the voltage of both V_o and V_H . The voltage V_H is controlled by the boost converter, the voltage V_o is controlled by the DP-AMI by using SPWM, and the voltage V_L is constant value [11, 12].

Table 3 represents harmonic contents in the control DP-AMI with various duty ratios of the boost converter and LCL filter. It is found that at the duty ratio of 0.5, the harmonic content in the output is less, i.e., THD = 0.24%.

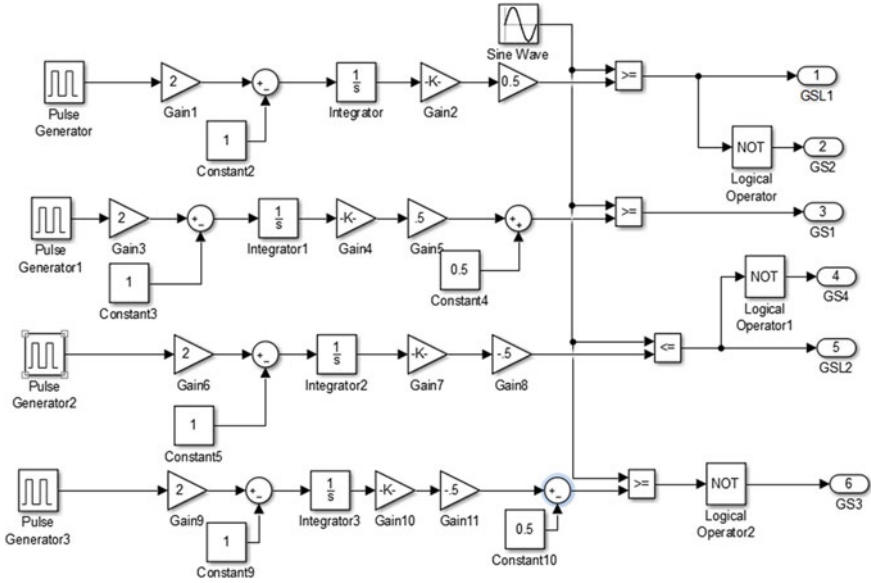


Fig. 7 Modulation strategy of DP-AMI

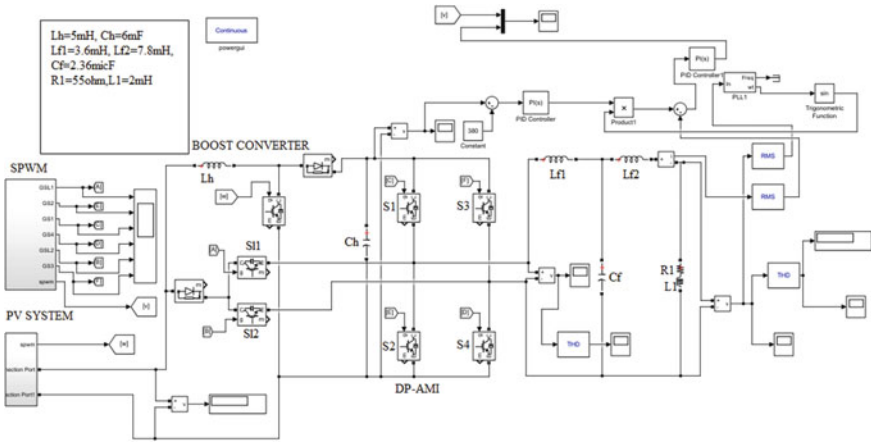


Fig. 8 MATLAB/Simulink control block diagram of DP-AMI

Table 3 Control of DP-AMI with different duty ratio of boost converter

Duty ratio	V_L (V)	V_H (V)	THD of V_{AB} (%)	THD of filtered V_o (%)
0.2	190	238	28.8	15
0.3	190	270.1	26.52	10.39
0.5	190	379.46	26.98	0.24
0.7	190	626.2	36.58	12.51
0.8	140	698.2	45.9	20.51

4 Time-Domain Simulation Results

4.1 Time-Domain Simulation Results of DP-AMI

The midpoint voltage of DP-AMI and its THD is as shown in Figs. 9 and 10, respectively. Filtered output voltage of DP-AMI and its THD are as shown in Figs. 11 and 12, respectively. The output voltage of boost converter and SPWM is as shown in Figs. 13 and 14, respectively.

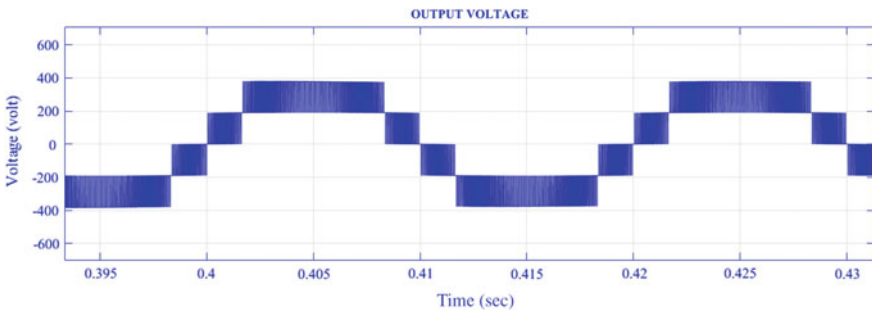


Fig. 9 Midpoint voltage of DP-AMI (for $V_L = 190$ V, the midpoint voltage $V_o = 380 \sin(100\pi t)$ V)

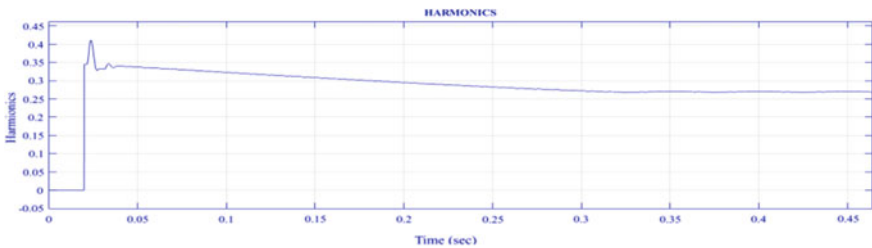


Fig. 10 THD of midpoint voltage (DP-AMI) (For $V_L = 190$ V, THD of midpoint voltage = 26%)

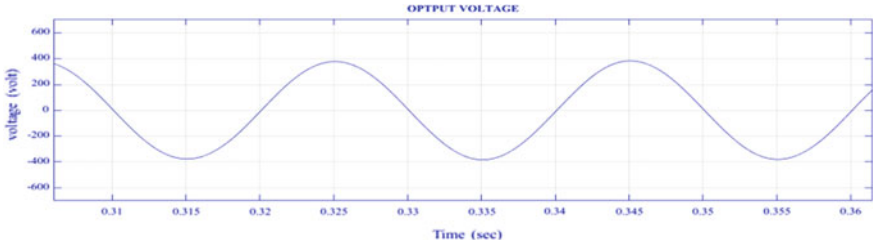


Fig. 11 Filtered output voltage of DP-AMI [for $V_L = 190$ V, the filtered output voltage $V_o = 380 \sin(100\pi t)$]

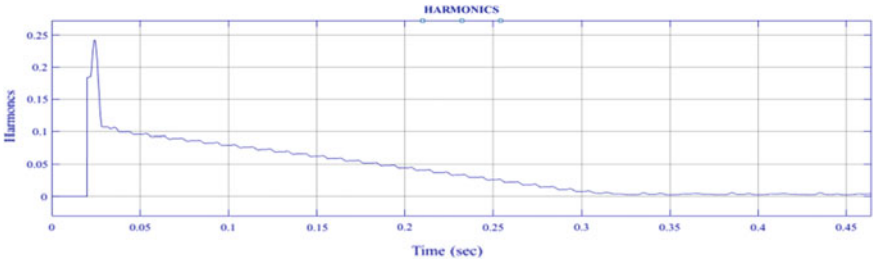


Fig. 12 THD of filtered output voltage (DP-AMI) (for $V_L = 190$ V, THD of the filtered output voltage is 0.24%)

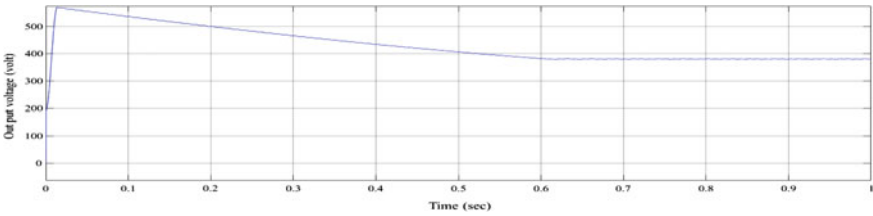


Fig. 13 Output voltage of boost converter (for $V_L = 190$ V and duty ratio of = 0.5, the output voltage of boost converter $V_H = 380$ V)

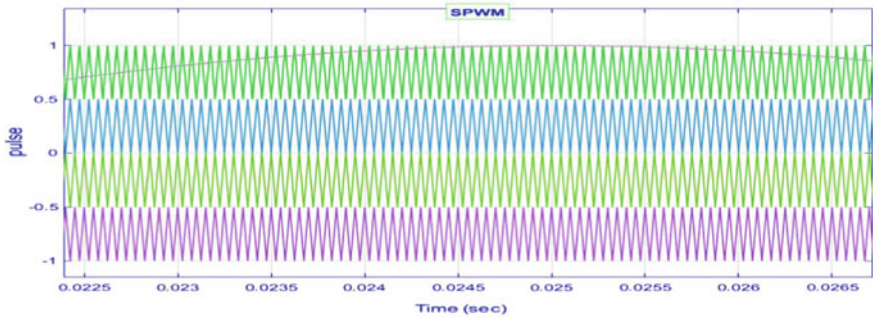


Fig. 14 Modulation scheme of DP-AMI by using SPWM

4.2 Time-Domain Simulation Results of Control DP-AMI

Figure 15 represents the control midpoint voltage of DP-AMI integrated with PV system. Initially this DP-AMI is not able to generate three voltage level because, the pulse generated by using MPPT algorithm is taking some time to track maximum power point then give pulse to the boost converter.

Total harmonic distortion (THD) is measure of resultant of all harmonics present in the output voltage with respect to the fundamental component.

The THD of the control midpoint voltage, filtered output voltage, and its FFT result are shown in Figs. 16, 17, and 18, respectively.

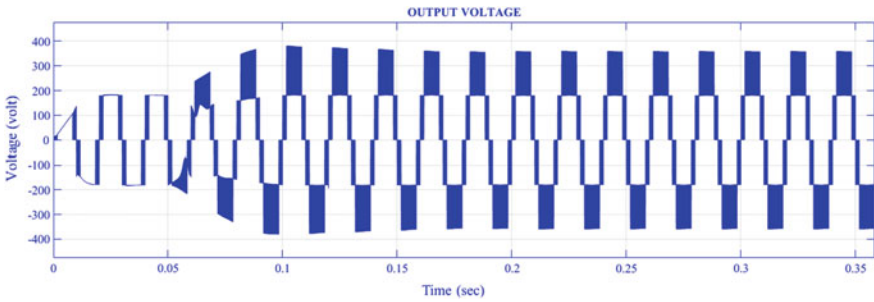


Fig. 15 Control midpoint voltage of DP-AMI (for $V_L = 180$ V, the midpoint voltage $V_o = 360 \sin$ (wt) V)

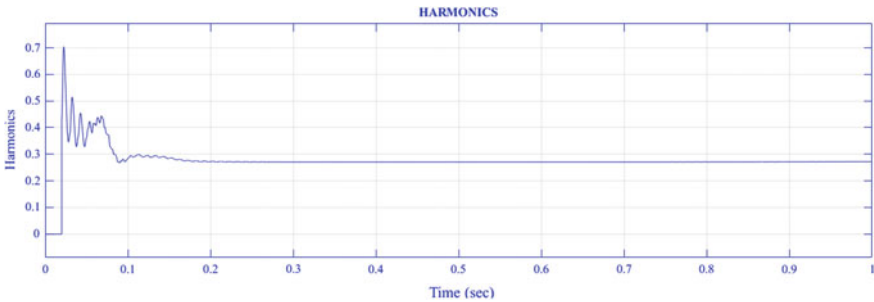


Fig. 16 THD of the midpoint voltage (DP-AMI) (for $V_L = 190$ V, THD of the midpoint voltage = 26%)

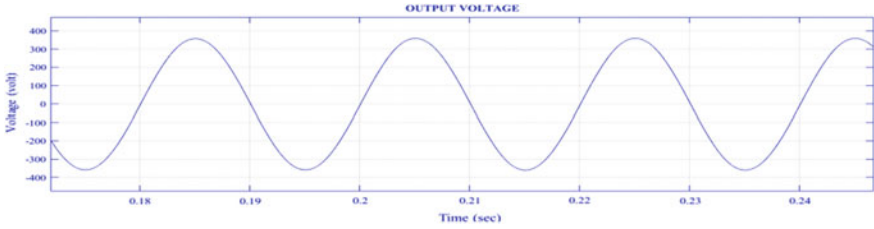


Fig. 17 Filtered output voltage of DP-AMI (for $V_L = 180$ V, the filtered output voltage $V_o = 360 \sin(\omega t)$ V)

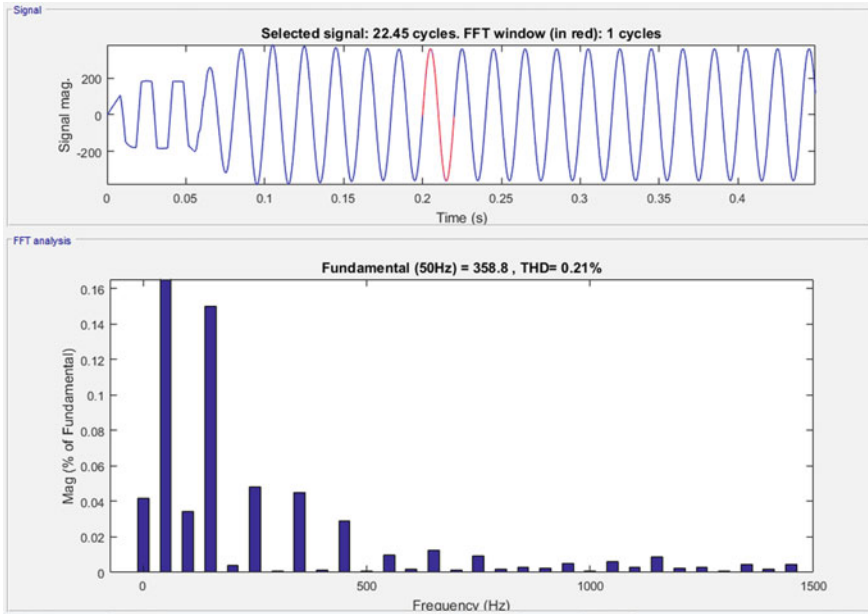


Fig. 18 FFT analysis result of output voltage (for $V_L = 180$ V, FFT result shown above)

4.3 Time-Domain Simulation Result of Various Multi-level Inverters

Figure 19 represents THD of three types converter midpoint voltage. These are control DP-AMI, DP-AMI and cascaded H-bridge. Here it is found that all the three converter contain same THD at the midpoint voltage that is 26%.

Figure 20 represents THD of three types of converter filtered output voltage. These are single phase control DP-AMI, DP-AMI and cascaded H-bridge. Here by considering same circuit condition for all, it is found that THD of single phase DP-AMI with or without control is 0.21%, where as in case cascaded H-bridge THD is

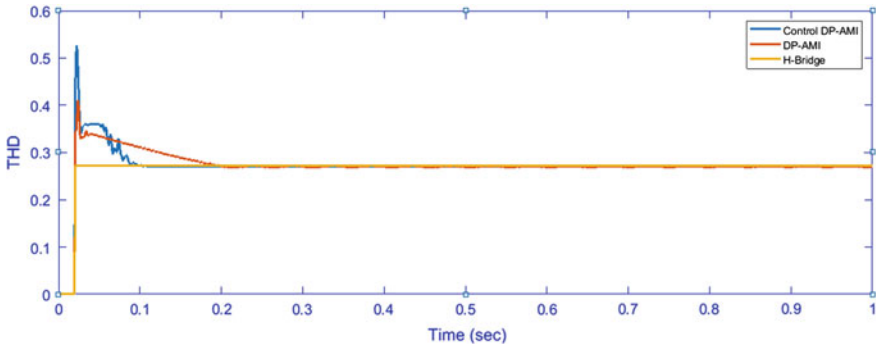


Fig. 19 THD analysis of output voltage

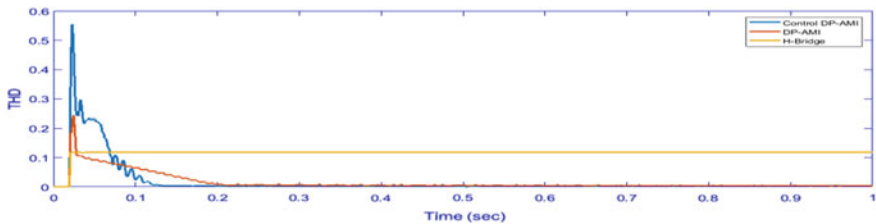


Fig. 20 THD analysis of filtered output voltages

12%. The DP-AMI improve the power conversion efficiency as well reduced THD as compared to cascaded H-bridge multilevel inverter.

5 Conclusion

The present research under investigation of open-loop control and closed-loop control of DP-AMI is done by using MATLAB/Simulink. In this research work, it is found that multi-level inverter (DP-AMI) output waveform has lower dv/dt and also lower harmonic distortions as compared to two-level and cascaded H-bridge inverter. As a result, switching and conduction losses of DP-AMI decreased for which the proposed method proved to be efficient. So DP-AMI is a new, simple, and straight-forward technique for efficiency improvement of the conventional two-stage DC/AC system and implemented in PV system. The control of DP-AMI is more preferable as compare to conventional DP-AMI. Furthermore, it can be extended to multi-phase DP-AMI, and good quality of output wave form can be obtained with less THD.

References

1. Manjrekar MD, Lipo TA (1998) A hybrid multilevel inverter topology for drive applications. In: IEEE applied power electronics conference, pp 523–529
2. Nabae A, Takahashi I, Akagi H (1981) A new neutral–point clamped PWM inverter. *IEEE Trans Ind Elect IA-A7(5)*:518–523
3. Rodriguez J, Lai JS, Peng FZ (2002) Multilevel inverter: a survey of topologies, control and applications. *IEEE Trans Ind Elect 49(4)*:724–738
4. Hongfei Wu, Zhu L, Yang F, Mu T, Ge H (2017) Dual-DC-Port asymmetrical multilevel inverters with reduced conversion stages and enhanced conversion efficiency. *IEEE Trans Industr Electron 64(3)*:2081–2091
5. Tolbert LM, Peng FZ, Cunyngham T, Chiasson JN (2002) Charge balance control schemes for multilevel converter in hybrid electric vehicles. In: *IEEE Trans Ind Electr 49(5)*
6. Zhang L, Sun K, Xing Y (2014) H6 transformer less full-bridge PV gridtied inverters. *IEEE Trans Power Electron 29(3)*:1229–1238
7. Hong F, Liu J, Ji B, Zhou Y, Wang J, Wang C (2015) Single inductor dual buck full-bridge inverter. *IEEE Trans Ind Electron 62(8)*:4869–4877
8. Nguyen MK, Le TV, Park SJ, Lim YC (2015) A class of quasi switched boost inverters. *IEEE Trans Ind Electron 62(3)*:1526–1536
9. Schweizer M, Kolar JW (2013) Design and implementation of a highly efficient three-level T-type converter for low-voltage applications. *IEEE Trans Power Electron 28(2)*:899–907
10. Peng FZ (2001) A generalized multilevel inverter topology with self voltage balancing. *IEEE Trans Ind Appl 37(2)*:611–618
11. Singh D, Yadav JR (2014) Perturb and observe method MATLAB Simulink and design of PV system using buck boost converter. *Int J Sci Eng Technol Res (IJSETR) 3(6)*:1692–1696
12. Savitha PB, Shashikala MS, Puttabuddhi KL (2014) Modelling of photovoltaic cell/module under environmental disturbances using MATLAB/Simulink. *Int J Eng Trends Technol (IJETT) 9(1)*:48–55

Fuzzy Granular Computing-Based Controller Design for Inverted Pendulum System with Delay



Srikanth Kavirayani

Abstract Fuzzy control as a method used in control design has been predominant when the plant mathematical model is unavailable. Granular computing has been seen as a process which speeds up the fuzzy methodology when combined to the fuzzy control design. Inverted pendulum control and stabilization are a classical problem investigated in this work. The stabilization of the pendulum is achieved with an advanced fuzzy granular computing-based controller under the influence of time delay. The controller which was a combination of fuzzy type-2 controller along with classical PID controller achieved the control. However, it was seen that the impact of time delay with advanced fuzzy controllers is significant even if there was a unit transportation delay in the system the output response suffers which becomes a major drawback and which indicates the need for possible boundaries in time delay systems.

Keywords Fuzzy granular computing · Time delay · Single inverted pendulum

1 Introduction

The popular magician's rope trick transforms itself into broom-stick balancing and the interesting control problem of the single inverted pendulum on a cart. Some of the major applications of this research involve studies on segway transport, missile launching and earthquake studies. Various versions of the inverted pendulum problem are investigated worldwide from a simple PID-based control to the latest fuzzy controllers. The focus being fuzzy in this context, some work on fuzzy is highlighted here.

Lin et al. [1] have developed decoupled control by hierarchical fuzzy sliding mode control for the double inverted pendulum system. Cheng et al. [2] have discussed a

S. Kavirayani (✉)
Department of EEE, Gayatri Vidya Parishad College of Engineering (A), Visakhapatnam,
Andhra Pradesh 530048, India
e-mail: kavirayanisrikanth@gvpce.ac.in

Q-value-based safe reinforcement learning scheme for neuro-fuzzy systems. Various researchers have applied fuzzy control to various types of acrobats, pendubots, pendulum systems and other underactuated systems. Yuan et al. [3] have performed simulations on linearized pendubot model in MATLAB environment by PSO and LQR algorithm separately, and the results were compared which proved the PSO algorithm is advantageous and achieved the expected goal for stabilization. A new algorithm to optimize the state feedback matrixes of the linearized two-link pendubot control system was applied and PSO led to smaller angular displacement and velocity of every link, less overshoots and shorter settling time. Omatu et al. [4] discussed a new architecture of a self-tuning neuro-PID control system and its application to stabilization of an inverted pendulum. A single-input multi-output system is considered to control the inverted pendulum by using the PID controller. Xu et al. [5] focused on experimental studies of real-time online learning control for nonlinear systems using kernel-based ADP methods. Specifically, the kernel-based dual heuristic programming (KDHP) method is applied and tested on real-time control systems. Feifei et al. [6] use the Newton-Euler method to derive the dynamic equation of the linear inverted pendulum. Mehrez [7] in their paper propose a control strategy to deal with highly dynamic systems. Li et al. [8] first describe the research background of inverted pendulum, and then derive the mathematical model of planar double inverted pendulum system by use of Lagrange modeling method. Yu et al. [9] in their paper have discussed a controller that takes the hybrid of BP neural network and least-squares algorithm to train parameters. Tharun et al. [10] have elaborated on the use of granular computing as a tool for expediting the rule explosion. Srikanth et al. [11] have contributed to the studies of inverted pendulum based on condition numbers in one of his recent works for a high-end complex dynamic system called the triple inverted pendulum.

Granular computing involves defining entities which classify certain characteristics of the system. In a hierarchy control, there are different levels of weights that define each of these characteristics which supersede or precede the given set of characteristics. When hierarchy-based granular computing is combined with fuzzy logic, fuzzy rules are defined based on the constraints of the system. The rule explosion happens based on the number of rules that define the system. There is little or no work on application of the fuzzy granular computing to the inverted pendulum system under the influence of time delay which is the proposed work in this case. The inverted pendulum modeled with transport delay yielded the condition various the serious limitation of an unwanted dead time can cause to the system is observed as part of this work. The novelty of this work can be attributed to the following important parameters.

- Inclusion of time delay into the system model and analysis.
- A novel fuzzy granular computing technique linked to the time delay and error rectification.

2 Research Methodology

The inverted pendulum on a cart is a benchmark model that is modeled under the influence of time delay here. The cart position (x) and the pendulum angle (theta) are the two parameters which are the control variables which need to be the dependent variables which are observed to be controlled by an input which is the force applied on to the cart. This cart movement causes the pendulum to swing up and stabilize the upright equilibrium position. The pendulum moves from the downward equilibrium position to the upward equilibrium position and then stays there indicating the control. Figure 1 indicates the basic mechanical structure of the pendulum on the cart whose mathematical representation is given in Eqs. 1 and 2.

Euler Lagrangian equations are used for modeling the system. These equations are derived from the basic Newtonian equations summing up the forces that are acting on the pendulum. If mass of pendulum (M) is subject to the force and x is the relative displacement of the cart position then the governing differential equation which models the dynamics of the system is given as in Eq. 1.

$$M\ddot{x} + a\dot{x} + k = F \tag{1}$$

where K and P are horizontal and vertical components of the interaction forces and 'a' is friction coefficient. The force exerted in the horizontal direction due to the moment on the pendulum is determined as in Eq. 2.

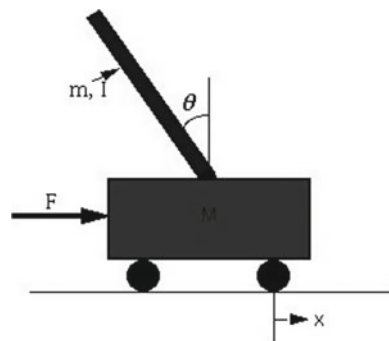
$$F = ml\ddot{\Theta} \tag{2}$$

The final dynamic equation of motions for the forces acting is based on [11]

$$(M + m)\ddot{x} + b\dot{x} - ml\ddot{\Theta} \cos \Theta + ml\dot{\Theta}^2 \sin \Theta = F \tag{3}$$

$$(I + ml^2)\ddot{\Theta} - mgl \sin \Theta = ml\ddot{x} \cos \Theta \tag{4}$$

Fig. 1 Inverted pendulum mechanical representation



The plant equation represented by Eqs. 3 and 4 take into effect the angular acceleration due to gravity, angular acceleration due to external disturbances and angular acceleration to motion of cart. On linearization of such a model, the inputs are divided into two parts out of which one input on which there is no control and the other where there is control on the input. The disturbances on which there is no control are not considered in this paper and the controlled inputs are only treated with fuzzy granular computing.

As we are aware fuzzy logic is designed for weak models with significant parameter variations and incomplete data sets, the stability analysis with fuzzy logic the implementation cycles are reduced as fuzzy sets are employed using rules. The crisp inputs for the variables are converted into fuzzy sets using membership functions as the available input and output data of the system is too vague and imprecise when a model like the inverted pendulum is considered.

2.1 Novel Fuzzy Preview Controller

The plant model has been modeled in Simulink and has been considered as a subsystem where in the transport delay was added to the system to understand the impact of time delay. The controller is designed based on PID controller and fuzzy is also developed as a subsystem which provides the necessary computation based on rule explosion defined. The cart position is taken as the reference zero and the computation is done strictly based on both the initial conditions for the pendulum and the cart position set to zero as reference condition. The developed Simulink model is given in Fig. 2 and the rule explosion is given in Fig. 3.

The controller design is based on earlier work based on pottem et al. [10] where PID-based controllers are designed, and the plant is modeled without the consideration of time delays. The rules that have been defined can be viewed as follows in Fig. 3. A weighted average method is adopted to calculate the hierarchical fuzzy PID controller as in [10] with type-1 fuzzy controller and type-2 fuzzy controller. However, the major difference is the transportation lag which would be introduced into the control loop.

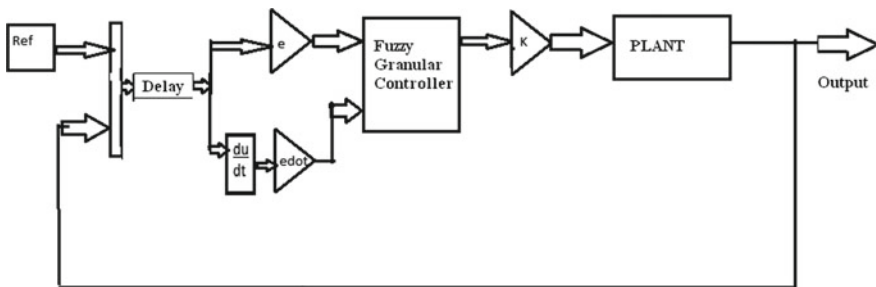


Fig. 2 Closed-loop system with transport delay for SIP

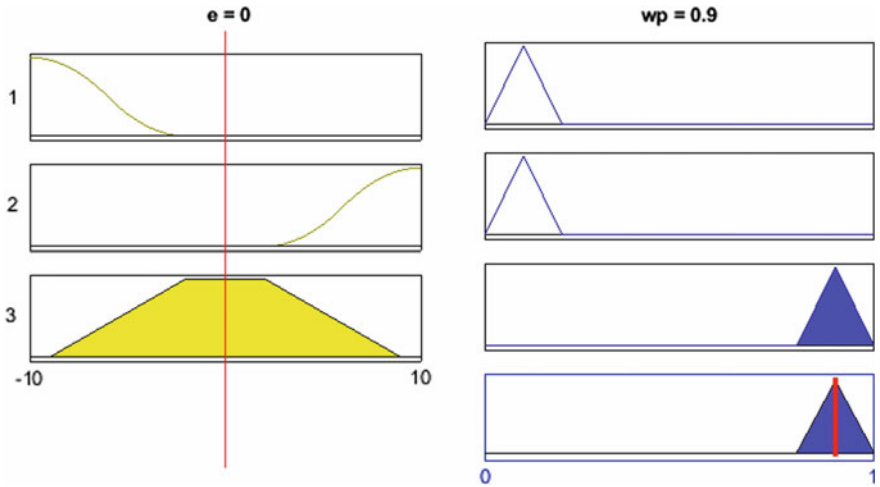


Fig. 3 Rule explosion in the fuzzy interface

$$u = e^{-st} + wp * u_{PID} + w_{type1} * u_{type1 \text{ fuzzy}} + w_{type2} * u_{type2 \text{ fuzzy}} \quad (5)$$

As given in Eq. 5, the inclusion of the time delay component causes incremental control action along with the time delays resulting in a better control strategy which is granulation causing refinement in the way the control effort is used for the smoother control of the plant model.

3 Results

The pendulum was stabilized successfully with the aid of a fuzzy granular computed controller and the PID controller which control both the angle and the pendulum. The output surface obtained using MATLAB fuzzy toolbox is given below in Fig. 4. The fuzzy toolbox output surface variation is shown in Fig. 4 which indicates the possible region in which the output angle varies.

However, as shown in the figure, the controller was not successful in stabilizing the pendulum when a unit delay was incorporated into the system dynamics. The significant impact of a unit delay which could be caused due to some suffering or due to some disturbance is considered as defined in Eq. 5 which will yield a system which will move out of the verge of stability from the input. Figures 5 and 6 indicate the variation for the cart position and Fig. 5 indicates that the system has runaway which is a sign of instability. Figure 6 indicates that the cart position is in permissible limits but is still not controlled. Figure 7 indicates the zero stability case where the pendulum was stabilizable, however, as it can be noticed in Fig. 8, the pendulum could not be stabilized even for a variation of unit delay and the pendulum oscillates about

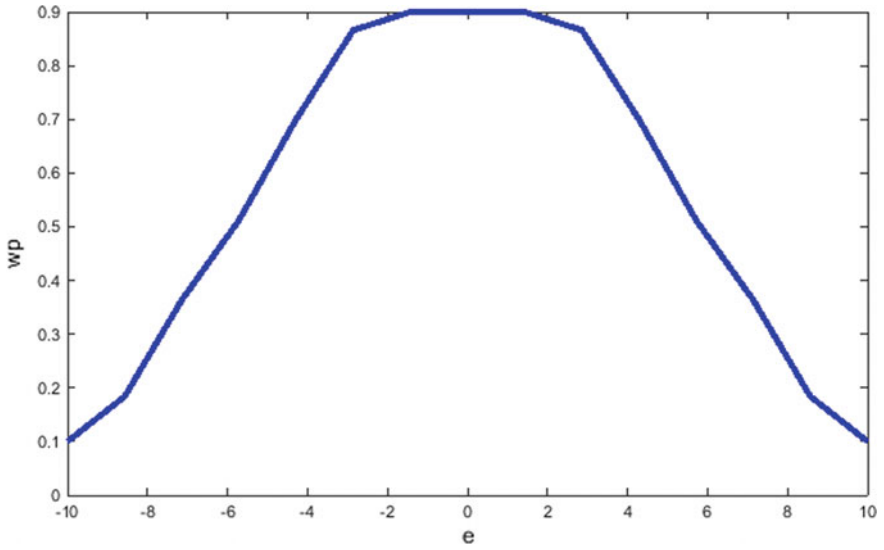


Fig. 4 Output surface variation

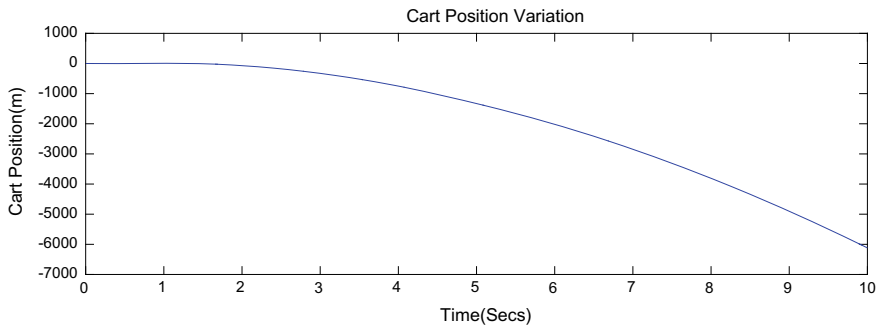


Fig. 5 Cart position variation with unit delay

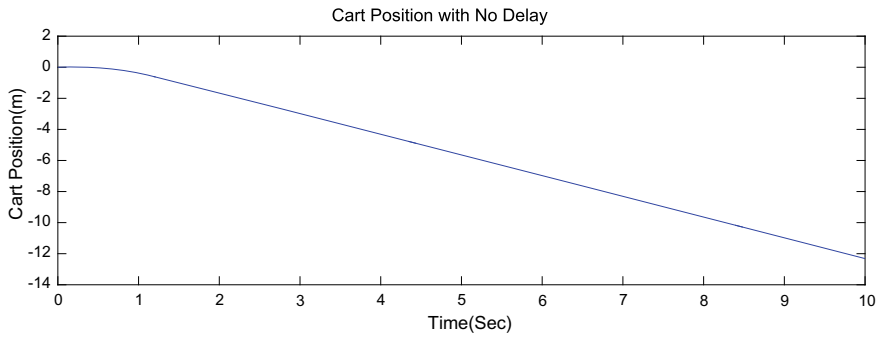


Fig. 6 Cart position variation with zero delay

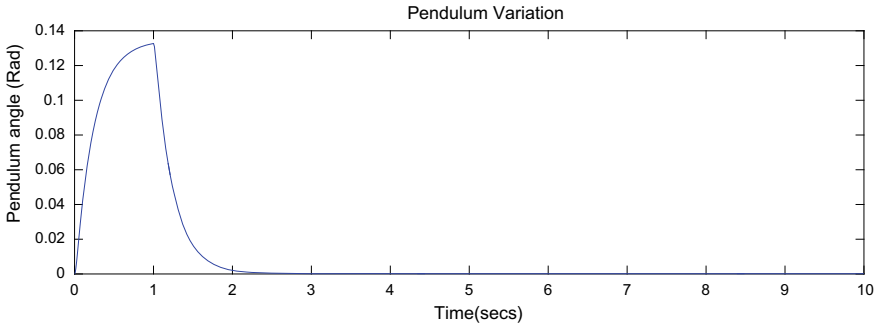


Fig. 7 Pendulum angle variation without delay

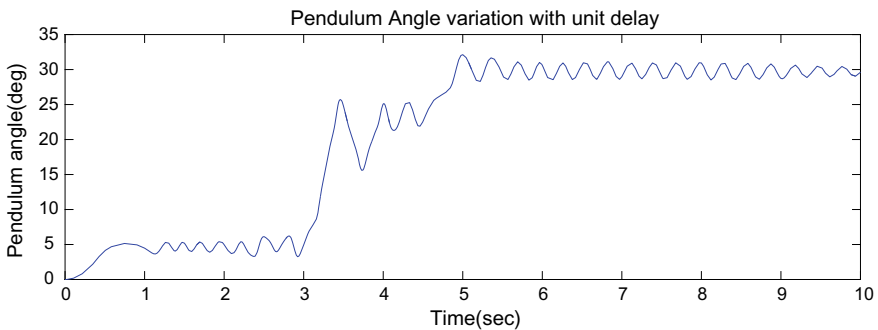


Fig. 8 Pendulum angle variation with unit delay

the final steady-state output which indicates that the system uses energy exhaustively even when a marginal delay is entered into the system. This becomes a bottleneck for high-end systems. It should be realized that traditional techniques like pole placement have limitations on the bounds defined during stability. The constraints with stability are very well handled with fuzzy preview control that is achieved in this particular case of the inverted pendulum. It is evident that the settling time and overshoot are parameters which are highly influenced. The saturation effect degrades the system stability and the eigenvalue analysis cannot be used to study stability, so in this case, the traditional techniques fail, whereas the fuzzy preview control succeeds.

In Fig. 9, the uncertainty in terms of variations with delay is studied using a funnel chart. As seen in Fig. 9, the effect on the cart position is high taking the logic 0 and logic 1 for the stability and unstable conditions. When the experiment is repeated for variations with delay, it is observed that the uncertainty mainly effects the cart position drastically than the pendulum position. This is clearly implied because the control input is immediately effecting the cart position and as a result major impact would be on the cart.

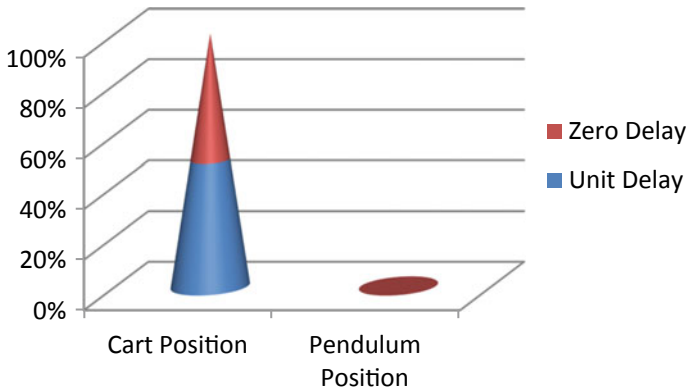


Fig. 9 Uncertainty analysis using inverted funnel chart

4 Conclusions

It can be concluded from this work that critical time delays are to be defined and considered when the system is being modeled when complex dynamic systems are being considered. The influence of dead time as suffering for the system which enters the system as transportation lag or delay is not bounded and the controller becomes ineffective when the dead time is present. This causes the system to suffer and also will destabilize the system if the delay is not in predefined bounds. Thus, when modeling robotic systems with fuzzy controllers, it is definitely a requirement that the system time delays are considered so that the system becomes robust and even under the influence of time delay the system becomes efficient. Thus, it can be concluded that when saturation effects degrade the system stability and the techniques like pole placement fail, the fuzzy preview granular computing-based controller would be a good alternative for systems with complex dynamics. Some of the major applications where the studies on the inverted pendulum system can be extrapolated are listed as (i) design of manipulator controls with conveyor-belts require proper fine tuning with inherent time delays and the model studies can be extrapolated to this hybrid system; (ii) design considerations in humanoid robots, for instance, in staircase stepping requires a lot of fuzzy information with preview and the analysis done using this method can be extended to this kind of systems; and (iii) complex higher-order dynamic systems can be evaluated using the test bed of inverted pendulum because in eigenspace analysis, the fuzzy sets involved only will change from larger sets to smaller sets with the eigenvalues that decide the control of a particular plant.

References

1. Lin CM, Mon YJ (2005) Decoupling control by hierarchical fuzzy sliding mode controller. *IEEE Trans Control Syst Technol* 13(4)
2. Cheng YC, Lin SF, Hsu CY, Q-value based particle swarm optimization for reinforcement neuro fuzzy system design. *Int J Comput Sci Eng* 3(10)
3. Yuan S, Wang D, Li X (2009) Research on control of pendubot based on PSO algorithm. In: 2009 International conference on computational intelligence natural computing, IEEE computer society, pp 346–349
4. Omatu S, Fujinaka T, Yoshioka M (2000) Neuro-PID control for inverted single and double pendulums. In: *IEEE 2000*, pp 2685–2690
5. Xu X, Lian C, Zuo L, He H (2013) Kernel-based approximate dynamic programming for real-time online learning control: an experimental study. *Control Syst Technol IEEE Trans* 22:99–110. <https://doi.org/10.1109/tcst.2013.2246866>
6. Feifei R, Lei Z, Le T, Yanhai H, Pengpeng Z (2013) Design and research of double closed-loop control strategy for inverted pendulum system. In: *Intelligent system design and engineering applications (ISDEA)*, third international conference, pp 550–553, 16–18 Jan 2013
7. Mehrez O, Ramadan A (2012) A control strategy for designing an intelligent controller for highly dynamic/perturbed systems. In: 2012 12th international conference on control, automation and systems (ICCAS), pp 924–929, 17–21 Oct 2012
8. Li Z, Zhang X, Chen C, Guo Y (2012) The modeling and simulation on sliding mode control applied in the double inverted pendulum system. In: 2012 10th world congress on intelligent control and automation (WCICA), pp 1089–1091, 6–8 July 2012
9. Yu J, Huang L, Zhou S (2012) Fuzzy Control of linear flexible double inverted pendulum system. In: *International conference on control engineering and communication technology (ICCECT)*, pp 342–345, 7–9 Dec 2012
10. Tharun PS, Nigam MJ (2013) Hierarchical fuzzy PID controller using granular computing for inverted pendulum. *Int J Electr Electron Data Commun Directory Open Access J (Sweden)*, 07-01-2013
11. Kavirayani S, Salma U (2019) Fuzzy granular computing controls Ill-conditioned matrix definitions for triple inverted pendulum. In: Nayak J, Abraham A, Krishna B, Chandra Sekhar G, Das A (eds) *Soft computing in data analytics. Advances in intelligent systems and computing*, vol 758. Springer, Singapore

Electrical Faults in Photovoltaic Modules: Analysis, Characterization and Detection



Priya Ranjan Satpathy, Sasmita Jena, Sobhit Panda and Renu Sharma

Abstract Photovoltaic (PV) modules are installed in the field to deliver possible maximum power to the load. However, the PV modules encounter various electrical faults during operation that results in severe power loss, failure and performance degradation of the system. Also, the lack of fault knowledge among the PV manufacturer and installers has resulted in severe accidents and fire hazards in some cases. The scope of this paper covers the description on various electrical faults, their occurrence and impact on the performance of PV modules. The faults include interconnect and connection faults, bridge and earth faults, shunt path development faults and mismatch faults that commonly occurs in the field-installed PV systems. The effect of these electrical faults on the equivalent circuit and characteristics curves of the PV modules has been studied using MATLAB/Simulink. The analysis presented clearly indicates the adverse effect of these faults in the power generation and performance of the PV modules. Also, a short survey on various fault detection techniques proposed in the literatures has been done.

Keywords Photovoltaic · Electrical faults · Power loss · Detection

P. R. Satpathy (✉) · S. Jena · R. Sharma
Department of Electrical Engineering, ITER, SOA Deemed to be University, Bhubaneswar, India
e-mail: priransat3@gmail.com

S. Jena
e-mail: sasmita.jena500@gmail.com

R. Sharma
e-mail: renusharma@soa.ac.in

S. Panda
Department of Instrumentation and Electronics Engineering, CET, Bhubaneswar, India
e-mail: sobhitpanda25@gmail.com

© Springer Nature Singapore Pte Ltd. 2020
R. Sharma et al. (eds.), *Innovation in Electrical Power Engineering, Communication, and Computing Technology*, Lecture Notes in Electrical Engineering 630,
https://doi.org/10.1007/978-981-15-2305-2_21

1 Introduction

Photovoltaic (PV) systems are considered as an integral solution for accomplishing energy security, social equity and mitigation of environmental impact challenges [1, 2]. Various advantages such as no moving parts, environmentally friendly nature, source abundance, low temperature operation, no sound production and low maintenance have made PV systems a promising source of renewable power generation [3]. PV modules are the core of a PV system that are connected in series and parallel configurations to form an array in order to deliver the power desired by the load [4]. However, the modules face enormous faults during operation that result in power losses, failures, accidents, efficiency degradation and reduced reliability. So, fault analysis and diagnosis of PV modules have been considered as an important field of research nowadays [5].

Fault monitoring systems are playing a key role in PV systems for analysis and detection of faults equipped with diagnosis algorithms [6]. However, monitoring systems (MS) add additional cost to the system, so the installation of MS in residential and small PV plants is mainly ignored. In general, small PV systems are not checked regularly for which undetectable faults can occur in the system that leads to energy and financial losses [7–9]. Also, undetected and unclear fault in the PV system for long term cannot only results in the power losses, components damage and failure but also leads to safety issues and fire hazards [10]. In fact, recent incidents (Bakersfield, California in April 5, 2009 and Mount Holly, North Carolina in April 16, 2011) have raised a major concern regarding the impact of faults that resulted in severe fire hazards [11]. In general, PV systems encounter various faults such as visual, thermal and electrical where the visual and thermal faults can be observed by color and thermal property change of the module and detected by using thermal cameras and other equipment. However, electrical faults are most promising to the PV systems that affect the system performance by reducing power generation and efficiency. Also, these faults can lead to system failure, severe damage to components such as modules and fire hazards [12, 13]. So, understanding the types of faults with their causes and effects in the PV arrays is one of the major aspects of preventing power losses, efficiency degradation and undesirable hazards like fire.

The aim of this paper is to perceive, simulate and discuss various electrical faults that occur in DC side (modules) of the PV system. The study has been carried out in MATLAB/Simulink environment and mainly focused on the electrical voltage and current inspection. The effect of various electrical faults has been studied by analyzing the characteristics curves of the PV module. Also, a literature survey of various fault detection techniques of PV system has been done.

2 System Description

2.1 Mathematical Modeling of the PV Module

A PV module mainly consists of series-connected cells given by a circuit (see Fig. 1) and can be modeled using the equations as given below.

$$I_{PV} = I_{ph} - I_o \left[\exp \left(\frac{V_{pv} + R_s I_{pv}}{A} \right) - 1 \right] - \left[\frac{(V_{pv} + I_{pv} R_s)}{R_{sh}} \right] \tag{1}$$

where I_{PV} and I_{ph} are the current output and photo generated current of module, A is the ideality factor, V_{PV} represents the voltage of the cell, R_S represents the series resistance and R_{Sh} represents the shunt resistance.

2.2 Specification and Characteristics of the PV Module

The specification of the PV module at standard testing condition (STC) considered for the study has been given in Table 1.

The PV module (WS-50 W) consists of 36 numbers of series-connected cells generating maximum power of 50 W at STC. The characteristics curves of the module operating under various irradiance levels and operating temperatures have been represented in Figs. 2 and 3, respectively. The curves clearly state the direct depen-

Fig. 1 Circuit representation of a PV module

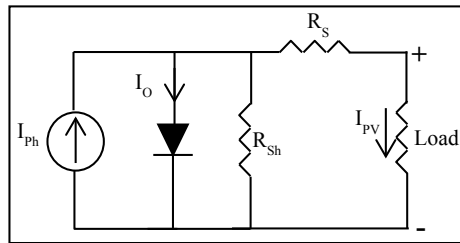


Table 1 Specification of PV module at STC (1000 W/m² and 25 °C)

Parameters	Rating
Maximum power (P_M)	50 W
Maximum voltage (V_M)	17.47 V
Maximum current (I_M)	2.862 A
Open-circuit voltage (V_{OC})	21.56 V
Short-circuit current (I_{SC})	3.10 A

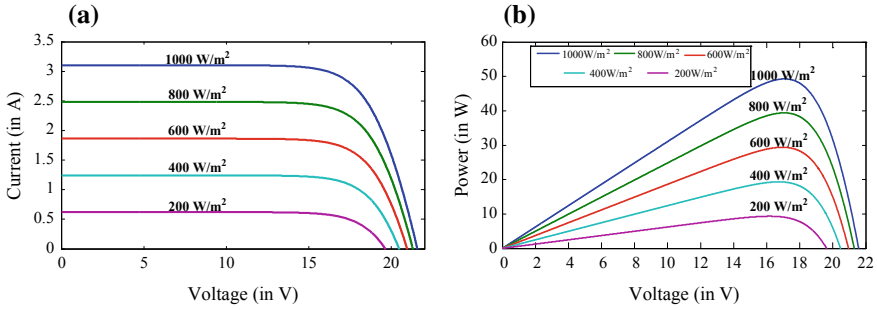


Fig. 2 Characteristics curves of the PV module under various irradiance levels. **a** Current–voltage ($I-V$) curve. **b** Power–voltage ($P-V$) curve

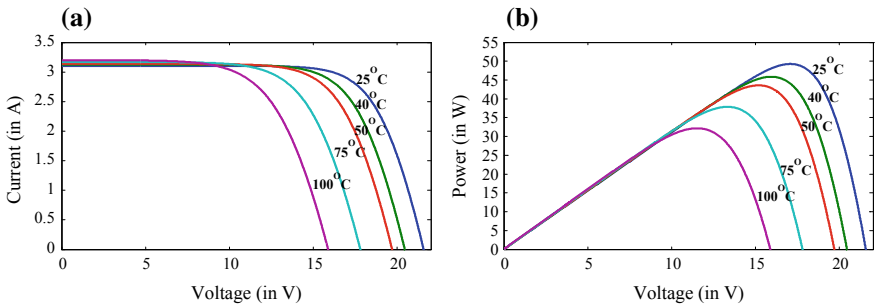


Fig. 3 Characteristics curves of the PV module under various operating temperatures. **a** Current–voltage ($I-V$) curve. **b** Power–voltage ($P-V$) curve

dependency of current on irradiance level and inverse dependency of voltage on operating temperature of the module.

3 Electrical Faults Analysis and Characterization

The most common electrical faults that occur in PV modules and their effect on the operation have been discussed in this section. The faults include: interconnect and connection faults, bridge and earth faults, shunt path development faults and mismatch faults. The effect of these faults on the equivalent circuit and characteristics curves of the module has been studied. The major parameter (voltage or current) associated with the power losses during each fault has been figured out. Also, the efficiency and performance ratio of module during each fault have been calculated mathematically.

3.1 Interconnect and Connection Faults

Overview: Though the PV cell is incapable of generating useful voltage or current, so a group of cells are connected in series and parallel to form a module and generate the useful voltage and current level. In general, the front surface of the cell is printed with a grid of silver fingers and series connection is carried out by soldering the cell’s silver fingers using copper ribbons (interconnects). However, the reliability of the module gets reduced by solder joint failure that can occur due to temperature, salt mist, humidity and thermal cycling leading to coarsening, stress and creep.

Effect: The interconnect and connection faults result in an increased series resistance (R_s) of the module and its equivalent circuit. This reduces the slope of $I-V$ curve near open-circuit voltage (V_{OC}) leading to power loss.

Analysis: The effect of interconnect and connection faults have been studied by operating the module at various irradiance levels (400–800 W/m²) having different series resistances ranging from 0 to 0.4 Ω . The characteristics curves of the module during faults have been shown in Fig. 4 that clearly indicate the notable reduction in voltage as compared to current of the module. The right-most curves during different irradiance correspond to fault free PV module.

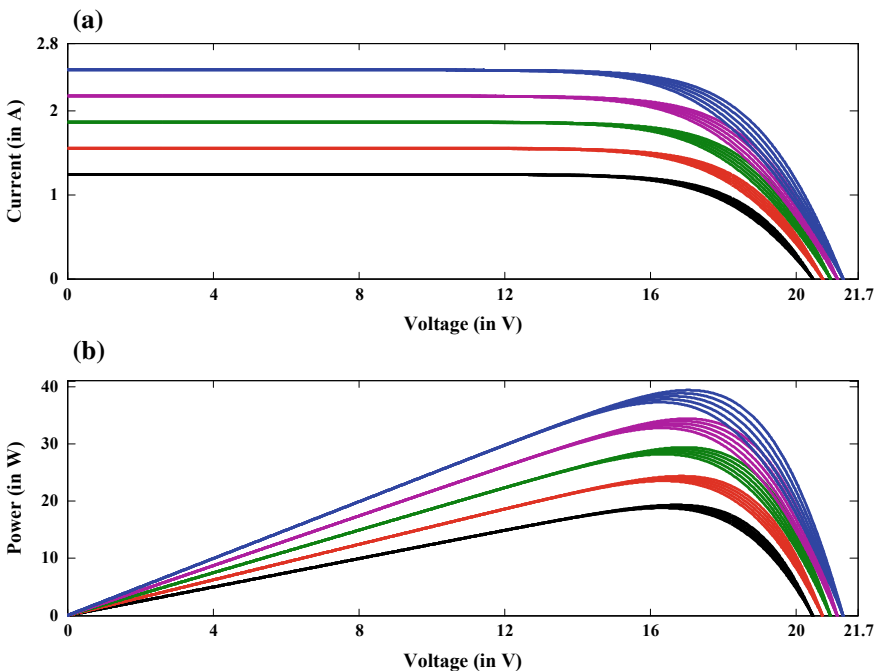


Fig. 4 Characteristics curves of the module operating at different irradiance levels during interconnect and connection faults. **a** Current–voltage ($I-V$) and **b** power–voltage ($P-V$) curve

3.2 Bridge and Earth Faults

Overview: When a connection occurs between interconnects or interconnects and earth or two points with different potential, earth fault takes place. Encapsulation deterioration, water corrosion, development of internal resistance, short circuit, disconnection due to bypass diodes, ion migration, metal corrosion, impact damage and surface conduction are stated as the main causes of earth faults. The peak reverse voltage and junction temperature are the main parameters that affect the lifespan of bypass diodes as high temperature disable them resulting in short-circuit failure causing bridge faults.

Effect: The bridge and earth faults result in short circuiting of the cells connected to the PV module and hence severely reduce the voltage proportional to the number of sorted cells.

Analysis: The effect of bridge and earth faults has been studied by sorting the cells of modules and operating them at different irradiance levels. The sorted cells number ranges from 0 to 10 cells where zero sorted cells correspond to the faults free module. The characteristics curves of the module during bridge and earth faults have been depicted in Fig. 5 that represent a serious voltage reduction of the module with an increasing sorted cells number.

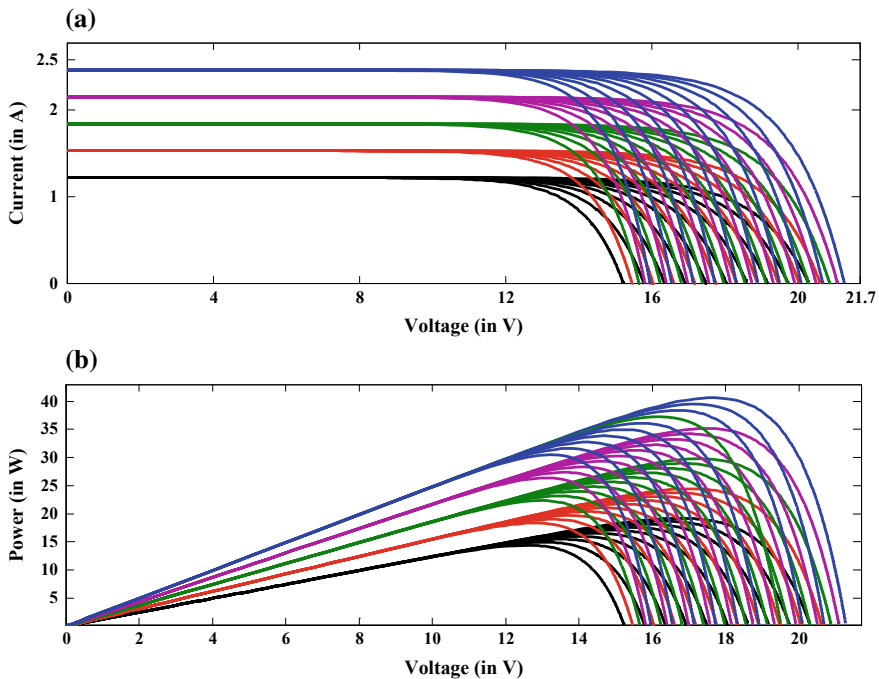


Fig. 5 Characteristics curves of the module operating at different irradiance levels during bridge and earth faults. **a** Current–voltage ($I-V$) and **b** power–voltage ($P-V$) curve

3.3 Shunt Path Development Faults

Overview: These faults mainly occur when a connection or moisture forms a shunt path between the positive and negative terminals of PV module due to deterioration in conductor insulation.

Effect: The shunt path development faults result in the decrement of shunt resistance (R_{Sh}) in the equivalent circuit of PV module that increases the slope of $I-V$ curve near short-circuit current (I_{SC}).

Analysis: The effect of shunt path development faults has been analyzed by operating the module at different irradiance levels (400–800 W/m²) with different values of shunt resistance ranging from 100 to 1000 Ω . The characteristics curves of the module during this fault have been presented in Fig. 6. The graphs clearly represent that the power generation of the modules reduces with a decrease in current output more than decrease in voltage.

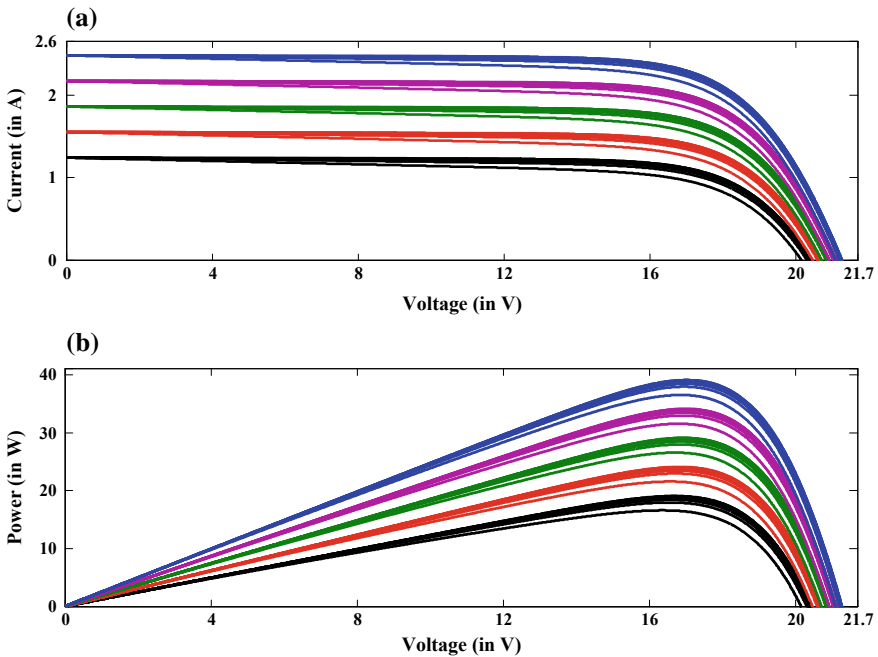


Fig. 6 Characteristics curves of the module operating at different irradiance levels during shunt path development faults. **a** Current–voltage ($I-V$) and **b** power–voltage ($P-V$) curve

3.4 Mismatch Faults

Overview: Mismatch faults mainly occur due to partial shading among the cells of the PV module. Partial shading can take place due to shadow of nearby buildings and trees, soiling, dust accumulation, bird litters, broken module glass, etc. During this situation, the cells of PV module receive different irradiance levels results in power loss. Generally, a bypass diode is connected in parallel with 18 numbers of series cells to bypass the higher current generated by the unshaded modules and remove hotspot effect. However, the failure of bypass diodes can result in severe power loss in the modules.

Effect: The mismatch faults reduce the power output of the modules leading to local heat (or hotspot) formation in the shaded cells that result in permanent damage of the module and fire hazards.

Analysis: The effect of mismatch fault has been studied by partially shading single cells (10th cell and 20th cell) and two consecutive cells (18th cell and 19th cell). The characteristics curves of the PV module during various mismatch fault conditions have been shown in Fig. 7.

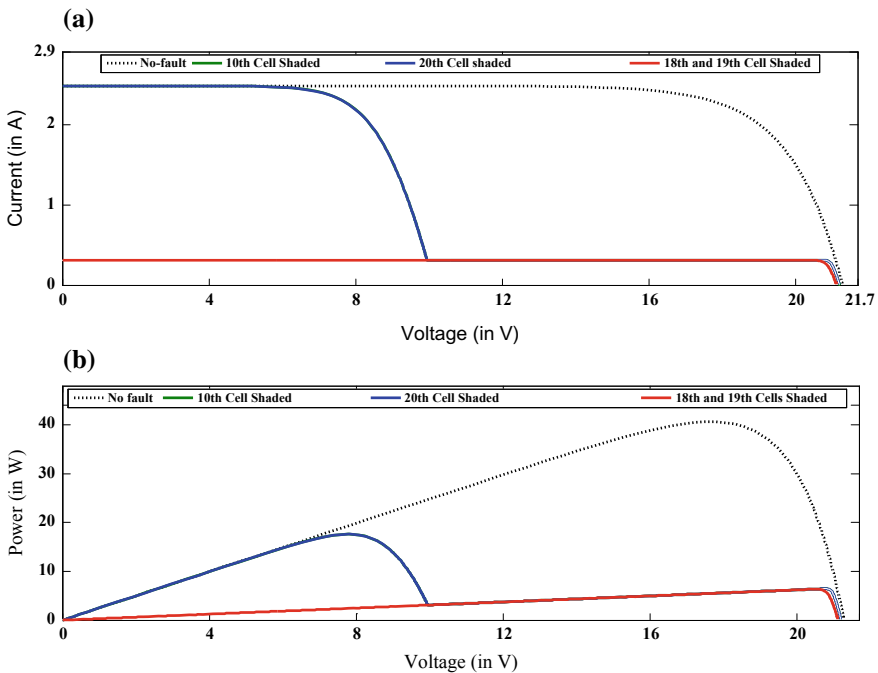


Fig. 7 Characteristics curves of the module operating during mismatch faults. **a** Current–voltage (I – V) and **b** power–voltage (P – V) curve

The graphs indicate that when cell belonging a single bypass diode group get shaded, the characteristics curve resulted in multiple peaks formation with maximum power point (MPP) lies at the first peak. However, when cells belonging to both the bypass diodes group get shaded, the curve formed a single peak with reduced power. Also, it has been noted that there is a significant reduction of maximum voltage generated by the module during mismatch faults.

4 Electrical Faults Detection and Diagnosis

Various PV fault detection techniques have been proposed in the literatures that utilize on-site data measurement such as irradiance, temperature, operating current and voltage, generated power, power loss and fill factor. An algorithm based on artificial neural network (ANN) to detect the normal, mismatch, ground and bridge faults using the operating temperature, current and voltage of the module has been proposed [14]. Another decision tree-based algorithm that requires past data under normal and faulty conditions to detect various faults in PV module with high accuracy has been proposed [15]. A string level fault detection technique that compares the current output of each string to locate the faulty string has been proposed in the literature [16]. A PV cell health monitoring system using infrared thermograph (IF) for hotspot detection has been proposed [17]. The quality of PV cell can be monitored using thermal camera with light beam induced voltage/Current (LBIV/LBIC), electroluminescence (EL), photoluminescence (PL) based instruments [18, 19]. A fault detection technique that compares the actual $I-V$ curve with expected curve of the PV array has been proposed [20]. The summary of other PV faults and their detection techniques have been presented in Table 2.

5 Conclusion

In this paper, the causes, effect and analysis of the most common faults, i.e., interconnect and connection faults, bridge and earth faults, shunt path development faults and mismatch faults on the equivalent circuit and characteristics curves of PV modules have been discussed. It has been established that the PV faults affect the characteristics curves and power generation of the module by either reducing the voltage and current. Also, the long term existence of these faults can result in permanent damage of module and fire hazards in some cases. Various faults detecting techniques proposed in the literatures have been surveyed.

Table 2 Different types of faults and their detection techniques in PV system

Fault type	Detection techniques	Fault locating equipment
Ground fault	Measurement of fault current	Ground fault detection interruption (GFDI), differential current measurement (DCM)
	Voltage and current measurement	Minimum covariance determinant (MCD) estimator [21]
	Reflectometry	Spread spectrum time domain reflectometry (SSTDR) [22]
Line-to-line fault	$I-V$ curve simulation and comparison	PV simulator [20]
	On-site measurement of voltage and current	ANN [14], decision tree algorithm [15]
	Reflectometry	Time domain reflectometry (TDR) [23]
Open fault	On-site measurement of voltage and current	Decision tree algorithm [15]
	Reflectometry	Time domain reflectometry (TDR) [23]
Series-arc fault	Voltage and current measurement	Minimum covariance determinant (MCD) estimator [21]
	PV current frequency domain analysis	Arc-fault circuit interrupter (AFCI) [24]
Parallel-arc fault	Current/voltage drop detection with frequency domain analysis	AFCI with current/voltage sensing and measuring equipment [24]
Bypass diode failure	Diode testing and sensing temperature	Multimeter and infrared [25]
Hotspot formation	Thermograph	Infrared [17]
Dust/soiling	Visual inspection, thermograph	Infrared [17]

References

- Jena S, Kar SK (2019) Setting a fostered energy network by decarbonizing the grid: hybridization, control, and future solutions upon storage. *Int J Energy Res* 43(1):455–474
- Satpathy PR, Sharma R (2019) Diffusion charge compensation strategy for power balancing in capacitor-less photovoltaic modules during partial shading. *Appl Energy* 255:113826
- Satpathy PR, Sharma R (2019) Power and mismatch losses mitigation by a fixed electrical reconfiguration technique for partially shaded photovoltaic arrays. *Energy Convers Manag* 192:52–70
- Satpathy PR, Sharma R, Dash S (2019) An efficient SD-PAR technique for maximum power generation from modules of partially shaded PV arrays. *Energy* 175:182–194
- Nehme B, M'Sirdi NK, Akiki T, Naamane A (2014) Contribution to the modeling of ageing effects in PV cells and modules. *Energy Procedia* 62:565–575
- Dhimish M, Holmes V, Mehrdadi B, Dales M, Mather P (2017) Photovoltaic fault detection algorithm based on theoretical curves modelling and fuzzy classification system. *Energy* 140:276–290

7. Ducange P, Fazzolari M, Lazzarini B, Marcelloni F (2011) An intelligent system for detecting faults in photovoltaic fields. In: 2011 11th international conference on intelligent systems design and applications (ISDA), pp 1341–1346
8. Shojaee S, Davarifar M, Varahram MH, Davari A (2006) Implementation of remote meter reading via power line. In: RCEE 2006, Gonabad Azad University, Iran
9. Davarifar M, Daneshi-Far Z, Fayyaz H (2009) Implementation of automate remote meter reading (AMR) via BPL in Kish Island. In: International power system conference (PSC), Tehran, Iran
10. Zhao Y, Lehman B, DePalma JF, Mosesian J, Lyons R (2010) Fault evolution in photovoltaic array during night-to-day transition. In: 2010 IEEE 12th workshop on control and modeling for power electronics (COMPEL), pp 1–6
11. Falvo MC, Capparella S (2015) Safety issues in PV systems: design choices for a secure fault detection and for preventing fire risk. *Case Stud Fire Saf* 3:1–16
12. Alam MK, Khan FH, Johnson J, Flicker J (2013, June) PV faults: overview, modeling, prevention and detection techniques. In: 2013 IEEE 14th workshop on control and modeling for power electronics (COMPEL), IEEE, pp 1–7
13. Buddha S, Braun H, Krishnan V, Tepedelenioglu C, Spanias A, Yeider T et al (2012) Signal processing for photovoltaic applications. In: 2012 IEEE international conference on emerging signal processing applications (ESPA), pp 115–118
14. Li Z, Wang Y, Zhou D, Wu C (2012, October) An intelligent method for fault diagnosis in photovoltaic array. In: International computer science conference, pp 10–16. Springer, Berlin, Heidelberg
15. Zhao Y, Yang L, Lehman B, de Palma JF, Mosesian J, Lyons R (2012, February) Decision tree-based fault detection and classification in solar photovoltaic arrays. In: 2012 twenty-seventh annual IEEE applied power electronics conference and exposition (APEC), IEEE, pp 93–99
16. Takehara N, Fukae K (1997) US Patent No. 5,669,987. Washington, DC, US Patent and Trademark Office
17. Ancuta F, Cepisca C (2011, July). Fault analysis possibilities for PV panels. In: Proceedings of the 2011 3rd international youth conference on energetics (IYCE), IEEE, pp 1–5
18. Colvin J (2009) Comparative failure analysis of photovoltaic devices. In: Conference proceedings of the 35th international symposium of testing and failure analysis, pp 149–156. ASM International
19. Alers GB (2011) Photovoltaic failure analysis: techniques for microelectronics and solar. In: PV module reliability workshop, Colorado, USA
20. Stellbogen D (1993, May) Use of PV circuit simulation for fault detection in PV array fields. In: Conference record of the twenty third IEEE photovoltaic specialists conference-1993 (cat. no. 93CH3283-9), IEEE, pp 1302–1307
21. Braun H, Buddha ST, Krishnan V, Spanias A, Tepedelenioglu C, Yeider T, Takehara T (2012, March) Signal processing for fault detection in photovoltaic arrays. In: 2012 IEEE international conference on acoustics, speech and signal processing (ICASSP), IEEE, pp 1681–1684
22. Alam MK, Khan F, Johnson J, Flicker J (2013, Sept) PV ground-fault detection using spread spectrum time domain reflectometry (SSTD). In: 2013 IEEE energy conversion congress and exposition, IEEE, pp 1015–102
23. Takashima T, Yamaguchi J, Otani K, Oozeki T, Kato K, Ishida M (2009) Experimental studies of fault location in PV module strings. *Sol Energy Mater Sol Cells* 93(6–7):1079–1082
24. Johnson J, Montoya M, McCalmont S, Katzir G, Fuks F, Earle J, Fresquez A, Gonzalez S, Granata J (2012, June) Differentiating series and parallel photovoltaic arc-faults. In: 2012 38th IEEE photovoltaic specialists conference, IEEE, pp 000720–000726
25. Kato K (2012) PV module failures observed in the field-solder bond and bypass diode failures. In: 27th EUPVSEC

Detection and Classification of Voltage Sag Causes Based on S-Transform and Extreme Learning Machine



**Bhaskar Patnaik, Rasmi Ranjan Panigrahi, Manohar Mishra,
Ranjan Kumar Jena and Manoj kumar Swain**

Abstract This manuscript presents a method based on S-transform (ST) and extreme learning machine (ELM) to identify the causes of voltage sag. Exact recognition of voltage sag causes (VSCs) can help decrease the problems initiated due to voltage dip in electric power system. ST is a well-known time–frequency analysis technique. Initially, the extracted voltage signals are pre-processed through ST and several statistical features are extracted, which are later applied as inputs to ELM classifier for voltage sag cause detection. Here, three significant causes are simulated for voltage sag in MATLAB/Simulink, like (i) single-phase and three-phase fault, (ii) starting of induction motor and (iii) energization of transformer. The performance of the proposed technique is compared with other existing voltage sag cause classification techniques. The classification results indicate the ability of the proposed technique for detection and classification of VSCs more accurately.

Keywords S-transform · Extreme learning machine · Voltage sag causes

B. Patnaik · R. K. Jena

Department of Electrical Engineering, CAPGS, Biju Patnaik University of Technology, Rourkela 769004, India

e-mail: bhaskar7310@gmail.com

R. K. Jena

e-mail: capgs.rkjena@bput.ac.in

R. R. Panigrahi (✉)

Department of Electrical Engineering, ITER, Siksha ‘O’ Anusandhan (Deemed to Be University), Bhubaneswar 751030, India

e-mail: rasmi.ranjanp@gmail.com

M. Mishra

Department of Electrical and Electronics Engineering, ITER, Siksha ‘O’ Anusandhan (Deemed to Be University), Bhubaneswar 751030, India

e-mail: manohar2006mishra@gmail.com

M. Swain

Department of Electrical Engineering, Gandhi Engineering College, Bhubaneswar 752054, India
e-mail: bappi.luna@gmail.com

© Springer Nature Singapore Pte Ltd. 2020

R. Sharma et al. (eds.), *Innovation in Electrical Power Engineering, Communication, and Computing Technology*, Lecture Notes in Electrical Engineering 630,

https://doi.org/10.1007/978-981-15-2305-2_22

1 Introduction

This modern era has been witnessing a meteoric rise in the presence of advanced power electronics converters in electrical power systems (EPSs), intensifying the concerns towards apprehensible threat to the power quality (PQ) [1]. If the sources and/or causes of voltage dip are detected timely and accurately, then it can very well help to plan and put in action the remedial measures [2, 3]. The most influential and apparently detrimental to a good power quality, amongst all PQ disturbances (PQDs), is voltage sag [4]. The main reasons behind this disturbance are faults due to short circuit (SC), switching on of an induction motor (IM) and energization of a transformer. Consequence upon a voltage sag phenomenon, the voltage magnitude (in terms of its RMS value), can decrease up to 0.9 pu within a time span of 1/2–30 cycles [4]. The characteristics of voltage sags produced by discrete sources are unique in several ways. For example, amplitude (A), time period (T), phase angle jump and harmonics contents are some of the distinctive features of a voltage sag [3]. This work confers the techniques for voltage sag cause (VSC) identification and their classification.

Several PQ detection approaches have been presented by academicians and people from industry relying on signal-processing tools like Fourier transform (FT), short-time Fourier transform (STFT), wavelet transform (WT), multi-resolution analysis (MRA) and Hilbert–Huang transform. Amongst these, a few have been depicted in the literature [3, 5, 6]. The authors in [3] enumerated a unique approach for detection of VSCs based on HHT. The methodology uses instantaneous frequency curve to determine the point of mutation, frequency components and signal amplitude. Afterwards, these indices have been utilized to ascertain the sources of voltage sag. Here, the instantaneous frequency curve was derived from the output of EMD followed by Hilbert transform. The average rate of accuracy was observed to be 96%. The authors in [5] proposed a different approach for detection of voltage sag causes. It is a combination of HHT and probabilistic neural network (PNN). While the EMD along with HT is for distinctive feature extraction, the PNN helped classifying the disturbances. In this case, the accuracy is 98.63%. Also, comparative studies amongst available techniques on WT-based feature as well as those available on multi-neural network (MNN)-based classification have been done. The overall accuracies were observed to be 83.63% employing WT-MNN, 96.36% with EMD-MNN and 85.90% with WT-PNN. Similarly, the authors in [6] presented HHT and PNN-based approach to identify voltage sag causes. The efficiency of the proposed approach was observed to be 97.66%. From this survey, it could be inferred that there is no method which could detect the VSCs with 100% accuracy. Moreover, the published literatures do not include noise-infested conditions for verification of detection proficiency.

In this work, the role of ST to detect and classify the causes of voltage sag has been analysed. The S-transform (ST) is an extension to WT. It is vastly similar to the FT. Moreover, the formulation of ST involves selection of a particular mother wavelet derived from a continuous WT and multiplying it with a phase correction factor. Thus, the ST is basically a phase-corrected continuous WT [7, 8]. The output matrix

of ST provides a range of distinctive features extracted from the disturbance signal. These features serve as feed to the ELM classifier for precise classification of VSCs. The results of this classification confirm that the technique proposed is capable of detecting and classifying VSCs quickly and more accurately. In this analysis, three significant causes of voltage sag are simulated in MATLAB/Simulink, for instance (i) single phase-to-ground and three-phase fault, (ii) switching on an IM and (iii) energization of a transformer.

The rest parts of this article are presented in a manner as follows: a concise description of S-transform theory and process involved in feature extraction using it is described in Sect. 2. The analysis of VSCs and the performance of ST on these disturbance signals visually are presented in Sect. 3. The theory behind ELM as a classifier of VSCs is described in Sect. 4. Finally, in Sects. 5 and 6, results and conclusions have been presented.

2 S-Transform and Feature Extraction

As reported by various articles cited in Refs. [7–9], by using ST to the measured voltage signals at the relaying point, numerous PQ events have been analysed. By considering the paper length policy, a shortened description of ST has been provided.

The continuous ST for input signal $v(t)$ is expressed in Eq. (1).

$$s(t, f) = \frac{|f|}{\sqrt{2\pi}} \int_{-\infty}^{\infty} v(t) e^{-\frac{(t-\tau)^2 f^2}{2}} e^{-i2\pi f t} d(t) \tag{1}$$

The Gaussian window width can be numerically presented as:

$$\sigma(f) = T = \frac{1}{|f|} \tag{2}$$

Let $v[kt]$, $k = 0, 1, \dots, N - 1$ be a discrete time-variant signal equivalent of $v(t)$ having sampling rate T .

Now, the discrete FT of $v[kt]$ can be obtained as [7–9]

$$V\left(\frac{n}{nT}\right) = \frac{1}{N} \sum_{k=0}^{N-1} v[kT] e^{-\frac{2\pi n k}{N}} \tag{3}$$

where $n = 0, 1, \dots, N - 1$. Applying Eq. (3), ST of a discrete time-variant signal $v[kt]$ is calculated by allowing f which tends to $\frac{n}{NT}$ and τ approaching to jT . Therefore, discrete ST can be specified as presented in Eq. (4).

$$S\left[jT, \frac{n}{NT}\right] = \sum_{m=0}^{N-1} V\left[\frac{m+n}{NT}\right] G(m, n) e^{\frac{2\pi m j}{N}} \tag{4}$$

where

$$G(m, n) = e^{-2\pi^2 m^2 \alpha^2} \tag{5}$$

And $\alpha = 1/b$;
 $n \neq 0; n = 1, 2, 3, 4, \dots, N - 1$;
 $j = m = 0, 1, 2, 3, 4, \dots, N - 1$;

where N is the number of samples and $b = 0.3-5$ considering different resolutions.

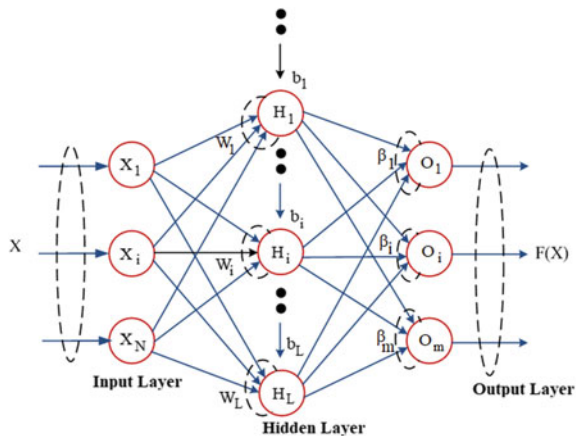
The overall computation of ST required $(N + N \log N)$ numbers of operation. The final result of S-transform is a $N \times M$ matrix named as the S-matrix, where the rows and columns relate to frequency (f) and time (t) information, respectively, and each element is a complex quantity. The S-matrix is denoted in a t versus f plot as in wavelet transform (WT).

In this work, several unique features, for example energy, standard deviation, kurtosis, etc., are extracted from the non-stationary power signals using S-matrix.

3 ELM

The extreme learning machine was at first proposed by Huang and his co-authors [10]. It is basically a feed-forward neural network with single hidden layer, as shown in Fig. 1. It delivers enhanced overall performance in terms of quicker learning, reduced computational requirement [11], with respect to other computational tools or processes. Each of the input layer nodes and hidden layer nodes is assigned

Fig. 1 Single-hidden layer feed-forward network (SLFN)



with weight matrix in a random manner. So to say, the weight matrix is computed mathematically only once.

Consider ‘ N ’ numbers of training samples (x_i, t_i) , where

$$\begin{aligned} x_i &= [x_{i1}, x_{i2}, \dots, x_{iN}]^T \in R^n \text{ and} \\ t_i &= [t_{i1}, t_{i2}, \dots, t_{im}]^T \in R^m \end{aligned} \tag{6}$$

Here, n is the length of the input vector, m stands for the total number of classes and L represents the numbers of hidden nodes.

The SLFNs can be mathematically put as:

$$F_L(x_j) = \sum_{i=1}^L \beta_i g_i(x_j) = \sum_{i=1}^L \beta_i G_i(w_i, b_i, x_j) = t_j \tag{7}$$

where $j = 1, 2, \dots, N$.

Now, Eq. (7) can be rewritten as:

$$H * \beta = T \tag{8}$$

where H is the output matrix of hidden layer, β is the output weight matrix and T is the target vector.

$$\begin{aligned} H &= \begin{bmatrix} h(x_1) \\ \vdots \\ h(x_N) \end{bmatrix}_{N \times L} = \begin{bmatrix} G(w_1, b_1, x_1) & \cdots & G(w_L, b_L, x_1) \\ \vdots & \cdots & \vdots \\ G(w_1, b_1, x_N) & \cdots & G(w_L, b_L, x_N) \end{bmatrix}_{N \times L} ; \\ \beta &= \begin{bmatrix} \beta_1^T \\ \vdots \\ \beta_L^T \end{bmatrix}_{L \times m} \text{ and } T = \begin{bmatrix} t_1^T \\ \vdots \\ t_L^T \end{bmatrix}_{N \times m} \end{aligned} \tag{9}$$

$\beta = H^\dagger T$ [as in Eq. (8)].

Here, H^\dagger signifies the ‘Moore–Penrose generalize inverse matrix’.

Addition of a small value of $1/\lambda$ to the diagonal of H^*H^T or H^T*H in order to remove non-singularities provides us the output weight matrix β :

$$\beta = H^\dagger * T = H^T \left(\frac{I}{\lambda} + HH^T \right)^{-1} T, \text{ for } N < L \tag{10}$$

$$\beta = H^\dagger * T = \left(\frac{I}{\lambda} + H^T H \right)^{-1} H^T T, \text{ for } N > L \tag{11}$$

The flow chart (Fig. 2) presents the ELM algorithm.

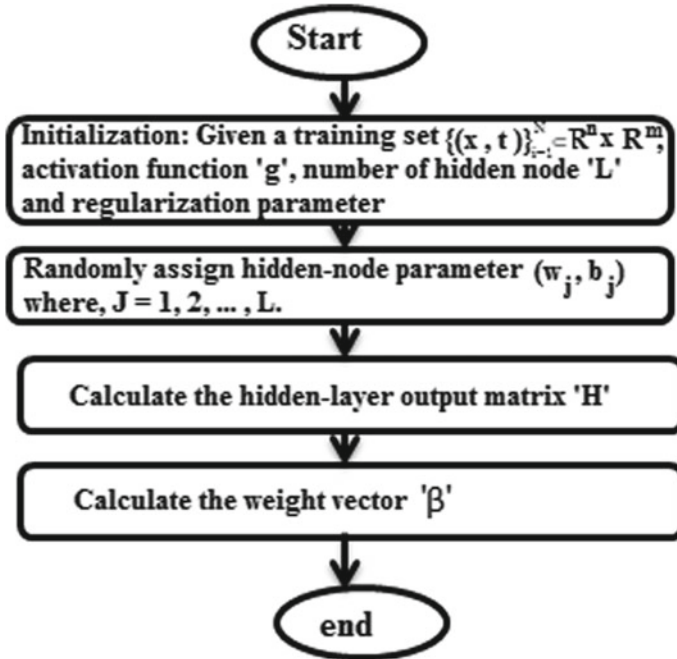


Fig. 2 Structure of ELM

4 The Analysis of VSCs and the Performance of ST on These Disturbance Signals Visually

Voltage sags occurred in electric power systems (EPSs) can be categorized as rectangular and non-rectangular type [5]. Rectangular voltage sags are the disturbances (voltage dips) occurred due to short-circuit fault events. Here, an instant fall of voltage at the beginning followed by an abrupt peaking towards the end of fault is witnessed. But in case of non-rectangular voltage sag, sudden drop in magnitude of voltage at the beginning followed by a sluggish recovery towards the end of disturbance is observed. Non-rectangular voltage sags occur during switching on of IMs as well as while energizing a transformer.

In this attempt, the use of ST for recognition of VSCs is examined. Three significant VSCs are simulated by MATLAB/Simulink. They are (i) single phase-ground along with three-phase fault (PQD-I), (ii) switching on of an IM (PQD-II) and (iii) energization of transformer (PQD-III).

4.1 Voltage Sag Due to SC Fault

SC fault taking place in electrical power system is symmetrical (three phases, e.g., abc-g or abc) or asymmetrical (single line-ground, line-line or line-line-ground) in nature. The magnitudes of voltage sags for each phase are similar or dissimilar, depending upon the types of fault.

To analyse the voltage sags due to SC fault events, a three-phase SC fault is simulated on a 13 kV distribution network. The features corresponding to this type of disturbances are (i) quick restoration of magnitude of voltage, (ii) variation in phase angle (Φ) and (iii) null harmonic distortion. Figure 3a shows the fluctuation in voltage signal (b-phase) as a result of three-phase SC fault occurring at 1 s. Figure 3b shows the corresponding three-phase RMS voltage variation. ST is applied to b-phases of disturbed voltage signal. The maximum amplitude versus time (MAT) plot

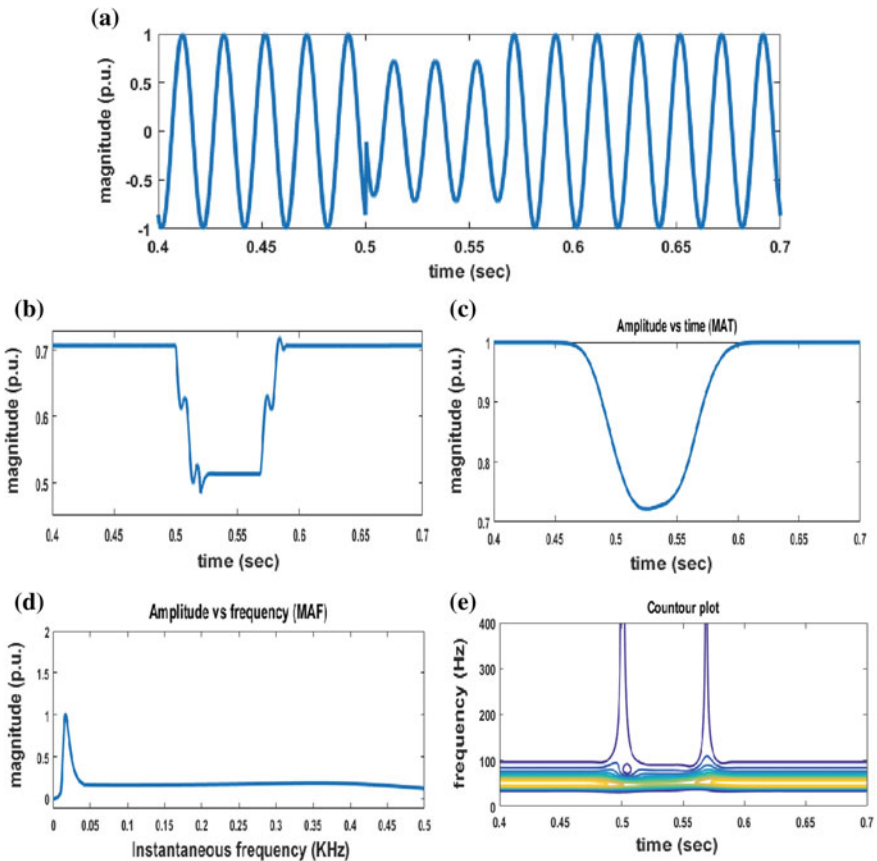


Fig. 3 Performance of ST on voltage sag caused by three-phase fault

is shown in Fig. 3c, which is obtained by scanning through the columns of S-matrix for each and every frequency value. Figure 3d shows the maximum amplitude versus frequency (MAF) plot, obtained by scanning through the rows of S-matrix. This graph demonstrates the frequency components of the disturbance and their corresponding amplitude. Figure 3e presents the frequency versus time plot of S-matrix named as time–frequency contour. The disturbance caused by the fault event can be clearly noticed by the variation of contour plot.

4.2 Voltage Sag Due to Energization of Transformer

The disturbances initiated due to energizing power transformer can produce non-rectangular voltage sags and interim harmonic distortion. The distinctive traits of this type of sags are: (i) uneven magnitude of sags in each phase, (ii) superficial voltage sag, (iii) slow but steady recovery of voltage, (iv) null phase shift and (v) harmonic distortions. In order to analyse the voltage sag due to the event of energization of a transformer, energization of an 11,000/400 V transformer, part of a 11 kV EPS, is simulated. The simulation has been carried out in various operational circumstances, such as varying the time instant for transformer energization and considering different types of transformer winding (γ/Δ , γ/γ and Δ/γ). The disturbance is termed as PQD-II. Figure 4a shows the fluctuation of three-phase voltage wave during energization of transformer at 1 s. Figure 4b shows the corresponding three-phase RMS voltage variation. ST is applied to b-phases of disturbed voltage signal. The MAT plot is shown in Fig. 4c.

Figure 4d shows the MAF plot. This graph demonstrates the frequency components of the disturbance and their corresponding amplitude. Figure 4e presents the frequency vs time plot of S-matrix named as time–frequency contour. The disturbance caused by the fault event can be clearly noticed by the variation of contour plot.

4.3 Voltage Sag Caused by IM Starting

The starting current of an IM is very large (approximately five times the FL current) at extremely low pf. This initial current creates shallow voltage sags because of which there will be no phase angle shift and harmonics distortion seen. However, low but equal magnitudes of sag in each phase, and slow and steady voltage recovery are some more characteristics of such type of voltage sags.

To analyse the voltage sag due to the initiation of an induction motor, a 75 kW induction motor has been loaded onto an 11 kV power system. The IM is simulated with activating the starter switch ON at 1 s. The driving rate of the IM during the

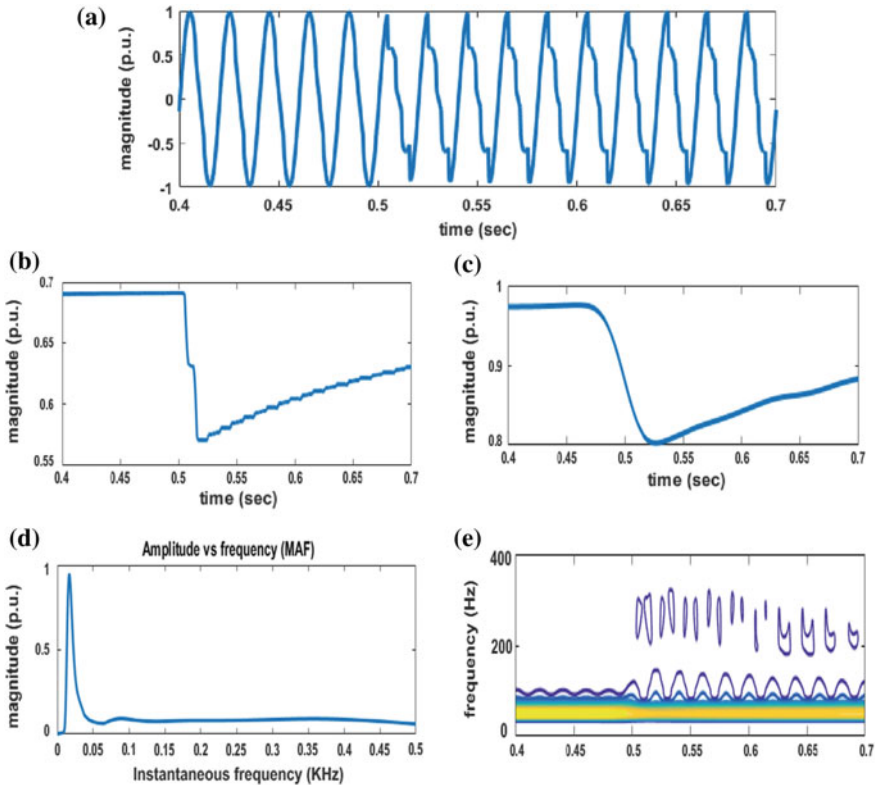


Fig. 4 Performance of ST on voltage sag caused by three-phase transformer energization

initiating is fixed at 1 rad/s. Figure 5a shows the fluctuation in three-phase voltage wave owing to the starting of the IM. Figure 5b shows the corresponding three-phase voltage (RMS) variation. ST is applied to b-phases of disturbed voltage signal. The MAT plot is shown in Fig. 5c. Figure 5d shows the MAF plot. Figure 5e presents the frequency versus time plot. The disturbance caused by the fault event can be clearly noticed by the variation of contour.

The MAT, MAF plot and contour of ST correctly detect the disturbance (voltage sag). Next, to classify each individual class (causes of voltage sag) through machine learning process, feature extraction process is carried out which pre-processed the extracted signal that transforms it into an appropriate new pattern to be followed with classification process. Here, the features are obtained from the output of ST using MAT plot and MAF plot, such as (1) distribution of energy, (2) standard deviation of the amplitude and (3) standard deviation of the phase.

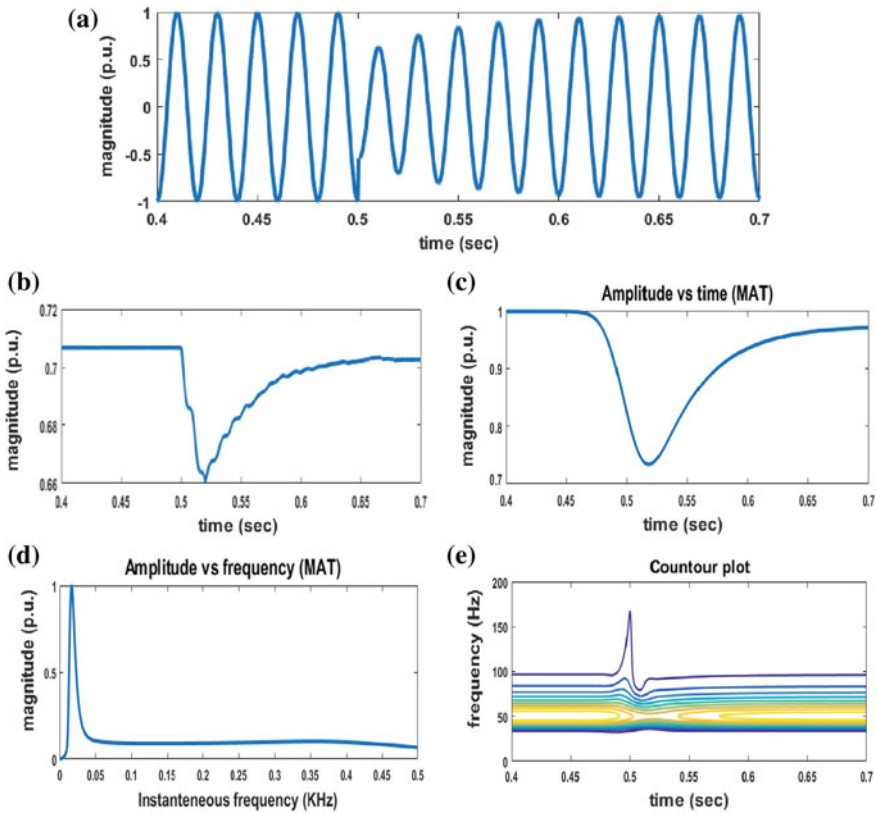


Fig. 5 Performance of ST on voltage sag caused by starting of IM

5 Evaluation

Figure 6 shows the flow chart for classification of VSCs using ELM classifier. Initially, ST is employed to extract various features out of the extracted PQD signals. These are then fed to the ELM classifier in order to identify the actual reasons for voltage sag. With an intention to test the performance of the proposed approach, 750 PQD events are simulated by using MATLAB/Simulink. Afterwards, the classifier is trained with a data set of 450 numbers of ST-based feature vectors which comprises 150 numbers of disturbances from each class (PQD-I, PQD-II and PQD-III). The rest of the data serves the purpose of testing of the ELM.

The accuracy of classification method proposed is put in Table 1. The result thus obtained signifies clearly that the overall accuracy of the proposed technique is 100%. Besides, the classification process of the proposed approach has been fed with some noise signals (signals with signal-to-noise ratio (SNR) of 20 dB) and the test output has been put in Table 2. It can be inferred that performance of ST along with ELM is very satisfactory with gross accuracy of 96.66%. Subsequently, Table 3 shows the

Fig. 6 Flow chart of proposed VSC detection and classification

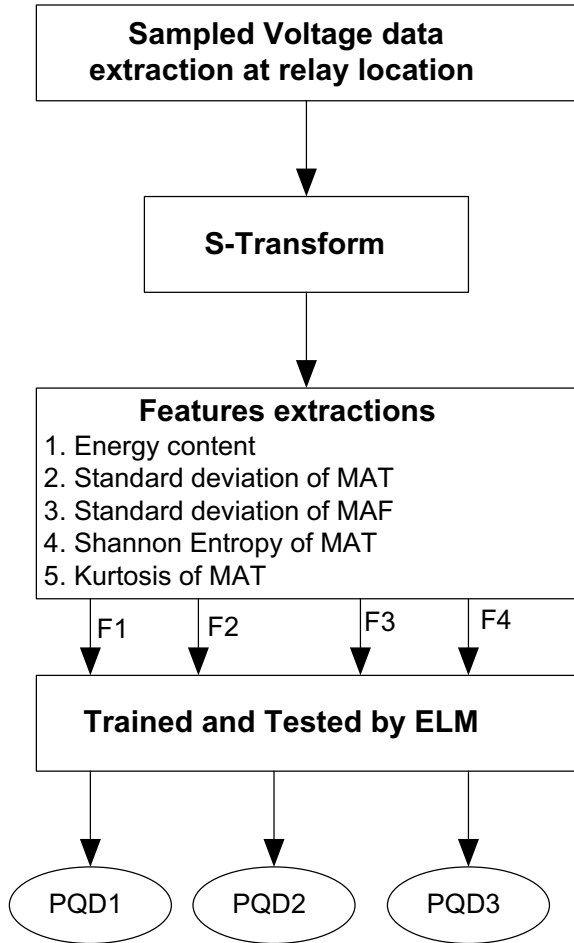


Table 1 Accuracy of classification by the proposed method (ST + ELM)

Disturbances	PQD-I	PQD-II	PQD-III
PQD-I	100	0	0
PQD-II	0	100	0
PQD-III	0	0	100
Overall accuracy	100%		

Table 2 Classification accuracy (using ST + ELM) considering 20 dB SNR

Disturbances	PQD-I	PQD-II	PQD-III
PQD-I	99	0	1
PQD-II	8	91	1
PQD-III	0	0	100
Gross accuracy	96.66%		

Table 3 Performance analysis table (in comparison with other recently cited works)

References	PQD-I (%)	PQD-II (%)	PQD-III (%)	Gross (%)
[3], EMD + FFT	93.33	100	100	96
[5], EMD + PNN	100	95.71	100	98.63
[5], EMD + MNN	100	88.57	100	96.36
[6], WT + PNN	100	82.85	72.85	85.90
[6], EMD + PNN	100	93	100	97.66
[6], WT + PNN	100	81	75	86.33
Proposed, ST + ELM	100	100	100	100

performance of the stated method (ST + ELM) has been compared with research works in earlier printed articles, which clearly indicates that it excels over all recently cited techniques.

6 Conclusion

In this article, ST based on ELM technique is applied to classify the type of VSCs. Applying ST, various unique information are extracted as features. Then, the ELM is applied to classify the causes of voltage sag occurrences. The results obtained from the simulation present that ST along with ELM, as a tool for identification of VSCs, is a better performer.

References

1. Mishra M (2018) Power quality disturbance detection and classification using signal processing and soft computing techniques: a comprehensive review. *Int Trans Electr Energy Syst* 29:e12008
2. Ding N, Cai W et al (2009) Voltage sag disturbance detection based on RMS voltage method. In: Conference APPEEC 2009. Wuhan, pp 1–4 (March 2009)
3. Yang L, Yu J, Lai Y (March 2010) Disturbance source identification of voltage sags based on Hilbert-Huang transform. In: 2010 Asia-Pacific power and energy engineering conference (APPEEC). IEEE, New York, pp 1–4
4. Bollen MHJ (2000) Understanding power quality problems. IEEE Press, Piscataway, NJ
5. Manjula M, Mishra S, Sarma AVRS (2013) Empirical mode decomposition with Hilbert transform for classification of voltage sag causes using probabilistic neural network. *Int J Electr Power Energy Syst* 44(1):597–603
6. Manjula M, Sarma AVRS, Mishra S (December 2011) Detection and classification of voltage sag causes based on empirical mode decomposition. In: 2011 annual IEEE India conference (INDICON). IEEE, New York, pp 1–5
7. Chilukuri MV, Dash PK (2004) Multiresolution S-transform-based fuzzy recognition system for power quality events. *IEEE Trans Power Delivery* 19(1):323–330

8. Kumar R, Singh B, Shahani DT, Chandra A, Al-Haddad K (2015) Recognition of power-quality disturbances using S-transform-based ANN classifier and rule-based decision tree. *IEEE Trans Ind Appl* 51(2):1249–1258
9. Mishra M, Rout PK, Routray SK, Nayak N (2014) Power quality disturbance recognition using hybrid signal processing and machine intelligence techniques. *Int J Ind Electr Drives* 1(2):91–104
10. Huang GB, Zhu QY, Siew CK (2006) Extreme learning machine: theory and applications. *Neurocomputing* 70(1–3):489–501
11. Huang GB, Wang DH, Lan Y (2011) Extreme learning machines: a survey. *Int J Mach Learn Cybernet* 2(2):107–122

Accelerated Deep Learning in Proteomics—A Review



Deeba Khan and Seema Shedole

Abstract Advent of deep learning in 2012 has revolutionized the plethora of researches including bioinformatics. This revolution is complemented by the progress in hardware technology and big omics data. Software mimicking human brain, powerful hardware and data to harness, these trio factors have benefited researches in image recognition, speech recognition, natural language processing and more so the life science domains involve omics. Deep learning has resolved the problem of transforming data into knowledge with much acceptable accuracy compared to their traditional counterparts. This paper condenses the problems addressed by different deep learning architectures in proteomics, which is a notable field of life science. The paper also summarizes the use of accelerators in addressing the problems.

Keywords Deep learning · Accelerators · Proteomics · Sequences · GPU frameworks

1 Introduction

Proteomics is a study that involves characterization of proteome in a living organism and predicts protein structures, protein functions and its solubility [1]. Proteins play a vital role in diagnosing disease, pharma research, drug design, etc., making its study imperative. Bioinformaticians' support to life scientists in enabling this study is remarkable. From stand-alone software to parallel software, workflows, cloud support, online databanks, bioscientists have array of solutions to their problems. This support is now fueled by deep learning (DL). The potential of deep learning in bio-science is its ability to better exploit the datasets that are large and high-dimensional.

D. Khan (✉) · S. Shedole
Ramaiah Institute of Technology, Bengaluru, Karnataka 560054, India
e-mail: deebamajeed@gmail.com

S. Shedole
e-mail: seemas@msrit.edu

© Springer Nature Singapore Pte Ltd. 2020
R. Sharma et al. (eds.), *Innovation in Electrical Power Engineering, Communication, and Computing Technology*, Lecture Notes in Electrical Engineering 630,
https://doi.org/10.1007/978-981-15-2305-2_23

Consequently, many problems are addressed by deep learning with acceptable accuracy compared to their traditional counterparts. The list of problems includes predicting protein structures, peptide sequencing, inferring protein using peptide profile, predicting protein residue–residue contacts, predicting protein secondary structures, protein fold recognitions, predicting protein solubility.

In this paper, we have discussed recent applications of deep learning of which few are accelerated, with a focus on proteomics. This review does not give a detailed background on all technical details, but provides an overview on current deep learning solutions to classification problems in proteomics, viz. peptide inference, protein structure prediction, solvent accessibility, contact map, fold classification, protein function prediction, etc. The applications covered are deliberately broad to illustrate differences and commonalities between approaches. The comprehensive information on each approach is cited in references.

2 Literature Survey

Software support for proteomics started in 1970. The protein similarity search program proposed by Needleman et al. [2]. Protein similarity search program proposed by Needleman was based on dynamic programming technique. Since many applications in bioinformatics are computer-intensive, even good solutions fail to perform with existing hardware. Much work was done to improve performance of computational methods to solve proteomics problem. BLAST stole the show in 1997. Proposed by Altschul et al. [3], these programs brought a big revolution in bioinformatics research. With high-performance computing (HPC) becoming popular a parallel version of BLAST, mpi-BLAST and many such programs were introduced. Details of mpi-BLAST work can be found in Darling et al. [4]. The hardware support to such parallel programs was traditionally given by clusters or dedicated parallel systems. Charalambous et al. [5] explored an economically feasible alternate architecture. The research group exploited the attributes offered by the graphics processing units (GPUs) to speed up applications in bioinformatics. The group developed a bioscience application RAXML for phylogenetic inference. RAXML was ported to the GPU. Oliver et al. [6] in their work used hardware based on field-programmable gate array (FPGA) for biosequence database scanning to accomplish higher results with minimum possible cost investment. NVIDIA [7] the renowned manufacturer of graphics card in their article gave a briefing on general-purpose GPU (GPGPU). The article also focuses on application of NVIDIA CUDA in bio-related information processing. Vouzis et al. [8] developed GPU-BLAST using general-purpose graphics processing unit. The popularity of powerful hardware, GPU, gave way to a remarkable era of deep learning. Applications of deep learning in bioinformatics with challenges and opportunities can be found in paper published by Ching et al. [9]. Uses of convolutional neural networks, a popular deep learning architecture, have widely been used to address many problems in proteomics.

3 Background

3.1 Proteomics

Proteomics is a research-based study of proteins and their connections and interactions with each other in a cell [1]. The completion of the Human Genome Project leads to emphasis on protein compliment of the humans. Since proteome exhibits accurately on dynamic state of tissue, a cell or an organism, it is expected from proteomics to help in predicting better disease biomarkers for monitoring treatment and in diagnosis. The dawn of proteomics technologies for detection of proteins and their quantitation creates new challenges and opportunities for researchers and clinicians seeking to gain better insight into diseases. High-throughput technologies for proteomics combined with advanced bioinformatics are intensively used to identify molecular signatures of diseases that depend on protein pathways. Mass spectrometry stages an important role in proteomics, and it has become a vital tool for cellular and molecular biology. Proteomics study has great potential since many issues and challenges remain to be addressed. The challenges include mining of low abundant proteins and integration of genomics with proteomics along with data in metabolomics. Proteomics is the stepping stone for extracting and constructing useful information that aids in biomedical research. In this review, a glimpse of current challenges in proteomics technologies is conferred.

3.2 Deep Learning

Deep learning methods have granted the computational power to resolve complex research questions related to classification. Its success has already been demonstrated by the revolutionizing achievements in the field of artificial intelligence, like image recognition, object detection, audio recognition, natural language processing, etc. Most problems in proteomics are classification-based. In fact, classification of protein structure can be traced back to the 1970s aiming to comprehend the process of protein folding and protein structure evolution. Grouping proteins into structural or functional categories also facilitate the understanding of increasing number of new sequences. Early methods for similarity measures mostly rely on sequence properties (i.e., alignment-based), such as FASTA [10], BLAST or PSI-BLAST [11], and were then upgraded by leveraging profiles derived from multiple sequence alignments and position-specific scoring matrices (PSSM) in addition to raw sequences or discriminative models like SVM which was adopted as a topological approach utilizing persistent homology to extract features for classification of protein domains.

The boom of deep learning is supported by the successive introduction of a variety of deep architectures like deep neural network (DNN), restricted Boltzmann machine (RBM), deep belief network (DBN), convolutional neural network (CNN),

Table 1 Popular deep learning architectures

Deep learning architectures	Description
DNN	This is a hierarchical neural network with multi-hidden deep layers of input and output of a neural network, input is feedforward processing, and optimizing is done with backpropagation
RNN	Cyclic connection and recurrent unit are used for handling sequential info hence causing previous data to be remembered implicitly in vectors
RBM	Generative neural network that is the building block for many deep learning approaches, having a single input and hidden layer. There is no connection among the nodes in each layer
LSTM	This is a special type of recurrence neural network. Its features enable models to capture longer-term dependencies
CNN	Contains multi-convolution layers that capture feature maps from regional connectivity. It is done through the polling layers and weighted filters to reduce data size. Fully connected neural network is included as the classifier
SAE	A built-in encoder and decoder are used in this model. The input vector is transformed into a hidden layer using encoder, and the representation of hidden layer is mapped by the decoder to the reconstructed input. This is regarded as the output result

recurrent neural network (RNN), long short-term memory (LSTM), stacked autoencoder (SAE), etc. The better application of deep learning methods and life science research may lead to a profound understanding of proteins that will benefit multiple fields including precision medicine, pharmacy, even agriculture, etc. For example, medical research and its applications such as gene therapies, molecular diagnostics and personalized medicine could be revolutionized by tailoring high-performance computing methods for analyzing available datasets. Also, the process of developing new drugs takes a long period and is usually very costly. To save time and cost, the general approach taken by pharmaceutical companies is to try to match the candidate protein identified by researchers with their known drug molecules. Table 1 summarizes the list of deep learning architectures and a brief description of each.

3.3 Accelerators

Many computer-intensive applications can be run on general-purpose processors coupled with hardware accelerators to reduce throughput time. The hardware accelerators comprise many processing units that enable concurrent execution. The prevalent hardware accelerators are GPUs [12], cell, field-programmable gate arrays (FPGAs) [13] and application-specific integrated circuits (ASICs) [14]. Popularity of computer-intensive bioinformatics applications can be owed to these accelerators.

In deep learning too, training neural networks and predicting are big challenges, and also there is a high computational cost in terms of energy, memory and time energy. These gains again can be owed to graphics processing units, since they surpass the vector operations which are the essence of deep learning.

Graphics processing units have inadequate memory, hence making grids of less complexity and useful dimensions difficult to program on machines having GPU. This difficulty has at times forced life science researchers to use replacements or restrict the sample size used for analysis. For instance, to predict gene's expression level using single neural network, genes were haphazardly segregated into two separate halves aimed at analysis due to memory limitations. In yet another case, researchers restricted the neural network size or the count of training occurrences. Researchers sometimes have also picked classic processing units (CPUs) for executions instead of GPUs, hence sacrificing performance or grid size.

While constant enhancements in these accelerators may remove these hurdles, it is doubtful whether such developments will happen fast enough to keep up with the big omics data and complex models of deep learning. Though there is pressing interest in specialized hardware, like FPGAs [15] and application-specific integrated circuits (ASICs) [16], software at disposal for such application-specific machines is minimal. ASIC, FPGAs and GPUs promise progress in models used for deep learning with energy, time and memory efficiency. Dedicated hardware is a hard investment which is not likely to do research or use DL. For community whose interest lies in deep learning, special accelerator solutions are likely to become prevalent. Distributed computing remains a common solution to resource savvy applications. Efforts put on many significant deep learning approaches that use distributed computing have increased. Distributed computing is not a solution for DL always, but many developments are observed in this area. Presently, a number of tools, algorithms and high-level libraries in the distributed environment are available to support deep learning. Consequently, a very complex network can be trained with minimal setup. Cloud computing has widely been adopted in genomics and proteomics. This can facilitate easier sharing of the datasets and may help in scaling DL. Cloud computing is affordable and flexible. It also enables the use of specialized hardware with decent investment. Hence, cloud computing is a popular choice among researchers. With all this said, among many hardware solutions GPUs are top ranked because the software framework to experiment is in place. Table 2 summarizes available GPU

Table 2 Popular GPU frameworks

GPU framework	Language	Deep learning architectures supported
Caffé	C++	CNN and RNN
CNTK	Python	CNN, RNN, LSTM
TensorFlow	C++	RNN, CNN, DBN
Theano	Python	RNN, DBN, SAE, CNN
Torch	Lua	CNN, DBN, SAE, RNN

frameworks and corresponding tools [17], the core language they are developed on and their support to different deep learning architectures.

4 Solutions to Problems in Proteomics

Many deep learning solutions have been proposed in recent years to different problems in proteomics, viz. peptide sequencing, predicting protein solubility, predicting protein secondary structures, residue–residue contact predictions, protein fold recognitions, protein inference using peptide profiles. Most of these predicting solutions are supported by GPU frameworks. This section discusses deep learning solutions briefly.

4.1 *DeepNovo—Model for Peptide Sequencing*

Tandem mass spectrometry sequencing of peptides is crucial to proteomics in the classification of proteins, especially for new sequences. DeepNovo [18] is a DNN model that is used for such de novo peptide sequencing. It combines the characteristics of RNN and CNN to learn features of fragment ions. It is also used to study sequenced pattern of peptides and identify proteins using tandem mass spectra. The networks in this model subsequently use local dynamic programming locally for de novo sequencing optimization. This method upon evaluation on a wide variety of species was found to have remarkably outperformed state-of-the-art methods, achieving 38.1–64.0% higher accuracy at the peptide level and 7.7–22.9% higher accuracy at the amino acid level. DeepNovo was also used to automatically reconstruct the complete sequences of antibody light and heavy chains of mouse, achieving 97.5–100% coverage and 97.2–99.5% accuracy, without help of datasets. Furthermore, DeepNovo can adapt to any database for predictions. It is a complete solution in the sense that it resolves both training and predicting problems related to sequencing.

4.2 *DeepSol—Model for Predicting Protein Solubility*

Solubility of a protein has an important role to play in pharma productions and finding. The degree of solubility is an important indicator for any given protein. This functionality can be well defined by protein's sequence. Thus, there is a necessity to come up with novel, precise in silico protein solubility predictors that are based on sequence. DeepSol [19] is a novel DL-based protein solubility predictor. The backbone of this framework is a CNN that exploits k-mer structure of proteins. In addition, structure-based features are mined from the protein sequence. Though many

sequence based prediction methods exist, DeepSol outperforms all known state-of-the-art solubility prediction methods. It boasts of an accuracy of 0.77 and Matthew's correlation coefficient of 0.55. The superior prediction accuracy of DeepSol allows to screen for sequences with improved production capacity, thus making it more reliable for protein solubility predictions.

4.3 DeepPep—Model for Protein Inference Using Peptide Profile

A basic challenge in proteomics is protein inference. The problem is identification of the protein set that is the origin of a given peptide profile. A DL model DeepPep [20] uses a neural network that is based on convolutional layers to address protein inference problem. The input to this model is the proteome blend that is searched across the protein database along with target peptide profile. In principle, DeepPep quantifies the alteration in probabilistic score of peptide spectrum matches in the absence or presence of a specific protein, hence selecting candidate proteins with the largest impact on the peptide profile. Application of this method across datasets claims for its higher predictive ability (AUC of 0.80 ± 0.18 and AUPR of 0.84 ± 0.28) in inferring proteins without need of peptide detectability on which the most competitive methods rely. This convolutional neural network architecture-based method outpaces the traditional DL architectures without convolution layers.

4.4 DeepCov—Model for Predicting Protein Residue–Residue Contacts

DeepCov [21] is CNN method used for predicting protein residue–residue contacts. It demonstrates that using DNN models, simple statistics for alignment contain adequate information to accomplish state-of-the-art accuracy unlike other methods that depend not only on substitution frequency but also from protein sequences taken from supplementary sources of data, or features to guess residue–residue contacts' solvent accessibility, secondary structure and numbers from other contact prediction methods. DeepCov uses CNN operating on amino acid pair occurrence or covariance data resulting directly from alignments, without involving global statistical methods such as sparse inverse covariance or predicting pseudo-likelihood.

Table 3 Deep learning-based solutions to prediction problems in proteomics

Deep learning models	Problem addressed	Deep learning architecture	GPU framework
DeepNovo	Peptide sequencing	CNN and RNN	TensorFlow
DeepPep	Protein inference	CNN	Torch
DeepCov	Predicting residue–residue contacts	CNN	Theano
DeepSol	Predicting protein solubility	CNN	Keras
DeepSF	Protein fold recognition	CNN	Theano

4.5 *DeepSF—Model for Protein Fold Recognition*

DeepSF [22], a one-dimensional CNN method, was designed to categorize proteins of varying length into 1195 known folds. These folds are listed in SCOP 1.75 data source. DeepSF uses protein sequence of varying size to mine hidden features through convolution transformation. Unlike the classical methods that use pairwise sequence alignment, this model categorizes folds by mapping all protein sequences in the data source to all the folds in the fold space precisely. This approach extracts features related to folds from protein sequences automatically. Such features are a way of resemblance measure among proteins. This method boasts of an accuracy that is 12.63–26.32% higher than HHSearch on template-free modeling targets and 3.39–17.09% higher on hard template-based modeling targets for top predicted folds.

Table 3 summarizes recent deep learning applications in proteomics. The deep learning architectures and GPU framework are also listed. It can be observed that most of the prediction problems use CNN architectures for their solutions.

5 Discussion

Application of deep learning techniques to proteomics may seem seamless and trivial, but it is not free of shortcomings. In this section, we discuss some challenges the researchers may face while using this technique. The main hurdle lies in the unequally distributed data [23] among different classes and the availability of data itself. For instance, in the clinical situations access to data is restricted. In circumstances where researchers have access to the clinical data, there are more diseased samples compared to healthier one. To minimize error rates in models built with such imbalanced data, appropriate measures like F-score and harmonic mean should be adopted for validations. There exist ample deep learning architectures to choose from. Better the understanding of capabilities of the architectures, easier it is to choose the appropriate architecture. The usefulness of each deep learning technique

is still unclear and poses a challenge when deep learning solutions are to be adopted. Study of proteomics may revolve around proteins, but in reality proteins are pieces of a big puzzle where other pieces are data from varied sources like electronic health records, drug responses, images from X-ray, MRI. Deep learning should be robust enough to handle data from different modes and integrate it. This still remains a challenge. Another limitation of using deep learning techniques lies in the model training time which is likely to increase drastically with increase in training data. The reasonable solution is to accelerate deep learning using parallel and distributed computing. Use of specialized hardware like GPUs is another feasible solution to address this problem. The GPU frameworks like TensorFlow are already in place to support deep learning. Use of specialized hardware is in its early stage, but once adapted they will prove to be much more helpful in long run.

6 Conclusion

The word deep learning is now getting attached to big data. Since life science provides a galore of omics data, use of deep learning becomes imperious to analyze such data. In this paper, we have discussed few models that solve problems in proteomics using deep learning. However, deep learning techniques can be used for any type of data that is sequenced, for instance DNA or RNA sequences. As future work, we may look into how deep learning frameworks can be exploited to different problems in genomics and compare them with their classical parts. It can be concluded that the focus of computing community is eventually shifting from algorithm designs to deep mining of data both in academics and for business solutions.

References

1. Cao C, Liu F, Tan H, Song D, Shu W, Li W, Zhou Y, Bo X, Xie Z (2018) Deep learning and its applications in biomedicine. *Genomics Proteomics Bioinform* 16(1):17–32. <https://doi.org/10.1016/j.gpb.2017.07.003>
2. Needleman SB, Wunsch CD (1970) A general method applicable to the search for similarities in the amino acid sequence of two proteins. *J Mol Biol* 443–453
3. Altschul SF, Gish W, Miller W, Myers EW, Lipman DJ (1990) Basic local alignment search tool. *J Mol Biol* 215(3):403–410
4. Darling AE, Carey L, Feng W (2003) The design, implementation, and evaluation of mpiBLAST. In: *Proceedings of cluster world*
5. Charalambous M, Trancoso P, Stamatakis A (2005) Initial experiences porting a bioinformatics application to a graphics processor 415–425. https://doi.org/10.1007/11573036_39
6. Oliver T, Schmidt B, Maskell D (2005) Hyper customized processors for bio-sequence database scanning on FPGAs. In: *13th ACM international symposium on field-programmable gate arrays*
7. NVIDIA (2007) NVIDIA compute unified device architecture (CUDA) programming guide, version 1.0
8. Vouzis PD, Sahinidis NV (2010) GPU-BLAST: using graphics processors to accelerate protein sequence alignment. *Bioinformatics* 27(2):182–188

9. Ching T, Himmelstein DS, Beaulieu-Jones BK (2018) Opportunities and obstacles for deep learning in biology and medicine. *J R Soc Interface* 15
10. Pearson WR, Lipman DJ (1988) Improved tools for biological sequence comparison 8
11. Altschul SF, Madden TL, Schaffer AA, Zhang J, Zhang Z, Miller W, Lipman DJ (1997) Gapped BLAST and PSI-BLAST: a new generation of protein database search programs. *Nucleic Acids Res* 3389–3402
12. Chetlur S, Woolley C, Vandermersch P, Cohen J, Tran J, Catanzaro B, Shelhamer E (2014) cuDNN: Efficient primitives for deep learning. *ArXiv e-prints*
13. Suda N, Chandra V, Dasika G, Mohanty A, Ma Y, Vrudhula S, Seo J, Cao Y (2016) Throughput-optimized OpenCL-based FPGA accelerator for large-scale convolutional neural networks. In: *Proceedings of the ACM/SIGDA international symposium on field-programmable gate arrays*. ACM, New York, NY, pp 16–25
14. Owens JD, Luebke D, Govindaraju N, Harris M, Krüger J, Lefohn AE, Purcell T (2007) A Survey of general-purpose computation on graphics hardware. *Comput Graphics Forum* 26:80–113
15. Qiu J, Wang J, Yao S, Guo K, Li B, Zhou E, Yu J, Tang T, Xu N, Song S, Wang Y, Yang H (2016) Going deeper with embedded FPGA platform for convolutional neural network. In: *Proceedings of the ACM/SIGDA international symposium on field-programmable gate arrays*. ACM, New York, NY, pp 26–35
16. Engel JJ, Guzowski TS, Hunt A, Lackey DE, Pickup LD, Proctor RA, Reynolds K, Rincon AM, Stauffer DR (1996) Design methodology for IBM ASIC products. *IBM J Res Develop* 40:387–406. <https://doi.org/10.1147/rd.404.0387>
17. Hung C-L, Tang C (2017) Bioinformatics tools with deep learning based on GPU 1906–1908. <https://doi.org/10.1109/bibm.2017.8217950>
18. Tran NH, Zhang X, Xin L, Shan B, Li M (2017) De novo peptide sequencing by deep learning. *Proc Natl Acad Sci* 114:201705691. <https://doi.org/10.1073/pnas.1705691114>
19. Khurana S, Rawi R, Kunji K, Chuang GY, Bensmail H, Mall R (2018) DeepSol: a deep learning framework for sequence-based protein solubility prediction. *Bioinformatics*
20. Kim M, Eetemadi A, Tagkopoulos I (2017) DeepPep: deep proteome inference from peptide profiles. *PLoS Comput Biol* 13(9):e1005661
21. Wang S, Peng J, Ma J, Xu J (2016) Protein secondary structure prediction using deep convolutional neural fields. *Sci Rep*. <https://doi.org/10.1038/srep18962>
22. Hou J, Adhikari B, Cheng J (2018) DeepSF: deep convolutional neural network for mapping protein sequences to folds. 565–565. <https://doi.org/10.1145/3233547.3233716>
23. Min S, Lee B, Yoon S (2017) Deep learning in bioinformatics. *Briefings Bioinform* 18:851–869. <https://doi.org/10.1093/bib/bbw068>

DSTATCOM Using Limit Cycle Oscillator FLL with Optimized Gains of Voltage Error Controllers



Jayadeep Srikakolapu, Sabha Raj Arya and Rakesh Maurya

Abstract In this paper, an algorithm depending on limit cycle oscillator-based frequency-locked loop is used to extract fundamental component of load current. The extracted fundamental components are used to control distribution static compensator (DSTATCOM). The major function of DSTATCOM is to make source current sinusoidal for compensation of power quality problems. This reduces the reactive burden on the source and helps in making source current sinusoidal. The reference grid current has been produced by extracting fundamental components from each phase of load current using limit cycle oscillator (LCO)-based frequency-locked loop (FLL). An optimization algorithm named multi-verse optimization (MVO) which is based on population has been used for estimation of PI gains as error controller in various modes of operation of DSTATCOM as mentioned. The error minimization of DC bus voltage and terminal voltage has been formulated as an unconstrained optimization problem, and gains have been estimated. To maximize the benefits of the MVO optimization process, the local search accuracy has been improved. This improvement has been achieved by increasing the wormholes in the universe. The suggested control scheme with gain values from the MVO optimization technique has controlled issues like reactive power compensation and mitigation of grid current harmonics caused due to an identified harmonic producing load, i.e. a three-phase AC voltage controller with resistive loads. This work provides results of d-SPACE-based realization of the suggested limit cycle oscillator-based frequency-locked loop algorithm for DSTATCOM.

Keywords AC voltage controller · DSTATCOM · FLL · MVO · PWM · PI controller · THD

J. Srikakolapu · S. R. Arya (✉) · R. Maurya
Department of Electrical Engineering, Sardar Vallabhbhai National Institute of Technology,
Surat 395007, India
e-mail: sabharaj1@gmail.com

J. Srikakolapu
e-mail: sjaideep1729@gmail.com

R. Maurya
e-mail: rmaurya@eed.svnit.ac.in

1 Introduction

The generation and utilization of electrical energy have taken numerous ways to fulfill human needs. Power electronics backs key role in this aspect [1]. This aspect in many areas like power supplies, drive controllers, energy conversion has included nonlinearity in the load [2]. In spite of the obligatory benefits, this nonlinearity raises poor power quality concerns like poor power factor, high THD, disturbed voltage and distorted supply current [3]. To rectify these issues at various voltage levels, various devices are used. At distribution level, custom power devices are used to rectify various power quality problems [4]. A shunt connected custom power device in the middle of the supply and load to preset the sinusoidal nature of the supply current is termed as DSTATCOM [5]. Driving DSTATCOM to overcome various issues is done using a control algorithm. The control scheme adopted helps in judging the performance of the DSTATCOM and the system. Performance of any control algorithm is judged by time taken to rectify and extent of handling an issue [6].

The effective load current handling to mitigate the power quality issues is based on the capability of the control scheme [7]. Methods like symmetrical components and extraction of fundamental components are identified [8]. Synchronous reference frame (SRF) PLL certifies righteous solution for dynamic condition for a three-phase system but during distortions SRF-PLL gets severely affected. Synchronous reference frame-based and instantaneous power theory-based schemes are used in constructing a basic three-phase PLL [9]. During adverse grid conditions for a unified power quality condition, a self-tuning filter-based instantaneous power p-q control is used to overcome the power quality problem [10]. The inability of proper harmonic mitigation of few control algorithms has seeded the advancement of various PLLs [11]. Moving average PLL (MA-PLL), modified synchronous reference frame PLL (MSRF-PLL) and auto adjustable synchronous reference frame PLL (ASRF-PLL) are few types of d-q-based PLLs. The stability of the system is highly affected by the loop gains in aforementioned PLLs. Multiple complex coefficient filter PLL (MCCF-PLL) and second-order generalized integrator PLL (SOGI-PLL) are types of α - β -based PLLs. These PLLs suffer with weak harmonic rejection capability [12–14]. Harmonic compensation is done by extracting the required harmonic amplitude using a SOGI based on two-cascaded synchronous reference frame PLL (SRF-PLL). Cascading SRF PLLs has increased the computational burden with poor dynamic response [15]. Power oscillations have been removed using DSOGI in a three-phase inverter with grid disturbances; however, it has not removed oscillations under voltage and current [16]. Although TOSSI has provided less settling time, it has no much effect on THD in its application in synchronization of the distributed generation system [17]. The basic differences between a phase-locked loop (PLL) and an FLL are in the reference frame with which they operate. In general, PLL operates in synchronously rotating (d-q) frame, where as an FLL works in a stationary reference frame [18].

LCO provides creditable immunity and robustness to harmonics and load imbalance. The complete information needed to estimate the fundamental current components from the highly polluted load current is considered with system analysis [19]. An adaptive frequency-locked loop has been made by integrating LCO in the control algorithm. Excluding the trigonometric functions in the control makes less computational burden for LCO-FLL [20]. A LCO-FLL is highly robust against supply voltage variation such as swells, sags, harmonics and phase frequency shifts. In synchronization process, with tolerable transient performance LCO-FLL synchronize with grid at any initial condition set [21]. In a highly harmonized load current condition with phase imbalance, the proposed scheme handles properly. These features are highly effective in area of power quality. Performance of the proposed scheme has made it a good alternative to PLL-based DSTATCOM control algorithm where fundamental current extraction under disturbed load current condition is required [22].

The DC voltage and the AC voltage are sustained by PI controllers. PI controller gains are chosen for required response of DSTATCOM [23]. Tuning of PI parameters using primitive methods takes significant time. To overcome this, many methods have been observed to get an optimized gain values. The process of reaching an optimized solution is called optimization; heuristic search helps in producing high-quality solutions in most of cases [24]. Mirjalili proposed a simple yet powerful, specific algorithm-based and less parameter optimization algorithm named multi-verse optimization algorithm (MVO) it is a meta-heuristic optimization algorithm [25, 26].

In this paper, a control algorithm for DSTATCOM system depending on limit cycle oscillator (LCO) has been proposed for minimizing effect due to load harmonics and reactive power demand on supply current. Fundamental components of load current have been estimated using a frequency-locked loop (FLL). An adaptive frequency-locked loop has been made by integrating LCO in the control algorithm. Excluding the trigonometric functions in the control makes less computational burden for LCO-FLL. The extracted fundamental components with tolerable transient performance synchronize with grid current irrespective of initial condition set with this the system has been settled within few fundamental cycles. The main features of the proposed FLL are its better stability during load dynamics, better performance with nonlinear type of AC voltage controller-type load.

2 System Configuration

The general configuration of the DSTATCOM is shown in Fig. 1. The basic constituent of the DSTATCOM considered in this study is a converter driven by voltage source. It is a current-controlled converter with a capacitor (C_{dc}) at the DC link for DC-link voltage maintenance. The power circuit consists of a AC voltage controller-type nonlinear load. The grid currents (i_{aG} , i_{bG} and i_{cG}) are disturbed due to the load currents (i_{aL} , i_{bL} and i_{cL}).

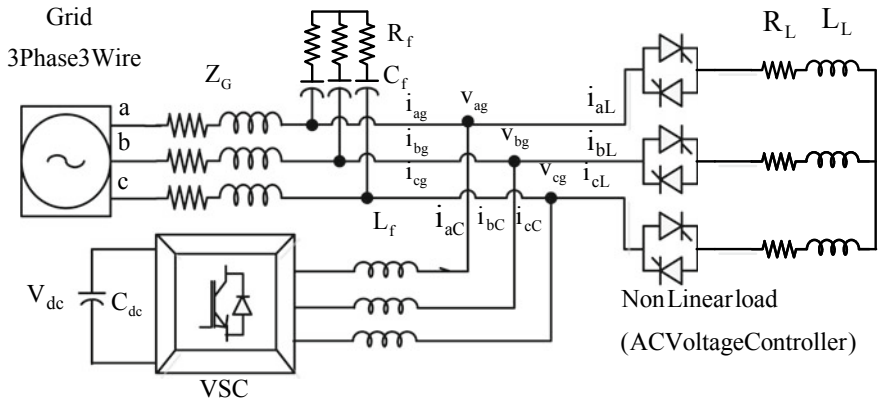


Fig. 1 System configuration with DSTATCOM and AC voltage controller-type nonlinear load

The compensating currents (i_{aC} , i_{bC} , and i_{cC}) are injected to the AC mains for maintaining the grid currents to reference value. Some more assisting components of the power circuit are filter inductance (L_f) at line and passive ripple filter (R_f , C_f) at point of common coupling (PCC) to smooth the wave shape of compensating current and the grid voltage, respectively. The AC grid mains consist of some source impedance (Z_G). The limit cycle oscillator FLL-based control scheme has been provided in Fig. 2, Hall Effect sensors for sensing various voltages and currents which are needed for the control algorithm are used. The pulse width modulated (PWM) firing pulses for controlling VSC are generated using the sensed signals.

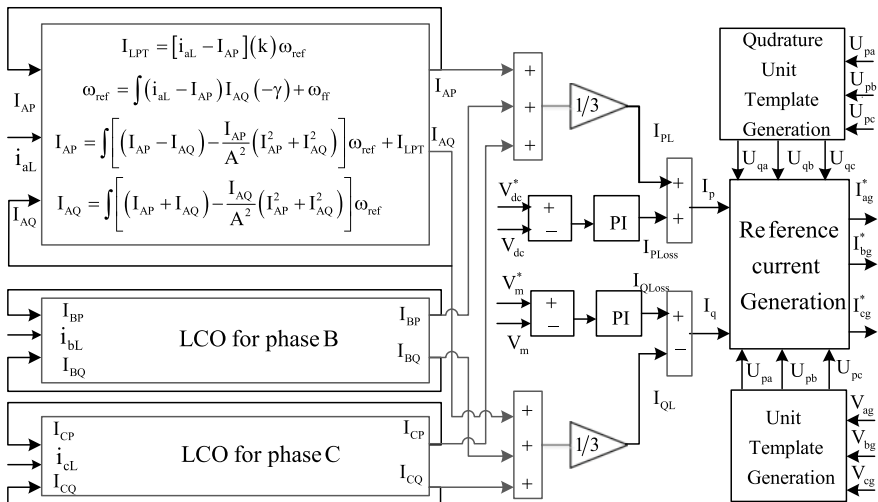


Fig. 2 Control algorithm of DSTATCOM using LCO-FLL

3 Control Algorithm

The LCO-FLL for the DSTATCOM system demonstrated in Fig. 1 has been illustrated in Fig. 2. The control scheme has been sectionalized mainly in two sections one for internal signal generation and the other section for gate signal generation. The disturbed load currents (i_{aL} , i_{bL} and i_{cL}), grid currents (i_{ag} , i_{bg} and i_{cg}), the DC-link voltage (V_{dc}) are sensed. In Fig. 2, the LCO-FLL is used for fundamental stationary components extraction from load current. The voltage error of DC bus voltage has been regulated using a PI controller in PFC mode. The active and reactive components of load current have been calculated and reference grid currents are estimated. Considering the estimated and actual grid currents, PWM pulses of VSC have been generated.

3.1 Unit Template Approximation

In phase unit, templates are approximated using the sensed grid voltages (V_{ag} , V_{bg} , and V_{cg}) at point of common coupling (PCC) and peak amplitude of the terminal voltage (V_m) using Eq. (1) as shown below [5].

$$V_m = \sqrt{\frac{2(V_{ag}^2 + V_{bg}^2 + V_{cg}^2)}{3}} \tag{1}$$

The unit vectors U_{pa} , U_{pb} and U_{pc} and its quadrature unit vectors U_{qa} , U_{qb} and U_{qc} using terminal voltage and voltage angle are approximated [3].

3.2 Design of LCO-FLL as a Part of Algorithm

An FLL based on LCO has been used to extract two in quadrature signals of the input quantity namely in phase quantity and in quadrature quantity indicated with suffix P and Q . Design analysis of phase ‘A’ is provided and the same is followed in both ‘B’ and ‘C’ phases. The extracted quantities of ‘A’ phase load current are I_{AP} and I_{AQ} ; they are in phase and in quadrature quantities, respectively. These extracted quantities from LCO-FLL are again fed back to the input of the LCO-FLL. The phase current quantity (I_{AP}) is compared with the actual load current. The error obtained is multiplied with a constant γ and ω_{ff} as shown in the equation below [19, 20] (Eqs. 2 and 3).

$$I_{LPT} = [i_{aL} - I_{AP}](k)\omega_{ref} \tag{2}$$

$$\omega_{\text{ref}} = \int (i_{aL} - I_{AP})I_{AQ}(-\gamma) + \omega_{ff} \quad (3)$$

The final output of the LCO-FLL is further integrated by multiplying with ω_{ref} and I_{LPT} is added to I_{AP} and both I_{AP} and I_{AQ} are estimated and final output is given as in Eqs. 4 and 5.

$$I_{AP} = \int \left[(I_{AP} - I_{AQ}) - \frac{I_{AP}}{A^2} (I_{AP}^2 + I_{AQ}^2) \right] \omega_{\text{ref}} + I_{\text{LPT}} \quad (4)$$

$$I_{AQ} = \int \left[(I_{AP} + I_{AQ}) - \frac{I_{AQ}}{A^2} (I_{AP}^2 + I_{AQ}^2) \right] \omega_{\text{ref}} \quad (5)$$

3.3 Calculation of Load Current Components

The load current active component (I_{PL}) has been calculated by averaging all active components of three-phase load currents as in Eq. 6 [5].

$$I_{PL} = \left(\frac{I_{AP} + I_{BP} + I_{CP}}{3} \right) \quad (6)$$

The load current reactive component (I_{QL}) is by averaging all reactive components of three-phase load currents as Eq. 7.

$$I_{QL} = \left(\frac{I_{AQ} + I_{BQ} + I_{CQ}}{3} \right) \quad (7)$$

3.4 Generation of Reference Current and PWM Pulses

The error obtained by comparing the reference terminal voltage (V_{dc}^*) with the obtained terminal voltage amplitude (V_{dc}) is processed through PI controller (PI_1) which provides I_{cp} as a loss components of converter. The error obtained by comparing the reference terminal voltage (V_m^*) with the obtained terminal voltage amplitude (V_m) is processed through PI controller (PI_2) which provides I_{cq} as an extra reactive components for voltage compensation. The reference components of grid currents namely active and reactive components are considered using Eqs. (8) and (9), respectively [5, 9] as follows.

$$I_p(n) = I_{p\text{Loss}}(n) + I_{PL}(n) \quad (8)$$

$$I_q(n) = I_{QLoss}(n) + I_{QL}(n) \quad (9)$$

Reference grid currents are calculated using unit templates with the following set of equations Eqs. 10, 11 and 12.

$$I_{aG}^* = U_{pa} * I_p + U_{qa} * I_q \quad (10)$$

$$I_{bG}^* = U_{pb} * I_p + U_{qb} * I_q \quad (11)$$

$$I_{cG}^* = U_{pc} * I_p + U_{qc} * I_q \quad (12)$$

Comparison of actual grid currents and reference grid currents obtains the error, which is input of the PWM generation block. The output of the PWM generation block is the gate pulses fed to the switches in VSC.

3.5 Calculation of PI Controller Gains Using MVO Algorithm

The error minimizations of DC bus and AC bus voltages have been formulated as an unconstrained optimization problem and gains have been estimated using multi-verse optimization (MVO) algorithm as follows. The voltage regulations of 0.28% and 10 numbers of iterations have been considered as termination criterion for this system. The objective function $f(x)$ to be minimized in this case is DC bus voltage error in PFC mode. The cost function (C_f) of the optimization technique has been defined with the error, $e(t)$ of actual and reference signals [26].

The cost function (C_f) is updated for every simulation with every search universe using the following equation.

$$C_f = \int te^2(t)dt \quad (11)$$

The variables which are to be optimized here are the proportional and integral controller gains K_1 and K_2 , respectively. So the size of the search agent is set to 2. As the variables are two in number and size is set to 2 for the search agent or universe. The controller gains in each mode of operation are obtained in such a way that the error is minimized to its lowest value.

MVO algorithm has been applied to the formulated problem using the mentioned equation set Eqs. 12–14.

$$M = M_{\min} + \left(\frac{j \times (M_{\max} - M_{\min})}{J_m} \right) \quad (12)$$

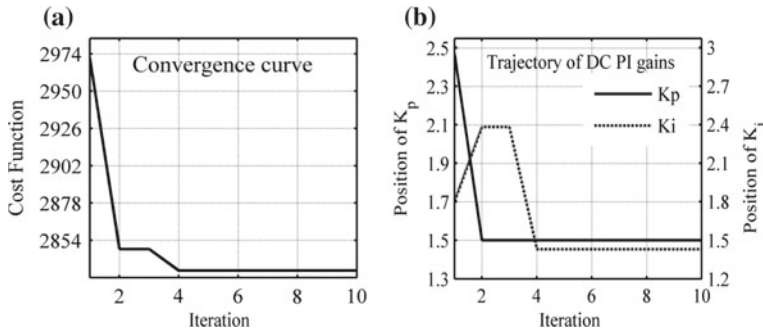


Fig. 3 Cost function optimization of DC and AC PI controller using MVO algorithm **a** Cost Function of DC PI **b** DC PI gains

$$D = 1 - \left(\frac{j}{J_m} \right)^{\frac{1}{E}} \tag{13}$$

$$P_s^{j+1} = \left\{ \begin{array}{l} \left\{ \begin{array}{l} P_s^j + D * (u_s - l_s) \text{ if } r_2 < 0.5 \\ P_s^j - D * (u_s + l_s) \text{ if } r_2 \geq 0.5 \end{array} \right\} \text{ if } r_1 < M \\ P_s^j \text{ if } r_1 \geq M \end{array} \right\} \tag{14}$$

In the above set of equations, the random variables r_1 and r_2 are selected from 0 to 1. The position of each variable is given by ‘ P_s^j ’. Here ‘ s ’ indicates the position of the variable and ‘ j ’ indicates the iteration values. The iterative exploitation is given by a constant ‘ E ’. The probability of existence of wormhole is given by M . The rate of distance travelled is given by ‘ D ’.

In this iterative optimization process, variables position varies with iteration number. In Fig. 3a, a plot depicting variation of C_f with respect to iterations is shown for PFC mode. The cost function (C_f) of the considered system has been optimized and settled stable at 4th iteration, i.e. 2835 for PI controller in PFC mode Fig. 3b is evident that at least by 4th iteration in PFC mode the optimized values for the considered variables have been obtained.

4 Simulation Work

The proper functioning of the proposed control algorithm for DSTATCOM has been verified in MATLAB SIMULINK environment. The simulated model consists of a supply AC mains of 415 V, 50 Hz with source impedance of $Z_s = (0.25 + j0.785)$ ohm feeding an AC voltage controller type of nonlinear load with load impedance of $(12 + j0.6283)$ ohm. Appendix 1 consists of the details of the parameters used in making simulated model. The model has been simulated for 1.5 s with a sampling time of 10 μ s the load dynamics in different phases have been included into the system from

0.95–1.1 s. The DSTATCOM has been operated with a PWM frequency of 5 kHz. Performance observation of the proposed control algorithm in time domain for power factor correction (PFC) mode is done. Appendix 1 provides necessary data used for simulation work.

4.1 System Performance During Load Dynamics

The performance of the DSTATCOM in power factor correction (PFC) and zero voltage regulation (ZVR) mode has been studied with load dynamics using three-phase grid voltages (V_g), distorted load currents (I_L), balanced grid currents (I_g), compensator currents (I_C), DC-link voltage (V_{dc}) and terminal voltage (V_m). Figure 4 illustrates the performance of DSTATCOM with nonlinear loads with load dynamics in PFC mode along with load balancing. Grid currents (i_{ag} , i_{bg} and i_{cg}) are shown in Fig. 4 at subplot (3, 4, 5). The proposed LCO-FLL has been validated with this demonstration.

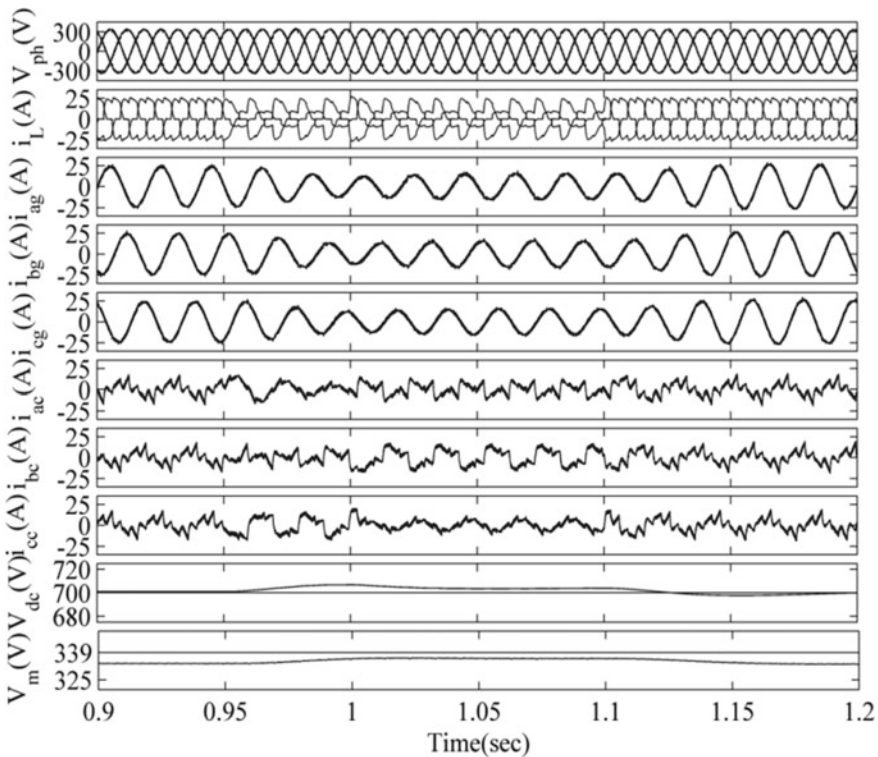


Fig. 4 Dynamic performance of the system with nonlinear load in PFC mode

Table 1 Simulation of LCO-FLL-based control For DSTATCOM with AC voltage controller as load

Harmonic current Mitigation and reactive power compensation		
Parameter	PFC mode	
	Magnitude	%THD
V_{ag}	333.2	3.22%
I_{ag}	23.99	4.73%
I_{aL}	25.14	21.22%
V_{dc}	700	–
Power	Active power	Reactive power
Source side	11,950	19.69
Load side	10,583	6031
Compensator side	959	5494
Power factor	Unity	–

The load balancing has been achieved during load elimination in phase ‘a’ load at time (t) equal to 0.9 – 1.0 s and load removal in phase ‘c’ load at time (t) equal 1.0 to 1.1 s. The balanced supply currents have been observed during the imbalance in load current due to phase removal with fast response. Subplot (6–8) shows the compensating currents of the VSC; it indicates the efficient reactive power compensation for supply current. Subplot (9) shows the self-sustaining DC bus voltage (V_{dc}) profile, and it is found that the controller effectively sets the DC bus voltage. Capability of the DSTATCOM system to compensate the sudden load variation is illustrated using these simulation results in PFC mode. By observing grid voltage (V_{ag}) and grid current (i_{ag}), it has been concluded that both are in phase this proves the proper PFC mode during load dynamics. The dynamic performance of the DSTATCOM in PFC mode has been studied using three-phase grid voltages (V_g), distorted load currents (I_L), balanced grid currents (I_g), compensator currents (I_C), DC-link voltage (V_{dc}) and terminal voltage (V_m). In Table 1, the total harmonic distortion (THD) values of the voltage at grid terminals (V_G), current at grid terminals (i_G) and current at load terminals (I_L) are 3.22%, 4.73% and 21.22%, respectively in PFC mode. These values are within the IEEE standards. This THD values illustrate the ability of the DSTATCOM system for sudden load variation.

5 Experimental Validation

Using d-SPACE DS1104, the experimental validation of a three-wire system with DSTATCOM has been implemented with sampling time of 40 μ s. With a four-channel digital storage oscilloscope, the performance has been captured. The voltage and current quantities have been sensed using LEM made Hall Effect sensors LV25P and LA55P. Gate pulses are being produced using d-SPACE-1104 with a sampling rate of 40 μ s for the proposed algorithm. The harmonic distortions of the system in

steady state have been observed using single-phase power quality analyzer (Fluke-43B) For harmonic analysis, results are taken for source voltage, source current and load current. Detailed data used for experimental work is given in Appendix 2.

5.1 Performance of DSTATCOM System in Steady State and Dynamic State

The steady-state performance of the system using source current (i_{ag}), load current (i_{al}) and compensator current (i_{ac}) is shown in Fig. 5a–c with respect to grid voltage (V_{abg}). Figure 5d shows THD analysis under steady state for grid current of phase ‘a’ and the current distortion is under acceptable range. Figure 5e shows the THD analysis for load current of phase ‘a’ under steady state. Figure 5f shows the THD analysis for grid voltage of phase ‘a’ under steady state. In UPF mode, the satisfactory performance of DSTATCOM has been justified by observing the THD of grid current, grid voltages and load current which are 4.6%, 3.2% and 23.1%, respectively. Figure 5g–i shows active and reactive powers at the grid (2.36 kW, 0.06 kVAR), at the load end (2.05 kW, 0.85 kVAR) and at the compensator (0.37 kW and 0.79 kVAR), respectively. The total active power is supplied by the grid to load and compensator and total reactive power supplied by the compensator to load and grid. This shows the power balance in the system. The power factor at the grid terminals has been improved to unity from 0.92 DPF.

The dynamic performance of the system with LCO-FLL has been analyzed using Fig. 6a, b. To show the effective operation of system in PFC mode, various system signals like phase currents of source, load and compensator have been sensed and plotted with respect to the grid voltage (V_{abg}) and DC-link voltage (V_{dc}) during load injection. Figure 6a shows the response of source current, load current and compensator current with respect to grid voltage. Figure 6b shows the response of source current (I_{ag}), load current (I_{al}) and compensator current (I_{ac}) with respect to DC-link voltage (V_{dc}). During load current injection, the variation in grid current amplitude has been observed, and DC-link voltage has been recovered within four cycles without crossing the controlled limit. These observations conclude that system operates satisfactorily during dynamic condition.

6 Conclusion

In crux, in this work a new method is proposed for fundamental extraction using FLL which is based on LCO. Stability analysis of the LCO-based FLL was considered which confirms the stability of the LCO-FLL. PFC mode is considered for DSTATCOM in which the considered LCO-FLL provides suitable performance for

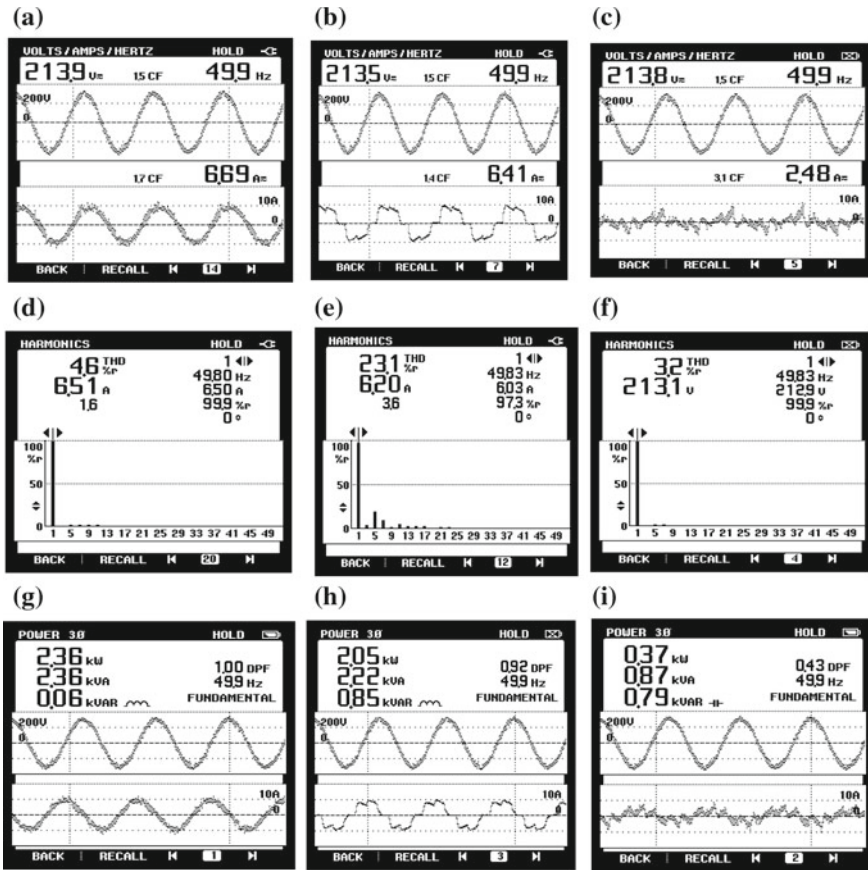


Fig. 5 Steady-state analysis of (a–c) i_{ag} , i_{aL} , i_{cC} with respect to v_{abg} (d–f) harmonics spectrum of i_{ag} , i_{aL} , v_{abg} (g–i) Active and reactive power analysis for system under study with (a) Active and reactive power supplied by the source (b) Active and reactive power delivered to load (c) Active and reactive power at compensator

highly polluted load current with phase imbalance. Harmonic mitigation capabilities can be observed since the LCO-FLL reduces the source current THD to less than 5% from 23%. The LCO-FLL produces synchronized fundamental signals with constant amplitude despite phase imbalance in the load currents. Three-phase LCO-FLL case was evaluated in MATLAB and then realized using d-SPACE-1104. The results obtained are appropriate which concludes that fundamental extraction using LCO-FLL is proper and done in less than one grid voltage cycle. The error minimization of DC bus voltage has been estimated in four iterations. The produced results using optimized PI gains have been analyzed through simulation and verified from experimental performance.

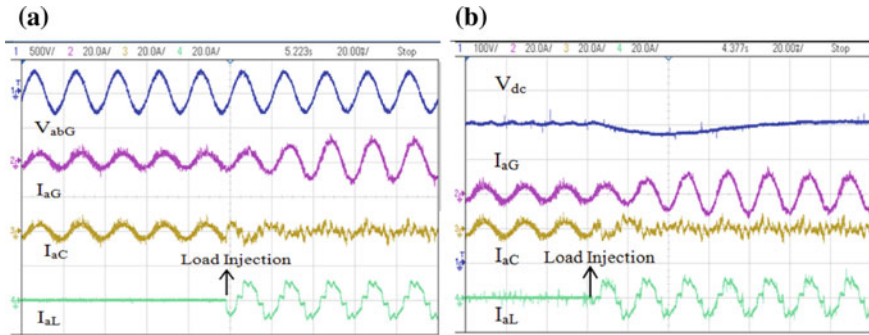


Fig. 6 System dynamic performance with DSTATCOM (a) Ch1: V_{abg} ; Ch2: I_{ag} ; Ch3: I_{aL} ; Ch4: I_{aC} (e) Ch1: V_{dc} ; Ch2: I_{ag} ; Ch3: I_{aC} ; Ch4: I_{aL}

Acknowledgements The authors are very thankful to Science and Engineering Research Board-New Delhi under Extra Mural Research Scheme for funding this Project through Grant No. SB/S3/EECE/030/2016, Dated: 17/08/2016.

Appendix 1

AC mains: 3 phase, 415 V (line), 50 Hz, source impedance: $R_s = 0.06 \Omega$, $L_s = 1$ mH; nonlinear type load: AC voltage controller with load ($R = 12 \Omega$ and $L = 2$ mH and $R = 50 \Omega$ and $L = 2$ mH during unbalance in one phase) DC-link voltage: 700 V; sampling time (t_s) = 10 μ s; Interfacing inductor: $L_f = 2.25$ mH; Switching frequency (f_s) = 5 kHz, DC-link cut-off frequency of LPF: 10 Hz.

Appendix 2

AC mains: 3 phase, 230 V (line) with distortion, 50 Hz; nonlinear type load: AC voltage controller with load; passive filter parameter (ripple filter): $R_f = 5 \Omega$, $C_f = 20 \mu$ F; sampling time (T_s) = 40 μ s, DC-link voltage: 400 V; DC-link capacitor (C_{dc}): 4500 μ F; Interfacing inductor: $L_f = 4$ mH; and DC-link PI controller $k_p = 0.3$ and $k_i = 0.06$.

References

1. Akagi H (2007) *Instantaneous power theory and applications to power conditioning*, 4th ed. Wiley, New Jersey
2. Dugan R et al (1996) *Electrical power systems quality*, 2nd edn. McGraw-Hill, New York
3. Bollen H, Understanding power quality problems. IEEE Press, New York
4. Kusko A, Thompson M (2007) *Power quality in electrical systems*. McGraw-Hill, New York
5. Singh B, Solanki J (2009) A comparison of control algorithms for DSTATCOM. *IEEE Trans Industr Electron* 56:2738–2745. <https://doi.org/10.1109/tie.2009.2021596>
6. Benysek G, Pasko M (2012) *Power theories for improved power quality*. Springer, Dordrecht
7. Blaabjerg F, Teodorescu R, Liserre M, Timbus A (2006) Overview of control and grid synchronization for distributed power generation systems. *IEEE Trans Industr Electron* 53:1398–1409. <https://doi.org/10.1109/tie.2006.881997>
8. Singh B, Al-Haddad K, Chandra A (1999) A review of active filters for power quality improvement. *IEEE Trans Industr Electron* 46:960–971. <https://doi.org/10.1109/41.793345>
9. Singh B, Bhuvaneswari G, Arya S (2012) Review on power quality solution technology. *J Asian Power Electron* 6:19–27
10. Ebadian M, Talebi M, Ghanizadeh R (2015) A new approach based on instantaneous power theory for improving the performance of UPQC under unbalanced and distortional load conditions. *Automatika* 56:226–237. <https://doi.org/10.7305/automatika.2015.07.750>
11. Rahmani S, Mendalek N, Al-Haddad K (2010) Experimental design of a nonlinear control technique for three-phase shunt active power filter. *IEEE Trans Industr Electron* 57:3364–3375. <https://doi.org/10.1109/tie.2009.2038945>
12. Rodriguez P, Pou J, Bergas J et al (2007) Decoupled double synchronous reference frame PLL for power converters control. *IEEE Trans Power Electron* 22:584–592. <https://doi.org/10.1109/tpe.2006.890000>
13. Karimi-Ghartemani M, Iravani M (2004) A method for synchronization of power electronic converters in polluted and variable-frequency environments. *IEEE Trans Power Syst* 19:1263–1270. <https://doi.org/10.1109/tpwrs.2004.831280>
14. Golestan S, Guerrero J, Vasquez J (2017) Three-phase PLLs: a review of recent advances. *IEEE Trans Power Electron* 32:1894–1907. <https://doi.org/10.1109/tpe.2016.2565642>
15. Xavier L, Cupertino A, de Resende J et al (2017) Adaptive current control strategy for harmonic compensation in single-phase solar inverters. *Electr Power Syst Res* 142:84–95. <https://doi.org/10.1016/j.epsr.2016.08.040>
16. Sun L, Ju P, Chen Y et al (2016) Optimal control strategy of voltage source converter-based high-voltage direct current under unbalanced grid voltage conditions. *IET Gener Transm Distrib* 10:444–451. <https://doi.org/10.1049/iet-gtd.2015.0749>
17. Chilipi R, Beig A, Al Hosani K, Al Sayari N (2016) Control scheme for grid-tied distributed generation inverter under unbalanced and distorted utility conditions with power quality ancillary services. *IET Renew Power Gener* 10:140–149. <https://doi.org/10.1049/iet-rpg.2015.0095>
18. Guo X, Wu Q, Gu H (2011) Phase locked loop and synchronization methods for grid interfaced converters: a review. *J PrzegladElektrotechniczny* 10:182–187
19. Teplinsky A, Feely O (2008) Limit cycles in a MEMS oscillator. *IEEE Trans Circuits Syst II Express Briefs* 55:882–886. <https://doi.org/10.1109/tcsii.2008.923402>
20. Pandey S, Kumar S, Singh B (2018) LCO-FLL control for single-phase utility integrated single-stage solar PV system. *IET Renew Power Gener* 12:1941–1948. <https://doi.org/10.1049/iet-rpg.2018.5405>
21. Oviedo E, Vazquez N, Femat R (2018) Synchronization technique of grid-connected power converters based on a limit cycle oscillator. *IEEE Trans Industr Electron* 65:709–717. <https://doi.org/10.1109/tie.2017.2703655>
22. Ahmed H, Amamra S, Bierhoff M (2019) Frequency-locked loop-based estimation of single-phase grid voltage parameters. *IEEE Trans Industr Electron* 66:8856–8859. <https://doi.org/10.1109/tie.2018.2873527>

23. Du K, Swamy M (2016) Search and optimization by metaheuristics. Springer International Publishing, Switzerland
24. Deb K (2007) Optimization for engineering design, 1st edn. Prentice Hall of India, New Delhi
25. Knowles J, Corne D, Deb K (2008) Multi-objective problem solving from nature. Springer, Berlin
26. Mirjalili S, Mirjalili S, Hatamlou A (2015) Multi-verse optimizer: a nature-inspired algorithm for global optimization. *Neural Comput Appl* 27:495–513. <https://doi.org/10.1007/S00521-015-1870-7>

Global Horizontal Irradiance Prediction Using Deep Neural Network Framework



Sambit Dash, Priya Ranjan Satpathy, Sobhit Panda and Renu Sharma

Abstract Due to uncertainty in solar radiation caused by cloud cover and other environmental conditions, it is necessary to accurately predict solar irradiance for time ahead planning and scheduling. In this paper, a comparative analysis of 1 h ahead forecasting of global horizontal irradiance using various popular machine learning technique and deep neural network is determined. The forecasting accuracy is analyzed using various error metrics such as mean absolute error (MAE) and mean square error (MSE). The number of time lags influencing 1 h ahead forecasting is determined using autocorrelation and partial autocorrelation function. The hyper-parameters of various machine learning techniques are tuned using random search method. It is observed the deep neural network provides the least prediction error as compared to other machine learning techniques.

Keywords Global horizontal irradiance (GHI) · Regression · Deep neural network (DNN)

S. Dash

Department of Electrical Engineering, IIIT, Bhubaneswar 751003, India
e-mail: sambitdash.2011@gmail.com

P. R. Satpathy (✉) · R. Sharma

Department of Electrical Engineering, ITER, SOA Deemed to Be University, Bhubaneswar 751030, India
e-mail: priransat3@gmail.com

R. Sharma

e-mail: renusharma@soa.ac.in

S. Panda

Department of Instrumentation and Electronics Engineering, CET, Bhubaneswar 751003, India
e-mail: sobhitpanda25@gmail.com

© Springer Nature Singapore Pte Ltd. 2020

R. Sharma et al. (eds.), *Innovation in Electrical Power Engineering, Communication, and Computing Technology*, Lecture Notes in Electrical Engineering 630,
https://doi.org/10.1007/978-981-15-2305-2_25

1 Introduction

With the advent of renewable power generation and simultaneous depletion of conventional sources such as coal and petroleum products, it has become necessary to adequately forecast the generation capability of renewable sources so as the schedule and plan usage of such sources along with conventional resources [1, 2]. There has been an exponential increase in the usage of photovoltaic (PV) systems which creates challenges for appropriate functioning of the grid as the power output of PV fluctuates depending on the weather pattern [3, 4]. Forecasting is necessary to adequately utilize the fluctuating energy of the PV system. Generally, load patterns which have been forecasted for few days ahead are used as basis for scheduling the conventional power plants and initiating transactions in the market to meet the supply and demand conundrum. The forecasted load data is utilized by various parties involved in the process of generation, transmission, and distribution of electrical energy such as utilities, transmission companies, and generation plants. For insulated microgrid, the importance of forecasting is more apparent. Since these grids are not interconnected and the power is generated in the territory itself, this creates a problem as PV power output can ramp up depending on the time of the day [5–8]. Thereby, proper forecasting can help the grid operators to adequately balance the power demand and power generation. There can be different forecasting horizons such as ultra-short-term forecasting of few minutes ahead to a forecasting horizon spreading a few days ahead. Although various parameters of solar irradiance can be forecasted, in this paper, we have considered forecasting the global horizontal irradiance (GHI) since it is the most essential parameter in forecasting. There can be various approaches to GHI prediction namely statistical approaches such as autoregressive (AR), autoregressive moving average (ARMA), or autoregressive integrated moving average (ARIMA). For long-term forecast, numerical weather prediction (NWP) models have been fairly accurate as compared to statistical models. For short-term forecasting, temporal elements in the cloud have been utilized to track movement of cloud which has been used to forecast solar irradiation. Currently, statistical machine learning algorithms such as artificial neural network (ANN) and support vector machines (SVM) have gained prominence for efficient forecasting of time series data. Although in recent times, advances in the field of deep learning has been enormous, deep neural networks (DNNs) have been particularly efficient in the field of computer vision and time series data analysis. In this paper, various machine learning classifiers such as ANN, SVM, and random forest (RF) are utilized for predicting solar irradiance and their accuracy is compared with DNN. Various error metrics such as mean absolute error (MAE) and mean square error (MSE) have been utilized for prediction accuracy comparison.

2 Different Aspects of Solar Irradiance

Solar irradiation can be defined as the electromagnetic radiation from sun striking the earth in terms of power per unit area [9]. The unit of solar irradiation is Wh/m^2 . Solar irradiance has three aspects to it.

- (a) Global horizontal irradiance (GHI)
- (b) Direct normal irradiance (DNI)
- (c) Diffuse horizontal irradiance (DHI)

DNI can be considered as the amount of solar radiation per unit area striking a surface which is held perpendicular to the rays of the sun. DHI is the radiation generated due to scattering of the sun's rays by the atmosphere. GHI is the total amount of radiation along the horizontal surface.

$$\text{GHI} = \text{DNI} \cdot \cos \varphi + \text{DHI} \quad (1)$$

where φ is the angle between normal of the surface and the sun's rays.

3 Data

In this paper, hourly GHI data is taken from rotating shadow band radiometer located at Sacramento Municipal Utility District, Anatolia-Rancho Cordova California [10]. The monitoring station measures GHI, DNI, and DHI for particular location and the data is open for public use. The entire dataset taken in this work is in month of April 2013. The hourly dataset is divided into training and testing data using scikit-learn function `sklearn.model_selection.train_test_split`.

4 Autocorrelation (ACF) and Partial Autocorrelation (PACF)

Before venturing into prediction, it is important to analyze the data at hand.

Figure 1 shows the time series data consisting of GHI for the entire month of April. The data is divided to training and test dataset.

4.1 Autocorrelation Function (ACF)

Autocorrelation can be defined as correlation of a signal with time-lagged values of the same signal. ACF can be an efficient tool to recognize repeating pattern in a

Fig. 1 GHI for the month of April 2013

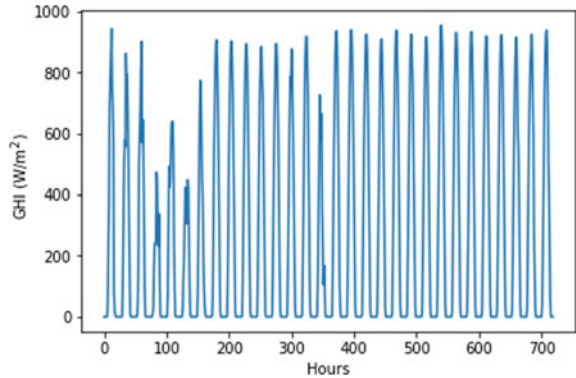
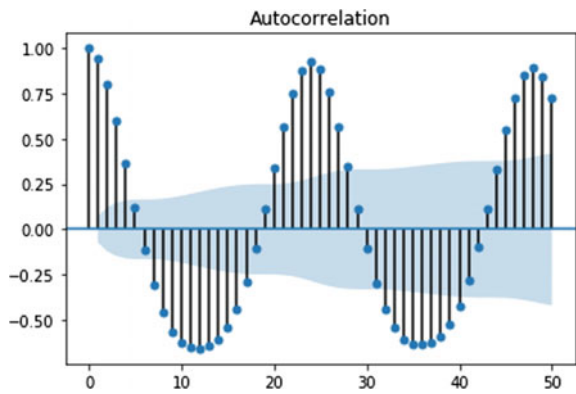


Fig. 2 ACF plot for 50 time lags



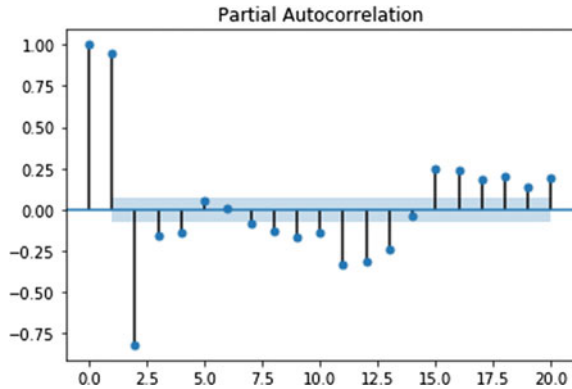
signal. Higher the value of ACF higher is the correlation of the current signal with time-lagged version of itself. The ACF plot for GHI values of April 2013 is shown in Fig. 2.

From the ACF plot, it can be concluded that the daytime values are correlated to each other and similarly nighttime values are correlated to each other. The points outside the cone show actual correlation, whereas points inside the cone are not correlated.

4.2 Partial Autocorrelation Function (PACF)

The partial autocorrelation at a particular lag is the direct correlation of the present data with that particular lagged value excluding the impact of intermediate values on the data points. ACF consists of both the direct and indirect correlations of the data with its lagged points, whereas PACF shows the correlation of the data directly with

Fig. 3 PACF for 20 time lags



its lagged points thereby making it effective tool to select the number of lagged values required for forecasting GHI. The PACF plot for the month of April is represented in Fig. 3.

From the partial autocorrelation, it can be observed clearly that the data is highly correlated to 1 and 2 h time lag. Thus, for forecasting of GHI, we use time series data of 1 h and 2 time lag.

5 Deep Neural Network (DNN)

DNN [11] is a form of artificial neural network (ANN) with multiple hidden layers between input and output. The power of DNN lies in mapping complex nonlinear relationship between input and output data. The configuration of DNN used in this work is given below:

- (a) Library: Keras [9]
- (b) Number of hidden layers: 1
- (c) Neurons in input and hidden layers: 32
- (d) Activation function for input, hidden, and output layers: Relu
- (e) Optimizer: rmsprop
- (f) Loss: mean square error
- (g) Metric: mean square error.

6 Configuration of Other Machine Learning Techniques

A brief discussion on the configuration of various other machine learning techniques has been given below.

6.1 Support Vector Machine (SVM)

SVM [12] is a supervised machine learning algorithm based on maximizing the margin between various classes of data. The data point which lie on the border of the hyper-plane are called as support vectors. The configuration of SVM is given as:

- (a) Library: scikit-learn [11]
- (b) Kernel: radial basis function
- (c) Penalty factor “C” tuned using random search
- (d) Epsilon: 0.0001.

6.2 Multilayer Perceptron (MLP)

MLP is a collection of nodes based loosely on functioning of biological brain. The input received by the MLP is combined with the activation function, and the generated data point is transferred to the next hidden layer where the data again combine with the activation function and the process continues till it reaches the output layer. The configuration of MLP is given as:

- (a) Library: Scikit-learn
- (b) Kernel: Rectified linear unit (ReLu)
- (c) Solver: Adam
- (d) Hidden Layer tuned using random search within {1, 25,000}
- (e) Learning rate tuned using random search within {0.001, 0.05}
- (f) Alpha tuned using random search within {0.001, 0.05}.

6.3 Random Forest (RF)

RF [13, 14] is based on an ensemble of decision trees which are built in parallel, and based on a majority vote, a strong learner is created. RF attempts to overcome general weakness of decision tree which tends to be over fitting to the dataset. The configuration of RF is given as:

- (a) Library: scikit-learn
- (b) Maximum depth: 5
- (c) Number of estimators chosen using random search.

6.4 Gaussian Process Regression (GPR)

In GPR [15], value at a particular point is predicted using weighted average of known values of the function in the neighborhood. The configuration of GPR used in this paper is:

- (a) Library: scikit-learn
- (b) Kernel: 5*RBF(length_scale = 1.0, length_scale_bounds = (1e-1, 10.0))*RationalQuadratic(length_scale = 1.0, alpha = 0.1).

7 Performance Metrics

The performance of the machine learning models [16] is evaluated on four statistical indices, i.e., mean absolute error (MAE), mean square error (MSE), root mean square error (RMSE), and coefficient of determination (R^2). The R^2 measure gives information with regard to how efficient the model is in quantifying the variability in data. MAE helps determining the absolute value of the error due to bias. MSE helps determining the quality of the regressor.

$$\text{MAE} = \frac{\sum_{i=1}^n |y_i - x_i|}{n} = \frac{e_1 + e_2 + \dots + e_n}{n} \quad (2)$$

$$\text{MSE} = \frac{1}{n} \sum_{i=1}^n (e_1 + e_2 + \dots + e_n)^2 \quad (3)$$

$$\text{RMSE} = \sqrt{\frac{e_1^2 + e_2^2 + \dots + e_n^2}{n}} \quad (4)$$

$$R^2 = \frac{\sum_{i=1}^n (y_i - \bar{y}_d)^2}{\sum_{i=1}^n (y_i - \bar{y}_d)^2 + \sum_{i=1}^n (y_i - \bar{y}_{d_i})^2} \quad (5)$$

8 Result Analysis

Figures 4, 5, and 6 show the actual GHI for the particular day and the forecasted GHI by various machine learning algorithms and their corresponding error margins. Table 1 shows the performance metrics of various techniques. It can be clearly observed that DNN has the least prediction error compared to all other algorithms in all performance metrics. It must be noted that although RF has lesser MAE as compared to GPR, it has a much higher MSE and RMSE as compared to GPR, whereas DNN has the least error across all metrics compared to other algorithms.

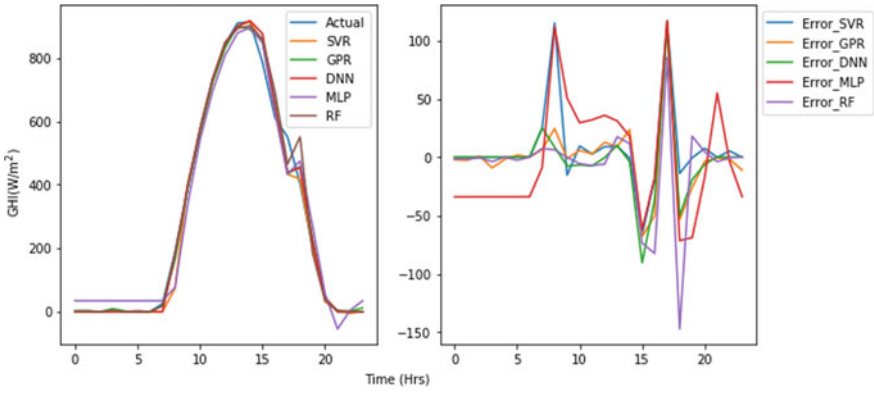


Fig. 4 Forecasted GHI and error in forecasted data for day 1

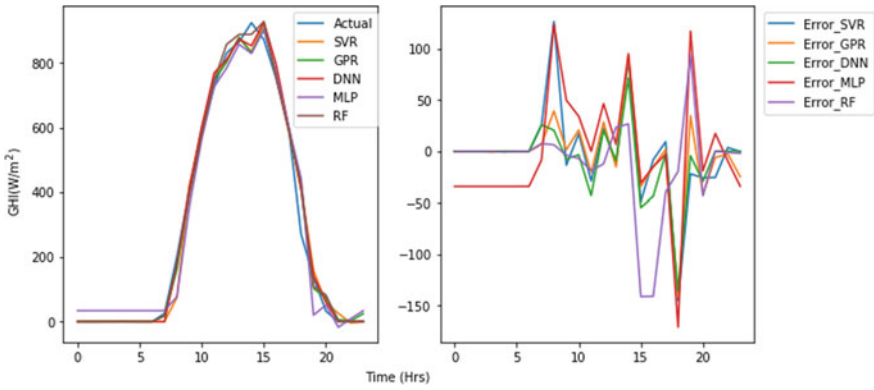


Fig. 5 Forecasted GHI and error in forecasted data for day 2

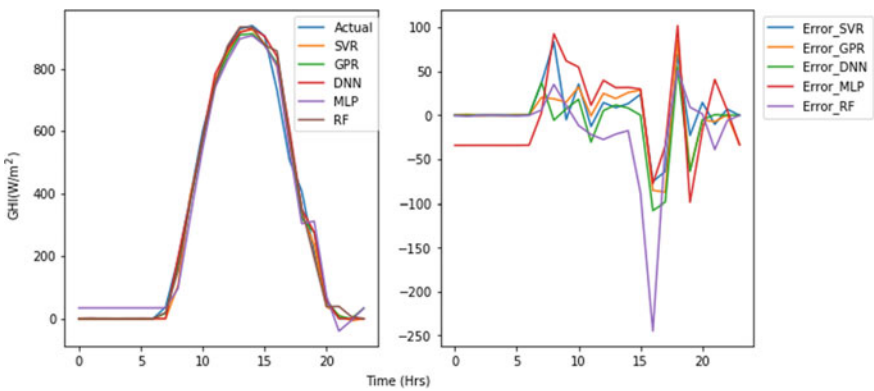


Fig. 6 Forecasted GHI and error in forecasted data for day 3

Table 1 Performance metrics for 3 days

	MLP	SVR	GPR	RF	DNN
MAE	42.13	21.41	21.13	19.90	18.19
MSE	2825.60	1546.70	1320.55	1471.15	1246.18
RMSE	53.15	39.32	36.33	38.35	35.30
R^2	0.9769	0.9873	0.9892	0.9880	0.9898

9 Conclusion

In this paper, we have taken GHI for the month of April 2013 and evaluated the number of time lags influencing the forecasting accuracy using ACF and PACF. Then, using the appropriate time lags, various machine learning classifiers are trained and tested. It was observed that DNN has the least prediction error on all performance metrics thereby making it the best regression algorithm for predicting GHI for 1 h ahead in the observed dataset.

Acknowledgements We thank Afshin Andreas and National Renewable Energy Laboratory (NREL) for providing the SMUD RSR dataset.

References

1. Jena S, Kar SK (2019) Setting a fostered energy network by decarbonizing the grid: hybridization, control, and future solutions upon storage. *Int J Energy Res* 43(1):455–474
2. Satpathy PR, Sharma R (2019) Power and mismatch losses mitigation by a fixed electrical reconfiguration technique for partially shaded photovoltaic arrays. *Energy Convers Manag* 192:52–70
3. Satpathy PR, Sharma R, Dash S (2019) An efficient SD-PAR technique for maximum power generation from modules of partially shaded PV arrays. *Energy* 175:182–194
4. Diagne M, David M, Lauret P, Boland J, Schmutz N (2013) Review of solar irradiance forecasting methods and a proposition for small-scale insular grids. *Renew Sustain Energy Rev* 27:65–76
5. Yadav AP, Kumar A, Behera L (December 2013) RNN based solar radiation forecasting using adaptive learning rate. In: *International conference on swarm, evolutionary, and memetic computing*. Springer, Cham, pp 442–452
6. Naveen Chakkaravarthy A, Subathra MSP, Jerin Pradeep P, Manoj Kumar N (2018) Solar irradiance forecasting and energy optimization for achieving nearly net zero energy building. *J Renew Sustain sEnergy* 10(3):035103
7. Kumar NM, Subathra MSP (2019) Three years ahead solar irradiance forecasting to quantify degradation influenced energy potentials from thin film (a-Si) photovoltaic system. *Results Phys* 12:701–703
8. Satpathy PR, Sharma R (2019) Diffusion charge compensation strategy for power balancing in capacitor-less photovoltaic modules during partial shading. *Appl Energy* 255:113826
9. Andreas A, Bank J (2009) Sacramento municipal utility district (SMUD): Rotating shadowband radiometer (RSR); Anatolia—Rancho Cordova, California (Data); NREL Report No. DA-5500-56513. <http://dx.doi.org/10.5439/1052554>

10. Hinton G, Deng L, Yu D, Dahl G, Mohamed AR, Jaitly N, Senior A, Vanhoucke V, Nguyen P, Kingsbury B, Sainath T (2012) Deep neural networks for acoustic modeling in speech recognition. *IEEE Sign Process Mag* 29
11. Chollet F (2015) Keras
12. Schölkopf B, Smola AJ, Bach F (2002) *Learning with kernels: support vector machines, regularization, optimization, and beyond*. MIT press, Cambridge
13. Pedregosa F, Varoquaux G, Gramfort A, Michel V, Thirion B, Grisel O, Blondel M, Prettenhofer P, Weiss R, Dubourg V, Vanderplas J (2011) Scikit-learn: machine learning in python. *J Mach Learn Res* 12(Oct):2825–s2830
14. Liaw A, Wiener M (2002) Classification and regression by randomForest. *R news* 2(3):18–22
15. Rasmussen CE (February 2003) Gaussian processes in machine learning. In: *Summer school on machine learning*. Springer, Berlin, Heidelberg, pp 63–71
16. Powar OS, Chemmangat K (2019) Dynamic time warping for reducing the effect of force variation on myoelectric control of hand prostheses. *J Electromyogr Kinesiol* 48:152–160

A Hybrid Approach for Path Planning of Multiple AUVs



Madhusmita Panda , Bikramaditya Das  and Bibhuti Bhusan Pati 

Abstract The autonomous underwater vehicles (AUVs) are the independent marine robots employed in many undersea operations starting from the field of underwater research to commercial oil industry surveys. The path planning of a team of AUVs is necessary as it is required to find a safe route from the start to endpoints for the team of AUVs to accomplish any mission goal. The group of AUVs has to trace a time or energy optimal locus in order to reduce the cost of any operation. This paper proposed a hybrid grey wolf optimization (h-GWO) algorithm for path planning of multiple AUVs by integrating features of genetic algorithm (GA) and grey wolf optimization (GWO). This allows a team of AUVs to move in an obstacle rich environment without colliding with obstacles and with each other. Here, path cost is a summation of distance travelled and penalty of collision. Simulation results are obtained for three AUVs in a three-dimensional grid map with static obstacles by applying GA, GWO, and h-GWO algorithm. A comparative study of obtained results made on the basis of computational time, path length and path cost. The results of the hybrid algorithm overcome the disadvantages of GA and GWO and provided a cost-optimized path for operations that are not time-sensitive.

Keywords Autonomous underwater vehicle (AUV) · Genetic algorithm (GA) · Grey wolf optimization (GWO) · Hybrid · Path planning (PP)

1 Introduction

An autonomous underwater vehicle (AUV) is a self-controlled and self powered underwater robot [1]. The AUV modelling is critical as it has to withstand the under seawater pressure, unavailability of the global positioning system (GPS) signal, low bandwidth sea channel while performing independently [2]. Path planning (PP) for

M. Panda (✉) · B. Das · B. B. Pati
Department of Electronics and Telecommunication, VSSUT, Burla, Odisha 768018, India
e-mail: mpanda_etc@vssut.ac.in

AUVs in a three-dimensional (3D) environment is needed for all applications involving AUV. A PP controller (PPC) is required to find an optimal and sub-optimal path from source to destination location while avoiding obstacles in the path.

GA is an optimization technique preferred to solve the multi-objective optimization problem. It is easy to implement and robust to local maxima and minima. But, it is difficult to define an objective function with proper genetic operators. GA takes more time to process which leads to an increase in the computational cost with the increase in complexity of the problem [3].

The “Grey wolf optimization (GWO)” is one of the “Swarm intelligence (SI)” algorithms that mimic the hunting process of the “Grey wolf (GW)” pack led by the “alpha wolf” [4]. GWO shows better exploration capability in comparison with contemporary methods and effectively avoids the local minimum [5]. The GWO has been effectively applied in many applications as discussed in [6]. The GWO has also applied for generating a cost-optimized path for a single AUV in [7]. Some of the path planner for both single AUV [8–10] and the team of AUVs [1, 11–13] are illustrated in the literature. In this research, an attempt has been made to propose a hybrid GWO (h-GWO) algorithm to address the PP problem of multiple AUVs and compare the result with the results obtained by applying the GA and the GWO to generate a cost-effective path for multiple AUVs. The AUVs follow the leader-follower topography. For this research, a leader AUV is followed by two follower AUVs.

This research paper is arranged into five sections. Section 2 derives the cost function used for path planning of multiple AUV. Section 3 reviews GA and GWO algorithms and describes h-GWO. Section 4 is for analysis of the obtained results by applying GA, GWO, and h-GWO to PP of multiple AUV and Sect. 5 concludes the paper.

2 Cost Function Modelling

The PP of multiple AUVs involves two different cost functions calculated in two phases:

Phase 1-The cost function for leader path

Phase 2-The cost function for the follower’s path.

2.1 Calculation of the Cost Function for Follower Path

The cost function for leader AUV’s PP is given by [9]

$$\text{path cost} = \mu * \text{path Length} + (1 - \mu) \times (\text{path penalty}) \quad (1)$$

In Eq. 1 μ is the weighting coefficient such that $\mu \in [0, 1]$. The $\mu \rightarrow 1$ indicates a lesser probability of collision that leads to shorter route while $\mu \rightarrow 0$ indicates a higher probability of collision, thus leads to the longer path to avoid the threat.

Path Length:

It is the total distance travelled from source to destination. Lesser the path length lesser will be the time of travel and energy expenses. It is calculated as

$$\text{path length} = \sum_{m=0}^M l(P_m, P_{m+1}) \quad (2)$$

Here, $l(P_m, P_{m+1})$ is the ‘‘Euclidian distance’’ between points P_m and P_{m+1} calculated as

$$l(P_m, P_{m+1}) = \sqrt{(x_{m+1} - x_m)^2 + (y_{m+1} - y_m)^2 + (z_{m+1} - z_m)^2} \quad (3)$$

Path Penalty:

The total penalty of the path depends upon how far the path points are from the centre of their nearest obstacle. For example, the path penalty for m th point on the j th path is calculated as

$$\text{path penalty} = \sum_{m=0}^M P_{jm} (1 + j \times m) \quad (4)$$

where P_{jm} is the penalty of the m th point on the j th path given by,

$$P_{jm} = \begin{cases} r_{\min} - l_{\min}, & \text{when } l_{\min} > r_{\min} \\ e^{\rho(r_{\min} - l_{\min})} & \text{when } l_{\min} \leq r_{\min} \end{cases} \quad (5)$$

In Eq. 5, l_{\min} is the distance of the m th point from the closest obstacle centre and r_{\min} is the radius of the closest obstacle. When the $l_{\min} > r_{\min}$, the m th point is outside the obstacle boundary otherwise the point selected is within obstacle boundary that leads to a collision. A collision leads to an exponential increase in path cost indicated by the positive penalty coefficient ρ .

2.2 Calculation of the Cost Function for Leader Path

The follower cost function is used to avoid the obstacle and another follower AUVs on the follower path. Thus, an extra parameter is added to the ‘‘path cost’’ equation.

$$\text{path cost} = \mu * \text{path Length} + (1 - \mu) \times (\text{path penalty} + \text{collision penalty}) \quad (6)$$

Collision Penalty:

It is the total collision penalty of a follower path when they collide with other AUVs given as,

$$\text{collision penalty} = \sum_{m=0}^M P_{cij}(m) \quad (7)$$

where $P_{cij}(m)$ is the penalty of m th point on the i th path due to m th point on j th path. Simply, the total collision cost is calculated by the summation of collision penalty due to every m th point of a path due to the corresponding point of all other paths formed. Now the individual collision penalty between two corresponding points of two different paths is given as,

$$P_c(m) = \begin{cases} s_d - d_{ij}(m), & \text{when } s_d < d_{ij}(m) \\ e^{d_{ij}(m)-s_d}, & \text{when } s_d > d_{ij}(m) \end{cases} \quad (8)$$

In the above equation, s_d is the safe distance and $d_{ij}(m)$ is the distance of the m th point of i th path and j th path. The equation describes that when two corresponding points of two paths are far enough to avoid collision then the distance between them is minimized up to a safe distance by providing a negative penalty. When two corresponding points of two paths are close enough that there is the chance of collision between them, then the paths are separated using a positive exponential penalty.

3 Algorithms

3.1 Genetic Algorithms

Genetic algorithms are inspired by biological evolution processes of “reproduction and natural selection” to solve for the “fittest” solutions. GA is a powerful and efficient random search algorithm that can solve optimization problems with incomplete information. The “performance” of the GA depends on the process of encoding the candidate solutions into chromosomes and defining the fitness function for a given application. The other determining factors are “crossover” probability, “mutation” probability, “population” size, and the total number of “iterations”. These values can be adjusted after assessing the algorithm’s performance on a few trials run. The basic components common to almost all genetic algorithms are shown in Fig. 1.

The solution of PP problem for multiple AUV by using GA is given in the following steps:

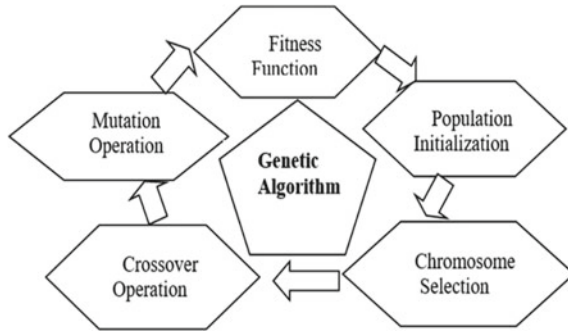


Fig. 1 Components of GA

Algorithm 1: Pseudo code of GA for PP of multiple AUVs	
Step 1:	The 3D environment is realized as a grid map consisting of different node points. AUV will move from node to node as it moves in the grid.
Step 2:	The starting and terminating points are properly defined.
Step 3:	The static obstacle locations on each node of the grid path is established
Step 4:	Generate the initial population consists of all feasible paths. Define max. no. of generation and number of followers AUVs
Step 5:	Compute the minimum cost path for leader AUV
Step 6:	for (t < max. no. generation) for all follower AUVs computation of minimum cost path apply crossover and mutation operator end for end for
Step 7:	if the path converges with leader path return the optimal path else repeat step 6

3.2 Grey Wolf Optimization

The GWO maintains the leadership hierarchy and group hunting features of grey wolves [4]. The “alpha (α) wolf” is at the top of the hierarchy followed by “beta (β)”, “delta (δ)” and “omega (ω)” wolves in order as in Fig. 2. The three phases of grey wolf hunting are shown in Fig. 3.

The encircling of prey can be modelled as distance “ d ” from prey given by:

$$d = |c \cdot xp - x(n)| \tag{9}$$

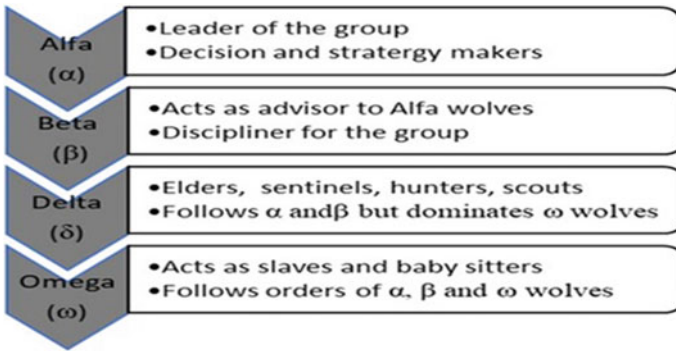


Fig. 2 Order of leadership and types of roles played in GW pack

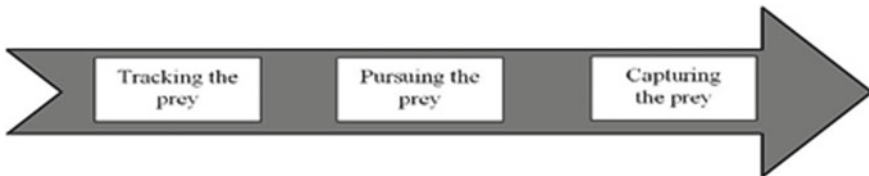


Fig. 3 Phases of GW pack hunting

where, n , x_p , and x indicate the current number of iterations, target location, and current location, respectively. The next position is calculated as:

$$(n + 1) = xp(n) - a \cdot d \tag{10}$$

The coefficient vectors “ a ” and “ c ” are calculated using two random vectors “ R_1 ” and “ R_2 ” varying between “0” and “1” as follows:

$$a = 2 \times AR_1 - A \quad \text{and} \quad c = 2 \times R_2 \tag{11}$$

Here “ A ” is a linearly decreasing variable with each iteration from 2 to 0. If the total number of iterations is N , then A is defined as

$$A = 2 - n \left(\frac{2}{N} \right) \tag{12}$$

The best three solutions from all feasible solutions are considered as α , β , and δ wolves and regarded as the best approximations of the target location. Other solutions are regarded as ω wolves and update their position with respect to the best three estimations as to the following equations:

$$x_1 = |x_\alpha - a_1 \cdot d_\alpha| \quad (13)$$

$$x_2 = |x_\beta - a_2 \cdot d_\beta| \quad (14)$$

$$x_3 = |x_\delta - a_3 \cdot d_\delta| \quad (15)$$

where a_1 , a_2 and a_3 are the coefficients for position updation of α , β and δ wolves and d_α , d_β , and d_δ are the distance vectors for α , β , and δ paths. The d_α , d_β , and d_δ are calculated as

$$d_\alpha = |c_1 \cdot x_\alpha - x| \quad (16)$$

$$d_\beta = |c_2 \cdot x_\beta - x| \quad (17)$$

$$d_\delta = |c_3 \cdot x_\delta - x| \quad (18)$$

The path updation is done as per the following equation

$$x(t + 1) = (x_1 + x_2 + x_3)/3 \quad (19)$$

Algorithm 2: Pseudo code of GWO for PP of multiple AUVs

Step 1:

The population of grey wolf is x_i , where $(i = 1, 2, \dots, n)$

Set the values of a , A , and c

Step 2:

For every x_i do

Compute the path cost

End for

Get the best three minimum cost paths x_α , x_β and x_δ

Step 3:

while $(n < N)$

For each AUV path

Update the next position

End for

Update the previous values of a , A , and c

For every x_i do

Compute the path cost

End for

Update the values of x_1 , x_2 and x_3

$n = n + 1$

End while

Step 4: Return the value of x_1

3.3 Hybrid GWO Algorithm

In this paper, a hybrid GWO (h-GWO) algorithm is proposed combining GA and GWO algorithms. Here GA is used to estimate the initial positions of AUVs to estimate the distance from the target. The best three estimations are selected as x_α , x_β , and x_δ . These estimations are used as initial positions of α , β , and δ wolves, respectively. Then the rest of steps follow as per GWO algorithms to generate cost minimum path.

Algorithm 3: Pseudocode of h-GWO for PP of multiple AUVs
<p>Step 1: <i>The 3D environment is realized as a grid map consisting of different node points.</i></p> <p>Step 2: <i>The starting and terminating points are properly defined.</i></p> <p>Step 3: <i>The static obstacle locations on each node of the grid path is established</i></p> <p>Step 4: <i>Generate the initial population consists of all possible next nodes directed toward the target</i></p> <p>Step 5: <i>For all next node points</i> <i>Calculate the minimum cost function w.r.t to target</i> <i>End for</i></p> <p>Step 6: <i>Select the best three node positions as x_α, x_β and x_δ. Set the values of a, A, and c</i></p> <p>Step 7: <i>For every AUV do</i> <i>Compute the path cost</i> <i>End for</i></p> <p>Step 8: <i>while ($n < N$)</i> <i>For each path</i> <i>Update the next position</i> <i>End for</i> <i>Update the previous values of a, A, and c</i> <i>For every AUV do</i> <i>Calculate pat cost</i> <i>End for</i> <i>Update the previous values of x_1, x_2 and x_3</i> <i>$n = n + 1$</i> <i>End while</i></p> <p>Step 9: <i>Return the value of x_1</i></p>

4 Result Analysis

The AUV path planning method intended to generate a safe route from a source position to destination location without colliding with obstacles. All the simulations are in MATLAB R2018a. Here, AUV is considered as a point object and the 3-D environment is modelled as a 3D grid map of (500 * 500 * 500) dimensions. The obstacle locations are predefined and fixed. For path planning the source co-ordinate

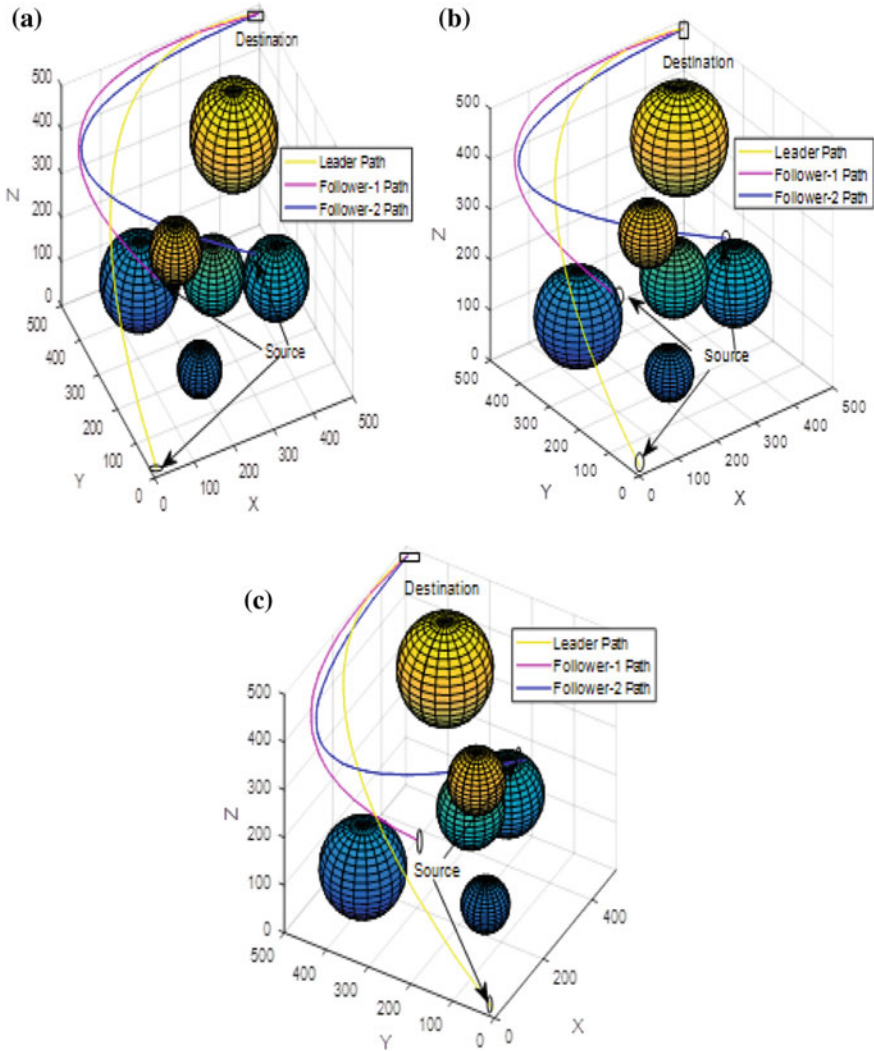


Fig. 4 Cost-optimized path for leader and follower AUVs planned by using **a** GA, **b** GWO, and **c** h-GWO

for three AUVs are taken at three different co-ordinates while the destination co-ordinate is same for all the three AUVs. For this research one leader AUV and two follower AUVs are considered. The leader source co-ordinate is [10], the Follower—1 source co-ordinate is [130, 260, 200], and Follower—2 source co-ordinate is [300, 100, 320]. The source points are shown by “ellipses” and the target by a “rectangle” in the simulation results.

Figure 4 shows the complete path in a 3-D map, while the best cost curves of the applied algorithms are shown in Fig. 5. The simulation results and tabulation analysis

as presented in Tables 1, 2 and 3 have been verified that the average path length obtained by GA, GWO and h-GWO is 1120.3, 1065.79, and 1063.82, respectively. Similarly, the average path costs calculated by GA, GWO, and h-GWO are -52.47 , -32.95 , and -19.49 , respectively. The larger the negative number the lesser the probability of collision and safer is the path. Thus, applying GA results in longer path in comparison with other two algorithms. The GWO and h-GWO result in almost equal path lengths, but the hybrid algorithm generates minimum path cost. The results obtained for h-GWO are better as compared to GA and GWO on the expanse of computation time.

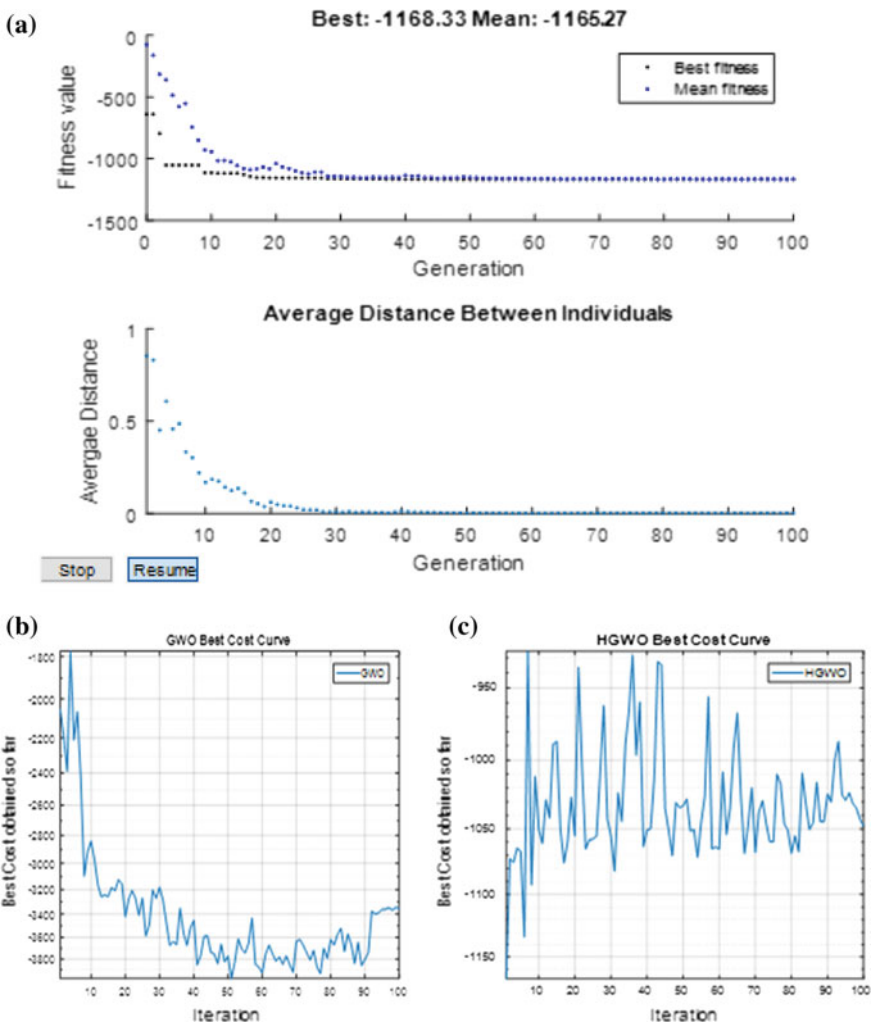


Fig. 5 Best cost curves for AUV path planners using a GA, b GWO, and c h-GWO

Table 1 Performance analysis of GA

Run number	Computation time (s)	Path length (m)	Path cost (m)
1	22.59	1100.04	-46.93
2	24.04	1136.70	-44.06
3	22.16	1126.23	-72.25
4	22.61	1134.72	-41.13
5	22.77	1103.94	-58.00
Average	22.83	1120.3	-52.47

Table 2 Performance analysis of GWO

Run number	Computation time (s)	Path length (m)	Path cost (m)
1	18.75	1060.03	-34.45
2	18.60	1066.59	-30.30
3	18.39	1079.25	-36.67
4	18.46	1053.13	-48.78
5	18.36	1069.95	-14.58
Average	18.51	1065.79	-32.95

Table 3 Performance analysis of h-GWO

Run number	Computation time (s)	Path length (m)	Path cost (m)
1	59.73	1043.17	-19.30
2	60.72	1090.45	-21.91
3	60.46	1073.03	-20.47
4	52.04	1055.44	-17.63
5	64.12	1057.05	-18.16
Average	59.41	1063.82	-19.49

5 Conclusion

The proposed h-GWO is applied for planning minimum cost and collision free safe routes for multiple AUVs employed in underwater missions. The simulation environment is statically realized as a 3-D map with known obstacles locations. It is intended to compensate for the demerits of the basic GA and GWO algorithms. The h-GWO optimizes the path cost. It reduces the path length but takes comparatively more computation time. Thus, this algorithm can only be employed for the applications where time is not a critical factor. But most of the underwater operations except the military missions are usually not time-critical, hence can afford the little increase in computational time. In future, the proposed algorithm may be used to find cost optimal path in 3-D dynamic environment.

Acknowledgements We acknowledge the help and facilities provided by the department of “Electronics and Telecommunication Engineering” and “TEQIP-III cell of the Veer Surendra Sai University of Technology, Burla, Odisha, India”.

References

1. Das B, Subudhi B, Pati BB (2016) Co-operative control of a team of autonomous underwater vehicles in an obstacle-rich environment. *J Mar Eng Technol* 15:135–151
2. Hyakudome T (2011) Design of autonomous underwater vehicle. *Int J Adv Robot Syst* 8:9
3. Aghababa MP, Amrollahi MH, Borjkhani M (2012) Application of GA, PSO, and ACO algorithms to path planning of autonomous underwater vehicles. *J Mar Sci Appl* 11:378–386
4. Mirjalili S, Mirjalili SM, Lewis A (2014) Grey wolf optimizer. *Adv Eng Softw* 69:46–61
5. Rezaei H, Bozorg-Haddad O, Chu X (2018) Grey wolf optimization (GWO) algorithm. In: *Studies in computational intelligence*, pp 81–91
6. Panda M, Das B (2019) Grey wolf optimizer and its applications: a survey. In: *Lecture notes in electrical engineering*. Springer, Berlin, pp 179–194
7. Panda M, Das B, Pati BB (2019) Grey wolf optimization for global path planning of autonomous underwater vehicle. In: *Proceedings of the third international conference on advanced informatics for computing research—ICAICR '19*, pp 1–6
8. Aghababa MP (2012) 3D path planning for underwater vehicles using five evolutionary optimization algorithms avoiding static and energetic obstacles. *Appl Ocean Res* 38:48–62
9. Ataei M, Yousefi-Koma A (2015) Three-dimensional optimal path planning for waypoint guidance of an autonomous underwater vehicle. *Robot Auton Syst* 67:23–32
10. Yao P, Zhao S (2018) Three-dimensional path planning for AUV based on interfered fluid dynamical system under ocean current. *IEEE Access* 6:42904–42916
11. Das B, Subudhi B, Pati BB (2014) Adaptive sliding mode formation control of multiple underwater robots. *Arch Control Sci* 24:515–543
12. Das B, Subudhi B, Pati BB (2015) Employing nonlinear observer for formation control of AUVs under communication constraints. *Int J Intell Unmanned Syst* 3:122–155
13. Das B, Subudhi B, Pati BB (2016) Cooperative formation control of autonomous underwater vehicles: an overview. *Int J Autom Comput* 13:199–225

A Hybrid Framework for Fault Classification and Location in Power Distribution System Using Wavelet and Support Vector Machine



Satyajit Panigrahy and A. K. Chandel

Abstract In this paper, a discrete wavelet transform and a radial basis function (RBF) kernel-based support vector machine are combined to form a hybrid technique for a short distance radial distribution line. The main objectives of the proposed method are to classifying the shunt faults and estimating its locations. Unlike a decision tree-based hybrid method, this technique is easy to implement and computationally less burden. Here, three-phase line current samples have been utilized to generate the features. Importantly, feature extraction has been handled by Daubechies mother wavelet. Six features (i.e., mean, standard deviation, energy, entropy, skewness, and kurtosis) of line currents have taken into consideration. The data extracted from the feature generation stage contain redundant feature values. Therefore, the principal component analysis tool has been applied to reduce the redundancy in the dataset by optimizing the features. Finally, the optimized features are sent as inputs to the kernel-based SVM for fault classification and estimating the location. MATLAB/Simulink simulation environment and Python programming interface have been utilized to test the performance of the developed model.

Keywords Continuous wavelet transform (CWT) · Discrete wavelet transform (DWT) · Support vector machine (SVM) · Principal component analysis (PCA) · Decision tree (DT) · Fault classification · Fault distance estimation

1 Introduction

The sole responsibility of the electric power distribution system (EPDS) is to supply electricity for the distributed residentials, large and small industrial users in an uninterrupted manner and within the cheaper price. A fault in the power system is

S. Panigrahy (✉) · A. K. Chandel
National Institute of Technology, Hamirpur, Himachal Pradesh 177005, India
e-mail: satyajit.panigrahy007@gmail.com

A. K. Chandel
e-mail: ashchandelin@gmail.com

© Springer Nature Singapore Pte Ltd. 2020
R. Sharma et al. (eds.), *Innovation in Electrical Power Engineering, Communication, and Computing Technology*, Lecture Notes in Electrical Engineering 630,
https://doi.org/10.1007/978-981-15-2305-2_27

the greatest threat as it discontinues the supply. As per the standard (ANSI/IEEE Std. 100–1992), fault is defined as a real-time condition which causes the failure of equipment to perform in an optimum manner. Once a fault occurs in a distribution system, it causes voltage sag, swell, temporary loss, or system blackout [1].

The fault is an abnormal condition where the system quantities (i.e., voltage, current, phase angle) exceed their threshold values [2]. Faults are classified considering the period of time and fault level. Temporary and permanent faults are classified under a specified time interval. Faults in the distribution system are of two types, i.e., series and shunt faults [3] as given in Fig. 1. By observing phase voltages, series faults can be easily identified. Open conductor faults are of one conductor, two conductors, and three conductors open type. Asymmetrical and symmetrical faults are grouped into the category of shunt faults. The line-to-ground (LG), line-to-line (LL), and double line-to-ground (LLG) faults are grouped under asymmetrical faults, whereas triple line (LLL) and triple line-to-ground (LLLG) faults are grouped under symmetrical faults. Various types of shunt faults are shown in Fig. 2.

The provision of adequate protection to find and isolate faulty components within the power system is an essential part of the grid structure [4]. Once the faulty phase is identified, it is necessary to analyze the major cause of the faulty condition. To achieve this, protection devices should work in synchronism with the existing diagnostic methods. The fundamental objectives of the proposed hybrid technique are to classify the fault events, verify the affected phases, and estimate the fault locations.

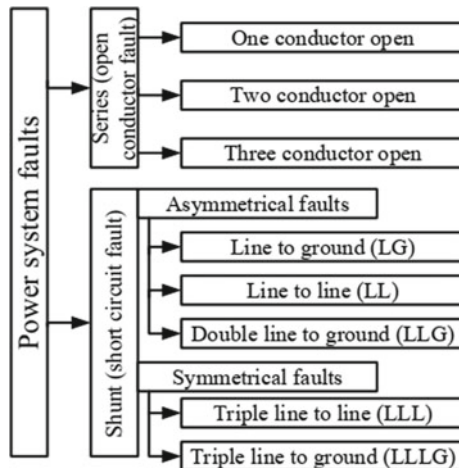


Fig. 1 Classification of faults

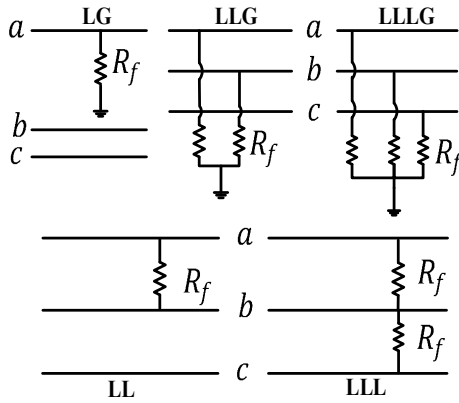


Fig. 2 Types of shunt faults

2 Modern Methods

2.1 Wavelet Transform (WT)

A signal in the time–frequency domain can be analyzed by time localized frequency information through WT [5, 6]. It is a mathematical tool for analyzing non-stationary signals since the frequency components of the signals vary with time. WT can be classified into CWT and DWT and are discussed subsequently.

– The CWT can be defined as follows:

$$X_{a,b}(t) = \frac{1}{\sqrt{a}} \int_{-\infty}^{+\infty} x(t)\Psi\left(\frac{t-b}{a}\right)dt \tag{1}$$

Herein, $x(t)$ and $\Psi(t)$ are signal and mother wavelet, respectively. The mother wavelet can be expressed as follows,

$$\Psi_{a,b}(t) = \frac{1}{\sqrt{a}}\Psi\left(\frac{t-b}{a}\right)$$

where a and b represent the dilated and translated parameters, respectively.

– The DWT applied to the signal is given as follows:

$$x(t) = \sum_{k=0}^{2^{M-j}-1} a_{jk}\phi_{jk}(t) + \sum_j \sum_{k=0}^{2^{M-j}-1} d_{jk}\Psi_{jk}(t) \tag{2}$$

$$\phi_{jk}(t) = 2^{-j/2}\phi(2^j t - n)$$

$$\Psi_{jk}(t) = 2^{-j/2}\psi(2^j t - n)$$

where a_{jk} and d_{jk} denote the approximation and detail coefficients, respectively, where $k = 0, 1, \dots, 2^{M-j-1}$.

The Daubechies wavelet approach is suited for identifying short-time, high-frequency transients, and low-frequency behavior over a long duration where the signals are non-periodic or non-stationary in nature [7].

2.2 Principal Component Analysis (PCA)

PCA is an appropriate tool to reduce the dimensionality of a dataset by removing the redundant or interrelated variables from the original dataset. To do that, a simple normalization process is employed which create the covariance matrix. From that covariance matrix, principal components are obtained. The covariance matrix can be computed as follows:

$$cov(P_{ia}^+, P_{ia}^-) = \frac{\sum[(P_{ia}^+ - \bar{P}_{ia}^+)(P_{ia}^- - \bar{P}_{ia}^-)]}{(k - 1)} \quad (3)$$

where P_{ia}^+ the symmetrical positive pattern and P_{ia}^- the symmetrical negative pattern obtained by using Eq. (3).

Detection of multiple faults, small perturbations and dealing of non-stationary signals will be the extension of PCA method in the future [8].

2.3 Support Vector Machine (SVM)

The concept of SVM is proposed by Vapnik et al. and became a novel tool for data analysis [9]. It uses kernel trick technique to transform the extremely complex data by mapping them into a high-dimensional feature space. Kernels can be of linear, polynomial, radial basis, and sigmoid types. SVM uses learning algorithm and statistical approaches for classification and estimation problems, respectively [10].

2.4 Decision Tree (DT)

A Classification and Regression Tree (CART) algorithm is utilized to construct a decision tree model based on the historical data. CART algorithm divides the input

data into a tree fashion where it provides either a piecewise constant estimator or a classifier for data fitting. The CART algorithm utilizes learning sample which is a set of historical data containing pre-assigned classes in all observations. DT-based hybrid technique can successfully differentiate the high impedance faults from the most normal operations like switching of loads, shunt capacitors, and load transformer inrush currents [11].

3 Proposed Hybrid Fault Detection and Diagnosis Technique

In this section, a flowchart of the proposed hybrid method with its implementation has been discussed. The proposed hybrid fault detection and diagnosis (HFDD) method has been divided into several steps, as shown in Fig. 3. Initially, a short radial distribution network has modeled in the MATLAB/Simulink environment which is shown in Fig. 4.

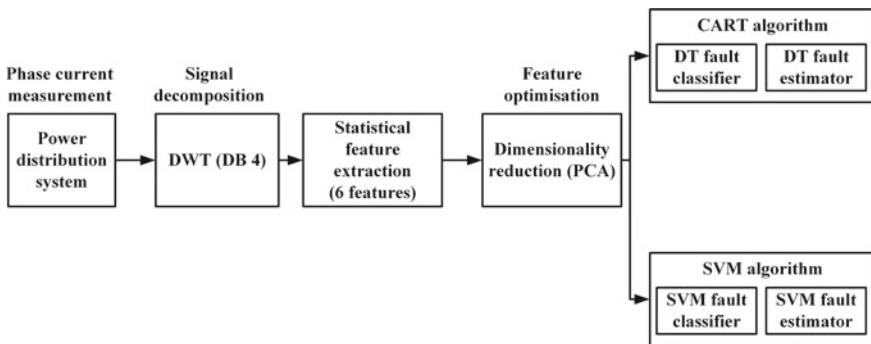


Fig. 3 Flowchart for HFDD method

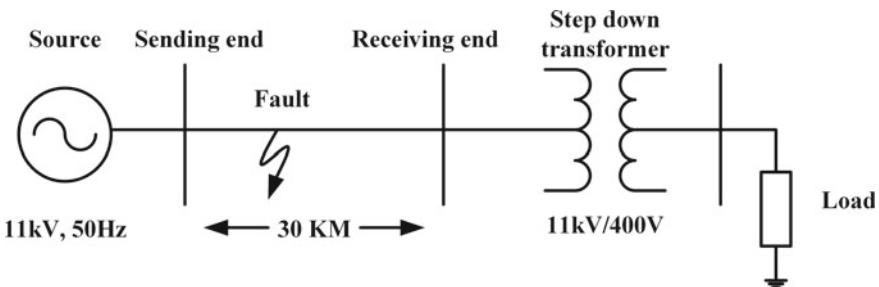


Fig. 4 Single-line diagram of the network under study

3.1 Data Generation

At first, the developed model has simulated for various fault conditions. Each phase current signals have been decomposed with the help of the Daubechies mother wavelet. Ten types of shunt faults (i.e., 3 LG, 3 LL, 3 LLG, 1 LLLG), seven values of fault resistances (i.e., 1, 5, 10, 15, 20, 35, 50 in ohm), and six values of fault distances (i.e., 5, 10, 15, 20, 25, 30 in km) have considered as the varying parameters. Thus, a total of 420 (42×10) patterns have been generated in the proposed work.

3.2 Feature Extraction and Reduction

After the data generation stage, feature extraction and reduction stage have initialized. In this stage, six statistical feature values for the aforementioned fault cases have computed. Further, these statistical features have a large number of redundant data which consumes more memory space. Hence, a PCA method has incorporated in the proposed work to reduce the computational complexity by selecting the optimized features among six features. Here, energy, entropy, and standard deviation are the three optimized features.

4 Implementation of HFDD

In this section, HFDD is implemented as a classifier and an estimator to classify the shunt faults and to measure the fault distance for a short radial distribution system, respectively. Further, the developed hybrid technique is compared with a DT-based method to determine the preciseness and robustness. To show the higher accuracy of the developed method, errors between the actual and predicated fault location have been calculated with the help of four types of statistical estimators (i.e., MAE, MAPE, RMSE, and R^2).

4.1 Algorithm

The steps involved in the algorithm development have written in the Python programming interface. Step 1: Importing the libraries, Step 2: Importing dataset, Step 3: Splitting the dataset into training and test set, Step 4: Feature scaling, Step 5: Implementation of learning methods to the classifiers: (a) Fitting kernel-based learning algorithm to the training set, (b) Fitting decision tree learning algorithm to the training set. Step 6: Making the confusion matrix, Step 7: Predicting the test set results.

4.2 Results and Discussions

In the distribution network, a double line fault is more dominating as compared to a single line-to-ground fault. The proposed algorithm has accurately identified the double line fault conditions shown in Table 1. It is evident from Table 1 that for a double line fault (C-A), proposed SVM-based hybrid method has successfully classified the faulty phase, whereas DT-based method has wrongly classified B-C phase instead of C-A phase. The accuracy percentages for classifying the shunt faults with SVM and DT are 96.25% and 92.15%, respectively. Table 2 combines the individual shunt fault phases represented in Table 1. From Table 3, it is observed that the dominant faulty double line phase is 5 km far from the source end. Table 4 shows the predicted fault distances, which are calculated by subtracting error values from the actual fault distances. Four types of statistical error estimators have used to determine the fault locations as shown in Table 5. SVM error estimators exhibit a greater accurate value than the DT for estimating the fault location at varying lengths.

Table 1 Accuracy variation for different types of shunt faults (each phase)

Fault type	Total no. of test cases	Support vector machine			Decision tree		
		Fault classified correctly	Fault classified incorrectly	Accuracy (%)	Fault classified correctly	Fault classified incorrectly	Accuracy (%)
A-g	8	8	0	100	8	0	100
B-g	9	9	0	100	9	0	100
C-g	9	8	1	88.88	7	2	77.77
A-B	8	8	0	100	8	0	100
B-C	9	9	0	100	8	1	88.88
C-A	9	8	1	88.88	9	0	100
A-B-g	8	8	0	100	8	0	100
B-C-g	9	8	1	88.88	8	1	88.88
C-A-g	9	9	0	100	8	1	88.88
A-B-C-g	9	9	0	88.88	9	0	100
Total cases	87	84	3	96.55	82	5	94.25

Table 2 Accuracy comparison for different types of shunt fault (combine phase)

Fault type	Total no. of test cases	Support vector machine		Decision tree	
		Correct predications	Accuracy (%)	Correct predications	Accuracy (%)
L-g	26	25	96.15	24	92.30
L-L	26	25	96.15	25	96.15
L-L-g	26	25	96.15	24	92.30
L-L-L-g	9	9	100	9	100

Table 3 Accuracy comparison for change in distribution line length

Fault type	Length (km)	No. of test cases	SVM		DT	
			Correct predications	Accuracy (%)	Correct predications	Accuracy (%)
L-G	5	5	5	100	5	100
L-G	10	5	4	80	4	80
L-G	15	5	5	100	5	100
L-G	20	5	5	100	5	100
L-G	25	5	5	100	4	80
L-G	30	5	5	100	5	100
L-L	5	5	5	100	5	100
L-L	10	5	5	100	5	100
L-L	15	5	5	100	5	100
L-L	20	5	4	80	4	80
L-L	25	5	5	100	5	100
L-L	30	5	5	100	5	100
L-L-G	5	5	4	80	4	80
L-L-G	10	5	5	100	5	100
L-L-G	15	5	5	100	5	100
L-L-G	20	5	5	100	5	100
L-L-G	25	5	5	100	5	100
L-L-G	30	5	5	100	4	80
L-L-L-G	5	5	5	100	5	100
L-L-L-G	10	5	5	100	5	100
L-L-L-G	15	5	5	100	5	100
L-L-L-G	20	5	5	100	5	100
L-L-L-G	25	5	5	100	5	100
L-L-L-G	30	5	5	100	5	100

Table 4 Fault location prediction based on statistical errors

Fault type	Actual distance (km)	Predicted distance (km)							
		Support vector machine				Decision tree			
		MAE	MAPE	RMSE	R^2	MAE	MAPE	RMSE	R^2
L-G	5	4.8	4.9	4.8	4.6	4.7	5.1	4.9	4.6
L-G	10	9.7	10.1	9.8	9.5	9.8	9.6	9.9	9.7
L-G	15	14.6	15.2	14.8	14.3	14.8	15.1	14.7	14.6
L-G	20	19.8	19.7	20.1	19.6	19.7	19.8	20.2	19.6
L-G	25	24.9	24.7	25.1	24.6	24.8	24.8	24.9	24.7
L-G	30	29.8	29.7	29.9	29.4	29.8	29.5	30.1	29.6
L-L	5	4.8	5.1	4.7	4.5	4.9	4.8	5.1	4.8
L-L	10	9.6	9.8	10.1	9.4	9.7	10.2	9.8	9.6
L-L	15	14.8	14.7	15.1	14.6	14.6	15.2	14.8	14.5
L-L	20	19.7	19.8	20.2	19.5	19.8	19.7	20.1	19.6
L-L	25	24.5	25.1	24.8	24.3	24.4	24.9	24.8	24.3
L-L	30	29.6	30.2	29.7	29.5	29.6	30.1	29.8	29.4
L-L-G	5	4.9	4.8	5.1	4.7	4.8	4.8	5.2	4.6
L-L-G	10	9.5	9.7	10.1	9.3	9.6	10.1	9.7	9.5
L-L-G	15	14.7	14.9	15.2	14.3	14.8	14.7	15.2	14.6
L-L-G	20	19.4	19.6	20.1	19.2	19.3	19.5	19.6	19.1
L-L-G	25	24.7	25.3	24.8	24.5	24.5	25.1	24.8	24.4
L-L-G	30	29.5	29.8	29.7	29.4	29.6	30.2	29.6	29.4
L-L-L-G	5	4.8	5.2	4.7	4.6	4.6	5.2	4.9	4.5
L-L-L-G	10	9.7	10.1	9.8	9.5	9.6	9.9	10.1	9.4
L-L-L-G	15	14.9	14.8	14.8	14.6	14.8	15.1	14.6	14.7
L-L-L-G	20	19.8	20.1	19.7	19.5	19.7	19.8	20.1	19.5
L-L-L-G	25	24.7	24.8	24.9	24.4	24.6	25.1	24.7	24.4
L-L-L-G	30	29.9	29.7	30.1	29.7	29.8	29.6	30.2	29.6

Table 5 Calculation of various statistical errors

Fault type	Actual distance (km)	Support vector machine				Decision tree			
		MAE	MAPE	RMSE	R^2	MAE	MAPE	RMSE	R^2
L-G	5	0.2150	0.07443	0.1987	0.31238	0.2511	0.07529	0.1103	0.35113
L-G	10	0.2985	0.09869	0.1873	0.52682	0.1544	0.31029	0.0511	0.29788
L-G	15	0.3619	0.18345	0.1584	0.62577	0.1502	0.01249	0.2503	0.35013
L-G	20	0.1973	0.21776	0.1238	0.35789	0.2509	0.26100	0.1984	0.35139
L-G	25	0.0116	0.27488	0.1342	0.37646	0.1864	0.18635	0.0112	0.27478
L-G	30	0.2016	0.24322	0.1079	0.32658	0.2012	0.45089	0.0846	0.34899
L-L	5	0.1856	0.16895	0.2984	0.43018	0.1121	0.18554	0.0915	0.18492
L-L	10	0.3531	0.22569	0.1186	0.55207	0.2538	0.17781	0.2258	0.35309
L-L	15	0.2176	0.27653	0.1426	0.38602	0.3865	0.19868	0.2168	0.45181
L-L	20	0.2684	0.23914	0.1627	0.44834	0.2392	0.26837	0.0987	0.44868
L-L	25	0.5068	0.13468	0.1876	0.61736	0.6103	0.87769	0.1789	0.61824
L-L	30	0.2577	0.08625	0.2319	0.48159	0.2562	0.07931	0.1876	0.55788
L-L-G	5	0.0519	0.14574	0.1642	0.31469	0.1739	0.14582	0.1659	0.35211
L-L-G	10	0.5019	0.25177	0.1122	0.62736	0.3510	0.07981	0.2520	0.50187
L-L-G	15	0.2648	0.10248	0.1753	0.62681	0.2102	0.26458	0.1984	0.40189
L-L-G	20	0.4831	0.28642	0.1039	0.75469	0.2863	0.48299	0.0867	0.30129
L-L-G	25	0.2164	0.28146	0.1329	0.48766	0.6016	0.08503	0.1334	0.48692
L-L-G	30	0.4517	0.17349	0.2786	0.55018	0.4511	0.09561	0.1585	0.51289
L-L-L-G	5	0.0577	0.15303	0.0945	0.30149	0.1612	0.15309	0.1853	0.35019
L-L-L-G	10	0.4511	0.25781	0.0862	0.65043	0.5018	0.07891	0.2580	0.45164
L-L-L-G	15	0.2531	0.05169	0.1742	0.62019	0.2017	0.25289	0.1593	0.38415
L-L-L-G	20	0.5532	0.35103	0.0821	0.75032	0.6541	0.45022	0.3509	0.80011
L-L-L-G	25	0.2550	0.15022	0.1504	0.40129	0.4013	0.01248	0.2019	0.52193
L-L-L-G	30	0.4103	0.15321	0.2502	0.51011	0.3202	0.19788	0.3218	0.52001

5 Conclusions

An HFDD technique has been proposed for a short radial distribution network (11 kV/30 km) by considering two hybrid modern approaches, i.e., DWT and kernel-based SVM. At first, DWT is utilized to extract six statistical features from three-phase currents of the modeled network. The extracted features from DWT contain a huge number of redundant data which increase system complexity. Therefore, PCA is used to enhance the feature selection by optimizing the features with the help of correlation approach which selects three most important features of the interest, i.e., energy, entropy, and standard deviation out of six features. Finally, the optimized features are provided to a kernel-based SVM as input. As per the training, SVM can determine the fault types and locations. At last, the proposed method is compared with a DT-based hybrid technique for accuracy comparison. It can be concluded that SVM is 4% accurate than a DT-based approach for fault classification and give accurate estimations for fault locations. The developed hybrid technique can be more accurate by considering various input parameters like fault inception angle, load angle, reluctance vector machine, gradient search approach, and a large number of datasets in the future.

References

1. Melhorn CJ, Davis TD, Beam GE (1998) Voltage sags: their impact on the utility and industrial customers. *IEEE Trans Ind Appl* 34(3):549–558
2. Prasad A, Edward JB, Ravi K (2018) A review on fault classification methodologies in power transmission systems: part-I. *J Electr Syst Inf Technol* 5(1):48–60
3. Gonen T (2009) *Electric power transmission system engineering, analysis and design*. California State University, Sacramento, CRC Press Taylor and Francis Group, USA
4. Bamber M, Darby A et al (May 2011) *Network protection and automation guide: protective relays. Measurement and control*, ALSTOM
5. Mallat S (1999) *A wavelet tour of signal processing*. Academic press, Cambridge
6. Sonka M, Hlavac V, Boyle R (2014) *Image processing, analysis, and machine vision*. Cengage Learning, Boston
7. Chul Hwan K, Raj A (2000) Wavelet transforms in power systems. I. General introduction to the wavelet transforms. *Power Eng J* 14:81–87
8. Deng X, Tian X, Chen S, Harris CJ (2018) Nonlinear process fault diagnosis based on serial principal component analysis. *IEEE Trans Neural Netw Learn Syst* 29(3):560–572
9. Cortes C, Vapnik V (1995) Support-vector networks. *Mach Learn* 20(3):273–297 (Elsevier)
10. Ray P, Mishra DP (2016) Support vector machine-based fault classification and location of a long transmission line. *Int J Eng Sci Technol* 19(3):1368–1380
11. Sheng Y, Rovnyak SM (2004) Decision tree-based methodology for high impedance fault detection. *IEEE Trans. Power Deliv.* 19(2):533–536

Effect of Soiling on Power Output of a Photovoltaic System



Sonali Goel, Sobhit Panda, Nallapaneni Manoj Kumar and Renu Sharma

Abstract The power output of a photovoltaic (PV) module depends on the geographical locations (latitude, longitude and solar irradiance), tilt angle and its climatic condition (humidity, temperature) and shading due to soiling, bird droppings, etc. This paper deals with the power loss in solar PV system due to deposit of dust particles on the PV surface. The loss of power due to soiling was studied for a rooftop solar PV system installed in SOA (Deemed to be University), Bhubaneswar, India. It was observed that power loss to an extent of 3.09% per day occurred during non-monsoon months, while it reduced to 0.93% per day during monsoon months due to accumulation of soil on PV modules.

Keywords Solar photovoltaic · Losses · Performance

1 Introduction

The energy demand across the globe has increased in many folds due to technological advancement, rapid growth in industries and increase in household energy demand. This led the engineers and planners to think and find the means to harvest the alternative energy sources other than the fossil fuel. Renewable sources such as solar PV, wind, biomass, biogas, small hydro, concentrating solar power are extensively

S. Goel (✉) · R. Sharma

Department of Electrical Engineering, SOA Deemed to be University, Bhubaneswar, Odisha 751030, India
e-mail: sonali19881@gmail.com

R. Sharma

e-mail: renusharma@soa.ac.in

S. Panda

Instrumentation and Electronics Engineering, CET, Bhubaneswar 751003, India
e-mail: sobhitpanda25@gmail.com

N. M. Kumar

School of Energy and Environment, City University of Hong Kong, Kowloon, Hong Kong
e-mail: nallapanenichow@gmail.com

© Springer Nature Singapore Pte Ltd. 2020

R. Sharma et al. (eds.), *Innovation in Electrical Power Engineering, Communication, and Computing Technology*, Lecture Notes in Electrical Engineering 630,
https://doi.org/10.1007/978-981-15-2305-2_28

used nowadays to generate electricity all over the world to reduce the pressure on fossil fuel and to reduce environmental pollution. Due to rapid cost reduction in PV modules all over the world, it is expected that PV system will become one of the major sources of electricity in future [1]. The power generation from PV module is reduced due to various losses such as array capture loss, degradation loss, shading, soiling, mismatch and ohmic losses. Accumulation of dust particles over the solar PV surface tends to reduction of significant power if not cleaned periodically. This is called soiling loss. Generally, horizontal surface tends to accumulate more dust than the inclined surface. Also, a low-speed wind promotes dust accumulation, while a high-speed wind prevents deposition of dust particles on PV surface and rather has a cleaning effect. The deposition and cleaning of dust due to wind movements depend on the property of dust (weight size and type) [2].

This paper deals with the study of losses associated with a solar PV system due to accumulation of dust particles. This study was conducted during 2015 for an experimental set up installed at the rooftop of fifth floor of a tall building (latitude 20.24 °N and longitude 80.85 °E) of SOA (Deemed to be University), Bhubaneswar, India. Several studies conducted by many researchers across the globe on soiling loss of PV systems. Denholm et al. [3] conducted a study on soiling loss of a PV system and opined that the module efficiency is reduced by 10–25% due to losses in inverter, wiring and soiling. Salim et al. [4] made a long-term study on a solar village PV system in Saudi Arabia and found that the performance of the system reduced by 32% due to deposition of dust for a period of eight months. Wakim [5] made a study on PV system in Kuwait city and concluded that the PV power is reduced by 17% due to accumulation of sand on PV panels during a period of six days. Sayigh et al. [6] found that tilt angle of a PV installation has a greater influence on reduction of solar transmittance as compared to horizontal installation. They observed that the useful energy is reduced by 30% for a horizontal PV system after three days of dust accumulation. Said [7] made a study on effect of dust accumulation on a PV panel in maritime desert zone and found that efficiency of PV panel reduced by 7% per month due to soiling. El-Shobokshy and Hussein [8, 9] made a study on the effect of dust accumulation on a PV system by using artificial dust like limestone, cement and carbon particulates and simulated it keeping light intensity constant by using halogen lamps. The study revealed that the fine carbon particulates (0.5 μm) have most deteriorating effect on PV efficiency as compared to the limestone particles (80 μm). Kimber et al. [10] made a study on effect of soiling on a large grid-connected PV system in California and observed that a reduction of efficiency to the tune of 0.2% per day without rainfall in dry season and annual losses ranges from 1.5 to 6.2% depending on the location of PV plant. They concluded that at least 20 mm rainfall is required to clean the surface of PV system. Hottel and Woertz [11] made a study on the effect of dust accumulation of solar panels for a period of three months and found that about 1% reduction of incident solar radiation resulted from dust accumulation on surface of solar panel at a tilt angle of 30°. Ramli et al. [12] made a study in Indonesia to study the effect of soiling on PV output power and concluded that dust accumulation for a period of two weeks reduced the PV power output by 10.8% in dry season.

2 Soiling Loss

Loss of power due to dust, dirt and snow falling over the surface of the PV module is called soiling loss. Deposit of dust on PV module depends on the location of the PV installation site and its environment. Accumulation of dust over the module reduces the overall efficiency and energy production from PV module. Annual loss due to soiling ranges from 1.5 to 6.2% depending on the location of the PV plant. After a slight rain, the efficiency of some PV panels may decline sharply due to adhesion of dust materials because of stickiness, and at least 20 mm rainfall is needed to clean the surface of PV module, otherwise the system will continue to experience power loss due to dust and soil deposition [13]. The usual values of loss due to soiling are taken as 2% for low degree of dirt and 8% for high degree of dirt location [14]. The power loss due to dust deposit in the present study was measured in reference module by measuring V_m and I_m and solar irradiance simultaneously of clean solar module and soiled module separately at solar noon (12 o' clock) every day for 15 days. After 15 days, solar modules are cleaned regularly to reduce soiling loss. The soiling loss was calculated in Eq. 1

$$\text{Soiling Loss(SL), \%} = \left(1 - \frac{X_{\text{soiled}}}{X_{\text{cleaned}}} \right) * 100 \tag{1}$$

where

X Short-circuit current (I_{sc}) or maximum power (P_{max}) or daily energy yield in kWh,
 I_{sc} and P_{max} values are recorded at solar noon for soiling loss calculation, and I_{sc} is widely used for soiling loss calculation.

Power and efficiency loss due to soiling can be calculated by [15]

$$\% \text{reduction in power} = \left(\frac{P_{\text{without dust}} - P_{\text{with dust}}}{P_{\text{without dust}}} \right) * 100 \tag{2}$$

$$\% \text{reduction in efficiency} = \left(\frac{\eta_{\text{without dust}} - \eta_{\text{with dust}}}{\eta_{\text{without dust}}} \right) * 100 \tag{3}$$

where

$P_{\text{without dust}}$ and $P_{\text{with dust}}$ are the PV generated power without dust and with dust on modules, respectively, $\eta_{\text{without dust}}$ and $\eta_{\text{with dust}}$ are the PV efficiency without dust and with dust, respectively.

Also, soiling loss can be calculated by [16]

$$L_{\text{dirtiness}} = 1 - \left(\frac{T_{\text{dirt}}(0)}{T_{\text{clean}}(0)} \right) \tag{4}$$

where

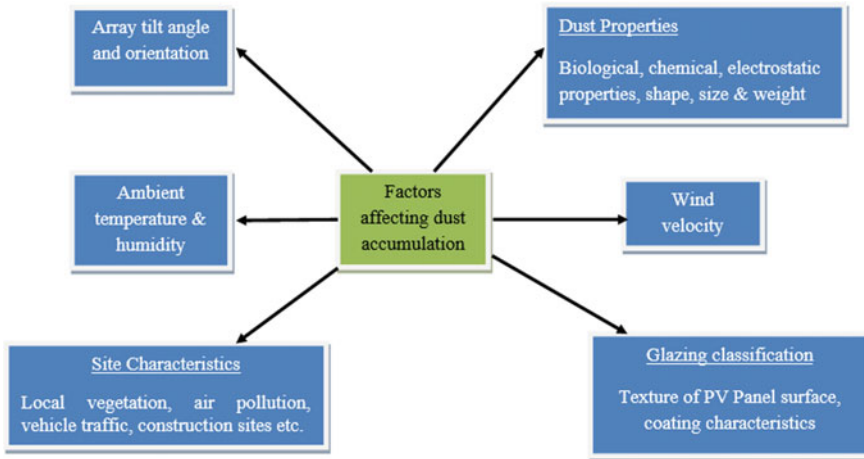


Fig. 1 Factors affecting soiling loss

$T_{\text{dirt}}(0)$ transmittance of normal incident light when the surface is dirty.

$T_{\text{clean}}(0)$ transmittance of normal incident light when the surface is clean.

$L_{\text{dirtiness}}$ Soiling loss due to dirt.

Various factors affecting the dust deposit over the module are shown in Fig. 1 which shows that site characteristics are very important due to local conditions. As the present research site is situated in crowded localities, lot of traffic and construction sites are in and around the building (where rooftop system is mounted) is causing more dust deposit on modules.

3 Materials and Methods

The experimental set up was installed on the rooftop of fifth floor of a 25 m high tall building of ITER, SOA (Deemed to be University), Bhubaneswar, India. For measurement of soiling loss, two 50 Wp solar panels were mounted separately at 21° tilt angle on the roof, and I_{sc} , V_{oc} and P_{max} for clean and soiled module were measured every day at 12 noon continuously for 15 days (Fig. 2). The specifications of the PV modules used for the experiment are shown in Table 1.

Weather data

The monthly daily average wind velocity, rainfall, humidity at one-hour interval was collected from the local metrology station, Bhubaneswar, for the year 2015 (January to December, 2015). The highest average ambient temperature of 33 °C and lowest of 20.8 °C was observed in May and December, respectively. The highest rainfall occurred during July to September ranging from 151.5 to 284 mm (Table 2).



Fig. 2 Measurement of soiling loss

Table 1 PV panel specification

PV panel	Specification
Type of panel	Polycrystalline
P_{max}	50 W
V_{mp}	17.47 V
I_{mp}	2.86 A
V_{oc}	21.56 V
I_{sc}	3.10 A
Maximum system voltage	1000 V

4 Results and Discussions

As rain occurred almost in all months during 2015 and the intensity of rain is more than 20 mm in some days of the month of March, April and June, natural periodic cleaning of modules was done by rain at least once a month. Besides this, frequent rain occurred during July to October, and hence, repeated cleaning of module surface was done by rain during these months. In rest of the months, cleaning of array was done by spraying water at an interval of 15 days. The P_{max} of both cleaned and soiled modules were measured every day at a particular time. The average power reduction due to soiling was observed by comparing the P_{max} of both the PV modules and presented in Table 3. It was found that during non-monsoon months (Jan–May), the power loss to the extent of 3.10% started from sixth day onwards, and it increased every day linearly and reached up to 4.27% on 15th day (Fig. 3). The average reduction of power during this period was calculated to be 3.09% per day. This higher soiling loss

Table 2 Measured weather data of the site

Month	Ambient temperature, °C			Wind speed		RH, %			Rainfall, mm	No. of rain days
	Max	Min	Mean	kmph	m/s	Max	Min	Avg		
Jan, 15	27.8	14.2	21	2.9	0.81	91	43	67	15	2
Feb, 15	32.5	17.0	24.75	3.2	0.89	94	39	66.5	9	1
Mar, 15	35.8	21.5	28.65	4.5	1.25	91	40	65.5	24.8	3
Apr, 15	37.1	24.2	30.65	7.5	2.08	88	50	69	84	6
May, 15	39.0	27.0	33.0	8.1	2.25	88	52	70	15	5
June, 15	36.2	26.1	31.15	6.7	1.86	88	62	75	75	13
July, 15	32.4	25	28.7	4.8	1.33	88	71	79.5	252	18
Aug, 15	3.0	24.4	28.7	4.9	1.36	90	68	79	284	16
Sept, 15	33.0	25.0	27.9	3.8	1.05	91	75	83	151.5	12
Oct, 15	33.0	23.5	26.95	2.2	0.61	93	66	79.5	75.5	7
Nov, 15	31.2	20.1	24.45	2.4	0.66	91	55	73	8.3	3
Dec, 15	29.2	17.5	20.8	3.0	0.83	86	52	69	14.8	3

Table 3 Soiling loss in monsoon and non-monsoon days

Day No.	Non-monsoon period (Jan–May)			Monsoon period (Jun–Sept)		
	P_{max} (clean), W	P_{max} (soiled), W	Soiling loss, %	P_{max} (clean), W	P_{max} (soiled), W	Soiling loss, %
0	31.56	31.56	0.00	30.54	30.54	0
1	29.23	28.66	1.92	30.64	30.52	0.39
2	41.00	38.97	2.56	32.32	32.01	0.96
3	34.65	33.75	2.60	34.41	33.98	1.25
4	39.93	38.88	2.63	36.43	35.97	1.26
5	33.12	32.24	2.66	29.27	28.86	1.40
6	32.87	31.85	3.10	15.67	9.87	0.37
7	35.77	34.65	3.13	9.76	9.10	0.06
8	29.92	28.96	3.21	10.34	8.76	0.15
9	31.63	30.60	3.26	34.62	34.42	0.58
10	32.20	31.08	3.48	39.60	39.32	0.71
11	37.60	36.12	3.94	42.50	42.11	0.92
12	33.41	32.00	4.22	38.90	38.54	0.93
13	34.40	32.95	4.22	32.64	32.14	1.53
14	36.67	35.12	4.23	38.89	38.23	1.70
15	35.36	33.85	4.27	33.24	32.65	1.77
Avg.			3.09			0.93

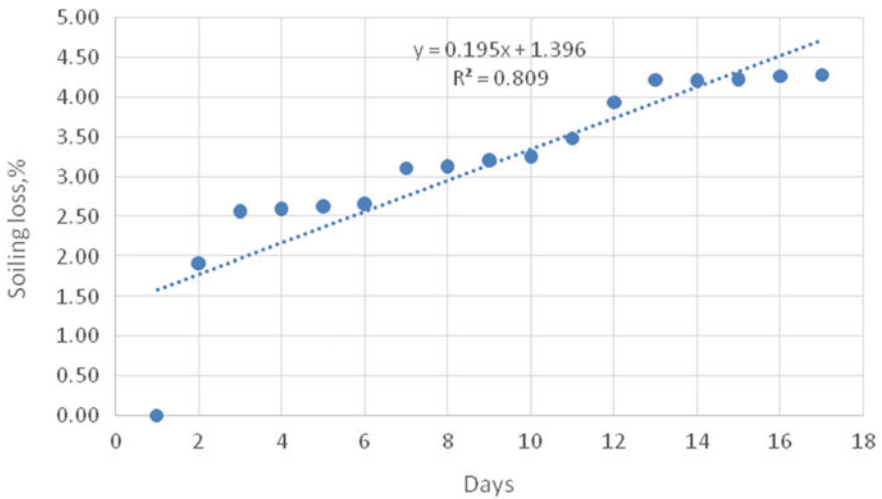


Fig. 3 Soiling loss in non-monsoon month (Oct–Nov)

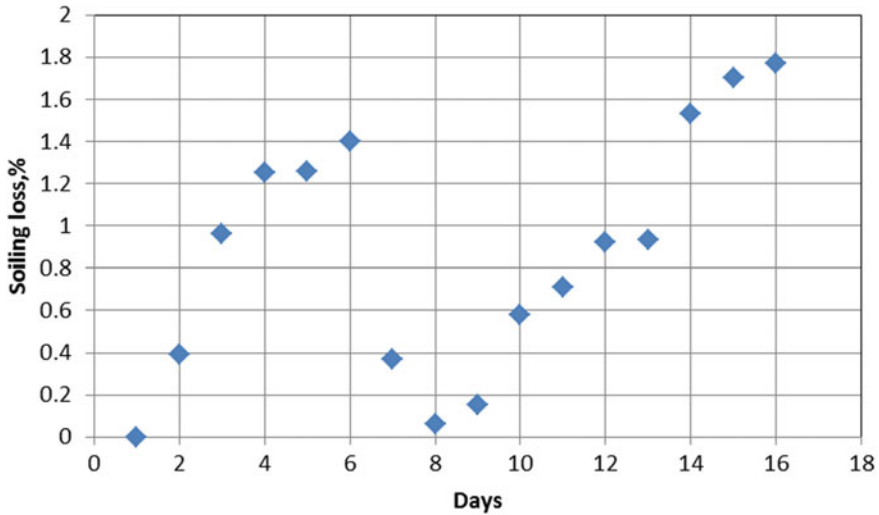


Fig. 4 Soiling loss in monsoon months (July–Aug)

is mainly due to deposit of cement and dust particles over the module as construction of buildings and lot of traffic are in and around the site of study. But during monsoon months, the power loss was observed to be non-uniform, and this may be due to frequent rainfall during these months which caused natural cleaning (Fig. 4). The average power loss due to soiling during this period was calculated to be 0.93% per day.

5 Conclusion

The objective of this paper is to find the power loss in solar PV system due to the effect of dust. Different climatic parameters such as wind speed, rainfall and humidity significantly affect the power output of photovoltaic module. The intensity of the rain was more than 20 mm in some days of non-monsoon months by which the module was cleaned by rain more than once during these periods, while during monsoon months due to frequent rain with intensity more than 20 mm in many days, module surfaces were cleaned many times causing very lower power loss due to dust. In rest of the months, cleaning was done by spraying water at an interval of 15 days. During non-monsoon days, the average soiling loss was found to be 3.09%/day, while it is only 0.93%/day during monsoon months. As power loss due to soiling increases linearly over the days, it requires cleaning by spraying water at 15 days intervals.

Acknowledgements The authors would like to thank the authorities of SOA (Deemed to be University) and local Meteorology Station, Bhubaneswar, for providing facilities for the research work.

References

1. Okello D, Van Dyk EE, Vorster FJ (2015) Analysis of measured and simulated performance data of a 3.2 kWp grid-connected PV system in Port Elizabeth, South Africa. *Energy Convers Manag* 100:10–15
2. Mani M, Pillai R (2010) Impact of dust on solar photovoltaic (PV) performance: research status, challenges and recommendations. *Renew Sustain Energy Rev* 14(9):3124–3131
3. Denholm P, Drury E, Margolis R, Mehos M, Sioshansi FP (2010) Solar energy: the largest energy resource. In: *Generating electricity in a carbon-constrained world*, pp 271–302
4. Salim AA, Huraib FS, Eugenio NN (1988) PV power-study of system options and optimization. In: *EC photovoltaic solar conference*, vol 8, pp 688–692
5. Wakim F (1981) Introduction of PV power generation to Kuwait. Kuwait Institute for Scientific Researchers, Kuwait City
6. Sayigh A, Al-Jandal S, Ahmed H (1985) Dust effect on solar flat surfaces devices in Kuwait. In: *Proceedings of the workshop on the physics of non-conventional energy sources and materials science for energy*, ICTP, Trieste, Italy, pp 353–367
7. Said SAM (1990) Effects of dust accumulation on performances of thermal and photovoltaic flat-plate collectors. *Appl Energy* 37(1):73–84
8. El-Shobokshy MS, Hussein FM (1993) Effect of dust with different physical properties on the performance of photovoltaic cells. *Sol Energy* 51(6):505–511
9. El-Shobokshy MS, Hussein FM (1993) Degradation of photovoltaic cell performance due to dust deposition on to its surface. *Renew Energy* 3(6–7):585–590
10. Kimber A, Mitchell L, Nagradi S, Wengar H (2006) The effect of soiling on large grid connected photovoltaic system in California and the South west region of the United States. In: *Conference record of 2006 IEEE 4th world conference on photovoltaic energy conversion*, vol 2, pp 2391–2395
11. Hottel HC (1942) Performance of flat-plate solar heat collectors. *Trans ASME* 64:91
12. Ramli MAM, Prasetyono E, Wicaksana RW, Windarko NA, Sedraoui K, Al-Tuki YA (2016) On the investigation of photovoltaic output power reduction due to dust accumulation and weather conditions. *Renew Energy* 99:836–844
13. Maghami MR, Hizam H, Gomes C, Radzi MA, Rezadad MI, Hajjighorbani S (2016) Power loss due to soiling on solar panel: a review. *Renew Sustain Energy Rev* 59:1307–1316
14. Mulcué-Nieto LF, Mora-López L (2014) A new model to predict the energy generated by a photovoltaic system connected to the grid in low latitude countries. *Sol Energy* 107:423–442
15. Rajput DS, Sudhakar K (2013) Effect of dust on the performance of solar PV panel. *Int J Chem Tech Res* 5(2):1083–1086. Mondol JD, Yohanis YG, Norton B (2007) Comparison of measured and predicted long term performance of grid a connected photovoltaic system. *Energy Convers Manag* 48(4):1065–1080
16. Baltus CWA, Eikelboom JA, Van Zolingen RJC (1997) Analytical monitoring of losses in PV systems. In: *Proceedings of the 14th European photovoltaic solar energy conference held at Barcelona*

Ant Colony Optimization in Data Mining: Critical Perspective from 2015 to 2020



Janmenjoy Nayak, Kanithi Vakula, Paidi Dinesh, Bighnaraj Naik and Manohar Mishra

Abstract Ant colony optimization (ACO) is a modern metaheuristic advance for resolving firm optimization problems. ACO is based on perception of swarm intelligence (SI). Many algorithms that are motivated by scavenging activity of ant colonies were utilized to result of complex distinct optimization problems. This paper intends to provide a detailed idea about the importance of ACO for data mining problems with a broad analysis on the structure of ACO as well as its applicability from 2015 to 2020. Many variations of ACO have also been utilized for solving diverse complex problems of data mining area. The main intent of this study is to inspire the researchers of optimization board to make use of ACO for explaining to those kinds of problems that were not used yet.

Keywords Optimization · ACO · Data mining and swarm intelligence

J. Nayak

Department of Computer Science and Engineering, Aditya Institute of Technology and Management (AITAM), K Kotturu, Tekkali, AP 532201, India
e-mail: mailforjnayak@gmail.com

K. Vakula · P. Dinesh

Department of Computer Science and Engineering, Sri Sivani College of Engineering, Srikakulam, AP 532410, India
e-mail: vakku.bi@gmail.com

P. Dinesh

e-mail: dinesh.pydi98@gmail.com

B. Naik

Department of Computer Applications, Veer Surendra Sai University of Technology, Burla, Sambalpur, Odisha 768018, India
e-mail: mailtobnaik@gmail.com

M. Mishra (✉)

Department of Electrical and Electronics Engineering, SOA Deemed to be University, Bhubaneswar, Odisha 751030, India
e-mail: manohar2006mishra@gmail.com

© Springer Nature Singapore Pte Ltd. 2020

R. Sharma et al. (eds.), *Innovation in Electrical Power Engineering, Communication, and Computing Technology*, Lecture Notes in Electrical Engineering 630,
https://doi.org/10.1007/978-981-15-2305-2_29

1 Introduction

Optimization is a frequently detected mathematical problem in all engineering restraints. It exactly means finding the best desirable solution. The problems of optimization are broad ranging and frequent. Therefore, techniques for resolving these problems became an energetic research topic and are mainly fixed by using various optimization algorithms. Gain and occurrence are the assets of our daily life which will have an extremely less growth in real world. In order to optimally utilize these assets, we require finding the solution from real world. Nature plays a vital and huge source of motivation in solving difficult and hard problems. Earlier techniques to resolve the problems of optimization need huge computational efforts which inclined to fail as the size of problem rises. This is the inspiration for using bio-inspired optimization algorithms (BIOA) as computationally well-organized substitutes to deterministic advance. The power behind the BIOA computing is that it constantly discovers optimal solutions to resolve its difficulty sustaining ideal steadiness along with its components. BIOAs investigating novel fields of applications as well as new opportunity for explaining an impressive range of problems. One of the successful and leading classes in BIOAs engages SI-based algorithms which are stimulated by the communal activities of animals correspondingly such as PSO [1], ACO [2], ABC [3], FF [4] and many more.

Ant colony optimization algorithm (ACO) [2] is a modern approach which is originally introduced by Marco Dorigo in his Ph.D. thesis in the year 1992. It is a probabilistic method for resolving complex combinatorial problems. Artificial ants set for multi-agent techniques motivated by the performance of real ants. The laying of pheromone trail and subsequent actions of real ants which utilize pheromones as a message medium is the inspiring source of ACO. ACO has been applied to numerous optimization problems such as data mining [5] and scheduling problems [6]. The major objective of data mining is to mine information from data that is not just exact but also understandable for the user. There are various data mining tasks such as classification [7], clustering [8], regression [9] and forecasting [10]. The employ of ACO for determining various sorting rules in the data mining perspective is a promising and new research area. ACO has the capability to carry out a flexible strong search for an excellent grouping of terms relating principles of the forecaster attributes.

The rest section of this paper is segmented as follows. Section 2 explains a brief summary of ant colony algorithm as well as its structure, while Sect. 3 gives a thorough perspective between applications of ACO in several research fields. Section 4 mentions various variants of ACO. Critical analysis has been clarified in brief (Sect. 5) in order to discover novel solutions for several problems. Section 6 concludes by providing significant future directions.

2 Ant Colony Optimization

In this section, the structure and natural behaviour of ants are described along with the working principles.

2.1 Concept Behind ACO

Ants exchange information to each other as well as alternative ants by placing a chemical substance released from them named ‘pheromones’ beyond their paths over the ant’s particular colony. Various species of ants move towards the food by smelling the heavy pheromone heed place on the ground which will be helpful to locate the sources of food easily. This pheromone organizes a path so that it grants the ants for locating the best food source that is recognized earlier by other ants. The preliminary behaviour of ant is depicted in Fig. 1. With the help of arbitrary strides as well as pheromones inside a ground comprising a single nest and a food source, ants start moving from the nest for finding the food. Later, they return to their nest. In a meanwhile, path that is under use by the ants will congregate to the shortest path.

While searching for food, any obstacle may be interrupted on the passing path, and that process is depicted in Fig. 2.

When interruption occurred by an obstacle, the ants will detect two paths by releasing a new pheromone, and those two paths will be detected by the ants to move all around the obstacle. This process of detecting the paths is depicted in Fig. 3.

After the detection of two paths, the ants will follow the shortest path by following the newly released pheromone. This process is depicted in Fig. 4.

Fig. 1 Ants following pheromone path in between food and nest



Fig. 2 Interruption of path by an obstacle

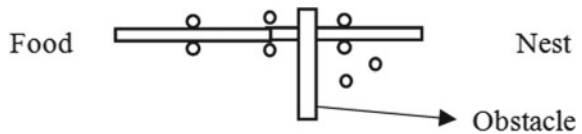


Fig. 3 Detection of two paths by ants for moving throughout the obstacle

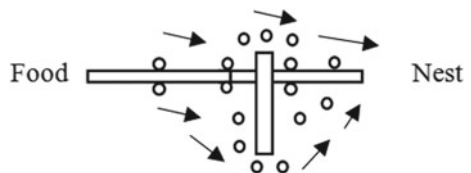
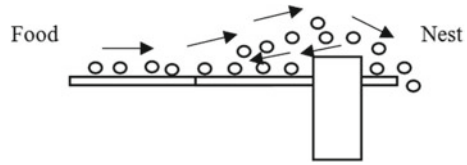


Fig. 4 Formation of the shortest path following new pheromone by ants



2.2 Structure of ACO

Whenever ants started searching from its source (nest) to its destination (food source), they left pheromones to spot the path which benefits the followed ants to detect the specific path of their team. The algorithm works on the basis of adjusting the pheromone on paths at individual node, which is depicted in Fig. 5. The path's choice will be directed on the basis of probability-based selection (PS) method. Ants are determined with the help of probability phenomenon for choosing their resolution to the problem, and it is named to be tour. The phenomenon of probability in between the two paths known to be pseudo-random-proportional action choice rule (PRPACR), and the phenomenon is specified as in Eq. 1 [2]. It relies upon the two aspects such as heuristic as well as metaheuristic.

$$p_{i,j} = \frac{(\tau_{i,j}^\alpha)(\eta_{i,j}^\beta)}{\sum (\tau_{i,j}^\alpha)(\eta_{i,j}^\beta)} \tag{1}$$

here,

- $\tau_{i,j}$ quantity of pheromone on i and j
- α controlling parameter for the influence of $\tau_{i,j}$
- $\eta_{i,j}$ attractiveness of edge i and j
- β controlling parameter for the influence of $\eta_{i,j}$.

Every ant adapts the situation in two dissimilar ways:

(A) Updation of local path

Since ants move between the paths, they update the expanse of pheromone on the edge, and it has been mentioned in Eq. 2 [2].

$$\tau_{i,j}(t) = (1 - \rho) \times \tau_{i,j}(t - 1) + \rho \cdot \tau_0 \tag{2}$$

here,

- ρ evaporation constant.
- τ_0 the initial value of pheromone path, and it can be evaluated using Eq. 3.

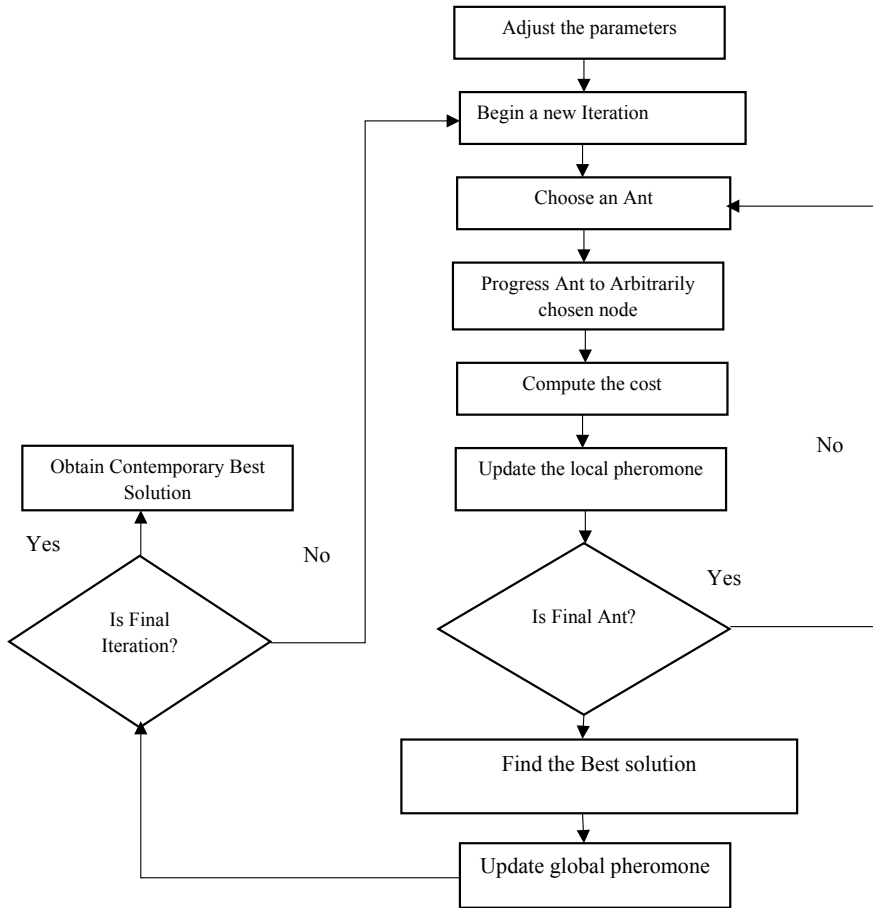


Fig. 5 Structure of ACO algorithm

$$\tau_0 = 1 - \left(\frac{n}{L_n} \right) \tag{3}$$

In Eq. 3,

n number of paths

L_n total distance covered between the complete paths which is formed with one among the structure heuristics.

(B) Updation of global Path

Whenever all the ants finished discovering total paths, the shortest path updates the edges in it (Eq. 4 [2]).

$$\tau_{ij}(t) = (1 - \rho) \times \tau_{ij}(t - 1) + \rho/L^+ \tag{4}$$

Here, L^+ = Length of contemporary best path which is created by one of the ants among all the ants.

3 Applications of Ant Colony Optimization

ACO algorithms have been used to numerous combinatorial problems sorting from quadratic task to routing vehicles. Many derived techniques have been modified to active problems in multi-targets, existent variables, stochastic problems and parallel executions. As the application areas of ACO are quite multidirectional, so in this work, we have considered its applicability in data mining problems with a specific range of years from 2015 to 2020. The problems of data mining such as classification, clustering, regression as well as forecasting are being applied by many researchers frequently and are depicted in Fig. 6.

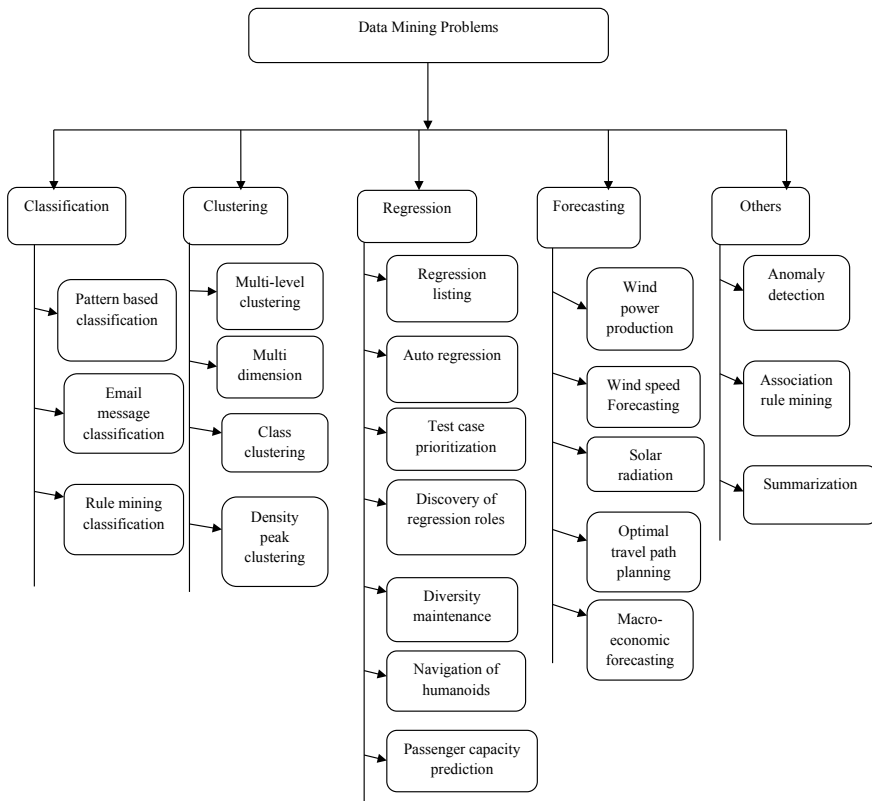


Fig. 6 Various data mining problems of ACO

Table 1 Other classifications of ACO

S. No.	Algorithm used	Problem name	Application area	Compared method	Authors	Year	Refs.
1	ACO	Classification rule mining	Data mining	Ant-miner	Hota et al.	2014	[13]
2	ACO	Optimization of data cluster	Data mining	c-means clustering algorithm	Salama and Abdelbar	2016	[14]
3	ACO and social network analysis	Automatic classification	Classification	Public Enron E-mail dataset	Probiez	2018	[15]

3.1 Classification

One of the frequently used methods in data mining is classification. It is a kind of supervised learning. The ACO is a bio-inspired pattern of SI for intending the metaheuristic advances for the problems of optimization. One of the application areas [11] of ACO is classification for determining promising patterns. The tree-based approach, that engages expansion and reduction of trees, is the majority of the obtainable algorithms for the detection of rising patterns. In this, SI-based algorithms used the assortment of ACO and evaded greedy search and difficulty of tree-based algorithms for detection of promising patterns. In another application [12], ACO algorithm is utilized effectively in categorization rule mining. Ant-MinerPAE is a novel enhanced ACO classification mining algorithm that affects ant searching to build categorization rules, compute the exposure of rules, set up the classification form and optimize the assembled classification method. This solution is utilized in 12 openly accessible datasets and proved to be statistically considerable superior to the analytical accurateness of other rule induction classifications like CN2, PSO, C4.5 rules, etc. Some of the other classifications of ACO that have been developed in recent years are depicted in Table 1.

3.2 Clustering

Clustering is the method of segregating the data into a group of related individuals. Clustering is a significant technique in data mining. In [16], ACO has been used in travelling salesman problem (TSP) that is based on clustering method. In this, a hybrid hierarchical algorithm for TSP according to the divide-and-conquer scheme has been observed. The TSP problem is decayed by density peaks clustering algorithm (DPC) into a small number of subproblems through small-scale nodes. TSP is a distinctive combinatorial optimization problem that tries to discover the shortest visit that navigates all nodes at one time. This algorithm has a noteworthy result

Table 2 Clustering applications using ACO

S. No.	Algorithm used	Problem name	Application area	Compared method	Authors	Year	Refs.
1	ACO	Multilevel clustering	Wireless sensor network	LEACH, EML and improved ACO	Bisht and Kumar	2017	[18]
2	CCACRO	Data categorization	Self-organizing map	Small/shallow C-TOSOM, small/deep C-TOSOM and TOSOM	Kourav et al.	2015	[19]
3	Big data fuzzy ant colony algorithm	Stability analysis	Dam slopes	Simulated annealing algorithm	Yang et al.	2019	[20]

on dropping runtime and has the advantage of higher accurateness and robustness. The other application area is [17] multidimensional clustering, which offers high variety in data set-up, size, processing obligation, etc. It is necessary to implement a successful and well-organized advance to cluster the rising quantity of physical health data for additional analysis. A new clustering technique for multidimensional health data based on simulated ACO has been observed for resolving the complex problems. The remaining clustering applications are depicted in Table 2.

3.3 Forecasting

ACO has been extensively used for solving complex problems of forecasting in data mining. In [21], ACO has been used for forecasting of wind power production with the help of extreme learning machine (ELM). ELM has been utilized due to its high capability of learning. Experimentations were made using two Spain wind farms. Though no feature selection is performed, the proposed forecasting model yields higher performance. In [22], a least square support vector machine (LSSVM) model has been proposed. An improved ACO has been utilized for developing the method. LSSVM and backpropagation neural network (BPNN) have been compared, and higher accuracy rate for the forecasting of data has been found in case of the proposed method. Some other applications of forecasting are depicted in Table 3.

Table 3 Applications of forecasting using ACO

S. No.	Algorithm used	Problem name	Application area	Compared method	Authors	Year	Refs.
1	ACO-BPNN	Macro-economic forecasting	Data mining	–	Kuang et al.	2017	[23]
2	MEMD-ACO-RF	Monthly rain forecasting	Data mining	Standalone RF, M5tree, MPMR	Prasad et al.	2019	[24]
3	ACO	Real-time planning and forecasting	Intelligent transportation system	–	Shan Xiao	2017	[25]

3.4 Regression

Regression is one of the mostly solvable problems in the field of data mining. In [26], ACO has been utilized for solving regression testing. The study made on [26] focuses on the problem of prioritization, and ACO acts as a tool for solving this problem in an effective manner and yields higher performance. Another study was done in [27] using ACO for time series forecasting. A method named auto-regression has been employed in the study, and Levenberg–Marquardt (LM) algorithm has been adopted. Stock index data of Taiwan capitalization has been used for evaluating the performance, and higher performance for auto-regressing the data has been found. Some of the other applications of regression are depicted in Table 4.

Table 4 Applications of regression using ACO

S. No.	Algorithm used	Problem name	Application area	Compared method	Authors	Year	Refs.
1	ACO	Prioritization	Regression testing	–	Zhao et al.	2015	[28]
2	Ant-Miner-RegMA	Regression rule discovery	Data mining	Ant-Miner-Reg	Helal et al.	2018	[29]
3	RA-AACO	Navigation of humanoids	Regression	Fuzzy-wind driven optimization (FWDO), Adaptive neuro-fuzzy inference system (ANFIS)	Kumar et al.	2018	[30]

4 Variations of ACO

Various distinct versions of ACO with excellent performance have been developed for determining several problems which have been used in several numbers of applications. Many investigations have been carried out to improve the ACO performance. Few of the research works concerning enhancements of ACO have been mentioned as variants. In [31], ACO has been used for fully controllable method (FCACA) in vector space for the grouping of text documents. In this, a novel report of necessary heuristic decision has drastically enhanced the convergence and better control above the procedure of the grouping data. In [32], a novel algorithm is proposed as a modified Max-MIN ant system (MMAS) to determine the capacitated clustering problem (CCP). They have made use of a compactness model on the local search and information heuristic modified from the harmed p-medians problem. Many variants of ACO such as Max-Min ant colony and ant colony system (ACS) have been proposed for solving several problems of different research areas. These variants have also used for solving various data mining problems such as classification, clustering, regression, forecasting and summarization. Some of the important works are taken into consideration and are depicted in Table 5.

5 Discussions

ACO is an enduring powerful NIO metaheuristic-based SI algorithm that has been utilized for determining foremost difficult problems. Various research fields, those were used with the aid of ACO, have been conferred in different sections. The most regularly applicable and solvable areas have been mentioned in Sect. 3 and are mainly concerned with attracted fields of different researches. The papers considered for this study have been extracted from the online standard databases such as Springer, Science direct and IEEE explore.

For retrieving the papers from these standard databases, we used a keyword search strategy. In order to retrieve papers related to classification problems, we used the keyword “Classification using Ant colony optimization”. Moreover, to gather the papers related to clustering, regression, forecasting, summarization, anomaly detection and association rule mining, we used the keywords “clustering using Ant Colony Optimization”, “Regression using Ant Colony Optimization”, “Forecasting using Ant Colony Optimization”, “Summarization using Ant Colony Optimization”, “Anomaly detection using Ant Colony Optimization” and “Association rule mining using Ant Colony Optimization”, respectively. Though huge numbers of papers are published, we consider only 30 papers related to ACO from the year 2015–2019 by removing the similar type applications. The survey conducted in this paper reviewed several data mining problems solved by ACO. Figure 7 demonstrates the usage levels of ACO for various data mining problems. It is evident to note that though different SI-based algorithms are developed and applied in many applications of data mining, the

Table 5 Variants of ACO in data mining problems

S. No.	Variant used	Problem name	Compared method	Authors	Year	Refs.
1	Hybrid of ACO-PSO	Wind energy forecasting	Hybrid of PSO and ANFIS	Rahmani et al.	2013	[33]
2	ACO	Classification	SVM, RIPPER, etc.	Martens et al.	2007	[7]
3	Ant clustering algorithm (ACA)	Fuzzy anomaly detection	Fuzzy-wind driven optimization (FWDO), Adaptive neuro-fuzzy inference system	Aminanto et al.	2017	[34]
4	ACO-LDS	Creep data, Linguistic data summarization (LDS)	HybridGA-LDS	Diaz et al.	2015	[35]
5	ACS	Associative rule mining	Apriori algorithm	Kuo and Shih	2007	[36]
6	ACS	Fuzzy data mining	–	Hong et al.	2008	[37]
7	Artificial ACS	Building regression tree	Recursive partitioning (RP) algorithm	Izrailev and Agraftotis	2001	[9]
8	ACO	Text summarization	PSO, GA	Hassan	2015	[38]

Applications of ACO in various data mining problems

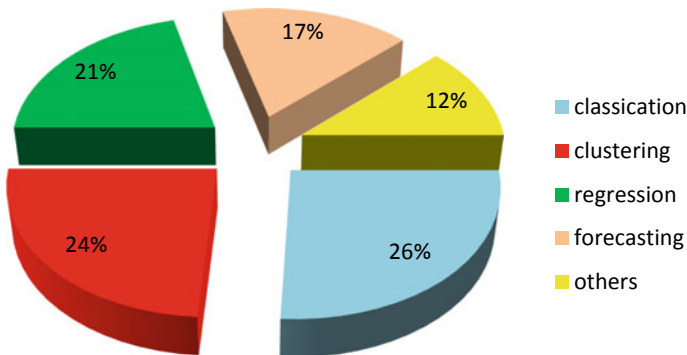


Fig. 7 Usage levels of ACO for various data mining problems

impact of ACO is quite impressive, especially in solving data mining problems. Some of the problems like classification (image, text, pattern, etc.), clustering (hard and soft), regression, forecasting and function approximation are being solved through ACO in an efficient manner. It will be worthy to mention that, being a SI-based algorithm, ACO can be considered as one of the most successful metaheuristics after PSO. Apart from these applications, ACO has remained as one of the leading choices for integration with neural network to solve data mining problems. With the advent development of ACO, the successful variations in terms of parameter tuning and other hybridizations made this optimization a global problem-solving approach. Some of its advantages like finding global optima, ability to parallel search in a population, quick detection of effective solutions, surety for convergence, etc., make it more fit to apply for NP-hard and other related complex combinatorial problems.

6 Conclusion

Undoubtedly, ACO is a powerful SI-based algorithm suitable for global solutions. Now-a-days, ACO has been concerned roughly in all areas correspondingly. The study presented in this paper represents the applicability of ACO in various data mining problems. The main motto of this paper has focused on the working procedure of ACO as well as its experimental investigations with some of the solved data mining problems. Many of its variations and other hybridizations are discussed in a brief way. Sections 3 and 4 are evidence that ACO has an enormous popularity and has received an attention from the researchers of data mining. Every research field has its specific necessity and applicability. ACO became an effective tool for data mining problems, and there is no doubt that the next decade will witness many improvements of variations as well as applications towards other industry. However, ACO is absolutely a bonus to data mining toolbox. Despite its crest success in data mining problems, some of its challenges such as change in probability distribution during each iteration, no independent decision for random sequence and uncertainty in time consumption for convergence indicate for novel advance research for successful results.

References

1. Eberhart R, Kennedy J (1995) A new optimizer using particle swarm theory. In: MHS'95, Proceedings of the sixth international symposium on micro machine and human science, IEEE
2. Colomi A, Dorigo M, Maniezzo V (1992) Distributed optimization by ant colonies. In: Proceedings of the first European conference on artificial life, vol 142
3. Karaboga D, Basturk B (2007) A powerful and efficient algorithm for numerical function optimization: artificial bee colony (ABC) algorithm. *J Global Optim* 39(3):459–471
4. Yang X-S (2010) Firefly algorithm, stochastic test functions and design optimisation. arXiv preprint [arXiv:1003.1409](https://arxiv.org/abs/1003.1409)

5. Parpinelli RS, Lopes HS, Freitas AA (2002) Data mining with an ant colony optimization algorithm. *IEEE Trans Evol Comput* 6(4):321–332
6. Blum C (2002) ACO applied to group shop scheduling: a case study on intensification and diversification. In: *International workshop on ant algorithms*. Springer, Berlin
7. Martens D et al (2007) Classification with ant colony optimization. *IEEE Trans Evol Comput* 11(5):651–665
8. Liu X, Fu H (2010) An effective clustering algorithm with ant colony. *JCP* 5(4):598–605
9. Izrailev S, Agrafiotis D (2001) A novel method for building regression tree models for QSAR based on artificial ant colony systems. *J Chem Inf Comput Sci* 41(1):176–180
10. Niu D, Wang Y, Wu DD (2010) Power load forecasting using support vector machine and ant colony optimization. *Expert Syst Appl* 37(3):2531–2539
11. Ali Z, Shahzad W (2018) EPACO: a novel ant colony optimization for emerging patterns based classification. *Cluster Comput* 21(1):453–467
12. Yang L et al (2017) Ant colony classification mining algorithm based on pheromone attraction and exclusion. *Soft Comput* 21(19):5741–5753
13. Hota S, Satapathy P, Jagadev AK (2015) Modified ant colony optimization algorithm (MAnt-Miner) for classification rule mining. In: *Intelligent computing, communication and devices*. Springer, New Delhi, pp 267–275
14. Salama KM, Abdelbar AM (2016) Using ant colony optimization to build cluster-based classification systems. In: *International conference on swarm intelligence*. Springer, Cham
15. Probiez B (2018) The mechanism to predict folders in automatic classification email messages to folders in the mailboxes. In: *International conference on computational collective intelligence*. Springer, Cham
16. Liao E, Liu C (2018) A hierarchical algorithm based on density peaks clustering and ant colony optimization for traveling salesman problem. *IEEE Access* 6:38921–38933
17. Huang X, Yao Y (2016) Multi-dimensions clustering approach for physical health data based on artificial ant colony optimization. In: *2016 8th international conference on intelligent human-machine systems and cybernetics (IHMSC)*, vol 2, IEEE
18. Bisht A, Kumar R (2017) An efficient multi-level clustering approach using improved ant colony optimization. In: *2017 3rd international conference on advances in computing, communication & automation (ICACCA)* (Fall), IEEE
19. Kourav D, Khilrani A, Nigam R (2015) Class clustering with ant colony rank optimization (CCACRO) for data categorization. In: *2015 international conference on applied and theoretical computing and communication technology (iCATccT)*, IEEE
20. Yang Y et al (2019) Stability analysis of earth-rock dam slopes based on big data fuzzy ant colony clustering. In: *2019 IEEE 3rd information technology, networking, electronic and automation control conference (ITNEC)*, IEEE
21. Carrillo M et al (2017) Wind power production forecasting using ant colony optimization and extreme learning machines. In: *International symposium on intelligent and distributed computing*. Springer, Cham
22. Li Y, Yang P, Wang H (2018) Short-term wind speed forecasting based on improved ant colony algorithm for LSSVM. *Cluster Comput* 1–7
23. Kuang Y et al (2017) A novel macroeconomic forecasting model based on revised multimedia assisted BP neural network model and ant colony algorithm. *Multimedia Tools Appl* 76(18):18749–18770
24. Prasad R et al (2019) Designing a multi-stage multivariate empirical mode decomposition coupled with ant colony optimization and random forest model to forecast monthly solar radiation. *Appl Energy* 236:778–792
25. Xiao S (2017) Optimal travel path planning and real time forecast system based on ant colony algorithm. In: *2017 IEEE 2nd advanced information technology, electronic and automation control conference (IAEAC)*, IEEE
26. Ahmad SF, Singh DK, Suman P (2018) Prioritization for regression testing using ant colony optimization based on test factors. In: *Intelligent communication, control and devices*. Springer, Singapore, pp 1353–1360

27. Cai Q et al (2015) A new fuzzy time series forecasting model combined with ant colony optimization and auto-regression. *Knowl Based Syst* 74:61–68
28. Gao D, Guo X, Zhao L (2015) Test case prioritization for regression testing based on ant colony optimization. In: 2015 6th IEEE international conference on software engineering and service science (ICSESS), IEEE
29. Helal A, Brookhouse J, Otero FEB (2018) Archive-based pheromone model for discovering regression rules with ant colony optimization. In: 2018 IEEE congress on evolutionary computation (CEC), IEEE
30. Kumar PB, Sahu C, Parhi DR (2018) A hybridized regression-adaptive ant colony optimization approach for navigation of humanoids in a cluttered environment. *Appl Soft Comput* 68:565–585
31. Dziwiński P, Bartczuk Ł, Starczewski JT (2012) Fully controllable ant colony system for text data clustering. In: *Swarm evolutionary computation*. Springer, Berlin, pp 199–205
32. de Franga FO, Von Zuben FJ, de Castro LN (2004) A max min ant system applied to the capacitated clustering problem. In: *Proceedings of the 2004 14th IEEE signal processing society workshop machine learning for signal processing*, IEEE
33. Rahmani R et al (2013) Hybrid technique of ant colony and particle swarm optimization for short term wind energy forecasting. *J Wind Eng Ind Aerodyn* 123:163–170
34. Aminanto ME et al (2017) Another fuzzy anomaly detection system based on ant clustering algorithm. *IEICE Trans Fundam Electron Commun Comput Sci* 100(1):176–183
35. Donis-Díaz CA, Bello R, Kacprzyk J (2015) Using ant colony optimization and genetic algorithms for the linguistic summarization of creep data. In: *Intelligent systems' 2014*. Springer, Cham, pp 81–92
36. Kuo RJ, Shih CW (2007) Association rule mining through the ant colony system for national health insurance research database in Taiwan. *Comput Math Appl* 54(11–12):1303–1318
37. Hong T-P et al (2008) Extracting membership functions in fuzzy data mining by ant colony systems. In: *2008 international conference on machine learning and cybernetics*, vol 7, IEEE
38. Hassan OF (2015) Text summarization using ant colony optimization algorithm. Diss, Sudan University of Science and Technology

Linear Quadratic Regulator Design for Stabilizing and Trajectory Tracking of Inverted Pendulum



Akshaya Kumar Patra, Alok Kumar Mishra, Anuja Nanda,
Ramachandra Agrawal, Abhishek Patra and Shekharesh Barik

Abstract This manuscript presents a SIMULINK model of inverted pendulum (IP) and design of a linear quadratic regulator (LQR) to control of cart position (CP) and angular position (AP) of the pendulum under uncertainties and disturbances. For designing of the LQR, a fourth-order state-space model of the IP is taken. The LQR is a novel approach whose gains dynamically vary with respect to the error signal. The validation of the improved control performance of LQR is established by comparative result investigation with other published control algorithms. The comparative results clearly reveal the better response of the proposed approach to control the system dynamics within the stable range with respect to accuracy, robustness, and ability to handle uncertainties.

Keywords Inverted pendulum · Angular displacement · Angular velocity · LQR

A. K. Patra (✉) · A. K. Mishra · A. Nanda
Department of EEE, ITER, SOA Deemed to be University, Bhubaneswar 751030, India
e-mail: hiakp@yahoo.com

A. K. Mishra
e-mail: alokmishra@soa.ac.in

A. Nanda
e-mail: anuja.sus@gmail.com

R. Agrawal · A. Patra
Department of EE, ITER, SOA Deemed to be University, Bhubaneswar 751030, India
e-mail: ramachandra1agrawal@gmail.com

A. Patra
e-mail: pabhishek720@gmail.com

S. Barik
Department of CSE, DRIEMS (Autonomous), Cuttack 754022, India
e-mail: shekharesh@gmail.com

1 Introduction

The control of IP is a standard problem among all other problems in the control system engineering field owing to non-minimum phase, nonlinear, and under-actuated characteristics as reported in Refs. [1–3]. Additionally, the IP system exhibits a significant number of industrial applications like self-balancing two-wheeled vehicles or a kind of Segway, guided missiles, rockets, intelligent robots, and other crane models [4]. In this present study, an adaptive law of control approach is being tested and analyzed to choose the IP system as it possesses a significant relevance with the control dynamics. During the past three decades, so many control strategy techniques are suggested and tested for control of AP of pendulum within the stable range. Time-discrete and switching PID control strategy is implemented in IP problems with variable control gains based on the measured AP of the pendulum [5, 6]. However, the optimal gain parameter setting, a lesser range of robust control, and need of change of gain setting with varying conditions are the major limitations to limit the real-time application of these controllers. Among other projected robust control algorithms implemented for limiting the AP of the pendulum are fuzzy [7], linear quadratic regulator (LQR) [8–10], neurocontrol [11], backstepping control [12], passivity control [13], state feedback control [14], H-infinity ($H\infty$) control [15], sliding mode (SM) control [16], fuzzy sliding mode (FSM) control [17, 18], and BLQG control [19]. However, even if these control techniques are implemented effectively to control the AP the pendulum with better accuracy, they still fail to handle various constraints and random change found in a trajectory of motion in the pendulum. These control techniques are not completely insensitive to the disturbances and the uncertainties of the model in spite of the improved performance. Hence, optimal control parameters setting for better performance and for avoiding slow response following process disturbance, the current work suggests an alternative novel technique implementing the linear quadratic regulator.

The LQR approach concept leads to an enhanced control performance with respect to robustness and delay of time compensation characteristics to counteract the negative impact of associated errors, disturbances, and uncertainties. The stabilizing control law $u(t)$ is developed based on the LQR approach [20–22]. Application of the LQR to control the AP of pendulum results to ensure a better robust controller in comparison with other contemporary well-accepted methods under both harmonized and incompatible uncertainties.

The highlights of this manuscript are as follows:

- Development of a SIMULINK model of an IP.
- Design of a LQR to control the AP of the pendulum within a stable range.
- Estimation of the control actions of the LQR under huge deviation of process disturbance.
- Comparative investigation to certify the better response of the LQR.

This manuscript is structured as follows. Section 2 concisely illustrates the IP system with mathematical details reflecting to its dynamic characteristics. Also, it

clearly demonstrates the simulation execution of the system on MATLAB environment. A detailed presentation on how the control technique is formulated and how it is implemented for this problem is presented in Sect. 3. Comparative results of the proposed approach with other published control techniques and the related analysis are provided in Sect. 4. The concluding comments are summarized in Sect. 5.

2 Problem Formulation and Modeling

2.1 System Overview

The closed-loop model of the IP is depicted in Fig. 1a. The applied horizontal force $F(t)$ and $v(t)$ are reflected as the process disturbance and the sensor noise, respectively, in this study. The controller receives information about the AP of the pendulum as an input to provide the optimal control force $u(t)$, and it balances the pendulum.

2.2 System Modeling

Figure 1b reflects the cart-pendulum model connected to a flexible cart rail with a free swinging pole. The CP is being controlled by a DC motor. The nonlinear IP modeling through the Newton's law-based mathematical equations has been carried out. It is presumed that the vertical force does not affect the CP and the CP is disturbed by the horizontal force $F(t)$ based on the operation of the DC motor [23–26]. All the physical activities of the IP system are expressed mathematically and specified by Eqs. (1) and (2). All nomenclature and specifications for IP are shown in Tables 1 and 2, respectively. The SIMULINK model of the IP is established with respect to Eqs. (1) and (2) as displayed in Fig. 1c.

$$(M + m)\ddot{x}(t) - ml\ddot{\theta}(t) \cos \theta(t) + ml\dot{\theta}(t)^2 \sin \theta(t) + b\dot{x}(t) = F(t) \quad (1)$$

$$(i + ml^2)\ddot{\theta}(t) - mgl \sin \theta(t) = ml\ddot{x}(t) \cos \theta(t) \quad (2)$$

2.3 Linearization of IP Model

The nonlinear IP system is linearized surrounding the operating point for the design of LQR to control the system dynamics within the stable range. The linearization of the IP system based on Eqs. (1) and (2) is done by neglecting the higher-order terms such as $\dot{\theta}(t)^2$. For linearization of the nonlinear IP system, the dynamic Eqs. (1) and

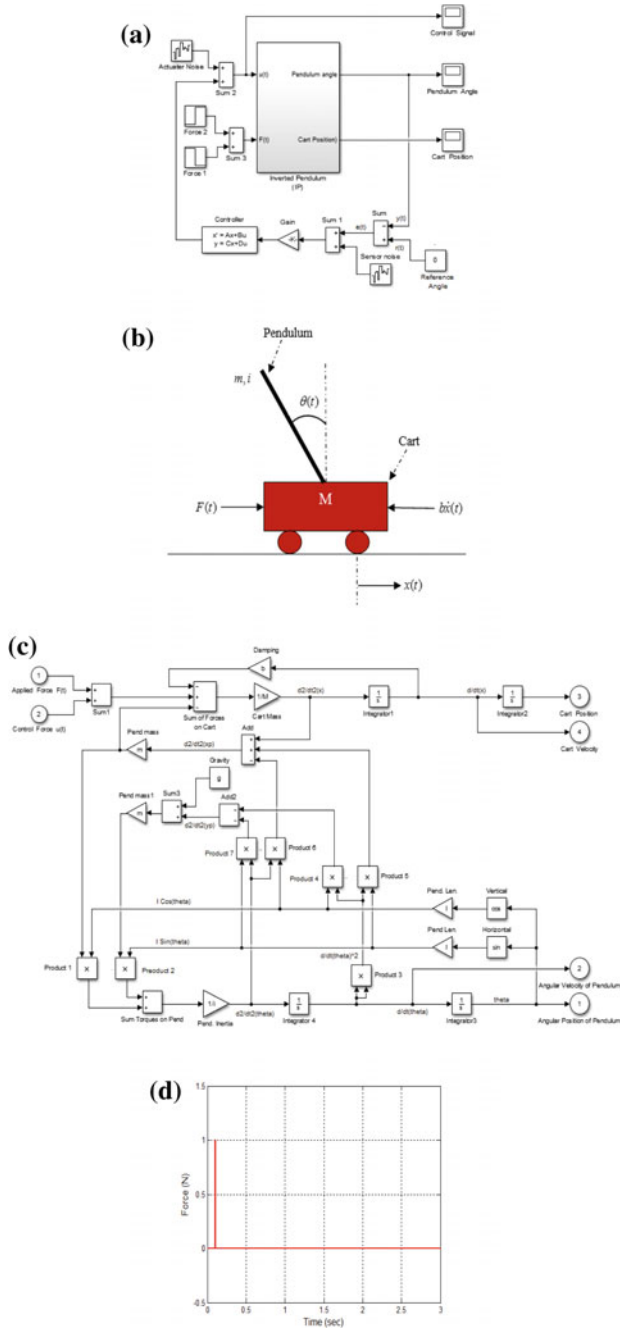


Fig. 1 **a** IP model with LQR; **b** schematic model of the IP system; **c** simulation model of the nonlinear IP system; **d** the horizontal force acting on the cart at the time of 0.1 s

Table 1 IP model states and parameters

Symbol	Description
$F(t)$	Horizontal force acting on the cart
$b\dot{x}(t)$	Frictional force acting on the cart
$x(t), \dot{x}(t), \ddot{x}(t)$	Cart position, cart velocity, and cart acceleration, respectively
$\theta(t), \dot{\theta}(t), \ddot{\theta}(t)$	AP, AV, and angular acceleration of pendulum, respectively

Table 2 IP model specification values

Symbol	Physical meaning	Value
M	Cart mass	0.5 kg
m	Pendulum mass	0.2 kg
i	Inertia	0.3 kg m ²
g	Gravitational acceleration	9.8 m/s ²
b	Frictional coefficient	0.1 N s/m
l	Pendulum length	0.3 m

(2) are reduced to Eqs. (3) and (4) based on the stable conditions such as $\theta(t) \cong 0$, $\dot{\theta}(t)^2 \cong 0$, and $\cos(0) = 1$.

$$(M + m)\ddot{x}(t) + b\dot{x}(t) - ml\ddot{\theta}(t) = F(t) \tag{3}$$

$$(i + ml^2)\ddot{\theta}(t) - mgl\theta(t) = ml\ddot{x}(t) \tag{4}$$

The transfer function (TF) of the CP and AP of the pendulum is derived as follows [23]:

$$\frac{X(s)}{U(s)} = \frac{\frac{(i+ml^2)s^2 - mgl}{\psi}}{s^4 + \frac{b(i+ml^2)}{\psi}s^3 - \frac{(M+m)mgl}{\psi}s^2 - \frac{bmg l}{\psi}s} \tag{5}$$

$$\frac{\theta(s)}{U(s)} = \frac{\frac{ml}{\psi}s}{s^3 + \frac{b(i+ml^2)}{\psi}s^2 - \frac{(M+m)mgl}{\psi}s - \frac{bmg l}{\psi}} \tag{6}$$

where $\psi = [(M + m)(i + ml^2) - ml^2]$. The linearized equation of the IP system with $F(t)$ and $v(t)$ based on Eqs. (5) and (6) can be expressed as follows [23]:

$$\dot{x}_m(t) = A_m x_m(t) + B_m u(t) + B_d F(t) \tag{7a}$$

$$y(t) = c_m x_m(t) = D_m u(t) \tag{7b}$$

where $x_m(t)$, $u(t)$, and $y(t)$ are represented as the state variable, control input, and regulated output, respectively. The state-space matrices of the IP system are represented as A_m , B_m , C_m , D_m , and B_d . The detailed description of linearization is described in the literature [23]. In MATLAB, the command ‘*linmod*’ is used to evaluate the state-space matrices on the SIMULINK model of IP as depicted in Fig. 1c.

2.4 Response of IP Model

There are four roots in IP system. One of them lies in right-hand side of the complex plane. As a result, the system becomes unstable. This needs the design of an adaptive controller for improving the stability of the system by means of shifting the roots into the left-hand side of the complex plane. The IP system SIMULINK model in the open-loop form is depicted in Fig. 1c. The IP system consists of two inputs and four outputs. The control force $u(t)$ and applied horizontal force $F(t)$ are the two inputs of the IP system. The CP and AP of the pendulum are two outputs of the IP system. An uncontrolled system dynamics such as AP of the pendulum and CP are being observed owing to the application of 1 N impulsive horizontal force $F(t)$ on the cart at the time $t = 1.0$ s. The uncontrolled system dynamics are illustrated in Fig. 2a, b. Figure 2a, b illustrates the unstable dynamics under various model uncertainties and disturbances. The unstable dynamics can be reduced by applying the suitable control techniques. In this case, the AP of the pendulum is the most essential outcome that needs to be controlled within a stable range through suitable control techniques, and CP is analyzed in order to view the motion trajectory.

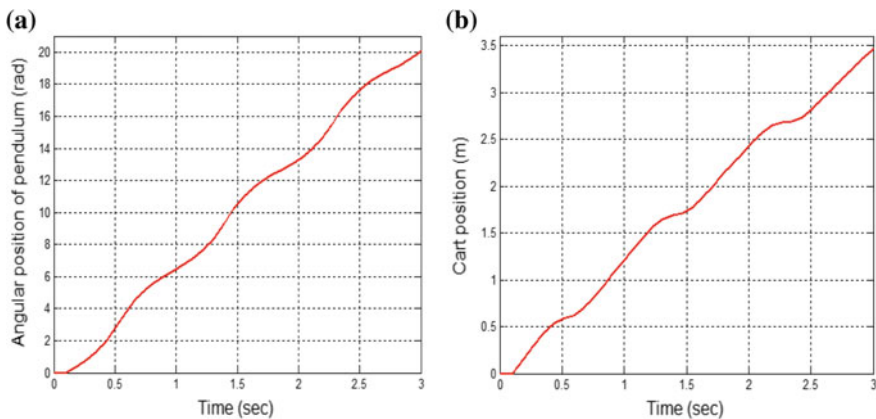


Fig. 2 a AP of pendulum with application of $F(t)$; b CP with application of $F(t)$

3 Control Algorithm

The LQR algorithm is demonstrated in this section. The closed-loop system response with respect to robustness, accuracy, and stability is analyzed. The control specifications such as settling time t_s , steady-state error e_{ss} , maximum overshoot O_{Max} , and maximum undershoot U_{Max} are also evaluated and examined with proper validation of the controller action.

3.1 LQR Design

The linearized model of the IP as discussed in Sect. 2.3 has been taken for the formulation of the LQR to regulate the CP and AP of the pendulum. For accomplishing an upgraded response and the adjustment of controller parameters of the suggested LQR, it is integrated to the linearized model of the IP as illustrated in Fig. 3. The linearized model of the patient with $F(t)$ and $v(t)$ is formulated as:

$$\dot{x}_m(t) = A_m x_m(t) + B_m u(t) + B_d F(t) \tag{8}$$

$$y(t) = C_m x_m(t) + v(t) \tag{9}$$

$$u(t) = -K_c e(t) \tag{10}$$

Figure 3 shows the linearized model of the diabetes patient with the LQR gain K_c . The evaluation procedures of K_c are mentioned in detail in Sect. 3.1.1. The evaluation of the TF of the LQR is described in Sect. 3.1.2.

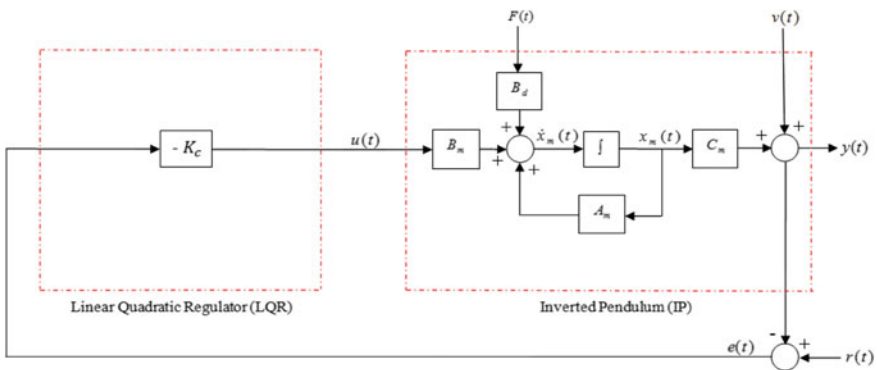


Fig. 3 IP model with suggested LQR in the state-space representation

3.1.1 LQR Gain K_c

The K_c is evaluated with respect to the IP dynamics for the minimum value of the quadratic performance index j as specified in Eq. (11).

$$j = \int_0^\infty [x_m(t)^T Q_1 x_m(t) + u(t)^T R_1 u(t)] dt \tag{11}$$

where $Q_1 = C_m^T q_1 C_m$. The Q_1 , q_1 , and R_1 are denoted as the positive semi-definite weighted matrix of state, the intensity of a weighted matrix of state, and the positive definite weighted matrix of input, respectively. The K_c is estimated for the minimum value of the quadratic performance index as specified in Eq. (12).

$$K_c = R_1^{-1} B_m^T \prod_k \tag{12}$$

\prod_k is the solution of the CARE. The CARE is specified as follows:

$$A_m^T \prod_k + \prod_k A_m - \prod_k B_m R_1^{-1} B_m^T \prod_k + C_m^T q_1 C_m = 0 \tag{13}$$

3.1.2 TF of LQR

The TF of suggested controller $K(s)$ is estimated with the use of K_c . The $K(s)$ of LQR is specified as follows:

$$K(s) = K_c (sI_n - A_m + B_m K_c)^{-1} B_m \tag{14}$$

The packed matrix notation of $K(s)$ is specified as follows:

$$K(s) = \begin{bmatrix} A_m - B_m K_c & B_m \\ \hline K & 0 \end{bmatrix} \tag{15}$$

For the design of suggested LQR, the optimal values of control parameters are evaluated with help of MATLAB and represented as in the Table 3.

Table 3 Optimal values of control parameters

Q_1	R_1
$1000 * C_m^T * C_m$	1

4 Outcomes and Discussions

The response of the closed-loop IP with proposed LQR is described in detail in this section. The proposed control approach (LQR) is compared with other popular control algorithms to justify its enhanced performance.

4.1 Performance Analysis of IP System with LQR

In this section, all physical activities of the closed-loop IP model with suggested LQR are examined under different conditions and the huge deviation of applied horizontal force. The closed-loop system dynamics with 1 N impulsive horizontal force $F(t)$ at the time of 1.0 s are displayed in Fig. 4a, b. The outcomes clearly specify the pendulum achieves the zero AP with less t_s and cart also attains the balance position where the system is absolutely stable. To achieve the enhanced system response, the required control force $u(t)$ is generated by the suggested LQR and demonstrated in Fig. 5.

4.2 Robustness of the LQR

Figure 6 illustrates the AP of the pendulum with suggested LQR under the huge deviation of applied horizontal force $F(t)$. The time-domain outcomes under huge deviation of applied forces show the enhanced performance of the closed-loop system with LQR. Overall in each case, the pendulum achieves finally zero AP with less

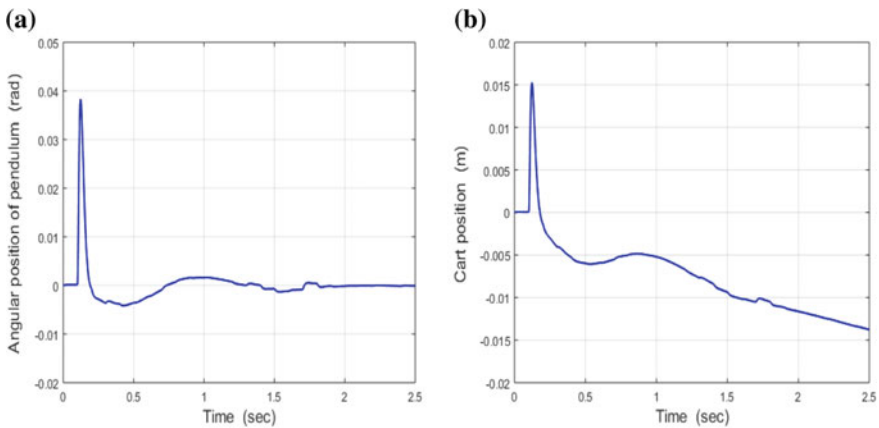


Fig. 4 **a** AP of the pendulum with the application of $F(t)$ based on LQR; **b** CP with the application of $F(t)$ based on LQR

Fig. 5 Controlled signal of the LQR

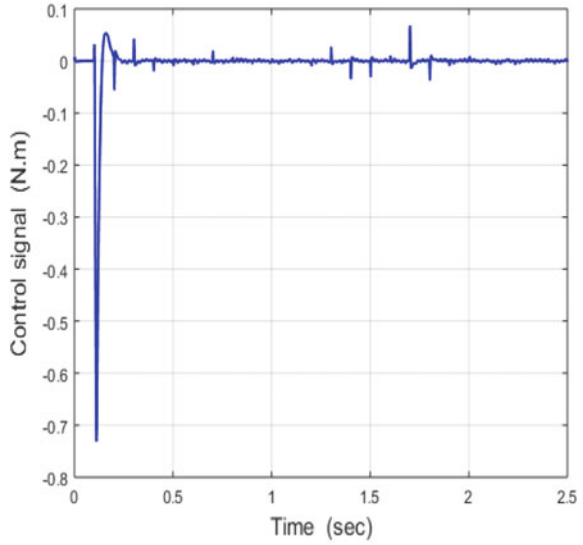
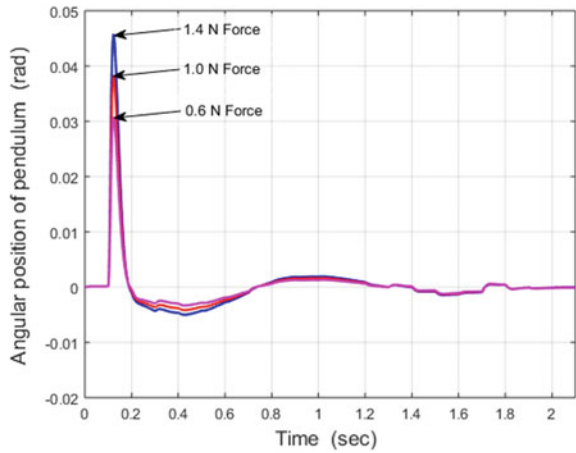


Fig. 6 AP of the pendulum with a deviation of $\pm 40\%$ applied $F(t)$ based on LQR



t_s . As indicated by the outcomes, the suggested LQR robust performance under the huge deviation of applied horizontal forces is much better.

4.3 Stability Investigation

Figure 7a, b illustrates the magnitude plots result of the open and closed-loop systems to verify and analyze the stability conditions. From both the magnitude plots, it is observed a better smoothness referring to the wider steady-state stability of

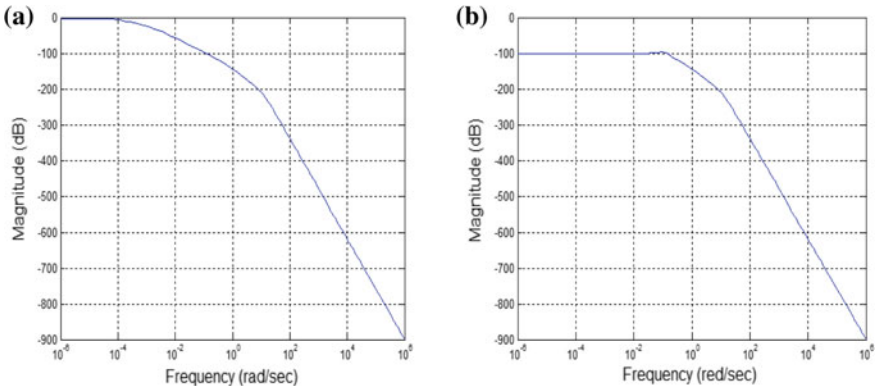


Fig. 7 a Magnitude plot of the IP system; b magnitude plot of the closed-loop IP system

closed-loop system (Fig. 7b) than the open-loop system (Fig. 7a). In other words, the bandwidth is increased in case of a closed-loop system with LQR than the open-loop system. This clearly indicates a faster dynamics, and also it results zero AP of pendulum with quick settling time in case of the closed-loop system. This justifies better stability during system operation.

4.4 Comparative Study

The suggested LQR approach is compared with other popular control approaches such as PID, LQR, H_∞ , FSM, and BLQG to justify its enhanced performance as a controller. Figure 4a illustrates the effect of applied force in the AP of the pendulum with the proposed LQR approach. Table 4 presents a comparative analysis with respect to t_s (s), O_{Max} (rad), U_{Max} (rad), noise (%), and e_{ss} (%). The effect of applied force in the AP of pendulum applying different control approaches as PID, LQR, H_∞ , FSM, and BLQG is also demonstrated in Table 4 based on the Refs. [5, 9, 15,

Table 4 Comparative result analysis related to AP of pendulum

Controller	PID [5]	LQR [9]	H_∞ [15]	FSM [18]	BLQG [19]	LQR (Proposed)
Applied force (N)	1	1	1	1	1	1
t_s (s)	2.8	2.0	2.1	1.8	1.9	1.7
O_{Max} (rad)	0.1	0.126	0.107	0.042	0.041	0.039
U_{Max} (rad)	0.01	0.087	0.045	0.151	0.01	0.005
Noise (%)	10	5	5	5	5	5
e_{ss} (%)	0	0	0	0	0	0

18, 19], respectively. Similar working conditions are followed with the same level of sensor noise in all control techniques application for comparison.

The AP of pendulum under 1 N impulsive horizontal force is tested. The corresponding results are presented for the various control approaches along with the proposed LQR with respect to time-domain specifications such as O_{Max} (rad), U_{Max} (rad), and t_s (s). The results signify the better controllability of the LQR. The simulation results also demonstrate the high noise and chattering elimination capability with high robustness for the proposed approach. Overall, by looking to the above comparative analysis, the findings of suggested approach advantages are the higher accuracy and stability, more robustness, high noise and chattering elimination capability, and better capability to handle uncertainty under various conditions and huge deviation of road disturbance.

5 Conclusions

The manuscript proposed a novel control strategy (LQR) to balance the pendulum. To justify its enhanced performance, it has been applied and tested to control the system dynamics of IP system within the stable range. Initially, the IP system is modeled as a fourth-order state-space representation. Then, the proposed control approach (LQR) is designed and implemented. The comparative results clearly reflect that the suggested LQR is arrived at better performance than the other control approaches such as PID, fuzzy, H_∞ , FSM, and BLQG with respect to stability, reliability, and robustness under various abnormal conditions and disturbances. The better performance of the suggested approach in terms of improved accuracy and stability, enhanced robustness, high noise and chattering elimination capability, and better ability to control uncertainty justifies its real-time application.

References

1. Iqbal J, Islam RU, Syed ZA, Abdul AK, Ajwad SA (2016) Automating industrial tasks through mechatronic systems—a review of robotics in industrial perspective. *Tehnik ki vjesnik – Technical Gazette* 23:917–924
2. Ajwad SA, Asim N, Islam RU, Iqbal J (2017) Role and review of educational robotic platforms in preparing engineers for industry. *Maejo Int J Sci Technol* 11:17–34
3. Bettayeb M, Boussaleh C, Mansouri R, Al-Saggaf U (2014) Stabilization of an inverted pendulum-cart system by fractional PI-state feedback. *ISA Trans* 53:508–516
4. Iqbal J, Ullah M, Khan SG, Khelifa B, Ukovic SC (2017) Nonlinear control systems—a brief overview of historical and recent advances. *Nonlinear Eng* 6:301–312
5. Ghosh A, Krishnan T, Subudhi B (2012) Brief paper—robust proportional-integral-derivative compensation of an inverted cart-pendulum system: an experimental study. *IET Control Theor Appl* 6(8):1145–1152

6. Wang C, Yin G, Liu C, Fu W (2016) Design and simulation of inverted pendulum system based on the fractional PID controller. In: IEEE 11th conference on industrial electronics and applications (ICIEA), June, pp 1760–1764
7. Magana ME, Holzapfel F (1998) Fuzzy-logic control of an inverted pendulum with vision feedback. *IEEE Trans Educ* 41(2):165–170
8. Ozana S, Pies M, Slanina Z, Hajovsky R (2012) Design and implementation of LQR controller for inverted pendulum by use of REX control system. In: IEEE international conference on circuits and systems, vol 1, pp 343–347
9. Kumar EV, Jerome J (2013) Robust LQR controller design for stabilizing and trajectory tracking of inverted pendulum. *Procedia Eng* 64:169–178
10. Prasad LB, Tyagi B, Gupta HO (2012) Modelling and simulation for optimal control of non-linear inverted pendulum dynamical system using PID controller and LQR. In: Modelling symposium (Ams), Sixth Asia, pp 138–143
11. Pasemann F (1998) Evolving neurocontrollers for balancing an inverted pendulum. *Netw Comput Neural Syst* 9:1–4
12. Deng L, Gao S (2011) The design for the controller of the linear inverted pendulum based on backstepping. In: International conference on electronic and mechanical engineering and information technology (EMEIT), vol 6, pp 2892–2895
13. Jörgl M, Schlacher K, Gattringer H (2013) Passivity based control of a cart with inverted pendulum. *Appl Mech Mater* 332:339–344
14. Žilić T, Pavković D (2009) Modeling and control of a pneumatically actuated inverted pendulum. *ISA Trans* 48:327–335
15. Lambrecht P, Vander G (1988) H-infinity control of an experimental inverted pendulum with dry friction. *IEEE Contr Syst Mag* 13(4):44–50
16. Wai RJ, Chang LJ (2006) Adaptive stabilizing and tracking control for a nonlinear inverted-pendulum system via sliding-mode technique. *IEEE Trans Ind Electron* 53:674–692
17. Tao CW, Taur J, Chang J (2010) Adaptive fuzzy switched swing-up and sliding control for the double-pendulum-and-cart system. *IEEE Trans Syst Man Cybern B Cybern* 40(1):241–252
18. Chen CS, Chen WL (1998) Robust adaptive sliding-mode control using fuzzy modelling for an inverted-pendulum system. *IEEE Trans Ind Electron* 45(2):297–306
19. Patra AK, Rout PK (2019) Backstepping linear quadratic gaussian controller design for balancing an inverted pendulum. *IETE J Res* 1–15
20. Khalil HK (2002) *Nonlinear systems*, 3rd edn. Prentice Hall, Upper Saddle River, New Jersey
21. Patra AK, Rout PK (2017) Adaptive sliding mode Gaussian controller for artificial pancreas in T1DM patient. *J Process Control* 58:23–27
22. Patra AK, Rout PK (2018) Backstepping sliding mode Gaussian insulin injection control for blood glucose regulation in T1DM patient. *J Dyn Syst Meas Control* 140(9):091006–091006-15
23. Irfan S, Mehmood A, Razzaq MT, Iqbal J (2018) Advanced sliding mode control techniques for inverted pendulum: modelling and simulation. *Eng Sci Tech Int J* <https://doi.org/10.1016/j.jestch.2018.06.010>
24. Ronquillo-Lomeli G, Ríos-Moreno GJ (2016) Nonlinear identification of inverted pendulum system using Volterra polynomials. *Mech Based Des Struct Mach* 44(1):5–15
25. Kajita S, Kanehiro F, Kaneko K, Fujiwara K (2003) Biped walking pattern generation by a simple three-dimensional inverted pendulum model. *Adv Robot* 17(2):131–147
26. Canete L, Takahashi T (2015) Modeling, analysis and compensation of disturbances during task execution of a wheeled inverted pendulum type assistant robot using a unified controller. *Adv Robot* 29(22):1453–1462

Real-Time Position Estimation of Mobile Platform in Indoor and GPS-Denied Environments



Sagar Dhatrak and Damayanti Gharpure

Abstract Indoor mobile platform localization plays an important role in autonomous navigation. This paper describes the development of a mobile platform localization approach based on wheel odometry and inertial measurement unit (IMU) sensors throughout the travel path. The correctness of the estimated position determines the accuracy with which the trajectory can be predicted. A number of experiments were carried out to understand the variation in IMU data with the sensor placed at different distances along the axis of the robot and its effect on heading angle of the mobile platform and the resulting trajectory. In the east and west directions, as distance between IMU and midpoint of axis joining left and right dc motors becomes greater than 8 cm, effect of positioning of dc motor starts reducing on heading angle θ and goes down to zero at distance greater than 12 cm. In north and south directions, as distance between IMU and midpoint of axis joining left and right dc motors becomes greater than 2 cm, effect of positioning of dc motor completely vanishes. The paper details the experiments carried out, results obtained, and discusses measures to improve the localization accuracy.

Keywords Mobile platform · Localization · IMU · Odometry

1 Introduction

Work on autonomous mobile platform, which can navigate in a given indoor as well as outdoor environment recognizes its surroundings using different types of sensors, is being carried out [1–3]. Mobile robot platforms have been used to autonomously navigate in hazard detection and avoidance techniques. Accurate navigation is based on its ability to produce state estimates of the mobile platform's pose with respect to specific reference frame [4]. The localization of a mobile platform in an indoor

S. Dhatrak (✉) · D. Gharpure
Department of Electronic Science, Savitribai Phule Pune University, Pune, India
e-mail: sagardhat333@rediffmail.com

D. Gharpure
e-mail: dcgharpure@gmail.com

© Springer Nature Singapore Pte Ltd. 2020
R. Sharma et al. (eds.), *Innovation in Electrical Power Engineering, Communication, and Computing Technology*, Lecture Notes in Electrical Engineering 630,
https://doi.org/10.1007/978-981-15-2305-2_31

environment is important for many applications like floor cleaning robots, elder assistance, hazard detection and robotic vacuum cleaner. Trajectory of the mobile platform is used to know its current location and travelled distance from the initial position.

Mobile platform position is measured by different absolute positioning methods such as the global positioning system (GPS), radio frequency identification (RFID) systems and ultrasonic local positioning systems. In the indoor mobile platform localization, GPS is not suitable to measure indoor locations, since microwaves are attenuated and scattered by walls, roofs and other objects [4] and RFID requires additional hardware, which is costly. The robot state estimation makes the use of IMU sensor to estimate rover attitude during remove a travelling and estimated attitude is combined with wheel odometry to estimate robot position [5]. The ultrasonic local positioning systems, used for measuring short distances, require additional installation, and signal interference is problem [6, 7].

Inertial navigation systems (INS) consist of accelerometers and gyroscopes. INS provides orientation and position [8]. Its stability is good at short distance but stability decreases over time. Systems which combine INS and odometry to provide more accurate position than stand-alone wheel odometry are reported [9]. Bong-Su Cho et al. present a dead reckoning localization system for mobile platforms using inertial sensors and wheel revolution encoding without using external signals in indoor environments [10]. The results also show errors occurred by the integrative nature of the rotating speed of wheel and the slippage between the wheel and ground surface and solution for this is provided by Kalman filter [11]. A system based on University of Michigan Benchmark test (UMBmark) is developed to compensate odometric error to find more accurate mobile platform position [6].

In indoor environment, measurements are unstable because of floor surface condition and obstacles inside room. Mobile platform position is obtained by fusing measurements from inertial measurement unit, an odometer and an active beacon system [2]. Fusing data of an IMU and an odometer provides mobile platform position, when an active beacon is losing its signal. Kalman filter are applied to reduce noise from sensors. David Tick et al. presented a novel approach to localize and control mobile platform fusing visual pose with optical encoder to estimate the pose and orientation of mobile robot [4]. The realization of this work supposes the availability of a great number of repetitions of samples responding to the same known theoretical model. In practice, as the theoretical model is unknown, we use the Monte Carlo method based on the generation of the data by computer according to a fixed theoretical model [12].

In this paper, the position estimate of the mobile platform in indoor environments such as building, houses and factories on a flat, mostly level surface is discussed. Dead reckoning system estimates a robot position from the inertial measurement sensors (IMU) and wheel encoder which does not depend on external signals [10]. Dead reckoning is used for real-time mobile platform state estimation because it offers advantages of being simple and low cost. IMU consists of three-axis accelerometer, three-axis gyroscope and magnetometer sensors. As mobile platform travels, mobile platform position and heading are obtained using wheel odometry and IMU [13]. The

mobile platform heading is measured using gyroscope and magnetometer sensor. dc motor affects the heading angle measured by IMU. The paper describes experiments carried out to study the effect of distance between IMU from the wheel dc motors on position estimation. Further experiments carried out to study the effect of localization errors on trajectory obtained are also discussed. Error due to wheel slippages is not considered for, in this paper. Extensive results from state estimation of mobile platform are presented. This paper deals with the errors in localization of mobile platform using wheel encoder and IMU and its effect on trajectory prediction.

2 System

This paper deals with autonomous localization of mobile platform named as 'Pragyan' in indoor environment and the errors in localization of mobile platform using wheel encoder and IMU and its effect on trajectory prediction. Experiments are carried out to study the effect of distance between IMUs from the wheel dc motors on position estimation. The mobile platform used consists of Arduino Nano microcontroller, IMU, two dc motors, wheels and IR sensors used as wheel encoder for left motor and right motor as shown in Fig. 1. Each wheel is fitted with a simple IR-based wheel encoder. Mobile platform travels 3.66 cm for each incremental count and wheel diameter is of 7 cm and in one complete rotation of wheel, it travels 21.98 cm distance.

2.1 Inertial Navigation System

The mobile platform has utilized two back wheels and front castor wheel and consists of two dc motors and GY-87 IMU. As Fig. 2 shows, d is distance between two motors

Fig. 1 Pragyan mobile platform

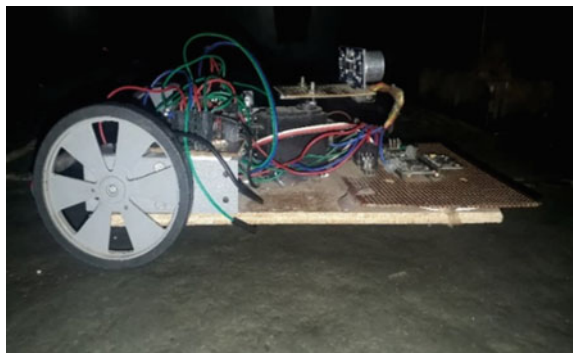
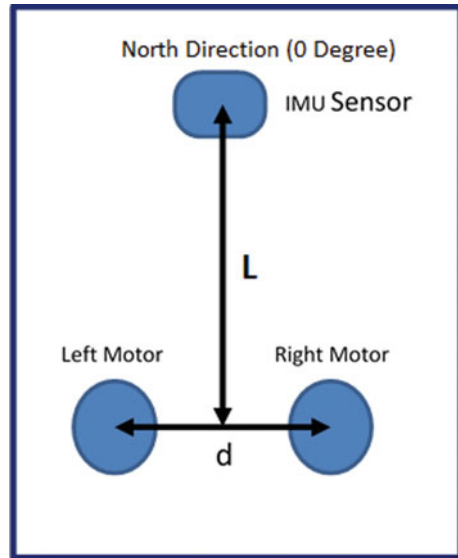


Fig. 2 Positioning of IMU and dc motors



which is 12 cm, L is distance from midpoint of axis joining two motors to IMU, which is 15 cm and mobile platform width is 14 cm and length is 24 cm.

Two IR sensors are equipped with each wheel as wheel encoder. In the initial positioning algorithm, the orientation of the mobile platform is calculated by the tri-accelerometers and the compass sensor. Mobile platform's roll and pitch angle are measured by accelerometer, and so it has low accuracy in attitude [2]. Magnetometer sensor is used for measuring yaw angle. Magnetometer sensor produces error in yaw angle measurement, when it is subjected to small magnetic field changes caused by metals found in the external environment [6]. So, errors due to attitude and yaw angle measurement have to be corrected in order to measure orientation of mobile platform.

The triaxial gyroscope measures the angular rate in the body frame and orientation of the mobile platform. The measurement is affected by drift and random walk noise which accumulates with time. Complementary filter is used for increased accuracy in attitude and yaw angle by reducing error due to small magnetic field changes and gyroscope drift problem. The combination of these three sensors with complementary filter provides accurate mobile platform heading irrespective of the angle and movement of the mobile platform. This algorithm steps are shown in Fig. 3. This section provides mobile platform heading yaw angle to positioning algorithm to estimate the state of mobile platform.

The mobile platform used for our research work is shown in Fig. 1. The position of mobile platform is shown in Fig. 4 by position vector P (Eq. 1).

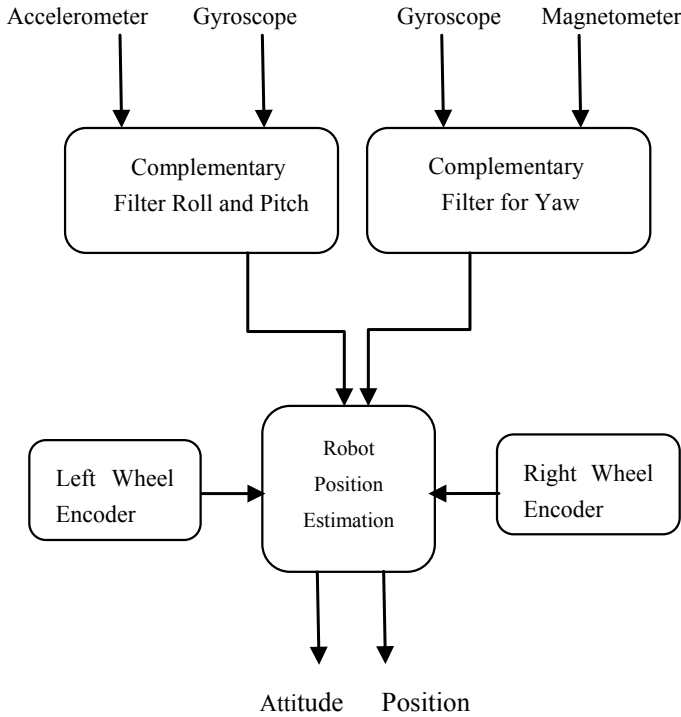
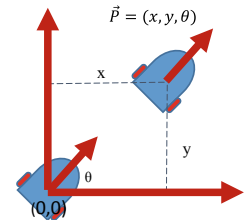


Fig. 3 Inertial navigation system algorithm

Fig. 4 Mobile platform new position



$$\vec{P} = \begin{pmatrix} x \\ y \\ \theta \end{pmatrix}. \tag{1}$$

where x and y are the two-dimensional coordinates and θ is the orientation of the mobile platform from IMU.

The mobile platform position is estimated starting from a known position by integrating the travel distances. After a fixed sampling interval Δt , the incremental travel distances Δx , Δy and $\Delta \theta$ are presented in Eqs. 2, 3 and 4, respectively.

$$\Delta x = \Delta d * \cos\left(\theta + \frac{\Delta\theta}{2}\right) \quad (2)$$

$$\Delta y = \Delta d * \sin\left(\theta + \frac{\Delta\theta}{2}\right) \quad (3)$$

The relative displacement Δd and orientation $\Delta\theta$ of the mobile platform between two steps are given as in Eqs. 5 and 4, respectively.

$$\Delta\theta = \frac{\Delta dl - \Delta dr}{B} \quad (4)$$

$$\Delta d = \frac{\Delta dl + \Delta dr}{2} \quad (5)$$

where Δdl and Δdr stand for the relative displacement of the left wheel and the right wheel of the mobile platform, respectively, which are measured by IR sensor used as encoders [14].

$\Delta x, \Delta y, \Delta\theta$ Mobile platform travelled position after Δt sampling interval
 $\Delta dl, \Delta dr$ Travelled distances by left and right wheel, respectively
 B Distance between the two wheels of mobile platform
 $\Delta\theta$ Heading angle of robot measured using IMU

If Δdl is not equal to Δdr , then

$$\begin{aligned} x_{i+1} &= x_i + \Delta x \\ y_{i+1} &= y_i + \Delta y \\ \theta_{i+1} &= \theta_i + \Delta\theta \end{aligned}$$

If Δdl is equal to Δdr , then

$$\begin{aligned} x_{i+1} &= x_i + \Delta x \\ y_{i+1} &= y_i + \Delta y \\ \theta_{i+1} &= \theta_i \end{aligned}$$

Trajectory of mobile platform is plotted using left, right wheel encoder and IMU. When mobile platform travels straight, Δdl and Δdr are equal and heading angle of mobile platform is only angle from IMU, and if it is not travelling straight, then heading angle of mobile platform is addition of angle in Eq. (4) and IMU.

3 Experimental Method

A number of experiments are performed using mobile platform to estimate the position and understand the error due to variation in distance ‘ L ’ of the IMU sensors from the wheels. Test environment used for experiments is shown in Fig. 5.

3.1 Effect of dc Motors on Mobile Platform Heading Angle

Experiments were carried out by varying distance between IMU and midpoint of axis joining left and right dc motors. Initially, distance is set to 1 cm and mobile platform heading angle θ is measured. Further distance L is increased by 1 cm up to 17 cm and heading angle θ is measured in each case. Experiments were also repeated by setting mobile platform pointing towards the North, south, east and west directions to study the effect of direction. The effect of variation in current of the dc motor was also studied but it was observed that there is no effect of dc motor changing current on mobile platform heading angle θ .

Heading angle θ is measured for each 1 cm distance and this step is repeated for 10 runs. From the above graph in east and west directions, as the distance between IMU and midpoint of axis joining left and right dc motors becomes greater than 8 cm, effect of positioning of dc motor starts reducing on heading angle θ and goes down to zero at distance greater than 12 cm. In north and south directions, as distance between IMU and midpoint of axis joining left and right dc motors becomes greater than 2 cm, effect of positioning of dc motor is completely vanished. It has been also

Fig. 5 Test environment

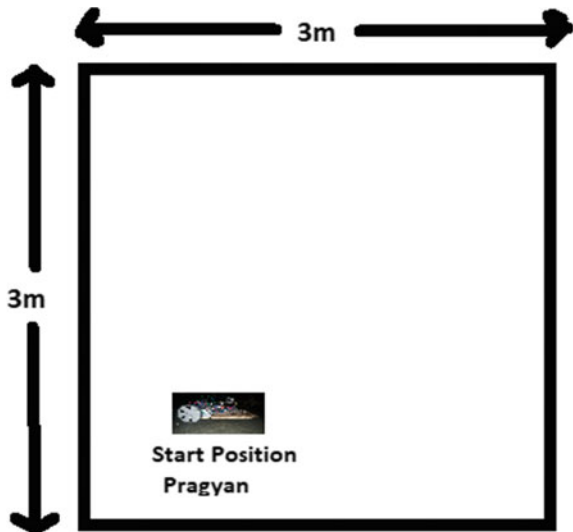
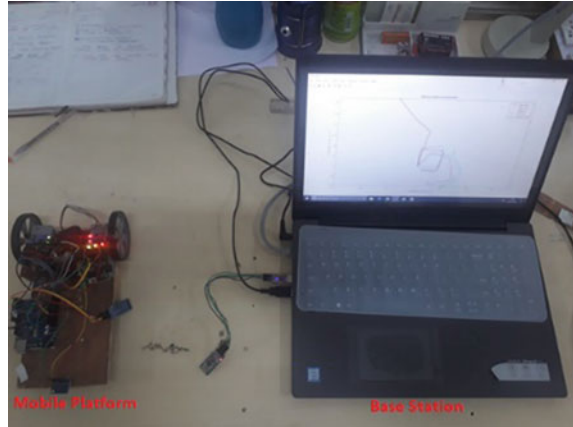


Fig. 6 Experimental set-up

found that, when current flowing through dc motor is changed, there is no effect on mobile platform heading angle θ . Same heading angle is obtained at different currents 0 mA, 45 mA, 50 mA and 55 mA, indicating driving current does not affect the IMU data.

3.2 Trajectory Estimation

The mobile platform Pragyan is programmed for following a square trajectory of 40 cm \times 40 cm in the 3 m \times 3 m environment. Left and right wheel encoder counts and robot heading angle θ are send to laptop using Bluetooth module HC-05. Experimental set-up is shown in Fig. 6. Throughout the travel, the position and heading angle data were recorded. MATLAB program is written to convert wheel encoder count and IMU angle into mobile platform position, and the position of mobile platform is plotted to obtain the trajectory as shown in Fig. 8. Experiment is performed to test the accuracy of mobile platform state and heading angle θ .

4 Result and Discussion

Effect of dc motor on IMU in the form of predicated heading angle is plotted for varying direction as well as distances. From the above graph in east and west directions, as distance between IMU and midpoint of axis joining left and right dc motors becomes greater than 8 cm, effect of positioning of dc motor on heading angle θ starts reducing and completely vanished at distance greater than 12 cm. In north and south directions, as distance between IMU and midpoint of axis joining left and right

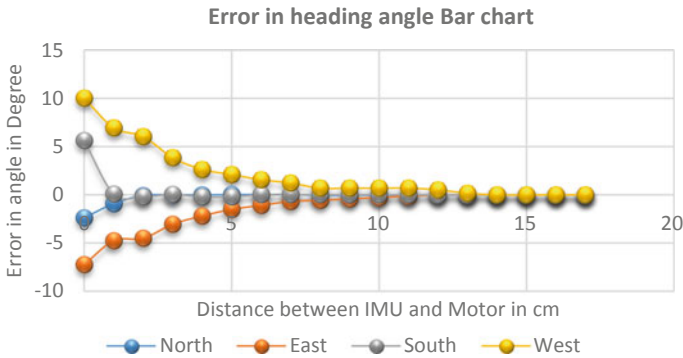


Fig. 7 Error in heading angle bar chart

dc motors becomes greater than 2 cm, effect of positioning of dc motor on heading angle is completely vanished.

The graph in Fig. 7 shows that effect of the dc motors on heading angle θ of mobile platform is affected by the distance between IMU and midpoint of axis joining left and right dc motors.

Experiments were also performed to test the effect of mobile platform state and heading angle θ on accuracy of the trajectory. For this purpose, the mobile platform was placed in the test environment and programmed to follow the square shape trajectory A, B, C and D with dimension 40 cm \times 40 cm. The predicted trajectories are plotted for distance 'L' varying as 0 cm, 5 cm, 10 cm and 15 cm are shown in Fig. 8.

The blue square indicates the ground truth, and in case of 0 cm distance, the predicted trajectory matches ground truth till B and then is totally erroneous. When the distance between IMU and midpoint of axis joining left and right dc motors is set to 15 cm on mobile platform then resultant trajectory is close to ground truth.

As the mobile platform travels through test environment, experimental coordinates are recorded. The end position experimental coordinates are compared with end position ground truth coordinates, as shown in Table 1 and graph is plotted root-mean-square error (RMSE)/cm versus distance between IMU and midpoint of axis joining left and right dc motors.

The root-mean-square error is calculated using ground truth coordinates (X_r, Y_r) and experimental coordinates (X_e, Y_e).

It can be seen that as the distance between IMU and midpoint of axis joining left and right dc motors increases, RMSE decreases, which is shown graphically in Fig. 9.

The method mentioned in [10] is complicated and the method used here is much simpler. When mobile platform travelled square-shaped trajectory, the total distance travelled by it is 160 cm and RMSE is 11.80 cm at 'L' greater than 12 cm. Mobile platform travelled trajectory is compared with ground truth, and positioning error is 7.375%.

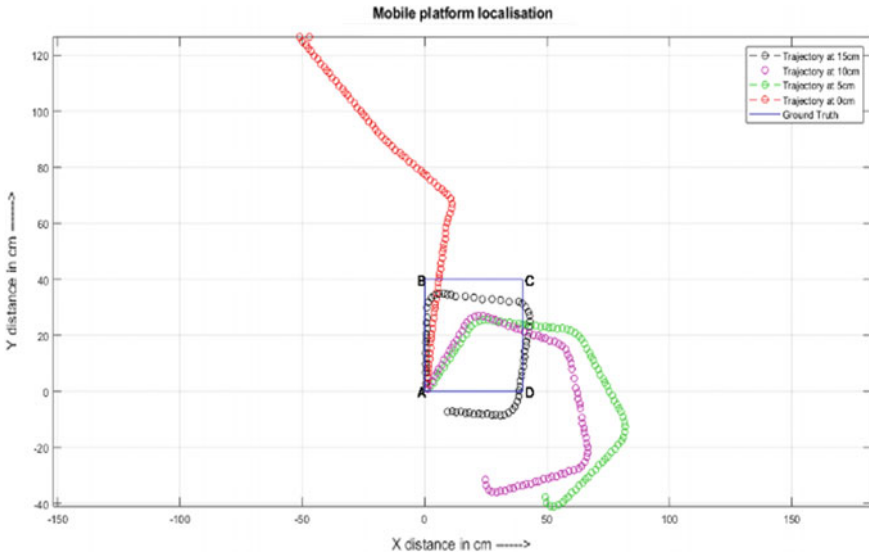
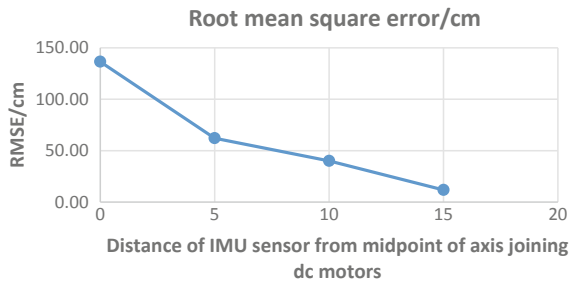


Fig. 8 Experimental mobile platform travel path

Table 1 Root-mean-square error analysis of mobile platform travel path

S. No.	Ground truth end position coordinates		Experimental end position coordinates		Distance L in cm	RMSE/cm
	Y_r	X_r	Y_e	X_e		
1	0	0	126.47	51.08	0	136.40
2	0	0	-37.7	49.30	5	62.06
3	0	0	-31.51	24.76	10	40.07
4	0	0	-7.27	9.30	15	11.80

Fig. 9 RMSE error analysis



5 Conclusion

This paper has outlined the experiments related to the accuracy of localization, using wheel encoder and IMU data. Estimation of mobile platform heading angle based on IMU data and travel distance measured via wheel encoder is described. Experiments were carried out by setting a mobile platform pointing towards the north, south, east and west directions to check the effect of position of IMU along the axis. The experiments indicate that the heading angle θ of mobile platform is affected by the distance between IMU and midpoint of axis joining left and right dc motors as well as the direction of movement. The error in position estimation is observed to be more in east and west direction, if IMU is placed at distance less than 12 cm. If IMU is placed at distance greater than 12 cm positioning error in all directions goes down to zero. It can be seen that as the distance between IMU and midpoint of axis joining left and right dc motors increases, RMSE decreases. It has been found that, when current flowing through dc motor is changed, there is no effect on the mobile platform heading angle. To understand the effect of error in heading angle on predicted trajectory, Pragyana was placed in the test environment and programmed to follow the square-shaped trajectory. The results clearly indicate the errors in trajectory prediction though the robot follows a square path.

Overall the error in heading angle could be attributed to dc motor. In future work, error generated due to placing of IMU near to the dc motors can be corrected mathematically. Further work on use extended Kalman filter (EKF) to remove error due to wheel slippages to obtain the more accurate trajectory of mobile platform is underway.

References

1. Baumgartner ET, Aghazarian H, Trebi Ollenu A (2001) Rover localization result for the FIDO rover. California Institute of Technology, Pasadena
2. Lee T, Shin J, Cho D (2009) Position estimation for mobile robot using in-plane 3-axis IMU and active beacon. In: IEEE international symposium on industrial electronics (ISIE 2009), Seoul Olympic Parktel, Seoul, Korea, July 5–8, 2009
3. Choi JM, Lee SJ, Won MC (2011) Self-learning navigation algorithm for vision-based mobile robots using machine learning algorithms. *J Mech Sci Technol* 25(1):247–254
4. Shen J, Tick D, Gans N (2010) Localization through fusion of discrete and continuous epipolar geometry with wheel and IMU odometry. Preprint submitted to 2011 American control conference. Received Sept 27, 2010
5. Baumgartner ET, Aghazarian H, Trebi-Ollenu A (2001) Rover localization results for the FIDO rover. In: Proceedings volume 4571, Sensor fusion and decentralized control in robotic systems IV, Intelligent systems and advanced manufacturing, Boston, MA, United States
6. Borenstein J, Feng L (1996) Measurement and correction of systematic odometry errors in mobile robots. *IEEE Trans Rob Autom* 12(6):869–880
7. Moon WS, Cho BS, Jang JW, Baek KR (2010) A multirobot positioning system using a multi-code ultrasonic sensor network and a Kalman filter. *Int J Control Autom Syst* 8(6):1349–1355
8. Barshan B, Durrant-Whyte HF (1995) Inertial navigation systems for mobile robots. *IEEE Trans Robot Autom* 11(3):328–342

9. Brossard M, Bonnabel S (2019) Learning wheel odometry and IMU errors for localization. In: International conference on robotics and automation (ICRA), May 2019, Montreal, Canada
10. Cho B-S, Moon W, Seo W-J, Baek K-R (2011) A dead reckoning localization system for mobile robots using inertial sensors and wheel revolution encoding. *J Mech Sci Technol* 25(11):2907–2917
11. Yi J, Zhang J, Song D, Jayasuriya S. IMU-based localization and slip estimation for skid-steered mobile robots. <https://www.researchgate.net/publication/221065982>
12. Dellaert F, Fox D, Burgard W, Thrun S (1999) Monte Carlo localization for mobile robots. Carnegie Mellon University, Pittsburgh, Institute of Computer Science III, University of Bonn, Bonn
13. El-Diasty M (2014) An accurate heading solution using MEMS-based gyroscope and magnetometer integrated system (preliminary results). In: ISPRS annals of the photogrammetry, remote sensing and spatial information sciences, vol II-2, 2014 ISPRS Technical Commission II symposium, 6–8 Oct 2014, Toronto, Canada
14. <http://www.cs.cmu.edu/~rasc/Download/AMRobots5.pdf>

Steady Model for Classification of Handwritten Digit Recognition



Anujay Ghosh, Aruna Pavate, Vidit Gholam, Gauri Shenoy and Shefali Mahadik

Abstract Handwritten digit recognition plays an important role not only in computer vision but also in pattern recognition. Handwritten digit recognition is the competence of a machine to receive, calculate and decipher a human handwritten input from sources such as handwritten manuscripts, especially created before the advent of a digital revolution and digital images. This work implements the system to read the handwritten digits with a custom novel method identical to the amalgamation of different techniques, including principal component analysis, support vector machine and K -nearest neighbours to recognize and classify handwritten digits into their respective labels. PCA algorithm finds out the best linear combinations of the original features so that the variance along the new feature is maximum. Recognition of characters is done using KNN nonparametric machine learning algorithm, and SVM lowers the generalization error of the overall classifier. The proposed work does the analysis on digit data set having a total of 70,000 image samples. The performance of the system is analysed using different measurement metrics like precision, recall, f1 score and support, and the recognition of the patterns in the images shows the result with classification accuracy of 97%.

Keywords K -nearest neighbour · Support vector machine · Principal component analysis · Classification · Handwritten digit

1 Introduction

The human capability to examine and categorize objects and scenes is a very useful skill, researchers have tried to implement this through machine learning algorithm in many domains including Education, Sports, Transportation, Oil and Gas, Financial Services, Marketing and Sales, Government, health care and in many safety-critical applications like fingerprint recognition, facial recognition and many more [1]. Handwriting digit recognition is one of the major applications in machine learning applied

A. Ghosh (✉) · A. Pavate · V. Gholam · G. Shenoy · S. Mahadik
Atharva College of Engineering, Mumbai University, Mumbai 400095, India

© Springer Nature Singapore Pte Ltd. 2020
R. Sharma et al. (eds.), *Innovation in Electrical Power Engineering, Communication, and Computing Technology*, Lecture Notes in Electrical Engineering 630,
https://doi.org/10.1007/978-981-15-2305-2_32

in many wide ranges of real-life applications such as signature identification and verification, zip code recognition in postal mail categorization, form processing, handwritten digit verification in bank, fraud detection etc. Handwritten digit recognition plays a crucial role in optical character recognition (OCR) and in pattern recognition [2]. There are many devices such as smart phones and tablets that can take handwriting as an input to a touch screen via a finger or using an electronic stylus. This allows user to quickly transfer the text to the devices which helps especially for the selective individuals who are not well versed with input devices such as keyboards to write text faster rather than typing slowly through input devices. Recognition of such text is very hard even by humans. Thus, a system that supports an automatic recognition of text would be very helpful in many applications.

1.1 Need of the System

Handwritten digit recognition system is developed to improve the accuracy of the existing solutions to achieve higher accuracy and reliable performance. Over the last decades, many machine learning algorithms made use of impressive handwritten digit recognition techniques such as baseline linear classifier, baseline nearest neighbour classifier, pairwise linear classifier, radial basis network, large fully connected Multilayer neural network, tangent distance classifier, optimal margin classifier [3], support vector machine (SVM) [4–8], CNN [5], fuzzy [9] neural network [7, 10–14], PCA [6, 15], CNN-SVM classifier [2, 16], KNN [17], recurrent neural network (RNN) [18] and DNN classifiers [19].

However, there are still some challenges that need to be solved. As handwritten characters are different in writing style, stroke thickness, deformation, rotation, etc., it is difficult to recognize [17, 18, 20, 21]. The main challenge in handwriting recognition system is to classify a handwritten digit based on black and white images. Furthermore, to meet the industry need, accuracy and robustness to the variation in writing style of the individual must be high.

1.2 Scope of the System

The digital world's advent began a mere century or two ago, but scriptures and books after books have been handwritten by human scholars from the beginning of mankind. Accepting the digital world first begins with the task of integrating the scripts that came into existence before the rise of computers and technology. Thus, this conversion and integration must begin with the most common values in the world that transcend different languages as well numbers.

The problem is to categorize handwritten digits into ten distinct classes with accuracy as high as possible. The digit ranges from zero (0) to nine (9). In this work, we utilized the support vector machines (SVMs), principal component analysis

(PCA) and K -nearest neighbour (KNN) techniques, by compounding to form a novel method to solve the problem. The experiment applied on digit data set [22, 23] is taken from the well-known Modified National Institute of Standards and Technology (MNIST) data set [23].

2 Related Work

For developing handwritten digit recognition, the literature presents a number of researches that have made use of machine learning techniques. Among them, a few techniques related to the work have been presented below.

Matan et al. developed a neural network architecture for recognizing handwritten digits in a real world. This network has 1% error rate with about 7% reject rate on handwritten zip code digits provided by the US portal service [24]. Jitendra Malik et al. developed simple and an easy approach for finding out the resemblance between shapes and utilized it for object recognition. The proposed approach was tested on COIL data set, silhouette, trademarks and handwritten digits [21].

S. M. Shamim et al. presented an approach to offline handwritten digit recognition. The main problem is the capability to develop a cost-effective algorithmic program that can acknowledge handwritten digits and which is submitted by users by the way of a scanner, tablet and other digital devices [14].

Caiyun Ma et al. proposed an approach based on specific feature extraction and deep neural network on MNIST database. The proposed work is compared with SOM() [6] and P-SVM [25], and the result shows the proposed algorithm with accuracy 94.2% with 24 dimensions and showed that the deep analysis is more beneficial than traditional in terms of visualization of features [19]. Anuj Dutt et al. compared the results of some of the most widely used machine learning algorithms like SVM, KNN and RFC 4 and with deep learning algorithms like multilayer CNN using Keras with Theano and TensorFlow. The result showed the accuracy of 98.70% using CNN (Keras + Theano) as compared to 97.91% using SVM, 96.67% using KNN, 96.89% using RFC and the lowest error rate 1.28% using convolution neural network [26]. Chayaporn Kaensar presented comparative analysis using three different algorithms like neural network, support vector machine and K -nearest neighbour. The analysis of the presented work demonstrates that the SVM is the best classifier with 96.93% accuracy with more time required for training as compared to neural network and K -nearest neighbour [7].

Mohd Razif Shamsuddin et al. presented handwritten digit recognition on MNIST data set. In this work, four different methods (logistic regression, random forest, extra trees classifier and convolution neural network) were applied on normalized MNIST data set and binary data set. The analysis result shows that the convolution neural network gives the system validation with the best result 99.4% on normalized data set and 92.4% on binary data set using extra trees algorithm. The analysis shows that the system works better on normalized data set [27]. Saeed AL-Mansoori proposed multilayer perceptron (MLP) neural network to solve the problem of the handwritten

digit recognition. The system performance is observed on MNIST data set by altering the number of hidden layers and the number of iterations, and the result showed the overall training accuracy of 99.32% and testing accuracy of 100% [8].

Cheng-Lin Liu et al. presented handwritten digit recognition on binary and grey images using eight different classifiers like KNN, MLP, PC, RBF, LVQ, DLQDF, SVC-poly and SVC-RBF tested on three different data sets CENPARMI, CEDAR and MNIST. The presented work is concluded as SVC-RBF gives the highest accuracy among all the algorithms, but this algorithm is extremely expensive in memory space and computation [28]. In addition to the above, other important works include research on local similarity [29], prototype generation techniques [30], handwriting verification [31], trajectory and velocity modelling [5] and feature extraction [15].

3 Materials and Methods

The work is implemented and tested in the following system requirements: Intel i 3 or later processor, minimum 2 GB RAM, minimum 2 GB graphics processing unit, operating system (Windows 7 and above), Anaconda Python 3.7. All the algorithms tried using scikit-learn Python library, version 0.17.1.

3.1 Data Set

The proposed system was implemented and tested using MNIST data set (Modified National Institute of Standards and Technology database). The MNIST data set contains handwritten digits having 60,000 examples in the training set and 10,000 examples in the test set. The MNIST data set was associated with MNIST data set which is the super-set of MNIST. The size of the image is 28×28 pixels = 748 pixels. There are close to 60,000 images in the combined data set that can be used for training and judging the system. The data set contains the input and likelihood that the image belongs to different classes (i.e. the machine-encoded digits, 0–9) [22, 23].

3.2 Methods

Figure 1 shows that proposed approach is an association of PCA, KNN and SVM algorithms to improve the classification accuracy. The PCA algorithm helps to reduce the number of attributes which contribute more towards classification. The first step is to load the data set and abstract the feature columns with target columns. The size of the data set is rather large (60,000 samples with 784 features); thus, extraction of features from the original large dimensional features of the data is done using PCA in the initial stage.

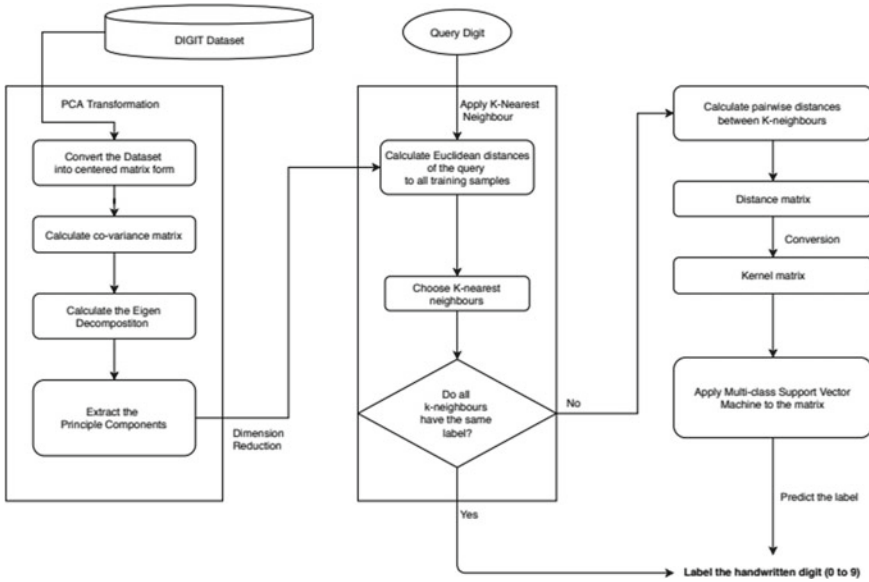
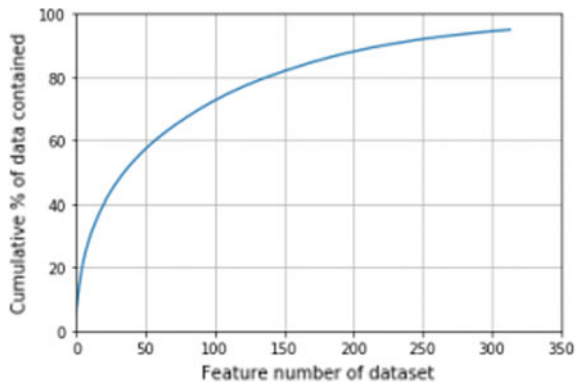


Fig. 1 Working of the proposed system for handwritten digit recognition

The first 60 features can explain approximately 97% of total substance (in terms of total variance retained), which fulfil to be typical of the information in the original data set as shown in Fig. 2. Thus, the first 60 principal components are implemented as the extracted features. The data is then split into training and testing sets. The simple implementation of SVM-KNN goes as follows: the KNN model is created and fit to the training set values, which trains the KNN classifier. For a query, it is necessary to compute the Euclidean distances of the query to all the training samples and pick the *K*-nearest neighbours. The general value of Euclidean distance (*d*) is calculated using Eq. 1.

Fig. 2 Amount of data versus component number first 314 principal components as the extracted features using PCA



$$d(p, q) = \sqrt{\sum_{i=1}^n (q_i - p_i)^2} \quad (1)$$

where p is the first data point, q is the second data point and n is the number of dimensions in data point.

If the K -neighbours (excluding the query) all have the same class, the query is flagged with the respective class same as its neighbours. Further, it calculates the distance between K -neighbour pairwise and converts the distance matrix into kernel matrix. Finally, the multiclass SVM is applied to the kernel matrix to flag the query. In the initial implementation, 314 principal components are extracted and use parameters values of $k = 2$ for KNN and $C = 0.5$ for SVM. This resulted in an accuracy score of 0.964 as shown in Table 1. Then, the number of iterations is used to tune the k parameter by changing its value while keeping the other parameter values as the same and observing the results. The same steps are applied for 20 distinct values of k (number of neighbours), keeping the c (penalty parameter) value constant.

Table 1 Initial test

# of features selected	Penalty parameter c	Prediction time (test)	Accuracy (train)	Accuracy (test)
2	0.5	51.002	1.0	0.964

Table 2 For different values of k with $c = 0.5$ accuracy observed

# of features selected	c	Prediction time (test) (s)	Accuracy (train)	Accuracy (test)
5	0.5	42.3	1	0.964
3	0.5	54.9	1	0.972
1	0.5	55.6	1	0.969
7	0.5	54.8	1	0.971
8	0.5	65.5	1	0.9673
9	0.5	66.5	1	0.9692
10	0.5	62.2	1	0.9694
11	0.5	69.9	1	0.9665
12	0.5	68.8	1	0.9658
13	0.5	70.1	1	0.9648
14	0.5	70.6	1	0.9646
15	0.5	71.6	1	0.9638
6	0.5	61.8	1	0.9692
17	0.5	68.6	1	0.9694
21	0.5	76.9	1	0.9593

Fig. 3 k versus accuracy (test)

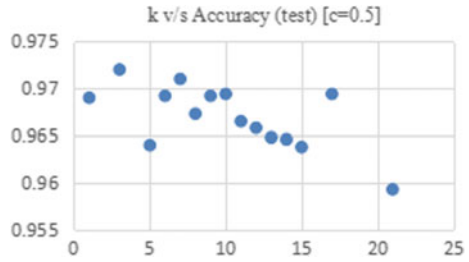
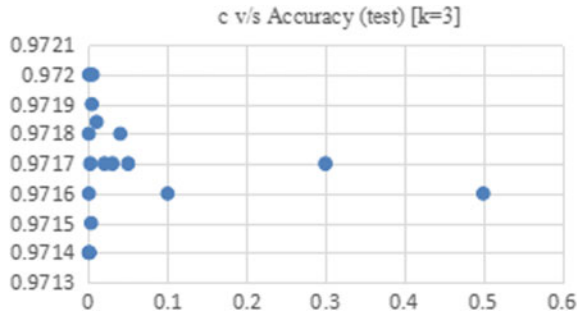


Fig. 4 Accuracy (test) with respect to C



The bold value in Table 2 highlights the best k value with respect to the highest test set accuracy achieved as well as fastest prediction time taken to do so. Figure 3 plots accuracy of test set with respect to changing k values taken from Table 2.

The value of $k = 3$ gives the highest accuracy as shown in Table 2, hence keeping $k = 3$ constant and changing the values of c to understand variation in accuracy with change in c as follows (Fig. 4; Table 3):

From the above result, it is concluded that the best value of k is $k = 3$. However, changes in the C value do not impact the final accuracy score. This result is quite unusual because the input space to the SVM is very small (size 3) and the SVM algorithm can classify the data set pretty quickly; hence, changing the parameters does not have much effect on the accuracy. The final solution then uses $k = 3$, $C = 0.005$ and yields an accuracy score of 0.9720 as shown in Table 2.

4 Results and Discussions

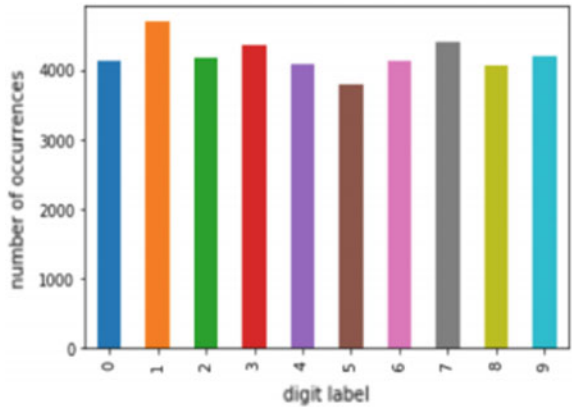
4.1 Data set Analysis

Digit data set has a total of 70,000 image samples (42,000 training set and 28,000 testing set samples, each with 784 features). Figure 5 represents the number of occurrences of all the digits versus labels (i.e. 0–9) present in the training data set of 42,000 samples.

Table 3 For $k = 3$ with $c = 0.5$ accuracy observed

# of features selected	c	Prediction time (test)	Accuracy (train)	Accuracy (test)
3	0.01	54.9	1	0.97184
3	0.02	55.2	1	0.9717
3	0.03	55.1	1	0.9717
3	0.04	55.3	1	0.9718
3	0.05	55.2	1	0.9717
3	0.001	55	1	0.9714
3	0.002	61.9	1	0.9717
3	0.003	54.9	1	0.9715
3	0.004	54.9	1	0.9719
3	0.005	54.58	1	0.972
3	0.1	55.14	1	0.9716
3	0.3	54.89	1	0.9717
3	0.5	55.28	1	0.9716
3	0.0001	55.35	1	0.9714
3	0.0002	55.95	1	0.9718

Fig. 5 Occurrence of each digit in the training set



4.2 Classification Report

Figure 6 displays the extensive classification report containing details about the precision of the model, recall, f1 score and support.

Fig. 6 Classification report

	precision	recall	f1-score	support
0	0.99	0.99	0.99	1653
1	0.98	0.99	0.98	1874
2	0.99	0.97	0.98	1671
3	0.97	0.96	0.96	1740
4	0.98	0.97	0.98	1629
5	0.96	0.96	0.96	1518
6	0.98	0.99	0.98	1655
7	0.97	0.97	0.97	1760
8	0.98	0.95	0.96	1625
9	0.93	0.97	0.95	1675
micro avg	0.97	0.97	0.97	16800
macro avg	0.97	0.97	0.97	16800
weighted avg	0.97	0.97	0.97	16800

Fig. 7 Images with their predicted labels



Fig. 8 Actual images with their true labels



4.3 Manual Result Testing

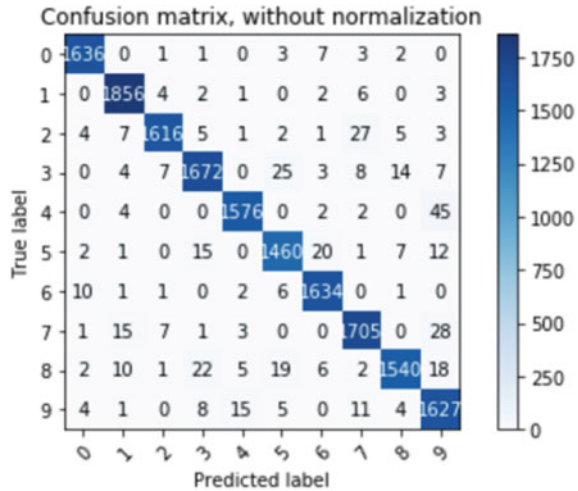
By manually taking out digits from the data set, plotting their 28 px by 28 px square image using image show function in matplotlib and comparing the results with the predicted outcome, we get the following:

The actual images and their labels are shown in Fig. 8. The same images were fed to the model, and the model’s prediction was shown in Fig. 7. This model incorrectly labels the fifth image and identifies it as 0, but the correct label is 9.

4.4 Confusion Matrix

Figure 9 visualizes the confusion matrix. It plots the predicted values versus actual values where the actual labels are represented on Y-axis and predicted values are represented on X-axis. This model has been applied to the testing data set. The model predicted the label to be 0 correctly 1636 times.

Fig. 9 Confusion matrix, without normalization



5 Conclusion and Future Scope

In this work, the model is acceptable for providing a solution for classifying handwritten digits into their respective labels in the MNIST data set as it is able to accurately categorize well with accuracy quite close to humans using a combination of two classification techniques such as support vector machine and *K*-nearest neighbours. However, the model is still in its rudimentary stages and useful in a limited domain. To solve large problem for recognizing multiple digits in an image or to recognize arbitrary multidigit information in unspecified or not constrained natural images, several changes need to be done in this work.

References

1. <https://www.outsource2india.com/software/articles/machine-learning-applications-how-it-works-who-uses-it.asp>. Last accessed date: Aug 2019
2. Niu X-X, Suen CY (2012) A novel hybrid CNN-SVM classifier for recognizing handwritten digits. *Pattern Recogn* 45:1318–1325
3. LeCun Y, Jackel L, Bottou L (1995) Comparison of learning algorithms for handwritten digit recognition. In: *Proceedings of the international conference on artificial neural networks*, Nanterre, France, pp 53–60
4. Decoste D, Scholkope B (2002) Training invariant support vector machines. In: *Machine learning*, vol 46. Kluwer Academic Publishers, Amsterdam, pp 161–190
5. Kherallah M, Haddad L, Alimi AM, Mitiche A (2008) On-line handwritten digit recognition based on trajectory and velocity modeling. *Pattern Recogn Lett* 29:580–594
6. Li R, Zhang S (2011) Handwritten digit recognition based on principal component analysis and support vector machines. In: *International conference on advances in computer science, environment, ecoinformatics, and education*, pp 595–599

7. Kaensar C (2013) A comparative study on handwriting digit recognition classifier using neural network, support vector machine and K-nearest neighbor. In: Meesad P et al (eds) IC2 IT2013, AISC 209. Springer, Berlin, pp 155–163. https://doi.org/10.1007/978-3-642-37371-8_19
8. Saeed AL-M (2015) Intelligent handwritten digit recognition using artificial neural network. J Eng Res Appl 5(5) (Part-3):46–51. www.ijera.com. ISSN: 2248-9622
9. Jou C, Lee H-C (2009) Handwritten numeral recognition based on simplified structural classification and fuzzy memberships. Expert Syst Appl 36:11585–11863
10. Kussul E, Baidyk T (2004) Improved method of handwritten digit recognition tested on MNIST database. Image Vis Comput 22(12):971–981
11. Desai AA (2010) Gujarati handwritten numeral optical character reorganization through neural network. Pattern Recogn 43:2582–2589
12. Meier U, Cireşan DC, Schmidhuber J (2011) Better digit recognition with a committee of simple neural nets. In: International conference on document analysis and recognition, vol 1, pp 1250–1254
13. Claudiu Cireşan D, Meier U, Gambardella LM (2013) Deep big simple neural nets excel on handwritten digit recognition. Neural Comput 22(12)
14. Shamim SM, Miah MBA, Angona Sarker MR, Al Jobair A (2018) Handwritten digit recognition using machine learning algorithms. Glob J Comput Sci Technol D Neural Artif Intell 18(1) (Version 1.0)
15. Lauer F, Suen CY, Bloch G (2007) A trainable feature extractor for handwritten digit recognition. Pattern Recogn 40:1816–1824
16. Tayeb S, Pirouz M, Cozzens B, Huang R, Jay M, Khembunjong K, Paliskara S, Zhan F, Zhang M, Zhan J, Latifi S (2017) Toward data quality analytics in signature verification using a convolutional neural network. In: 2017 IEEE international conference on big data (Big Data), pp 2644–2651
17. Ilmi N, Budi WTA, Nur RK (2016) Handwriting digit recognition using local binary pattern variance and K-nearest neighbor. In: 2016 Fourth international conference on information and communication technologies (ICOICT)
18. Chherawala Y, Roy PP, Cheriet M (2016) Feature set evaluation for offline handwriting recognition systems: application to the recurrent neural network. IEEE Trans Cybern 46(12)
19. Ma C, Zhang H (2015) Effective handwritten digit recognition based on multi-feature extraction and deep analysis. In: 2015 12th international conference on fuzzy systems and knowledge discovery (FSKD), pp 297–301
20. Belongie S, Malik J, Puzicha J (2002) Shape matching and object recognition using shape contexts. IEEE Trans Pattern Anal Mach Intell 24(24):509–522
21. Belongie S, Malik J, Puzicha J (2016) Shape matching and object recognition using shape contexts. IEEE Trans Pattern Anal Mach Intell 24(24)
22. <http://www.pymvpa.org/datadb/mnist.html>
23. <http://yann.lecun.com/exdb/mnist/>
24. Matan O, Kiang RK, Stenard CE, Boser B, Denker JS, Henderson D, Howard RE, Hubbard W, Jackel LD, Lecun Y (1990) Handwritten character recognition using neural network architecture. In: Proceedings of the 4th USPS advanced technology conference, Washington D.C., pp 1003–1011, Nov 1990
25. Yimu W, Yun P, Yan Chen L (2014) Parallel implementation of handwritten digit recognition system using self-organizing map. J Zhejiang Univ 48:742–747
26. Dutt A, Dutt A (2017) Handwritten digit recognition using deep learning. Int J Adv Res Comput Eng Technol (IJARCET) 6(7):990–997. ISSN: 2278-1323
27. Shamsuddin MR, Abdul-Rahman S, Mohamed A (2019) Exploratory analysis of MNIST handwritten digit for machine learning modelling. In: Yap BW et al (eds) SCDS 2018, CCIS 937, pp 134–145
28. Liu C-L, Nakashima K, Sako H, Fujisawa H (2003) Handwritten digit recognition: benchmarking of state-of-the-art techniques. Pattern Recogn 2271–2285
29. Hua Q, Bai L, Wang X (2012) Local similarity and diversity preserving discriminant projection for face and handwriting digits recognition. Neurocomputing 86:150–157

30. Impedovo S, Mangini FM, BarbuZZi D (2014) A novel prototype generation technique for handwriting digit recognition. *Pattern Recogn* 47:1002–1010
31. Kutzner T, Dietze M, Bönninger I, Travieso CM, Dutta MK, Singh A (2016) Online handwriting verification with safe password and increasing number of features. In: 2016 3rd international conference on signal processing and integrated networks (SPIN)

Optimal TCSC Location for Reactive Power Optimization Using Oppositional Salp Swarm Algorithm



Sheila Mahapatra , Saurav Raj  and S. Mohan Krishna 

Abstract The research work proposed in this article involves a nature-inspired technique of salp swarm algorithm (SSA) which is proposed for finding the optimal reactive power dispatch of an interconnected power network. Oppositional-based learning is a promising technique for improving convergence and is used in this work coupled with SSA algorithm as a new hybrid method of oppositional salp swarm algorithm (OSSA). The proposed techniques are successfully implemented on standard IEEE 57 benchmark system for deprecating of real power losses as well as overall cost of operation of the power system along with retention of bus voltages under acceptable limits. The performance of the proposed algorithms is also examined with inclusion of optimal thyristor-controlled series compensator (TCSC) placement and sizing. The identification of weakest branch in the power network is initially done for optimal TCSC placement and it is tendered through line stability index method (LSI).

Keywords Reactive power planning (RPP) · Salp swarm algorithm (SSA) · Oppositional salp swarm algorithm (OSSA) · Thyristor-controlled series compensator (TCSC) · Line stability index method

1 Introduction

During the past few decades, there has been manifold increase in demand for electrical energy from power industry. This requires stringent planning, management, and real-time operation of power utilities and owing to large interconnected systems, it has become immensely complicated coupled with unfolding of competitive power

S. Mahapatra · S. Raj (✉) · S. Mohan Krishna
Alliance University, Bangalore 562106, India
e-mail: sauravsonusahu@ee.ism.ac.in

S. Mahapatra
e-mail: mahapatrasheila@gmail.com

S. Mohan Krishna
e-mail: smk87.genx@gmail.com

© Springer Nature Singapore Pte Ltd. 2020
R. Sharma et al. (eds.), *Innovation in Electrical Power Engineering, Communication, and Computing Technology*, Lecture Notes in Electrical Engineering 630,
https://doi.org/10.1007/978-981-15-2305-2_33

markets. Further open market principles and power quality demand calls for electrical energy to be treated as a commodity and so power network should ensure maximizing cost reduction, minimizing transmission losses, and revamping voltage profile. These aspects ultimately require effective reactive power planning which is an arduous optimization problem for a deregulated power structure.

Reactive power optimization primarily deals with diminishing of real power loss and constructive management of various reactive power sources such as generators, shunt capacitors, and tap changing transformers. Decisions regarding reactive power injections and maintaining bus voltages in their permissible limits should be taken to ensure reliability and economic dispatch on a large-scale system. Further, with the advent of renewable sources, new challenges have emerged for reactive power optimization [1]. The authors in [2] proposed a genetic algorithm-based optimal reactive power planning which is implemented on a real-time new-planned 380 kV West–East transmission line inter-tie networks of Saudi Arabia to depict the capabilities in reactive var compensation. Binary search technique is proposed by the authors in [3] for reactive power planning keeping in view operating and security constraints by utilizing both discrete and continuous variables. A reactive power optimization model is proposed by the authors in [4] which is based on two-step procedure carried out on large test system. To harvest maximum benefit in current deregulated power system structure, various control methodologies and optimization techniques are applied to FACTS controllers which was first established by Hingorani in 1988 [5]. TCSC has tremendous application potential for achieving satisfactory performance by rapidly changing the reactance and controlling power flow in transmission lines [6–8]. Opposition-based learning is introduced by the authors in [9] to meet challenging real-time problems and provides a comparison between genetic algorithm and oppositional genetic algorithm. Authors in [10] employ opposite points in differential evolution for population initialization and generator jumping for enhancing the convergence of the algorithm. The reactive power planning solution was obtained through optimal capacitor placement by authors in [11, 12]. Bio-inspired algorithms were used by authors in [13, 14] for improved reactive power planning solution. A loss sensitivity approach is implemented to analyze the bus sensitivity and obtain optimal reactive power planning [15]. Optimal reactive power dispatch is rendered through seeker optimization algorithm on a 118-test bus system [16].

Implementation of efficient optimization methods yields maximum benefits which are cost-effective and improve the secured operation in a power network as cost of FACTS controller is a pivotal issue which needs to be addressed during its installation. So, SSA and hybrid OSSA algorithms are implemented in the current work as they are immensely suitable owing to swift convergence, reduced computation time and provide consistent accuracy in results with numerous trials. The relevance of these algorithms is also justified being easily implementable, not getting trapped in local optima and ensuring global optimality.

Two pivotal concerns are accounted for: first is optimal TCSC sizing by determining the weak branch for diminished active power losses and overall operating

cost and second is TCSC installation for improving the voltage profile. Problem definition and system constraints are presented in Sect. 2 followed by the details about the optimization algorithms applied for solving the problem. Section 4 provides the result analysis on two standard IEEE test systems.

2 Problem Formulation

The objective function is also extended to optimal TCSC placement which further improves the effectiveness of the proposed method.

2.1 Objective Function

a. Real power loss minimization:

The minimization of real power loss is formulated as

$$P_L = \sum_{k=1}^N g_k [V_m^2 + V_n^2 - 2V_m V_n \cos(\delta_m - \delta_n)] \quad (1)$$

where P_L = real power loss, g_k is the conductance in k th branch connected between m th and n th buses, V_m and V_n are voltage magnitudes and δ_m and δ_n are voltage phase angles at m th and n th buses, respectively. N specifies the number of lines or branches.

b. Optimal TCSC Placement:

The FACTS device used in the work is TCSC controller which provides series compensation, and its optimal placement is done by line stability index (LSI) method.

c. Minimization of operating cost:

The complete operating cost of the power network is a combination of TCSC installation cost and the cost due to energy loss. The energy cost data are taken from [11, 12].

$$\begin{aligned} \text{Energy cost} &= 0.06 \text{ \$/kWh} \\ \text{Energy rate} &= 0.06 \times 100,000 \times 8760 \end{aligned} \quad (2)$$

$$\text{Energy cost } C_E = P_L \times E_R \quad (3)$$

The TCSC cost with the cost coefficients and s as operating range of TCSC in MVAR is given as follows:

$$C_{\text{TCSC}} = 0.0015s^2 - 0.7130s + 153.75 \quad (4)$$

So, total operating cost

$$T_C = C_E + C_{\text{TCSC}} \quad (5)$$

2.2 Objective Function

In the present work, power balancing condition both for active and reactive is observed as equality constraints.

$$P_{Gm} - P_{Dm} - V_m \sum_{N=1}^{N_b} V_n [G_{mn} \cos(\delta_{mn}) + B_{mn} \sin(\delta_{mn})] = 0 \quad (6)$$

$$Q_{Gm} - Q_{Dm} - V_m \sum_{N=1}^{N_b} V_n [G_{mn} \sin(\delta_{mn}) - B_{mn} \cos(\delta_{mn})] = 0 \quad (7)$$

Similarly, the generator reactive power, the voltage magnitude, transformer tap settings, and the TCSC reactance are regarded as inequality security constraints.

$$V_m^{\min} \leq V_m \leq V_m^{\max}, \quad m = 1, 2, \dots, N_b \quad (8)$$

$$Q_{gm}^{\min} \leq Q_{gm} \leq Q_{gm}^{\max}, \quad m = 1, 2, \dots, N_g \quad (9)$$

$$T_m^{\min} \leq T_m \leq T_m^{\max}, \quad m = 1, 2, \dots, N_t \quad (10)$$

$$-0.7X_{\text{line}} \leq X_{\text{TCSC}} \leq 0.2X_{\text{line}}, \quad i = 1, 2, \dots, N_{\text{TCSC}} \quad (11)$$

where V_m is the magnitude of voltage in m th bus, G_{mn} and B_{mn} are transfer conductance and susceptance between m th and n th buses, P_{gm} and Q_{gm} are real and reactive power injected to the m th bus, and P_{Dm} and Q_{Dm} are the real and reactive power demanded at m th bus. δ_{mn} is the voltage angle between the buses. N_b is the total number of buses, N_g is the number of generator buses specified in the given system under study, and N_t corresponds to number of transformer tap settings. N_{TCSC} is the number of TCSC installed in the network with the compensation range fixed between 20% inductive and 70% capacitive as provided in Eq. (11) in order to prevent over-compensation.

The voltage deviation at load bus is calculated as

$$V_D = \sum_{k=1}^N (V_n - V_1) \quad (12)$$

where V_D is the voltage deviation at load bus, V_n is voltage during normal loading, and V_1 is voltage at initial value set at 1 p.u.

2.3 Modeling of FACTS Controller

The series FACTS controller implemented in the present study is TCSC which consists of sequences of compensating capacitors connected in parallel to thyristor-controlled reactor. This involves the controllable reactance XTCSC which is inserted in series to the transmission line of fixed reactance X_{mn} . The new value of net reactance $X_{mn\text{new}}$ with TCSC and degree of series compensation acquired by installing TCSC is given in Eq. (13).

$$X_{mn\text{new}} = (1 - k)X_{mn} \quad \text{where, } k = \frac{X_{\text{TCSC}}}{X_{mn}} \quad (13)$$

This leads to change in active and reactive power flow in the lines and effective reduction in real power losses. The modified real power in the transmission line is given by

$$P_{mn} = \frac{V_m V_n}{X_{mn\text{new}}} \sin(\delta_m - \delta_n) \quad (14)$$

where P_{mn} is the power flow between bus m th and n th buses, V_m , V_n , δ_m and δ_n are the magnitude and angle of voltage at m th and n th bus, respectively. In the problem formulation, XTCSC is a function of thyristor firing angle where maximum and minimum value of the thyristor firing angle are 90° and 0° , respectively.

3 Implementation of Computational Techniques

Salp swarm algorithm (SSA) is a swarm-inspired stochastic collective based algorithm which can be employed to yield better solution to real-time problem.

3.1 Salp Swarm Algorithm

SSA is based on the swarming behavior of salps which are sea creatures resembling jelly fish. The swarming behavior of salp is interesting as it forms a salp chain and

it is mathematically modeled into the SSA algorithm. The formation of salp chain is believed to provide them better coordination and mobility for searching the food [17].

Working Process of SSA

Mathematical modeling of salp chain is initiated by dividing the population into leader and followers. The leader is the first salp in the chain and rest are followers guided by the leader directly or indirectly. The salp population is generated in “n”-dimensional search space. These arbitrarily generated swarms of salp are deemed as the objective functions in the search space. The fitness function is food source F and in the proposed problem it is minimizing the real power loss and cost of operation. The SSA updates the position of the leader salp with respect to food source and the follower salp updates their position with respect to each other.

$$x_k^1 = \begin{cases} F_k + c_1((ub_k - lb_k)c_2 + lb_k) c_3 \geq 0 \\ F_k - c_1((ub_k - lb_k)c_2 + lb_k) c_3 < 0 \end{cases} \tag{15}$$

where x_k^1 shows the leader salp position in k th dimension, F_k is the position of food source in k th dimension, ub_k and lb_k indicates the upper and lower bounds of the k th dimension, and c_2, c_3 are random numbers which define the step size and are uniformly generated in the interval of $\{0, 1\}$.

$$c_1 = 2e^{-\left(\frac{4m}{M}\right)^2} \tag{16}$$

where c_1 is the controlling parameter, m is the current iteration and M is the total number of iterations. The salp followers are updated based on Newton’s law of motion and is given as:

$$x_k^i = \frac{1}{2}(x_k^i + x_k^{i-1}) \tag{17}$$

where x_k^i is the position of i th salp follower in k th dimension and $i \geq 2$. This procedure continues until the termination iteration is arrived with output being classified in accordance with their inputs. From the output of SSA technique, the real power loss, energy cost, and TCSC cost are evaluated.

3.2 Opposition-Based Learning

Opposition-based learning (OBL) was first instituted by Tizhoosh [9] which can potentially accelerate the convergence of optimization techniques and has proved immensely beneficial for computational intelligence. Fitness evaluation or the chances to arrive at the optimal solution enhances by checking the opposite guesses. This forms the basic framework of opposition-based learning. So, the fitter one

whether guess or opposite guess can be applied to initial solution and subsequently to each solution in the current population to intensify convergence.

Let X_j^o is a control variable $\in [X^{\max}, X^{\min}]$, then corresponding opposition variable is obtained as

$$OX_n = X_n^{\max} + X_n^{\min} - X_n^0 \tag{18}$$

The oppositional matrix is presented below:

$$OX = \begin{bmatrix} X_{11}^{\max} + X_{11}^{\min} - X_{11}^0 & \dots & X_{1n}^{\max} + X_{1n}^{\min} - X_{1n}^0 \\ \dots & \dots & \dots \\ X_{i1}^{\max} + X_{i1}^{\min} - X_{i1}^0 & \dots & X_{in}^{\max} + X_{in}^{\min} - X_{in}^0 \end{bmatrix} \tag{19}$$

where i = number of population generated and n = number of variables.

The convergence speed is accelerated by selecting opposite population matrix OX as initial population. The initial population is modified in the OSSA hybrid technique as per Eq. (19). The modified population is incorporated in SSA optimization to enhance the efficacy and strength of the algorithm. It also accelerates the convergence toward optimality.

4 Results and Discussion

In the work presented in this article, SSA and hybrid technique of OSSA are employed to ascertain the optimal location, parameter setting and cost sizing of TCSC for improving the reactive power planning, and the voltage profile of the transmission network. The proposed techniques are implemented on the MATLAB R2013b platform and their performances are evaluated by applying them to the IEEE standard bench mark 57 bus system. The proposed method outcomes are obtained without TCSC device and effectiveness of the algorithm is further tested by TCSC installation in the weak branch for RPP and improvement of voltage profile. The proposed algorithms are executed for 500 iterations and population size is taken 40.

4.1 Case 1: IEEE 57 Bus Test System-Uncompensated

The standard IEEE 57 bus connected system comprises of 6 generator buses with 80 interconnected power lines and tap changing transformers located on 17 branches. Three shunt capacitors are utilized for reactive power compensation prior to TCSC optimal placement. At 100 MVA base, demand for total real power is 1251.70 MW and its VAR power demand is 335.70 MVAR. Real power loss without reactive power planning is 0.2799 p.u. and its cost of operation is 1.471×10^7 \$. The reactive

power generation minimum and maximum value are taken from [18]. Initially, shunt capacitors are placed at locations detected by LSI method. Thereafter, SSA and OSSA algorithms are implemented to minimize transmission loss as well as operating cost. The computational time per iteration with SSA algorithm is 26.275 s and using OSSA algorithm is 26.02 s.

4.2 Case 2: IEEE 57 Bus Test System-Compensated (TCSC)

The TCSCs are placed at the locations detected by LSI method. Then SSA and OSSA optimization techniques are applied to find the optimal coordination of reactive power generation, transformer tap settings, and TCSC for minimizing transmission losses and ameliorating the voltage profile. The optimal locations for four TCSCs by both optimization techniques for compensated system are 14-46, 3-15, 10-51, and 11-43.

It also depicts that the optimal parameter settings obtained by SSA and OSSA techniques are satisfying equality and inequality constraints. Table 1 provides the optimal settings for TCSC compensated system. The result comparison with various hybrid optimization techniques like SPSO, APSO, EPSO, GWO, and OGWO is also shown with the proposed methods in Table 2 and the results clearly depicts the superiority of the proposed algorithms. The convergence curve of active power loss and operating cost for uncompensated along with compensated system for SSA and OSSA technique are shown in Figs. 1 and 2, respectively. The computational time per iteration with SSA algorithm is 25.42 s and using OSSA algorithm is 25.241 s.

5 Conclusion

The research work proposed in this article emphasizes on attaining improved reactive power dispatch by execution of two algorithms of SSA and hybrid technique of OSSA by optimizing real power loss and overall cost of operation. This is integrated with upgrading voltage profile of the test system. The techniques are tested for various cases of uncompensated and compensated with (TCSC) system. The algorithms were successfully executed to determine the global or near global optimal settings of control variables on IEEE 57 bus test system. So, the proposed OSSA algorithm can be endorsed as a promising algorithm to solve complex power system engineering problem.

Table 1 Optimal setting of control variables in IEEE 57 bus system with TCSC

Variable	Minimum	SSA	OSSA	Maximum
Q_{GEN} (2)	-0.17	0.1599	0.1501	0.50
Q_{GEN} (3)	-0.10	0.5826	0.4295	0.60
Q_{GEN} (6)	-0.08	0.0255	0.2390	0.25
Q_{GEN} (8)	-1.40	-1.2926	-0.5282	2.0
Q_{GEN} (9)	-0.03	0.0842	0.0899	0.09
Q_{GEN} (12)	-0.5	1.5391	1.2641	1.55
Tap (19)	0.9	0.9259	0.9949	1.0
Tap (20)	0.9	0.9225	0.9897	1.0
Tap (31)	0.9	0.9669	0.9882	1.0
Tap (35)	0.9	0.9437	0.9948	1.0
Tap (36)	0.9	0.9210	0.9391	1.0
Tap (37)	0.9	0.9692	0.9200	1.0
Tap (41)	0.9	0.9563	0.9200	1.0
Tap (46)	0.9	0.9241	0.9712	1.0
Tap (54)	0.9	0.9524	0.9962	1.0
Tap (58)	0.9	0.9941	1.0	1.0
Tap (59)	0.9	0.9200	0.92	1.0
Tap (65)	0.9	0.9212	0.9897	1.0
Tap (66)	0.9	0.9670	0.9884	1.0
Tap (71)	0.9	0.9377	0.9712	1.0
Tap (73)	0.9	0.9559	0.9789	1.0
Tap (76)	0.9	0.9463	0.9887	1.0
Tap (80)	0.9	0.9917	0.9364	1.0
TCSC1 (14-46)	0.0	0.0963	0.1003	0.11
TCSC2 (3-15)	0.0	0.0862	0.1056	0.11
TCSC3 (10-51)	0.0	0.0925	0.0556	0.11
TCSC4 (11-43)	0.0	0.0171	0.0599	0.11

Table 2 Comparison of results for active power loss minimization and operating cost in IEEE 57 bus test system

Active power loss (p.u) Base case	Operating cost (\$) $\times 10^7$ Base case	Algorithms	Real power loss after RPP without TCSC (p.u)	Real power loss after RPP with TCSC (p.u)	Operating cost after RPP without TCSC $\times 10^7$ (\$)	Operating cost after RPP with TCSC $\times 10^7$ (\$)
0.2799	1.471	NLP [16]	0.2590	-	-	-
		CGA [16]	0.2524	-	-	-
		L-DE [16]	0.2781	-	-	-
		LSACP-DE [16]	0.2791	-	-	-
		SPSO [13]	0.2522	-	1.325	-
		EPSO [13]	0.2526	-	1.327	-
		SSA	0.2584	0.2512	1.3583	1.3202
		Proposed OSSA	0.2523	0.2504	1.3260	1.3163

Fig. 1 Convergence of active power loss for uncompensated and compensated system with SSA and OSSA

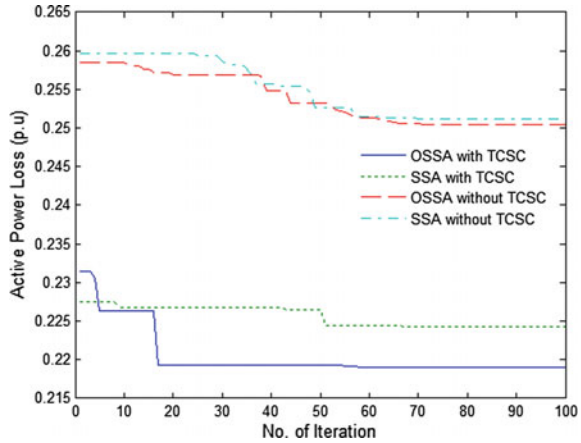
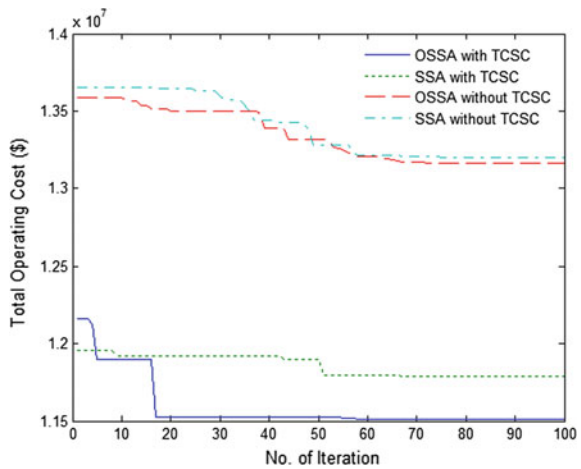


Fig. 2 Convergence of operating cost for uncompensated and compensated system with SSA and OSSA



References

1. Shen X, Liu Y, Liu Y (2018) A multistage solution approach for dynamic reactive power optimization based on interval uncertainty. *Math Prob Eng*
2. Shwehdi MH, Raja Mohamed S, Devaraj D (2018) Optimal capacitor placement on West–East inter-tie in Saudi Arabia using genetic algorithm. *Comput Electr Eng* 68:156–169
3. Mazzini AP, Asada EN, Lage GG (2018) Minimisation of active power losses and number of control adjustments in the optimal reactive dispatch problem. *IET Gener Trans Distrib* 12(12):2897–2904
4. Shaheen AM, El-Sehiemy RA, Farrag SM (2017) A reactive power planning procedure considering iterative identification of VAR candidate buses. *Neural Comput Appl* 1–22
5. Hingorani NG (1993) Flexible AC transmission. *IEEE Spectr* 30(4):40–45
6. Sakr WS, El-Sehiemy RA, Azmy AM (2016) Optimal allocation of TCSCs by adaptive DE algorithm. *IET Gener Trans Distrib* 10(15):3844–3854

7. Mahapatra S, Jha AN, Panigrahi BK (2016) Enhanced secured optimal power flow by TCSC parameter optimization using RBFNN based GSA. *Int J Electr Eng Inf* 8(2)
8. Bhattacharyya B, Kumar S (2016) A novel approach for the solution of transmission congestion with multi type FACTS devices. *IET Gener Trans Distrib*
9. Tizhoosh HR (2005) Opposition-based learning: a new scheme for machine intelligence. In: *Computational intelligence for modelling, control and automation, 2005 and international conference on intelligent agents, web technologies and internet commerce, international conference on*, vol 1, pp 695–701, IEEE
10. Rahnamayan S, Tizhoosh HR, Salama MM (2007) Quasi-oppositional differential evolution. In: *Evolutionary computation, CEC 2007. IEEE Congress on*, pp 2229–2236, IEEE
11. Chiang H-D, Wang J-C, Cockings O, Shin H-D (1990) Optimal capacitor placements in distribution systems. I. A new formulation and the overall problem. *IEEE Trans Power Delivery* 5(2):634–642
12. Chiang H-D, Wang J-C, Cockings O, Shin H-D (1990) Optimal capacitor placements in distribution systems. II. Solution algorithms and numerical results. *IEEE Trans Power Delivery* 5(2):643–649
13. Bhattacharyya B, Raj S (2016) PSO based bio inspired algorithms for reactive power planning. *Int J Electr Power Energy Syst* 74:396–402
14. Raj S, Bhattacharyya B (2018) Reactive power planning by opposition-based grey wolf optimization method. *Int Trans Electr Energy Syst* e2551
15. Bhattacharyya B, Goswami SK, Bansal RC (2009) Loss sensitivity approach in evolutionary algorithms for reactive power planning. *Electr Power Compon Syst* 37(3):287–299
16. Dai C, Chen W, Zhu Y, Zhang X (2009) Seeker optimization algorithm for optimal reactive power dispatch. *IEEE Trans Power Syst* 24(3):1218–1231
17. Mirjalili S, Gandomi AH, Mirjalili SZ, Saremi S, Faris H, Mirjalili SM (2017) Salp Swarm Algorithm: a bio-inspired optimizer for engineering design problems. *Adv Eng Softw* 114:163–191
18. Pai MA, Chatterjee D (2014) *Computer techniques in power system analysis*. McGraw-Hill Education, India

THD Reduction of On-Grid Solar Photovoltaic System Employing SPWM Technique



Suraj Kumar Panigrahi, Renu Sharma and Satyanarayan Bhuyan

Abstract The grid-connected photovoltaic (PV) system is gaining more and more attention due to its associated abilities of uninterrupted electrical power supply. The increasing demand for sustainable energy production has led us to focus on the power electronic circuit interfaced with the renewable energy sources. To increase the efficiency of the produced solar energy, DC–DC boost converters with an advantage of maximum power point tracking (MPPT) are considered as a far-fetched solution. In this paper, a PV module with MPPT has been designed. This study also includes the design and control of inverter as well as cascaded inverter with SPWM, which helps reduce the total harmonic distortion (THD) and gives a better dynamic response and accuracy in tracking references. A comparison between different inverter topologies has been proposed here for better result analysis.

Keywords PV · DC–DC converter · MPPT · SPWM · THD

1 Introduction

With the steep decline in our conventional sources of energy, i.e., the fossil fuels and an ever-increasing power demand, the search for alternative sources has become a dire necessity of this era [1]. The process of industrialization re-defining its peak demand for electrical energy every now and then needs to be indemnified with surplus energy sources [2]. This is mostly due to limited resource and harmful ecological impacts of

S. K. Panigrahi (✉) · R. Sharma
Department of Electrical Engineering, ITER, SOA Deemed to be University, Bhubaneswar,
Odisha 751030, India
e-mail: gm.surajkumar@gmail.com

R. Sharma
e-mail: renusharma@soa.ac.in

S. Bhuyan
Department of Electronics and Communication Engineering, ITER, SOA Deemed to be
University, Bhubaneswar, Odisha 751030, India
e-mail: satyanarayanbhuyan@soa.ac.in

© Springer Nature Singapore Pte Ltd. 2020
R. Sharma et al. (eds.), *Innovation in Electrical Power Engineering, Communication,
and Computing Technology*, Lecture Notes in Electrical Engineering 630,
https://doi.org/10.1007/978-981-15-2305-2_34

the conventional energy. Now, for future sustainability, it is very important to search alternative energy resources or renewable energy sources. Photovoltaic (PV) energy has become one of the important renewable energy sources [3]. The main aim of PV systems is to increase the gained energy abundantly by maintaining the maximum power point of PV panel. PV modules are very simple for harnessing the sun's energy. Photovoltaic cells (solar cells) can directly transform the incident solar radiation into electricity. It has no noise, pollution or moving parts, which makes them robust, reliable and long lasting. The PV output is dependent on the surface temperature and the intensity of the sun irradiance. One can achieve maximum power output from the PV array by introducing solar trackers (mechanical-based) for maximization of power generation from the amount of light received and a maximum power point tracking (MPPT) algorithm to operate the PV array around its maximum power point for a given load under varying weather conditions. This kind of energy can be fed to load through power electronic converters like boost converter and voltage source inverter [4]. However, the effectiveness of the inverter needs to be upgraded further in order to compensate the effects of the losses caused by self-consumption, unbalanced load on inverter output voltage, nonlinearity and output voltage flickering [5], electromagnetic interference and higher-order harmonics content [6]. To overcome all the above disadvantages, a cascaded inverter topology has been introduced. In addition to this, it is very vital to the inverter system meets the ability to run with high speed and frequency to generate the sinusoidal pulse width modulation (SPWM) signals. The SPWM controller plays a key role in the improvement of the performance of the inverter connected to grid.

2 Grid Connection of PV System

Figure 1 shows a grid-connected solar PV system. In the very first stage, PV array is linked to the DC–DC converter which gives maximum and fixed PV output to the inverter through a DC link. A three-phase cascaded inverter is used to transform constant DC into AC voltage with constant frequency of 50 Hz. An LC filter is used for reducing the ripple generated in AC voltage, and consequently, it is connected to

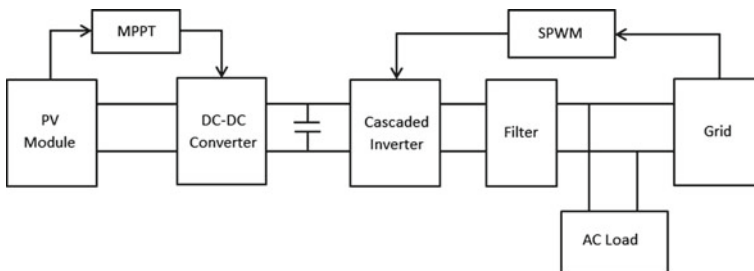


Fig. 1 Grid-connected PV system

the load and grid side. The inverter needs to be controlled in order to get minimum harmonics in the voltage waveform to obtain good power quality. In order to get the gate pulse for the inverter circuit, SPWM technique is used. Figure 1 shows a basic block diagram of grid-connected PV system.

2.1 Modeling of PV Cell

The key element of a solar panel is a photovoltaic cell. A single PV cell can be represented as a current source connected with one diode and two resistors which is shown in Fig. 2. By connecting many PV cells in series and parallel manner, a PV module can be designed [7, 8].

In Fig. 2, the current source I_{ph} indicates the photocurrent, whereas R_{sh} and R_{se} indicate the shunt and series resistances of the solar PV (SPV) cell, respectively. Ideally, the value of R_{sh} is very large, and R_{se} tends to be very small, and hence, in order to simplify the analysis, the values are neglected. Grouped PV cells termed as PV modules. Further organization of PV modules in parallel-series pattern make PV arrays.

The photoelectric phenomenon is responsible for the conversion of solar energy into electricity in a transparent way. These solar PV cells are nothing but a p-n junction-based diode which is fabricated in a thin wafer of semiconductor materials. Photons having energy which is greater than that of the semiconductor band gap energy create electron-hole pairs while exposed to sunlight. The number of electron-hole pairs generated in this process is proportional to the incident irradiation. The output voltage generated by the SPV cell is basically a function of the photocurrent produced by the cells which in turn depends on the irradiation received by the cells during its operation [9]. The output current of PV module is shown in Eq. (1).

$$I_{PV} = N_p * I_{ph} - N_p * I_0 \left[\exp\left(\frac{q * (V_{PV} + I_{PV}R_S)}{N_S AkT}\right) - 1 \right] \tag{1}$$

where I_{PV} refers to PV module output current, V_{PV} refers to PV module output voltage, R_S refers series resistance, I_{ph} refers to photo current, T is the operating temperature k indicates the Boltzmann constant ($1.38e-23$ J/K), A indicates ideality

Fig. 2 Electrical model of a PV cell

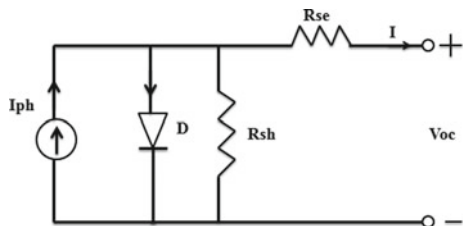


Table 1 Photovoltaic parameters

Parameters	Values
Open-circuit voltage (V_{oc})	30.6 V
Short-circuit current (I_{sc})	8.5 A
Maximum power voltage (V_{mp})	24.3 V
Maximum power output current (I_{mp})	7.8 A
Maximum power (P_{mp})	189.54 W

factor, N_P is parallel number of cells, and N_S is the series number of cells [10]. Table 1 shows PV module parameters.

Below are the specifications of the PV module:

2.2 MPPT Technique

In order to improve the efficiency of PV module maximum power point, tracking mechanism is adopted to deliver maximum power generated by the PV module. There are many algorithms exist to track maximum power point. In this work, Perturb and Observe (P and O) method which is also known as hill climbing method is used. It is one of the most popular algorithms due to its simplicity. As the name indicates, the method will perturb the system by changing the duty cycle of the converter [11].

A slight perturbation is given to the system which causes the variation of output power. If the PV power increases, then the next perturbation is made in the same direction if the power decreases, and then, the next perturbation is made in the opposite direction. In this manner, one can track the maximum power continuously. Figure 3 shows how the algorithm works.

3 DC–DC Converter

In this paper, a boost converter is used to step up the DC output voltage of the PV module. Boost circuit consists of DC input voltage source V_s , input inductor L , controllable switch S , energy transfer capacitor C , a diode D and a load resistance R . Advantage of this boost converter is that we are getting a desired output voltage which is greater than the supply input voltage [12]. Figure 4 shows a circuit diagram of boost converter.

Now, two cases arise, 1. Switch is close, 2. Switch is open.

i. Switch is close

When switch is close, the path is short circuited, and no current flows toward diode.

Now, applying KVL in the above circuit, Fig. 5, Eqs. (2), (3) can be obtained.

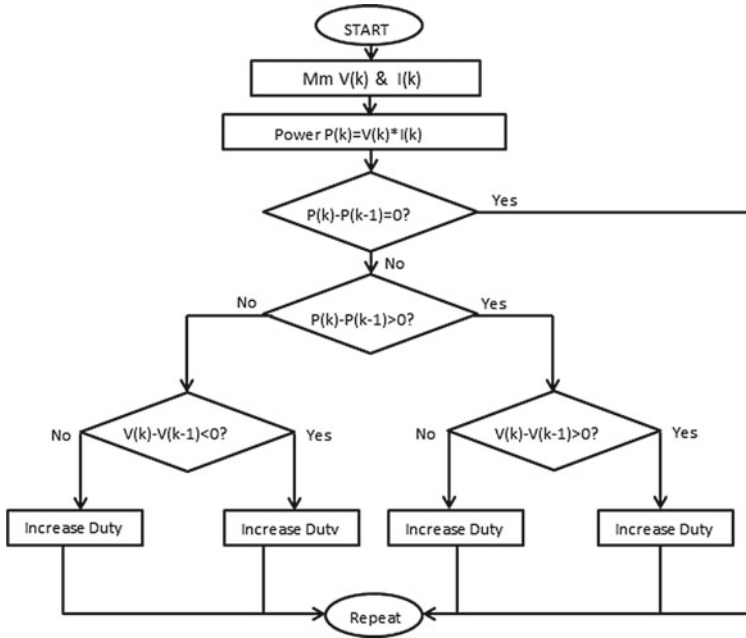


Fig. 3 Flow chart of P & O algorithm

Fig. 4 Circuit diagram of DC-DC boost converter

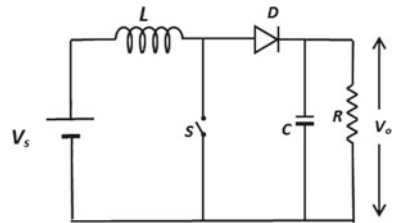
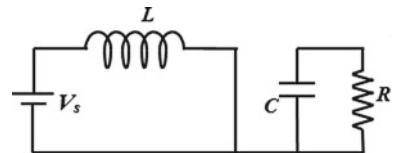


Fig. 5 Circuit diagram of boost converter when switch is close

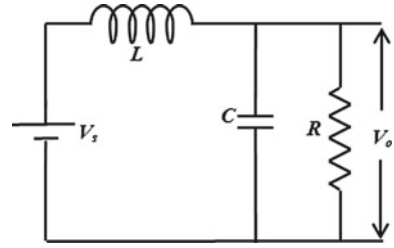


$$V_s = L \frac{di}{dt} \tag{2}$$

$$(I_L)_{close} = \frac{V_s}{L} \tag{3}$$

where V_s = supply voltage, L = inductance, I_L = inductance current.

Fig. 6 Circuit diagram of boost converter when switch is open



ii. Switch is open

When switch is open, the diode becomes forward bias, and current flows through capacitor which results in capacitor charging.

Now, applying KVL in Fig. 6, Eqs. (4), (5) and (6) can be obtained.

$$V_s - L \frac{di}{dt} - V_o = 0 \tag{4}$$

$$V_s = V_o + L \frac{di}{dt} \tag{5}$$

$$V_o = \frac{1}{1 - D} \times V_s \tag{6}$$

where

V_o output voltage

D duty cycle.

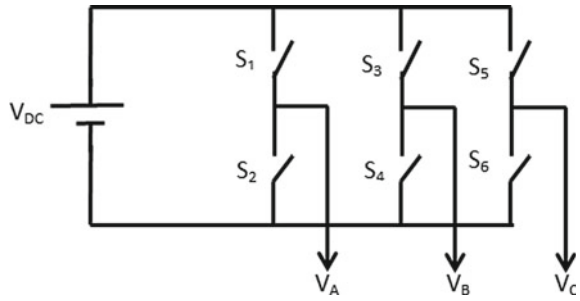
The duty cycle is generated from the MPPT algorithm, and it is given as gate pulse to the DC–DC converter.

4 Three-Phase Inverter

An inverter is an arrangement of power electronics devices which converts a constant DC voltage to AC voltage. Three-phase voltage source inverter (VSI) helps to convert fixed DC voltage into three-phase AC voltage and provides power to consumer loads as well as utility grid. The three-phase inverters are broadly used for grid connection of PV systems. A three-phase inverter uses a minimum of six switching devices [13] shown in Fig. 7.

Cascaded inverters are used for getting higher voltage output with lower harmonic distortion.

Fig. 7 Circuit diagram of three-phase VSI



Control Strategy of Inverter

Sinusoidal pulse width modulation technique (SPWM) is the simplest way to generate sinusoidal that can be changed by changing the amplitude and frequency of modulating voltage to obtain the desired output. As high frequency leads to better output, modifying wave matched with a very high-frequency triangular wave, shown in Fig. 8.

The reference signal is taken from mains supply through PLL and compared with repeating carrier signal. The frequency of carrier signal must be very high then the reference signal. In three-phase VSI, three sinusoidal waves, which are 120° out of phase, were taken and compared with triangular wave. Thus the generated gate pulse is given to the switching devices of inverter.

Cascaded Inverter

The two inverters are connected in parallel and phase of one is connected to neutral of other and vice versa. This connection leads to higher voltage level and lower ripple or harmonics [14]. Figure 9 shows the circuit diagram of a single-phase cascaded inverter.

We are getting the pulse from SPWM. The inverter was designed in such a way that the switch S_1, S_4 of first inverter and S_5, S_8 of second inverter is ON at the same time. The other switches get ON in the next half. By doing this, we are getting two times the input voltage.

Fig. 8 Block diagram of SPWM

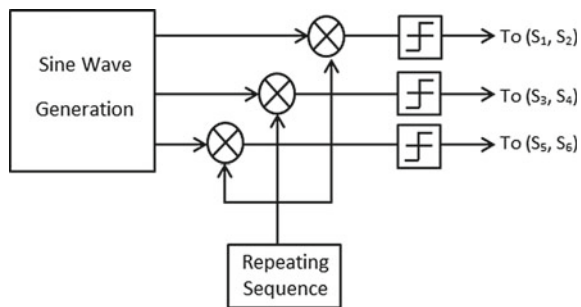
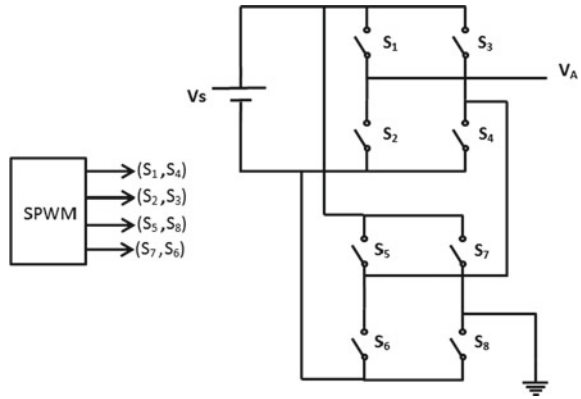


Fig. 9 Circuit diagram of cascaded inverter



5 LC Filter Design

The inverter output is not a pure sine wave, and it contains harmonics. An LC-type filters are used to deliver a desired output to the electric load. Various elements are there which choose the capacitor and inductor of the filter. It eliminates higher-order harmonics [15]. Inductors smooth the current curve, and capacitors smooth the voltage curve.

Generally, the resonant frequency of a filter must be six times of desired output frequency in order to remove the higher-order harmonics [16]. By applying KCL in the filter circuit in Fig. 10, Eqs. (7), (8) and (9) can be obtained.

$$i_{iA} + i_{ca} = i_{ab} + i_{LA} \Rightarrow i_{iA} + C_f \frac{dV_{LCA}}{dt} \tag{7}$$

$$i_{iB} + i_{ab} = i_{bc} + i_{LB} \Rightarrow i_{iB} + C_f \frac{dV_{LAB}}{dt} \tag{8}$$

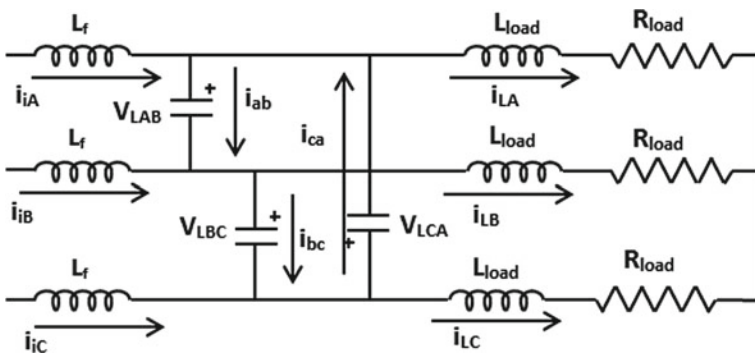


Fig. 10 Circuit diagram of LC filter

Table 2 Filter parameters

Filter component	Value
L_f	0.05 H
C_f	400 μ F

$$i_{iC} + i_{bc} = i_{ca} + i_{LC} \Rightarrow i_{iC} + C_f \frac{dV_{LBC}}{dt} \tag{9}$$

In order to get state-space equations of LC filter circuit given in Eq. (10), KVL is applied to both load side and inverter side.

$$\dot{X}(t) = AX(t) + Bu(t) \tag{10}$$

$$X = \begin{bmatrix} V_L \\ I_i \\ I_L \end{bmatrix}_{9 \times 1} \quad A = \begin{bmatrix} 0 & \frac{1}{3C_f} I_{3 \times 3} & \frac{-1}{3C_f} I_{3 \times 3} \\ \frac{-1}{L_f} I_{3 \times 3} & 0 & 0 \\ \frac{1}{L_{load}} I_{3 \times 3} & 0 & \frac{-R_{load}}{L_{load}} I_{3 \times 3} \end{bmatrix}_{9 \times 9} \quad B = \begin{bmatrix} \frac{1}{L_f} I_{3 \times 3} \\ 0 \end{bmatrix}_{9 \times 3}, \quad u = [V_i]_{3 \times 1}$$

Table 2 shows the calculated filter parameter.

6 Simulink Results and Analysis

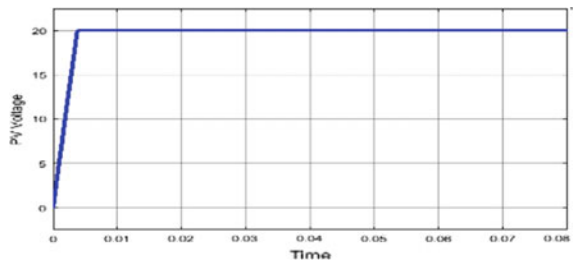
The output of PV, boost converter, THD calculation of inverter without cascaded and cascaded inverter is shown below:

Figure 11 shows the output voltage of PV module when irradiance is 700 W/m² where number of series cell is five and parallel cell is ten.

Figure 12 shows the boost converter output which is settled at 40 V in 0.04 s. This DC voltage is fed to inverter through DC-link capacitor. The inverter output is stepped up using step-up transformer.

Figure 13 shows the sinusoidal output voltage of inverter with LC filter, where $L = 0.05$ H, $C = 0.4$ mF. In order to use this output voltage, it must be stepped up by transformer.

Fig. 11 Output voltage of PV module



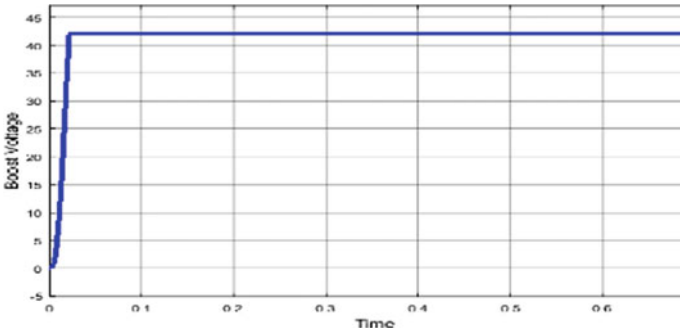


Fig. 12 Output voltage of boost circuit

Fig. 13 Output voltage of inverter after filter

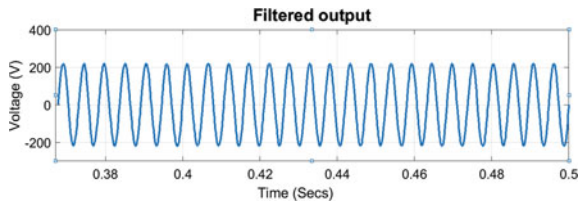


Figure 14 shows the total harmonic distortion (THD) of inverter output for solo inverter connection. It is calculated as 43.16%, which is very high to be fed to the grid.

Figure 15 shows the total harmonics distortion of inverter output for cascaded inverter connection, and it is calculated as 37.05%, which is comparatively low.

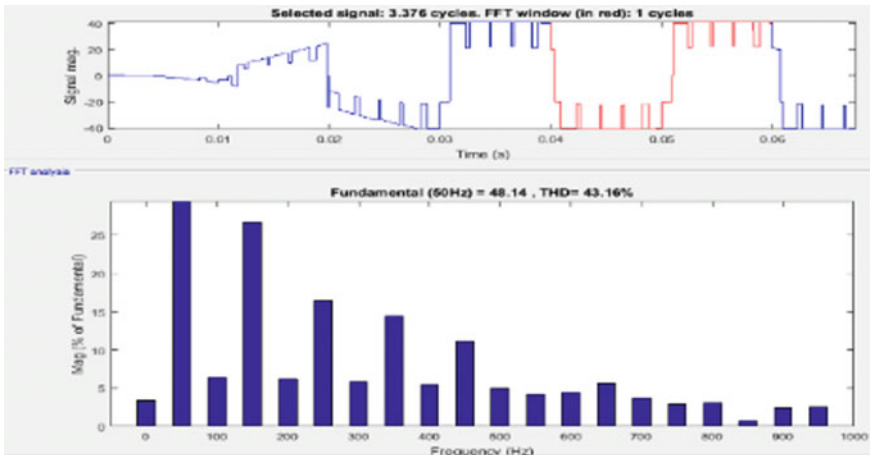


Fig. 14 THD calculation of without cascaded inverter

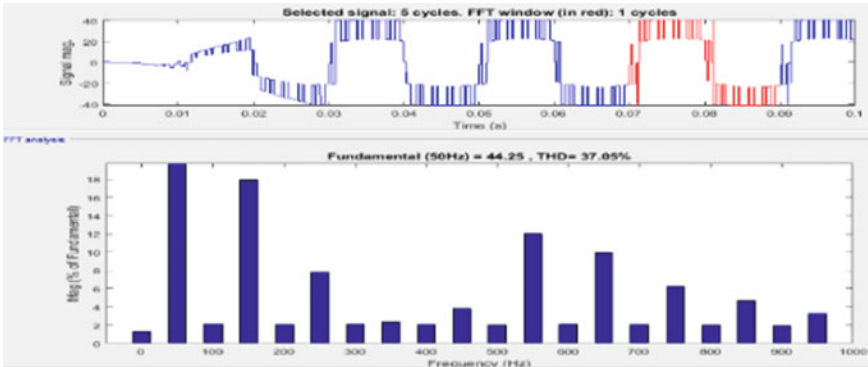


Fig. 15 THD calculation of cascaded inverter output

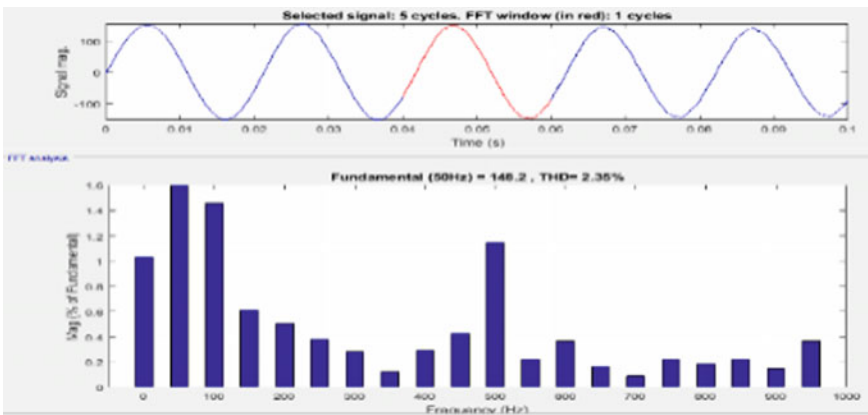


Fig. 16 THD calculation of filter output without cascaded inverter

Figure 16 shows the THD of filter output when the inverter is connected alone, and it is calculated as 2.35%.

Figure 17 shows the THD of filter output when cascaded inverter is connected, and it is calculated as 1.15%, which is very minimum and can be connected to the utility grid.

Table 3 shows us that the cascaded-type inverter with filter is most preferred as we get only 1.15% of harmonics.

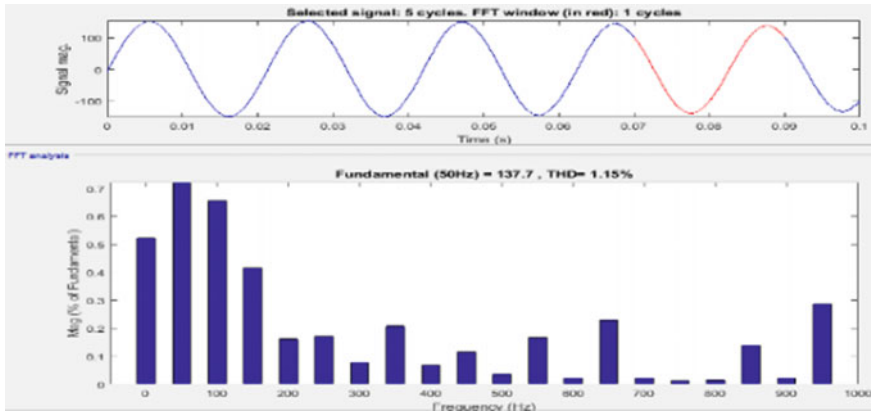


Fig. 17 THD calculation of filter output with cascaded inverter

Table 3 Performance results

Connection type		THD values (in %)
Non-cascaded-type inverter	Without filter	43.16
	With filter	2.35
Cascaded-type inverter	Without filter	37.05
	With filter	1.15

7 Conclusion

Nowadays, grid-connected PV systems are used for fulfilling the heavy demand of sustainable energy requirement. In this paper, cascaded three-phase inverter with SPWM technique has been deliberated. The LC filter circuit has been used in this system to remove the distortion present in the inverter output. The filter circuit has been designed by applying state-space analysis method. The SPWM technique has been implemented on both single three-phase voltage source inverter and cascaded three-phase voltage source inverter. Simulation results of both inverters have been analyzed, and a comparison table has been provided. From our observations, we can conclude that the inverters with SPWM technique give us better output by reducing total harmonic distortion.

References

1. Jena S, Kar SK (2019) Setting a fostered energy network by decarbonizing the grid: hybridization, control, and future solutions upon storage. *Int J Energy Res* 43(1):455–474
2. Satpathy PR, Sharma R, Dash S (2019) An efficient SD-PAR technique for maximum power generation from modules of partially shaded PV arrays. *Energy* 175:182–194

3. Ahmad GE, Hussein HMS, El-Ghetany HH (2003) Theoretical analysis and experimental verification of PV modules. *Renew Energy* 1159–1168
4. Blaabjerg F, Chen Z, Kjaer S (2004) Power electronics as efficient interface in dispersed power generation system. *IEEE Trans Power Electron* 1184–1194
5. Gounden NA, Peter SA, Nallandula H (2009) Fuzzy logic controller with MPPT using line-communicated inverter for 3-phase grid-connected PV system. *Renew Energy* 909–915
6. Eltawil MA, Zhao Z (2010) Grid-connected PV power system: technical and potential problem-a review 112–129
7. Satpathy PR, Sharma R (2019) Diffusion charge compensation strategy for power balancing in capacitor-less photovoltaic modules during partial shading. *Appl Energy* 255:113826
8. Satpathy PR, Sharma R (2019) Power and mismatch losses mitigation by a fixed electrical reconfiguration technique for partially shaded photovoltaic arrays. *Energy Convers Manage* 192:52–70
9. Balouktsis A, Karapantsios TD, Antoniadis A, Paschaloudis D, Bazerianidou A, Bilalis N (2006) Sizing stand-alone photovoltaic system. *Int J Photoenergy* 1–8
10. Salas V, Olias E (2009) Overview of state of technique for PV inverter used in low voltage grid-connected PV system 1541–1550
11. Sadeghzadesh SM, Soleimani A, Ghassami AA (2013) A high performance MPP tracker for PV system. *Electr Power Energy Syst* 237–243
12. Lakshmanan SA, Rajpourhit BS, Jain A (2014) Modeling and analysis of 3-phase VSI using SPWM technique for grid connected solar PV system. In: 2014 IEEE students' conference on electrical, electronics and computer science, pp 1–6, IEEE
13. Hosseini E (2015) Modeling and simulation of chopper switching via MATLAB simulink. In: Scientific bulletin of the Petru Maior University of Tirgu Mures, pp 10–17
14. Kumar AM, Shaker KC (2018) Grid connected solar system of 3-phase multilevel inverter with SPWM technique. *Indian J Sci Res* 143–148
15. Kouro S, Moya A, Villanueva E, Correa P, Wu B, Rodriguez J (2009) Control of a cascaded H-bridge converter for grid-connected photovoltaic system. In: IEEE 35th annual conference of the Industrial Electronics Society, pp 1–7
16. Mariethozz S, Morari M (2009) Explicit model-predictive control of a PWM inverter with an LCL filter. *IEEE Trans Ind Electron* 389–399

Estimation of Simple, Energy and Carbon Payback Periods of a 1 MWp Ground-Mounted Solar PV Plant at Tirupati Airport: A Case Study



S. Mohan Krishna , Sheila Mahapatra , Saurav Raj 
and J. L. Febin Daya 

Abstract As India is slowly transiting from the fossil fuel to the renewable energy format for power generation, the concept of energy security, efficiency, usage of clean energy sources and less environmental degradation are the points of focus. The high capital cost involved in the setting up of a solar PV system makes it necessary to evaluate the feasibility based on the economic indices. The work proposed in this article is to evaluate the payback periods for a solar ground-mounted photovoltaic (PV) system installed in the Tirupati Airport (Airports Authority of India) and reflect on the economic feasibility for the same. The results obtained indicate that the investment is feasible, both technologically and economically. The payback periods and the carbon emissions are reduced drastically and making it a clean energy technology.

Keywords Solar photovoltaic power plant · Energy economics · Economic index · Payback period · Renewable energy

1 Introduction

1.1 Motivation

Fossil fuels have for long played a major role in electrical energy generation. Most thermal power plants in India are coal-fired due to the abundance in the availability of coal reserves, but these are source of carbon emissions and greenhouse gases. This has adversely affected the environment by compounding the issue of global warming and climate change. Besides, the efficiency of these plants was also less. For the energy generated to be sustainable, it is necessary to ensure that the environment is

S. Mohan Krishna (✉) · S. Mahapatra · S. Raj
Alliance College of Engineering and Design, Alliance University, Bangalore 562106, India
e-mail: smk87@gmail.com

J. L. F. Daya
Vellore Institute of Technology, Chennai 600127, India
e-mail: febindaya.jl@vit.ac.in

© Springer Nature Singapore Pte Ltd. 2020
R. Sharma et al. (eds.), *Innovation in Electrical Power Engineering, Communication, and Computing Technology*, Lecture Notes in Electrical Engineering 630,
https://doi.org/10.1007/978-981-15-2305-2_35

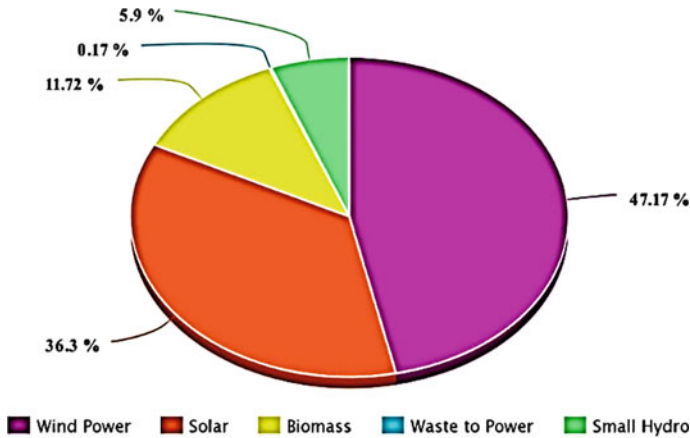


Fig. 1 Grid-connected renewable energy-based installed capacity of India [11]

not degraded and the world shifts from the traditional fossil fuel format to renewable energy format of energy generation. Fossil fuel-based energy generation still occupies 79.8% while renewable energy-based energy generation occupies 17.3% of the energy mix. The greenhouse gas emissions from electricity generation were 2194.74 MtCO₂, with fossil fuels contributing a major share owing to their dominant presence in the resource mix of India. By 2017, the thermal power plants in India contributed to increased levels of sulphur dioxide (SO₂) of around 32% and that of particulate matter of around 34%. Therefore, this resulted in the government coming up with more policy measures and incentives to accelerate setting up of renewable energy-based power plants. Figure 1 shows the current installed capacity (as of 31 May 2019) of the renewable energy-based generation plants in India. Solar power generation is rapidly picking up with the government initiating the national solar mission with an ambition of setting up a target of 100 GW by 2022 as shown in Fig. 2. Besides, the move got another head start when the governments of India and France launched the International Solar Alliance (ISA). The aim of the ISA is to promote and develop the solar power amongst 121 solar-rich member countries by mustering investment to the tune of 1 trillion USD by 2030. The central government has also constituted a 350 million USD fund to finance solar-based power projects. Many commercial installations are gradually being solarized in order to keep pace with the National Solar Mission. Cochin Airport is the first green airport in India which is 100% solar powered.

However, the high capital cost involved in the setting up of a solar PV system makes it necessary to evaluate the feasibility of the same. The motivation for the present work is to evaluate the economic value of electricity produced by solar PV in terms of sustainability by applying economic indices which are significant aspect to ensure reasonable return on investment.

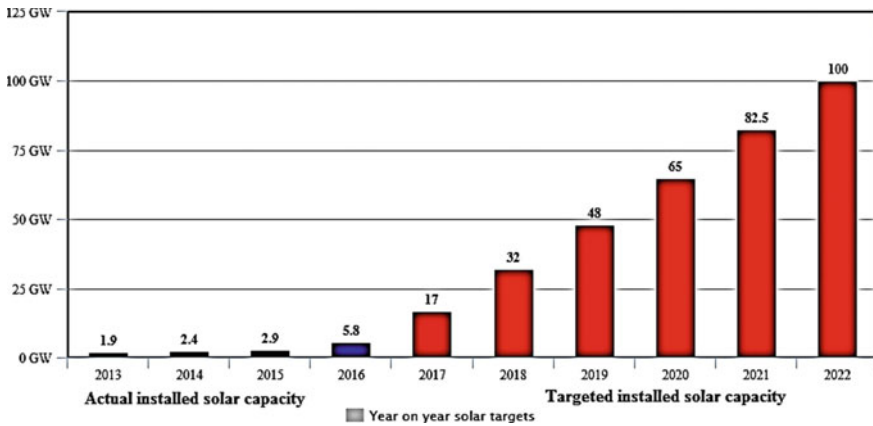


Fig. 2 Targeted installed solar capacity by 2022 [11]

1.2 Literature Review

Sharma and Goel [1] analysed the performance of a 11.2 kWp rooftop grid-connected PV installed at Siksha ‘O’ Anusandhan University, India. Parameters of performance like the final yield, performance ratio and system efficiency were analysed with respect to the existing research. Some of the significant findings of the study are, the yearly average final yield of the proposed system is 1339.55 kW h/kWp/year which is comparatively higher than most other systems considered in the literature. Also, the average PV and inverter efficiency were 13.42 and 89.83%, which showed improvement over other projects in the study. Besides, the carbon footprint was also reduced by 14.661 tons of CO₂ from the atmosphere per annum. Khatri [2] assessed the performance of a solar PV plant with respect to several economic parameters like the discount rate, effective discount rate, rate of escalation of electricity cost, salvage value of the plant. Kumar and Nagarajan [3] presented an economic study and energy loss analysis of a grid-tied transformer less rooftop solar PV plant. Energy losses in the form of switching devices, temperature, network, and interconnection were determined. Kumar and Sudhakar [4] considered a plant with a seasonal tilt and having a good average solar radiation for analysis of power losses and the performance ratio. The plant yielded 1.96–5.07 h/d, with an annual performance ratio of 86.12%. Mulcué-Nieto and Mora López [5] developed a new model which could predict the energy generated by a grid-tied PV system installed in countries having low latitude. The factors considered for the study in Colombia are the angular losses and losses due to dirt, the temperature losses, the DC–AC conversion losses and the performance ratio of the system. Peerapong and Limmeechokchai [6] discussed the incentives on investment in the form of proposed feed-in tariffs framework for a solar PV plant installed in Thailand. They investigate the same for solar plants in three categories, namely residential rooftop, integrated ground-mounted and utility scale with the installed capacity larger than 1 MW. Vasisht et al. [7] presented a

performance study of the rooftop solar PV system installed in the Indian Institute of Science campus, under different seasons and climatic conditions of Bangalore. The grading systems used for the evaluation are the capacity utilization factor (CUF) and performance ratio (PR). Sudhakar et al. [8] estimated the photosynthetically active radiation (PAR), which is an important part of the solar radiation and is significant for modelling biological growth system. Six different Indian latitudes' data are considered for PAR estimation based on monthly and hourly average of global radiation everyday. It is found that the performance does vary for different climatic conditions as shown by the power regression model. Kessler [9] states that, for a capital-intensive solar rooftop project, the financial component generally takes precedence over the environmental component. He does a comparative analysis of simple payback and energy payback period for four solar PV plants employing crystalline-Si technology, where three are commercial installations in the Northeastern United States. Peng et al. [10] examined the sustainability and environmental performance of PV-based energy generation system through a comprehensive review of the life cycle assessment (LCA) of the systems. Marimuthu et al. [11], Winkler [12] and Darghouth et al. [13] also discussed the different economic indices in addition to the carbon payback period to consider the carbon inventory (emissions) data during the manufacture of the PV cells.

The research work is presented in the sections as described: Sect. 2 provides the detail about methodology. It also gives an overview about the needs of a systematic evaluation tool for capital or investment expenditures. Section 3 offers a detailed view of the proposed technique, result analysis and discussion. The conclusion of the research work is delivered in Sect. 4.

2 Methodology

2.1 Economic Indicator Payback Period for Solar PV Module

There are various economic indicators available for power sector economics and planning. This work considers the payback period. Payback period is the time taken by the cash flow of the incomes from a particular investment to become equal to the initial investment. In other words, it is time taken by a project for break-even (between initial investment and the returns). The payback period has several advantages:

- Simplicity and faster solution
- Preferred over liquidity
- Preferred during uncertainty.

However, there also some concerns which need to be addressed as it is opined that, not all cash flows are considered, and it ignores the time value of money. The different payback periods considered for a solar PV installation life cycle assessment are shown in Fig. 3. The environmental impact of a solar PV installation must be seriously

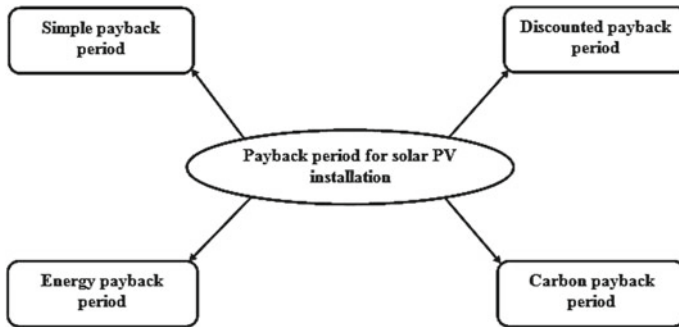


Fig. 3 Payback periods for solar PV calculations

considered since the purpose of installing the same is to ensure minimal environmental degradation. There must be a trade-off between the conventional power plants and the solar installation in terms of the cost and environmental impact.

2.2 Technical Specification and Data Inventories for the Solar PV Plant

As part of India’s National Solar Mission, many airports in India are being solarized. The Airports Authority of India (AAI) recently inaugurated a 1 MWp solar PV plant (875 kW AC) at Tirupati’s Renigunta International Airport as shown in Fig. 4. With this, the temple town joins the group of other solar-powered airports’ in India like the Cochin, Trivandrum and Vijayawada airports. The solar plant is slated to cater to 75% of the airport’s daytime power consumption. This plant was installed and commissioned by the distributed solar developer, Fourth Partner Energy. The firm has commissioned around 20 projects in Andhra Pradesh for several reputed clients. With an operational portfolio of over 170 MWp of distributed solar assets spread around 23 states, it was the second-largest rooftop installer in 2018 with a 193% year-on-year (YoY) growth rate. The ground-mounted solar installation is set up across four acres of land, parallel to the airport runway and its isolation bay. Also, the excess power generated at the airport can be fed to the national grid via net metering.

There are several data inventories and specifications which are required for comprehensive research on the economic indices for solar PV installation. These data should be preferably real-time in the sense, and a commercial installation should be considered along with the associated data. Some of them are:

- Specification of solar PV power plant
- Life cycle inventory comprising
- Material inventory



Fig. 4 Ground-mounted solar PV plant at Renigunta Airport, Tirupati

- Energy inventory
- Carbon inventory.

Table 1 provides the details about the site location.

Many resources exist for estimating the average solar radiation on a site. Some of them are NASA-SSE, METEONORM and Solar GIS. Through METEONORM resource datasheet, it was estimated that the annual average solar radiation at the airport was 5.1 kW h/m²/day (horizontal) and 5.2 kW h/m²/day (13.6° tilted). Table 2 gives the solar PV plant details.

Table 1 Site location of the 1 MWp ground-mounted solar PV plant

Place	Tirupati Airport, Renigunta
District	Chittoor
State	Andhra Pradesh
Latitude	13.63° N
Longitude	79.54° E
Altitude	104 m

Table 2 Solar PV plant details at Tirupati Airport

SPV system capacity	875 kW AC
System DC capacity	1 MWp DC
PV module type	Polycrystalline silicon
Make	Adani Solar (Mundra)
P_{\max}	325 Wp
<i>Physical dimensions</i>	
Length	1960 mm
Width	992 mm
Thickness	35 mm/40 mm
Rated voltage (V_{mp})	37.29 V
Rated current (I_{mp})	8.72 A
Open circuit voltage (V_{oc})	45.26 V
Short circuit current (I_{sc})	9.21 A
Temperature coefficient	0.4%/°C
Module efficiency	16.71%

Details regarding the solar PV modules and the electrical parameters of the same are also provided in Table 2 [at standard test conditions (STC), for solar irradiation of 1 kW per m², a module temperature of 25 °C and a solar irradiation angle of 45°], respectively. The material data inventory details are provided in Table 3.

The following boundary conditions and assumptions have been considered for this case study:

- The PV module manufacture, material for balance of system (BOS) (all components of a photovoltaic system other than the photovoltaic panels like the glass, encapsulant, frame, junction box, connector and cable) and energy consumed during PV module manufacture have been considered.
- Raw material mining is excluded.
- Recycling and transportation have also been excluded.

Table 3 Material data inventory

PV module weight	22 kg
Cell size	156.75 mm * 156.75 mm
Cell number	72
Glass type	Anti-reflection coating, high transmittance
Encapsulant type	ethylene-vinyl acetate (EVA)
Frame type	Anodized aluminium alloy
Junction box protection class	IP67
Connector type	MC4
Cable length	1200 mm

3 Results and Discussion

Here, the tools and calculators from Solar Mango (open-source platform provides a considerable collection of calculators and tools for the estimation of rooftop area, generation estimation, cost of power, CO₂ reduction and energy consumption) are used for the estimation of certain critical aspects of the solar plant at Tirupati Airport. Certain assumptions are also made. This is followed by the determination of the payback periods.

3.1 Energy Generation Which Can Be Met by Solar

Considering the airport requires around 4 lakh units of electricity a month, the solar plant meets around 1.4 lakh units with the rest being taken care of conventional coal-based electricity. Tables 4 and 5 present the inputs to the energy generator tool and the results obtained. The following assumptions were made:

- Only 80% of the available area is considered for calculations and to accommodate for shading losses.
- 10 m² is considered as the required area for 1 kW solar panels.

3.2 CO₂ Emission Reduction Calculator

Tables 6 and 7 present the inputs, and the results obtained from the CO₂ emission reduction calculator. The assumptions made are:

- Reduction of CO₂ emission per 1 kW h of solar power = 1 kg of CO₂.
- The reduction in CO₂ emissions for the electricity generated from a solar power plant versus a coal plant and does not take into account CO₂ from other parts of the value chain.

Table 4 Inputs to the energy generator tool

Electricity consumption per month	400,000 kW h
Ground area available	16,187 m ²
Rate of sunshine availability	3.5 kW h per day

Table 5 Results from the energy generator tool

Solar energy that can be generated for a month	135,974 units
Percentage of monthly consumption that can be met with solar	33.99%

Table 6 Inputs to the CO₂ emission reduction calculator

Solar plant capacity (AC)	875 kW
Approximate units per kW per day	3.5 kW h

Table 7 Results obtained from CO₂ emission reduction calculator

CO ₂ emissions reduced	1117.8125 tons per year
-----------------------------------	-------------------------

3.3 Estimation of Payback Periods

Simple payback period—In capital budgeting decisions, payback period is the period of time required to regain the amount disbursed in an investment. It literally explains the period something takes to pay for itself. The simple payback period (SPB) is the time in years, between initial outlay of capital on a solar installation and the return on initial investment.

The simple payback period is calculated using the following formula (Eq. 1):

$$\text{Simple payback period (PB)} = \frac{\text{Capital cost of the project (CC)}}{\text{Net annual savings (AS)}} \tag{1}$$

where PB = payback period (years), CC = capital cost of the project (in Rs.) and AS = net annual savings (in Rs.).

For the solar plant considered here, the CC = Rs. 54,000,000
 The monthly electricity charges saved approximately = Rs. 1,000,000
 Annual electricity charges saved approximately = Rs. 12,000,000

Considering the maintenance charges are negligible, let us assume it to be around Rs. 40,000 annually. Therefore,

$$PB = \frac{54,000,000}{12,000,000 - 40,000} \approx 4.5 \text{ years}$$

Energy payback period—It relates to energy consumption. The time required to generate as much energy as is consumed during production and the lifetime operation of the system. As discussed before and as portrayed by the energy generation tool, for 4 lakh units of electricity consumption, the solar energy generated per month is 135,974 units. However, it is not exactly possible to determine the energy consumed for manufacturing the different components of the solar system for this plant as the energy and the carbon data inventory is not available. However, there is a claim that the solar panel industry used more electricity than it produced until 2010. It is safe to assume that around 2 times as much energy is used to produce a unit of electricity as is delivered [13]. Therefore,

Energy produced per month = 135,974 units

$$\begin{aligned} \text{Energy produced per annum} &= 135,974 * 12 = 1631,688 \text{ units} = 1631.688 \text{ MW h} \\ \text{Energy consumed for manufacture of solar plant components (including BOS)} & \\ &= 2 * 1631.688 \text{ MW h} \end{aligned}$$

The energy payback period is calculated using the following formula (Eq. 2):

$$\text{Energy payback period (years)} = \frac{\text{Energy consumed by solar plant (in MW h)}}{\text{Energy produced by solar plant per year (in MW h)}} \quad (2)$$

$$\text{Therefore Energy payback period} = \frac{2 * 1631.688 \text{ MW h}}{1631.688 \text{ MW h}} = 2 \text{ years}$$

Carbon payback period—The carbon payback period is a measure of how long a CO₂ mitigating process needs to run to compensate the CO₂ emitted to the atmosphere during the life cycle stage of a solar PV system. According to a study [14], around 50–75 g of CO₂ is emitted per kW h of electricity produced. Accordingly,

The life time of the solar plant is generally considered to be = 25 years

Total kW h generated over 25 years = 40,792,200 kW h

$$\begin{aligned} \text{Now, the CO}_2 \text{ emissions for the life cycle of the plant} &= 40,792,200 * 50 = 2,039,610,000 \text{ g} \\ &= 2,039,610 \text{ kg} \\ &= 2039.61 \text{ tons} \end{aligned}$$

From, the emission reduction calculator (Source: Solar Mango), by installing this plant, the CO₂ emissions reduced

$$= 1117.8125 \text{ tons per year}$$

The carbon payback period is calculated using the following formula (Eq. 3):

$$\text{Carbon payback period (years)} = \frac{\text{Life cycle carbon dioxide emissions (in tons)}}{\text{Gross carbon dioxide emission avoided per year (in tons)}} \quad (3)$$

$$\text{Carbon payback period} = \frac{2039.61}{1117.8125} = 1.824 \text{ years}$$

4 Conclusion and Scope for Future Work

The estimation of the simple, energy and carbon payback periods for this case study on the ground-mounted solar PV system in Tirupati International Airport indicates that the payback time is considerably less, and the capital cost can be recovered in a short duration of time. Therefore, it is economically feasible. Besides, it works well as an emission reduction technology where the carbon payback time is very less, thereby mitigating the effect of the carbon emissions emitted during the life cycle of the plant. Therefore, it is also technologically feasible. As compared to a coal-fired thermal power plant which gives rise to more greenhouse gas emissions per unit of energy generated, this technology is cleaner and less environmentally degrading. The space occupied, the fuel used and the plant efficiency all in all indicate a better investment as compared to fossil fuel-based plants. The payback period was chosen to determine the economic feasibility in the case study owing to its simplicity and ease of use. However, it comes with its own set of limitations like ignoring the time value of money and not considering the time after the payback period. Other economic metrics can be used for feasibility studies which take into account the time value of money, discounted payback, etc. Also, the effect of seasonal variations and solar radiation needs to be taken into account for feasibility studies. This, in turn, may aid the policy-makers and future solar investors to target the regions with considerable solar potential.

Acknowledgements The authors would like to thank Dr. Guruprasad Mohapatra, IAS, Chairman, Airports Authority of India (AAI), for sparing his precious time for the facilitation of real-time data and are also indebted to Shri. S. Singh, Jt. GM (Engg-E) and Shri. Manish Chaudhury, AGM (E-E), AAI, for the technical data of manufacturer of solar PV plant at Tirupati.

References

1. Sharma R, Goel S (2017) Performance analysis of a 11.2 kWp roof top grid-connected PV system in Eastern India. *Energy Rep* 3:76–84
2. Khatri R (2016) Design and assessment of solar PV plant for girls hostel (GARGI) of MNIT University, Jaipur city: a case study. *Energy Rep* 2:89–98
3. Kumar SS, Nagarajan C (2016) Performance-economic and energy loss analysis of 80 kWp grid connected roof top transformer less photovoltaic power plant. *Circuits Syst* 7(06):662
4. Kumar BS, Sudhakar K (2015) Performance evaluation of 10 MW grid connected solar photovoltaic power plant in India. *Energy Rep* 1:184–192
5. Mulcué-Nieto LF, Mora-López L (2014) A new model to predict the energy generated by a photovoltaic system connected to the grid in low latitude countries. *Sol Energy* 107:423–442
6. Peerapong P, Limmeechokchai B (2014) Investment incentive of grid connected solar photovoltaic power plant under proposed feed-in tariffs framework in Thailand. *Energy Procedia* 52:179–189
7. Vasisht MS, Srinivasan J, Ramasesha SK (2016) Performance of solar photovoltaic installations: effect of seasonal variations. *Sol Energy* 131:39–46

8. Sudhakar K, Srivastava T, Satpathy G, Premalatha M (2013) Modelling and estimation of photosynthetically active incident radiation based on global irradiance in Indian latitudes. *Int J Energy Environ Eng* 4(1):21
9. Kessler W (2017) Comparing energy payback and simple payback period for solar photovoltaic systems. In: *E3S web of conferences*, vol 22. EDP Sciences, p 00080
10. Peng J, Lu L, Yang H (2013) Review on life cycle assessment of energy payback and greenhouse gas emission of solar photovoltaic systems. *Renew Sustain Energy Rev* 19:255–274
11. Marimuthu C, Kirubakaran V, Rajasekaran R (2014) Energy pay back period and carbon pay back AQ5 285 period for solar photovoltaic power plant. *Int J Chem Sci* 12(1): 293–305
12. Winkler SC (2015) Small-scale solar photovoltaic investment: payback periods, net present value, and the impact of EPA 111 (D)
13. Darghouth NR, Barbose G, Wiser RH (2014) Customer-economics of residential photovoltaic systems (part 1): the impact of high renewable energy penetrations on electricity bill savings with net metering. *Energy Policy* 67:290–300
14. <https://www.popsi.com/science/article/2013-04/solar-panels-now-make-more-electricity-they-use/>

Average Current-Controlled SEPIC Converter with High Power Factor Correction



Alok Kumar Mishra, Akshaya Kumar Patra, Ramachandra Agrawal, Lalit Mohan Satapathy, Anuja Nanda, Samarjeet Satapathy and Jnana Ranjan Swain

Abstract This paper presents a comparative analysis between the two controllers, PI and fuzzy logic controllers that used for power factor correction using DC-to-DC single-ended primary-inductor converter (SEPIC) converter. MATLAB/Simulink models of SEPIC converter are developed to improve the power factor and output voltage regulation. Average current control technique is used for input power factor correction to get a regulated voltage at the output PI or fuzzy logic controller (FLC) is adopted. The system is tested at both steady-state and transient conditions, and its performance is then estimated and compared in terms of various parameters like total harmonic distortion (THD), input power factor, output voltage ripple for PI and FLC.

Keywords PID · FLC · SEPIC converter · Average current control · Power factor correction circuits

A. K. Mishra (✉) · A. K. Patra · L. M. Satapathy · A. Nanda
Department of EEE, ITER, SOA Deemed to be University, Bhubaneswar 751030, India
e-mail: malok2010@gmail.com

A. K. Patra
e-mail: hiakp@yahoo.com

L. M. Satapathy
e-mail: lalitsatapathy@soa.ac.in

A. Nanda
e-mail: anujananda@soa.ac.in

R. Agrawal · S. Satapathy · J. R. Swain
Department of EE, ITER, SOA Deemed to be University, Bhubaneswar 751030, India
e-mail: ramachandra1agrawal@gmail.com

S. Satapathy
e-mail: samarajeets832@gmail.com

J. R. Swain
e-mail: jnana5500@gmail.com

1 Introduction

According to the international standards and for the best power transfer and utilization, power factor correction has become a necessity. To get a DC output voltage, we use a rectifier and a parallel capacitor [1, 2] as shown in Fig. 1a. The input voltage and current are shown in Fig. 1b. Figure 1b depicts a pulse-shaped input current with much harmonics content causing a very poor power factor. The IEEE and IEC are some international entities to define or standardize the permissible limits of the harmonic content in line current such as IEEE 519 and IEC 61000-3-2 [3]. The design of an AC-to-DC power converter to overcome these power quality issues like obtaining a unity power factor at the AC input mains, and a close regulation of the DC output voltage has been discussed in [4–9]. So, for small power uses in single-phase supplies, DC–DC converters are used which are switch-based and controlled accordingly to ensure high power factor at the input side. The main motive is to emulate a resistive circuit when seen from the input side and improve power factor. Theoretically, there exist three families of non-isolated power factor correction topologies which are buck, boost and buck–boost topology [1, 10–13]. The buck topology is generally used when low output voltage is required but has high frequency commuted current at input. Due to the commuted nature, it exhibits a discontinuous nature and hence should be connected with high-speed recovery circuit. The major drawback faced by buck topology is the inclusion of a filter of high-frequency range within the diode bridge and the power source [14]. The filtering inductor causes a soft variable current in the input end in the topology of a boost converter. This topology provides high output voltage and leads to over-voltage stress at the switches [5, 15]. The third family is buck–boost topology and finds its applications in power factor correction circuits. It includes Cuk converter and single-ended primary-inductor converter (SEPIC converter) [16, 17]. The output voltage polarity makes these two converters different from each other. In case of Cuk converter, the position of free-wheeling diode and the inductor is reversed from that of the SEPIC converter to obtain reversed output voltage polarity [18, 19]. In this paper, we have used SEPIC-type PFC circuit to improve the input side power factor of the diode bridge rectifier and lowered the THD factor with decreased ripple that contained voltage at output [1, 20, 21]. The entire modelling and the design scheme of power factor rectified AC-to-DC power converters are carried out in the MATLAB/Simulink environment.

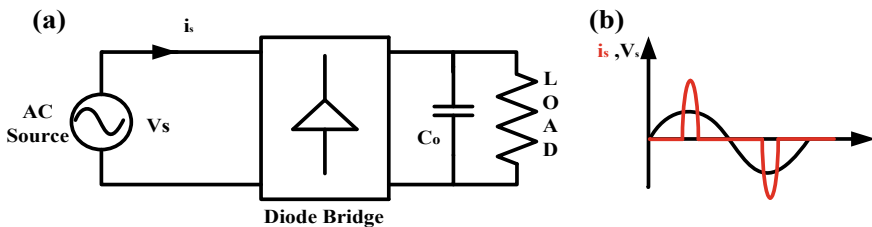


Fig. 1 a AC–DC rectifier, b source voltage and current waveform

2 Circuit Configuration and Design Equation

To improve the power factor at the input and to get a regulated voltage at the output, we have to interface SEPIC in between the bridge rectifier and the load as shown in Fig. 2.

By adopting this SEPIC topology, for a low voltage DC bus, it provides a low ripple current at its input, which is rare in the case of conventional converters of buck–boost type. With adequate coupling coefficient design in a SEPIC converter, the same magnetic core can accommodate the output and input inductors. The basic circuit diagram of DC–DC SEPIC converter is shown in Fig. 3. When switch is ON, inductors L_1 and L_2 store energy; inductor current increases linearly; output capacitor supplies power to the load, and the diode is reverse biased as depicted in Fig. 4.

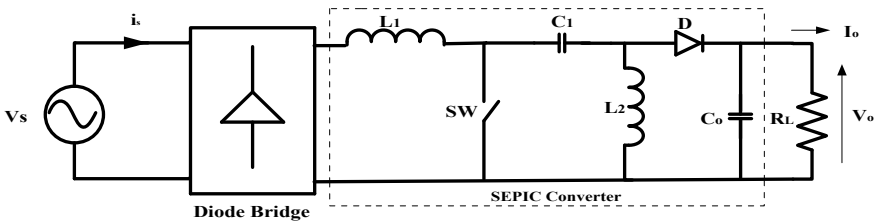


Fig. 2 SEPIC converter topology for power factor correction

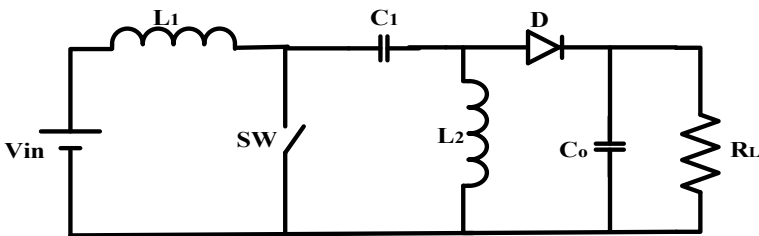


Fig. 3 Basic circuit diagram of DC–DC SEPIC converter

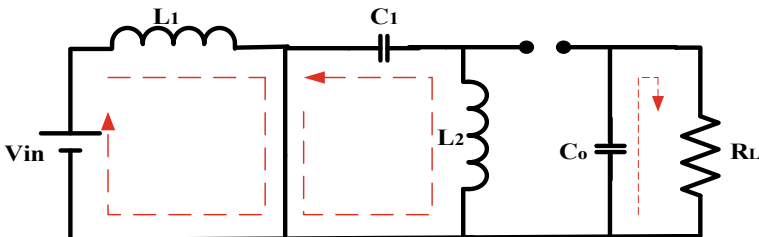


Fig. 4 SEPIC converter when switch is ON

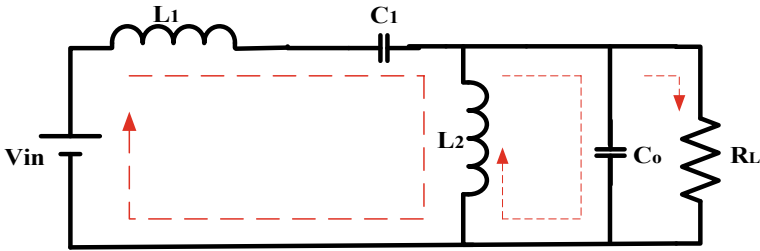


Fig. 5 SEPIC converter when switch is OFF

When switch is ON, after applying KVL and KCL the voltage and current are represented in Eqs. (1)–(4).

$$L_1 \frac{di_1}{dt} = v_{in} \quad (1)$$

$$L_2 \frac{di_2}{dt} = v_{C_1} \quad (2)$$

$$C_1 \frac{dv_{C_1}}{dt} = iL_2 \quad (3)$$

$$C_0 \frac{dv_{C_0}}{dt} = -\frac{v_{C_0}}{R} \quad (4)$$

When switch is OFF as depicted in Fig. 5, applying KVL and KCL the voltage and current are represented in Eqs. (5)–(8).

$$L_1 \frac{di_1}{dt} = v_{in} - v_{C_1} - v_{C_0} \quad (5)$$

$$L_2 \frac{di_2}{dt} = -v_{C_1} \quad (6)$$

$$C_1 \frac{dv_{C_1}}{dt} = iL_1 \quad (7)$$

$$C_0 \frac{dv_{C_0}}{dt} = iL_1 + iL_2 - \frac{v_{C_0}}{R} \quad (8)$$

Using the above equations, we can find the values of circuit components, which are represented in Eqs. (9)–(12), where v_s is the RMS source voltage, d is the duty cycle, ΔiL represents inductor current ripple, Δv_c , Δv_o are the voltage ripple of the output voltage and capacitor voltage, respectively. f_s is the switching frequency. P_o is the output power, V_o is the output voltage, I_o is the output current.

$$L_1 = \frac{v_s * d}{\Delta i L_1 * f_s} \quad (9)$$

$$L_2 = \frac{v_s * d}{2 * \Delta i L_2 * f_s} \quad (10)$$

$$C_1 = \frac{i L_2 * d}{\Delta v_{c_1} * f_s} \quad (11)$$

$$C_o = \frac{P_o}{4\pi * f_s * V_o * \Delta v_o} \quad (12)$$

3 Different Methods of Power Factor Correction

There are two objectives of power factor correction: (1) To get a regulated voltage at the output, (2) the wave shape of current at the input must be a sine wave. To achieve the first objective, we have to use a feedback loop at the output. There are two methods to achieve the second objective. First method is called “multiplier approach” and the second is called “voltage follower approach”. In multiplier approach, a feedback loop of input current is used to govern the DC-to-DC power converter to function as an input voltage programmed current sink as shown in Fig. 6. In this paper, multiplier approach is used. Multiplier approach control is further sub-divided into four different methods for generating the gate pulse for the SEPIC converter, such as

1. Hysteresis current control
2. Peak current control
3. Average current control
4. Borderline current control.

In this paper, average current control method is considered which allows a better input current waveform, which is depicted in Fig. 6. In this technique, the sensed inductor current is to be filtered with the help of a current error amplifier and the output of the same drives the PWM modulator. Hence, the error between input current I_g and its reference gets minimized with the help of inner current loop. The reference current is generated by a voltage error amplifier (PI or fuzzy logic controller). Due to the PWM modulator, average current control method gives a constant switching frequency because of current filtering commutation noises get eliminated. This method does not need any compensation ramp. Inductor current must have to sense which is the demerits of this method.

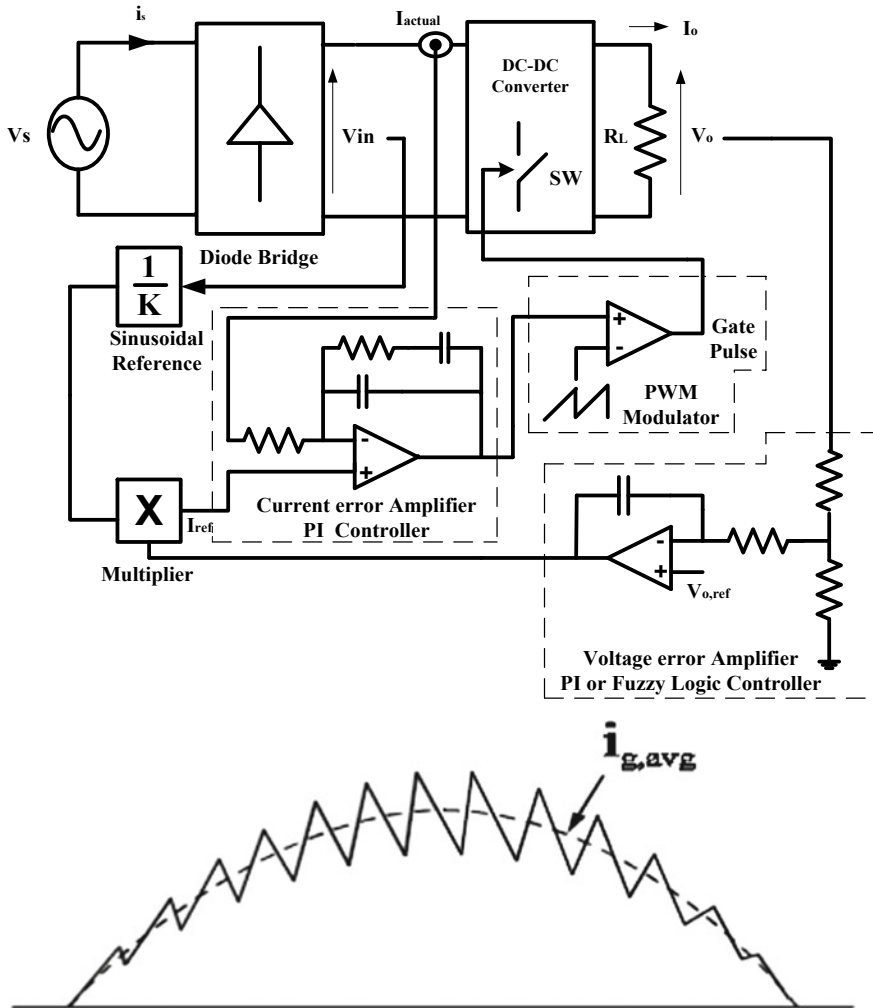


Fig. 6 Multiplier approach with average current control technique

4 PID Controller for Output Voltage Regulation

The name itself proportional–integral–derivative controller is a type of control loop mechanism adopted in continuous modulated operation of control. A PID controller repeatedly calculates the error in between a set point (SP) value and measured process value (PV) and gets a correction accordingly in PID base. In real-time operation, it accordingly provides an accurate and respective change of correction to a control function. For example, furnace temperature controls that it applies a derivative term to effectively correct the error in spite of a huge change.

5 Fuzzy Logic Controller for Output Voltage Regulation

The basic block diagram of the proposed fuzzy logic controller for output voltage regulation of SEPIC converter is shown in Fig. 7.

Any object has a degree of membership which varies from 0 to 1 in the fuzzy set theory, which makes fuzzy logic to handle all situations in a natural way. The shape of membership functions can also be trapezoidal or Gaussian, depending on the applications, and can be symmetrical or asymmetrical. The power converter voltage error is defined in linguistic variables such as positive big (PB), negative big (NB), positive medium (PM), negative medium (NM), positive small (PS), negative small (NS), zero (ZE), where each variable is defined by a gradually varying triangular membership function. For error (e) and change in error (de), seven fuzzy sets are chosen. For a particular application, depending on the input resolution, the number of fuzzy levels is selected, which is not fixed. Higher will be the input resolution, more has to be the number of fuzzy levels. Each input is assigned a membership function μ which is not quantized in the classical sense to each fuzzy set. To diminish the difficulty in calculation, here triangular fuzzy set values are used and we may also use bell-shaped or trapezoidal fuzzy set depending on the application. For n number of variables, the fuzzy rules are n dimensional. The sum of rules is known as rule R . Fuzzy inference system editor edits the input and output variables, which are e , de and output. After editing, we have to design the membership function for each variable. The final step involves in writing rules in rule editor using the rule given in Table 1.

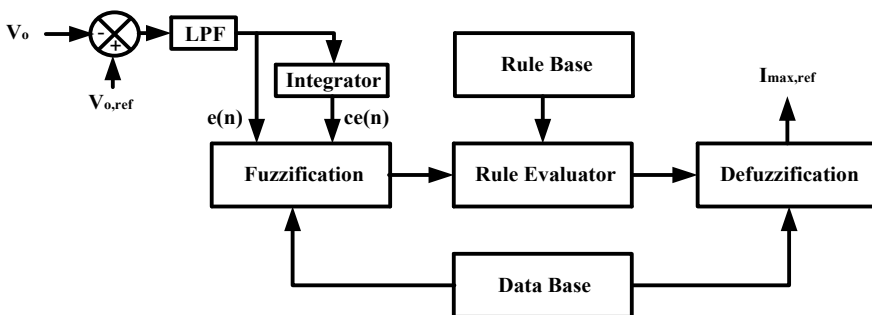


Fig. 7 Basic block diagram of FLC

Table 1 Fuzzy rules for closed-loop control of SEPIC converter

e\de	NB	NM	NS	ZE	PS	PM	PB
NB	NB	NB	NB	NB	NM	NS	ZE
NM	NB	NB	NB	NM	NS	ZE	PS
NS	NB	NB	NM	NS	ZE	PS	PM
ZE	NB	NM	NS	ZE	PS	PM	PB
PS	NM	NS	ZE	PS	PM	PB	PB
PM	NS	ZE	PS	PM	PB	PB	PB
PB	ZE	PS	PM	PM	PB	PB	PB

6 Results and Discussion

To investigate the performance of the proposed system, a Simulink model of a SEPIC converter used for power factor correction is developed as shown in Fig. 8.

The designed parameter used in the simulation is given in Table 2. The system performance is investigated in four steps. Step: 1: when SEPIC converter is not connected to the system. Step: 2: when SEPIC converter is connected to the system with inner current loop only and without the output voltage feedback loop. Step: 3: when SEPIC converter is connected to the system with PI controller in the feedback loop. Step: 4: when SEPIC converter is connected to the system with fuzzy logic controller in the feedback loop. To convert AC to DC, we generally connect a bridge rectifier and filter capacitor across the load as shown in Fig. 1, and simulation result of the same along with its harmonic spectrum is shown in Fig. 9a–d. To improve the performance of the input current and output voltage, SEPIC converter is used as discussed in Fig. 2. Various waveforms at steady state in open loop are shown in

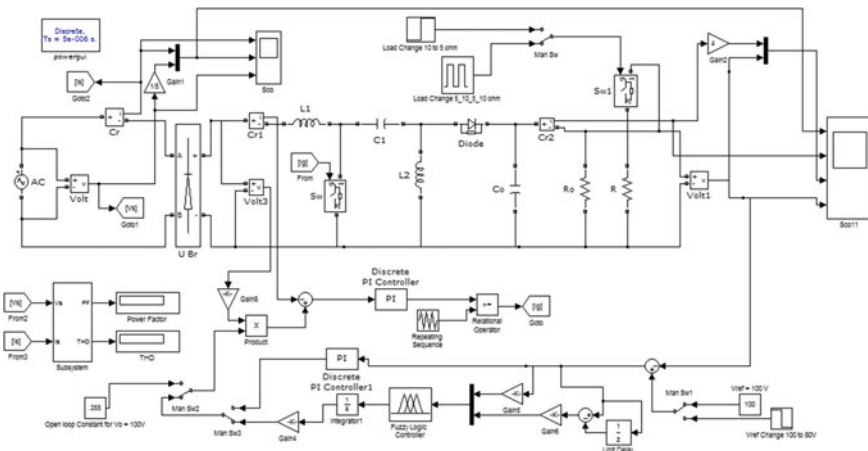


Fig. 8 Simulink model of SEPIC converter

Table 2 Designed parameter of SEPIC converter

Parameters	Values
Input voltage RMS value	120 V
Supply frequency	50 Hz
L_1, L_2	6 mH, 10 mH
C_1, C_o	10 mF, 10 mF
Load power	1 kW
Reference output voltage	100 V
Switching frequency	40 kHz
Voltage and current ripple	0.05
Duty cycle	0.45

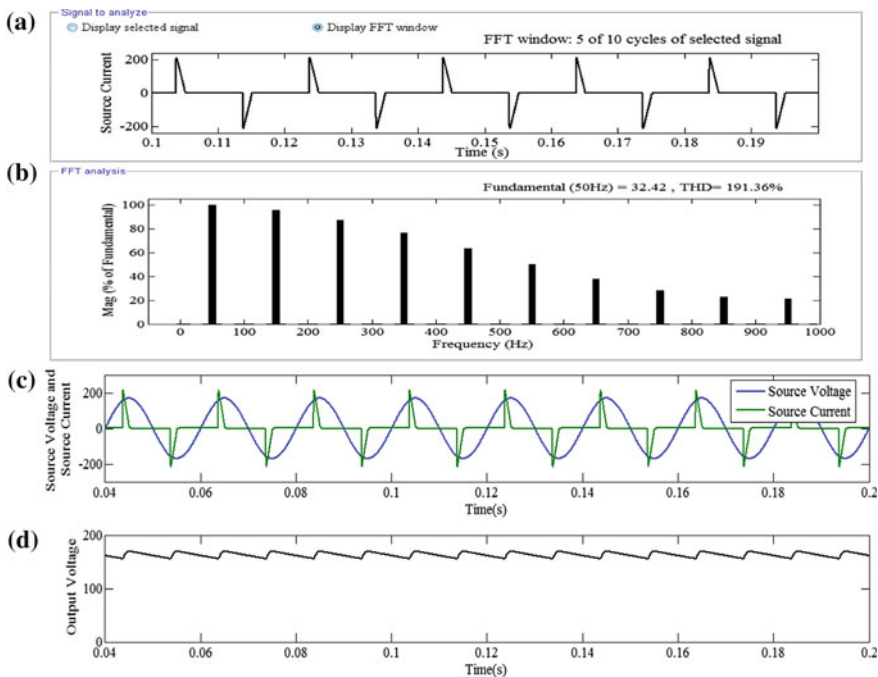


Fig. 9 Simulation results of the proposed system without SEPIC converter

Fig. 10a–e. From Fig. 10d, it is clear that when load is increased at $t = 2.5$ s, load voltage is not a regulated one. To get a regulated output voltage and improved input current wave, PI or fuzzy logic controller is used in the output feedback loop. The dynamic response of the system is shown in Figs. 11a–f and 12a–f, respectively, for PI and fuzzy logic controller in the outer loop. To test the validity of the PI and fuzzy logic controller, a load change and reference voltage change are created at $t = 1$ s

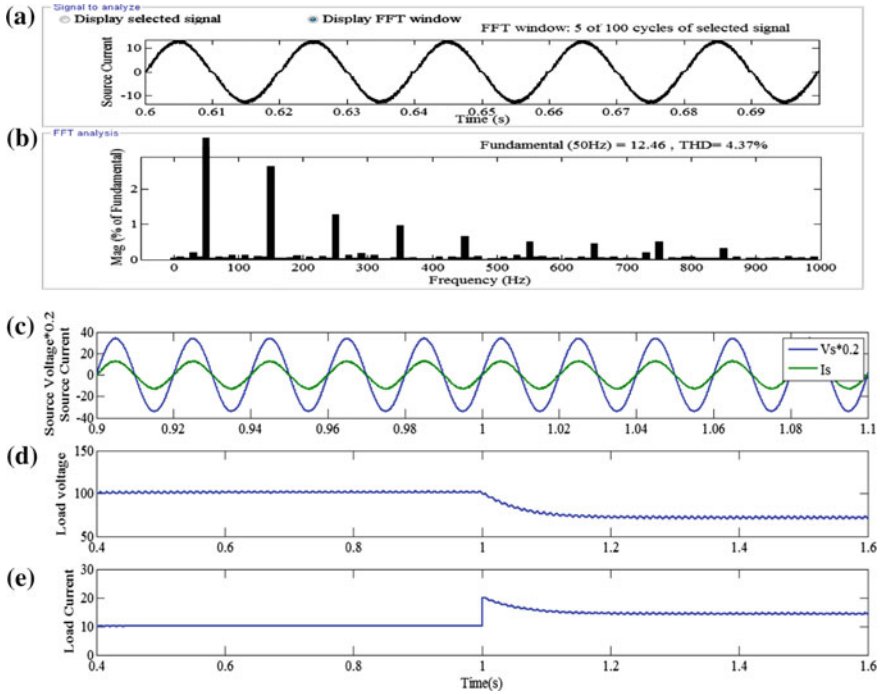


Fig. 10 Simulation results of the proposed system in open loop

and at $t = 2$ s, respectively. With this dynamic change, the regulated output voltage is obtained which can be clearly seen from Figs. 11e and 12e, respectively, for PI and fuzzy logic controller. Various performance parameters obtained in simulation are given in Table 3 for comparison.

7 Conclusion

The design, modelling and simulation of SEPIC converter for power factor correction purposes considered in MATLAB/Simulink environment. The outcomes of the simulation work provided low THD of the supply current with upgraded AC mains power factor and reduced output voltage ripple. Comparing with PI and FLC used in the output feedback loop, FLC gives better results in terms of THD of supply current, input power factor and output voltage ripple which is given in Table 3. From Fig. 12e, it is clear that FLC gives a well-regulated output voltage with reduced ripple when load disturbance and reference change occur. The prototype of the proposed SEPIC converter can be developed, which would be attempted as future work.

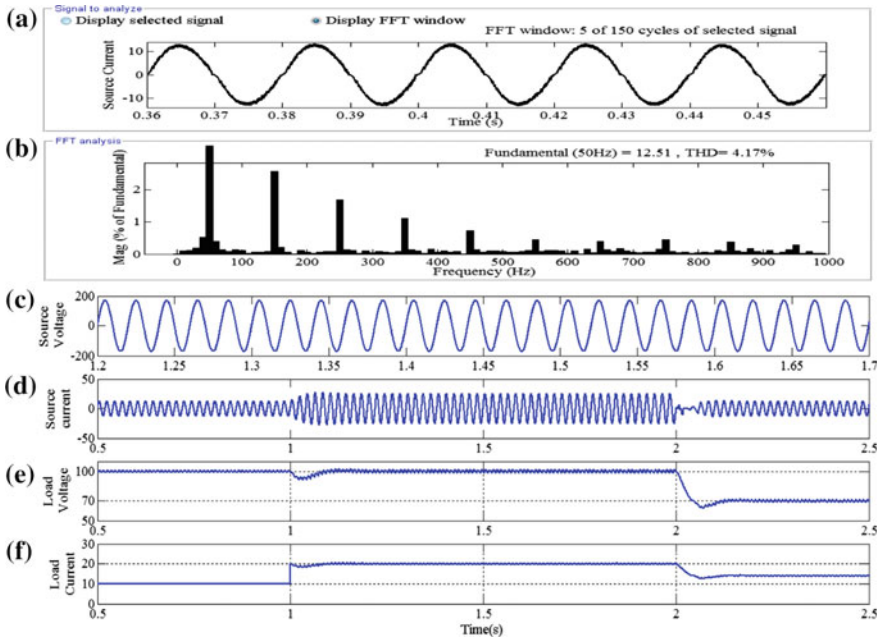


Fig. 11 Simulation results of PI-controlled SEPIC converter

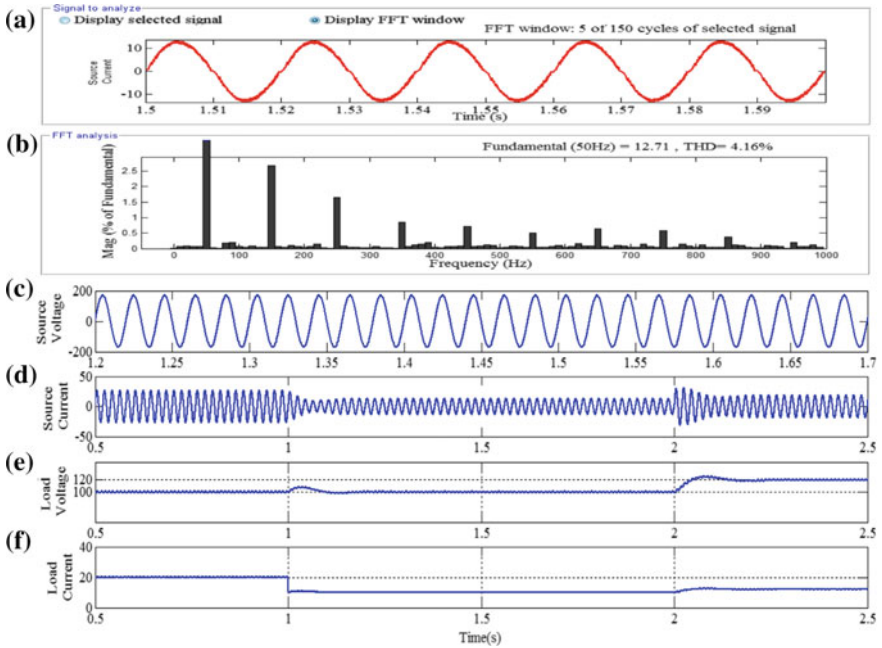


Fig. 12 Simulation results of fuzzy logic-controlled SEPIC converter

Table 3 Performance parameters of the system under different conditions

Different condition	Performance parameter		
	THD %	Power factor	Output voltage ripple %
Without SEPIC converter	191.36	0.4479	9.2
Open loop SEPIC converter	4.37	0.9986	2.0
PI-controlled SEPIC converter	4.17	0.9983	2.1
Fuzzy logic-controlled SEPIC converter	4.16	0.9997	1.5

References

- Mishra AK, Pathak MK, Das S (2011) Isolated converter topologies for power factor correction—a comparison. In: IEEE international conference on energy, automation and signal, 28 Dec 2011, pp 1–6
- Kuiyuan W (2006) The comparison and choice of several power factor correction methods. In: IEEE vehicle power and propulsion conference, Sep 2006, pp 1–5, IEEE
- 519–2014: IEEE recommended practice and requirements for harmonic control in electric power systems, 11 June 2014, pp 1–29
- Pressman I (1991) Switching power supply design. McGraw-Hill, New York
- Patra AK, Rout PK (2017) Adaptive continuous-time model predictive controller for implantable insulin delivery system in type I diabetic patient. *Optimal Control Appl Methods* 38:184–204
- Patra AK, Rout PK (2014) Optimal H-infinity insulin injection control for blood glucose regulation in IDDM patient using physiological model. *Int J Autom Control* 8:309–322
- Singh B, Singh BN, Chandra A, Al-Haddad K, Pandey A, Kothari DP (2003) A review of single-phase improved power quality AC-DC converters. *IEEE Trans Ind Electron* 50(5):962–981
- Batarseh I (2003) Power electronics circuits, 3rd edn. Wiley, London
- Richard R (1994) The fundamentals of power factor correction. *Int J Electr Eng Educ* 31:213–229
- Dah D, Ki SK (2013) Light-load efficiency improvement in buck-derived single-stage single-switch PFC converters. *IEEE Trans Power Electron* 28(5):2105–2110
- Patra AK, Mishra AK, Rout PK (2018) Backstepping model predictive controller for blood glucose regulation in type-I diabetes patient. *IETE J Res.* <https://doi.org/10.1080/03772063.2018.1493404>
- Patra AK, Rout PK (2017) Adaptive sliding mode Gaussian controller for artificial pancreas in T1DM patient. *J Process Control* 58:23–27
- Liu X, Xu J, Chen Z et al (2015) Single-inductor dual-output buck–boost power factor correction converter. *IEEE Trans Ind Electron* 62(2):943–952
- Kanaan HY, Al-Haddad K, Fnaiech F (2004) Switching-function-based modeling and control of a SEPIC power factor correction circuit operating in continuous and discontinuous current modes. In: IEEE international conference on industrial technology, vol 1, no 8, pp 431–437, Dec 2004
- Umamaheswari MG, Uma G (2013) Analysis and design of reduced order linear quadratic regulator control for three phase power factor correction using Cuk rectifiers. *Electr Power Syst Res* 1(96):1–8
- Mahdavi M, Farzanehfard H (2011) Bridgeless SEPIC PFC rectifier with reduced components and conduction losses. *IEEE Trans Ind Electron* 58(9):4153–4160
- Umamaheswari MG, Uma G, Isabella LA (2014) Analysis and design of digital predictive controller for PFC Cuk converter. *J Comput Electron* 13(1):142–154

18. Poorali B, Adib E (2016) Analysis of the integrated SEPIC-flyback converter as a single-stage single-switch power-factor-correction LED driver. *IEEE Trans Ind Electron* 63(6):3562–3569
19. Melo PF, Gules R, Ribeiro EF et al (2010) A modified SEPIC converter for high-power-factor rectifier and universal input voltage applications. *IEEE Trans Power Electron* 25(2):310–321
20. Sudhakarababu C, Veerachary M (2004) Zeta converter for power factor correction and voltage regulation. In: 2004 IEEE region 10 conference TENCN 2004, 24 Nov 2004, vol 500, pp 61–64, IEEE
21. Patra AK, Rout PK (2018) Backstepping sliding mode Gaussian insulin injection control for blood glucose regulation in T1DM patient. *J Dyn Syst Meas Control* 140(9):091006-091006-15

Smartgrids/Microgrids in India: A Review on Relevance, Initiatives, Policies, Projects and Challenges



Ashutosh Nayan Dey, Basanta K. Panigrahi and Sanjeeb Kumar Kar

Abstract Microgrid and smartgrids are quickly moving from laboratories/demonstration benches to being deployed in increasing number across wide range of applications along with integration of renewable energy sources. This paper attempts to (i) Explain the concept of renewable energy-based microgrid/smartgrids and their relevance in solving India's energy needs in a smart and sustainable way. (ii) Describes the various initiatives taken by Govt. to achieve the smartgrid vision of India along with brief on acts/policies enabling Renewable Energy Integration. (iii) Tracks the present status on smartgrid/microgrid activities across various parts of the country and does a comparative study on features of those projects. (iv) Analyzes the key benefits, opportunities as well the challenges faced during implementation of such smart and sustainable projects. (iv) Lastly, the author proposes a brief framework for deployment of new projects concerning microgrids/smartgrids.

Keywords Microgrid (MG) · Renewable energy · Smartgrid

1 Introduction

Total installed capacity of power generation in India as on 21/08/2019 is 360,456 MW [1]. The energy mix consists of conventional as well as renewable sources as shown in Table 1. While share of energy obtained from oil/coal/gas is reducing, at the same time, the share of renewable energy has gradually increased from 7.8% in 2008 to 22% in 2019 (Source CEA Statistics).

A. N. Dey · B. K. Panigrahi (✉) · S. K. Kar
Department of Electrical Engineering, ITER, SOA Deemed to be University, Bhubaneswar
751030, India
e-mail: basanta1983@gmail.com

A. N. Dey
e-mail: ashu4567@gmail.com

S. K. Kar
e-mail: sanjeebkar@soa.ac.in

© Springer Nature Singapore Pte Ltd. 2020
R. Sharma et al. (eds.), *Innovation in Electrical Power Engineering, Communication, and Computing Technology*, Lecture Notes in Electrical Engineering 630,
https://doi.org/10.1007/978-981-15-2305-2_37

Table 1 Percentage share of different sources in meeting India's energy needs

Type of energy source		Contribution in percent (out of total installed capacity of 360,456 MW)
Thermal	Coal (54.3%)	63.2%
	Lignite (1.7%)	
	Gas (6.9%)	
	Diesel (0.2%)	
Hydro		12.6%
Nuclear		1.9%
Renewable energy		22%
Total		100%

With increasing focus of Govt. to meet our energy needs from renewable sources, it has become more essential to have a highly adaptive grid which is smart enough in meeting the variable dynamics of demand and supply, especially considering the intermittent nature of renewable energy which cannot be controlled. Thus, the relevance of smartgrids and microgrids has increased considerably for meeting India's energy needs.

Traditional grids are inclined toward centralized generation mostly from conventional sources with one-directional power flow but microgrids are basically small networks of energy having own local energy source and they are capable of bidirectional power transfer in grid-connected mode but at the same time, they can function independently on stand-alone basis for off-grid applications or during islanded mode of operation.

Generally, microgrids integrate local power generation from renewable sources like solar, wind, etc., but considering the intermittent nature of generation from renewable sources, there is a need for energy storage systems which are discussed in [2, 3]. Then at the heart of microgrid is the controller which monitors overall parameters. Details related to microgrid controller are given in [4, 5]. Bidirectional power flow increases the complexity for need of system protection and stability as discussed [6, 7]. PCC or point of common coupling serves as a junction between local microgrid and utility grid allowing it to function in either grid-connected mode or islanded mode. A sample schematic diagram of microgrid is presented in Fig. 1.

When several clusters of local microgrid connected to main grids are enhanced with smart technologies involving digital communication, control and monitoring which are dynamic in nature, then it forms smartgrids. Various components of smartgrids are smart meters, advanced storage, smart integration, SCADA, etc. Detailed reviews on smartgrid technologies are mentioned in [8]. The various stakeholders are mentioned in Fig. 2

The remaining of this paper is organized as follows. Initiatives by Govt. of India are elaborately described in Sect. 2, while Sect. 3 describes the status of various projects in India and Sect. 4 demonstrate the challenges, opportunities and benefits. Lastly,

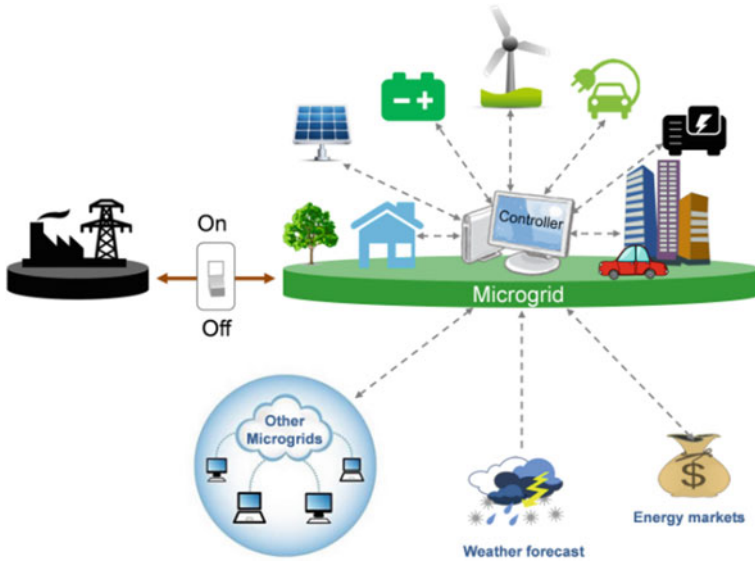
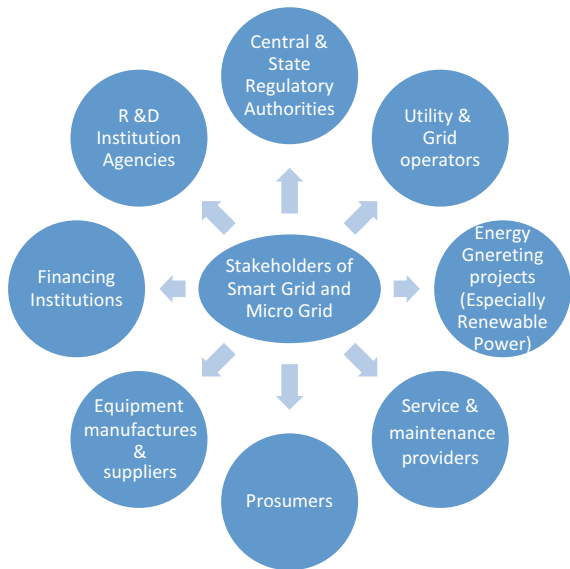


Fig. 1 Schematic of a basic microgrid. *Image source* Berkeley Laboratory Microgrid

Fig. 2 Stakeholders of microgrid and smartgrid



Sect. 5 describes the brief framework for implementation of microgrids/smartgrid projects. The closing comments of this paper are indicated in Sect. 6.

2 Initiatives by Govt. of India

Electricity is a concurrent subject in constitution hence while Central Govt. frames overall rules and regulations, whereas each state formulates its own policy inside the overall regulatory framework.

The vision statement of Govt. on smartgrids is to “Transform the Indian Power sector into a secure, adaptive, sustainable & digitally enabled ecosystem that provides reliable & quality energy for all with active participation of stakeholders” [Source: National Smart Grid Mission (NSGM)].

Given the necessity of transition from traditional grids to smartgrids and microgrids, Ministry of Power (MOP)—Govt. of India approved a vision and roadmap document in August 2013 and accordingly National Smart Grid Mission (NSGM) started in 2015. It plans, monitors and implements various activities related to smartgrids on national level and focuses on capacity building at state level by establishing state level project management units (SLPMU). Huge investments have been made under NSGM for study, research, consumer awareness and encouraging participation in various initiatives. Similarly, an alliance of many countries named as International Solar Alliance was initiated by India on November, 30, 2015. Some of the NSGM key milestones are showcased in Table 2, while the legal and institutional frameworks of our country dealing with our energy infrastructure are presented in Table 3.

Table 2 Some of the NSGM milestones for smartgrid rollout

Goals relation to smartgrid rollout	Phase 1 (up to 2020)	Phase 2 (2020–2025)
State level project management unit setup	100%	
SLPMU regulations and policies for SG	100%	
SLPMU roadmap for SG		100%
Preparedness of utility in mature-level framework for SG and self-assessment in a finalized frame work	100%	
Utility with AMI rollouts	10%	100%
Network mapping and consumer indexing by utilities	100% (urban)	100% (rural)
Automation of distribution system (SCADA/DMS)		100%
Utility with ability to manage RE integration	10%	100%
Utility with ability to deploy infrastructure for EV	10%	100%

Table 3 Legal and institutional framework

Electricity Act 2003	It provides for policy formulation by central Govt. and mandates SERC of states for optional utilization of all resources
NEP 2005	It targets to exploit RE resources, reduce capital cost, promote competitive building and encourage Pvt. sector participation
NTP 2006	Among other things, it formulates preferential tariff determined by SERC for procurement of RE
Integrated Energy Policy IEP 2006	Emphasis importance of RE to meet energy demand of industry
NAPCC 2008	It identifies eight core national mission to address global warming and some of it relates for gradual increase of RE percentage
JNNSM 2009	It is one of the eight mission of NAPCC and it promotes solar energy development for both on-grid and off-grid
NCEF 2010	It is a fund which uses carbon tax/cess for providing funds to promote R&D in clean energy technology

NSGM has targeted strengthening of existing Grid by IT and SCADA implementation which is ready to support smartgrids technology under RAPDRP programme and automation of T&D activities.

Components in smartgrids implementation are basically as follows [9]

- (i) Deploying of advanced metering infrastructure (AMI) and smart meters, renovation and modernization of sustain along with integrating GIS wherever possible (NSGM will promote microgrids in islands special industrial facilities, research institutions and commercial complexes).
- (ii) Development of microgrids and distributed generation.
- (iii) It will seek to promote RE generation as well as its seamless integration.
- (iv) Deployment of charging infrastructure facility for EV under national mission for electric mobility can be coordinated with NSGM.
- (v) Promotion off-grid-connected roof top solar under JNNSM (National Solar Mission) shall be encouraged.
- (vi) Projects related to real-time monitoring and control of distribution transformers with improving power factor like having provision for harmonic filter and reliability shall be partially funded under NSGM.
- (vii) Outage/blackout management system.
- (viii) Some other enabling components are peak load management, cyber security, network management, smart appliances, energy storage, rules for consumer data privacy and protection, dynamic pricing, etc.

3 Projects in India

Many small-scale microgrid projects (mostly solar based) are operating across India, some prominent among them are those running by M/S Husk Power System (villages across Bihar, UP, Odisha, Jharkhand, etc.); MeraGao Power (Villages across UP); Sagar Island Microgrid in West Bengal, etc. Similarly, Under NSGM the Govt has implemented many smartgrid projects whose detailed status report as obtained from [10, 11] has been concisely presented in Tables 4 and 5.

4 Challenges, Opportunities and Benefits

This section describes briefly the challenges, opportunities and benefits for any microgrid or smartgrid project.

4.1 Challenges

The major challenges faced by smartgrids and microgrids are discussed in [12] which can be summarized as (i) Integration of RE sources with the grid considering the intermittent nature of supply (ii) High capital required for implementing smart IT-enabled technologies for modernizing existing grids (iii) High cost of renewable technology installation especially when storage technology is integrated (iv) lack of sufficiently trained manpower for service, installation and maintenance (v) Some States still have absence of cohesive/comprehensive policy and regularity frame work for smartgrid development (vi) Obtaining finance for the projects from financial institutions (vii) Considering the complex technologies involved protection and control of power (viii) Cost sensitive Indian market.

4.2 Opportunities in India

(i) Regulations, policies and institutional frameworks have already been developed at level of central Government along with budgetary support and subsidies extended at various levels (ii) Renewable resource potential is very good in India (iii) Gradual emergence of indigenous manufacturing companies and technology developers providing on-grid and off-grid solutions (iv) Inadequate access of energy in many remote rural off-grid locations can be solved by implementing the concept of stand-alone microgrid rather than extension of grid which will be uneconomical (v) Considering the frequent disruption of power due to natural calamity or otherwise microgrids for critical installations can provide power backup for longer period.

Table 4 Status report on NSGM smartgrid projects [10]

S. No.	Name of project	Project as status on August 2019	Area catered	Project funding data		Implementing agency	No. of consumers	Functionality
				Total cost	Govt. share			
1	CED, Chandigarh	Design of Network in Progress. Inspection call of 500 smart meters started on 03.09.19	Sub-division 5 of Chandigarh	28.58 Crore	8.57 Crore	M/S Analogics, M/S synergy	29,433	AMI, DTMU, SCADA
2	JBVNL, Jharkhand (Ranchi)	Bids opened on 05.07.19. Technical Education is Progress	Ranchi	228.06 Crore	68.6 Crore	NA	3.6 Lakh	AMI, DTMU
3	OPTCL, Odisha (Rourkela)	Bid opening date 05.09.19	Rourkela	96.9 Crore	29.09 Crore	NA	0.87 Lakh	AMI, SCADA, DTMU
4	CED, Chandigarh (complete city exclude, SD-5)	Sanction Accepted	Chandigarh City (except SD-5)	241.4 Crore	72.4 Crore	NA	1.84 Lakhs	AMT, SCADA, DTMU
5	KSEB, Kerala (Kochi)	Sanction Letter issued on 28.09.18	Kochi City	90.07 Crore	27.26 Crore	NA	0.9 Lakhs	AMI, PLM, DTMU, EVCI, PV

Table 5 Status report on smartgrid pilot projects in India as on August 2019

S. No.	Project name	Project status	Area catered	Project funding data		Implementing agency	No. of consumer	Functionality
				Total cost	GOI share			
1	CESU Mysore	Completed	VV Mohalla, Mysore	32.5 Crore	16.28 Crore	M/S Enzen	21,824	AMI, OMS, PLM, DG
2	UHBVN, Haryana	Completed	Panipat city sub-division	Grant given by NEDO (Japan)		M/S Fuji Electric	10,188	AMI, OMS, PLM
3	Manesar smartgrid knowledge Center	Completed	Powergrid complex, Manesar	5.96 Crore	5.96 Crore	M/S Genus	NA	AMI, OMS, DG, EV, HEMS, Cyber security
4	HPSEB, Himachal	Completed	Kala Amb Industrial Area	19.4 Crore	9.73 Crore	M/S GE T&D	1335	AMI, OMS, PLM
5	UGVCL, Gujarat	Project completed	Naroda	23.1 Crore	11.59 Crore	M/S Genus	22,230	AMI, OMS, PLM, PQ
6	PED, Puducherry	Project live on Dec 2018	Div 1 of Puducherry	35.5 Crore	17.76 Crore	M/S DFE, China	33,499	AMI
7	WBSEDCC, West Bengal	Project live on 31.12.18	Siliguri Town	7.03 Crore	3.53 Crore	M/S Chemtrols	5265	AMI, PLM
8	TSECL Tripura	Project live on 30.06.19	Electrical Division 1 Agartala	63.4 Crore	31.7 Crore	M/S Wipro	45,290	AMI, PLM
9	TSS PDCL, Telangana	Project live on 30.03.19	Jeedimetla Industrial Area	32.9 Crore	17.4 Crore	M/S ECIL	11,906	AMI, PLM, OMS, PQ
10	APDCL, ASSAM	Project live on 02.05.19	Guwahati Division	20.9 Crore	10.4 Crore	M/S Fluentgrid	15,083	AMI, PLM, OMS, PQ, DG

AMI advanced metering infrastructure, PLM peak load management, OMS outage management system, PQ power quality, PQM power quality monitoring, HEMS home energy management system, EV electric vehicle

4.3 Benefits

- (i) For consumers—They become “Prosumers” by possibility of two-way power transfer, i.e. they can sell power to grid during excess generation by RE sources and importing from grid during shortages. In case of consumers with critical loads, when there is power blackout, backup power shall be available for longer periods by operating microgrids in islanding mode of operation.
- (ii) For environment—Integration of renewable sources and distributed generation into microgrids is environment-friendly as it reduces our dependence on power generated from conventional sources thereby reducing greenhouse emissions and carbon.
- (iii) For utilities—Energy cost can be reduced by load shifting, peak load management, reduction of T&D losses by decentralized power generation, etc., leads to better efficiency and management of power dynamics and also preservation of critical loads.
- (iv) For society—Society will get access to reliable and better quality of power, people in remote locations/islands can benefit from off-grid microgrids using renewable energy as this is economically a better alternative than extending traditional grids to remote location.

5 Brief Framework for Implementation of Microgrids/Smartgrid Projects

In this section, an attempt has been made toward presenting a concise framework which can be followed during implementation of a microgrid or smartgrid project.

- (i) Resources assessment (Extensive mapping for identifying RE potential of a place)
- (ii) Load profiling (Demand variation across various time periods needs to be studied)
- (iii) Identification of financial instruments and supports (Enhancing loans and finances, interaction with bank and investors)
- (iv) Project valuation and technology deployment (Implementation of suitable hardware and technologies based on optimal resource mix and load profiling and integration of RE technology with grid)
- (v) Strategy to upscale deployment if pilot project area is successful.

6 Future Scope and Conclusion

With advent of Internet of things (IoT), scope of research is huge in integrating the concept of microgrids with IoT which can alter the future of energy infrastructure and some of latest researches in the area have been discussed in [13].

Successful implementation of smart/microgrids will require participation of all stakeholders for which a structural approach is necessary along with necessity to adapt, understand and evolve based on consumer behavior. If we look at scale of implementation of smart grid/microgrid projects, then they are still at nascent stages in our country but there has been consistent rise in interest from all stakeholders to adopt these new technologies and given governments encouragement, in next few years, the stage is all set for exponential increase of such projects. Microgrids will hence no doubt be the building block for a smarter and superior grid of future which can meet the energy needs of our nation.

References

1. Central Electricity Authority Website. <http://cea.nic.in/monthlyinstalledcapacity.html>
2. Arani AAK, Gharehpetian GB, Abedi M (2019) Review on energy storage systems control methods in microgrids. *Int J Electr Power Energy Syst* 107:745–757
3. Tan X, Li Q, Wang H (2013) Advances and trends of energy storage technology in microgrid. *Int J Electr Power Energy Syst* 44(1):179–191
4. Basak P, Chowdhury S, Nee Dey SH, Chowdhury SP (2012) A literature review of integration of distributed energy resources in the perspective of control, protection and stability of microgrid. *Renew Sustain Energy Rev* 16(8):5545–5556
5. Kaur A, Kaushal J, Basak P (2016) A review of microgrid central controller. *Renew Sustain Energy Rev* 55:338–345
6. Gopalan S, Sreeram V, Mishra Y, Iu H (2017) Protection issues in microgrids and multi-microgrids. In: Bansal R (ed) *Handbook of distributed generation*. Springer, Cham
7. Solano J, Rey JM, Bastidas-Rodríguez JD, Hernández AI (2019) Stability issues in microgrids. In: Zamboni de Souza A, Castilla M (eds) *Microgrids design and implementation*. Springer, Cham
8. Dileep G (2020) A survey on smart grid technologies and applications. *Renew Energy* 146:2589–2625 (to be published)
9. Website of National Smart Grid Mission. www.nsgm.gov.in, <https://doi.org/10.1080/03772063.2018.1454344>
10. NSGM Project Status. <https://www.nsgm.gov.in/en/sg-status>
11. India Country Report. Research, development, demonstration and deployment of smart grids in India, Department of Science and Technology, Govt of India, June 2017
12. Yoldas Y, Onen A, Muyeen SM, Vasilakos AV, Alan I (2017) Enhancing smart grid with microgrids: challenges and opportunities. *Renew Sustain Energy Rev* 72:205–214
13. Reka SS, Dragicevic T (2018) Future effectual role of energy delivery: a comprehensive review of Internet of Things and smart grid. *Renew Sustain Energy Rev* 91:90–108

LFC Analysis in PV-Thermal System Using Non-integer Controller



Jyoti Ranjan Padhi, Manoj Kumar Debnath, Sanjeeb Kumar Kar and Binod Kumar Sahu

Abstract This chapter contains the non-integer proportional–integral controller tuned by firefly algorithm for the regulation of frequency. Here, the results of the two-area system using PI controller are challenged using the new non-integer PI controller which expectedly gave the better results as compared to the standard PI controller. The system which is considered here for the study is the two-area interconnected system: One area has the thermal system, and the other one contains the photovoltaic system. The firefly algorithm helps here to find the controller’s scaling factors which help the system to come back to the normal state after the system is subjected to the 1% step load perturbation. The results of the surveyed systems with different controllers are compared on the basis of peak overshoots, undershoots, and settling time.

Keywords Non-integer PI controller · Firefly algorithm · Automatic generation control · PV-thermal system · Fractional calculus

1 Introduction

The first and foremost function of an interconnected power system is to maintain the electrical energy’s generation, transmission, and distribution in all the areas at nominal voltage and frequency levels. The certain changes in the real power and reactive power directly affect the frequency and voltage magnitude, respectively.

J. R. Padhi · M. K. Debnath (✉) · S. K. Kar · B. K. Sahu
Siksha ‘O’ Anusandhan Deemed to be University, Bhubaneswar, Odisha 751030, India
e-mail: mkd.odisha@gmail.com

J. R. Padhi
e-mail: jyotipadhi@soa.ac.in

S. K. Kar
e-mail: sanjeebkar@soa.ac.in

B. K. Sahu
e-mail: binoditer@gmail.com

© Springer Nature Singapore Pte Ltd. 2020
R. Sharma et al. (eds.), *Innovation in Electrical Power Engineering, Communication, and Computing Technology*, Lecture Notes in Electrical Engineering 630,
https://doi.org/10.1007/978-981-15-2305-2_38

Whenever it is observed that there is a sudden change in the load, the current drawing capacity gets heavily affected and hence because of this the electrical torque varies (i.e., increases or decreases) with respect to the mechanical torque, and this thus affects the accelerating torque, and due to this, the turbine speed gets reduced or gets increased [1]. To maintain the interconnected system's frequency and the tie-line power flow is main target of a researcher so as to do that in a shorter period of time. The researchers Concordia and Kirchmayer worked upon the challenges that are faced in making the system's parameters stable after it was subjected to a step load perturbation, effectively [2].

K. H. Ang worked upon a research work that describes the PID controller's designing and the technology used [3]. Khodabakhshian and Hooshmand further worked more on the PID controllers especially in automatic generation control of a hydro power plant [4]. While discussing here about the controllers, apart from PID, many other controllers are also being used. Implementation of fuzzy logic controller in a load frequency control of a two-area power system was described by Cam and Kocaarslan [5]. K. P Singh together with other researchers worked upon the LFC of a power system having a multi-source power generation [6]. S. Panda and B. Mohanty worked together upon the AGC of linear and even nonlinear interconnected power system by implementing a hybrid bacteria foraging optimization algorithm–particle swarm optimization algorithm [7]. Sudha and Santhi researched upon the LFC of a reheat thermal interconnected system by using type-2 fuzzy system which includes SMES units [8]. Debnath et al. worked upon the LFC of a multi-source power system by using a fuzzy PID controller tuned by a new hybrid algorithm known as GWO-TLBO. It was found that the results were far better than the results after implementing only the PID controller [9]. Raju More's and Lalit Chandra Saikia's paper which is upon AGC of a multi-area system uses a new controller named as PID plus second-order derivative controller which was optimized by ant-lion optimizer algorithm. The results and outcomes by using such controllers were finer and accurate [10]. The implementation and usability of the fractional-order controllers in LFC and AGC were analyzed by Alomoush [12]. Arya and Yogendra worked upon the new fractional-order fuzzy PID controller which is applied to AGC of multi-area, multi-source generating stations optimized by the bacteria foraging optimization algorithm [13]. Pan, Indranil, and Saptarshi Das worked upon the fractional-order fuzzy controller of a hybrid power system with a renewable generation using chaotic particle swarm optimization technique [14].

Here, in this paper, the system to be used is the two-area interconnected power system containing the photovoltaic grid in area 1 and the thermal system with a reheat turbine in the other area. The controllers which are used in this paper are the non-integer proportional–integral (NPI) controllers which are present in both the areas. The NPI controllers here are optimized by using the firefly algorithm, and the values of the controller gains are gathered. The researcher named as Abd-Elazim and E. S. Ali worked upon the same system by using the PI controllers [11], and here, the outcomes of the NPI controller are to challenge with the result outcomes of the PI controller and both the controllers are optimized by the firefly algorithm. The results

were found to be better than the results of PI controller in every aspect like settling time, peak overshoot, and undershoot.

2 System Investigated

The model upon which this research paper is entirely based upon consists of a thermal system in one area and the PV system on the other represented in Fig. 1. The thermal system which is considered here is the one with reheat turbine. On the other hand, the PV system here contains a photovoltaic current source which is proportional to the intensity of the sunlight. Both the systems here have the same non-integer PI controllers which are optimized by firefly algorithm. The value of the controller parameters is obtained after the optimization procedure, and thus, it helps to bring the system back to a stable condition after being subjected to 1% step load perturbation (SLP), and with the help of this, we are able to check the system transient response. The presence of area control error in both the areas helps to minimize the tie-line power flow and frequency fluctuations.

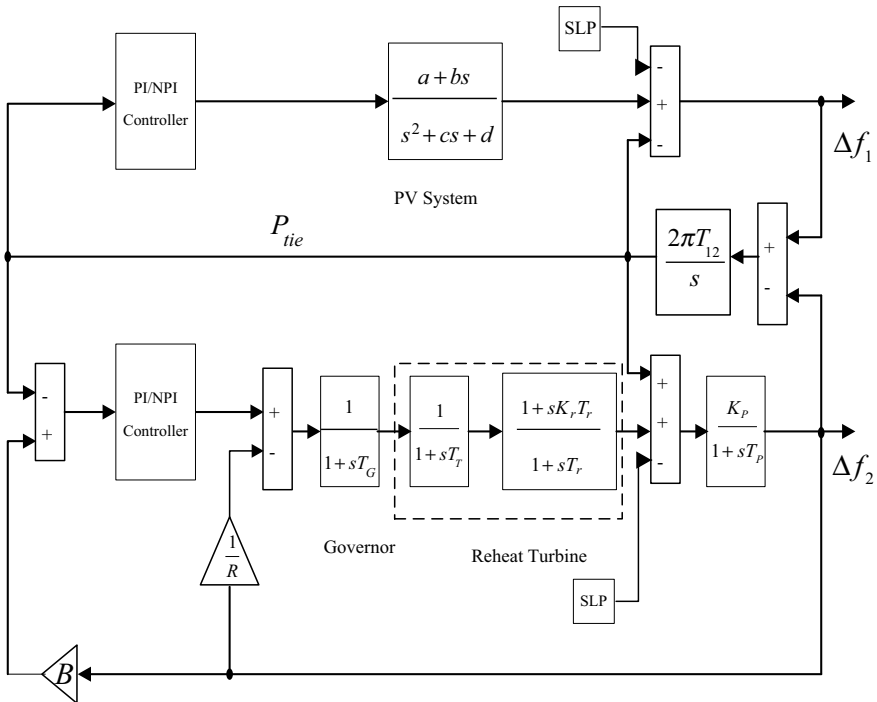


Fig. 1 PV-thermal-based interconnected system

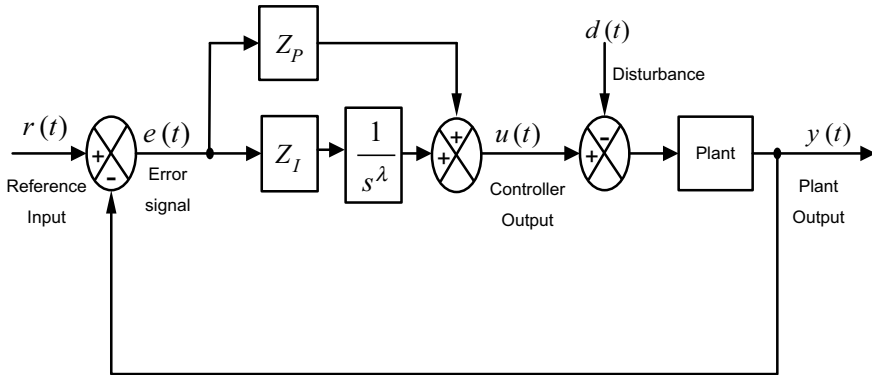


Fig. 2 Non-integer PI controller layout

3 Controller Structure (Non-integer PI Controller)

The system considered in this paper consists of the non-integer proportional–integral controllers in both the areas. The controller proposed, i.e., non-integer PI, is used so as to challenge the PI controller’s result. The controller’s performance basically depends upon the controller parameters output like Z_P , Z_I and λ . So as to get closed-loop system’s healthier performance, the values of Z_P , Z_I , and λ should be picked up properly. The proposed controller structure is represented here in Fig. 2. It is basically a single-loop constructed controller, which works upon the fractional calculus. The PI controller already exists, but it is modified a little more so as to get a better control action. The gain parameters of the proposed controller are optimized by using the firefly algorithm.

4 Optimization Technique (Firefly Algorithm)

Instead of using the simple and some of the modern optimization techniques, the nature-inspired and population-based algorithms are considered to be far as better than others. Such algorithms are inspired from many organisms or their behavior which are present in our ecosystem. Some examples of such algorithms which are derived are bacteria foraging optimization, particle swarm optimization algorithm, grasshopper optimization algorithm, symbiotic organism search algorithm, bat inspired algorithm, etc., and the firefly algorithm [15] is too considered among all these and is a population-based algorithm. The firefly algorithm was developed by a researcher named as Yang. Various fireflies are characterized on the basis of their flashing light which is produced by the biochemical process known as the bioluminescence. The flashing light of the flies may serve as the main courtship signals

for mating. The three main behavioral characteristics of fireflies that inspired the development of this algorithm are:

- i. Each and every firefly is attracted toward each other irrespective of their sex, because they are considered to be unisex in nature.
- ii. The attractiveness between the fireflies directly depends upon the brightness of each of them. Here, the less bright individual moves toward the brighter one. If it was observed that the distance is increased, as the post-consequences we can see that both attractiveness and brightness will start to decrease. Further, if it is found that both the fireflies are having the same brightness, then they move in open spaces randomly.
- iii. The light intensity of the fireflies is affected by the objective function which is to be optimized. For a bigger problem, the objective function will be proportional to the brightness (light intensity).

Attractiveness:

The attractiveness of the firefly is described by Eq. (1) given:

$$\beta_r = \beta_0 * \exp(-\gamma r^m) \tag{1}$$

where $m \geq 1$

Here

- r the distance between the two fireflies
- β_0 initial attractiveness, after satisfying the condition $r = 0$
- γ absorption's coefficient that helps to control the changes in the light intensity.

Distance and Movement:

Two flies are considered to be as i and j . The distance between these flies present at the co-ordinates x_i and x_j is treated as Cartesian distance conveyed by Eq. (2).

$$r_{ij} = \|x_i - x_j\| = \sqrt{\sum_{K=1}^d (x_{i,k} - x_{j,k})^2} \tag{2}$$

Here

- $x_{i,k}$ the K th component of the i th firefly of the spatial co-ordinates X_i .
- d the number of dimensions considered to be present
- x determines problem's dimensionality.

Whenever the firefly i gets attracted to firefly j which is brighter, then this movement is determined by Eq. (3).

$$x_i = x_i + \beta_0 * e^{-\gamma r_{ij}^2} (x_j - x_i) + \alpha \left(\text{rand} - \frac{1}{2} \right) \tag{3}$$

Here

- x_i = fireflies' current position (the first term)
- The second term is the resultant we got due to attraction
- The third term is named as randomization; it consists of a coefficient of randomization parameter as α
- In above equation rand = the function to be used to generate random numbers in between 0 and 1 range.

5 Result and Discussion

The model considered in this paper was examined under many cases with various load demands. The model was tuned using the firefly algorithm in the MATLAB software. All the cases are mentioned below to analyze the results of the system.

A. Case-1

In this case, 5% step disturbances of load demand are applied in thermal system. The result in Fig. 3 represents the time (in s) versus Δf_1 (in Hz), and Fig. 4 characterizes the time (in s) versus Δf_2 (in Hz), and Fig. 5 signifies the time (in s) versus ΔP_{tie} (in pu). These results are seen here to be compared with the results of the same system which is having PI controller as per as information [11]. It was observed that our system having non-integer proportional–integral controller which is tuned by the firefly algorithm gives the better results and improves the damping characteristics of the power system significantly. The firefly algorithm optimized controllers' gains like proportional gain, integral gains, and also the value of lambda (λ) are mentioned in Table 1. Other values such as peak overshoot (O_{sh}), settling time (T_{sh}), and peak undershoot (U_{sh}) which are noted for the deviations like Δf_1 of area 1, Δf_2 of area 2, and ΔP_{tie} in between area 1 and area 2 are represented in Table 2.

Fig. 3 Area 1 frequency abnormalities

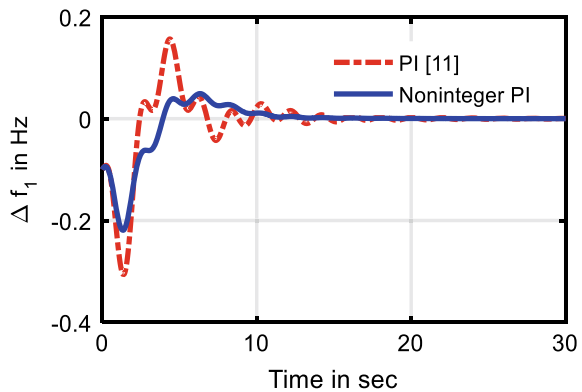


Fig. 4 Area 2 frequency abnormalities

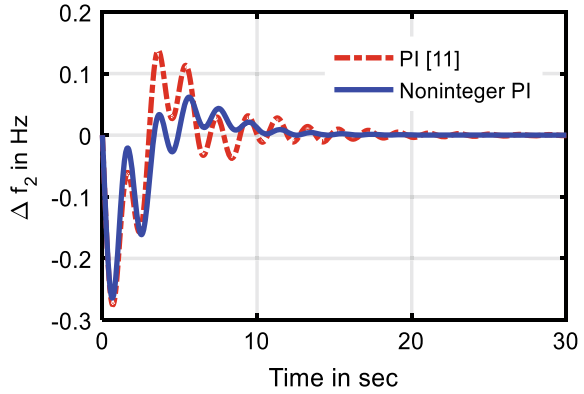


Fig. 5 Tie-line power frequency abnormalities

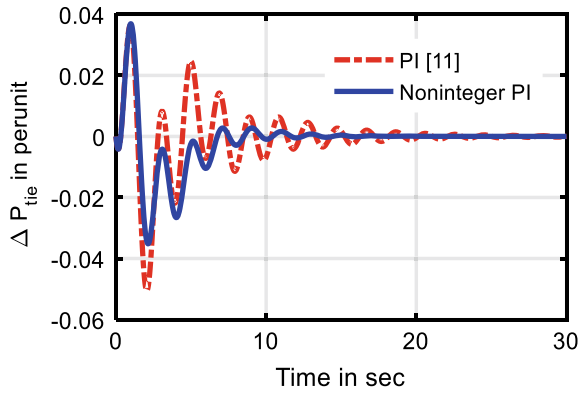


Table 1 Firefly optimized optimum controller constraints (PI/non-integer PI)

Controller	PV unit			Thermal unit		
	Z_P	Z_I	λ	Z_P	Z_I	λ
Non-integer PI	-0.4946	-0.1364	0.98	-1.0000	-0.6663	0.89
PI [11]	-0.8811	-0.5765	NA	-0.7626	-0.8307	NA

B. Case-2

Here, the load demand of the thermal system is increased by 10%. This case helps us to examine the robustness of the model and also allows us to check the robustness of the controller. The results after increasing the demand are given in Fig. 6 which is the graph between time (in s) versus Δf_1 (in Hz) of area 1, Fig. 7 represents the graph between time (in s) versus Δf_2 (in Hz) of area 2, and Fig. 8 displays the graph between time (in s) versus ΔP_{tie} (in pu). What we found here is that with the help of proposed controller, the system’s oscillations are attenuated. The results in the field of peak overshoot, settling time, and peak undershoot were thoroughly gone through,

Table 2 Comparison of response indices of different methods

Variations	Performance indices	PI [11]	Non-integer PI
ΔP_{tie}	Settling time (s)	11.0335	6.4614
	Undershoot in PU	-0.0505	-0.0352
	O_{sh} in PU	0.0364	0.0363
Δf_1	Settling time (s)	16.4262	11.0290
	Undershoot in Hz	-0.3063	-0.2194
	O_{sh} in Hz	0.1565	0.0492
Δf_2	Settling time (s)	17.4897	11.9645
	Undershoot in Hz	-0.2756	-0.2644
	O_{sh} in Hz	0.1376	0.0616

Fig. 6 Area 1 frequency abnormalities due to increase in load

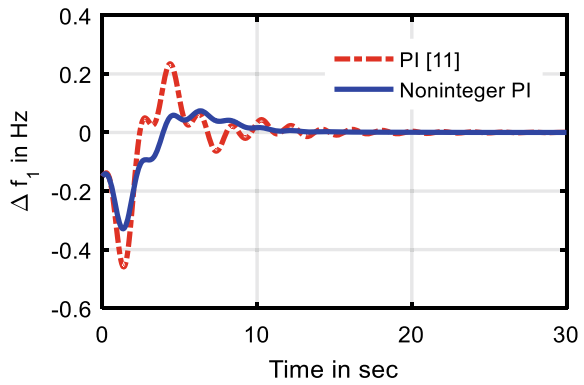


Fig. 7 Area 2 frequency abnormalities due to increase in load

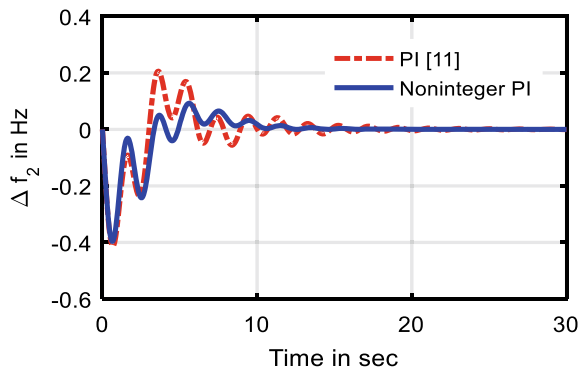
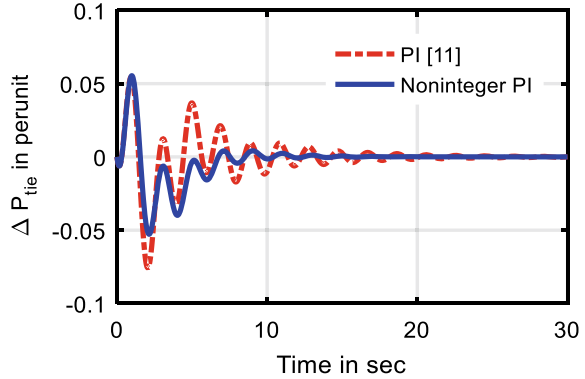


Fig. 8 Tie-line frequency abnormalities due to increase in load



and it was found that the system with the help of the non-integer PI controller still handles the transients in a better way and brings back the system stability in faster way.

6 Conclusion

This chapter is all about the model having a thermal system in one area and a PV system on the other which are working as an interconnected power system. Both the areas have their own individual non-integer proportional–integral controllers. The controllers are tuned by using a very effective optimization method known as the firefly algorithm (FA). While working on this model, a published paper was targeted and the results of the controller were challenged by using the proposed NPI controller. As far as the results/outcomes are considered, the controller NPI as expected gives a decent and the best results. Even the robustness check was cleared so easily by the NPI controller. Hence, it is concluded that the proposed NPI controller is far better than the PI controller.

References

1. Kundur P, Balu NJ, Lauby MG (1994) Power system stability and control, vol 7. McGraw-Hill, New York
2. Concordia C, Kirchmayer LK (1953) Tie-line power and frequency control of electric power systems [includes discussion]. *Trans Am Inst Electr Eng. Part III: Power Appar Syst* 72(3):562–572
3. Ang KH, Chong G, Li Y (2005) PID control system analysis, design, and technology. *IEEE Trans Control Syst Technol* 13(4):559–576
4. Khodabakhshian A, Hooshmand R (2010) A new PID controller design for automatic generation control of hydro power systems. *Int J Electr Power Energy Syst* 32(5):375–382

5. Çam Ertuğrul, Kocaarslan İlhan (2005) Load frequency control in two area power systems using fuzzy logic controller. *Energy Convers Manag* 46(2):233–243
6. Parmar, KPS, Majhi S, Kothari DP (2012) Load frequency control of a realistic power system with multi-source power generation. *Int J Electr Power Energy Syst* 42(1):426–433
7. Panda S, Mohanty B, Hota PK (2013) Hybrid BFOA–PSO algorithm for automatic generation control of linear and nonlinear interconnected power systems. *Appl Soft Comput* 13(12):4718–4730
8. Sudha KR, Vijaya Santhi R (2012) Load frequency control of an interconnected reheat thermal system using type-2 fuzzy system including SMES units. *Int J Electr Power Energy Syst* 43(1):1383–1392
9. Debnath MK, Jena T, Mallick RK (2017) Optimal design of PD-Fuzzy-PID cascaded controller for automatic generation control. *Cogent Eng* 4(1):1416535
10. Saikia LC, Sinha N (2016) Automatic generation control of a multi-area system using ant lion optimizer algorithm based PID plus second order derivative controller. *Int J Electr Power Energy Syst* 80:52–63
11. Abd-Elazim SM, Ali ES (2018) Load frequency controller design of a two-area system composing of PV grid and thermal generator via firefly algorithm. *Neural Comput Appl* 30(2):607–616
12. Alomoush MI (2010) Load frequency control and automatic generation control using fractional-order controllers. *Electr Eng* 91(7):357–368
13. Arya Y, Kumar N (2017) BFOA-scaled fractional order fuzzy PID controller applied to AGC of multi-area multi-source electric power generating systems. *Swarm Evolut Comput* 32:202–218
14. Pan I, Das S (2016) Fractional order fuzzy control of hybrid power system with renewable generation using chaotic PSO. *ISA Trans* 62:19–29
15. Yang X-S (2010) Firefly algorithm, stochastic test functions and design optimisation. arXiv preprint [arXiv:1003.1409](https://arxiv.org/abs/1003.1409)

Power Generation from Various Interconnecting Solar PV Networks for an Electrically Coupled Solar PV-TEG System Under Healthy and Partly Cloudy Condition



Sasmita Jena, Shalini Patro, Subham Subrajeet Barik, Sambit Tripathy, Keshav Krishna, Priya Ranjan Satpathy and Sanjeeb Kumar Kar

Abstract With the extensive demand for energy harvesting systems from various renewable resources, researches have been carried out in several areas among which thermo-electric generator (TEG) based system is an emerging one. In this paper, eight solar PV modules are interconnected in numerous fashions in order to investigate the behavior of the hybrid system. The transiency of the solar PV modules inside the network has been examined under Healthy Irradiance and Sectional Irradiance. Rise in solar concentration tends to decrease the solar PV module efficiency and this curse to solar PV becomes the boon to the TEG giving rise to higher power output at the terminals. Incorporation of solar photovoltaic (SPV) and thermoelectric (TE), termed as solar photovoltaic-thermoelectric (SPV-TE) hybrid system is found to be a very promising technique to broadening the utilization of solar spectrum and enhancing the power output effectively-cum-efficiently. This hybrid architecture caters electrical energy with additional thermal energy that signifies upon harnessing of solar insolation in an exceptional way.

S. Jena (✉) · S. Patro · S. S. Barik · S. Tripathy · K. Krishna · P. R. Satpathy · S. K. Kar
Department of Electrical Engineering ITER, Siksha O Anusandhan Deemed to be University,
Bhubaneswar, Odisha, India
e-mail: sasmita.jena500@gmail.com

S. Patro
e-mail: shalinipatro4@gmail.com

S. S. Barik
e-mail: subhamsubhrajitbarik@gmail.com

S. Tripathy
e-mail: aryanroy0953@gmail.com

K. Krishna
e-mail: keshavkrishnasonal@gmail.com

P. R. Satpathy
e-mail: priransat3@gmail.com

S. K. Kar
e-mail: sanjeebkar@soa.ac.in

Keywords Hybrid system (SPV + TEG) · Thermoelectric generator · Operating temperature · PV networking · Power generation

1 Introduction

Lower quantum efficiency is found to be a major demerit of solar photovoltaic cells in these days. Though only a smaller portion of incident radiation is converted into electricity directly, hence efficiency is found to be a crucial factor to be improved so that the popularity will be gained for solar Photovoltaic cells [1, 2]. Further, the non-convertible radiations will heat the panels that reduce efficiency. Hence at present cooling systems have been integrated so that the temperature could be decreased to a greater extent and enhancing the efficiency of the solar panels. Therefore realization of photovoltaic-thermoelectric systems comes into the picture [3]. Direct conversion of sunlight into electrical energy is an effective-cum-efficient way in this renewable era. Furthermore, some significant part has been absorbed as heat; to get rid of this some of the heat recovery system has been proposed in combination of conventional solar photovoltaic cells. Thus TEG has come into picture so that the non-convertible radiation which is dissipated as heat can be further converted to electrical energy. Researches have been going on such hybrid system for gaining popularity upon the renewable-based generation system [4]. The concept of solar energy spectrum energy utilization by a solar PV-Thermoelectric module and finding of an optimized geometry for SPV-TE based hybrid systems has been outlined. Current SPV-TE modules based hybrid systems are mostly based upon dye-sensitized solar cells(DSSC), a-Si based solar cells for the solar PV part while Bi-Te modules for the thermoelectric part. Also, maximum power point tracking plays a vital role in all solar PV based systems. Such combination based systems generally rely upon absorption of light spectrum by solar cells and secondly on the optimum operating temperature of the TE modules [5]. Many researchers are also working upon Perovskite solar cells which are found to be a reasonable choice for SPV-TEG based hybrid systems. It has been found that the temperature coefficient of the Perovskite solar cells is lower than 2% and this is found to be advantageous for Perovskite solar cells-TE based systems. There are near about 1% difference in Perovskite solar cell-TE based system (18.8%) and only Perovskite solar cells (17.9%). Also by altering the thermal concentration the volume of thermoelectric material can be lowered and at the same time cost will be cut-off remarkably. For analyzing such influence of thermal concentration upon the desired hybrid system a 3-D numerical model has been also developed [6].

In this paper, the solar PV modules are connected in parallel in order to form an array that is helpful in system requiring higher amount of power. In this paper, eight modules are connected in several manners in order to analyze and predict system performance. The array thus formed by the SPV modules is connected with TEG in order to produce power. Solar panels receive solar irradiance to generate power which can be termed as conversion of light energy into electrical energy. But the demerit lies upon the heat lost at the panel surface which causes a rise in surface temperature.

This, in turn, declines the solar PV performance at a greater rate and the panel suffers from lower quantum efficiency. Thus the TEGs use this lost heat and convert this heat energy into electricity. Hence the power generated using solar irradiance and power generated by using the excess heat of panel gives a significant output at the solar panel terminals. This system also aims to provide another perspective of understanding the volatility of SPV-TEG hybrid module under partly cloudy conditions. The system is tested for single SPV module integrated with TEG and then tested upon five different types of SPV networking structures with integrated TEG. The entire study has been carried out using eight solar PV modules with networking namely:

- Network I
- Network II.

The entire study is subjected to be tested under two types of irradiance namely:

- Healthy Irradiance (HI)
- Sectional Irradiance (SI).

Though daily solar insolation which is an inevitable part of solar energy to generate power is very reliant to time, factually it has an impact upon the temperature of SPV-TEG hybrid system, consequently the power generation and hence the efficiency of the system. Therefore, light has been put upon the implication of changing weather conditions on the system performance and power generation. This Sectional Irradiance (SI) is further subdivided into two parts such as:

- 1/2nd (50% shaded)
- Fully shaded (100% shaded).

The paper organization is as follows. In Sect. 2, the hybrid PV-TEG system is modeled, and hence the theoretical approach is outlined, Sect. 3 is followed by the interconnection of solar PV panels with TEG integration. Section 4 consists of power generation from the hybrid interconnection.

2 System Modeling and Description

The modeling of thermoelectric generator (TEG) and solar PV modules (SPV) have been performed by insertion of the corresponding number of modules in parallel and series as per the requirement. After being designed individually, both the systems have been combined in order to perform the study upon the hybrid system. The power generated from SPV array, i.e., conversion of light energy into electrical energy and power generated from TEG, i.e., conversion of lost heat into electrical energy is added in order to obtain the required power from the hybridized SPV-TEG system. Generally, the inconstancy nature of weather specifically partly cloudy conditions plays a vital role in the system's cohesion and hence marking critical issues like power generation, efficiency, etc. The model is described in individual subsection namely:

- Modeling of Solar PV array
- Modeling of TEG.

2.1 Modeling of Solar PV Array

Solar irradiation and temperature on the solar PV module surface are solely responsible for the characteristics of SPV array. As the solar irradiance upon the SPV array is increased, the power generated from SPV array is also increased. In order to construct an SPV array, number of SPV modules need to combine in a particular fashion either in series or parallel to obtain the requisite power. The equivalent circuit of the solar cell is shown in Fig. 1.

The output current of the solar PV module, i.e., I_{pv}

$$I_{pv} = Np * I_{ph} - Np * I_o \left[\exp \left\{ \frac{q * (V_{pv} + I_{pv}R_s)}{NsAkt} \right\} - 1 \right] - I_{sh} \tag{1}$$

where $k =$ Boltzmann’s constant $= 1.3805 \times 10^{-5}$ J/K, $A =$ ideality factor of the solar PV cell depend on PV manufacturing technology, some of them are presented in Table 1, $T =$ operating temperature of the module, $q = 1.6 \times 10^{-19}$ C

Fig. 1 Equivalent circuit of solar PV module

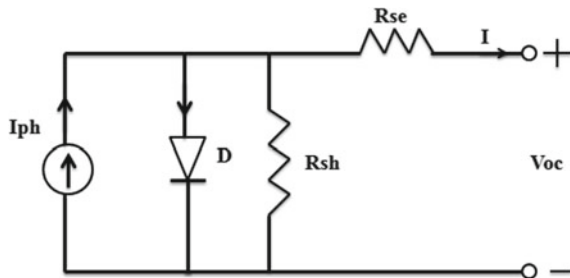


Table 1 The specification of solar PV module used (WAREE solar PV modules)

Parameters	Values
Maximum power voltage	17.47 V
Maximum power current	2.86 A
Maximum power	50 W
Short circuit current (I_{sc})	3.1 A
Open circuit voltage (V_{oc})	21.57 V

2.2 Modeling of Thermoelectric Generator

The working of TEG constitutes of three elementary thermoelectric effects with two accessorial effects. The three elementary effects are named as Seebeck effect, Peltier effect, and Thomson effect while the accessorial effect can be named as Joule effect and Fourier effect. Seebeck effect is responsible for electromotive force (EMF) and Peltier heat, Thomson heat and Joule heat are caused by the effect of Peltier, Thomson, and Joule respectively. As a matter of fact, Peltier effect is not an interface effect; it produces heat only at the end sides of the semiconductors. Volumetric effects like Thomson and Joule heat production are pretended to be uniformly transferred to the cold and hot junctions of the semiconductor elements [7]. Though Thomson effect is very small it is often neglected in many cases.

For steady-state analysis at cold and hot junction of TEG an energy balance equation is used which can be expressed as follows:

Mathematically

$$Q_h = \alpha * T_h * I - k_{tc} \Delta T - 0.5I^2 R \quad (2)$$

$$Q_c = \alpha * T_c * I - k_{tc} \Delta T + 0.5I^2 R \quad (3)$$

The electrical current can be expressed as follows:

$$I = \frac{\alpha \Delta T}{(1 + n)R} \quad (4)$$

The short circuit current is the maximum current at a load voltage of zero, i.e., $V_L = 0$. Hence can be written as follows:

$$I_{SC} = 2I_m = \frac{2W_m}{V_m} \quad (5)$$

Finally, the voltage of TEG can be expressed by using Ohm's Law, and the corresponding equation obtaining short circuit current and current through TEG, i.e.,

$$V = -R(I - I_{SC}) \quad (5)$$

A model of TEM specified by TEPI-12656-0.6 has been used over here to model the hybrid system and the behavioral analysis has been conducted. The parameter specifications of the thermoelectric Module (TEM) have been listed in Table 2. The constraints that have been considered for modeling are presented in Table 3.

Table 2 TE module parameters

Parameters	Values
Open circuit voltage (V)	8.8
Cold junction temperature (°C)	30
Hot junction temperature (°C)	300
Load resistance (Ω)	1.25
Load output voltage (V)	4.27
Load output power (W)	15
Load output current (A)	3.52
Heat flow density (W/cm^2)	~12
Heat flow across the module (W)	~370

Table 3 The modeled parameters at steady state

Parameters	Symbols	Corresponding values
Seebeck coefficient	α	0.035 V/K
Resistance	Ω	1.22
Thermal conductivity	k_{tc}	20.91 W/K
Figure of merit	Z	$0.387 \times 10^{-6} K^{-1}$

3 Results and Discussion

The solar PV panel receives solar irradiation and generates electricity directly through the photo-voltaic effect. Though solar panels are considered as less quantum efficient due to excess heat absorption at the surface, the heat recovered from the module surface is considered to be reused and generate power. Thence thermoelectric generator comes into picture that effectively as well as efficiently use this lost heat and produce electricity. The solar PV modules and the TEG combinedly deliver substantial amount of power. This makes the solar PV modules much more efficient-cum-effective. The system is tested under two types of irradiance namely:

- Healthy Irradiance (HI)
- Sectional Irradiance (SI).

The HI shows the system receiving sunlight at Standard Testing Condition (STC), i.e., at $1000 W/m^2$ and the modules receiving solar irradiance generate power and subsequently the heat absorbed by the modules is further reused by the TEG that are connected in parallel. The system is tested for only solar PV based, only TEG based and both SPV-TEG based sources in order to verify the results. All the connections have been subjected to be tested under sectional irradiance (partly cloudy condition). The following types of sectional irradiance (SI) are considered over here.

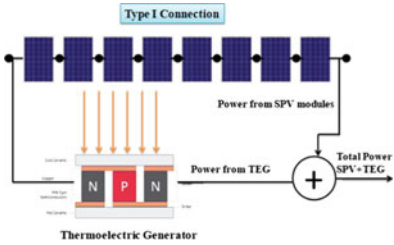
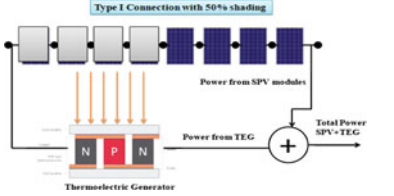
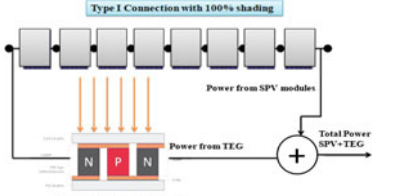
- 1/2nd (50% shaded) and
- Fully shaded (100% shaded).

3.1 Type I Network: Table 4

Healthy irradiance (HI) means system performance during non-shading conditions. During the experiment the irradiance varies from 900 to 1000 W/m²; that’s why the theoretical analysis is also done at 1000 W/m² in MATLAB/Simulink.

The power obtained from hybrid SPV and TEG system is much significant than that of only SPV based or only TEG based system which can be seen in Fig. 4. The result for every sub-conditions of SI has been shown in Fig. 2, 3 and 4. It can be interpreted from the graph that the every time shading occurs, power is decreasing gradually. It can also be seen that the power obtained from SPV and TEG based hybrid system is always very significant than that of only SPV based system and only TEG based system no matter what type of shading occurs.

Table 4 Type I network

Type of connection	Connection diagram	Output values obtained	
At healthy irradiance (non-shading condition)		Experimental 1. Only SPV 322 W 2. Only TEG 3881 W 3. SPV + TEG 4203 W	Theoretical 1. Only SPV 326 W 2. Only TEG 3886 W 3. SPV + TEG 4212 W
At sectional irradiance 1/2nd section (50% shaded)		Experimental 1. Only SPV 300.9 W 2. Only TEG 2395.5 W 3. SPV + TEG 2696.4 W	Theoretical 1. Only SPV 302.3 W 2. Only TEG 2398 W 3. SPV + TEG 2700 W
At Sectional Irradiance Whole section (100% shaded)		Experimental 1. Only SPV 275 W 2. Only TEG 1898.3 W 3. SPV + TEG 2173.3 W	Theoretical 1. Only SPV 280 W 2. Only TEG 1902 W 3. SPV + TEG 2182 W

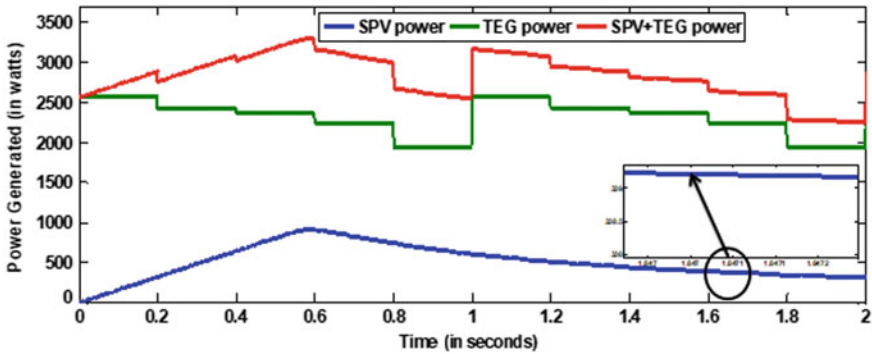


Fig. 2 Power obtained using Type-I network at healthy irradiance (HI)

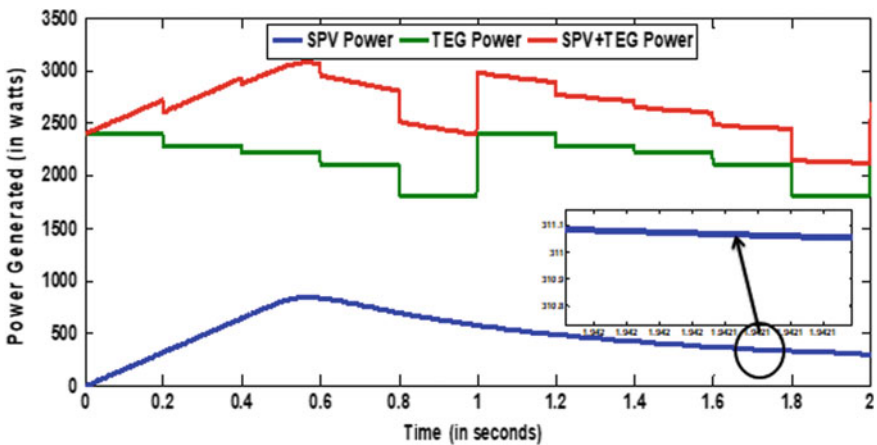


Fig. 3 Power obtained due to sectional irradiance (SI)-1/2nd of shading

3.2 Type II Network: Table 5

The connection diagram has shown below with showing the connection diagram.

The connection diagrams have been shown with values that are obtained experimentally and theoretically that can be seen in Table 5. The modeling was done by using MATLAB/Simulink and the experiment has been carried out at the rooftop of ITER, Siksha O Anusandhan (Deemed to be university) that can be seen in Fig. 8.

It can be interpreted from the graph that the every time shading occurs, power is decreasing gradually. It can also be seen that the power obtained from SPV and TEG based hybrid system is always very significant than that of only SPV based system and only TEG based system no matter what type of shading occurs. It can also be outlined that the TEGs work according to the sunlight incident on the SPV modules. During HI, the solar irradiance has incident on panel that in turn raising the temperature of

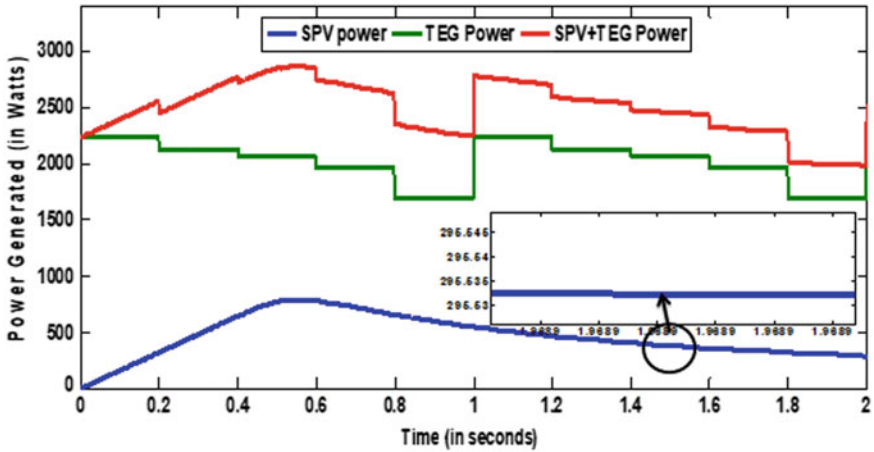


Fig. 4 Power obtained due to sectional irradiance (SI) 100% of shading

Table 5 Type II network

Type of connection	Connection diagram	Output values obtained	
At healthy irradiance (non-shading condition)		Experimental 1. Only SPV 120.85 W 2. Only TEG 3881 W 3. SPV + TEG 4001.85 W	Theoretical 1. Only SPV 123.7 W 2. Only TEG 3886 W 3. SPV + TEG 4010 W
At sectional irradiance 1/2nd section (50% shaded)		Experimental 1. Only SPV 115.66 W 2. Only TEG 2395.5 W 3. SPV + TEG 2511.16 W	Theoretical 1. Only SPV 117.7 W 2. Only TEG 2398 W 3. SPV + TEG 2516 W
At sectional irradiance whole section (100% shaded)		Experimental 1. Only SPV 275 W 2. Only TEG 1898.3 W 3. SPV + TEG 2173.3 W	Theoretical 1. Only SPV 280 W 2. Only TEG 1902 W 3. SPV + TEG 2182 W

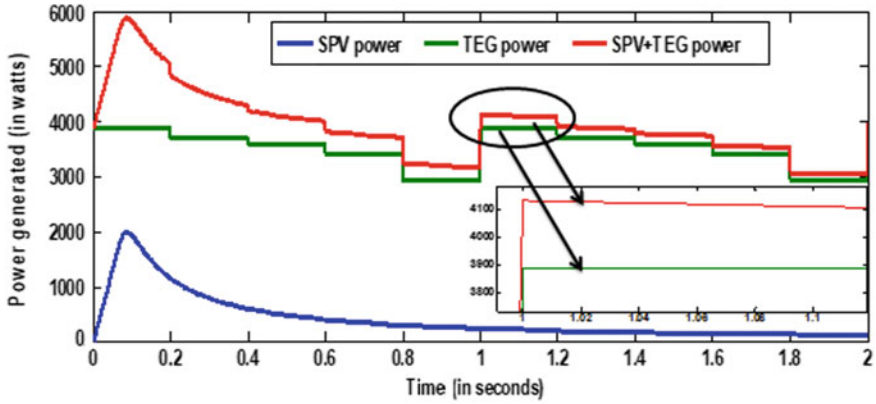


Fig. 5 Power obtained using Type-Ii network at healthy irradiance (HI)

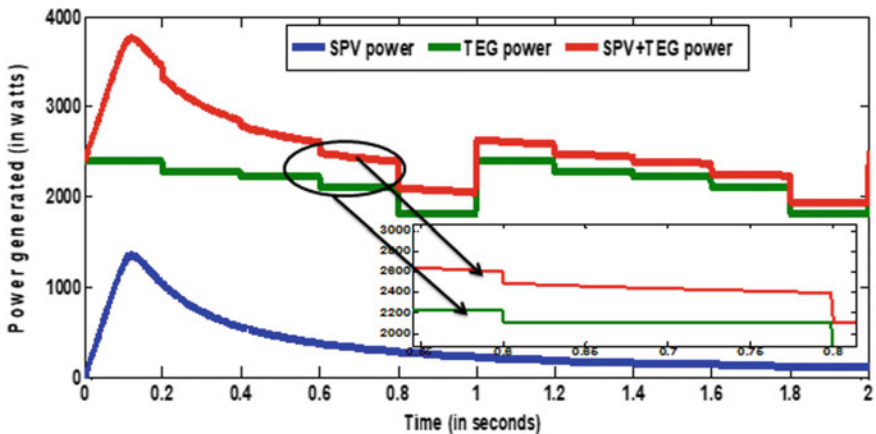


Fig. 6 Power obtained due to sectional irradiance (SI)-1/2nd of shading

the SPV module surface; and hence yields a significant amount of power from the hybrid system such as for Network = 4212 W (4.212 Kw) and Network IV = 4010 W (4.010 Kw), respectively. Whereas during SI, the solar irradiance became lesser than that of HI; this leads to lesser power generation from TEG and consequently from hybrid SPV + TEG. Because lesser is the irradiance, lesser what will be absorbed and lesser will be the power generation.

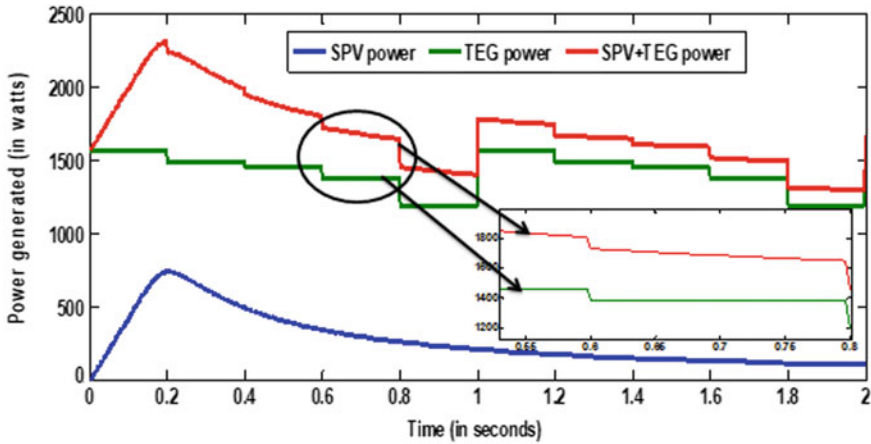


Fig. 7 Power obtained due to sectional irradiance (SI) 100% of shading

4 Experimental Setup for the Proposed Solar PV Networks

The experiment was carried out at the rooftop of ITER, Siksha O Anusandhan (Deemed to be University), Bhubaneswar, India that can be seen in Fig. 8.

Eight PV modules are interconnected under earlier mentioned networking structures namely Network-I and Network-II. All the modules are interconnected as per the connection diagram is shown in Tables 4 and 5. The experiment was carried out under HI and SI. Under HI, the irradiance was found to be varied between 850 and 950 W/m². The experiment has been conducted in April though in summer, the irradiance received by the Solar PV module is higher consequently rising the surface temperature. This, in turn, lowers the module efficiency. To overcome this lowering of quantum efficiency, the TEG is connected in order to use the higher temperature and generate power. The power obtained at the output terminals will be the combination of power generated from solar PV module using photovoltaic effect and power generated from TEG using thermoelectric effect.

5 Conclusion

Thermoelectric Generator is integrated with solar PV system in order to process the lost heat by thermoelectric effect. The conversion of light energy into electricity by photoelectric effect and converting heat into electricity by thermoelectric effect combinedly generate significant amount of power from solar PV array. During HI, the power generated is much higher than that of SI conditions. Because the irradiance thud incident on the modules during HI is higher that it tends to excessive heat absorption at the junction of TEG. The experimental and theoretical evaluation has



Fig. 8 Experimental setup of the system

been conducted in order to verify the output power for only SPV based system, only TEG based system, and hybrid SPV-TEG based system. This study clearly states that the power during hybridization is much significant as compared to the other two. The augmentation of the solar concentration decreases the SPV module efficiency and this, in turn, helpful for TEG for increasing its efficiency. This concept has been validated in this study. Employment of hybrid SPV-TEG based system delivers steady power for varying weather conditions than only SPV/only TEG. Elementary understanding of the overall output performance of the studied system has been made by consideration of thermoelectric effect and can be implemented in the places where rapid fluctuation of solar insolation and partly cloudy conditions degrades the solar PV array output with the procurement of stability.

References

1. Jena S, Kar SK (2018) Setting a fostered energy network by decarbonizing the grid: Hybridization, control, and future solutions upon storage. *Int J Energy Res*
2. Wang N (2017) Photovoltaic–thermoelectric hybrid energy conversion. In: *Thermoelectric energy conversion: basic concepts and device applications*
3. Zhang J, Xuan Y, Yang L (2016) A novel choice for the photovoltaic–thermoelectric hybrid system: the perovskite solar cell. *Int J Energy Res* 40(10):1400–1409
4. Xu L, Xiong Y, Mei A, Hu Y, Rong Y, Zhou Y, Hu B, Han H (2018) Efficient Perovskite photovoltaic-thermoelectric hybrid device. *Adv Energy Mater* 8(13):1702937
5. Willars-Rodríguez FJ, Chávez-Urbiola EA, Vorobiev P, Vorobiev YV (2017) Investigation of solar hybrid system with concentrating Fresnel lens, photovoltaic and thermoelectric generators. *Int J Energy Res* 41(3):377–388
6. Le Pierrès N, Cosnier M, Luo L, Fraisse G (2008) Coupling of thermoelectric modules with a photovoltaic panel for air pre-heating and pre-cooling application; an annual simulation. *Int J Energy Res* 32(14):1316–1328
7. Francioso L, De Pascali C (2017) Thermoelectric energy harvesting for powering wearable electronics. In: *Thermoelectric energy conversion: basic concepts and device applications*

Constraint Based Design of Multi-stage Core Type Multipole Field Electromagnetic Launching System (CMFELS) and Its Possible Use in the Catapult System



Srichandan Kondamudi  and Sandhya Thotakura

Abstract Some of the issues in linear drive are critical combination of an air gap, inadequate use of magnetic flux, external vibrations with disturbances, low dissipation of thermal energy, etc. With linear drives, these problems have become drawbacks to extend them to any application. Multipole Field Electromagnetic Launching System (MFELS) is a system in the linear electromagnetic drive family that can provide enough linear force with minimal problems. Core type MFELS is considered for this paper and an attempt is made to implement Core type MFELS for the application of the launching system for aircraft catapult. A step-by-step iterative type design algorithm is developed. Exit velocity is considered to be the objective feature and the accelerating coil's size, diameter and thickness are considered to be constraints. Comparison results for various pole cases were tabulated.

Keywords Catapult electromagnetic launch · Electromagnetic launch · Multi-field system · Exit velocity · Flux density · Lorentz force · Career-based aircraft

1 Introduction

The Electromagnetic Catapult (EMCAT) device can be scalable and appropriate for a variety of applications, which may be integrated into the company within a reasonable time limit based on proven models. In view of the brief writing review on the electromagnetic aircraft catapult system [1–5], each current system or structure is finished utilizing direct electric engines.

For keeping up a strong errand at speeds over the state-of-the-craftsmanship in the airship catapult framework, new structures must be created which can defeat the issues and could impel the airship with higher power/volume proportion. Multipole

S. Kondamudi (✉) · S. Thotakura
GITAM Deemed to be University, Visakhapatnam, India
e-mail: srichandank@gmail.com

S. Thotakura
e-mail: sandhyathotakura@gmail.com

© Springer Nature Singapore Pte Ltd. 2020
R. Sharma et al. (eds.), *Innovation in Electrical Power Engineering, Communication, and Computing Technology*, Lecture Notes in Electrical Engineering 630,
https://doi.org/10.1007/978-981-15-2305-2_40

Field Electromagnetic Launching System (MFELS) appears to have brilliant confirmation as an idea for what's to come; its rational affirmation predicts the progress of an outline that is enough solid to be able to pass on the payloads. Concerning the writing overview of the Multipole Electromagnetic propeller [6–10], proposed the basic blueprint and examination of Multipole Field Electromagnetic Propeller. In electromagnetic Aircraft Catapult system, the multipole field Electromagnetic propelling system can be an interesting option. In this paper, an attempt is made to implement the concept of Core type MFELS (CMFELS) for aircraft propelling system. A design algorithm for the CMFELS is developed considering various constraints. Comparison results for various pole cases were tabulated. In addition, the inductance value obtained in the FEM analysis was validated. After the approval, the performance of CMFELS is examined in the electromagnetic acceleration of aircraft for conceivable use as a propeller.

2 Core Type Multipole Field Electromagnetic Launching System

2.1 Basic Design and Analysis of CMFELS

The key components of CMFELS are an electromagnetic field (primary) and an electrically conductive body (secondary). The magnetic field is provided by arranging the coils around the tube, to provide an equal amount of magnetic field for the conductive body in all directions, which makes the conductive body to levitate from all directions, leading to a uniform alignment of air gap throughout the cylinder. Figure 1 shows the basic arrangement for CMFELS. The coils are excited using DC voltage, which produces a magnetic field in the armature (which is fixed). Based on the depth of diffusion of flux lines, Lorentz force is exerted on the moving part.

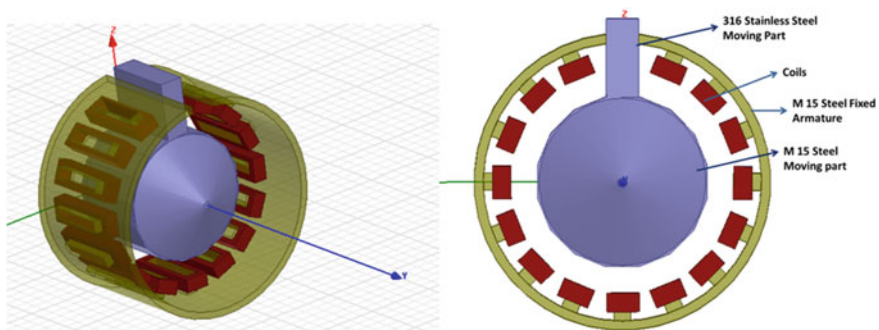


Fig. 1 Three-dimensional view of proposed single stage CMFELS with core

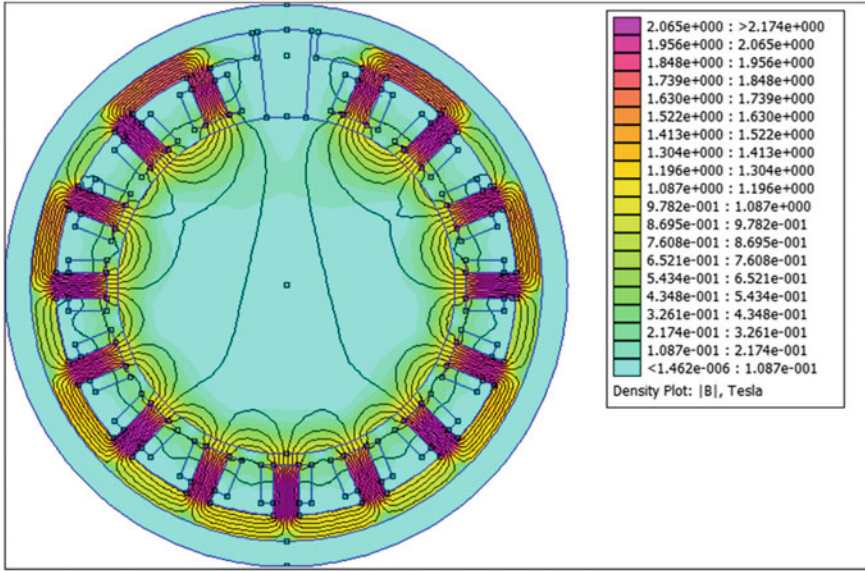


Fig. 2 Flux distribution in CMFELS

Based on the different iterations and results, if the coils are excited alternatively the flux penetration depth in the secondary will increase.

Using FEMM, the flux lines are attained as shown in Fig. 2. Since a major part of the flux is concentrated inside the armature, the amount of magnetic flux utilization will increase. The investigation begins with a single coil’s flux linkages and extended to all the coils. The magnetic parameters need more careful definitions as the magnetic flux flow in more regions with different areas. Based on Fig. 2, flux is initiated in the coil which crosses the air gap and then divides in the secondary similarly.

Using flux distribution method, expression for permeance is developed with the help of Fig. 2. In the flux path, six unique parts are distinguished by material, region and area and. For each part, permeance values are derived [11–14].

$$P_{13} = \frac{2\sqrt{2}\mu_o\mu_r \left(w_p h_m - \frac{8\sqrt{2}h_m l_p w_p}{\sqrt{(6l_p)^2 + (2h_m)^2}} \right)}{\pi \sqrt{(2l_p)^2 + \left(\frac{15h_m}{18}\right)^2}} \tag{3}$$

$$P_{14} = \frac{\mu_o w_p l_p}{(l_c + l_g)} \tag{4}$$

$$P_{15} = \frac{8\mu_o w_c l_p}{\pi} \left(\frac{3(l_c + l_p)}{\sqrt{(3l_p)^2 + (l_c + l_p)^2}} - \frac{2l_c}{\sqrt{(2l_p)^2 + l_c^2}} \right) \times \frac{1}{\sqrt{\left(\frac{5l_p}{2}\right)^2 + \left(\frac{2l_c + l_p}{2}\right)^2}} \tag{5}$$

$$P_{16} = \frac{8\mu_0 w_c l_c}{\pi} \left(\frac{3(h_c)}{\sqrt{(h_c)^2 + (2l_c)^2}} - \frac{4(h_c + t)}{\sqrt{(2l_p)^2 + l_c^2}} \right) \times \frac{1}{\sqrt{\left(\frac{3l_c}{2}\right)^2 + (0.9h_c + 0.1t)^2}} \tag{6}$$

Flux path 2:

$$P_{21} = \frac{2\mu_0 \mu_r w_c (h_c - t)}{5l_c} \tag{7}$$

$$P_{22} = \frac{8\mu_0 w_c}{\pi} \left(\frac{(4h_c + t)(3l_g + 2h_m)}{\sqrt{(3(4h_c + t))^2 + (5(3l_g + 2h_m))^2}} - \frac{(2h_c + 3t)l_g}{\sqrt{((2h_c + t))^2 + (5(l_g))^2}} \times \frac{1}{\sqrt{\left(\frac{6l_g + 2h_m}{6^2}\right)^2 + \left(\frac{3h_c + 2t}{5}\right)^2}} \right) \tag{8}$$

$$P_{23} = \frac{32\mu_0 \mu_r l_p h_m w_c}{\pi} \left(\frac{1}{\sqrt{(6l_p)^2 + (2h_m)^2}} \times \frac{1}{\sqrt{(2l_p)^2 + \left(\frac{2h_m}{3}\right)^2}} \right) \tag{9}$$

$$P_{24} = \frac{\mu_0 l_p w_p}{(l_c + l_g)} \tag{10}$$

$$P_{25} = \frac{8\mu_0 l_p w_c l_c}{\pi} \left(\frac{2}{\sqrt{(2l_p)^2 + (l_c)^2}} - \frac{3}{\sqrt{(5l_p)^2 + (3l_c)^2}} \right) \times \frac{1}{\sqrt{\left(\frac{3l_p}{2}\right)^2 + \left(\frac{4l_c}{5}\right)^2}} \tag{11}$$

$$P_{26} = \frac{8\mu_0 w_c l_c}{\pi} \left(\frac{(4h_c + t)}{\sqrt{(5l_c)^2 + (4h_c + t)^2}} - \frac{3(2h_c + 3t)}{\sqrt{(2h_c + 3t)^2 + (3l_c)^2}} \right) \times \frac{1}{\sqrt{\left(\frac{4l_c}{5}\right)^2 + \left(\frac{3h_c + 2t}{5}\right)^2}} \tag{12}$$

Identically, the permanence for all the flux paths are been derived.

Equivalent Reluctance of Flux path 1

$$\mathfrak{R}_{Fluxpath1}(x) = \frac{1}{P_{11}} + \frac{1}{P_{12}} + \frac{1}{P_{13}} + \frac{1}{P_{14}} + \frac{1}{P_{15}} + \frac{1}{P_{16}} \tag{13}$$

Equivalent Reluctance of Flux path 2

$$\mathbb{R}_{Fluxpath2}(x) = \frac{1}{P_{21}} + \frac{1}{P_{22}} + \frac{1}{P_{23}} + \frac{1}{P_{24}} + \frac{1}{P_{25}} + \frac{1}{P_{26}} \tag{14}$$

Equivalent Reluctance of single coil is

$$\begin{aligned} \mathbb{R}_{Total}(x) = & \mathbb{R}_{Fluxpath1}(x) + \mathbb{R}_{Fluxpath2}(x) + \mathbb{R}_{Fluxpath3}(x) + \mathbb{R}_{Fluxpath4}(x) + \\ & \mathbb{R}_{Fluxpath5}(x) + \mathbb{R}_{Fluxpath6}(x) + \mathbb{R}_{Fluxpath7}(x) + \mathbb{R}_{Fluxpath8}(x) + \\ & \mathbb{R}_{Fluxpath9}(x) \end{aligned} \tag{15}$$

This methodology is extended to discover the reluctance equations for x , y , and z -plane. The total inductance of the CMFELS of the secondary in z -plane is presented as

$$L_z(x) = \frac{N^2}{\mathbb{R}_{total}(x)} \tag{16}$$

The Lorenz force stems from the principles of transfer of electromechanical power as

$$F_{(x,y,z)} = \frac{1}{2} I^2 \frac{dL_{(x,y,z)}(x)}{dx} \tag{17}$$

where

N is coil turns, I is coil current, (l_c is coil length, l_g is air gap length, h_c is coil height, l_p is projecting object length, h_p is height of the projecting, h_m is metallic sheath's height, w_c is coil width, w_p is the projecting object's width, t is coil thickness, x is a secondary position) in meters, μ_o is air permeability, μ_{rp} is projecting object's permeability.

2.2 Inductance and Lorentz Force Expression

The above derived Lorentz force Eq. (16) indicates specifically how the CMFELS scale with the adjustment in inductance and current qualities. To illustrate the effect of the inductance on the drag force (F_x) and lift force (F_z) on the secondary in the xyz plane, the cause for build-up drag and lift force shall be analyzed. From the observations, the drag force (F_x) and lift force (F_z) are developed by the vertical and horizontal flux components in the secondary. On the other hand, the Lateral axis force component (F_y) also affects the secondary of the system. Based on the equation of Lorentz force (17), the rate of change of inductance is the main cause for generating a force in any direction. It is observed that the rate of change in inductance is less in x -plane and z -plane (concerning FEM analysis), which leads to a condition that $F_y \gg F_x \gg F_z$. Regarding the above condition, the most prevailing force is Lateral

Table 1 Dimensions of simulation and properties of the material

Symbol	Description	Value	Units
d_w	Wire diameter	5.8	(mm)
t	Coil thickness	0.4	(m)
l_g	Length of air gap	0.001	(m)
d_p	Projectile diameter	1.28	(m)
h_m	Thickness of sheet	0.12	(m)
w_p	Side length of the secondary	0.25	(m)
N	Number of turns	900	(1)
h_c	Height of the coil	0.066075	(m)
v	Speed	50	(m/s)
μ_{iron}	Permeability of the pure iron	5000	(Vs/Am)

axis (F_y), due to which the secondary will be swift in y -plane. Whereas the lift force component and drag force component will improve the uniform alignment of the air gap, decrease the extra vibrations.

3 Verification: Proposed Equation Versus FEM

Dimensions in Table 1 are used in 3D FEM simulations in this section for the verification of the analytically derived inductance equation and Lorentz force equation. It is observed that from the derived equations, the maximum and minimum CMFELS inductances are 5.2879 mH and 0.0283 mH, respectively. From the FEM, the maximum inductance value attained is 5 mH and the minimum inductance value observed is 0.0235 mH.

Figure 3 demonstrates the analytically calculated inductance and FEM simulation results for chosen dimensions and speed. The derived equation and 3D FEM results agree well. Figure 4 displays the distribution of flux density in the CMFELS.

4 Proposed Design Algorithm of CMFELS

In this segment, a design algorithm is proposed. The main objective in CMFELS' design is to achieve required exit velocity, taking into account the materialistic aspects such as coil length, coil turns, coil thickness, and coil height as the constraints. In the CMFELS design process, the objective function is

$$v_{\text{max}} = f(w_c, h_c, t, l_g, l_p w_p, N, \text{nop}, \text{nol}, m_g) \quad (18)$$

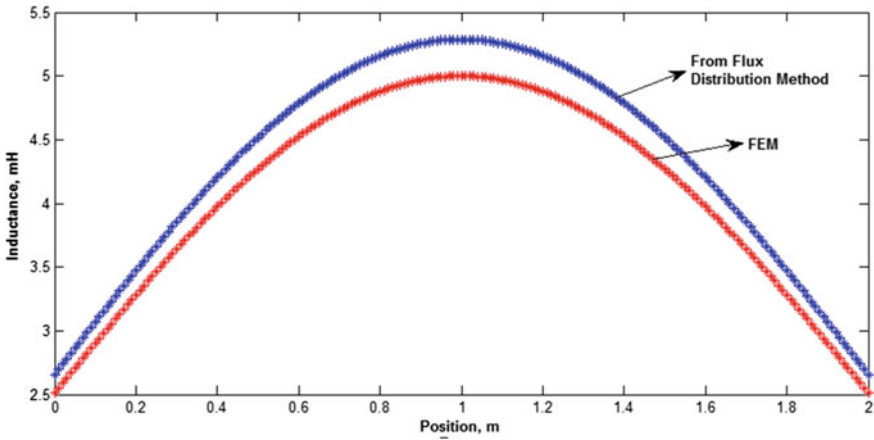


Fig. 3 Position versus inductance

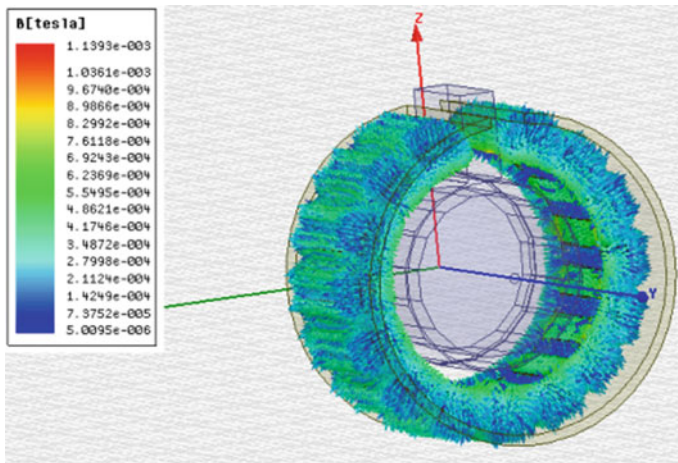


Fig. 4 3D FEM simulations of single stage CMFELS

where nol is layers in coil; nop is poles count; m_g is moving part's weight [13]. The final dimensions of the CMFELS are performed at the point where the industry gives the required speed. Using the flowchart shown in Fig. 5, the development process is illustrated. User-defined parameters are initiated such as required exit velocity, projectile mass, moving part's length and applied voltage. So the moving part's diameter is determined depending on the number of poles. The coil thickness and coil length are the factors that have boundary conditions as $0 < t < t_{max}$ and $0 < l_c < d_b$.

If the error is within a reasonable limit between the required velocity and the measured velocity, the problem converges by meeting the constraints.

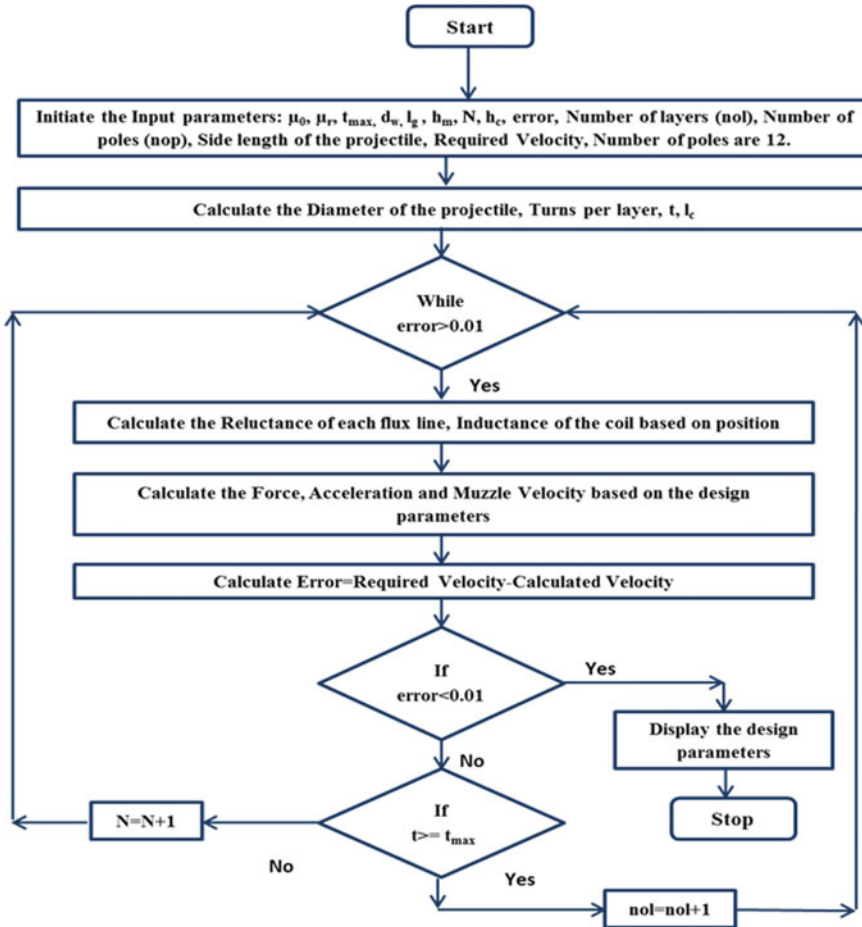


Fig. 5 Proposed design flowchart of CMFELS

5 Results and Analysis

Table 2 describes the inductance profile for different number of coils. As the number of poles has increased, it is observed from Table 2 that the minimum inductance decreases. And the peak inductance is different for some of the cases because to obtain the same necessary velocity when the pole increases the number of turns decreases. A

Table 2 Profile of inductance for different number of poles

Description	6 poles	8 poles	10 poles	12 poles	16 poles
L_{min} (H)	0.0072	0.0057	0.0048	0.0041	0.0038
L_{max} (H)	0.0169	0.0170	0.0176	0.0172	0.0171

step-by-step interactive process is created based on the design algorithm, and results are tabulated for different conditions.

Table 3 shows the design values of CMFELS in different cases. It is observed that the coil turns, coil height, coil thickness, and iteration count decreased when the number of poles increases. And the required speed, applied voltage, and projectile mass are maintained the same in all cases.

Figure 6 expound the relationship between iterations count and speed variations. It is witnessed that when the pole number increases, the force produced has increased and the required output velocity is achieved in fewer iterations.

Table 3 Design values for various poles in CMFELS

Description	6 poles	8 poles	10 poles	12 poles	16 poles
Diameter of projectile (mm)	40	52.2	64.7	77.27	102.51
Velocity required (m/s)	10	10	10	10	10
Velocity obtained (m/s)	10.0	9.99	10.19	10.06	10.018
Force obtained (N)	101.74	99.95	103.94	101.20	100.324
Turns/layer	22	22	22	22	22
Coil turns	352	286	242	220	176
Layers in coil	16	13	11	10	8
Coil height (mm)	5.9	4.7	4.3	3.568	3.178
Coil thickness (mm)	10	10.1	9.6	10.12	8.225
Iteration count	329	263	240	197	173

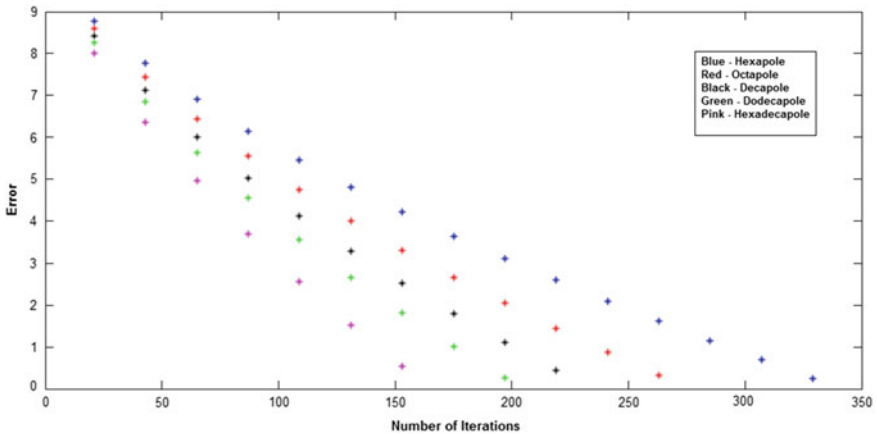


Fig. 6 Number of Iteration versus error for different number of poles

6 CMFELS Implementation for the Catapult System

Figure 7a, b shows the configuration of a CMFELS system for applying the Aircraft Catapult system. All the coils are connected in series, to attain contrast flux direction in adjacent coils. The coils are ready to accelerate with a 600 μ F capacitor bank loaded with 1 kV. Based on the values obtained in Table 2, the drag force and lift force will help secondary to levitate and move in the field without friction. Now, from Fig. 2, it is observed that because the magnetic field is uniform on walls of the secondary, the secondary will levitate uniformly though the system. The distance between each stage is 90% of secondary length, such that every time secondary is levitated by two stages of coils.

In Fig. 8, the force characteristics are plotted to validate the proposed model. The proposed model can be scaled to any velocities. Nevertheless, the results turn in favor of the CMFELS when it is compared to state-of-the-art EMALS in aircraft catapult system at speeds above 40 m/s.

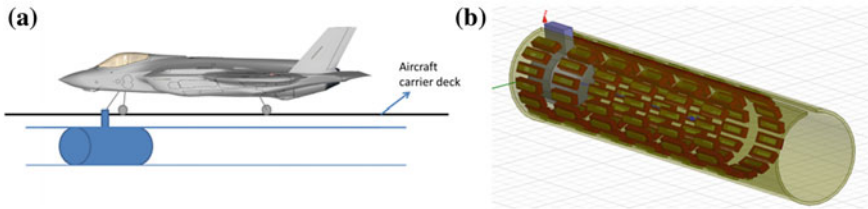


Fig. 7 a The structure of the EM launch system for aircraft, b proposed CMFELS model for aircraft propelling system operation

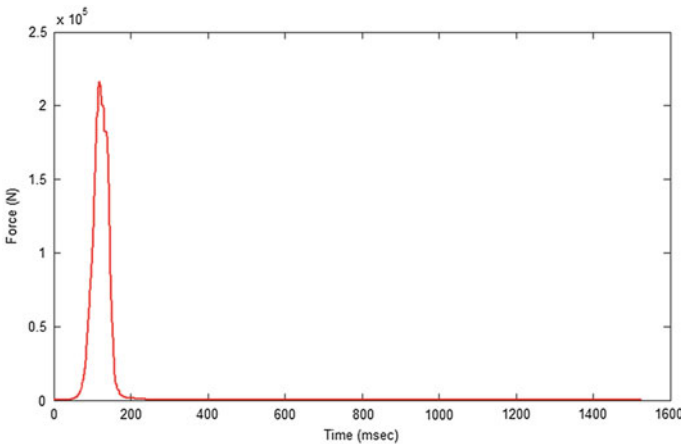


Fig. 8 Simulation results for Force generated by CMFELS

7 Conclusions

This paper addressed the Core type Multipole Field Electromagnetic Launching System (CMFELS) with a comprehensive numerical analysis. A step-by-step iterative design algorithm is developed. The materialistic aspects of the coil are considered as boundaries for achieving the speeds needed. A descriptive analysis is conducted for various pole conditions. The model's reliability was checked by comparison with the study of FEM. The model is established by omitting assumptions such as uniform magnetic field, estimated inductance, and values of reciprocal inductance, and negligible current layer. The force and inductance profile analysis provided a claim that the lifting force and drag force created in the model would help maintain the uniform air gap between the armature and the moving body. Therefore, the issue of critical air gap alignment in EMALS is answered.

Some of the observations are: (a) when the number of coils or poles increases, the number of turns and layers decreases, (b) several coils will improve the movement of an object because the flux applied is three-dimensional, (c) number of coils will increase the force exerted on the object, (d) depending on the orientation of the coils; flux lines flow within the moving object resulting in optimum use of flux. It is, therefore, to be inferred that the model proposed has a significant impact on improving CMFELS' launch reliability, structure, and configuration. In addition, by considering different constraints, the user-interactive algorithm provides versatility in choosing different necessary velocities.

References

1. Robertson H, Matt Bolton RN, Mick Thomson RN (2005) An advanced linear motor system for electromagnetic launch: development and opportunities. IET 11070
2. Doyle MR, Samuel DJ, Conway T, Klimowski RR (1995) Electromagnetic aircraft launch system-EMALS. IEEE Trans Magn 31(1):528–533
3. Bertonecelli T, Monti A, Patterson D, Dougal R (2002) Design and simulation of an electromagnetic aircraft launch system. In: IEEE 33rd annual IEEE power electronics specialists conference. Proceedings (Cat. No.02CH37289)
4. Reck B (2003) First design study of an electrical catapult for unmanned air vehicles in the several hundred kilogram range. IEEE Trans Magn 39(1):310–313
5. Becherini G, Sebastiano DF, Tellini B (2011) Analysis of the dynamic behavior of a linear induction type catapult. IEEE Trans Plasma Sci 39(1):59–64
6. Musolino A, Rizzo R, Tripodi E (2013) The double-sided tubular linear induction motor and its possible use in the electromagnetic aircraft launch system. IEEE Trans Plasma Sci 41(5):1193–1200
7. Zhu Y, Wang Y, Yan Z, Dong L, Xie X, Li H (2010) Multipole field electromagnetic launcher. IEEE Trans Magn 46(7):2622–2627
8. Zhu Y, Wang Y, Chen W, Yan Z, Li H (2012) Analysis and evaluation of three-stage twisty octapole field electromagnetic launcher. IEEE Trans Plasma Sci 40(5):1399–1406
9. Musolino A, Rizzo R, Tripodi E (2013) Travelling wave multipole field electromagnetic launcher: an SOVP analytical model. IEEE Trans Plasma Sci 41(5):1201–1208

10. Luo W, Wang Y, Yan Z, Chen W, Zhixing G (2013) Connection pattern research and experimental realization of single stage multipole field electromagnetic launcher. *IEEE Trans Plasma Sci* 41(11):3173–3179
11. Kondamudi S, Pasumarthi MR (2019) Computations of magnetic forces in multipole field electromagnetic launcher. *Int J Math, Eng Manag Sci* 4(3):761–774
12. Kondamudi S, Pasumarthi MR, Thotakura S (2019) Design and analysis of cored type multipole field electromagnetic launcher (C-MFEML). *Int J Innov Technol Explor Eng* 8(6):391–395
13. Kondamudi S, Pasumarthi MR (2019) Constraint based design of multipole field electromagnetic launcher using gauss method. *Int J Eng Adv Technol (IJEAT)*, 8(6S2):907–911
14. Thotakura S, Kondamudi S, Pasumarthi MR (2020) A novel configuration of multi-stage out-runner electromagnetic launching for aircraft catapult system. Springer Science and Business Media LLC, chapter 44

Performance Analysis of Fractional-Order High-Pass Filter



Kumar Biswal, Madhab Chandra and Sanjeeb Kumar Kar

Abstract In this paper, analysis of fractional order passive RC high-pass filter circuit is presented. The time-domain expressions for different values of fractional order α were calculated. The output of fractional-order high-pass filter for order α has been simulated by MATLAB software. The effect of fractional order α on frequency response is observed. The design of these filters using an approximation of the fractional Laplacian operator is outlined. A fractance device of order α which uses usual expression s^α is analyzed and presented using continuous fraction expansion (CFE) method. The fractional-order operator α is rationalized approximately by using different methods (Oustaloup, Newton and CFE method) that are presented and compared with the ideal response of circuit. The fractional-order circuits have better design flexibility than the integer-order circuits. The performance of integer-order circuit is improved by the replacement of fractional component as it has greater degree of freedom.

Keywords Step response · Impulse response · CFE · Rise time · Peak time · Settling time · Peak overshoot

K. Biswal (✉)

School of Electronics Engineering, Kalinga Institute of Industrial Technology (KIIT),
Bhubaneswar 751024, India
e-mail: kumar.biswalfet@kiit.ac.in

M. Chandra

Department of Instrumentation & Electronics Engineering, CET, BPUT, Bhubaneswar 751054,
India
e-mail: mctripathy@cet.edu.in

S. K. Kar

ITER, SoA, Deemed to be University, 751030 Bhubaneswar, Odisha, India
e-mail: sanjeebkar@soa.ac.in

© Springer Nature Singapore Pte Ltd. 2020

R. Sharma et al. (eds.), *Innovation in Electrical Power Engineering, Communication, and Computing Technology*, Lecture Notes in Electrical Engineering 630,
https://doi.org/10.1007/978-981-15-2305-2_41

1 Introduction

Fractional order differential and integral equations are the generalization of conventional integral and differential equations that can be used for modeling the real world we live in. The integer-order models were used due to the absence of solution methods for fractional differential equations. At present many methods have been developed for realizing the applications based on fractional derivative and integration [1, 2]. The term “fractional” covers all non-integer numbers including fractions and irrational numbers, therefore, this is sometimes known as non-integer order calculus [3]. The integer-order filters have integer coefficients in its mathematical representation which leads to some design criterion that makes it difficult to obtain sharp cutoff frequency. The exact design requirements can be satisfied by fractional-order filters which is not possible in conventional integer-order filters [4–8]. This fractional concept adds a little bit of safety in the design specifications as compared to the integer-order filters. The circuit design specifications which can be easily achieved in case of fractional-order filters along with tuning parameters. The roll-off frequency can be varied and set to any desired slope, which is only possible by using fractional-order filters. Hence fractional-order filters provide more flexibility compared to integer-order filters [9–12]. This paper is organized as follows. Section 2 deals with model, transfer function and response of fractional-order high-pass filter. Section 3 illustrates the time response of single stage fractional-order high-pass filter. Similarly, Sect. 4 deals with frequency response of single stage fractional-order high-pass filter. Finally, conclusion is presented in Sect. 5.

2 Fractional-Order High-Pass RC Circuits

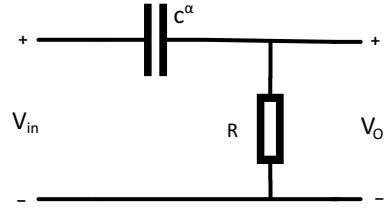
High-pass filters are primarily used to pass high-frequency signals and attenuate low-frequency signals. The cutoff frequency (ω_c) locates the pass band ($\omega > \omega_c$) and the stop band ($\omega < \omega_c$) in a complete frequency response. A high-pass filter allows high-frequency signals to pass and attenuates low signals having frequencies lower than the cutoff frequency.

High-pass filters have many applications both in analog and digital filters. The filter is characterized by its cutoff frequency and rate of frequency roll off. So the order of the filter determines the value of attenuation for frequencies lower than the cutoff frequency [13]. The circuit model for the single stage fractional-order high-pass filter is shown in Fig. 1

The characteristic equation for the circuit is given by the expression (1):

$$\frac{V_O}{R} + C^\alpha \frac{d^\alpha V_O(t)}{dt^\alpha} = C^\alpha \frac{d^\alpha V_{in}}{dt^\alpha} \quad (1)$$

Fig. 1 Circuit model of a single stage fractional-order high-pass filter



Taking Laplace transform, the transfer function of the circuit is presented through Eq. (2)

$$H(s) = \frac{V_o(s)}{V_i(s)} = \frac{S^\alpha}{S^\alpha + \tau} \tag{2}$$

Here $\tau = \frac{1}{RC^\alpha}$ is a constant (i.e., time constant).

$H(s)$ represents the transfer function of (integer) first-order high-pass filter. From the above transfer function $H(s)$, the magnitude and phase of the (fractional) first-order high-pass filter [14–17] are

$$|H(w)| = \frac{\tau w^\alpha}{\sqrt{\tau^2 w^{2\alpha} + 1 + 2w^\alpha \cos(\alpha\pi/2)}}$$

and $\theta(w) = -\tan^{-1}\left[\frac{\pi w^\alpha \sin(\alpha\pi/2)}{\tau^2 w^{2\alpha} + \tau w^\alpha \cos(\alpha\pi/2)}\right]$ respectively

The step response is calculated as:

$$v_o(t) = E_{\alpha,1}(-\tau t^\alpha) \tag{3}$$

The impulse response is found to be:

$$h(t) = 1 - \tau t^{\alpha-1} E_{\alpha,\alpha}(-\tau t^\alpha) \tag{4}$$

$$|H(w)| = \frac{wRC}{\sqrt{1 + (wRC)^2}} \tag{5}$$

and

$$\theta(w) = -\tan^{-1}(wRC) \tag{6}$$

Equations (5) and (6) represent the transfer function expressions for magnitude and phase of (integer) first-order high-pass filter.

3 Time Response of a Single Stage High-Pass Filter

In fractional-order filter, the time-domain response defines the different measuring parameters such as the transfer function, magnitude, phase, stability, maximum (peak) overshoot (M_p), settling time (t_s) and rise time (t_r) [6, 18]. The step response and impulse response of single stage fractional high-pass filter are plotted for the above parameters having different order α of fractional capacitor.

Settling time: The time required for the response of the system to be within the fraction of the steady state value and to remain there.

Rise time: The time taken for the response of a system to go from 10 to 90% of the steady state value at the first instant.

Peak time: It is the time taken for the response of a system to reach the peak (maximum) overshoot.

The time at which the peak overshoot occurs is given by Eq. (7)

$$t_p = \frac{0.131(\alpha - 0.255)^2}{(\alpha - 0.921)\omega_c} \quad (7)$$

The step response of single stage fractional high-pass filter shown in Fig. 2 is obtained for a range of α . This figure can be used for comparing the responses of fractional-order and integer-order filters. A standardized value of time constant, i.e., $RC = 1$, is assumed for all simulations.

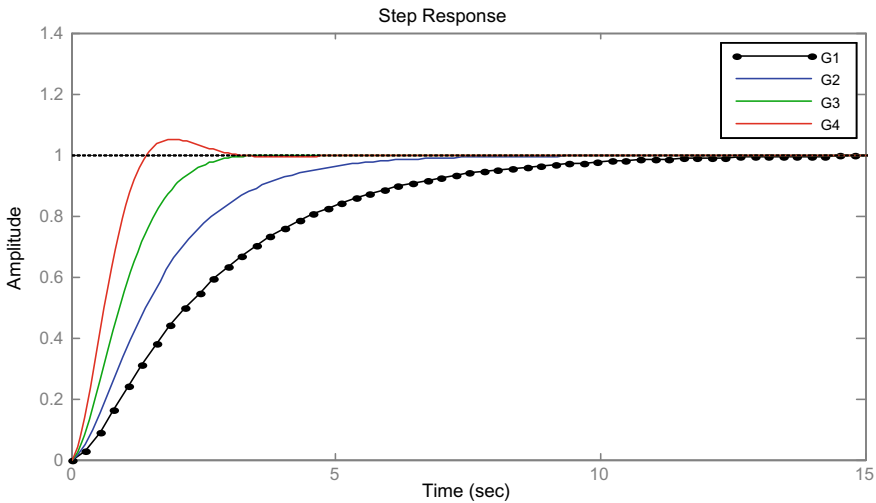


Fig. 2 Step response of single stage high-pass filter where order **a** G1 = 0.1, **b** G2 = 0.4, **c** G3 = 0.6, **d** G4 = 0.8

An impulse is a short duration signal that goes from zero to a maximum value and comes to zero again in a short time. The impulse response of a filter is obtained by applying an impulse input and studied with order α of filter as shown in Fig. 3.

Furthermore, when α varies from 0 to 1, the circuit’s behavior approaches toward an equivalent second-order system as observed is shown in Fig. 3. The different measuring specifications such as rise time, settling time, peak overshoot and peak time are shown in Table 1 by changing order α of fractional capacitor.

From Figs. 4, 5 and 6, the circuit’s response like percent overshoot, rise time and settling time is studied for different values of α . So by using the results of figures

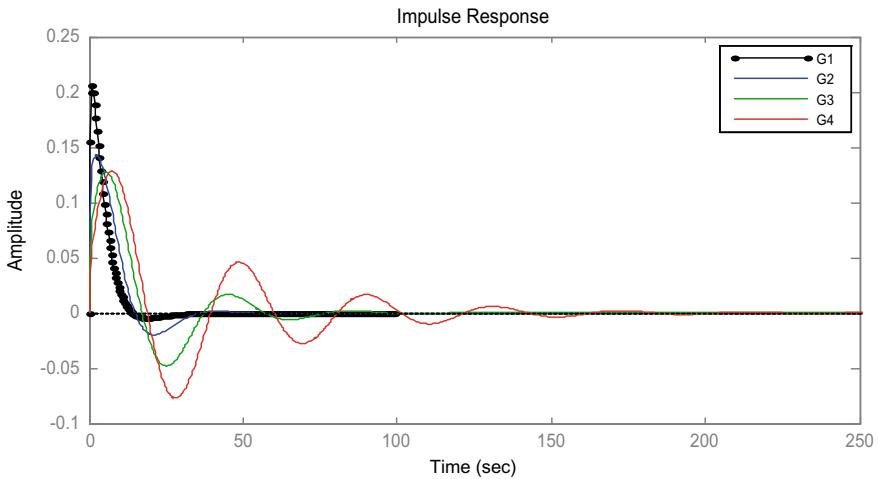


Fig. 3 Impulse response of a single stage high-pass filter where order **a** G1 = 0.1, **b** G2 = 0.4, **c** G3 = 0.6, **d** G4 = 0.8

Table 1 Time-domain response specification of a fractional high-pass filter

α	Rise time	Settling time	Overshoot	Peak time
0.1	0.262	0.436	3.4851	13.5730
0.2	0.332	1.681	9.0582	12.3646
0.3	0.414	2.396	16.9966	12.4480
0.4	0.457	2.841	27.7046	12.9948
0.5	0.559	3.120	41.5232	13.8923
0.6	0.677	3.308	54.7398	15.0238
0.7	0.814	3.383	68.9874	16.2049
0.8	0.733	5.309	79.0789	17.3486
0.9	0.806	7.939	89.6854	18.7509
1	0.880	10.970	98.7256	19.8979

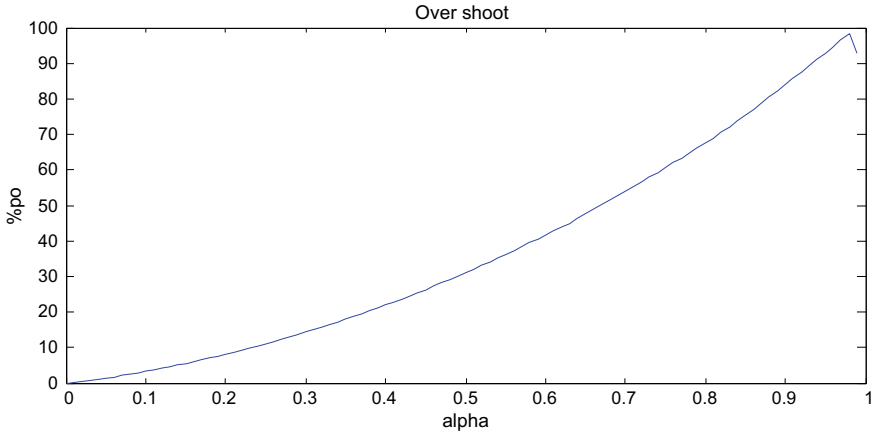


Fig. 4 Percent overshoot versus alpha for single stage fractional high-pass filter

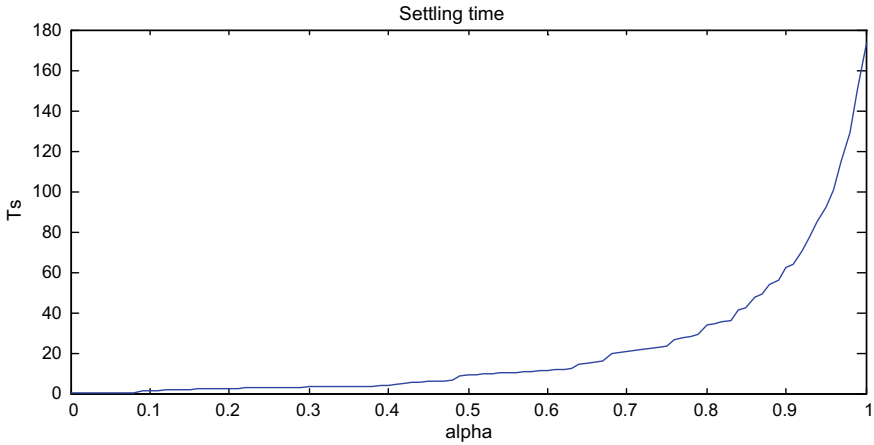


Fig. 5 Settling time versus alpha for single stage fractional high-pass filter

shown below, an approximate fractional capacitor can be chosen to meet the desired parameters given in Table 1.

Figure 4 shows the percentage overshoot versus order of the fractional capacitor α used in the high-pass filter. From Fig. 4, it is clear that overshoot decreases when order of the fractional capacitor decreases as it is maximum in classical capacitor.

Figure 5 indicates the variation of settling time by varying the order of the fractional capacitor. The settling time is maximum at $\alpha = 1$ i.e., when normal capacitor is used. This shows the circuit output stabilizes quickly when fractional capacitor is used.

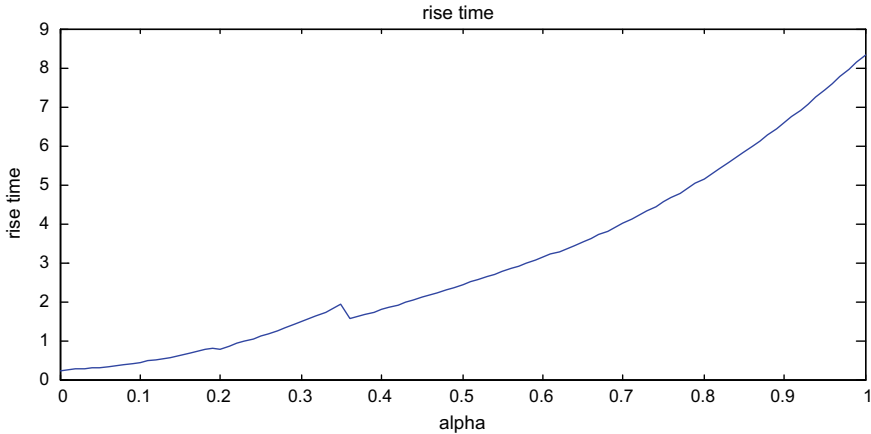


Fig. 6 Rise time versus alpha for single stage fractional high-pass filter

Figure 6 shows rise time versus order of the fractional capacitor α . It is clear from the figure that rise time decreases when fractional capacitor replaces the classical capacitor. This indicates that fractional circuits have less delay, high speed and thus the circuit gives a speed of response having less delay time.

4 Frequency Response of a Single Stage High-Pass Filter

The Bode plots for magnitude and phase of a fractional-order filter with order α are shown in Fig. 7; it is observed that the slope of the magnitude plot in the stop band region varies proportionally to α . As observed from Fig. 7, the asymptotic approximation becomes inaccurate for very small values of α , whereas the asymptote in the high-frequency region have greater slope which increases with increase of α . Hence the cutoff frequency becomes sharper, which leads to an increase in speed of response obtained in time-domain response as shown in Fig. 7.

The Bode plot for phase also shown in Fig. 7 indicates for small value of α , the phase variation is almost linear over a narrow frequency range. From the figure it is also observed that as α increase, the phase plot moves toward saturation state having asymptotic values of 0° and 90° for low and high frequencies, respectively.

5 Conclusions

In this article, the fractional-order RC high-pass filter has been analyzed both in time and frequency domains. First the fundamentals of impedance and phase characteristics have been systematically worked out as the groundwork for the design of

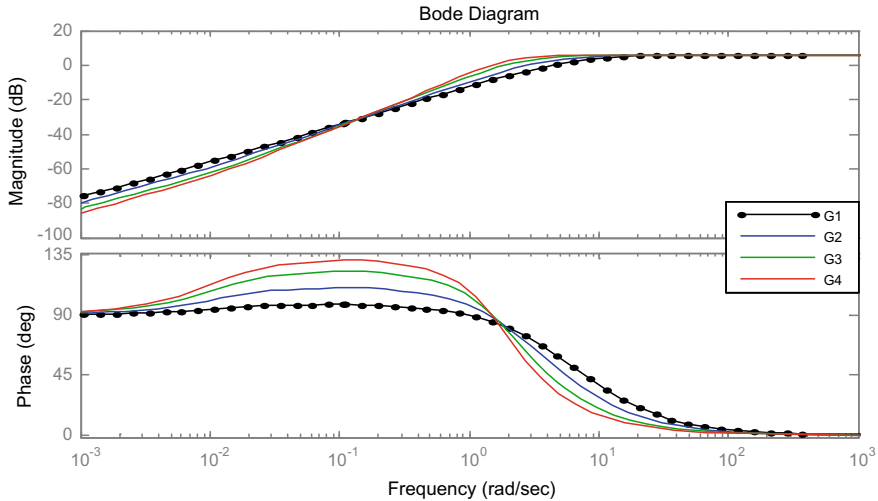


Fig. 7 Bode plot of single stage fractional high-pass filter where order **a** $G1 = 0.1$, **b** $G2 = 0.4$, **c** $G3 = 0.6$, **d** $G4 = 0.8$

the fractional-order filter circuit. Secondly, from the filter's response, the amplitude-frequency characteristics, phase-frequency characteristics and cutoff frequency are studied in detail with respect to time constant τ having different order α to show the better flexibility of the fractional-order filter circuit. The filter behavior is studied and represented by varying the order α . Finally, it is concluded that the speed of the response increases with increase in fractional order. In frequency domain, the magnitude and phase plots change almost linearly with the fractional order in the region of stop band.

References

1. Debnath L (2003) Recent applications of fractional calculus to science and engineering. *Int J Math Math Sci* 54:3413–3442
2. Rousan AA, Ayoub NY, Alzoubi FY, Khateeb H, Al-Qadi M, Hasan(Qaseer) MK, Albiss BA (2006) "A fractional LC-RC circuit", fractional calculus and applied analysis. *An Int J Theory Appl* 9(1):33–41
3. Ortigueira MD (2008) An introduction to the fractional continuous-time linear systems, the 21st century systems. *IEEE Circuits Syst Mag* 8(3):19–26
4. Elwakil AS (2010) Fractional-order circuits and systems: an emerging interdisciplinary research area. *IEEE Circuits Syst Mag* 10(4):40–50
5. Machado JT (2013) Fractional generalisation of memristor and higher order elements. *Commun Nonlinear Sci Numer Simul* 18:264–275
6. Walczak J, Jakubowska A (2015) Analysis of resonance phenomena in series RLC circuit with super capacitor. In: *Analysis and simulation of electrical and computer systems, Lecture Notes in Electrical Engineering*, vol 324, Springer, pp 27–34

7. Moreles MA, Lainez R (2017) Mathematical modelling of fractional order circuit elements and bioimpedance applications. *Commun Nonlinear Sci Numer Simulat* 46:81–88
8. Zahra WK, Hikal MM, Bahnasy TA (2017) Solutions of fractional order electrical circuits via Laplace transform and nonstandard finite difference method. *J Egypt Math Soc* 25:252–261
9. Obeidad A, Gharaibeh M, Al-Ali M, Rousan A (2011) “Evaluation of a current in resistor”, fractional calculus and applied analysis. *An Int J Theory Appl* 14(2):247–250
10. Gómez-Aguilar JF, Escobar-Jiménez RF, Olivares-Peregrino VH, Taneco-Hernández MA, Guerrero-Ramírez GV (2017) Electrical circuits RC and RL involving fractional operators with bi-order. *Adv Mech Eng* 9:1–10
11. El-Sayed MA, Nour HM, Raslan WE, El-Shazly ES (2012) Fractional parallel RLC circuit. *Alex J Math* 3:11–23
12. Radwan AG, Salama KN (2012) Fractional-order RC and RL circuits. *Circuits Syst Signal Process* 31(6):1901–1915
13. Jakubowska A, Walczak J (2016) Analysis of the transient state in a series circuit of the class $R-L_\beta-C_\alpha$. *Circuits Syst Signal Process* 35:1831–1853
14. Gorenflo R, Kilbas AA, Mainardi F, Rogosin SV (2014) Mittag-Leffler functions, related topics and applications. Theory and applications. Springer, Heidelberg, New York, Dordrecht, London
15. Garrappa R (2015) Numerical evaluation of two and three parameter Mittag-Leffler functions. *SIAM J Numer Anal* 53(3):1350–1369
16. Sierociuk D, Podlubny I, Petráš I (2013) Experimental evidence of variable-order behavior of ladders and nested ladders. *IEEE Trans Control Syst Technol* 21:459–466
17. Podlubny I (1999) Fractional differential equations. Academic Press, London
18. Hua Y, Luo Y, Lu Z (2008) Analytical solution of the linear fractional differential equation by a domain decomposition method. *J Comput Appl Math* 215:220–229

Application of 2DOF and 3DOF Controller for LFC Analysis in Multi-generation System



Gayatri Mohapatra, Manoj Kumar Debnath
and Krushna Keshab Mohapatra

Abstract In this article, a spider monkey optimization technique (SMO) is suggested to make the gains of the controller in harmony with the hybrid plants to analyze the load frequency control (LFC) using two degree of freedom (2DOF_PID) and the degree of freedom (3DOF_PID). Each area comprises solar thermal system (DSTS), conventional steam power plant (SPP) and a geothermal power plant (GTPP) to scrutinize the vigorous performance of the system for load frequency control. For more analysis, governor dead-band (GDB) and generation rate constraints (GRC) of the SPP have been considered 0.036 and 0.003, respectively. The dynamic responses of the systems are observed by implementing different controllers independently. The investigation exposes the dominance of 3DOF_PID controller over other controllers.

Keywords Load frequency control · Spider monkey optimization · 3DOF-PID controller

1 Introduction

Enchantment of a stable equilibrium between the increasing demand and load is the essential stipulation of the system. The interconnected power sources in modern power engineering lead to the interchange of power between the tie-lines by virtue of semiconductor devices. The dynamic nature of the load and power insists on a perfect equilibrium between both during disturbances. The frequency and the voltage of the generating system are the vital constraints that need to be maintained at their stated value for the favorable operation. The system voltage is coordinated by an automatic voltage regulator (AVR), and the frequency of the system, which varies with the load,

G. Mohapatra · M. K. Debnath (✉) · K. K. Mohapatra
Siksha 'O' Anusandhan Deemed to be University, Bhubaneswar, Odisha 751030, India
e-mail: mkd.odisha@gmail.com

G. Mohapatra
e-mail: gayatrim79@gmail.com

K. K. Mohapatra
e-mail: krushnakmohapatra@gmail.com

© Springer Nature Singapore Pte Ltd. 2020

R. Sharma et al. (eds.), *Innovation in Electrical Power Engineering, Communication, and Computing Technology*, Lecture Notes in Electrical Engineering 630,
https://doi.org/10.1007/978-981-15-2305-2_42

is controlled by AGC. With any divergence from the set, the frequency and tie-line powers get deviated from their required values. AGC eliminates these deviations by regulating the speed of the governor and continuously maintaining a balance in the generation and load (load frequency control) thereby helps in restoring the frequency [1, 2]. Providing reliable and good quality of power is a challenging task in the modern era due to the booming and complex systems interconnection. The electric network is distributed into multiple areas on the strength of electric links of the generating units. These areas are dedicated to having the structural energy exchanges by transmission system operators where the integral time absolute error (ITAE) is taken as an objective function to have better functionality [3, 4].

By extensive literature survey, it is found that many of the researchers concentrated their work in different types of controllers like particle swarm optimization (PSO), Sine Cosine Algorithm (SCA)-based PID, I, PI, PID, FOPI-FOPID controller for AVR and LFC of unified power system with different objective functions (ISE, IAE, ITSE and ITAE) based on frequency deviation, power deviation in the tie-line, time error and unplanned load variation [5–7]. Mathematical modeling of the tie-line power with SSSC and damping control strategy with PID, FOPID and fuzzy controllers to find the adjustable parameters [8, 9] is also raised for controller tuning. A multi-area and multi-source deregulated power system with an optimized controller like I, PI, PID, cascade combination of FO PI, FO PD integral double derivative (IDD) and proportional integral double derivative (PIDDD) controller and other parameters using the SCA technique are compared in order to find the best solution [10–17]. The gains of the PID, fuzzy-PID and fuzzy-PIDF controller are set with different processes of optimization with FACTS devices. A multi-staged PID controller has also been developed for LFC of solar thermal system [18–20] with communication time delay in the connected system and also in hybrid controllers.

A detailed research analysis intimates that the PID controller is employed in most of the cases due to its simplicity but with an inefficacy to perform cogently in many control processes operated in a combined controller state. So, an innovative fractional order PID controller tuned with SMO is deliberated in this article to solve the numerous AGC issues. The salient points of the research work in this article are as follows:

- i. To construct a two equal area multi-source (GTPP, DSTS and SPP) model in MATLAB Simulink framework.
- ii. Governor dead-band (GDB) and generation rate constraint (GRC) have been considered for more analysis of SPP for LFC.
- iii. Modeling and enactment of a novel SMO tuned PID controller for LFC.
- iv. To estimate and compare the performance of the 2DOF-PID and 3DOF-PID control approach with PID controller to face LFC problems.

2 System Investigated

Figure 1 deliberates the transfer function model of examined two equal area power system interconnected by a tie-line. Both the area comprises a GTPP, a DSTS and a SPP as a source of generating power. The reheat turbine of solar power plant is considered along with governor dead-band (0.036) and generation rate constant (3%). The values of different constraints of this scrutinized system are given in appendix. The parameters of FOPID and PID controller are tuned by employing SMO technique. Area of controller (ACE) works as input to the controller of each area, and the expression of (ACE) for the two-area system is represented in Eqs. (1) and (2).

To achieve the desired responses of spider monkey optimization technique, integral time absolute error has been considered as cost function. Equations (1) and (2) explain the ACE of area 1 and 2, respectively. Equation (3) signifies the expression for ITAE objective function, where Δf_1 , Δf_2 , ΔP_{tie} are the change of frequency of the area 1, area 2 and the change in the tie-line power, respectively.

$$ACE_1 = \Delta P_{12} + B_1 \Delta \omega_1 \tag{1}$$

$$ACE_2 = \Delta P_{21} + B_2 \Delta \omega_2 \tag{2}$$

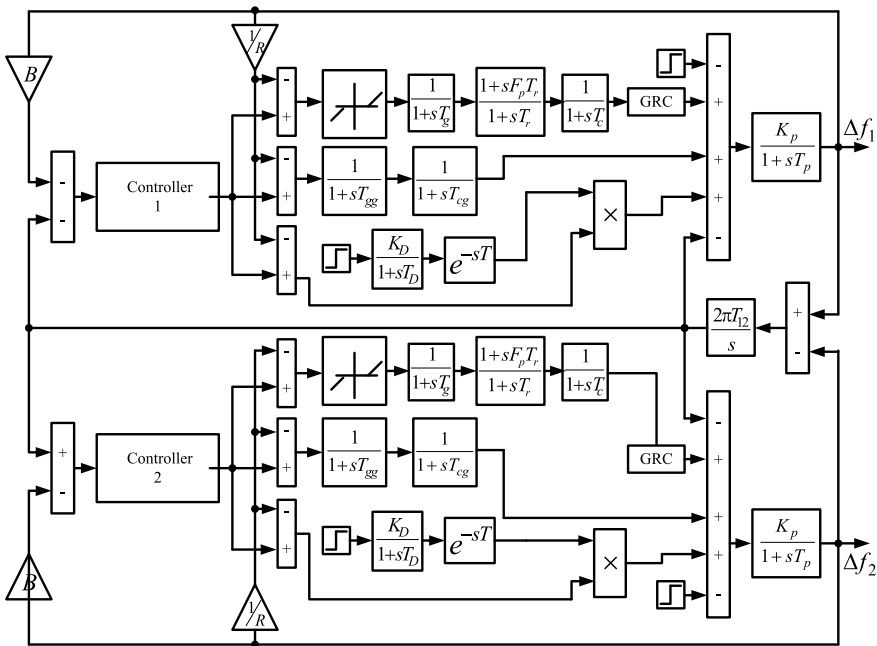


Fig. 1 Gives the transfer function Simulink model of the hybrid power system under study

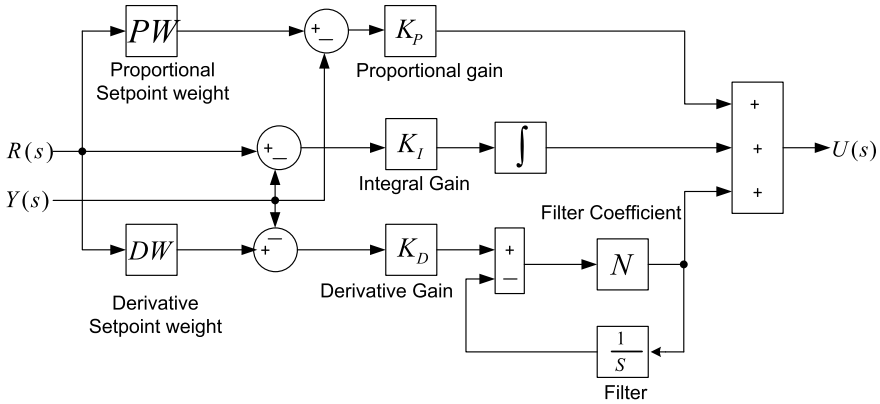


Fig. 2 Gives the structure of 2DOF-PID controller

$$ITAE = \int_0^t (|\Delta f_1| + |\Delta f_2| + |\Delta P_{tie}|) \times t dt \tag{3}$$

3 Controller Structures and Their Optimal Design

The degree of freedom of the system is the possible number of self-sufficient controllable loops. The increased number of loop enhances the stability of the system.

In this article, a 3DOF-PID controller for AGC is introduced in a hybrid system. The superiority of the same on a 2DOF-PID and PID is established. The internal structure of the 2DOF-PID and 3DOF-PID controller is explained in Figs. 2 and 3, respectively. The controller takes an input of $R(s)$ and the output, and $U(s)$ is fed to the generating unit. $Y(s)$ signifies the output of the system which conveys the change in the oscillation of the area with $D(s)$ as the disturbance. The 3DOF-PID has an additional loop for faster control with a scaling factor of seven which is one extra than the 2DOF-PID.

4 Spider Monkey Optimization (SMO) Method

This is an optimization based on the food foraging of the spider monkeys with a study on the nature and the social activities of the animal. In this method, a community, dictated by a female, seeking of food in the form of tiny singulars is in focus. The process of searching the food is replicated till it is found. For latest updates in their locus, inspection of expanded search territory and selection of food are considered. The following steps are to be followed for the successful execution of SMO technique.

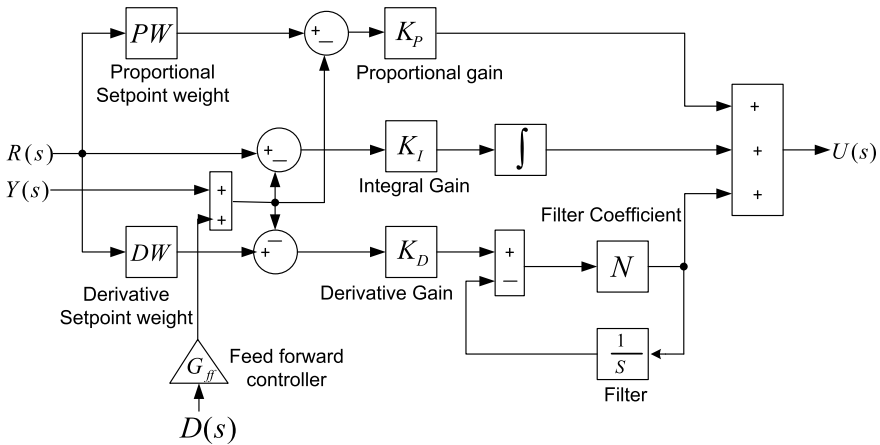


Fig. 3 Explains the block diagram of 3DOF-PID controller

- i. Initialize the population of monkeys by knowing their strength. At initial condition, mention the higher band, lower band local head learning limit (LHL_limit), global head learning limit (GHL_limit) and perturbation rate, p (where $p \in [0.1, 0.9]$) of the monkeys as per Eq. (4).
- ii. Determine fitness (each individual space from between source and the food) by Eq. (5).
- iii. Greedy selection to be used to choose the global and local heads depending on their fitness values.
- iv. New locations for group community using local head phase(LHP) to be applied depending upon their self-experience.
- v. Selection strategy needs to be employed based on the robustness of the group members.
- vi. Probabilities F_j from Eq. (6) for all companions are assessed and generate new locations for the distance as given in Eq. (7).
- vii. Global head phase (GHP) and a Grabby selection method are applied to modify global and local heads' locations by Eq. (8).
- viii. Any local head of a group if fails to modify her locus within LHL_limit, then further foraging is chosen using local head decision (LHD) phase by Eq. (9).
- ix. If the Global Head Decision (GHD) as per Eq. (10) is not able to set the position of the GHP, then smaller groups are made for further searching.
- x. Repeat the steps from (iv) to (vii) if termination criteria are not satisfied.

$$M_{ij} = (ub(i) - lb(i)) * rand + lb(i) \tag{4}$$

$$S(M_i, F_j) = D_i \cdot e^{bt} \cdot \text{Cos}(2\pi t) + F_j \tag{5}$$

$$F_j = 0.1 + \left(\frac{\text{fit}_i}{\text{fit}_{\max}} \right) \times 0.9 \tag{6}$$

$$D_i = |F_j - M_i| \tag{7}$$

$$M_{\text{new}ij} = M_{ij} * (\text{GL}_j - M_{ij}) + R(1, 1) * (M_{rj} - M_{ij}) \tag{8}$$

$$M_{\text{new}ij} = M_{ij} + R(0, 1) \times (\text{GL}_j - M_{ij}) + R(-1, 1) \times (M_{rj} - M_{ij}) \tag{9}$$

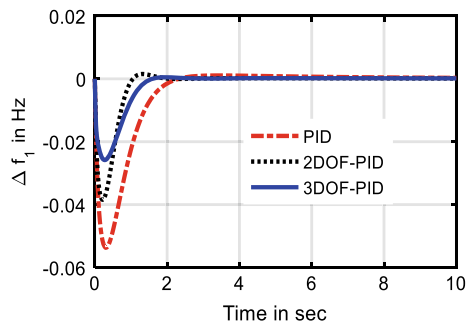
$$M_{\text{new}ij} = M_{ij} + R(0, 1) \times (\text{GL}_j - M_{ij}) + R(0, 1) \times (M_{rj} - LL_{kj}) \tag{10}$$

Here, i and j signify the number of monkey and food, respectively. $\text{ub}(i)$ and $\text{lb}(i)$ are the upper band and lower band of the i th variable. D_i is the distance between the monkey and the prey, and b is the operator for optimization.

5 Result and Discussion

Simulation of two equal area of power system has been done by using MATLAB/Simulink circumstances. Simulink model is called through SMO program to optimally design the controllers by minimizing the ITAE. The efficacy and sturdiness of this designed hybrid system along with PID, 2DOF_PID and 3DOF_PID controller are perceived from the dynamic responses. The analysis of this recommended controller has been done by subjecting 0.01 p.u SLP for both controllers separately. The instabilities of frequency of area 1 and area 2 and deviation interline power are represented in Figs. 4, 5 and 6 by tuning the gains of PID controller with spider monkey technique. Table 1 signifies the gains of suggested controllers as well as the time constant of geothermal power system. The transient response analysis on the basis of maximum overshoot, undershoot and settling time of all deviations is listed in Table 2. From the responses (Figs. 4, 5 and 6) and Table 2, it is proved that the offered technique provides more stability in the scrutinized system for AGC.

Fig. 4 Explains the abnormalities of frequency in area 1



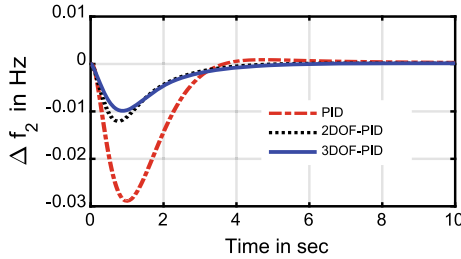


Fig. 5 Gives the abnormalities of frequency in area 2

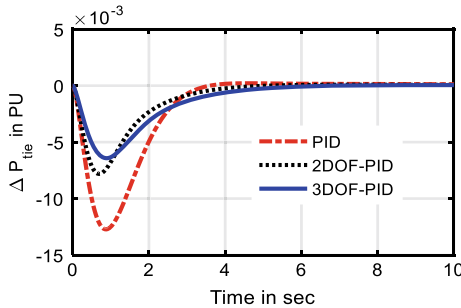


Fig. 6 Shows the tie-line power abnormalities between area 1 and area 2

Table 1 Tuned parameters of 3DOF and 2DOF controllers

Parameters	Area 1			Area 2		
	3DOF-PID	2DOF-PID	PID	3DOF-PID	2DOF-PID	PID
N	198.11	210.21	NA	150.6	185.1	NA
PW	2.6554	4.98	NA	3.0577	4.95	NA
DW	0.0100	1.0238	NA	4.9988	3.0509	NA
G_{ff}	0.1100	NA	NA	0.2101	NA	NA
K_P	0.9534	0.4138	1.3258	1.0150	1.5306	1.0426
K_I	2.0000	2.0000	2.0000	0.0100	0.0100	0.8539
K_D	0.5236	0.1834	0.5211	1.1940	0.7959	0.6939

6 Conclusion

The objective of the current study is to analyze PID, 2DOF-PID and 3DOF-PID controller to stabilize the frequency in a hybrid system. A two-area system (GPP, DSTS and SPP) comprising six units is observed by employing ITAE as cost function. A SLP of 0.01 p.u is offered to confirm the efficacy of the employed FOPID controller is introduced over a multi-source hybrid scrutinized system. The performance of

Table 2 Performance evaluating parameters of different response

Observation	Performance evaluative indices of response	PID	2DOF PID	3DOF PID
Δf_1	T_s in s (0.05% band)	7.2267	1.7500	1.5552
	Undershoots (Hz)	-0.0537	-0.0385	-0.0258
	Overshoots (Hz)	0.0011	0.0015	0.0005
Δf_2	T_s in s (0.05% band)	7.4100	3.9125	3.8084
	Undershoots (Hz)	-0.0289	-0.0121	-0.0099
	Overshoots (Hz)	0.0009	0.0002	0.0001
ΔP_{tie}	T_s in s (0.05% band)	3.1105	3.4417	3.2352
	Undershoots (PU)	-0.0127	-0.0078	-0.0064
	Overshoots (PU)	0.0002	0.0001	0.00005

the recommended controller is analyzed in terms of settling time, undershoot and overshoot as well as it helps to reduce the oscillation in the dynamic responses of system during perturbation.

Appendix

The system parameters are assigned as follows,

$$T_P = 20, K_P = 120, T_c = 0.3, T_g = 0.08, F_P = 0.5, T_r = 10, B = 0.425, R = 2.4, T_{12} = 0.086, T_d = 5, K_d = 1, T_{gg} = 0.08, T_{cg} = 0.1.$$

References

1. Kundur P, Balu NJ, Lauby MG (1994) Power system stability and control, vol 7. McGraw-Hill, New York
2. Singh R, Jain K, Pandit M (2011) Comparison of PSO variants with traditional solvers for large scale multi-area economic dispatch
3. Nanda J, Mishra S, Saikia LC (2009) Maiden application of bacterial foraging-based optimization technique in multiarea automatic generation control. *IEEE Trans Power Syst* 24(2):602–609
4. Pan I, Das S (2015) Fractional order AGC for distributed energy resources using robust optimization. *IEEE Trans Smart Grid* 7(5):2175–2186
5. Mohanty PK, Sahu BK, Pati TK, Panda S, Kar SK (2016) Design and analysis of fuzzy PID controller with derivative filter for AGC in multi-area interconnected power system. *IET Gener Transm Distrib* 10(15):3764–3776
6. Tasnin W, Saikia LC (2018) Deregulated AGC of multi-area system incorporating dish-stirling solar thermal and geothermal power plants using fractional order cascade controller. *Int J Electr Power Energy Syst* 101:60–74

7. Morsali J, Zare K, Hagh MT (2018) A novel dynamic model and control approach for SSSC to contribute effectively in AGC of a deregulated power system. *Int J Electr Power Energy Syst* 95:239–253
8. Mohanty B, Hota PK (2018) A hybrid chemical reaction-particle swarm optimization technique for automatic generation control. *J Electr Syst Inf Technol* 5(2):229–244
9. Tasnin W, Saikia LC (2018) Performance comparison of several energy storage devices in deregulated AGC of a multi-area system incorporating geothermal power plant. *IET Renew Power Gener* 12(7):761–772
10. Pathak N, Verma A, Bhatti TS, Nasiruddin I (2018) Real-time parameter estimation based intelligent controllers for AGC operation under varying power system dynamic conditions. *IET Gener Transm Distrib* 12(21):5649–5663
11. Saikia LC, Sinha N (2018) Load frequency control of a multi-area system incorporating distributed generation resources, gate controlled series capacitor along with high-voltage direct current link using hybrid ALO-pattern search optimised fractional order controller. *IET Renew Power Gener* 13(2):330–341
12. Kouba NEY, Menaa M, Hasni M, Boudour M (2018) A novel optimal combined fuzzy PID controller employing dragonfly algorithm for solving automatic generation control problem. *Electric Power Compon Syst* 46(19–20):2054–2070
13. Mohanty B (2019) Performance analysis of moth flame optimization algorithm for AGC system. *Int J Model Simul* 39(2):73–87
14. Debnath MK, Sinha S, Mallick RK (2018) Automatic generation control including solar thermal power generation with fuzzy-PID controller with derivative filter. *Int J Renew Energy Res (IJRER)* 8(1):26–35
15. Debnath MK, Mallick RK, Sahu BK (2017) Application of hybrid differential evolution–grey wolf optimization algorithm for automatic generation control of a multi-source interconnected power system using optimal fuzzy–PID controller. *Electric Power Compon Syst* 45(19):2104–2117
16. Tasnin W, Saikia LC (2019) Impact of renewables and FACT device on deregulated thermal system having sine cosine algorithm optimised fractional order cascade controller. *IET Renew Power Gener* 13(9):1420–1430
17. Nayak N, Mishra S, Sharma D, Sahu BK (2019) Application of modified sine cosine algorithm to optimally design PID/fuzzy-PID controllers to deal with AGC issues in deregulated power system. *IET Gener, Transm Distrib*
18. Debnath, MK, Jena T, Mallick RK (2017) Optimal design of PD-Fuzzy-PID cascaded controller for automatic generation control. *Cogent Eng* 4(1):1416535
19. Patel NC, Sahu BK, Bagarty DP, Das P, Debnath MK (2019) A novel application of ALO-based fractional order fuzzy PID controller for AGC of power system with diverse sources of generation. *The Int J Electr Eng Educ.* 0020720919829710
20. Debnath MK, Jena T, Sanyal SK (2019) Frequency control analysis with PID-fuzzy-PID hybrid controller tuned by modified GWO technique. *Int Trans Electr Energy Syst* e12074

Automatic Recognition of the Early Stage of Alzheimer's Disease Based on Discrete Wavelet Transform and Reduced Deep Convolutional Neural Network



Bhanja Kishor Swain, Mrutyunjaya Sahani and Renu Sharma

Abstract In this paper, the classification of normal controls (NC), very mild cognitive impairment and mild cognitive impairment (MCI) from structural magnetic resonance imaging (MRI) are proposed, based on the discrete wavelet transform (DWT) and reduced deep convolutional neural network (RDCNN). Multi-resolution analysis using DWT is applied to the digital images for decomposition purposes. The automatic feature extraction, selection and optimization are performed using the proposed RDCNN. The classification accuracy and learning speed of the DWT-RDCNN method are compared with RDCNN by taking the MRI data as input. The superior classification accuracy of the proposed DWT-RDCNN method over RDCNN method as well as other recently introduced prevalent methods is the major advantage for analyzing the biomedical images in the field of health care.

Keywords Magnetic resonance imaging (MRI) · Alzheimer's disease (AD) · Reduced deep convolutional neural network (RDCNN) · Discrete wavelet transform (DWT)

1 Introduction

Alzheimer's disease (AD) is a degenerative brain disease described by progressive dementia identified by the presence of neurofibrillary tangles and neuritic plaques, and the degeneration of specific nerve cells. It is an incessant neurodegenerative ailment that normally begins gradually and compounds over time. It is portrayed by memory hindrance, language dysfunction, and debilitation of acknowledgment, and

B. K. Swain (✉) · M. Sahani · R. Sharma
Institute of Technical Education and Research, Siksha 'O' Anusandhan (Deemed to Be University), Bhubaneswar, Odisha 751030, India
e-mail: bkswain123@gmail.com

M. Sahani
e-mail: mrutyunjayasahane@gmail.com

R. Sharma
e-mail: renusharma_india@yahoo.com

© Springer Nature Singapore Pte Ltd. 2020
R. Sharma et al. (eds.), *Innovation in Electrical Power Engineering, Communication, and Computing Technology*, Lecture Notes in Electrical Engineering 630,
https://doi.org/10.1007/978-981-15-2305-2_43

thus disturbs a patient's everyday life. Alzheimer's disease currently has turned into the 6th driving reason for death [1], and as indicated by a study, individuals who are experiencing dementia everywhere throughout the world is around 47 million and it is evaluated that there will be one individual with AD in every 85 individuals by 2050 [2]. Accordingly, it is of utmost importance to recognize the biomarkers that can allow exact and early judgements of abnormalities in the MRI scans. Furthermore, it is of utmost importance to recognize the MRI biomarkers that can allow exact and early judgements of abnormalities in the MRI scans. Many research articles provide the information about the utilization of different imaging modalities, for example, functional magnetic resonance imaging (fMRI), positron emission tomography, etc. with significant result of classification between normal controls and AD subjects. A precise and early analysis of the Alzheimer's disease and the possibility of the danger of converting from the prodromal state of AD to moderate AD, give patients the familiarity with the condition's seriousness and enable them to take deterrent measures, for example, making way of life changes and taking drugs. At present, many neurologists and medicinal experts have been investing significant energy in examining methods to take into consideration the prodromal state of AD, and empowering results have been often achieved [3]. MRI is an influential, non-invasive brain imaging technique that provides higher-quality information about the shape and volume of the brain than computed tomography (CT), SPECT, and PET scans. The high spatial resolution of MRI scans gives prominent information about small abnormalities in the brain with better contrast and tissue differentiation [4]. In addition, the analytic utilization of MRI has been hugely improved due to the mechanized and exact labelling of MR images, which plays out a significant job in distinguishing AD patients from normal controls (NC) [5]. Initially, a larger part of diagnosis work was practiced manually or semi-manually for estimating from the region of interest (ROI) of MRI, in view of the fact that patients with AD have progressively cerebral decay in comparison with NCs. A large portion of this ROI-based assessment focused with respect to the contracting of the cortex and hippocampus and amplified ventricles. Owing to the shortcomings of ROI-based methods it was important to concentrate on exploring other potential areas that may be linked to AD as segmentation of the complete MRI is of more importance [6]. Therefore, computer-aided automatic approaches are used to help the physicians to diagnose the disease from the MRI. A few artificial intelligence (AI) techniques have been proposed for the exact determination of AD. The surmised volume estimation [7] and the cerebral metabolic rate of glucose (CMRGlc) [8], were regularly processed from fragmented 3D brain region of interest (ROI) and were utilized for AD classification with support vector machine (SVM) [9] and Bayesian method [10]. The strategies dependent on these traditional machine learners regularly function admirably in binary classification, for example, diagnosing AD subjects from normal controls (NC), however, it is not the same for multiclass classification. Therefore, despite the fact that the determination of AD ought to be normally displayed as a multiclass classification issue, it was typically simplified as a lot of paired classification assignments that separate AD or MCI subjects from NC subjects. A strategy dependent on the graph cut algorithm was proposed as of late by Liu et al. [11]. This workflow balanced

the algorithm with parameters comparing to the connections between various phases of AD. In spite of the fact that such customization will in general yield promising classification results, the workflow can be delicate to changes in the informational index and can be difficult to reach out to a large scale. Another way of AD categorization is to use the biomarkers as an input to an unsupervised machine learning approach. Some other works have used the biomarkers with some feature modalities in some supervised machine learning approaches [12–14]. Such workflows suffer the problem of dimensionality decrease and loss of integral data. The traditional feature engineering methods cause feature repetition but deep data representation is efficient in multiclass classification. Deep learning methods separate the important features automatically using different layers and activation functions [15]. Brosch and Tam used a multi-layered deep learning structure to report that the proposed algorithm effectively identifies the variation in the shape of the brain region such as ventricle size [16]. Suk et al. [17], proposed a combined effect of stacked autoencoders (SAEs) and multi-kernel support vector machine (MKSVM) for the classification of AD from the NC but this type of framework may ignore the synergy between different modalities in the feature learning.

In this paper, first, we propose a novel reduced deep convolutional neural network (RDCNN) to automatically extract the discriminative features for the classification of normal controls (NC), very mild cognitive impairment and mild cognitive impairment (MCI). Second, a discrete wavelet transform based reduced deep convolutional neural network (DWT-RDCNN) is proposed for classification purposes. DWT is applied to decompose the input MR images and the decomposed images are fed to RDCNN for detection of affected brain images of MCI subjects. Finally, the DWT-RDCNN method proves its superiority with better classification accuracy and higher learning speed over the RDCNN method.

The rest of the article is organized as follows, Sect. 2 contains the information about the selected dataset for classification, Sect. 3 provides a brief introduction of the discrete wavelet transform, Sect. 4 represents the proposed RDCNN classifier, Sect. 5 discusses the results obtained followed by the conclusion in Sect. 6.

2 Materials and Methods

In this work, the MRI data is collected from the Open Access Series of Imaging Studies (OASIS). OASIS is a publicly available data set containing the compilation of MRI of brains for the easy access to the research and scientific community. The information is publicly available with the demographic data of cohorts at <http://www.oasis-brains.org>.

Figure 1 shows an image of the collected data set depicting the pictorial difference between the MRI of normal control and an early stage of AD patient. The data set of OASIS has two types of collection, the cross-sectional MRI data called as OASIS 1 and the longitudinal MRI data called as OASIS 2. This study concentrates on the automatic diagnosis of MCI considering the cross-sectional data set with 416

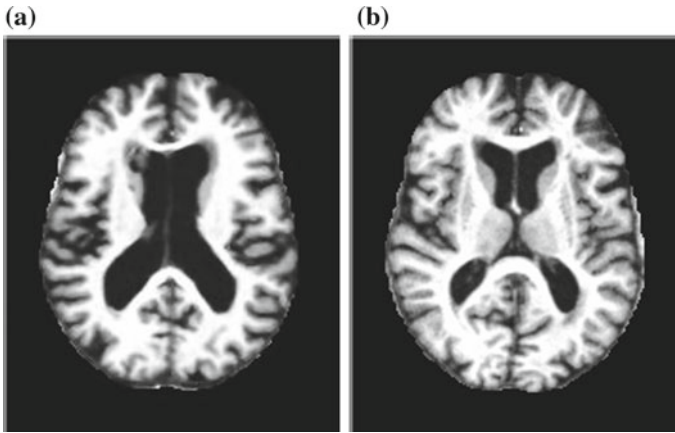


Fig. 1 Axial view of MRI dataset sample of **a** normal control and **b** MCI

subjects between 18 and 96 years old. Out of 416 subjects 196 samples are selected in our study which contains 98 normal controls, 70 very mild cognitive impairment and 28 MCI patients. The statistical information about the subjects from which the 196 samples are selected is presented in Table 1.

The selected data set includes the socio-economical information of the subjects and the handedness. All the subjects included in the data set are right-handed and the statistic highlights of the selected subjects contain gender (M/F), age, mini-mental state examination (MMSE) and the clinical dementia rating (CDR). The mini-mental state examination (MMSE) is a short 30-point questionnaire test generally conducted to observe the state of very mild dementia and mild cognitive impairment. Clinical dementia rating (CDR) is a number within a range of 0–4, estimating the seriousness of different stages of dementia.

Table 1 Cohort's statistical data

Factors	Normal controls	Very mild cognitive impairment	Mild cognitive impairment
No. of patients	98	70	28
Age	75.91 ± 8.98	74.87 ± 7.64	77.75 ± 6.99
CDR	0	0.5	1
MMSE	28.95 ± 1.20	27.28 ± 1.71	21.67 ± 3.75
Gender (M/F)	26/72	29/41	9/19

3 Feature Extraction

The wavelet transform (WT) has been used as a stationary and non-stationary wave-form analyzing tool for removal of disturbances from the desired signal, detection of abrupt discontinuity in electrical signals and compression of large amount of data especially in digital image processing [18]. Unlike the Fourier Transform, the wavelet transform possesses the capability of analyzing a signal in both the time and frequency domains giving information on the evolution of the frequency content of a signal over time. The process of sampling a continuous signal applying wavelet transform can be defined as discrete wavelet transform (DWT). It produces adequate data to analyze a non-stationary signal. WT stands true in analyzing a non-stationary signal by eliminating the resolution problem of STFT. Recently, WT has proved itself as a dominating signal processing tool especially in the application of signal decomposition. WT has applications in the field of image denoising, image compression, feature extraction and also in various fields of power system protection. The perfect signal reconstruction property of WT makes it a propitious method for signal decomposition.

Mathematically continuous wavelet transform (CWT) can be defined as [19]

$$CWT_g^\varphi(\tau, s) = \int_{-\infty}^{\infty} g(t) \cdot \varphi^*(\tau, s, t) dt \quad (1)$$

$$\varphi(\tau, s, t) = \frac{1}{\sqrt{s}} \varphi\left[\frac{t - \tau}{s}\right] \quad (2)$$

where s is the scaling parameter which is used to compress and dilate mother wavelet $\varphi(t)$ to obtain both high and low-frequency information of signal $g(t)$, to be analyzed.

Translational parameter is used to obtain time information. To overcome the calculation problem DWT is used, mathematically:

$$DWT_g^\varphi(m, n, k) = (P_0^m)^{-\frac{1}{2}} \sum_n g(n) \cdot \varphi^*\left[\frac{k - nq_0P_0^m}{P_0^m}\right] \quad (3)$$

where $g(n)$ is the discrete version of $g(t)$ which is discretely dilated by scaling parameter P_0^m and translated by translational parameter $nq_0P_0^m$ where q_0 is a constant with m and n are integers. Generally, $P_0 = 2$ and $q_0 = 1$ were chosen for dyadic transform.

Figure 2 shows three bi-dimension band limited intrinsic mode functions (BBLIMFs) of a sample affected by the early stage of Alzheimer's disease called as MCI.

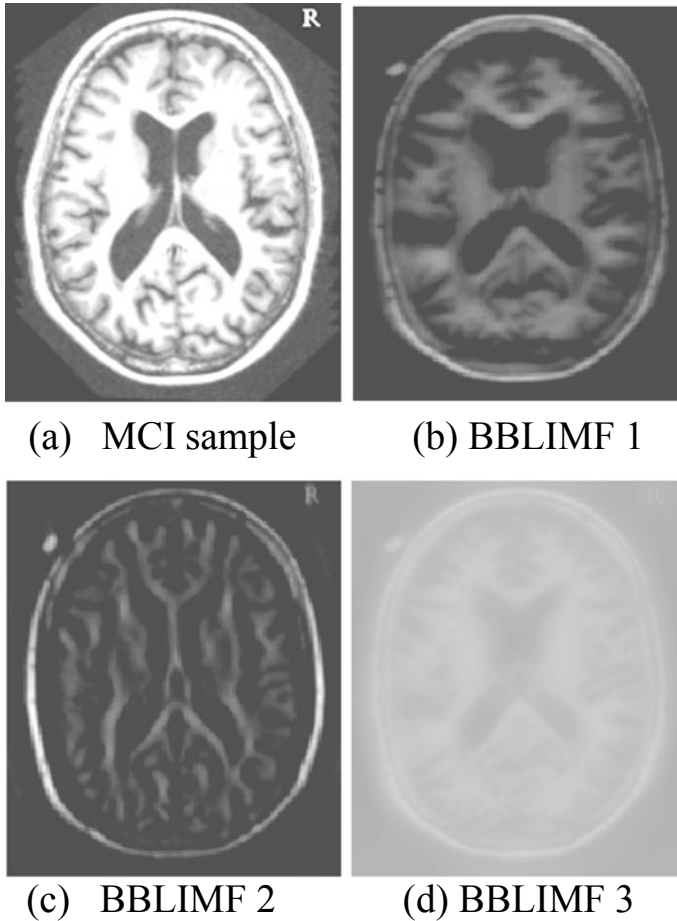


Fig. 2 The MCI sample and three BBLIMFs of DWT

4 The Reduced Deep Convolutional Neural Network (RDCNN)

The reduced deep convolutional neural networks (CNN) have layers with the capability of extracting local features of an image through convolution. The RDCNN architecture comprises of mainly four types of layers: (1) convolutional layer, (2) pooling layer, (3) fully connected layer and (4) softmax layer.

4.1 Convolutional Layer

Every node in a convolutional layer is associated with a subset of spatially connected neurons. The weights in the convolutional layer are shared among the nodes keeping an objective of searching for the same features in the input image. Each set of shared weights is known as a convolution kernel. In this layer, the convolution operation is performed by allowing the selected filters to slide over the input signal and the feature map is obtained by using the following equation

$$C_m = \sum_{n=0}^{N-1} f_n k_{m-n} \quad (4)$$

where k , f , C and N denote signal, filter, output, and the number of data points in k , respectively. The subscript n indicates the n th element of the filter vector while m corresponds to the m th output element that is being calculated. The prime objective of the convolution operation is to extract meaningful features from the input signal to train the algorithm.

Further, the rectified linear unit activation function is employed to speed up learning rate and to reduce non-linearity. The ReLU function does the thresholding operation by assigning zero to the values less than zero and is given as follows

$$f(r) = \begin{cases} R; & r \geq 0 \\ 0; & \text{Otherwise} \end{cases} \quad (5)$$

The batch normalization operation is performed on the output of ReLU layer to reduce the problem of overfitting.

4.2 Pooling Layer

To decrease computational complexity, each succession of convolutional layers is followed by a pooling layer [20]. The max-pooling layer is the most widely recognized and used for pooling operation very often. The main function of the pooling layer is to reduce the dimension of feature map preserving the important features. In this work max-pooling operation is used with a stride of two.

4.3 Fully Connected Layer

The normalized output of pooling layer is flattened and fed to the fully connected layer in which all the neurons in one layer are connected to all the neurons in the successive layers using the following equation

$$x_i = \sum_j w_{ji} y_j + b_i \quad (6)$$

where x and y are the outputs of current and previous layer, respectively with w weights and b biases.

4.4 Softmax Layer

Finally, the softmax function is used for classification by receiving the inputs from the last fully connected layer. It predicts the class of a signal applied at the input and the value of the output of the softmax layer lies between zero and one. The softmax activation function is given as

$$P(x_i) = \frac{e^{x_i}}{\sum_{m=0}^k e^{x_i}} \quad (7)$$

where $P(x_i)$ is the probability of the input to belong to the class of x_i .

5 Result and Discussion

In this work, OASIS1 dataset is used to verify the proposed work in an Intel Core i5-8000U CPU at 2.6 GHz processor of 16 GB RAM using MATLAB/Simulink software environment to detect the affected brain MRI images with MCI. The proposed RDCNN structure for computation, selection and optimization of most discriminate features automatically, is presented in Table 2. The developed architecture is shown in Fig. 3, where the same padding is used before each max-pooling layer and softmax layer is used to classify the non-demented, very mild demented and the early stage of AD input image data based on the probability function. The max-pooling and drop out layer of the novel RDCNN method reduce the major overfitting problem for detecting the MCI affected MRI images accurately. 70% images of each class are used for training and the remaining 30% for testing, in both the proposed RDCNN and DWT-RDCNN methods. The database images are fed to RDCNN to train the network with maximum training accuracy and minimum training cross-entropy loss by taking a smaller number of iterations and is shown in Fig. 4. After training, 30% of images of each class are used to test the network in noise-free and noisy conditions. Furthermore, Daubechies-4 wavelet of discrete wavelet transform is applied on the input images to extract three bi-dimension band limited intrinsic mode functions (BBLIMFs). The BBLIMFs of an image is fed to the proposed RDCNN method to improve the classification accuracy of multi-class classification. The processing time of DWT-RDCNN method is more as compared to RDCNN method but the higher learning speed, minimum training and testing loss, superior classification accuracy

Table 2 The developed structure of the proposed RDCNN

Layer	Name	Output nodes	Filter size	Stride
0–1	Convolution	$[204 \times 172 \times 1] \times 5$	5	1
1–2	Rectified linear unit	$[204 \times 172 \times 1] \times 5$	1	1
2–3	Batch normalization	$[204 \times 172 \times 1] \times 5$	10	10
3–4	Max-pooling	$[102 \times 136 \times 1] \times 5$	2	2
4–5	Convolution	$[93 \times 127 \times 1] \times 10$	10	1
5–6	Rectified linear unit	$[93 \times 127 \times 1] \times 10$	1	1
6–7	Batch normalization	$[93 \times 127 \times 1] \times 10$	10	10
7–8	Max-pooling	$[47 \times 64 \times 1] \times 10$	2	2
8–9	Convolution	$[33 \times 50 \times 1] \times 15$	15	1
9–10	Rectified linear unit	$[33 \times 50 \times 1] \times 15$	1	1
10–11	Batch normalization	$[33 \times 50 \times 1] \times 15$	10	10
11–12	Max-pooling	$[17 \times 25 \times 1] \times 15$	2	2
12–13	Fully connected	6375×1	0	0
13–14	Fully connected	3000×1	0	0
14–15	Fully connected	1000×1	0	0
15–16	Fully connected	100×1	0	0
16–17	Fully connected	3×1	0	0

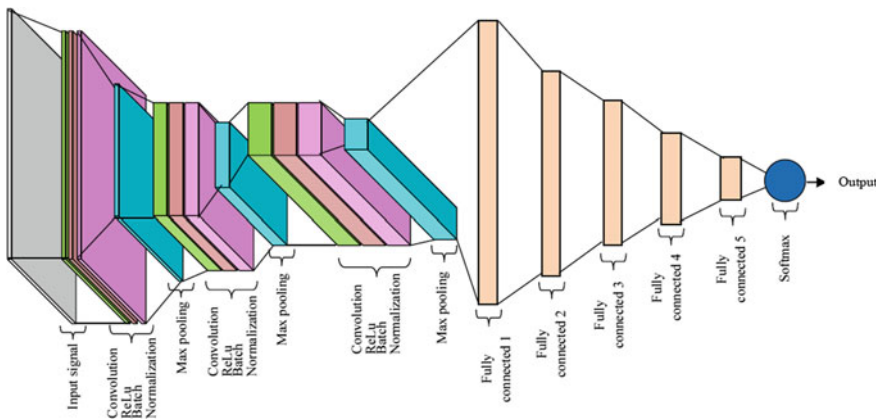


Fig. 3 Architecture of reduced deep convolutional neural network (RDCNN)

and anti-noise performance are the major advantages of DWT-RDCNN method over RDCNN method. The detailed comparison of classification accuracy of both the RDCNN and DWT-RDCNN methods are presented in Table 2.

Finally, Table 3 concludes that the proposed DWT-RDCNN method is the utmost

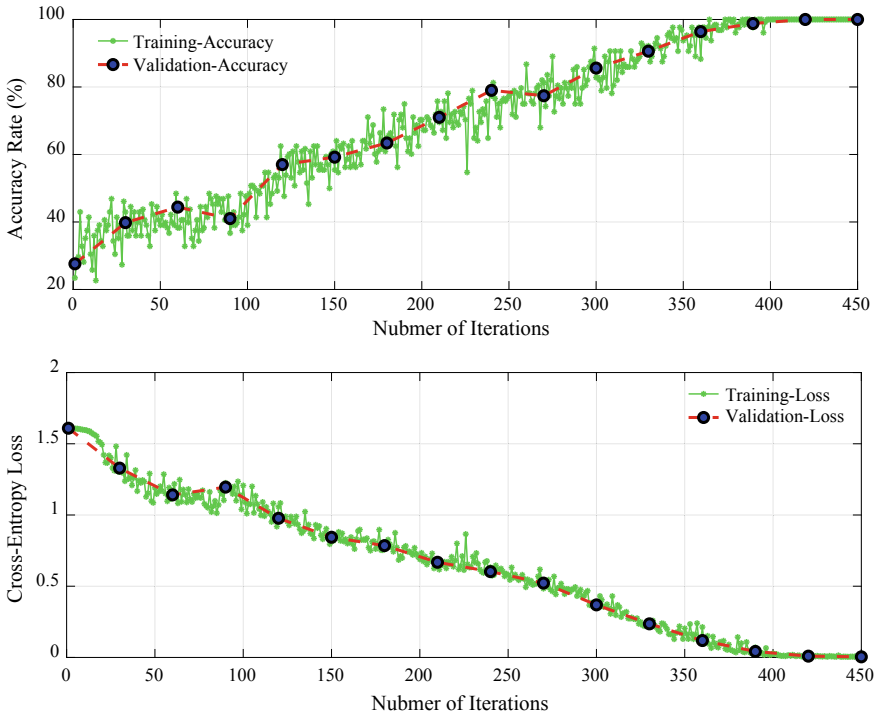


Fig. 4 Training and testing accuracy and loss

Table 3 Comparison of classification accuracy of RDCNN method and DWT-RDCNN method

Proposed model	Noise-free condition	SNR values		
		20 dB	30 dB	40 dB
RDCNN	95.4	90.3	92.3	94.3
DWT-RDCNN	97.9	95.9	96.4	96.9

choice for the recognition of AD at its early stage, called as the stage of MCI, efficiently.

6 Conclusion

The novel reduced deep convolutional neural network (RDCNN) architecture is developed and implemented to detect the early stage of Alzheimer’s disease from brain magnetic resonance images as input. Discrete wavelet transform (DWT) is used to decompose the input brain MRI images into number of images with different

frequency bands. Three decomposed images are fed to the proposed reduced deep convolutional neural network structure to extract the discriminative feature at the last fully connected layer automatically. The extracted features are fed to the softmax layer to classify the non-demented, very mild demented and the early stage of AD patients with superior classification accuracy. The higher learning speed and superior classification accuracy of the proposed DWT-RDCNN method prove its superiority over RDCNN method in both noise-free and noisy environments. Finally, the robustness of the proposed method confirms its application to other digital image classification.

References

1. Alzheimer's Association (2018) Alzheimer's disease facts and figures. *Alzheimer's Dementia* 14(3):367–429
2. Brookmeyer R, Johnson E, Ziegler-Graham K, Arrighi HM (2007) Forecasting the global burden of Alzheimer's disease. *Alzheimer's Dementia* 3(3):186–191
3. Tabaton M, Odetti P, Cammarata S et al (2010) Artificial neural networks identify the predictive values of risk factors on the conversion of amnesic mild cognitive impairment. *J Alzheimer's Dis* 19(3):1035–1040
4. Mahanand BS, Suresh S, Sundararajan N, Aswatha KM (2012) Identification of brain regions responsible for Alzheimer's disease using self-adaptive resource allocation network. *Neural Netw* 32:313–322
5. Jeurissen B, Leemans A, Sijbers J (2014) Automated correction of improperly rotated diffusion gradient orientations in diffusion weighted MRI. *Med Image Anal* 18(7):953–962
6. Zhang Y, Wang S, Ji G, Dong Z (2013) An MR images classifier system via particle swarm optimization and kernel support vector machine. *Sci World J*, Article ID 130134, 9 pp
7. Risacher SL et al (2009) Baseline MRI predictors of conversion from MCI to probable AD in the ADNI cohort. *Curr Alzheimer's Res* 6(4):347–361
8. Cai W et al (2010) 3D neurological image retrieval with localized pathology centric CMRGlc patterns. In: *Proceedings of 17th IEEE international conference in image processing*, pp 3201–3204
9. Zhang D et al (2011) Multimodal classification of Alzheimer's disease and mild cognitive impairment. *NeuroImage* 55(3):856–867
10. Liu S et al (2013) Multifold Bayesian kernelization in Alzheimers diagnosis. In: *Proceedings of international conference in medical image computing and computer-assisted intervention*, pp 303–310
11. Liu S et al (2013) Neuroimaging biomarker based prediction of Alzheimer's disease severity with optimized graph construction. In: *Proceedings of IEEE international symposium on biomedical imaging: from nano to macro*, pp 1324–1327
12. Singh N et al (2012) Genetic, structural and functional imaging biomarkers for early detection of conversion from MCI to AD. In: *Proceedings of international conference in medical image computing and computer-assisted intervention*, pp 132–140
13. Liu S et al (2013) A supervised Multiview spectral embedding method for neuroimaging classification. In: *Proceedings of 20th IEEE international conference on image process*, pp 601–605
14. Che H et al (2014) Co-neighbor multi-view spectral embedding for medical content-based retrieval. In: *Proceedings of IEEE International Symposium on biomedical imaging: from nano to macro*, pp 911–914
15. Bengio Y et al (2013) Representation learning: a review and new perspectives. *IEEE Trans Pattern Anal Mach Intell* 35(8):1798–1828

16. Brosch T, Tam R (2013) Manifold learning of brain MRIs by deep learning. In: Proceedings of international conference in medical image computing and computer-assisted intervention, pp 633–640
17. Suk H-I et al (2013) Latent feature representation with stacked auto-encoder for AD/MCI diagnosis. *Brain Struct Func* 1–19
18. Sahani M (2019) Detection and classification of power quality events using empirical wavelet transform and error minimised extreme learning machine. *Int J Power Energy Conv* 10(4)
19. Mishra M, Rout PK, Routray P (2015) High impedance fault detection in radial distribution system using wavelet transform. In: Annual IEEE India conference (INDICON), pp 1–6. IEEE
20. Tajbakhsh N, Shin JY, Gurudu SR, Hurst RT, Kendall CB, Gotway MB, Liang J (2016) Convolutional neural networks for medical image analysis: full training or fine tuning? *IEEE Trans Med Imag* 35(5):1299–1312

Employing Thermoelectric Coupled Solar PV Hybrid System in Non-conventional Distribution Generation



Sasmita Jena, Keshav Krishna, Sambit Tripathy, Subham Subrajeet Barik, Shalini Patro, Priya Ranjan Satpathy and Sanjeeb Kumar Kar

Abstract The inflation of clean, efficient, sustainable, effective, secure, and reliable electricity demand has been triggered much interest for distribution generation at a miraculous and quickened pace. The necessity of reliability enhancement, diversity of fuel, cutback of greenhouse gases, severe weather fluctuation, etc. has stimulated the inclusion of Microgrid concept not only in utility level but also in customer and community level. Incorporation of solar photovoltaic (SPV) and thermoelectric (TE), termed as Solar photovoltaic-thermoelectric (SPV-TE) hybrid system is found to be a very promising technique to broadening the utilization of solar spectrum and enhancing the power output effectively-cum-efficiently. This hybrid architecture caters electrical energy with additional thermal energy that signifies upon harnessing of solar insolation in an exceptional way. This paper portrays on implementation of the aforementioned SPV-TEG coupled system in Non-conventional Distribution Generation in order to retrieve enough power from SPV array giving rise to higher active power delivery to the system and lower the reactive power absorbance by the system. The comparative analysis is done under subsystem such as SPV-TEG-Wind

S. Jena (✉) · K. Krishna · S. Tripathy · S. S. Barik · S. Patro · P. R. Satpathy · S. K. Kar
Department of Electrical Engineering, Institute of Technical Education and Research,
Siksha O Anusandhan (Deemed to be University), Bhubaneswar 751030, Odisha, India
e-mail: sasmita.jena500@gmail.com

K. Krishna
e-mail: keshavkrishnasonal@gmail.com

S. Tripathy
e-mail: aryanroy0953@gmail.com

S. S. Barik
e-mail: subhamsubhrajitbarik@gmail.com

S. Patro
e-mail: shalinipatro4@gmail.com

P. R. Satpathy
e-mail: priransat3@gmail.com

S. K. Kar
e-mail: sanjeebkar@soa.ac.in

Energy system (WES) over SPV-WES on the basis of active and reactive power. The system is modeled, analyzed and validated under MATLAB-Simulink environment.

Keywords Solar PV system · TEG · Non-conventional distribution generation · Wind energy system · Reactive power · Active power

1 Introduction

Supplementary energy resources are becoming mandatory upon the enduring energy reserves to cope with the energy demand of surging population and technological advancement in the world [1]. Though the Sun is a boundless energy resource which also clean as well as unreservedly available energy resource from nature, it suffers from the curse of having lower efficiency upon the most used renewable energy resources. Concentrated solar photovoltaic modules (CPV) are also sunlight based energy generator that converts a portion of solar irradiance into electrical energy having much more efficient than traditional solar PV system. Several portions of the solar irradiation have wasted as heat while converting sunlight into electricity. SPV system suffers from having lower quantum efficiency as it dissipates greatly (around more than half) of the solar irradiation as heat. Hence by utilizing the dissipated heat into the conversion of electricity the power generation and ultimately efficiency can be increased. Many researchers have been working on the hybridization of solar PV-Wind energy system (WES)-FCT, its control aspect, storage. In the source side design of MPPTs for SPV and WES such as optimization-based MPPT, Modified MPPT raises the system cost as well as mathematical complexity [2]. As per our knowledge, implementation of SPV-TEG based system has not been employed in non-conventional distribution generation yet. Most of the researchers have been working upon the hybridization of solar PV, WES and FCT based power generating sources in Microgrid resulting substantial generation of active power and reactive power [3–5]. These papers lag the complete use of solar irradiation for extracting a significant amount of power from the solar PV array resulting in higher electrical efficiency. But as far as our concern, implementation of solar PV-TEG based hybrid system in conventional Microgrid has not been studied yet. The novelty of the paper lies in the employment of aforementioned technique (SPV-TEG hybrid system) for availing higher active power and lesser reactive power from the traditional Microgrid. Finally, system performance has been studied in this paper for employment of SPV-TEG based system in non-conventional distribution generation system under zero fault and numerous faulty conditions.

2 System Modeling and Description

The modeling of thermoelectric generator (TEG) and solar PV modules (SPV) have been performed by insertion of corresponding number of modules in parallel and series as per the requirement. After being designed individually, both the systems have been combined in order to perform the study upon the hybrid system. The model is described in individual subsection namely:

- Modeling of Solar PV array
- Modeling of TEG
- Modeling of WES
- Modeling of DC–DC Converter
- Modeling of VSC (Voltage Source Converter)
- Modeling of Control Algorithm
- Modeling of Filter
- Modeling of Electrolyzer and its bidirectional converter.

2.1 Modeling of Solar PV Array

Solar irradiation and temperature on the solar PV module surface are solely responsible for the characteristics of SPV array. As the solar irradiance upon the SPV array is increased, the power generated from SPV array is also increased. In order to construct an SPV array, number of SPV modules need to combine in a particular fashion either in series or parallel to obtain the requisite power. The equivalent circuit of the solar cell is shown in Fig. 1 where I_{ph} defines the function as current source, R_{sh} defines the internal shunt resistance, R_{se} is the series resistance and a diode connected in parallel with the current source [6]. The output current of the solar PV module

$$i.e. I_{pv} = N_p I_{ph} - N_p I_0 \left[\exp \left\{ \frac{q(V_{pv} + I_{pv} R_s)}{N_s A k T} \right\} - 1 \right] - I_{sh} \quad (1)$$

Fig. 1 Equivalent circuit of solar cell

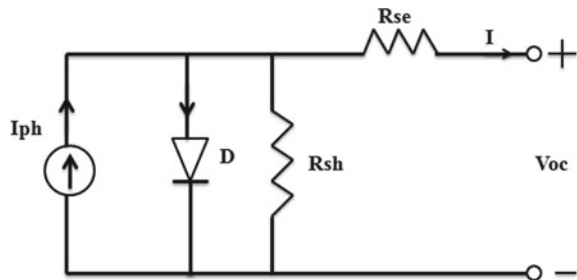


Table 1 Specification of TEG module

Parameters	Values
Open circuit voltage (V)	8.8
Cold junction temperature (°C)	30
Hot junction temperature (°C)	300
Load resistance (Ω)	1.25
Load output voltage (V)	4.27
Load output power (W)	15
Load output current (A)	3.52
Heat flow density (W/cm ²)	~12
Heat flow across the module (W)	~370

where $k = \text{Boltzmann's constant} = 1.3805 \times 10^{-5} \text{ J/K}$, $A = \text{ideality factor of the solar PV cell}$ depend on PV manufacturing technology, some of them are presented in Table 1, $T = \text{operating temperature of the module}$, $q = 1.6 \times 10^{-19} \text{ C}$.

2.2 Modeling of Thermoelectric Generator

The working of TEG constitutes of three elementary thermoelectric effects with two accessorial effects. The three elementary effects are named as Seebeck effect, Peltier effect, and Thomson effect while the accessorial effect can be named as Joule effect and Fourier effect. Seebeck effect is responsible for electromotive force (EMF) and Peltier heat, Thomson heat and Joule heat are caused by the effect of Peltier, Thomson, and Joule, respectively. As a matter of fact, Peltier effect is not an interface effect; it produces heat only at the end sides of the semiconductors. Volumetric effects like Thomson and Joule heat production are pretended to be uniformly transferred to the cold and hot junctions of the semiconductor elements [7]. Though the Thomson effect is very small it is often neglected in many cases.

For steady-state analysis at cold and hot junction of TEG an energy balance equation is used which can express as follows (2) and (3):

Mathematically

$$Q_h = \alpha * T_h * I - k_{tc} \Delta T - 0.5I^2 R \tag{2}$$

$$Q_c = \alpha * T_c * I - k_{tc} \Delta T + 0.5I^2 R \tag{3}$$

The electrical current can be expressed as (4):

$$I = \frac{\alpha \Delta T}{(1 + n)R} \tag{4}$$

Table 2 Modeling parameters at steady state

Parameters	Symbols	Corresponding values
Seebeck coefficient	α	0.035 V/K
Resistance	Ω	1.22
Thermal conductivity	k_{tc}	20.91 W/K
Figure of merit	Z	$0.387 \times 10^{-6} K^{-1}$

The short circuit current is the maximum current at a load voltage of zero i.e. $V_L = 0$. Hence can be written as (5):

$$I_{SC} = 2I_m = \frac{2W_m}{V_m} \tag{5}$$

Finally, the voltage of TEG can be expressed by using Ohm’s Law, and the corresponding equation obtaining short circuit current and current through TEG is shown in Eq. (5)

$$V = -R(I - I_{SC}) \tag{6}$$

A model of TEM specified by TEPI-12656-0.6 has been used over here to model the hybrid system and the behavioral analysis has been conducted. The parameter specifications of the thermoelectric module (TEM) have been listed in Table 1. The constraints that have been considered for modeling are presented in Table 2.

2.3 Modeling of Wind Turbine

About 350–400 W power is generated from a permanent magnet based self-regulated variable speed wind turbine at a wind speed of 12 m/s. Stall control or self-control can be achieved by adjustment of wind turbine blades in a particular direction. At a wind speed of 17 m/s this wind turbine can be able to extract power from the wind.

The aerodynamics of the rotor can be stated as (7)

$$P_w = \frac{C_p \rho A v_w^3}{2} \tag{7}$$

where P_w = wind power,
 C_p = Power coefficient.

2.4 Modeling of Electrolyzer

A resistor (contact resistance) connected in series with the controlled voltage source (CVS) is considered for modeling of an Electrolyzer. A shepherd's model has been used for representation of nonlinear voltage which varies with amplitude of current and amplitude of the actual voltage. The CVS can be represented mathematically as (8):

$$E = E_0 - K \frac{Q}{Q - \int i dt} + A \exp(-B \int i dt) \quad (8)$$

where E is No Load Voltage, E_0 is Constant Electrolyzer Voltage, K is the Polarization Voltage, Q is the Capacity of Electrolyzer, A is the Exponential Voltage, B is the Exponential Capacity, i is the Current of the Electrolyzer. Bidirectional converter is an integral part of connecting an Electrolyzer with a system. As the name suggests the flow of power is in both the directions. Generally, system integrated with Fuel Cell, Supercapacitors use bidirectional converter for power flow in both directions.

2.5 Modeling of DC-DC Converter

In order to step up the voltage at the output of the terminal, dc-dc converter is used which is also termed as boost converter.

It can be stated as (9)

$$V_0 = \frac{V_s}{1 - D} \quad (9)$$

where

V_0 denotes Output Voltage of the System

V_s denotes Input/Source Voltage of the System

D denotes Duty Cycle (it varies from 0 to 1).

2.6 Modeling of Voltage Source Converter (VSC)

For mitigation of power quality issues, converting dc side voltage into ac voltage for feeding it to the grid; VSC is connected to the system. This can also act as an active shunt filter. Natural a-b-c reference frame has been considered for modeling of the VSC. The following equations have been used in order to model the VSC.

Mathematically,

$$S_a = 2S_1 - 1 \quad (10)$$

$$S_b = 2S_3 - 1 \quad (11)$$

$$S_c = 2S_5 - 1 \quad (12)$$

$$V_{ia} = \left(\frac{2}{3}\right) * \frac{V_{dc}}{2} * S_a - \frac{1}{3}S_b - \frac{1}{3}S_c \quad (13)$$

$$V_{ib} = \left(\frac{2}{3}\right) * \frac{V_{dc}}{2} * S_b - \frac{1}{3}S_a - \frac{1}{3}S_c \quad (14)$$

$$V_{ic} = \left(\frac{2}{3}\right) * \frac{V_{dc}}{2} * S_c - \frac{1}{3}S_a - \frac{1}{3}S_b \quad (15)$$

where,

- S_a, S_b, S_c define three-phase Switches (Eqs. 10–12);
- S_1, S_3, S_5 define Switching state of switches;
- V_{ia}, V_{ib}, V_{ic} define Voltage output of inverter (Eqs. 13–15);
- V_{dc} define DC link voltage.

2.7 Modeling of Control Strategy of VSC

There is a self-uniqueness of this control strategy for operation during healthy as well as faulty conditions. The control strategy thus used is found to be efficient as after the clearance of fault, it brings the system back to the steady-state. No controller will be going to work during fault; hence the control strategy is designed in such a way that as soon as the fault is cleared the system comes back to the initial position as soon as possible. Whatever non-conventional sources are proposed to integrate this strategy holds well every time. A multiplication factor of 0.0045 is considered for phase voltages. The control strategy thus used can be shown in the block diagram in Fig. 2.

2.8 Filter Modeling

Though the system uses many power electronics-based switches there is the chance of generation of harmonics in the system. In order to lessen the harmonics filter circuits have been implemented. The Synchronous reference frame (SRF) has been used in order to model the filter circuit that can be explained below.

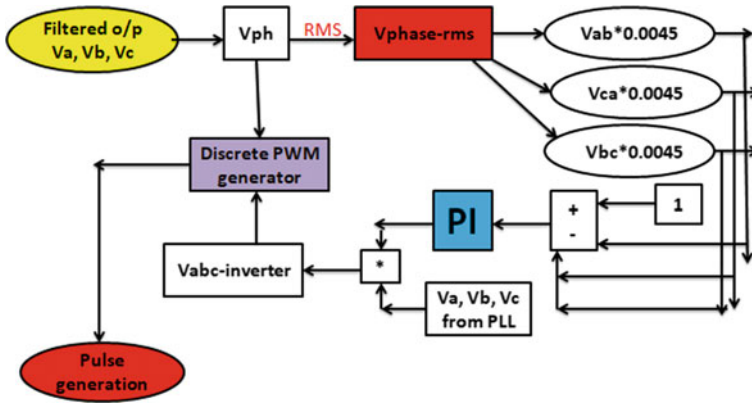


Fig. 2 Control strategy of VSC generating gate signal

$$V_{id} = R_f i_d + L_f \frac{di_d}{dt} - \omega_e L_f i_q \tag{15}$$

$$V_{iq} = R_f i_q + L_f \frac{di_q}{dt} + \omega_e L_f i_d \tag{16}$$

where,

- R_f denotes Resistance of Filter;
- L_f denotes Inductance of Filter;
- ω_e Denotes Angular Frequency;
- i_d, i_q denotes d and q-axis inverter currents;
- V_{id}, V_{iq} denotes d and q-axis inverter voltages.

3 Proposed System Configuration

Figure 3 shows the pictorial presentation of the proposed system.

The figure represents the proposed system of employing thermoelectric generator (TEG) in NDG. The newness of this work lies in integrating TEGs with solar PV array so that the power generation from the RE sources could be maximized in a significant manner. As per our knowledge, implementation of TEGs has not yet considered for Microgrid. Hence the proposed system is compared with conventional NDG to infer the superiority of employing TEGs to NDG.

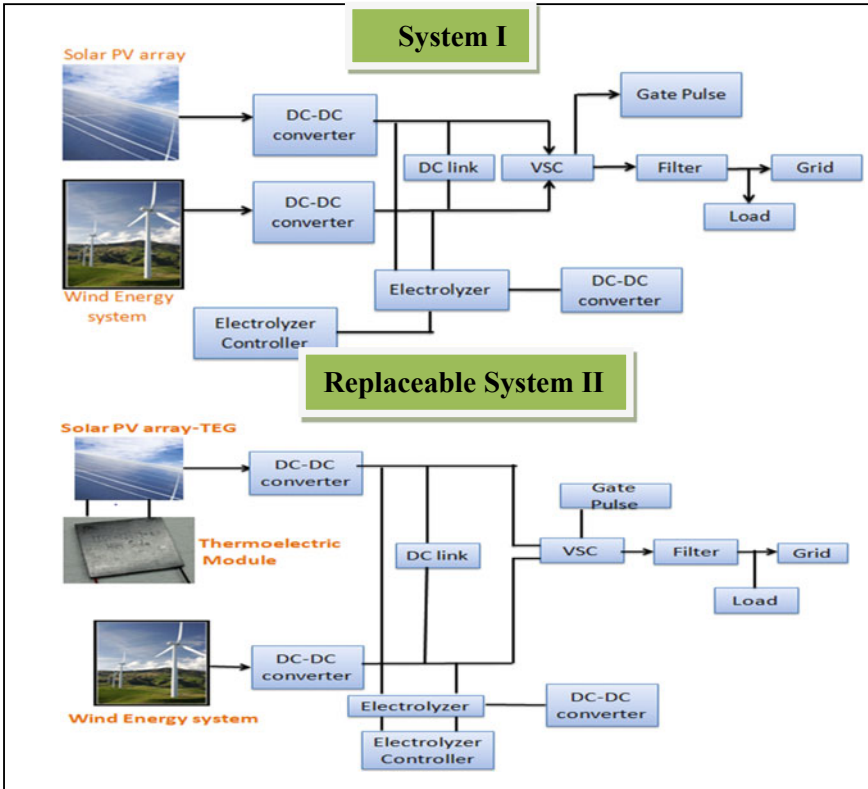


Fig. 3 System I to be compared with proposed system configuration

4 Results and Discussion

The system is subjected to healthy condition as well as several variations (fault conditions). The reliability of the whole NDG system is studied for several parameters such as active power delivered to the system by the RE sources (P) and Reactive power supplied to the system (Q). The control strategy applied to the system has been studied precisely during variations. Because the main aim of control strategy will be defined best when the fault is cleared means as soon as the fault is cleared the control strategy starts its action in order to retain the system back to the initial condition. Thus the applicability of the proposed system is verified for healthy condition (during zero fault), and faulty conditions such as Line-to-Ground (L-G) fault.

4.1 During Healthy Condition (Zero Fault Condition)

The proposed system is integrated with TEG in order to utilize the significantly lost heat by solar PV modules which are integrated into conventional Microgrid integrated with WES.

Solar PV array receives solar insolation for the generation of electricity. In Fig. 4, the active power thus generated by the proposed system is about 1.86 times to the conventional NDG. Similarly in Fig. 5, the reactive power generation is found to quite lesser i.e. equivalent to 2.93 times than the system I.

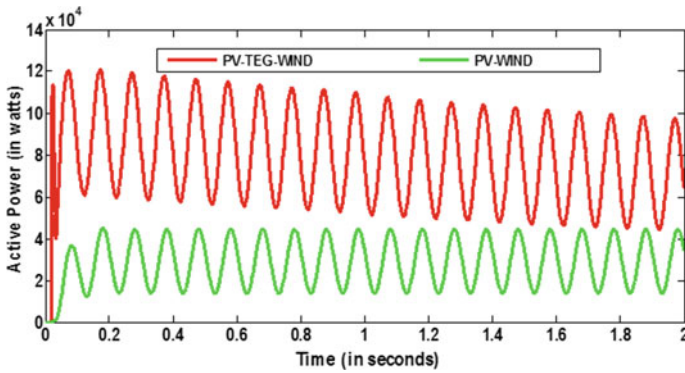


Fig. 4 Active power delivered for PV-TEG-WIND and PV-WIND system

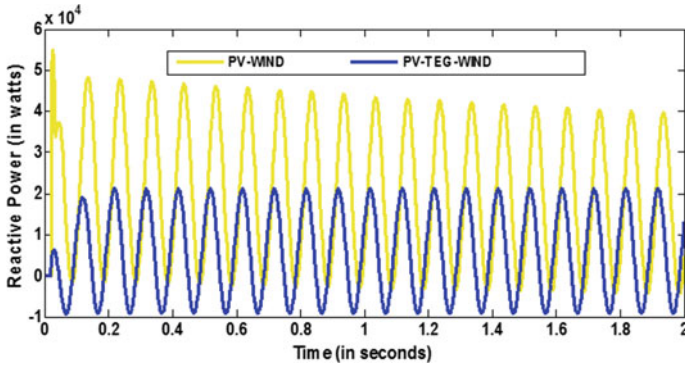


Fig. 5 Reactive power delivered for PV-TEG-WIND and PV-WIND system

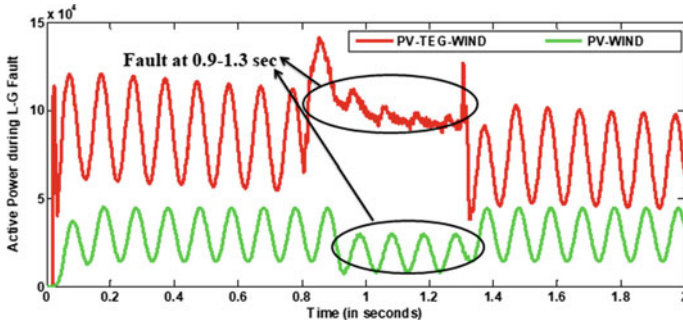


Fig. 6 Active power during L-G fault for PV-TEG-WIND and PV-WIND system

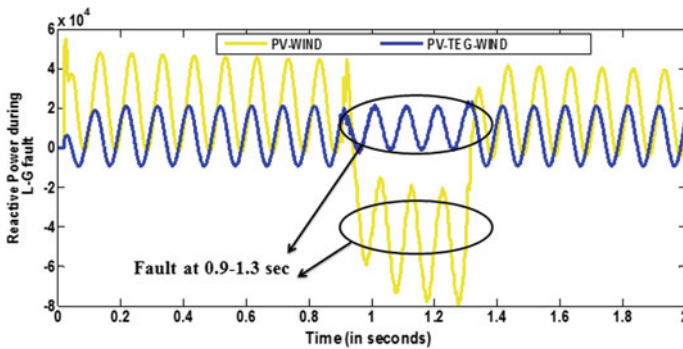


Fig. 7 Reactive power during L-G fault for PV-TEG-WIND and PV-WIND system

4.2 During Line to Ground Fault Condition

The proposed system is studied under fault conditions in order to check the reliability of the controller during disturbances. The system fault is created in virtual scenario. In the above studied single L-G fault active power, reactive power, solar power is shown in Figs. 6 and 7. It can be inferred that the controller acts precisely as the overall system comes back to steady-state just after the fault is cleared. The fault duration is set to be 0.9–1.3 s. In Fig. 6 the active power delivered by the proposed system is about 1.867 times to the conventional one though it suffers from disturbances, similarly, the reactive power absorbed is quite lesser i.e. about 2.95 times than that of conventional one in Fig. 7.

5 Observational Analysis

The observational analysis of the study has been shown in Table 3.

Table 3 Observation analysis of replaced system with conventional in terms of active and reactive power

During healthy condition		During L-G fault condition	
System I	Replaced system II	System I	Replaced system II
$P = 3.458 \times 10^4 \text{ W}$	$P = 6.443 \times 10^4 \text{ W}$	$P = 3.447 \times 10^4 \text{ W}$	$P = 6.435 \times 10^4 \text{ W}$
$Q = 1.37 \times 10^4 \text{ W}$	$Q = 4660 \text{ W}$	$Q = 1.378 \times 10^4 \text{ W}$	$Q = 4671 \text{ W}$
$\Delta P = 2.985 \times 10^4 \text{ W}$	% of increase = 46.32%	$\Delta P = 2.988 \times 10^4 \text{ W}$	% of increase = 46.43%
$\Delta Q = 1193 \text{ W}$	% of decrease = 19%	$\Delta Q = 1177 \text{ W}$	% of decrease = 19.61%

6 Conclusion

Thermoelectric Generators (TEG) are integrated with solar PV system in order to process the lost heat by thermoelectric effect. The conversion of light energy into electricity by photoelectric effect and converting heat into electricity by thermoelectric effect combinedly generate a significant amount of power from solar PV array. Hence this technique is implemented on conventional DG. In the proposed SPV-TEG-WES based system, about 45–50% more active power is delivered to the system while about 67–70% lesser reactive power is absorbed than that of conventional SPV-WES. The proposed system is studied on several constraints like active power, reactive power, and solar power. The entire system is modeled, studied, analyzed and validated using MATLAB/Simulink environment. The combined PV-TEG has shown a greater impact on traditional Microgrid giving rise to higher active power delivery to the system, lower reactive power absorbance. Hence the TEG integration is found to be very fruitful to the conventional hybridization where solar PV array is employed. The work can be extended to experimental verification with the theoretical determined results and thereafter the conventional system can be integrated with the TEGs for significant extraction of power from the solar PV array.

References

- Jena S, Kar SK (2019) Setting a fostered energy network by decarbonizing the grid: Hybridization, control, and future solutions upon storage. *Int J Energy Res* 43(1):455–474
- Grubišić-Čabo F, Nižetić S, Giuseppe Marco T (2016) Photovoltaic panels: a review of the cooling techniques. *Trans FAMENA* 40(SI-1):63–74
- Nižetić S, Čoko D, Yadav A, Grubišić-Čabo F (2016) Water spray cooling technique applied on a photovoltaic panel: the performance response. *Energy Convers Manag* 108:287–296
- Nižetić S, Grubišić-Čabo F, Marinić-Kragić I, Papadopoulos AM (2016) Experimental and numerical investigation of a backside convective cooling mechanism on photovoltaic panels. *Energy* 111:211–225
- Senthilkumar J, Charles Raja S, Srinivasan D, Venkatesh P (2018) Hybrid renewable energy-based distribution system for seasonal load variations. *Int J Energy Res* 42(3):1066–1087

6. Wu YY, Wu SY, Xiao L (2015) Performance analysis of photovoltaic–thermoelectric hybrid system with and without glass cover. *Energy Convers Manag* 93:151–159
7. Beerl O, Rotem O, Hazan E, Katz EA, Braun A, Gelbstein Y (2015) Hybrid photovoltaic-thermoelectric system for concentrated solar energy conversion: experimental realization and modeling. *J Appl Phys* 118(11):115104

Design of Artificial Pancreas Based on Fuzzy Logic Control in Type-I Diabetes Patient



Akshaya Kumar Patra, Anuja Nanda, Shantisudha Panigrahi
and Alok Kumar Mishra

Abstract This manuscript presents a SIMULINK model of Glucose Metabolism (GM) process and design of a Fuzzy Logic Controller (FLC) to regulate the Blood Glucose (BG) concentration in Type-I Diabetes Mellitus (T1DM) patients. The FLC is a novel approach whose gains dynamically vary with respect to the error and change in error signal. The validation of improved control action of FLC is established by comparative result investigation with other published control algorithms. The comparative results clearly reveal the better performance of the proposed approach to control the BG concentration (level) within the *normoglycaemic* range in terms of accuracy, stability, and robustness.

Keywords Diabetes · Insulin dose · Glucose concentration · MID · FLC

1 Introduction

As per the World Health Organization report, one among the widespread diseases is diabetes mellitus and is resulted due to the malfunctioning of the pancreas. This reduces insulin sensitivity affecting the *normoglycaemic* range of BG concentration (70–120 mg/dl) in a healthy human being. At present, numerous research projects are undertaken by several researchers to get rid of this problem by devising advanced

A. K. Patra (✉) · A. Nanda · A. K. Mishra
Department of EEE, Institute of Technical Education and Research, Siksha 'O' Anusandhan
(Deemed to Be University), Bhubaneswar 751030, Odisha, India
e-mail: hiakp@yahoo.com

A. Nanda
e-mail: anuja.sus@gmail.com

A. K. Mishra
e-mail: alokmishra@soa.ac.in

S. Panigrahi
Department of CSE, Institute of Technical Education and Research, Siksha 'O' Anusandhan
(Deemed to Be University), Bhubaneswar, Odisha 751030, India
e-mail: santisudha.nanda@gmail.com

© Springer Nature Singapore Pte Ltd. 2020
R. Sharma et al. (eds.), *Innovation in Electrical Power Engineering, Communication, and Computing Technology*, Lecture Notes in Electrical Engineering 630,
https://doi.org/10.1007/978-981-15-2305-2_45

medical equipment like automated MID. Till date, BG concentration is manually controlled to adopt the open-loop control strategy. The hypoglycaemic or hyperglycaemic conditions may evolve due to the difficulties in handling the internal system changes and external disturbances by implementing the control loop technique. The development of implanted Artificial Pancreases (AP) enabling the adequate dose of insulin delivery proportionate to the sensor measurement in the patient's body may provide the means to incorporate the closed-loop control strategy. Figure 1a describes a closed-loop patient model with an AP. The AP consists of glucose sensor, MID, and controller (FLC). The sensor measures the BG concentration of the human body continuously and sends signal to the controller (FLC) for generating the desired control actions. The control signal $u(t)$ generated by this controller (FLC) also depicts the association of the additional model uncertainties and disturbances. Thereafter, according to the $u(t)$, the optimal insulin dose is infused into the patient's Venous Blood (VB) by MID to achieve the *normoglycaemic* range of BG concentration [1, 2].

To determine an optimal solution for the AP like building an appropriate model of the complex BG regulatory system, a number of obstacles and challenges such as the effects of nonlinear behavior, time-dependent dynamics, presence of several sources of disturbance, uncertainty and lack of glucose sensing are to be faced. Additionally, the challenges and constraints related to control, specifically for BG regulation controller design are considerable glucose measurement delay, insulin absorption delay after being injected, irreversible action of insulin, meal detection, and estimation, model parameter variation, asymmetric risk of extreme BG concentration variations and time-based control needs, etc. [1]. Despite of technical progress and considerable development on aforesaid issues, substantial improvement is still required in the control algorithm. Assessment of the glucose excursions following the insulin dose adjustment needs a controller for BG regulation in AP and many authors suggested the PID controller as a viable solution [3, 4]. However, due to glucose sensing time delay, insulin action, and non-variable gain parameters, the desired performance, assuring high accuracy, reliability and robustness could not be achieved. The fuzzy control [5, 6], LQG control [7], H_∞ control [8–10], Sliding Mode (SM) control [11–14], and MP control [15, 16] are some of the well-proven controllers to deal with the BG regulation issues. The BG control in the diabetic patients within the *normoglycaemia* range inculcating the above controllers enhanced the accuracy and robustness to some extent compared to the PID controllers. However, these control approaches are not entirely insensitive to the disturbances and the uncertainties of the model in spite of the improved performance. Hence, optimal control parameters setting for better performance and for avoiding slow response following meal disturbance, the current work suggests an alternative novel technique implementing the fuzzy logic control.

The FLC approach concept leads to enhanced control performance with respect to robustness and delay of time compensation characteristics to counteract the negative impact of associated errors, disturbances, and uncertainties. The stabilizing control law $u(t)$ is developed based on the FLC approach. Application of the FLC to control the BG concentration in T1DM patient results to ensure a better robust controller in

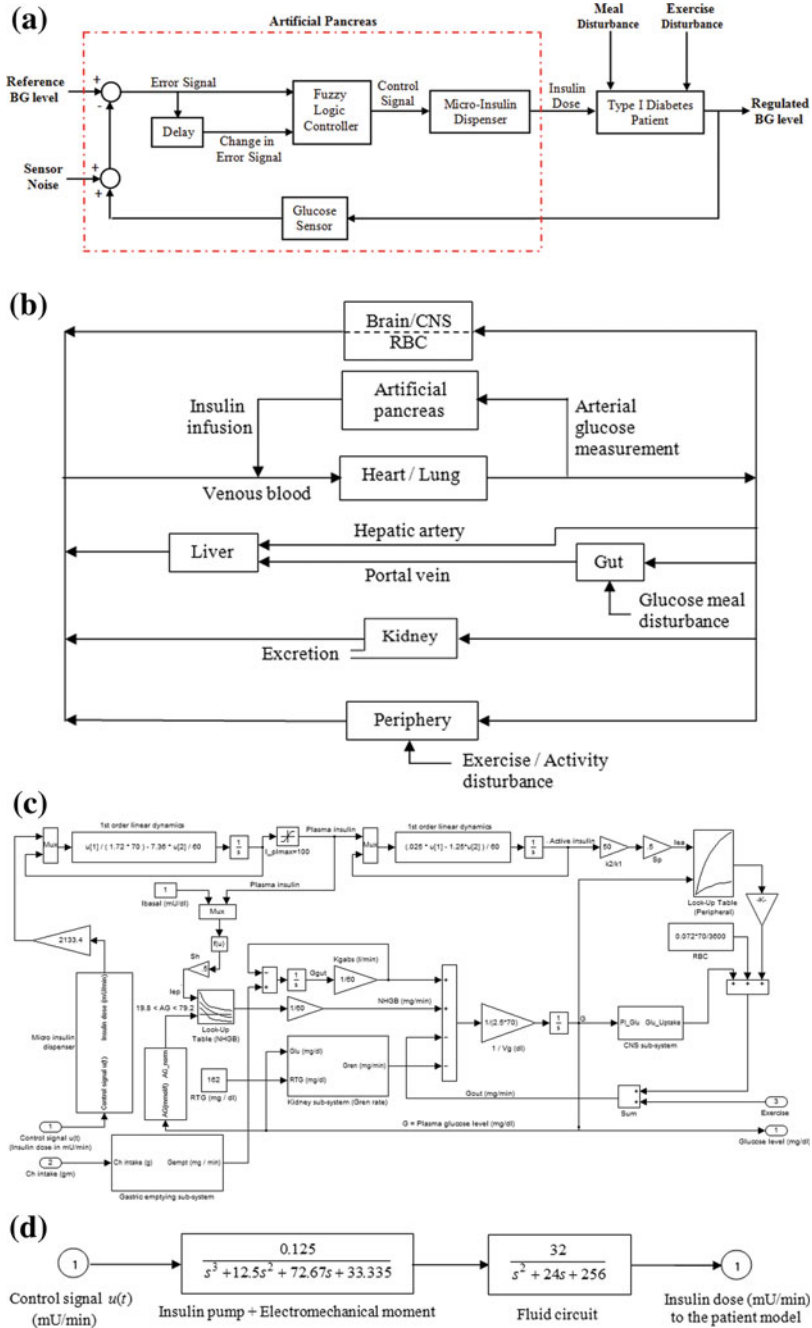


Fig. 1 a Overview of T1DM patient model with AP; b compartmental model of T1DM patient with AP; c SIMULINK model of T1DM patient with MID; d SIMULINK model of MID

comparison to other contemporary well-accepted methods under both harmonized and incompatible uncertainties.

The highlights of this manuscript are as follows:

- Development of a SIMULINK model of the T1DM patient.
- Design of a novel FLC to control the BG concentration within the stable range.
- Evaluation of the control actions of the FLC under several abnormal conditions.
- Comparative investigation to certify the better response of the FLC.

This manuscript is organized as follows. Section 2 concisely illustrates the T1DM patient model with mathematical details reflecting its dynamic characteristics of its GM process. Also, it clearly demonstrates the simulation execution of the system on MATLAB environment. A detailed presentation on how the control technique is formulated and how it is implemented for this problem is presented in Sect. 3. Comparative results of the proposed approach with other published control techniques and the related analysis are provided in Sect. 4. The concluding comments are summarized in the Sect. 5.

2 Problem Formulation and Modeling of T1DM Patient

The problem formulation and all dynamics of patient model are described in this section.

2.1 System Overview

The compartmental model schematic diagram as depicted in Fig. 1b reveals the GM dynamics of the human body. The proposed controller is tested using the above model. The human body has liver, kidney, periphery, heart/lungs, gut, and brain as different functional parts and is shown as six compartments separately. The blood flow directions or circulation are indicated by the arrow marks. The controller receives the measured arterial glucose value as input to provide the optimal insulin dose to be injected as an output with the help of MID.

2.2 Clinical Background

A human body with a prolonged high arterial BG level that exceeds 144 mg/dl is known to suffer from *hyperglycaemia* disease. This type of clinical disorder is also termed as diabetes mellitus. The insulin deficiency along with its less resistive or insensitiveness independently or combinedly cause *hyperglycaemia* and are some of the major reasons as discussed in [17, 18]. Diabetes Mellitus may occur if the blood

glucose remains unutilized effectively under any normal human life cycle. Diabetes is classified as type-I and type-II as per the rate of insulin creation in the patient's body. In the type-I diabetic patients, the insulin creation by the pancreatic cells is completely impossible, but in the case of the type-II is at a bit smaller rate, which also gets inhibited in due course. Hence, in the present situation, an immediate insulin injection to restore the normal BG level is essential that also prevents allied adverse impacts on the normal operation of any human body. Subject to diverse fooding, fasting and exercise behaviors, the regulation of the BG levels is not very easy in the real human life cycle.

The external sources like the carbohydrate foods are digested down into glucose at gut, and then filtered. The filtered glucose is added to the VB. Later on, the liver stores this glucose after being transferred from the venous blood as glycogen. When the BG concentration in the VB is less than *normoglycaemic* range of glucose concentration, glycogen is re-injected as glucose by the liver into venous blood and is known as the internal glucose source. The glucose utilization and production by the liver is known as the Net Hepatic Glucose Balance (NHGB), which is the general phenomena in the glucose metabolism process. The total energy needed by human body organs irrespective of insulin dependency derives from the degree of glucose utilization.

The creation of insulin is due to the β -cells present in the pancreas and thus the BG level is regulated. A normal human with high BG level has two major functions of insulin, firstly to allow the liver for the glucose absorption along with storing it in the form of glycogen, specifically under the meal intake conditions. As a result, the production of excess 'internal' glucose by the liver and muscles is stopped. Secondly, insulin speeds up the glucose absorption in the muscles and fulfills the peripheral energy needs of the body. But, in case of diabetes patients the abnormality in the MP dynamics, both the aforementioned functions are found to impair partially or completely. In case of diabetes patients, the cells stop the glucose utilization and internal glucose is produced by the liver, then an uncontrolled BG level is noticed. Later, as the BG level is more than the RTG value of 162 mg/dl, venous BG in excess is extracted through the kidney.

2.3 Modeling of a T1DM Patient

In the present scenario, with due consideration of the dynamics of the glucose metabolism process, several simulation models are proposed to control the BG concentration in the T1DM patients [19–22]. Owing to the simplified structure and desired approximation to the dynamics of human metabolism with reduced error, the model suggested by Parker et al. [19], Parker and Doyle [20] and Lehmann and Deutsch [21, 22] are among the widely accepted ones. The testing and verification of the proposed technique using Lehmann and Deutsch [21, 22] model for BG control are considered in the present study. Figure 1b describes the compartmental set up of a diabetic patients with the implanted AP. The controller computes the insulin injection amount to the VB at 5 min interval using an integrated implanted insulin pump.

Depending on the supporting device and sensing technology, the sampling rate varies when is being applied in the real-time domain [23, 24]. The gut compartment input is the meal and the peripheral input is the exercise for integrating and executing the process disturbances. Compartmental modeling method considering the equations of the fast principle has been used to develop the GI interaction process with a MID model of the patient [21, 22]. Figure 1c demonstrates the simulated model of the patient with MID.

2.4 *Micro-insulin Dispenser*

In this study, a 5th order model suggested by Cochin and Cadwallender [24] is taken up to devise the MID model. Figure 1d represents all dynamics of the major components of the MID model like the suitable control circuit, fluid circuit, insulin pump with return valve and the insulin storage capsule. The dynamics of its operation are based on the principle of the variable pumping rate. The BG concentration is regulated with the injection of the required insulin dose by the MID into venous blood with respect to $u(t)$.

2.5 *Analysis of Patient Dynamics*

The patient model dynamic and characteristic operations are verified under several operating constraints like the actuator and sensor noises, intake amount of carbohydrates, and varying exercises, etc. The BG concentration and the insulin dose of the considered patient model with 60 gm meal at 600 min and the exercise for half-an-hour at 1300 min are illustrated in Fig. 2a. The glucose production and consumption rate of liver, and glucose consumption rate by the BG profile organs such as gut compartment, CNS, and peripheral cells are shown in Fig. 2b.

The overall BG regulation in the human body is carried out naturally through glucose utilization by the organs such as peripheral cells (adipose tissues, muscle cells) and the liver that exclusively depends on insulin. The peripheral cells and liver consume the least amount of glucose under the condition of lack of insulin. Under this situation, BG level rises abnormally and goes beyond the glucose level of 144 mg/dl. This results in the *hyperglycaemia* problem. The kidney removes part of the glucose from VB under the condition when the BG concentration rises up to RTG value. The rate of glucose excretion of the kidney proportionate to the BG level is represented by Fig. 2c. Figure 2a–c illustrate the unstable dynamics under various model uncertainties and disturbances. These abnormal dynamics can be reduced by applying the AP based on a suitable control algorithm.

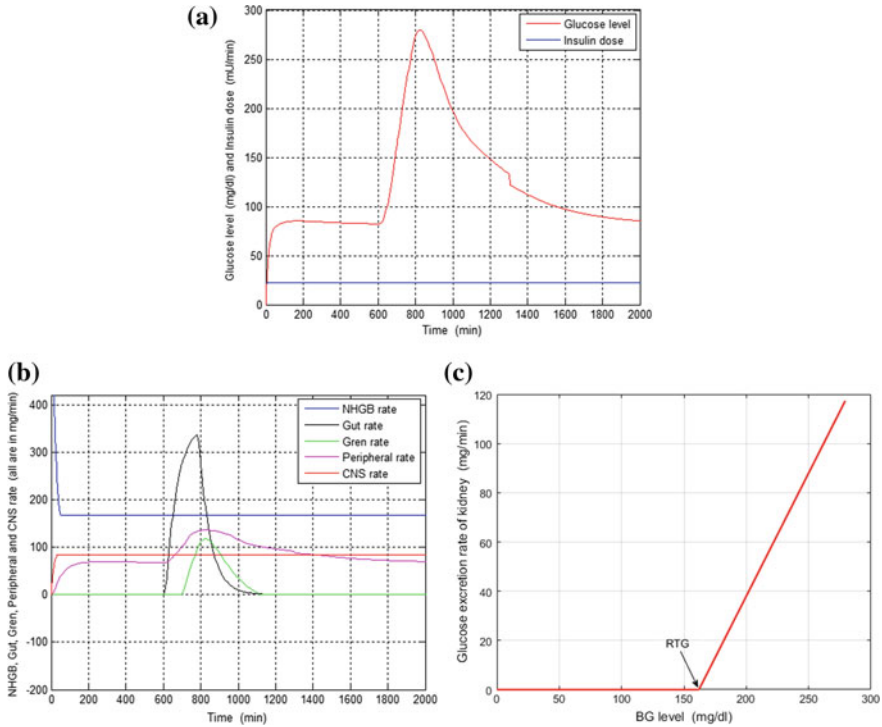


Fig. 2 **a** BG concentration with respect to insulin dose; **b** glucose production and consumption rate by GM organs; **c** glucose extraction rate of kidney versus BG level

3 Control Algorithm

The FLC control algorithm is demonstrated in this section. The closed-loop system response with respect to stability, accuracy, and robustness are analyzed. The control specifications such as settling time (min), steady-state error e_{ss} (%), overshoot (mg/dl) and undershoot (mg/dl) are also evaluated and examined with proper validation of the controller actions.

3.1 FLC Design

The basic block diagram of the proposed fuzzy logic controller for BG regulation in patient model is shown in Fig. 1a. There are two separate meanings of fuzzy logic. Generally, fuzzy logic is the further application of multivalued logic and is also known as logic system. We can also say fuzzy logic is the same as fuzzy sets theory, which relates to collection of objects with unsharp boundaries and the membership

Table 1 Fuzzy rules for closed-loop control of BG level

$e(t)/de(t)$	NB	NM	NS	ZE	PS	PM	PB
NB	NB	NB	NB	NB	NM	NS	ZE
NM	NB	NB	NB	NB	NS	ZE	PS
NS	NB	NB	NM	NS	ZE	PS	PM
ZE	NB	NM	NS	ZE	PS	PM	PB
PS	NM	NS	ZE	PS	PM	PB	PB
PM	NS	ZE	PS	PM	PB	PB	PB
PB	ZE	PS	PM	PM	PB	PB	PB

is a point of degree. There is a specific object which degree of membership in a given set which can vary between the range 0–1 in fuzzy set theory. Fuzzy logic is based on sound quantitative and also deals with imprecise information and data. Mathematical theory the values of fuzzy variables are expressed by proper English language. Error in BG level of a T1DM patient can be defined in linguistic variables like Negative Big (NB), Negative Medium (NM), Negative Small (NS), Zero (ZE), Positive Small (PS), Positive Medium (PM), Positive Big (PB), and each variable can be defined by varying triangular membership function. Seven fuzzy levels were chosen and were defined by fuzzy set library which values of the error signal is $e(t)$ and change in error signal is $de(t)$. The larger the number of fuzzy levels, the higher the input resolution. We know that a rule is n-dimensional and n is the number of variable included in the rule. The sum of rules is known as rule R. FIS editor edits the input and output variables, which are $e(t)$, $de(t)$ and output. After editing, the membership function for each variable is established [5]. The final step involves writing rules in rule editor using the rule given in Table 1.

4 Result and Discussions

Tim-domain response of glucose profiles, stability, and robustness of the closed-loop model with proposed FLC are described in detail in this section. The proposed control approach is compared with other popular control algorithms to justify its enhanced performance.

4.1 Analysis of Patient Dynamics with FLC

In this section, all glucose profiles of the nonlinear patient model with FLC is examined under different operating conditions such as variation of exercise, intake amount of carbohydrate, and noise of sensors and actuators. All glucose profiles like BG level, insulin dose, NHGB rate, Gut rate, CNS and peripheral glucose utilization rate in

T1DM patient model with the proposed controller are illustrated in Fig. 3. Compared to the condition of the uncontrolled process, the result obtained evidence a higher utilization of the plasma glucose by the peripheral cells and liver, those are dependent on the insulin availability and sensitivity. These bring back the BG level to 81 mg/dl with the quick settling time that results in the reduction or prevention of the hyperglycaemia occurrence probability as shown in Fig. 3a. The insulin-independent organ like the CNS, consume the plasma glucose at a constant rate. Figure 3b illustrates the constant rate of glucose utilization by CNS at 84 mg/min. As the BG level is below the RTG level, the kidney does not extract any glucose and is depicted in Fig. 3c by the constant glucose excretion rate at zero levels. By implementing the proposed control techniques to the MID, different operational parameters are evidenced and have enhanced performances.

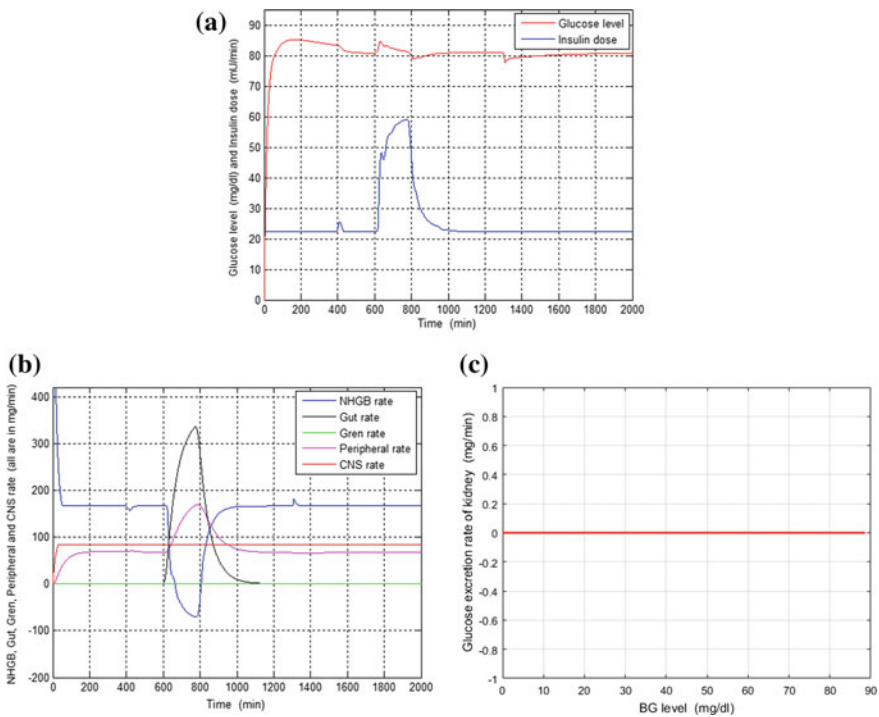


Fig. 3 Control action of FLC in glucose profiles of T1DM patient model: **a** BG concentration with respect to insulin dose; **b** glucose production and consumption by GM organs; **c** glucose extraction rate of kidney versus BG concentration (level)

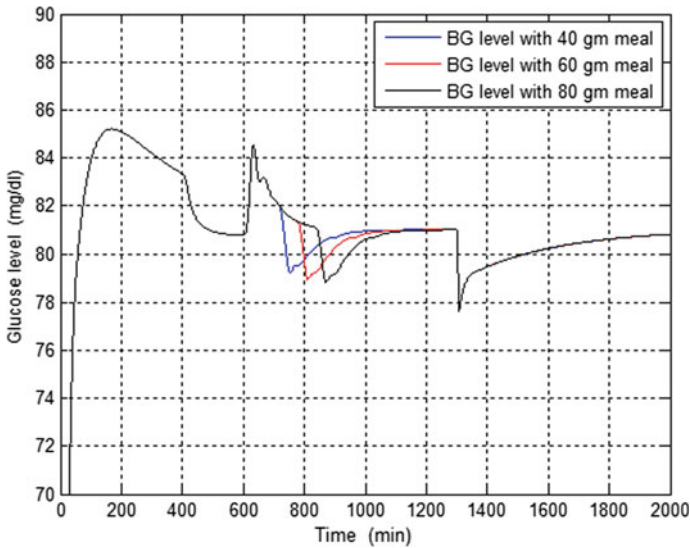


Fig. 4 BG concentration (level) with deviation of $\pm 30\%$ meal intake based on FLC

4.2 Robustness of the FLC

Figure 4 illustrates the BG concentration of the patient model with suggested FLC under the large variation of disturbance of the meal. The time-domain outcomes under different quantities of meal intake show the enhanced performance of the patient model with suggested approaches. Overall in each case, the patient model achieves finally BG concentration of 81 mg/dl with less settling time. As indicated by the results, the suggested controller's robust performance under the huge deviation of meal disturbances compared to FLC and other published control techniques is much better.

4.3 Stability Analysis

Figure 5a, b illustrates the magnitude plots result of the open-loop and closed-loop patient model to verify and analyze the stability conditions. From the magnitude plots, it is observed a better smoothness referring to the wider steady-state stability of closed-loop system (Fig. 5b) than the open-loop system (Fig. 5a). In other words, the bandwidth is increased in case of a closed-loop system with proposed controllers than the open-loop system. This clearly indicates a faster stable dynamics, and also closed-loop patient model with FLC archives BG concentration of 81 mg/dl with less settling time. This justifies better stability during system operation with FLC.

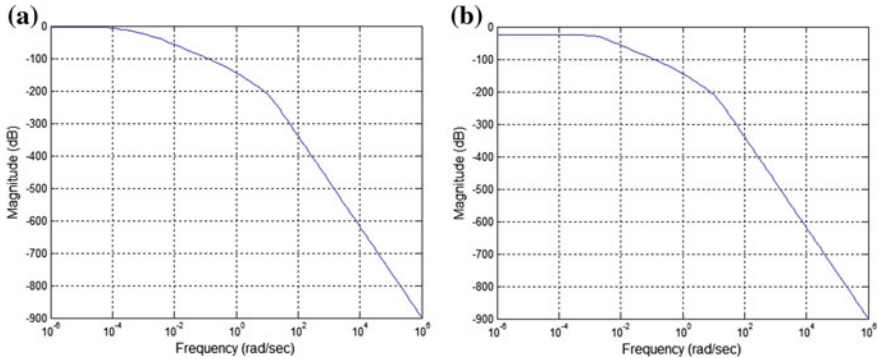


Fig. 5 a Magnitude plot of the patient model; b magnitude plot of the patient model with FLC

4.4 Comparative Study

The suggested FLC approach is compared with other popular control approaches such as PID, fuzzy, H_∞ , and SM to justify its enhanced performance as the controllers. Figure 3 illustrates the effect of meal disturbance in the BG concentration of the patient with the FLC approaches. Table 2 presents a comparative analysis with respect to settling time (min), peak overshoot (mg/dl), peak undershoot (mg/dl), noise (%), and steady-state error e_{ss} (%). The effect of meal disturbance in the BG concentration of the patient model applying different control approaches are also presented in Table 2. Similar working conditions are followed with the same level of actuator and sensor noise in all control techniques application for comparison.

The BG concentration in T1DM patient model ingested to 60 gm meal under different controllers is tested. The corresponding results are presented for the various control approaches along with the proposed FLC with respect to control specifications such as overshoots (mg/dl), undershoots (mg/dl) and settling time (min). The results signify the better controllability of the FLC. The simulation results also

Table 2 Comparative result analysis related to the BG concentration

Controller	PID [4]	Fuzzy [5]	H_∞ [10]	SM [14]	FLC (proposed)
Meal intake (mg)	60	60	60	60	60
Insulin infusion rate (mU/min)	59.6	59.2	59.1	59	59.1
Settling time (min)	290	260	255	250	265
Peak overshoot (mg/dl)	5.2	5.3	6.6	6.5	4.4
Peak undershoot (mg/dl)	3.1	2.1	1.2	1.5	1.3
Noise (%)	10	10	5	5	5
e_{ss} (%)	0	0	0	0	0

demonstrate the high noise elimination capability with high robustness for the proposed approach. Overall, by looking at the above comparative analysis, the findings of suggested approach advantages are higher accuracy and stability, more robustness, high noise elimination capability, and better capability to handle uncertainty under various abnormal conditions and huge variation meal disturbance.

5 Conclusions

In this paper, a novel control strategy FLC is proposed for BG control in T1DM patient model. To justify its enhanced performance, it has been applied and tested to control the BG concentration in patient within *normoglycaemic* range. Initially, a simulation model of the T1DM patient is formulated. Then the FLC is designed for BG regulation. The comparative results clearly reflect the suggested FLC arrives at better performance than the other control approaches such as PID, fuzzy, H_∞ , and SM, with respect to stability, reliability, and robustness under various abnormal conditions and disturbances. The related better performance of the suggested approach (FLC) with respect to improved accuracy and stability, enhanced robustness, high noise elimination capability, and better capability to handle uncertainty justify its real-time application.

References

1. Chee F, Fernando T, Vernon van Heerden P (2003) Closed-loop glucose control in critically ill patients using continuous glucose monitoring system (CGMS) in real time. *IEEE Trans Inf Technol Biomed* 7(1):43–53
2. Kamath S, George VI, Vidyasagar S (2009) Simulation study on closed loop control algorithm of type 1 diabetes mellitus patients. *IETE J Res* 55(5):230–235
3. Chee F et al (2003) Expert PID control system for blood glucose control in critically ill patients. *IEEE Trans Inf Technol Biomed* 7(4):419–425
4. Sutradhar A et al (2002) Analysis and design of an optimal PID controller for insulin dispenser system. *J Inst Eng (India) Electr Eng Div* 82:304–313
5. Kardar L, Fallah A (2008) Application of fuzzy logic controller for intensive insulin therapy in type I diabetes mellitus patient by subcutaneous route. In: *WSEAS transactions on systems and control* (2009), vol 3, no 9, pp 712–721. Biomedical Engineering, Amirkabir University of Technology
6. Singh M et al (2007) A new algorithm-based type-2 fuzzy controller for diabetic patient. *Int J Biomed Eng Technol* 1(1):18–40
7. Patra AK, Rout PK (2015) An automatic insulin infusion system based on LQG control technique. *Int J Biomed Eng Technol* 17(3):252–275
8. Chee F et al (2005) Optimal H_∞ /spl infin/insulin injection control for blood glucose regulation in diabetic patients. *IEEE Trans Biomed Eng* 52(10):1625–1631
9. Yasini S, Karimpour A, Sistani MBN (2012) Knowledge-based closed-loop control of blood glucose concentration in diabetic patients and comparison with H_∞ control technique. *IETE J Res* 58(4):328–336

10. Patra AK, Rout PK (2014) Optimal H_{∞} insulin injection control for blood glucose regulation in IDDM patient using physiological model. *Int J Autom Control* 8(4):309–322
11. Hernández AGG et al (2013) High-order sliding-mode control for blood glucose: practical relative degree approach. *Control Eng Pract* 21(5):747–758
12. Abu-Rmileh A, Garcia-Gabin W (2012) Wiener sliding-mode control for artificial pancreas: a new nonlinear approach to glucose regulation. *Comput Methods Programs Biomed* 107(2):327–340
13. Patra AK, Rout PK (2018) Backstepping sliding mode Gaussian insulin injection control for blood glucose regulation in type I diabetes patient. *J Dyn Syst Measur Control* 140(9):091006
14. Patra AK, Rout PK (2017) Adaptive sliding mode Gaussian controller for artificial pancreas in T1DM patient. *J Process Control* 59:13–27
15. Patra AK, Mishra AK, Rout PK (2018) Backstepping model predictive controller for blood glucose regulation in type-I diabetes patient. *IETE J Res* 1–15
16. Patra AK, Rout PK (2017) Adaptive continuous-time model predictive controller for implantable insulin delivery system in type I diabetic patient. *Opt Control Appl Methods* 38(2):184–204
17. Guyton JR et al (1978) A model of glucose-insulin homeostasis in man that incorporates the heterogeneous fast pool theory of pancreatic insulin release. *Diabetes* 27(10):1027–1042
18. Berger M, Rodbard D (1989) Computer simulation of plasma insulin and glucose dynamics after subcutaneous insulin injection. *Diab Care* 12(10):725–736
19. Parker RS, Doyle FJ, Peppas NA (1999) A model-based algorithm for blood glucose control in type I diabetic patients. *IEEE Trans Biomed Eng* 46(2):148–157
20. Parker RS, Doyle FJ (1997) Variable-rate implantable insulin infusion pumps—closed loop maintenance of normoglycaemia under patient variability for type 1 diabetes. In: *Proceedings of the 11th world congress, international society for artificial organs*
21. Lehmann ED, Deutsch T (1992) A physiological model of glucose-insulin interaction in type 1 diabetes mellitus. *J Biomed Eng* 14(3):235–242
22. Lehmann ED, Deutsch T (1998) Compartmental models for glycaemic prediction and decision-support in clinical diabetes care: promise and reality. *Comput Methods Programs Biomed* 56(2):193–204
23. Spera G (1997) Biosensor research targets medical diagnostics. In: *Medical device and diagnostic industry magazine*
24. Cochin L, Cadwallender W (1997) *Analysis and design of dynamic systems*, 3rd edn. Addison-Wesley, New York

Comparative Analysis of LMS-Based Control Algorithms for Grid Integrated PV System



Satish Choudhury, Byomakesh Dash, Bidyadhar Subudhi and Renu Sharma

Abstract In the power sharing scenario, maintaining power quality at its standard value is a challenging task. Insertion of various types of nonlinear load in the LT line not only deteriorate the quality of power flow but also unwanted harmonics are injected to the system. To maintain stability in the utility system adhering to quality of power flow, different least mean square (LMS) based adaptive control schemes are adopted. Comparative analysis between those LMS-based control algorithms is cited in this paper following steady and dynamic state analysis. In this paper, comparative dynamic analysis between LMS, sign error-LMS (SELMS), sign-data LMS (SDLMS) and sign-sign LMS (SSLMS) is made to evaluate the performance of the said algorithms.

Keywords Photovoltaic · Total harmonic distortion · LMS · SELMS · SDLMS · SSLMS

1 Introduction

The mission of the energy transition from unsustainable to more sustainable and equitable in the near future persuade to analyze the PV-based sustainable energy integrated system under different detrimental conditions. The integrated system basi-

S. Choudhury (✉) · B. Dash · R. Sharma
ITER, SOA University (Deemed to be University), Bhubaneswar, Odisha 751030, India
e-mail: satishchoudhury@soa.ac.in

B. Dash
e-mail: byomakeshdash@soa.ac.in

R. Sharma
e-mail: renusharma@soa.ac.in

B. Subudhi
School of Electrical Sciences, Indian Institute of Technology Goa,
Veling, Goa, India
e-mail: bidyadhamitrkl@gmail.com

© Springer Nature Singapore Pte Ltd. 2020
R. Sharma et al. (eds.), *Innovation in Electrical Power Engineering, Communication, and Computing Technology*, Lecture Notes in Electrical Engineering 630,
https://doi.org/10.1007/978-981-15-2305-2_46

cally encounters power quality issues owing to induction of nonlinear activities such as hard and soft switching of power semiconductor switches, sudden change in demand, bidirectional flow of power, and variation of solar temperature and irradiance. The process of encounter involves different types of control technologies such as second-order generalized integrator (SOGI), third-order generalized integrator (TOGI), SOGI-FLL, synchronous reference frame phase-locked loop (SRFPLL), and LMS-based control algorithm to get rid of aforementioned adversities. All the methodologies involved in the process of integration also uses MPPT techniques [1] such as incremental conductance (IC), perturb & Observe (P&O) technique, estimated perturb-perturb technique, incremental conductance with integral regulator, and hybrid MPPT techniques [2] which are widely used to extract the ultimate power from the solar PV system.

The control technologies mentioned above either use peak extraction or fundamental extraction technique to generate reference grid current which enables to create a pulse pattern using hysteresis controller for the switches of voltage source converter (VSC) involved in single-stage grid integrated PV (SSGIPV) system. The objective of different tools used in SSGIPV system is to maintain the quality of power flow, ensuring unit power factor (UPF) and reduction in THD as per IEEE-519 [3] standard. To achieve the said objectives, the system goes under dynamic performance evaluation. In this evaluation process, the percentage of steady-state error and the convergence rate is observed to give judgment on the control algorithm. Tools like improved linear sinusoidal tracer (ILST) [4], filtered-x-LMS [5], and least mean fourth (LMF) [6] focus on convergence rate and transient errors to evaluate the performance of the controller. It has been found that ILST and LMF have a faster convergence rate than that of Fx-LMS. The above-mentioned algorithms are also used variable step size instead of fixed step to have a faster dynamic response as given in the literature [7–11]. In LMS type of control algorithm, squared error is considered as a cost function for updating the weight matrix to estimate the active and reactive component of the load current required for generation of reference grid current. Further, the reference grid current along with the actual grid currents is used to generate required pulses for the controlled switches of the interfacing VSC through hysteresis current controller. The self-regulation of step sizes fastens the rate of convergence and also enhances the performances of the overall system by estimating the weights under steady and transient states.

In this paper, a comparative dynamic analysis of LMS-based control algorithms is made to select the suitable controller for effective grid integration. The overall behavior of SSGIPV system is analyzed by taking the selective control algorithm from the comparison made before with respect to different abnormalities. In LMS-based control algorithm, the range of step size is minimum and it directly depends upon the maximum value of the eigenvalues of the system, and it is also found that the minimum is the step size, the slower is the convergence rate, but the mean squared error (MSE) is smaller. Hence, the step size maintains balance between convergence rate and steady-state MSE [12]. Unlike LMS, in SELMS step size does not depend upon eigenvalues, but the step size is chosen to be a power of two. In SDLMS, time-varying step size is chosen for updating the weight vector, whereas SSLMS is

chosen the fixed step size to update the coefficient in the weight vector. Generally, the settling time of SSLMS is slower than that of LMS.

The objectives of the paper are as follows.

- Active and reactive component of the load current is estimated using aforementioned control algorithms.
- Comparative analysis of LMS, SELMS, SDLMS, and SSLMS on basics of average active weight pertaining to abnormalities is discussed.
- Dynamic analysis of the overall SSGIPV is analyzed using LMS control algorithm.

The paper is organized as follows. Following Introduction in Sects. 1 and 2 describes the modeling of PV grid system and computational analysis of LMS-based control scheme. The comparative analysis of LMS, SELMS, SDLMS, and SSLMS is explained in Sect. 3. The simulation result under unbalanced condition is discussed in Sect. 4, and the brief conclusion is presented in Sect. 5 followed by Appendix.

2 PV Grid Integrated System

The overall SSGIPV system is shown in Fig. 1. It consists of PV arrays, where the PV modules are connected in series and parallel fashion to get required current, voltage, and power rating. It has also consists of a voltage source converter, harmonic filters to remove the ripple content of the inverter output currents, utility grid, requisite control algorithm to generate switching pulses, P&O MPPT [1] controller to extract maximum power and the customized nonlinear load. The system parameters are calculated as in [13] and are given in Appendix.

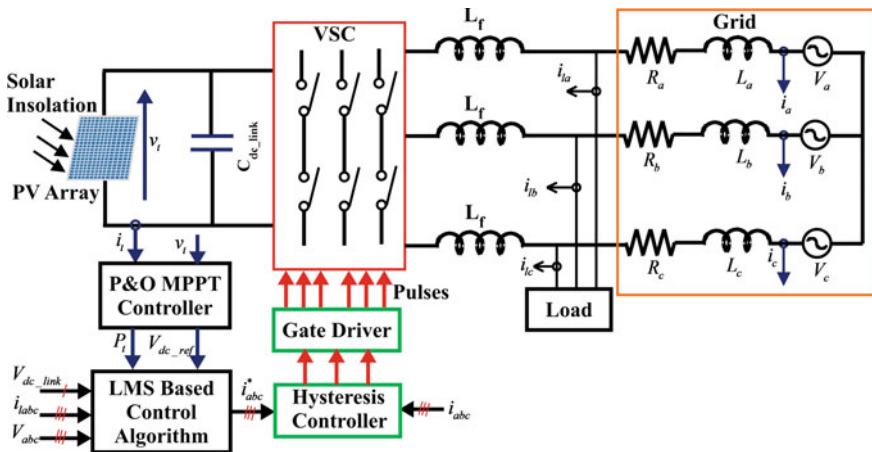


Fig. 1 Overall layout of PV grid integration system

2.1 MPPT and LMS-Based Control Scheme

The basic element of SSGIPV system is P&O MPPT controller. It is working in twofolds. In first fold, it extracts maximum power from the PV array, and in second fold, it helps to estimate the dc-link reference voltage (V_{dc_ref}) which will be further used along with other system parameters by LMS-based control algorithms as shown in Fig. 2 to estimate reference grid currents. Taking the aforesaid estimated V_{dc_ref} and actual voltage (V_{dc_link}) across dc-link capacitor (C_{dc_link}), the DC power loss component is calculated. Similarly, AC loss component can be calculated using the PV power (P_t) and the amplitude of the terminal voltage (V_{tp}). Further, the active and reactive weights required for estimating the reference grid currents (i_a^* , i_b^* , i_c^*) are calculated using loss components and the average weights estimated through different LMS-based control algorithms. The desired quality of power flow ensuring UPF is only achieved through controlled switching pulses of VSC which is the key element for effective grid integration under adverse condition. The required switching pulses are obtained by passing the current error through a hysteresis band of width 0.01, where the unit of the bandwidth is depending upon the error which is passing through it. In this case, it follows the unit of the current i.e., ampere. The following section depicts the estimation of different control parameters using LMS-based control algorithms.

Estimation of Parameters Using LMS Control Scheme: As stated before, the basic parameters for obtaining controlled switching pulses are the reference grid currents. So in this section, the step-by-step calculation of i_a^* , i_b^* , i_c^* are explained.

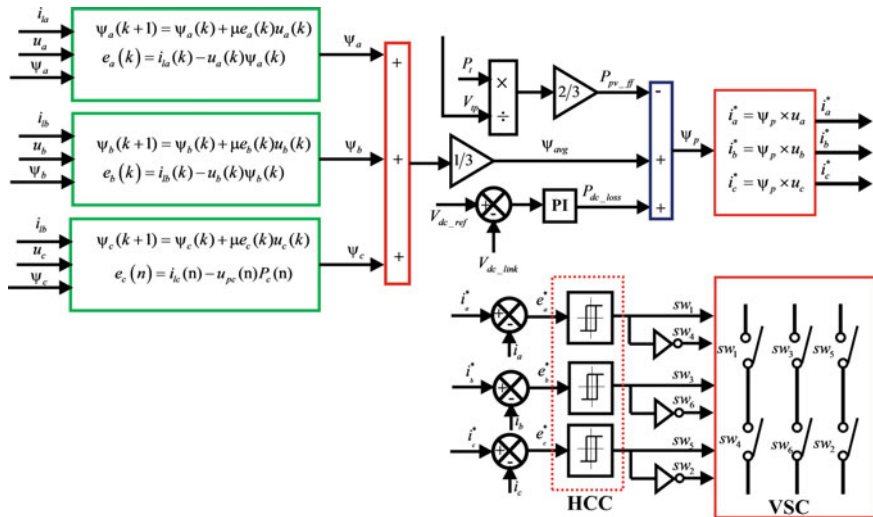


Fig. 2 Basic layout and implementation of LMS control scheme

Step 1: Calculation of in-phase templates:

The in-phase templates (u_a, u_b, u_c) are calculated using (1) and (2).

$$\begin{bmatrix} u_a \\ u_b \\ u_c \end{bmatrix} = \frac{1}{V_{ip}} \begin{bmatrix} V_a \\ V_b \\ V_c \end{bmatrix} = \frac{1}{V_{ip}} \begin{bmatrix} 2/3 & 1/3 \\ -1/3 & 1/3 \\ -1/3 & -2/3 \end{bmatrix} \begin{bmatrix} V_{ab} \\ V_{bc} \end{bmatrix} \quad (1)$$

where V_a, V_b and V_c are the phase voltages of 'a,' 'b,' and 'c' phase, respectively, and V_{ab} and V_{bc} are the line voltages across phase 'ab' and 'bc,' respectively. All the voltages are rated in volts.

$$V_{ip} = \sqrt{\frac{2}{3} (V_a^2 + V_b^2 + V_c^2)} \quad (2)$$

Step 2: Calculation of DC power loss:

To maintain the constant V_{dc_link} irrespective of disturbances in grid as well as in PV side, it is necessary to calculate DC power loss (P_{dc_loss}) as in (3).

$$P_{dc_loss}(k) = P_{dc_loss}(k-1) + K_c \left(1 + \frac{1}{\tau_i s} \right) (V_{dc_link}(k) - V_{dc_link}(k)) \quad (3)$$

where K_c is the proportional gain and τ_i is the integral time constant of PI controller.

Step 3: Calculation of feed-forward component:

The feed-forward components for the PV system (P_{pv_ff}) is calculated as in (4)

$$P_{pv_ff} = \frac{2P_t}{3V_{ip}} \quad (4)$$

Step 4: Calculation of Average weight:

The active weight of 'a' phase load current at each instant k is updated as in (5).

$$\psi_a(k+1) = \psi_a(k) + \mu e_a(k) u_a(k) \quad (5)$$

where $\psi_a(k)$ is the estimated weight of a-phase load current at 'kth' instant and $e_a(k)$ is the error. The error is calculated in (6).

$$e_a(k) = i_{la}(k) - u_a(k) \psi_a(k) \quad (6)$$

Similarly, the active weights of 'b' and 'c' phase load current $\psi_b(k)$ and $\psi_c(k)$, respectively, at each instant k is calculated using (5) and (6) replacing the unit templates and error of the respective phases in place of 'a' phase component. For example, e_a will be replaced by e_b and u_a will be replaced by u_b and so on. The average active weight is calculated using (7)

$$\psi_{avg} = \frac{\psi_a(k) + \psi_b(k) + \psi_c(k)}{3} \quad (7)$$

Step 5: Calculation of resultant active weight:

The resultant active weight (ψ_p) is calculated in (8)

$$\psi_p = \psi_{avg} + P_{dc_loss} - P_{pv_ff} \quad (8)$$

Step 6: Calculation of reference grid currents:

The i_a^* , i_b^* , i_c^* are calculated in (9)

$$i_a^* = \psi_p \times u_a, \quad i_b^* = \psi_p \times u_b, \quad i_c^* = \psi_p \times u_c \quad (9)$$

The parameters of SELMS, SDLMS, and SSLMS control scheme are calculated in the succeeding sections following the steps of LMS control scheme. In the process of parameter estimation, only the Step 4 of LMS control scheme will be modified and the remaining Steps will be unaltered. Figure 2 only shows the implementation of LMS control scheme, but this figure can be modified for other LMS-based control schemes discussed in succeeding section.

Estimation of Parameters Using SELMS Control Scheme: As discussed above, the changes made in the calculation of Step 4 in the preceding section are given below. The active weight of ‘a,’ ‘b,’ and ‘c’ phase load current is obtained using (10).

$$\begin{aligned} \psi_{ph}(k+1) &= \psi_{ph}(k) + \mu \text{sgn}\{e_{ph}(k)\} u_{ph}(k) \\ e_{ph}(k) &= i_{lph}(k) - u_{ph}(k) \psi_{ph}(k) \end{aligned} \quad (10)$$

where ‘ph’ indicates the parameters of a particular phase and being replaced by ‘a,’ ‘b,’ and ‘c’ for calculation of a-phase, b-phase, and c-phase parameters, respectively. Here, a sign function is used for the purpose of estimation and is given in (11).

$$\text{sgn}\{e_{ph}(k)\} = \begin{cases} 1; & e_{ph}(k) > 0 \\ 0; & e_{ph}(k) = 0 \\ -1; & e_{ph}(k) < 0 \end{cases} \quad (11)$$

Estimation of Parameters Using SDLMS Control Scheme: The active weight of ‘a,’ ‘b,’ and ‘c’ phase load current using SDLMS scheme is obtained using (12).

$$\psi_{ph}(k+1) = \psi_{ph}(k) + \mu e_{ph}(k) \text{sgn}\{u_{ph}(k)\} \quad (12)$$

where ‘ph’ indicates the parameters of a particular phase and being replaced by ‘a,’ ‘b,’ and ‘c’ for calculation of a-phase, b-phase, and c-phase parameters, respectively. The sign function used in (12) is given in (13).

$$\text{sgn}\{u_{ph}(k)\} = \begin{cases} 1; & u_{ph}(k) > 0 \\ 0; & u_{ph}(k) = 0 \\ -1; & u_{ph}(k) < 0 \end{cases} \quad (13)$$

Estimation of Parameters Using SSLMS Control Scheme: Similar to (12) the active weight of ‘a,’ ‘b,’ and ‘c’ phase load current using SSLMS control scheme is found using (14). Sign function used in (14) is given in (11 and 13).

$$\psi_{ph}(k + 1) = \psi_{ph}(k) + \mu \text{sgn} \{e_{ph}(k)\} \text{sign} \{u_{ph}(k)\} \quad (14)$$

2.2 Generation of Switching Pulses Using Hysteresis Controller

The error to be compensated using control algorithms stated above is obtained by comparing the calculated reference current from (9) with that of sensed current from utility grid. Then, the error is passed through the hysteresis current controller operating at width of 0.01. Within the band, the actual grid current is tracked to follow the reference grid current through controlled switching patterns of VSI.

3 Comparative Analysis of LMS, SELMS, SDLMS, and SSLMS

In the preceding section, the detail theoretical analysis of LMS, SELMS, SDLMS, and SSLMS is explained. In the LMS algorithm, the cost function is taken as in (15), whereas in sign function-based algorithm like SELMS, SDLMS and SSLMS uses the cost function as (16).

$$\xi(k) = E \{|e(k)|^2\} \quad (15)$$

$$\xi(k) = |e(k)| \quad (16)$$

The objective of the algorithms is to minimize the error either by using steepest descent or gradient descent methods. It is found from the analysis [12] that in LMS, the range of step size (μ) is $0 < \mu < \frac{2}{\lambda_{\max}}$, where λ_{\max} is the maximum value of the eigenvalues. The smaller step size indicates the slower convergence rate, but the error becomes smaller. So in sign-based algorithm, the equations are modified without increasing the computational complexity to achieve the requisite rate of convergence and the MSE. In SELMS, a sign function is used which does not allow to alter the direction of update vector and is robust in nature. The range of step size is increased, and the rate of convergence and MSE is modified accordingly. In SDLMS, the robustness is decreased as compared to SELMS because the equation allows to change the direction of the update vector. At each instant ‘k,’ the ‘nth’ coefficient in the sign of unit template may be written as in (17).

$$\text{sgn}\{u_{ph}(k - n)\} = \frac{u_{ph}(k - n)}{|u_{ph}(k - n)|} \tag{17}$$

Therefore, SDLMS has different step sizes for each coefficient in the weight vector, and it allows to adjust the rate of convergence and MSE. Similarly in SSLMS, the quantization of both error and the in-phase templates updates the coefficient of the update vectors, and it is found that the convergence rate is slower as compared to LMS. The methodologies mentioned in this section are simulated using MATLAB/Simulink, and the comparison is shown in Fig. 3. The comparison detail is shown in Table 1. The data given in Table 1 is an analysis with respect to a fixed step size of 0.002. It shows only the comparison between the control scheme cited in this paper under a particular case study when ‘a’ phase is disconnected for the period of 0.5–0.7 s and the grid is unbalanced. It does not claim to be superior than the other existing LMS-based algorithm or allied algorithms.

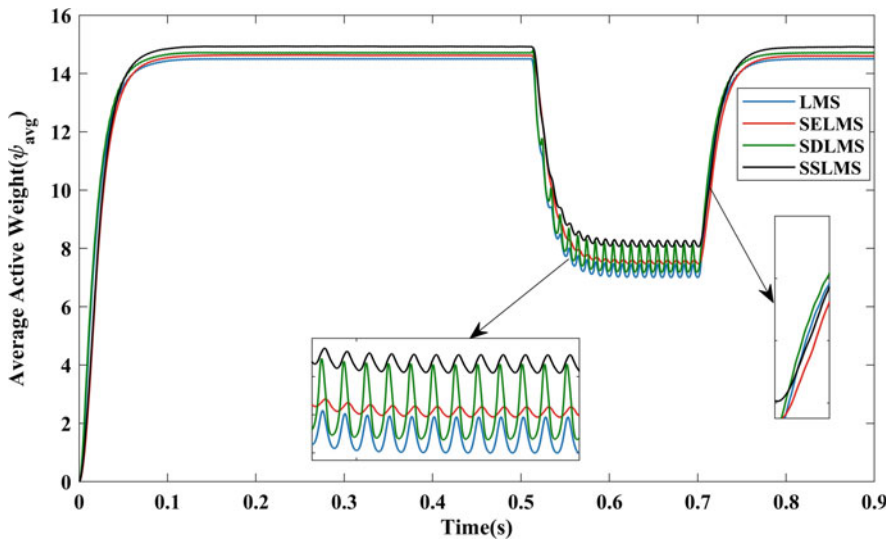


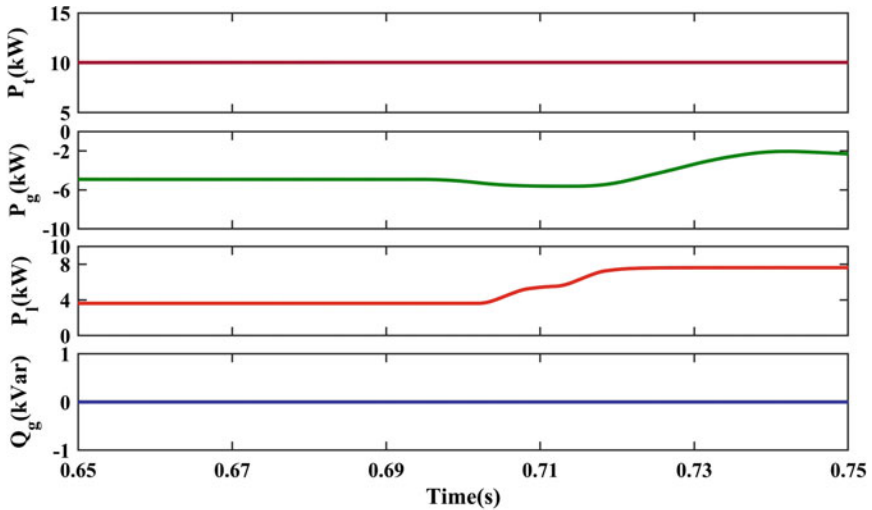
Fig. 3 Comparative analysis of LMS-based control scheme

Table 1 Comparative result analysis of LMS, SELMS, SDLMS, and SSLMS

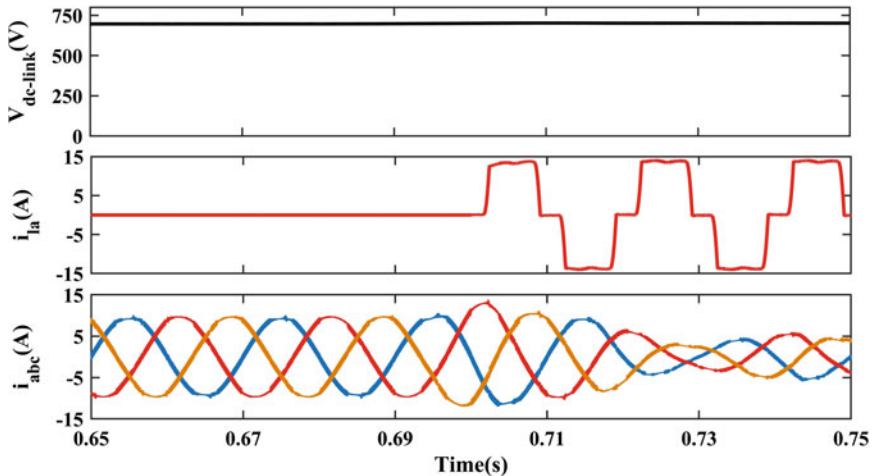
Control algorithms	Steady-state error	Dynamic state	
		Amplitude of oscillation	Convergence rate
LMS	Less	Less	Fast
SELMS	Less	Less	Slower
SDLMS	Medium	More	Medium
SSLMS	Medium	Less	Medium

4 Result Analysis

The performance analysis of SSGIPV is analyzed under the unbalanced condition where a-phase is disconnected for the period 0.65–0.7 s. Some of the characteristic curve of performance parameters are shown in Fig. 4 to perceive the performance of the control scheme explained in the preceding sections. From the given load



(a) Performance analysis of power flow (P_t, P_g, P_l, Q_g)



(b) Other performance parameters ($V_{dc-link}, i_a, i_{abc}$)

Fig. 4 Transient performances of the SSGIPV system under unbalanced nonlinear load

parameter, the load voltage is calculated [14] as $V_0 = 560.4$ V. and the power consumed by the load is $P_l = 7.851$ kW, which is noticed in Fig. 4a after 0.7 s (after completion of the unbalanced period). At the same time, it is noticed that the remaining power $P_l(10) - P_l(7.851) \approx P_g(2.15$ kW) is fed to the grid. Negative power indicates the power flow in the reverse direction, i.e., PV source to the grid. During period 0.65–0.7 s, the power consumed by the load is less than that of actual consumption because of unbalancing in the load side. It is noticed that the power consumption is decreased from 7.851–3.5 kW. Thus, the power fed to the grid increases to approximately 6.5 kW as shown in Fig. 4a. It is noticed in Fig. 4b that the V_{dc_link} is maintained constant through MPPT technique and the reactive power (Q_g) is maintained zero to ensure UPF operation under adverse condition. It is also shown in Fig. 4b that the flow of current from PV to grid is increasing during unbalanced period.

5 Conclusion

In this paper, the comparative analysis of LMS, SELMS, SDLMS and SSLMS is made by employing the algorithm with the PV grid integrated system. The performance is observed under certain unbalance condition. It is found that all the control schemes are able to operate the SSGIPV system under different abnormalities. Though for informative purpose, one abnormality, i.e., unbalancing in the load side, is taken into consideration, it has been tested for other abnormalities like sudden change in supply frequency, sudden hop in phase angle, change in solar insolation, temperature, etc. In a concluding remark, it can be said that the LMS scheme is useful for the system requiring faster convergence rate and less steady-state error as compared to other sign LMS-based control scheme. It is also commented that for lesser computational complexity, sign LMS-based control scheme can be adopted. Basically, it is found that the SSLMS scheme is preferable over other sign-based LMS algorithm because of very fast computation.

Appendix

PV grid integrated system specifications: PV voltage (V_{pv}) = 700 V, PV power = 10 kW, total number of PV modules in series (N_s) = 24, total number of PV modules in parallel (N_p) = 2, DC-link capacitor (C_{dc_link}) = 1624 μ F, DC-link voltage (V_{dc_link}) \cong 700 V, interfacing inductor (L_f) = 5.8 mH, proportional controller gain (K_c) = 0.4 and integral time constant (τ_i) = 40), line voltage at grid (V_{ab}) = 415 V(rms), sampling time (T_s) = 10^{-6} s. Nonlinear Load containing load resistance (R) = 40 Ω and load inductance (L) = 100 mH.

References

1. Subudhi B, Pradhan R (2013) A comparative study on maximum power point tracking techniques for photovoltaic power systems. *IEEE Trans Sust Energy* 4(1):89–98
2. Rout A, Samantara S, Dash GK, Choudhury S, Sharma R, Dash B (2014) Modeling and simulation of hybrid mppt based standalone PV system with upgraded multilevel inverter. In: India conference (INDICON), 2014 annual IEEE. IEEE, pp 1–6
3. IEEE standard for interconnection and interoperability of distributed energy resources with associated electric power systems interfaces (2018)
4. Singh B, Jain C, Goel S (2014) Ilt control algorithm of single-stage dual purpose grid connected solar PV system. *IEEE Trans Power Electron* 29(10):5347–5357
5. Garanayak P, Panda G (2016) Fast and accurate measurement of harmonic parameters employing hybrid adaptive linear neural network and filtered-x least mean square algorithm. *IET Gener Trans Distrib* 10(2):421–436
6. Walach E, Widrow B (1984) The least mean fourth (lmf) adaptive algorithm and its family. *IEEE Trans Inf Theory* 30(2):275–283
7. Badoni M, Singh A, Singh VP, Tripathi RN (2018) Grid interfaced solar photovoltaic system using za-lms based control algorithm. *Electric Power Syst Res* 160:261–272
8. Badoni M, Singh A, Singh B (2016) Adaptive neurofuzzy inference system least-mean-square-based control algorithm for dstatcom. *IEEE Trans Ind Inf* 12(2):483–492
9. Chen J, Richard C, Song Y, Brie D (2016) Transient performance analysis of zero-attracting lms. *IEEE Signal Process Lett* 23(12):1786–1790
10. Song P, Zhao H (2019) Filtered-x least mean square/fourth (fxlms/f) algorithm for active noise control. *Mech Syst Signal Process* 120:69–82
11. Beniwal N, Hussain I, Singh B (2017) Hybrid vss-lms-lmf based adaptive control of spv-dstatcom system under distorted grid conditions. *IET Renew Power Gener* 12(3):311–322
12. Hayes MH (2009) *Statistical digital signal processing and modeling*. Wiley
13. Akagi H, Watanabe EH, Aredes M (2017) *Instantaneous power theory and applications to power conditioning*, vol 62. Wiley
14. Mohan N, Undeland TM, Robbins WP (2003) *Power electronics: converters, applications, and design*. Wiley

Comparative Analysis of Adaptive Filtration Techniques Using DSTATCOM for Distribution System



Byomakesh Dash, Satish Choudhury, Bidyadhar Subudhi and Renu Sharma

Abstract This paper presents a comparative analysis between different adaptive filters such as LMS, LMF and RLS to study the dynamic performance of PV-DSTATCOM system. Various power quality issues such as power factor correction, reactive power control and harmonic elimination are addressed. To nullify the power quality issues and to adhere to the grid codes DSTATCOM is placed in shunt at the point of common coupling (PCC). In PV-DSTATCOM mode it maintains power flow to grid as well as to load under unity power factor and in DSTATCOM mode it sustains the load demand by maintaining power flow from grid to load. In addition, extraction of in phase and quadrature components of polluted load current is presented so as to produce suitable gate pulse for VSI. Performance evaluation of these filters is done on the basis of comparison of estimated active weight during unbalanced loading condition.

Keywords Photovoltaic (PV) · Distribution static compensator (DSTATCOM) · Voltage source inverter (VSI) · Total harmonic distortion (THD)

B. Dash (✉) · S. Choudhury · R. Sharma

Department of Electrical Engineering, Institute of Technical Education and Research, Siksha 'O' Anusandhan (Deemed to Be University), Bhubaneswar, Odisha 751030, India
e-mail: byomakesh19@gmail.com

S. Choudhury

e-mail: satishchoudhury@soa.ac.in

R. Sharma

e-mail: renusharma@soa.ac.in

B. Subudhi

School of Electrical Sciences, Indian Institute of Technology Goa, Ponda, Goa, India
e-mail: bidyadhamitrk1@gmail.com

© Springer Nature Singapore Pte Ltd. 2020

R. Sharma et al. (eds.), *Innovation in Electrical Power Engineering, Communication, and Computing Technology*, Lecture Notes in Electrical Engineering 630,
https://doi.org/10.1007/978-981-15-2305-2_47

1 Introduction

In recent years, the major concerns for power engineers are to fill the gap between increasing demand for electricity from consumer side and energy generation by fossil fuels which are in a declining state. To overcome these issues dependence on renewable energy has increased in recent years. As solar energy is available in abundance and low cost throughout the year researchers are working in the direction of PV grid integration of the system to address various power quality issues.

Distribution systems get polluted by harmonics due to large penetration of nonlinear loads with solid-state devices. This causes major power quality problems such as distorted grid currents, voltage fluctuation, poor power factor, distorted waveforms, etc. To overcome these power qualities issues various custom power devices (CPDS) are used depending on requirements. Out of all CPDs, DSTATCOMS are extensively used in distribution systems. DSTATCOM is a VSC connected at load end in parallel with the load and basically used to mitigate current related power quality issues [1].

Literature reveals several control strategies to mitigate harmonics and extraction of harmonics free component from polluted load current. Many conventional techniques such as IRPT, SRF, PBT and $I \cos(\phi)$ [2] have been reported in the literature to accomplish the above-mentioned objectives. Apart from this many other control algorithms have been cited in the literature to extract reference currents such as model reference adaptive control [3], single-phase active reactive power theory [4], implicitly closed-loop control and resonant controller [5]. Many adaptive filtering techniques have been reported in the literature such as Least Mean Square (LMS) [6], VSS-LMS, DNLMS, variable leaky LMS [7], Least Mean Fourth (LMF) [8], LMT, Recursive Least Square (RLS) [9], artificial neural network based (ANN) adaptive control and robust adaptive control strategy. Main advantages of adaptive filtering are better filtering capabilities and better performances under dynamic conditions.

In this paper performances of three commonly used adaptive filters LMS, RLS and LMF are compared both in steady-state and dynamic state. In addition accuracy, convergence speed and oscillations of LMS, LMF and RLS filters are compared during unbalanced loading condition. Again harmonic analysis is done to show the filtration capabilities of RLS adaptive filter so as to prove its worthiness in PV-DSTATCOM application to mitigate power quality issues.

The rest of the paper is organized as follows: Sect. 2 describes the modelling and design of grid integrated PV DSTATCOM system. Section 3 describes the control algorithms. Section 4 describes performance evaluation and comparison using MATLAB/SIMULINK. Section 5 concludes this paper.

2 Modelling and Design of PV-DSTATCOM System

Figure 1 shows the schematic diagram of PV DSTATCOM system. It consists of a 50 KW PV source, VSC in shunt at load side acting as DSTATCOM to mitigate PQ issues, dc-link capacitor, interfacing inductance, ripple filter and a nonlinear load.

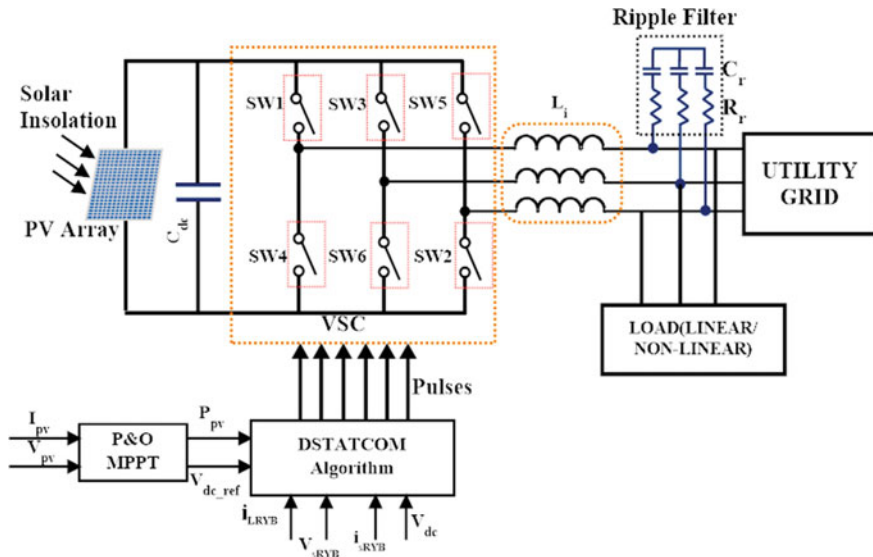


Fig. 1 Schematic of proposed system

Power flow from source to load is achieved under unity power factor condition. Here P&O method is used to extract maximum power from PV source.

A 50 kW PV system is connected to a 415 V, 50 Hz, three-phase system. The parameters of PV modules are calculated in (1), (2) and (3)

$$N_s = \frac{V_{dc}}{V_{mpv}} = \frac{700}{26.3} = 26.7 \cong 27 \tag{1}$$

$$N_p = \frac{P_{max}}{V_{dc} I_{mp}} = \frac{50,000}{700 \times 7.61} = 9.386 \cong 10 \tag{2}$$

$$V_{dc} = \frac{2V_{Lm}}{\sqrt{3}k} = \frac{2\sqrt{2} \times 415}{\sqrt{3} \times 1} = 677.69 \tag{3}$$

where \$V_{Lm}\$ is the peak line voltage of the grid and \$k\$ is the modulation index. The value of DC bus voltage \$V_{dc}\$ is taken as 700 V.

The value of interfacing inductance (\$L_i\$) is calculated in (4) [10]

$$L_i = \frac{\sqrt{3}mV_{dc}}{12h_0f_s\Delta I} = \frac{\sqrt{3} \times 1 \times 700}{12 \times 1.2 \times 10,000 \times 0.03 \times 71.43} = 3.9 \text{ mH} \cong 4 \text{ mH} \tag{4}$$

where \$h_0\$ is the overloading factor, \$f_s\$ is the switching frequency, and \$\Delta I\$ is the percent (3%) of ripple current.

The voltage source converter DC link capacitance is computed in (5)

$$C_{dc} = \frac{P_{dc}}{2V_{dc}\omega V_{dcr}} = \frac{50,000}{2 \times 700 \times 314 \times 0.02 \times 700} = 8124.3 \mu\text{F} \quad (5)$$

where V_{dcr} is percentage of ripple voltage and ω is the angular frequency. The ripple filter is designed with capacitance $C_r = 10 \mu\text{F}$ and resistance $R_r = 10 \Omega$ respectively [10].

3 Control Algorithms

In the first stage of PV-DSTATCOM control algorithm MPPT is used to extract maximum power from PV source. In this work P&O based MPPT algorithm is used to generate reference voltage so as to maintain the dc link voltage at its set value. This reference voltage thus produced is compared with actual dc link voltage and is then passed through a controller circuit so as to produce dc loss component. Then ac loss component is calculated by comparing peak voltage and reference ac voltage. Active and reactive weight components are estimated using adaptive filter algorithm. Resultant weight is calculated from the data obtained above and is then utilized to produce reference grid current. The reference current thus obtained is compared with actual current and is passed through hysteresis band current controller to produce suitable gate pulse for converter.

Phase voltages (V_{sR} , V_{sY} , V_{sB}) can be computed from line voltages (V_{sRY} , V_{sYB}) as per the Eq. (6)

$$\begin{aligned} V_{sR} &= \frac{2}{3}V_{sRY} + \frac{1}{3}V_{sYB} \\ V_{sY} &= \frac{-1}{3}V_{sRY} + \frac{1}{3}V_{sYB} \\ V_{sB} &= \frac{-1}{3}V_{sRY} - \frac{2}{3}V_{sYB} \end{aligned} \quad (6)$$

Peak value of terminal voltage can be computed as in (7)

$$V_p = \sqrt{\frac{2}{3} \sum_{x=R,Y,B} V_{sx}^2} \quad (7)$$

The in-phase and quadrature unit templates are calculated in (8) and (9)

$$u_{ax} = \frac{V_{sx}}{V_p} \quad (8)$$

where x represents R, Y, B phases and u_{ax} is in-phase active unit template of respective phases.

$$\begin{aligned} u_{bR} &= \frac{1}{\sqrt{3}}(-u_{aY} + u_{aB}) \\ u_{bY} &= \frac{1}{2\sqrt{3}}(3u_{aR} + u_{aY} - u_{aB}) \\ u_{bB} &= \frac{1}{2\sqrt{3}}(-3u_{aR} + u_{aY} - u_{aB}) \end{aligned} \quad (9)$$

where u_{bR}, u_{bY}, u_{bB} represents quadrature unit template.

The difference between the reference voltage provided by MPPT control ($V_{dc,ref}$) and voltage across dc link capacitor (V_{dc}) is the dc voltage error and is computed in (10)

$$V_{de}(m) = V_{dc,ref}(m) - V_{dc}(m) \quad (10)$$

The dc loss component is computed in (11)

$$\delta_{ca}(m) = \left(k_p + k_i \frac{1}{s} \right) \times V_{de}(m) \quad (11)$$

where k_p and k_i are proportional and integral gain.

The ac voltage error is calculated by subtracting peak value of terminal voltage (V_p) from its reference value V_{pref} in (12)

$$V_{pe}(m) = V_{pref}(m) - V_p(m) \quad (12)$$

The ac loss component is computed in (13)

$$\delta_{cb}(m) = k_p \left(1 + \frac{k_i}{k_p} \frac{1}{s} \right) \times V_{pe}(m) \quad (13)$$

To show the effect of PV system $\delta_{pv}(m)$ is added to the system and is computed in (14)

$$\delta_{pv}(m) = \frac{2P_{pv}(m)}{3V_p} \quad (14)$$

where P_{pv} is the output power of PV system.

3.1 Adaptive Filters

Figure 2 depicts the basic structure of adaptive filter. Where $r(n)$ is the input, $y(n)$ is filter output, $d(n)$ is the desired output and $e(n)$ is the error. This error is then used to find the cost function of the system required to find the weight coefficients of the adaptive filters.

3.1.1 LMS Algorithm

The cost function of LMS algorithm is given in (15) and (16)

$$C(m) = \frac{1}{2}e^2(m) \tag{15}$$

$$e_x(m) = d(m) - y(m) = i_{Lx}(m) - \delta_{ax}^T(m)u_{ax} \tag{16}$$

where $x = R, Y, B$ phases, respectively, $i_{Lx}(m)$ is the load current, $e_x(m)$ is the error and u_{ax} is the unit template of respective phases and $\delta_{ax}(m)$ is estimated filter coefficient of adaptive filter.

The filter coefficients are then updated as in (17)

$$\delta_{ax}(m + 1) = \delta_{ax}(m) - \mu \frac{\partial C(m)}{\partial \delta_{ax}(m)} = \delta_{ax}(m) + \mu e_x(m)u_{ax} \tag{17}$$

where $x = R, Y, B$ phases, respectively, μ is called step size for the proposed algorithm which governs the convergence speed and stability of the system. The value of μ is chosen a very small positive number in the range 0–1. Similarly, reactive filter coefficients $\delta_{bx}(m)$ can be calculated.

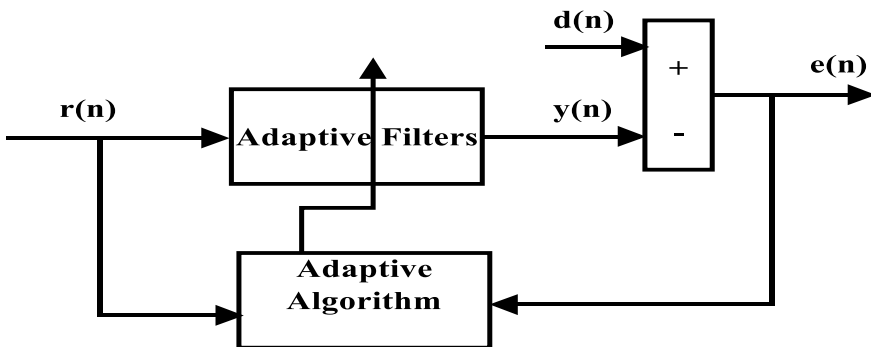


Fig. 2 Structure of adaptive filter

3.1.2 LMF Algorithm

The cost function of LMF algorithm is given by (18) and (19)

$$C(m) = \frac{1}{4}e^4(m) \quad (18)$$

$$e_x(m) = d(m) - y(m) = i_{Lx}(m) - \delta_{ax}^T(m)u_{ax} \quad (19)$$

The filter coefficients are updated as in (20)

$$\delta_{ax}(m+1) = \delta_{ax}(m) - \mu \frac{\partial C(m)}{\partial \delta_{ax}(m)} = \delta_{ax}(m) + \mu e_x^3(m)u_{ax} \quad (20)$$

where $x = R, Y, B$ phases, respectively, μ is fixed step size for the proposed algorithm which governs the convergence speed, The value of μ is chosen a very small positive number in the range 0–1. Reactive weight component $\delta_{bx}(m)$ can be calculated as Eq. (20).

3.1.3 RLS Algorithm

It falls in the category of recursive algorithm. Objective of this algorithm is to minimize the sum of square of the difference between desired signal and filter output. The cost function for RLS algorithm is represented as in (21)

$$C(m) = \sum_{n=1}^m F_m(n)e_m^2(n) \quad (21)$$

where $F_m(n) = \lambda^{m-n}$.

The filter coefficients are represented in (22) and (23)

$$\delta_{ax}(m+1) = \delta_{ax}(m) + K_x(m)e_x(m) \quad (22)$$

$$K_x(m) = \frac{M_{ax}(m)u_{ax}}{\lambda + u_{ax}^T(m)M_{ax}(m)u_{ax}} \quad (23)$$

$$M_{ax}(m+1) = \frac{M_{ax}(m) - K_x(m)u_{ax}^T M_{ax}(m)}{\lambda} \quad (24)$$

$$e_x(m) = i_{Lx}(m) - u_{ax}(m)\delta_{ax}(m+1) \quad (25)$$

where $x = R, Y, B$ phases, respectively, $K_x(m)$ is Kalman gain, $M_{ax}(m+1)$ is the inverse correlation matrix of and λ is forgetting co-efficient. The value of λ is taken between 0.95 and 1. Similarly, reactive weight component $\delta_{bx}(m)$ can be computed.

3.2 Generation of Reference Grid Current and Gate Pulse

Average and resultant active and reactive weights are computed in (26)–(29)

$$\delta_{\text{avga}} = \frac{1}{3} \sum_{x=R,Y,B} \delta_{ax} \quad (26)$$

$$\delta_{ra} = \delta_{\text{avga}} + \delta_{ca} - \delta_{pv} \quad (27)$$

where δ_{avga} is the average active weight, δ_{ra} is the resultant active weight, and δ_{pv} is the feed-forward term.

$$\delta_{\text{avgb}} = \frac{1}{3} \sum_{x=R,Y,B} \delta_{bx} \quad (28)$$

$$\delta_{rb} = \delta_{cb} - \delta_{\text{avgb}} \quad (29)$$

where x represents R, Y, B phases, respectively.

The resultant active weight (δ_{ra}) and reactive weight (δ_{rb}) determine the active (i_{sax}^*) and reactive (i_{sbx}^*) reference grid currents as in (30)

$$\begin{aligned} i_{sax}^* &= \delta_{ra} u_{ax} \\ i_{sbx}^* &= \delta_{rb} u_{bx} \end{aligned} \quad (30)$$

where x represents R, Y, B phases, respectively.

Then the total reference grid currents are computed in (31)

$$i_{sx}^* = i_{sax}^* + i_{sbx}^* \quad (31)$$

Here x represents R, Y, B phases and i_{sx}^* represents reference grid currents of respective phases.

After generating the reference grid currents ($i_{sR}^*, i_{sY}^*, i_{sB}^*$) they are compared with the actual grid currents (i_{sR}, i_{sY}, i_{sB}) sensed at the point of common coupling. The error is then passed through a hysteresis band of width 0.01 for generating the gate pulses.

4 Comparison Between LMS, LMF and RLS Filter

Figure 3 gives a comparative performance analysis between LMS, LMF and RLS filter algorithms during unbalanced loading condition. At 0.8 s phase, R is disconnected from the load and reconnected at 1 s. Transient behaviour of an algorithm is analyzed on the basis of oscillations during unbalancing and convergence capabilities

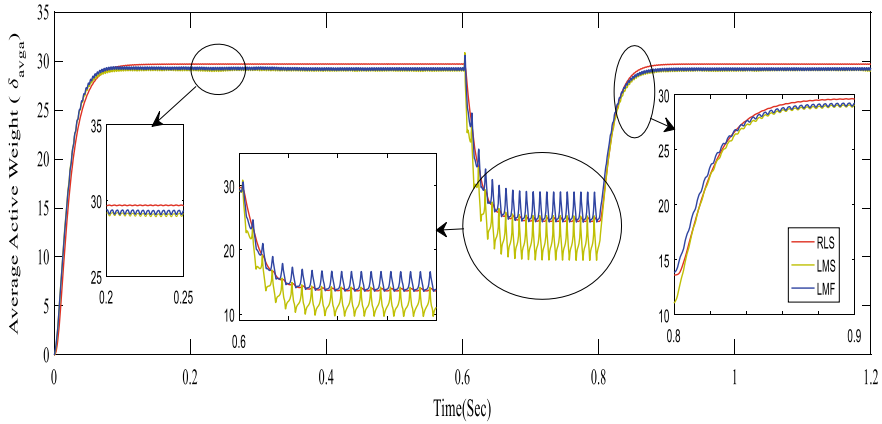


Fig. 3 Comparison of estimated average active weight of RLS with LMS and LMF

to steady-state. From Fig. 3 it is observed that during unbalanced condition oscillations is more in case of LMS and LMF filter whereas in RLS algorithm oscillation is almost zero. Oscillation of LMS filter is more as compared to LMF filter during unbalanced period. Comparing the weight curve for LMS, LMF and RLS filter it is observed that RLS has better convergence rate as compared to LMS and LMF filter.

4.1 Result Analysis of RLS Filter

The performance analysis of the PV-DSTATCOM system is analyzed under the condition when a-phase of the three-phase system is withdrawn at 0.6 s and it is reconnected at 0.8 s. As from the above analysis, it is observed that RLS filter outperforms LMF and LMS filter, hence dynamic performance of the system is observed using RLS algorithm and is shown in Fig. 4. At 0.6 s. When load is removed load power decreases and in the meantime power transferred to grid is increased as shown in Fig. 4a. Negative grid power means power is transferred to grid after meeting load demand. Zero reactive power indicates unity power factor operation. From Fig. 4b it is clear that after 0.6 s. Load current decreases whereas grid current increases. Voltage across dc link capacitor maintains constant value throughout the operation. Figure 5 depicts the transition of the system from PV-DSTATCOM to DSTATCOM mode and vice versa. At 0.5 s when PV source is removed, it operates as STATCOM. From Fig. 5a it is clear that at 0.5 s. PV current becomes zero, grid current changes its direction and remains sinusoidal and hence power flow takes place from grid to load. DC voltage remains constant during this period. During PV-DSTATCOM mode PV current increases, grid current increases, grid power becomes negative, i.e., it takes power from PV source as shown in Fig. 5b. Figure 6 shows the THD analysis of grid current and voltage and it satisfies IEEE-519 and 547 standards.

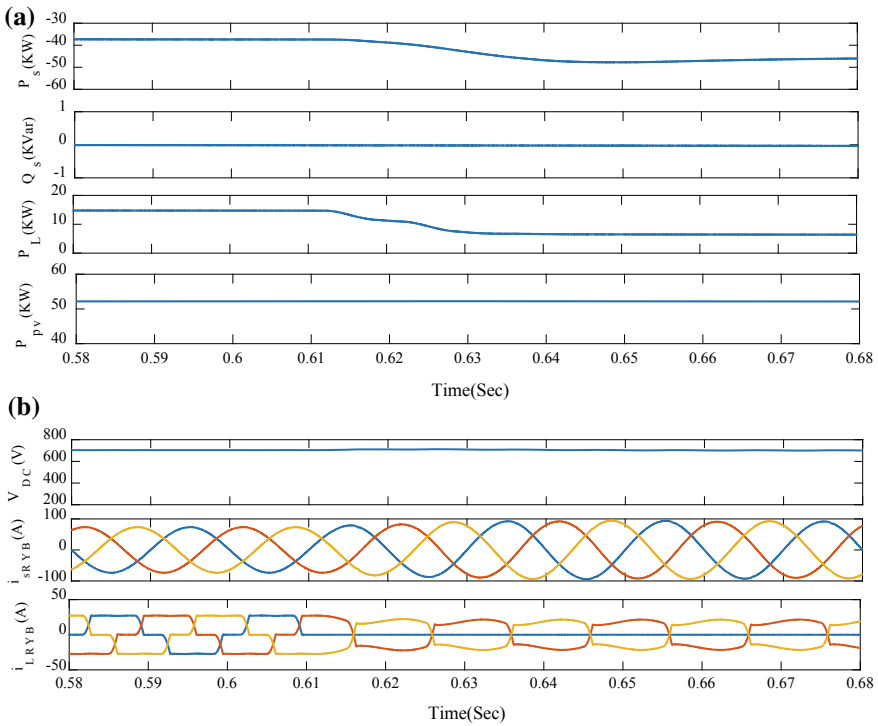


Fig. 4 Performance analysis of RLS based PV-DSTATCOM system when load is disconnected at 0.6 s. **a** P_s, Q_s, P_L, P_{pv} . **b** $V_{dc}, i_{sRYB}, i_{LRYB}$

5 Conclusion

In this paper, comparison between LMS, LMF and RLS algorithms are given for a PV-DSTATCOM system. The performances of the systems are observed under various abnormalities. But the performance under unbalanced condition is shown in the paper. It is concluded that the RLS algorithm performs better against LMF and LMS irrespective of abnormalities. Its convergence rate is better and there are no oscillations during unbalancing as compared to other algorithms. Harmonic contents of the grid current and voltage are within IEEE prescribed limit.

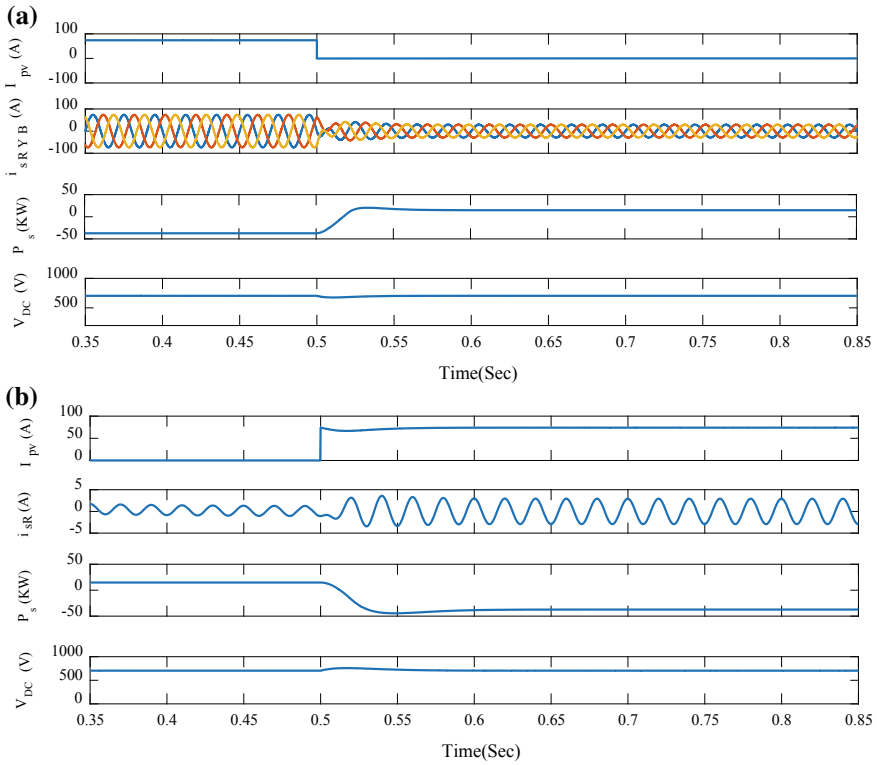


Fig. 5 PV-STATCOM to STATCOM mode and vice versa **a** I_{pv} , i_{sRYB} , P_s , V_{dc} . **b** I_{pv} , i_{sR} , P_s , V_{dc}

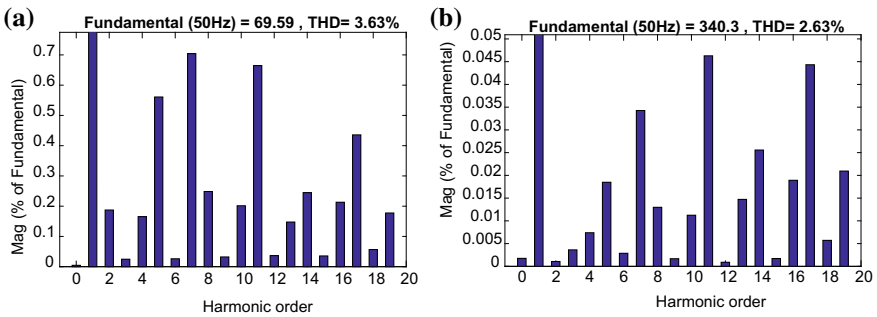


Fig. 6 Harmonic analysis of **a** grid current i_{sRYB} , **b** grid voltage V_{sRYB}

References

1. Myneni H, Siva Kumar G, Sreenivasarao D (2017) Dynamic dc voltage regulation of split-capacitor DSTATCOM for power quality improvement. *IET Gener Trans Distrib* 11(17):4373–4383
2. Singh B, Chandra A, Al-Haddad K (2015) *Power quality: problems and mitigation techniques*. Wiley, Chichester
3. Akhtar S, Bernstein DS (2005) Lyapunov-stable discrete-time model reference adaptive control. In: *Proceedings of the 2005, American control conference*, vol 5, pp 3174–3179. Portland, OR (2005)
4. Khadkikar V, Chandra A, Singh BN (2009) Generalised single-phase p-q theory for active power filtering: simulation and DSP-based experimental investigation. *IET Power Electron* 2(1):67–78
5. Angulo M, Ruiz-Caballero DA, Lago J, Heldwein ML, Mussa SA (2013) Active power filter control strategy with implicit closed-loop current control and resonant controller. *IEEE Trans Industr Electron* 60(7):2721–2730
6. Pradhan AK, Routray A, Basak A (2005) Power system frequency estimation using least mean square technique. *IEEE Trans Power Deliv* 20(3):1812–1816
7. Subudhi B, Ray PK, Ghosh S (2012) Variable leaky least mean-square algorithm-based power system frequency estimation. *IET Sci Meas Technol* 6(4):288–297
8. Walach E, Widrow B (1984) The least mean fourth (LMF) adaptive algorithm and its family. *IEEE Trans Inf Theory* 30(2):275–283
9. Badoni M, Singh A, Singh B (2015) Variable forgetting factor recursive least square control algorithm for DSTATCOM. *IEEE Trans Power Deliv* 30(5):2353–2361
10. Mohan N, Undeland TM, Robbins WP (2003) *Power electronics: converters applications and design*, Wiley, New York, NY

Fractional Order PID Controller Design for Stabilizing and Trajectory Tracking of Vehicle System



Akshaya Kumar Patra, Alok Kumar Mishra and Ramachandra Agrawal

Abstract The aim of this paper is to design a fractional order proportional-integral-derivative controller (FOPIDC) for a vehicle suspension (VS) system to improve the ride comfort by absorbing the shocks due to a rough and uneven road. In this control strategy, the conventional proportional and integral controller (CPIC) is reformulated with fractional orders of the integrator and differentiator to improve the control performance. The FOPIDC is a novel approach whose gains dynamically vary with respect to the error signal. The validation of the improved control performance of FOPIDC is established by comparative result investigation with other published control algorithms. The comparative results clearly reveal the better response of the suggested approach to control the oscillation of the VS system within a stable range with respect to the accuracy, robustness, and capability to control uncertainties.

Keywords Ride comfort · Road profile · Vehicle suspension system · FOPIDC

1 Introduction

In recent times, many researchers in the field of vehicle suspension (VS) system dynamics have devoted to arrive at an optimal solution with a compromise between vehicle handling, ride comfort, and stability. There is a need for better approach today as the above problems are very much evident in the modern vehicle cases. Specific to the large sedan and luxury cars, even if excellent ride qualities are achieved, it

A. K. Patra (✉) · A. K. Mishra
Department of EEE, ITER, Siksha 'O' Anusandhan (Deemed to be University), Bhubaneswar
751030, India
e-mail: hiakp@yahoo.com

A. K. Mishra
e-mail: alokmishra@soa.ac.in

R. Agrawal
Department of EE, ITER, Siksha 'O' Anusandhan (Deemed to be University), Bhubaneswar
751030, India
e-mail: ramachandra1agrwal@gmail.com

© Springer Nature Singapore Pte Ltd. 2020
R. Sharma et al. (eds.), *Innovation in Electrical Power Engineering, Communication, and Computing Technology*, Lecture Notes in Electrical Engineering 630,
https://doi.org/10.1007/978-981-15-2305-2_48

is limited to acquiring adequate handling behaviour. With reference to sports vehicles, it is provided with very good handling capability, but fails to provide desirable ride quality. There are many options in between for variations in the designing stage of the vehicle manufacturers to meet the customer needs. Designing point of view, passenger comfort and vehicle control are the two primary objectives to be considered. Road disturbances such as bumps or potholes are to be handled not to sacrifice the passenger comfort. At the control stage, these factors are generally considered either through keeping the vehicle body from rolling and pitching excessively, or by maintaining good contact between the tire and the road.

Nowadays hydraulic dampers (shock absorbers) and springs are extensively used for vehicle suspensions. As a principle, these are charged with the job of absorbing bumps, minimizing the vehicle's body motions during acceleration, braking and turning of the vehicle, and keeping the tires in contact with the road surface. However, from the designing point of view, these objectives are contradictory to each other to achieve all simultaneously at their optimum level.

The spring and the damper are the two essential components in VS design. The spring design mostly depends on the weight of the vehicle. The damper design is based on the suspension placement on the compromise curve, and so it is essential to be perfectly chosen to make the optimal vehicle performance for any type of vehicle. For ideal performance, the damper should act such that passengers isolate from low-frequency road disturbances and absorb high-frequency road disturbances. High damping is essential to achieve for best isolation of passengers from low-frequency disturbances.

However, even though it is desirable to design a high damping system, it is on the other degrade the high-frequency absorption rate. In other way providing low damping, the damper offers adequate high-frequency absorption in terms of scaring low-frequency isolation. To meet these contradictory objectives, it is essential to design and focus on automotive suspensions without compromising any of the factors mentioned above. As a solution to the above, three types of suspensions can be improved. These are passive, fully active, and semi-active type of suspensions. The spring and damper are the two basic components of the conventional passive suspension. Both the components are considered and fixed at the design stage. The suspension stores energy in the spring. Later it dissipates energy through the damper.

It is very much needed for further research to develop robust control algorithms to enhance the performance of VS system. This in turn enhances the vehicle capabilities to handle the aforementioned issues. An ideal design of VS system needs to achieve many performance characteristics such as (1) control of body movement and (2) control of suspension movement and force distribution. Performance point of view, the VS should able to isolate the body for comfort against the road impact and inertial disturbances. These are generally associated with cornering and braking or acceleration of the vehicle system [1]. As discussed above, many performance objectives are conflicting in nature that to enhance one, the other factor degrades. Considering all the objectives as a goal for the designing of a suspension system is difficult to meet [2]. Minimization of vertical force to the passengers can be achieved

by minimizing the vertical vehicle body acceleration of the suspension. Another factor which plays a vital role in passenger comfort is the optimal contact between wheel and road surface, and this is essential in various driving conditions in order to maximize safety factor [3]. Among a few designs in the past, the system presented in [4] based on unconstrained optimizations for passive suspension (PS) system case is widely accepted and used. This successfully performs to achieve the desirability of low suspension stiffness, reduced unsprung mass (UM), and an optimum damping ratio for the better controllability. As the PS system performs satisfactorily to some extent, it is considered in many applications for the VS system. However, both the suspension spring and damper do not supply energy to the suspension system. They only control the motion of the vehicle body and wheel by limiting the suspension velocity. This is computed according to the rate specified by the designer. To overcome this issue, the active suspension (AS) system is considered as an efficient option for this application. The AS systems have the ability to dynamically respond to changes in the road profile. It is due to this fact that it can supply energy to produce relative motion between the body and the wheel. Sensors are provided in suspension system to measure the parameters dynamically. The parameters such as body velocity, suspension displacement, and wheel velocity and wheel and body acceleration are sensed and computed for the controller as input parameters [5]. An AS can be thought as the integration of the passive components to actuators that supply additional forces. These additional forces are computed by a feedback control law based on the input data from the sensors fixed to the vehicle. For modelling the real-time dynamic conditions, the uncertainties due to system design and other external disturbances are needed to be considered for the controller. This motivates for a better control design to increase the robustness and controllability under uncertainties and disturbances.

During the past three decades, so many control strategy techniques are suggested and tested by absorbing the shocks due to a rough and bumpy road in case of VS system. Time-discrete and switching PID control strategy is implemented in VS problems with variable control gains based on the measured suspension variables [6, 7]. However, the optimal gain parameter setting, a lesser range of robust control, and need of change of gain setting with varying conditions are the major limitations to limit the real-time application of these controllers. Among other projected robust control algorithms applied for limiting the oscillation and velocity of the VS system are fuzzy-logic control [8–13], fuzzy-PID control [14], genetic algorithm [15], neural network [16], neuro-fuzzy (NF) control [17], linear quadratic regulator (LQR) [18], H-infinity control [19], and sliding mode (SM) control [20, 21]. However, the above control techniques are implemented effectively by absorbing the shocks due to the rough and bumpy road in case of VS system, still fail to handle various constraints and random change found in a suspension environment. These approaches are not fully insensitive to the disturbances and the uncertainties of the model in spite of the improved performance. Hence, optimal control parameters setting for still better performance and for avoiding slow response following road disturbance (road impact), the current work suggests an alternative novel technique based on the fractional PID control concept. Application of the suggested approach to control the

oscillation and velocity in vehicle suspension system results to ensure a better robust controller in comparison with other contemporary well-established approaches under both harmonized and incompatible uncertainties.

The highlights of this manuscript are as follows:

- Development of a Simulink model of a VS system.
- Design of a novel FOPIDC to regulate the oscillation of the VS system within a stable range from -5 to $+5\%$ of road disturbance and return to smooth ride within 5 s.
- Evaluation of the control actions of the FOPIDC under huge deviation of road disturbance.
- Comparative investigation to certify the better response of the FOPIDC.

This manuscript is organized as follows. Section 2 concisely illustrates the VS model with mathematical details reflecting its dynamic characteristics of its suspension vibration process. Also, it clearly demonstrates the simulation execution of the system on MATLAB environment. A detailed presentation on how the control technique is formulated and how it is implemented for this problem is presented in Sect. 3. Comparative results of the proposed approach with other published control techniques and the related analysis are provided in Sect. 4. The concluding comments are summarized in Sect. 5.

2 Problem Formulation and Modelling

The problem formulation and modelling of patient model are described in this section.

2.1 System Overview

The overall closed-loop model of VS system is depicted in Fig. 1a. The road disturbance $w(t)$ and $v(t)$ are reflected as the process disturbance and the sensor noise respectively in this study. The controller receives information about the oscillation of the VS system as input to provide the optimal control force $u(t)$, and it is applied in $bw(t)$ between the UM and the sprung mass (SM) to reduce the relative motion between them.

2.2 Modelling of VS System

In the year 1958, the concept of VS system was emerged into limelight. It has been found in the later period that the vibration suppression capability is limited in case of traditional PS and semi-active suspension systems. This leads to focus on an AS

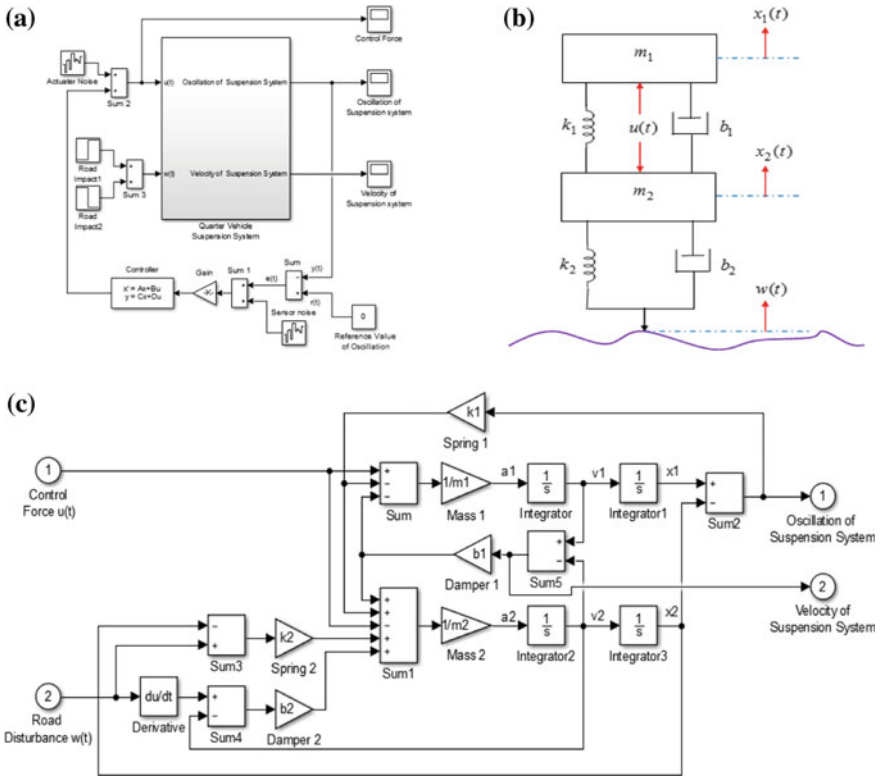


Fig. 1 a VS model with STPIC; b schematic model of the VS system; c simulation model of the non-linear VS system

system with additional control forces as a better alternative to the above drawbacks to suppress the oscillations and used in modern vehicle industry. The major factor that differentiates the active suspension system performance wise is the ability to inject energy into vehicle dynamic system via actuators unlike dissipates energy in case of conventional suspension system. To produce a desirable control force to handle the variety of road disturbances (road impact) in real-time applications, actuators are placed in between the UM and the SM in AS system. The most challenging task of designing an AS system is to enhance the ride comfort by absorbing the shocks due to the rough and bumpy road. The force actuator in the case of the AS system is capable to add and also dissipate energy from the system. This results in an increase in the ride comfort and vehicle handling due to the capability of the suspension system to regulate the vehicle altitude and to eliminate the adverse effects of braking and vehicle roll during cornering and braking. The schematic model of the VS system is illustrated in Fig. 1b.

All the physical activities of the VS system are mathematically expressed and specified by Eqs. (1) and (2). All states and parameters of the model are represented

Table 1 VS model states and parameters

Symbol	Description
$w(t)$	Road impact acting on the UM
$x_1(t)$	Displacement of the SM in vertical direction
$x_2(t)$	Displacement of the UM in vertical direction
$\dot{x}_1(t)$	Velocity of the SM in vertical direction
$\dot{x}_2(t)$	Velocity of the UM in vertical direction
$[x_1(t) - x_2(t)]$	Oscillation of suspension system
$u(t)$	Applied control force between the SM and the UM

Table 2 VS model specification values

Symbol	Quantity/meaning	Value
m_1	SM (mass of the vehicle supported by the suspension)	2500 kg
m_2	UM (mass of the axle and wheel)	320 kg
k_1	Spring constant of suspension system	80,000 N/m
k_2	Spring constant of wheel and tire	500,000 N/m
b_1	Damping coefficient of suspension system	350 Ns/m
b_2	Damping coefficient of wheel and tire	15,020 Ns/m

in Table 1. All specifications of the VS model are documented in Table 2. The Simulink diagram of the VS model is established with respect to Eqs. (1) and (2) as displayed in Fig. 1c.

$$m_1 \left(\frac{d^2 x_1(t)}{dt^2} \right) = -b_1 \left(\frac{dx_1(t)}{dt} - \frac{dx_2(t)}{dt} \right) - k_1(x_1(t) - x_2(t)) + u(t) \quad (1)$$

$$m_2 \left(\frac{d^2 x_2(t)}{dt^2} \right) = b_1 \left(\frac{dx_1(t)}{dt} - \frac{dx_2(t)}{dt} \right) + k_1(x_1(t) - x_2(t)) + b_2 \left(\frac{dw(t)}{dt} - \frac{dx_2(t)}{dt} \right) + k_2(w(t) - x_2(t)) - u(t) \quad (2)$$

2.3 Performance Analysis of VS System

There are four poles in VS system. One of them lies in right-hand side of the complex plane. As a result, the system becomes unstable. This needs the design of an adaptive controller for improving the stability of the system by means of shifting the poles into the left-hand side of the complex plane. The VS system Simulink model in the open-loop form is depicted in Fig. 1c. The VS system has two inputs and two

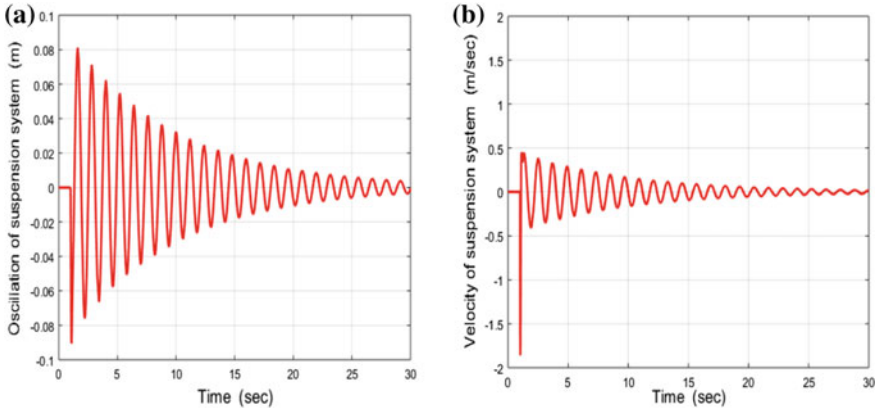


Fig. 2 **a** Response of oscillation of the suspension system with road impact; **b** response of velocity of the suspension system with road impact

outputs. The control force $u(t)$ and road disturbance $w(t)$ are the two inputs of the VS system. The oscillation and velocity of the suspension system are the two outputs of the VS system. An uncontrolled oscillation and velocity of the suspension system are being observed owing to the application of 0.1 m impulsive road disturbance on the unsprung mass at the simulation time of 1.0 s. The irregular oscillation and velocity of the suspension system are illustrated in Fig. 2a, b. Figure 2a, b illustrates the unstable dynamics under various model uncertainties and disturbances. These unstable dynamics can be reduced by applying the suitable control algorithms. In this case, the oscillation of the suspension system is the most essential outcome needs to be controlled within a stable range through suitable control techniques, and velocity of the suspension system is analysed in order to view the motion trajectory.

3 Control Algorithm

The FOPIDC control algorithm is demonstrated in this section. The closed-loop system response with respect to robustness, accuracy, and stability are analysed. The control specifications such as settling time t_s , steady-state error e_{ss} , maximum overshoot O_{Max} , and maximum undershoot U_{Max} are also evaluated and examined with proper validation of the controller action.

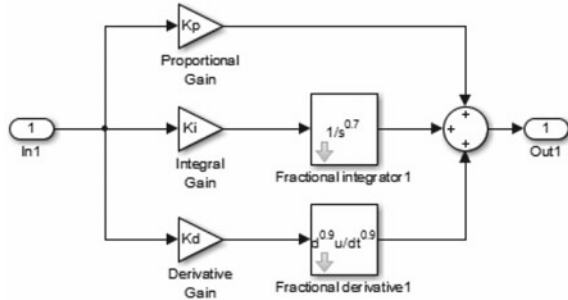
3.1 FOPIDC Design

The VS model with fractional order $PI^\alpha D^\gamma$ controller is shown in Fig. 1a. In fractional order $PI^\alpha D^\beta$ control, the error signal $e(t)$ is used to generate control signal

Table 3 Optimal values of control parameters

K_p	K_d	K_i	α	β
18	6	1.5	0.7	0.9

Fig. 3 Simulink diagram of FOPIDC



$u(t)$. The transfer function (TF) of the proposed controller can be formulated as [22]:

$$TF = K_p + \frac{K_i}{s^\alpha} + K_d s^\beta \tag{3}$$

where α and β are the fractional orders of the integrator and differentiator of the proposed controller, respectively. K_p , K_i , and K_d are denoted for the proportional, integral, and derivative gains of the proposed controller, respectively.

Essential steps for controller design:

- (1) Add K_p to reduce the rise time and reduce the steady-state error.
- (2) Add K_d to reduce the overshoot and reduce the settling time.
- (3) Add K_i to eliminate the steady-state error.
- (4) Adjust each of K_p , K_d , K_i , α , and β in such a manner to obtain the desired output.

The optimal values of the FOPIDC parameters are considered based on the MATLAB/Simulink environment and FOMCON toolbox as represented in Table 3. The structure of FOPIDC is shown in Fig. 3, which is designed based on Eq. (3).

4 Result and Discussions

The performance of the closed-loop VS system with FOPIDC is described in detail in this section. The suggested control approach is compared with other popular control algorithms to justify its enhanced performance.

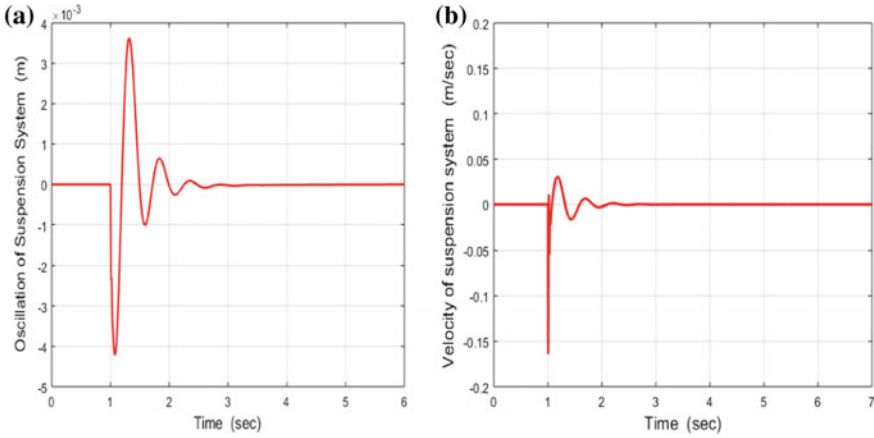


Fig. 4 **a** Response of oscillation of the suspension system with road impact based on FOPIDC; **b** response of velocity of the suspension system with road impact based on FOPIDC

4.1 Performance Analysis of VS System with FOPIDC

In this section, all physical activities of the closed-loop VS model with suggested FOPIDC are examined under different conditions and the huge deviation of road disturbance. The time-domain response of the oscillation and the velocity of the suspension system with 0.1 m impulsive road disturbance at the simulation time of 1.0 s are displayed in Fig. 4a, b. The output results clearly specify the suspension system attains the zero oscillation and zero velocity with less settling time and also attains the balance position where the system is absolutely steady. To achieve the enhanced system response, the required control force $u(t)$ is generated by the suggested FOPIDC and demonstrated in Fig. 5.

4.2 Robustness of the FOPIDC

Figure 6a, b illustrates the oscillation and the velocity of the VS system with suggested FOPIDC under the huge deviation of road disturbance $w(t)$. The time-domain outcomes under huge deviation of road disturbances show the enhanced performance of the closed-loop VS model with FOPIDC. Overall in each case, the VS system achieves finally zero oscillation and zero velocity with less settling time. As indicated by the results, the suggested controller’s robust performance under the huge deviation of road disturbances compared to other published control techniques is much better.

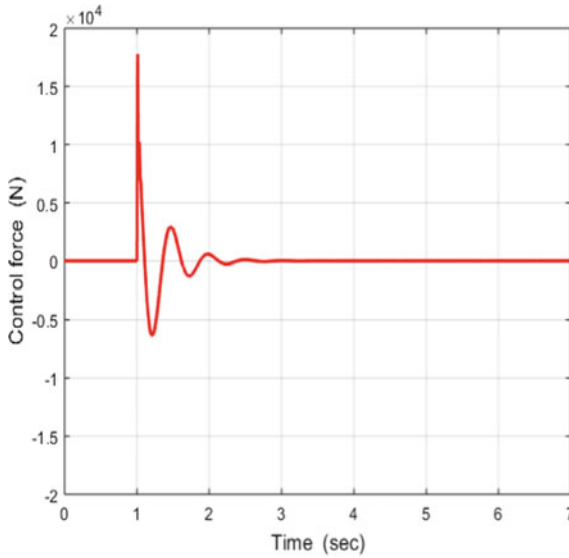


Fig. 5 Control force generated by FOPIDC

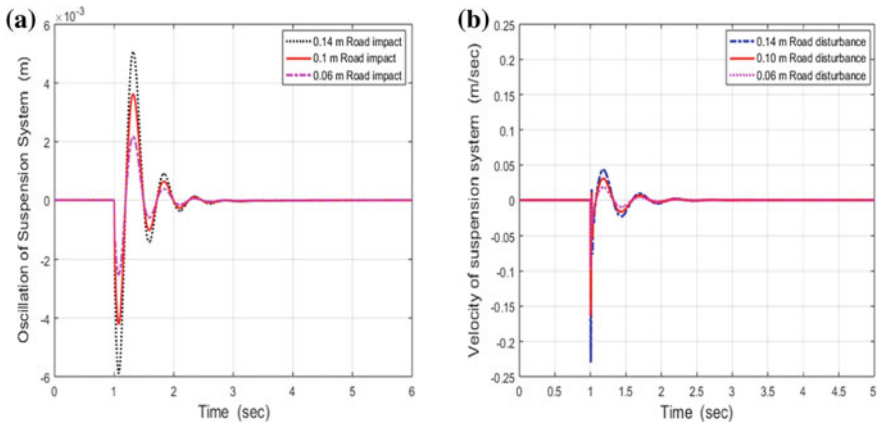


Fig. 6 a Oscillation of the suspension system with deviation of $\pm 40\%$ road disturbance based on FOPIDC; b velocity of the suspension system with deviation of $\pm 40\%$ road disturbance based on FOPIDC

4.3 Verification of Stability

There are four poles in VS system. One of them lies in the right-hand side of the complex plane as displayed in Fig. 7a. It signifies the system dynamics are unstable in nature. For enhancement of stability of the VS system, the FOPIDC is developed and implemented in the VS system. As a result, four poles of the VS system are

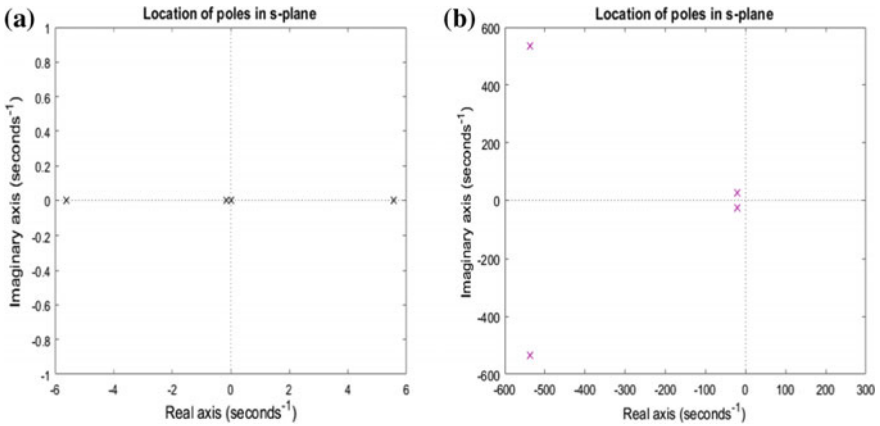


Fig. 7 **a** Location of VS system poles in complex plane; **b** location of closed-loop VS system poles in the complex plane

dragged towards the left-hand side of the complex plane as displayed in Fig. 7b. Consequently, the system stability is enhanced due to the suggested FOPIDC.

4.4 Comparative Study

The proposed FOPIDC control approach is compared with other popular control approaches such as PID, fuzzy, NF, LQR, H ∞ , and SM to justify its enhanced performance as a controller. Figure 4a illustrates the effect of road impact in the oscillation of the suspension system with the suggested FOPIDC approach. Table 4 presents a comparative analysis with respect to t_s (s), O_{Max} (m), U_{Max} (m), noise

Table 4 Comparative result analysis related to oscillation of the suspension system

Controller	PID [6] [ref. Fig. 6a]	Fuzzy [11] [ref. Fig. 2a]	NF [17] [ref. Fig. 3a]	H ∞ [19] [ref. Fig. 2a]	SM [21] [ref. Fig. 5a]	Proposed FOPIDC [ref. Fig. 4a]
Road disturbance (m)	0.1	0.1	0.1	0.1	0.1	0.1
t_s (s)	4.2	4.1	3.7	3.1	3.0	2.5
O_{Max} (m)	0.0050	0.0049	0.0047	0.0043	0.0040	0.0036
U_{Max} (m)	0.0042	0.0045	0.0046	0.0041	0.0048	0.0041
Noise (%)	10	10	5	5	5	1
e_{ss} (%)	0	0	0	0	0	0

(%), and e_{ss} (%). The effect of road disturbance in the oscillation of the suspension system applying different control approaches such as PID, fuzzy, NF, $H\infty$, and SM is also documented in Table 4 based on the references and [6, 11, 17, 19] and [21], respectively. Similar working conditions are followed with the same level of sensor noise in all control techniques application for comparison.

The oscillations of the suspension system under 0.1 m impulsive road disturbance are tested. The corresponding results are presented for the various control approaches along with the proposed FOPIDC with respect to time-domain specifications such as O_{Max} (m), U_{Max} (m), and t_s (s). The results signify the better controllability of the STPIC. The simulation results also demonstrate the high noise and chattering elimination capability with high robustness for the proposed approach. Overall, by looking to the above comparative analysis, the findings of suggested approach advantages are the higher accuracy and stability, more robustness, high noise and chattering elimination capability, and better capability to handle uncertainty under various conditions and huge deviation of road disturbance.

5 Conclusions

In this manuscript, a novel control strategy FOPIDC is proposed based on self-tuned approach. To justify its enhanced performance, it has been applied and tested to control the oscillation and the velocity of the suspension system in the vehicle. In suggested FOPIDC, self-tuned algorithm is utilized to enhance the control performance. The comparative results clearly reflect that the suggested FOPIDC is arrived at better performance than the other control approaches such as PID, fuzzy, NF, LQR, $H\infty$, and SM with respect to stability, reliability, and robustness under various abnormal conditions and disturbances. The better performance of the suggested approach in terms of improved accuracy and stability, enhanced robustness, high noise elimination capability, and better ability to control uncertainty justifies its real-time application.

References

1. Wright PG (1984) The application of active suspension to high performance road Vehicles, microprocessors in fluid engineering. IMechE Conference Publications
2. Fateh MM, Alavi SS (2009) Impedance control of an active suspension system. J Mechatron 19:134–140
3. Lin JS, Kanellakopoulos I (1995) Nonlinear design of active suspension. In: 34th IEEE Conference 1995, vol 17, pp 45–59
4. Alleyen A, Hedrick JK (1995) Nonlinear adaptive control of active suspensions. IEEE Trans Contr Syst Technol 3(1):845–860
5. Esmailzadeh E, Taghirad HD (1997) Active vehicle suspensions with optimal state feedback control. J Mech Sci 200(4):1–18

6. Kumar MS (2008) Development of active suspension system for automobiles using PID controller
7. Talib MHA, Darns IZM (2013) Self-tuning PID controller for active suspension system with hydraulic actuator. In: 2013 IEEE symposium on computers & informatics (ISCI), April, pp 86–91
8. Pekkökgöz RK, Gürel MA, Bilgehan M, Kisa M (2010) Active suspension of cars using fuzzy logic controller Optimized By genetic algorithm. *Int J Eng Appl Sci (IJEAS)* 2(4):27–37
9. Li H (2012) Reliable fuzzy control for active suspension systems with actuator delay and fault. *IEEE Trans Fuzzy Syst* 20(2):342–357
10. Lin Y-J, Lu T-Q, Padovan J (1993) Fuzzy logic control of vehicle suspension systems. *Int J Veh Des* 14(5):457–470
11. Yoshimura T, Nakaminami K, Kurimoto M (1998) Active suspension of passenger cars using linear and fuzzy logic controls. *Control Eng Pract* 1:41–47
12. Yeh EC, Tsao YJ (1994) A fuzzy freeview control scheme of active suspension for rough road. *Int J Veh Des* 15(1):166–180
13. Yang C (2007) Active suspension system of automobile based on fuzzy control. Northeastern University
14. Yang Q, Zhou K, Zhang W, Xing X, Yuan C (2008) Fuzzy-PID control on semi-active air suspension, transactions of the Chinese Society for Agricultural. Machinery 39(9):24–29
15. Du H, Lam J, Sze KY (2003) Non-fragile output feedback H1 vehicle suspension control using genetic algorithm. *Eng Appl Artif Intell* 16:667–680
16. Wang YJ (2007) Analysis of vehicle suspension control using neural networks. Northeastern University
17. Aldair AA, Wang WJ (2012) A neurofuzzy controller for full vehicle active suspension systems. *J Vib Control* 18(12):1837–1854
18. ElMadany MM, Abduljabbar ZS (1999) Linear quadratic Gaussian control of a quarter-car suspension. *Veh Syst Dyn* 32(6):479–497
19. Kaleemullah M, Faris WF, Hasbullah F (2011) Design of robust H_{∞} , fuzzy and LQR controller for active suspension of a quarter car model. In: 2011 4th international conference on mechatronics (ICOM), May. IEEE, pp 1–6
20. Li H, Yu J, Hilton C, Liu H (2013) Adaptive sliding-mode control for nonlinear active suspension vehicle systems using T-S fuzzy approach. *IEEE Trans Industr Electron* 60(8):3328–3338
21. Chen PC, Huang AC (2005) Adaptive sliding mode control of nonautonomous active suspension systems with time-varying loading. *J Sound Vib* 282:1119–1135
22. Bingul Z, Karahan O (2018) Comparison of PID and FOPID controllers tuned by PSO and ABC algorithms for unstable and integrating systems with time delay. *Optimal Control Appl Methods* 39(4):1431–1450

Optimum Design of PV-Battery-Based Microgrid with Mutation Volatilization-Dependent Water Cycle Algorithm



Shaktinarayana Mishra, Saumya Ranjan Lenka, Prachitara Satapathy and Pravati Nayak

Abstract This paper presents mutation volatilization-based water cycle algorithm (MVWCA) to improve the performance of a photovoltaic (PV)-based microgrid system by optimizing different regulators gain parameters during grid normal and uncertain situation. An inclusive optimization of different regulators gain parameters is studied by minimizing the cost function which constitutes active and reactive power losses at the VSC. A weak microgrid is considered to realize the prominent impact of different less inertia contributing element-based system. An auxiliary battery storage (BS) is integrated with PV to compensate the load during insufficient PV generation. The PV–BS generation is incorporated into the microgrid through a voltage source converter (VSC) using a second-order phase-locked loop (PLL) system to achieve grid synchronization. The proposed microgrid is modeled in the MATLAB script platform. Different rigorous case studies are realized to evaluate the performance of the proposed technique.

Keywords Photovoltaic systems · Battery storage · Voltage source converter · Water cycle algorithm

S. Mishra
Gandhi Institute of Technology and Management, Bhubaneswar, India
e-mail: shakti.n.mishara@gmail.com

S. R. Lenka
Vijai Electricals Ltd., Hyderabad, Telangana, India
e-mail: saumyaranjanlenka@gmail.com

P. Satapathy (✉)
College of Engineering and Technology, Bhubaneswar, India
e-mail: prachitara.satapathy@gmail.com

P. Nayak
Siksha 'O' Anusandhan (Deemed to be University), Bhubaneswar, India
e-mail: pravatinayak@soa.ac.in

© Springer Nature Singapore Pte Ltd. 2020
R. Sharma et al. (eds.), *Innovation in Electrical Power Engineering, Communication, and Computing Technology*, Lecture Notes in Electrical Engineering 630,
https://doi.org/10.1007/978-981-15-2305-2_49

1 Introduction

With the growing demand of electricity, the renewable-based distributed generations (DGs) are the perfect solutions to fulfill the requirement and have no negative environmental impact. The other key features of the renewable-based DGs are its less maintenance cost, power regulation versatility and portability. To increase the performance and reliability of the microgrid network during normal and uncertain situation, it is connected to the centralized grid. Microgrid can operate in islanded mode as well as in grid-connected mode. PV generation is intermittent in nature due to the unpredictable nature of solar irradiance and temperature. Hence, selections of optimal controller gain parameters are crucial to improve the system performance and for an optimal power system design with improved power quality and stability [1].

Various linear and nonlinear techniques are discussed in [2–12] to control the power flow at the PCC. Different AI techniques like neural network and fuzzy as discussed in [11, 12] provide better result but have slower convergence speed. The optimization techniques discussed in [8–10] are time consuming and inaccurate to produce optimal gain parameters. Different nature-inspired algorithm, like genetic algorithm [6, 7] and particle swarm optimization [2, 3], also suffers from different disadvantages. The GA could not solve certain variant problems and does not have a stable response time. The PSO method performs in a better way but has a defect of untimely convergence.

The water cycle algorithm (WCA) is also a meta-heuristic technique inspired from the natural water cycle process which is an efficient one for highly nonlinear problem [13]. To make it diversified to cope up with the PV intermittency, a mutation operation is included with the conventional WCA. Hence, this paper presents a mutated volatilization-based WCA (MVWCA) which is very adaptive to provide better solutions for improved performance. The MVWCA is applied at VSC to estimate optimal control parameters to provide faster system restoration during various uncertainties.

This paper is organized as follows. After a brief introduction, the proposed PV–BS-based microgrid is presented with all dynamic equations in Sect. 2. The proposed MVWCA technique is discussed in detail in Sect. 3. In Sect. 4, performance of the proposed optimization scheme is evaluated through rigorous case studies in *MATLAB script* environment. A comparative study of proposed optimization scheme with the basic harmonic search (HS) is also studied in Sect. 4. Lastly, concluding remarks are given in Sect. 5.

2 Modeling of Proposed Microgrid

To check the dynamic functioning with proposed MVWCA, a simple PV-BS-based microgrid is considered here as shown in Fig. 1. The considered microgrid is weak in nature with short-circuit ratio (X/R) of 0.13. A 10 kW PV system is included

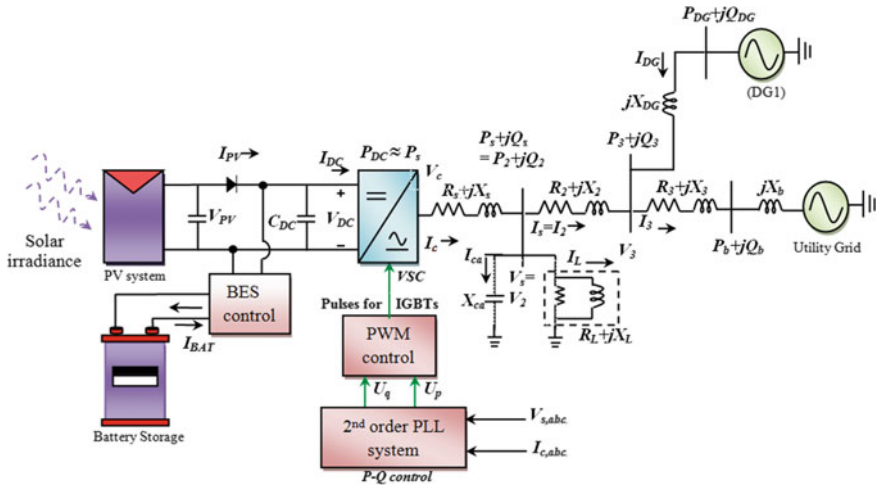


Fig. 1 Schematic diagram of PV-battery-DG-based multiple DER microgrid

according to the IEEE 1547 and UL1741 standard to control the active power injection to the grid. The PV–BES system provides power to the microgrid system through a voltage source converter (VSC). The DC link voltage (V_{DC}) is maintained constant by PV–BS system and is the voltage reference for active power requirement. The battery discharges power during deficient in PV generation (e.g., solar inconsistency, load variation) which is controlled by BS control. The PWM control of VSC uses a second-order phase-locked loop (PLL) for the grid synchronization. The proposed microgrid parameters are given in Table 1, and each element is discussed later in this section.

Table 1 Proposed microgrid parameters

Components	Data	Parameter values		
		R	L	C
PV–VSC (AC)	11.5 kVA, 120 V	1.36 mΩ	41.3 μH	–
Local load (R-L)	7.5 kW, 2 kVAR	0.3 mΩ	0.006 mH	–
$R_1 + jX_1$	1.5 kms	0.96 Ω	0.51 mH	510 μF
$R_2 + jX_2$	1 kms	0.64 Ω	0.34 mH	340 μF
$R_3 + jX_3$	2 kms	1.28 Ω	0.68 mH	678 μF
Filter capacitor (X_c)		–	–	52 mF
System operational frequency	50 Hz	–	–	–

2.1 PV-BES Generation

A 10 kW PV system is incorporated which uses *ELDORA-40* as the basic PV module whose details are given in [14]. There are 46 parallel strings where each consists of six modules in series that are integrated to generate 10 kW PV array. The mathematical model uses a single diode model, and details are given in [14]. The PV system operates at peak power for the maximum utilization of PV system through a MPP controller.

To maintain the DC link voltage constant during various contingencies, the battery storage system is applied. A 4.2 kW lead-acid battery is integrated with the PV as an auxiliary supply in the proposed microgrid system.

The battery voltage (V_{BAT}) for discharging and charging model [15] is as given in Eqs. (1) and (2), respectively.

$$V_{\text{BAT}} = E - R \times I_{\text{BAT}} - K \left(\frac{Q}{Q - I_{\text{BAT}}t} \right) (I_{\text{BAT}}t + I_{\text{BAT}}^*) + (\text{Exp}(I_{\text{BAT}}t)) \quad (1)$$

$$V_{\text{BAT}} = E - R \times I_{\text{BAT}} - K \left(\frac{Q}{I_{\text{BAT}}t - 0.1Q} \right) (I_{\text{BAT}}^*) + K \left(\frac{Q}{Q - I_{\text{BAT}}t} \right) (I_{\text{BAT}}t) + (\text{Exp}(I_{\text{BAT}}t)) \quad (2)$$

where E , Q and R represent battery constant voltage (V), battery capacity (Ah) and internal resistance (Ω), respectively. The K is the polarization constant (V/Ah), V_{BAT} is the battery voltage, and I_{BAT} is the battery current. I_{BAT}^* is the filtered current flowing through the polarization resistance. In this paper, the state of charge (SoC) is assumed as 100% initially. The SoC is managed within the limit (40–80%) by the BS control according to the power demand and PV generation. The power supplied by the battery is the power difference between the reference DC link power and the PV power and can be represented as in Eq. (3)

$$P_{\text{BAT}} = P_{\text{DC_ref}} - P_{\text{PV}} \quad (3)$$

2.2 Second-Order PLL-Based VSC Dynamics

The DC power from the PV-BS is supplied to the AC microgrid through IGBT-based VSC with second-order PLL control to achieve grid synchronization. The dynamics of VSC can be represented by the help of the Kirchoff's law in between VSC and PCC [14] and is given in Eq. (4).

$$V_c(t) = R_s i_s(t) + L_s \frac{di_s(t)}{dt} + V_s(t)$$

$$\Rightarrow \frac{di_s(t)}{dt} = \frac{-R_s}{L_s} i_s(t) + \frac{V_c(t) - V_s(t)}{L_s} \quad (4)$$

where V_c is the output of the converter in abc frame, V_s is the PCC voltage in abc frame, and i_s is the current in between the VSC and PCC in abc frame. The equation can be transformed from abc frame to a power synchronized rotating dq frame using Park's transformation. The phase synchronized angle (ωt) is provided by the PLL for the rotating dq frame.

The DC side dynamics of the converter can be deduced from the power balance between DC side and the PCC side of the converter. By neglecting the converter loss, the power balance equation is as expressed in Eq. (5):

$$\frac{dV_{DC}(t)}{dt} = \frac{1}{C V_{DC}(t)} \left[\frac{3}{2} (V_{sd} i_{sd} + V_{sq} i_{sq}) \right] \quad (5)$$

The DC link power availability is as given in Eq. (6).

$$\left. \begin{aligned} P_{DC} &= P_{PV} & \text{if } P_{PV} &\geq P_{\text{demand}} \\ P_{DC} &= P_{PV} + P_{BAT} & \text{if } P_{PV} < P_{\text{demand}} \end{aligned} \right\} \quad (6)$$

The VSC dynamics in terms of active power (P_s) and reactive power (Q_s) at PCC can be derived from I_d - I_q dynamics and is written as in Eq. (7).

$$\begin{bmatrix} \dot{P}_s \\ \dot{Q}_s \end{bmatrix} = \frac{-R_s}{L_s} \begin{bmatrix} P_s \\ Q_s \end{bmatrix} + \omega \begin{bmatrix} 0 & -1 \\ 1 & 0 \end{bmatrix} \begin{bmatrix} P_1 \\ Q_1 \end{bmatrix} + \frac{1}{L_s} \left(\begin{bmatrix} V_{cd} \\ V_{cq} \end{bmatrix} - \begin{bmatrix} V_{sd} \\ V_{sq} \end{bmatrix} \right) + \frac{1}{L_s} \begin{bmatrix} U_Q \\ U_P \end{bmatrix} \quad (7)$$

The control inputs (U_P and U_Q) for PWM generator in Eq. (7) are calculated by the second-order PLL and as expressed in Eq. (8).

$$\begin{aligned} U_P &= (3/2)(V_{cd} V_{sq} - V_{cq} V_{sd}) \\ U_Q &= (3/2)\{V_{cd} V_{sd} + V_{cq} V_{sq} - (V_{sd}^2 + V_{sq}^2)\} \end{aligned} \quad (8)$$

The VSC's second-order PLL uses a loop filter of the PLL system which takes PCC active and reactive power error as inputs and provides the control inputs as output (Eqs. 9 and 10). The phase detector provides the error difference between the current power and its reference value. The K_{p1} , K_{p2} , K_{i1} and K_{i2} are the proportional and integral gains which are used to calculate control inputs for VSC dynamics. P_{sref} and Q_{sref} are the reference values of PCC power.

$$U_q = \left(K_{p1} + \frac{K_{i1}}{s} \right) (P_{sref} - P_s) \quad (9)$$

$$U_P = \left(K_{p2} + \frac{K_{i2}}{s} \right) (Q_{sref} - Q_s) \quad (10)$$

The active (P_s) and reactive (Q_s) power errors at PCC of PV dynamic relations are considered for proposed optimization to improve the performance. The proposed MVWCA (discussed in Sect. 3) is used to tune the regulators gain (VSC PLL gains: $K_{p1}, K_{p2}, K_{i1}, K_{i2}$) for the optimal achievements of the proposed microgrid system. Instead of fixing the controller parameters through an iterative tuning method, the parameters are selected through the proposed MVWCA technique. This optimal selection of controller parameters provides the optimum performance of the system.

3 Proposed Mutated Volatilization-Based Water Cycle Algorithm (MVWCA)

The water cycle algorithm is a swarm-based meta-heuristic technique which inspired from the natural water cycle process [16]. In this process, the water travels through different stages in different forms. The stages are vaporization, transpiration of plants, condensation of water and precipitation. After the raining process, the raindrops are generated which are then combined to form streams. Streams flow toward the river, and finally all the raindrops reach at the sea through different stages like stream and river. The sea is the final destination of the raindrops, and hence, the optimum point.

The considered optimization problem is a minimization problem where the goal is to reduce the power losses to improve the microgrid stability. The cost function is as expressed in Eq. (11) which is equivalent to the flow intensity. The controller gains (K) are equivalent to the raindrops.

$$\text{Minimize cost function } f(K) = \sum_{p=1}^S e_p$$

$$\text{error } (e) = \underbrace{(P_{sref} - P_s)^2}_{\text{Active Power Error}} + \underbrace{(Q_{sref} - Q_s)^2}_{\text{VAR Error}} \tag{11}$$

Different steps to calculate the optimum solution are given in Algorithm 1. The details of the proposed MVWCA are given in Table 2.

Table 2 Parameters values for proposed MVWCA algorithm

Parameters	Values
No. of decision variables	4
Total number of raindrops (T)	40
Number of rivers (R)	4
D_{max}	0.0001
Maximum no. of iteration (itr)	50
bw_{max}, bw_{min}	0.2,0.1
par_{max}, par_{min}	0.5,0.3

Algorithm 1

- (1) Randomly generate the group of raindrops (G) within the boundaries of the controller gains. In Eq. (12), j describes a single raindrop.

$$G_{T \times 4} = \left[K_{p1}^j \ K_{i1}^j \ K_{p2}^j \ K_{i1}^j \right]_{j=1 \rightarrow \text{Total raindrops (T)}} \quad (12)$$

- (2) The flow intensity is calculated for each raindrop which is the cost functional value (Eq. 11). The raindrop with minimum flow intensity is chosen as sea here. Then, the rivers (values nearer to the sea) and streams (raindrops excluding sea and river) are decided according to the flow.
- (3) The streams flow toward the river and sea. The positions are changed by using Eqs. (13) and (14). The rivers flow toward the sea by using Eq. (15).

$$K_{\text{stream}}(t+1) = K_{\text{stream}}(t) + \text{rand} \times P \times (K_{\text{sea}}(t) - K_{\text{stream}}(t)) \quad (13)$$

$$K_{\text{stream}}(t+1) = K_{\text{stream}}(t) + \text{rand} \times P \times (K_{\text{river}}(t) - K_{\text{stream}}(t)) \quad (14)$$

$$K_{\text{river}}(t+1) = K_{\text{river}}(t) + \text{rand} \times P \times (K_{\text{sea}}(t) - K_{\text{river}}(t)) \quad (15)$$

$$\text{Adaptive parameter (P)} = \text{rand} \times \text{range}(z) + \min(z) \quad (16)$$

To improve the performance and capability of the mutation operation is added. The mutation operation generates better and effective raindrops with better flow intensity to perform efficiently. Here, a harmonic search technique [17] is implemented to calculate the new streams.

- (4) The new raindrops are generated by Eqs. (17) and (18).

$$\text{If } \left(\|K_{\text{sea}} - K_{\text{river}}^j\| < D_{\text{max}} \right) \text{ or } (\text{rand} < \text{PAR})$$

$$\text{If } \|K_{\text{sea}} - K_{\text{stream}}^j\| < D_{\text{max}}$$

$$K_{\text{stream}} = K_{\text{stream}} + \text{rand}(1, 4) \times \text{bw} \quad (17)$$

Else

$$K_{\text{stream}} = K_{\text{stream}} - \text{rand}(1, 4) \times \text{bw} \quad (18)$$

End

End

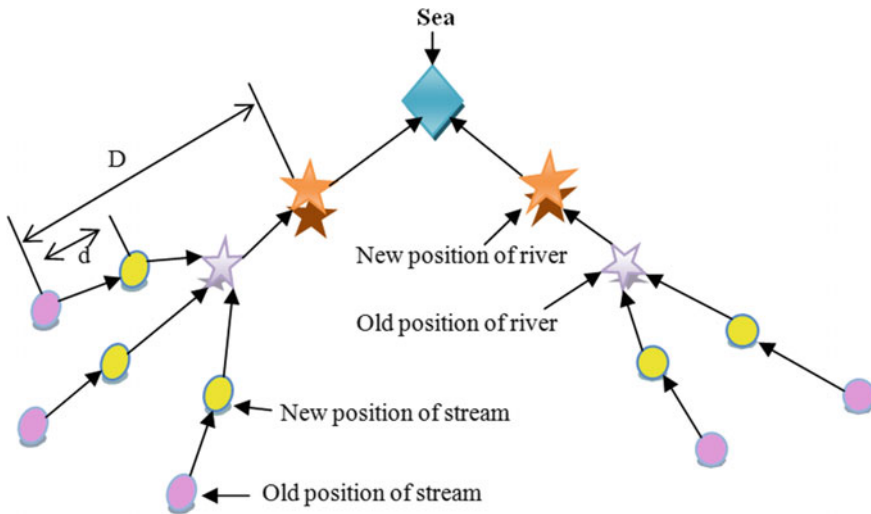


Fig. 2 Schematic diagram of proposed MVWCA

The expressions of bandwidth (bw) and pitch adjustment rate (par) are as calculated by Eqs. (19) and (20), respectively.

$$bw(t) = bw_{max} + e^{\left(\frac{\log(bw_{min}/bw_{max})}{itr}\right)} \times t \tag{19}$$

$$par(t) = par(t - 1) + e^{\left(\frac{par_{max} - par_{min}}{itr}\right)} \times t \tag{20}$$

(5) The new flow intensities are calculated by using Eq. (11) with the modified position. Thus, the step 2 to step 4 repeats up to maximum iteration (itr).

where ‘ub’ and ‘lb’ are the upper bound and lower bound of the controller gains. The schematic representation of the proposed water cycle algorithm is shown in Fig. 2. The performance of the proposed MVWCA technique is evaluated against the existing basic harmonic search technique for a comparative study.

4 Result and Discussion

To analyze the performance of the proposed microgrid system (shown in Fig. 1) with the optimal controller gain parameters, the microgrid system is modeled using *MATLAB editor* platform. The performance evaluation of the proposed MVWCA optimization technique is accomplished by considering different grid uncertainties like partial shading and three-phase PCC fault. A comparative study of the proposed

MVWCA technique against the basic harmonic search (HS) technique is also given in this section to show the superiority of the proposed algorithm.

4.1 *Partially Shaded Condition*

Partial shading is a PV side contingency where different PV modules receive dissimilar solar irradiance. PV generation is reduced due to partial shading situation, and hence, the supply to utility grid is reduced. Because of different illumination at different modules, the PV system has several local peaks and one global peak. Here, the PV array receives three different irradiances (no shading 1000 W/m^2 , partly shading 600 W/m^2 and full shading 200 W/m^2) at the time instant of $t = 4 \text{ s}$. During the fault, the behavior of grid and battery parameters is illustrated in Fig. 3. The MPPT technique tracks the global peak, and the characteristic curves for the basic PV array are as shown in Fig. 3a, b. Five of such 2 kW arrays are connected in parallel to provide the 10 kW PV system. It can be seen from Fig. 3c that the proposed MVWCA restores the system within 25 cycles, but the harmonic search method takes more time (125 cycles). Figure 3d–f shows the nature of current, active power and reactive power at the PCC (bus 2), respectively. The proposed technique gives less transient oscillations with less fault clearance time. During shading as the PV power is reduced, the battery is feeding the load and that is illustrated in Fig. 3h. The battery voltage and current nature are as shown in Fig. 3g, and it can be seen that the voltage is decreasing due to the discharging process. The cost function magnitude is as shown in Fig. 3i. The proposed MVWCA is taking only ten iterations to provide the optimum gains for the optimal operation; whereas, the HS technique is taking 33 iterations.

4.2 *Three-Phase Fault at PCC*

The performance of the proposed system with the optimal gain parameters is also studied for a three-phase fault scenario at PCC. Response of various grid parameters is shown in Fig. 4 by introducing a three-phase fault in the PCC for five cycles at $t = 1.5 \text{ s}$ time instant. The proposed technique provides high damping to make the system stable within 25 cycles (as shown in Fig. 4a). But, the basic HS method takes 100 cycles for the system restoration after the fault occurrence. Figure 4b, e shows the nature of current and frequency at the PCC due to the occurrence of the fault. Figure 4c, d shows the nature of active and reactive power at the PCC. The proposed MVWCA takes only 11 iterations to converge the cost function and is shown in Fig. 4f. The optimal gain parameters provide a reduced transient profile and a system with optimum response.

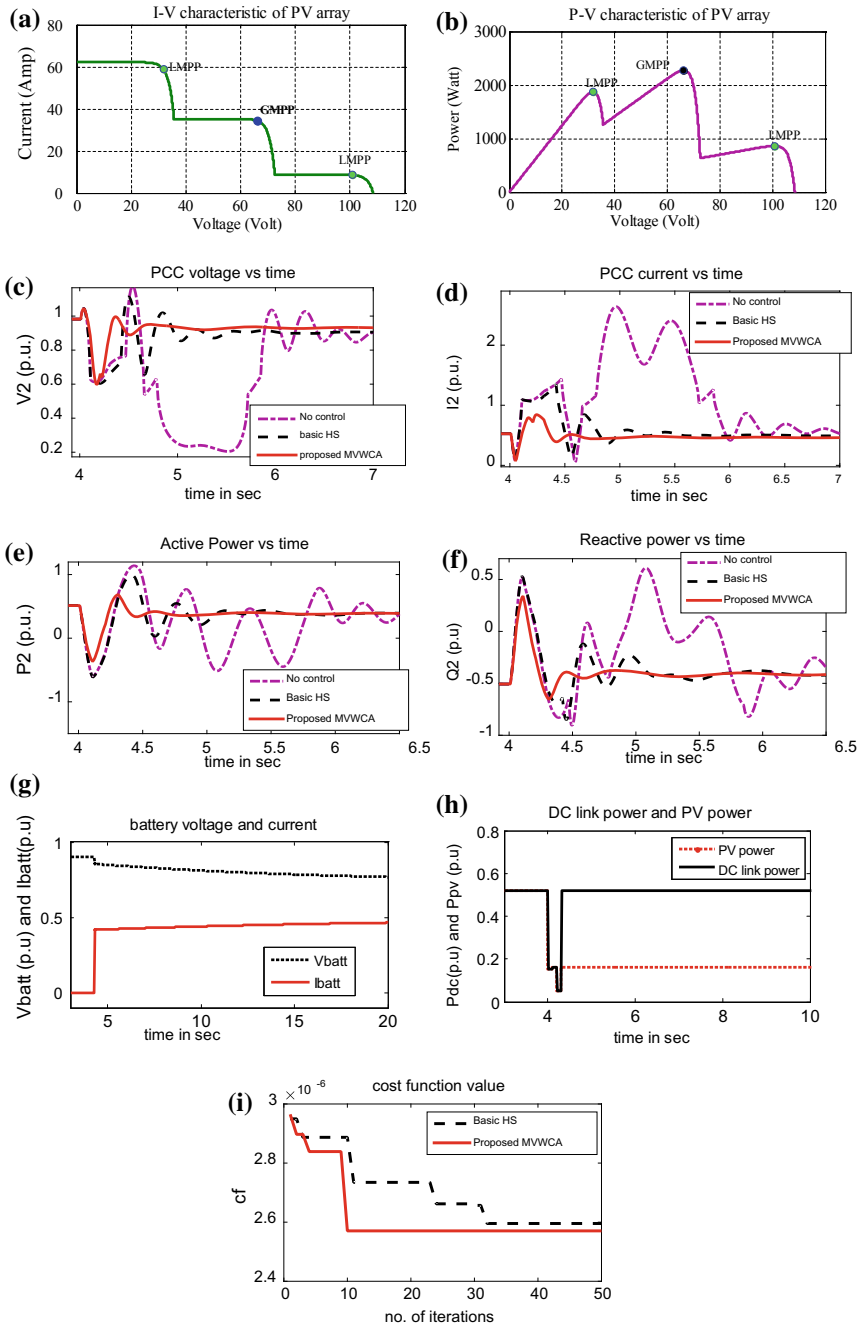


Fig. 3 Comparative results of various grid parameter responses during partial shading: **a** P–V curve and **b** I–V curve of PV system with global MPP; **c** voltage at PCC (V_1), **d** current at PCC (I_1), **e** active power at PCC (P_1), **f** reactive power at PCC Q_1 , **g** battery parameters (V_{batt} , I_{batt}), **h** DC link power and PV power (P_{DC} , P_{PV}), **i** cost function (f)

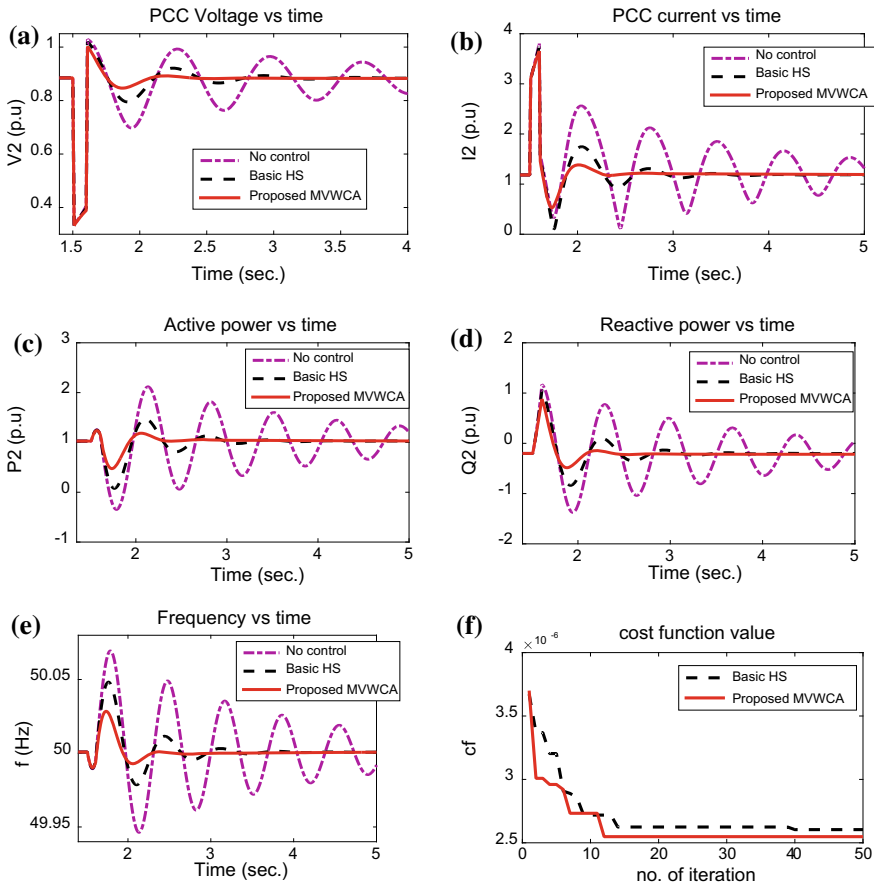


Fig. 4 Comparative results of various grid parameter responses during three-phase fault at PCC, **a** voltage at PCC (V_1), **b** current at PCC (I_1), **c** active power at PCC (P_1), **d** reactive power at PCC (Q_1), **e** operating frequency (f), **f** fitness function (f)

4.3 A Comparative Study of Basic HS and Proposed MVWCA Optimization Schemes

In this section, a comparative analysis is presented in Table 3 to show the supremacy of the proposed MVWCA technique over HS method. The dominance is proved through various parameters like system restoration time (after disturbances), cost function value (in terms of root mean square error) and convergence speed (as given in Table 3). The system with the MVWCA method is more damped and so mitigates the low-frequency oscillations in less number of cycles. The system restoration time after any type of disturbances is less with proposed method. The proposed scheme has faster convergence speed with less magnitude of cost function value as compared

Table 3 Performance evaluation of proposed MVWCA technique

Different faults	Method	Error mitigation time (cycles/s)	Cost function value (RMSE)	Speed (in terms generation)
Case 1 (partial shading)	Basic HS	125 (2.5 s.)	2.601×10^{-6}	34
	MVWCA	25 (0.5 s.)	2.521×10^{-6}	10
Case 2 (PCC fault)	Basic HS	100 (2 s.)	2.711×10^{-6}	15
	MVWCA	25 (0.5 s.)	2.548×10^{-6}	11

to the basic HS method. These parameters confirm the supremacy of the proposed MVWCA method, and hence, can be applied to establish an optimal microgrid system through various optimum regulator gains.

5 Conclusion

The improved performance of the proposed microgrid system with a mutated volatilization-based water cycle algorithm has been presented in this paper. The proposed MVWCA-based optimization is expressed in terms of parametric error minimization of microgrid dynamics. The proposed microgrid with PV and auxiliary battery energy storage system is modeled in MATLAB editor platform and integrated through VSC to achieve grid integration. To control the VSC dynamic performance, a second-order PLL is applied in the proposed microgrid. The system performance is improved with reduced transient dynamic oscillations by applying control gains optimized with the proposed MVWCA optimization technique. The dynamic responses of different grid parameters are studied during the solar and grid uncertainties. The system restoration time is minimum with the application of the proposed MVWCA technique. The optimization technique establishes effectiveness with fast convergence as compared with basic HS optimized system responses.

References

1. Huang W, Sun C, Wu Z, Zhang J (2009) A review on microgrid technology containing distributed generation system. *Power Syst Technol* 9:006
2. Hassan MA, Abido MA (2011) Optimal design of microgrids in autonomous and grid-connected modes using particle swarm optimization. *IEEE Trans Power Electron* 26(3):755–769
3. Gaing ZL (2004) A particle swarm optimization approach for optimum design of PID controller in AVR system. *IEEE Trans Energy Convers* 19(2):384–391
4. Zmood DN, Holmes DG, Bode GH (2001) Frequency-domain analysis of three-phase linear current regulators. *IEEE Trans Ind Appl* 37(2):601–610
5. Tabesh A, Iravani R (2009) Multivariable dynamic model and robust control of a voltage-source converter for power system applications. *IEEE Trans Power Delivery* 24(1):462–471

6. Panda S (2011) Multi-objective PID controller tuning for a FACTS-based damping stabilizer using non-dominated sorting genetic algorithm-II. *Int J Electr Power Energy Syst* 33(7):1296–1308
7. Daneshfar F, Bevrani H (2012) Multiobjective design of load frequency control using genetic algorithms. *Int J Electr Power Energy Syst* 42(1):257–263
8. Pogaku N, Prodanović M, Green TC (2007) Modeling, analysis and testing of autonomous operation of an inverter-based microgrid. *IEEE Trans Power Electron* 22(2):613–625
9. Katiraei F, Iravani MR, Lehn PW (2007) Small-signal dynamic model of a micro-grid including conventional and electronically interfaced distributed resources. *IET Gener Transm Distrib* 1(3):369–378
10. Sao CK, Lehn PW (2008) Control and power management of converter fed microgrids. *IEEE Trans Power Syst* 23(3):1088–1098
11. Seng TL, Khalid MB, Yusof R (1999) Tuning of a neuro-fuzzy controller by genetic algorithm. *IEEE Trans Syst Man Cybern B Cybern* 29(2):226–236
12. Sousa GC, Bose BK, Cleland JG (1995) Fuzzy logic based on-line efficiency optimization control of an indirect vector-controlled induction motor drive. *IEEE Trans Ind Electron* 42(2):192–198
13. Naik J, Satapathy P, Dash PK (2018) Short-term wind speed and wind power prediction using hybrid empirical mode decomposition and kernel ridge regression. *Appl Soft Comput* 70:1167–1188
14. Prachitara S, Dhar S, Dash PK (2017) Stability improvement of PV-BESS diesel generator-based microgrid with a new modified harmony search-based hybrid firefly algorithm. *IET Renew Power Gener* 11(5):566–577
15. Prachitara S, Dhar S, Dash PK (2017) An evolutionary online sequential extreme learning machine for maximum power point tracking and control in multi-photovoltaic microgrid system. *Renew Energy Focus* 21:33–53
16. Eskandar H, Sadollah A, Bahreininejad A, Hamdi M (2012) Water cycle algorithm—a novel metaheuristic optimization method for solving constrained engineering optimization problems. *Comput Struct* 110:151–166
17. Osama MA, Mandava R (2011) The variants of the harmony search algorithm: an overview. *Artif Intell Rev* 36(1):49–68

New Modified Water Cycle Optimized Fuzzy PI Controller for Improved Stability of Photovoltaic-Based Distributed Generation Towards Microgrid Integration



M. Mohamed Hamad Adam, Naeem M. S. Hannon and Snehamoy Dhar

Abstract In this paper, a new modified water cycle (WC)-based optimization is incorporated for independent distributed generation controllers' (IDGCs') gain parameters tuning. Photovoltaic (PV)-based distributed generation (DG) is considered for active distribution network/microgrid tied operation, where the IDGC feedback path is designed with fuzzy Proportional-Integral (PI) scheme. The PI controller is linear and hence unable to address operational uncertainties (e.g. variation in irradiation profile, partial shading, symmetrical/asymmetrical faults, load variations, etc.) for a PV-based DG incorporation. The fuzzy rule-based adaptive gains are also limited towards unbounded uncertainties (grid connected to autonomous mode operation). Thus, to improve the system stability with effective feedback gain parameters' selection, the modified WC algorithm is designed in this paper. The proposed WC scheme is included with a sinusoidal chaos map to address the nonlinearities. The performance of the proposed IDGC feedback path is evidenced under various grid operational contingencies. The efficacy measure of proposed scheme is recorded in terms of dynamic oscillation damping. This performance validation is implemented in MATLAB *Script* environment.

Keywords Photovoltaic · Independent distributed generation controller · Water cycle algorithm · Fuzzy PI control

1 Introduction

In recent energy framework, our planet is subjected to a catastrophe because of decreased fossil fuel, for which administrations are implementing novel energy models with renewable energy source (RES)-based distributed generations (DGs) [1, 2]. DGs are power generation units based on RES (i.e. PV, wind, etc.) which are

M. M. H. Adam · N. M. S. Hannon
Universiti Teknologi MARA, Shah Alam, Malaysia

S. Dhar (✉)
Siksha 'O' Anusandhan (Deemed to Be University), Bhubaneswar, India
e-mail: snehamoydhar@gmail.com

© Springer Nature Singapore Pte Ltd. 2020
R. Sharma et al. (eds.), *Innovation in Electrical Power Engineering, Communication, and Computing Technology*, Lecture Notes in Electrical Engineering 630,
https://doi.org/10.1007/978-981-15-2305-2_50

erratic in character and thus be able to pose grid (especially active distribution network/microgrid) stability concerns [3]. Hence power electronics converters (i.e. voltage source converter/VSC, DC-DC converters, etc.) are incorporated prior to these DGs integration to propose grid stability at point of common coupling (PCC). Noteworthy benefits like power in a bidirectional course, individualistic active-reactive power regulation to the microgrid, decoupling operation of AC side and DC side, etc. make the choice of VSC as conspicuous for PV operation [4]. PV-VSC-based DG systems are expressed in terms of non-linear dynamic relations towards feedback system (phase-locked loop: PLL with PCC), where contingencies are possible to reduce from grid stability by proper control design [5–8]. Standard proportional–integral (PI)-based feedback designs have implemented effectively for last fifty years [5] and utilized rigorously for industrial converter control till date. The primary cause of that is because of their less operational complexity, simple architecture, economical maintenance, and effectiveness for most grid-tied converters (bounded uncertainties to be handled with). Lately, inspired by the escalated development of advanced microcontrollers and digital signal processors, conventional PI-based converter control gets high importance in renewable market, from DGs’ feedback controllers to battery charge controllers [5, 6].

PV-based DGs are also well cited with PI-based feedback path against grid PLL operation [5, 7]. However, these PI-based controllers normally unable to perform under unbounded uncertainties (e.g. PV side contingencies: partial shading; grid side contingencies: islanding condition, etc.), especially for higher order (fractional derivative relation-based VSC) and time-delayed dynamic systems (VSC operation with primary controllers: PCs). To cope with these challenges, different improvements are incorporated into conventional PI design. Auto-tuning operation and adaptive PI-based feedback paths are recently added to literature [8]. Further new types of PI-based independent DG controllers (IDGCs) with fuzzy logic (FL) are implemented for DG PLL [9, 10]. The FL-PI-based IDGC for PV-VSC-based DG integration is having operational features like:

- (1) Better grid stability under contingencies: these IDGCs are having the similar linear architecture as classical PI-based design, but equipped with fixed coefficients, self tuned feedback P and I gains under VSC dynamic input.
- (2) These IDGCs are implemented depending on the conventional discrete PI design, by virtue of which fuzzy rules (FRs) are estimated.
- (3) Membership functions (MFs) are designed simple by triangular formula with minimum (maximum four) *IF–THEN* logics. The *Fuzzification*, FRs’ accomplishment, and *Defuzzification* operations are incorporated in the end derivation of the FR rules. The whole operation is based on PI gains adaptive switching under different VSC to PCC relations (control error) for different contingency profile. Thus, the *Fuzzification–FRs–Defuzzification* process is not required for every control instance (sample rate of VSC dynamics).

FL-PI-based controllers’ stability analysis is established in [11] where bounded uncertainty (within stability limit dynamic behaviour) has emphasized. The FL-PI is

established as superior to conventional PI architecture. Optimal operation of FL-PI-based IDGC is confirmed with single-objective as well as multi-objective problem [12]. But optimal operation of FL-PI-based DG feedback control for PV-VSC application (especially under unbounded uncertainties: partial shading, symmetric faults, islanded operation, etc.) is yet to be addressed in literature. In this paper, a new modified water cycle (WC)-based less computational optimization of FL-PI IDGC is proposed for PV-based DG integration towards microgrid.

After a brief introduction in Sect. 1, the considered PV-based DG integrated microgrid architecture with VSC dynamics is presented in Sect. 2. The PV operation is obtained as single-stage conversion for better reflection of IDGC effects on grid dynamics (without voltage stability by DC-DC). The proposed FL-PI-based feedback controller design is described in Sect. 3, where *FL* design is emphasized. The modified WC-based PI gains optimization is presented in Sect. 4. The performance of the proposed IDGC scheme is evaluated with small-signal analysis and operational contingency (partial shading) in Sect. 5. This evaluation study is obtained in MATLAB Script environment. The improved VSC-PCC-based PLL profile is evidenced as compared to conventional approaches. Finally, conclusion of the work is presented in Sect. 6.

2 Considered PV-Based Microgrid

For the PV application as DG, microgrid integration requires three-phase AC power and thus a 6-pulse IGBT-based voltage source converter (VSC) is considered here (Fig. 1). The considered single-stage conversion-based PV-DG is incorporated with local loading (AC) with parallel capacitor (for voltage stability) at PCC. The MPPT scheme is implemented in terms of measured/historical (DAS based) solar irradiation and PV panel temperature profile. The voltage, current (PV output profile)-dependent MPPT techniques are limited towards internal fault (DC arcs, DC cable faults, etc.) characteristics. The maximum power value may get estimated erroneously under such circuit contingencies at DC link. The irradiation and temperature (PV input profile) are directly proportional to maximum power value and having null influence under internal faults. Thus, to obtain an accurate MPPT technique under any DG side contingencies, the proposed MPPT is designed with irradiance and temperature feedbacks. The VSC injected power at PCC ($P_1 + jQ_1$) is directly influenced by feedback path (PWM generation). The feedback path or IDGC is designed based on PCs' reference (maximum power point tracking: MPPT-based estimation) and local measurements (PCC voltage: $V_{1, abc}$ and $I_{1, abc}$). The grid design parameters are as mentioned in Table 1.

The PV system model is further described with proper mathematical descriptions here. The MP data generation from local DG is possible to achieve while understanding the PV modelling. The single diode equivalent model is considered for present focus.

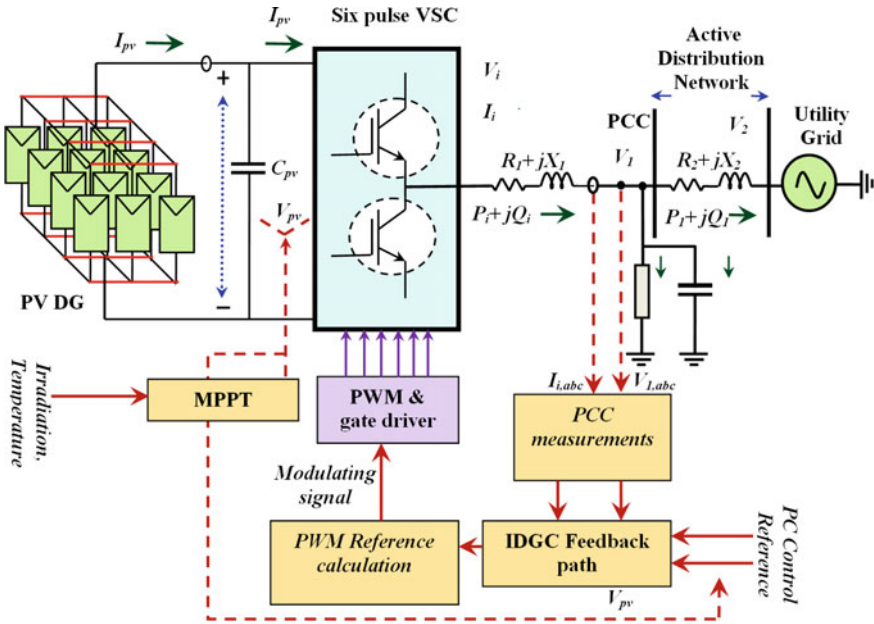


Fig. 1 Considered PV-based DG integration to microgrid operation

Table 1 Numerical data of the simulation system

Parameters	Values
VSC to PCC interfacing resistance (R_i)	15 m Ω
VSC to PCC interfacing inductance (L_i)	0.63 mH
Angular frequency (ω)	314.15 rad/s
PCC to grid interfacing resistance (R_g)	10 m Ω
PCC to grid interfacing inductance (L_g)	0.5mH
Filter capacitor (C_f)	0.64 mF
DC link capacitor (C_{pv})	0.5 mF
Conductance of local load (g_2)	1.54 p.u
Susceptance of the local load (b_2)	1.03 p.u

2.1 PV System Modelling

The solar cell is the elemental unit of any PV systems (array or module). A $p-n$ junction diode exposed to sunlight is able to transform light intensity (photon energy) into the form of electrical energy (DC) by photoconduction effect. PV single diode equivalent circuit is considered here for solar irradiation (W/m^2) data to PV parameter (MP power: P_{PV} , voltage: V_{PV}) calculation [13, 14]. This PV model is simulated in *MATLAB/Script* environment for present focus where PV array (number of series, parallel connected modules) is depicted as:

Table 2 Major descriptions of *ELDORA-40* PV at standard test condition: STC (= 1 kW/m², 25 °C)

Parameters	Values
MP power (P_{PV})	40 W
Voltage at MP (V_{PV})	17.4 V
Current at MP (I_{PV})	2.3 A
Short circuit current (I_{sc})	2.63 A
Open-circuit voltage (V_{oc})	21.9 V

$$I_{PV} = N_{pp} \times I_{ph} - N_{pp} \times I_{rst} \left[e^{\left(\frac{1}{V_T a} \left(\frac{V_{PV} + I_{PV} R_s}{N_{se}} \right) \right) - 1} \right] - \left(\frac{(N_{sc} / N_{pp}) \times V_{PV} + I_{PV} \times R_s}{R_{sh}} \right) \tag{1}$$

where $I_{PV} \rightarrow$ PV array’s output current, $N_{se} \rightarrow$ number of series modules, and $N_{pp} \rightarrow$ number of parallel modules, $V_T = kT/q \rightarrow$ thermal voltage. A real solar module *ELDORA-40* (10 kW PV system: 46 parallel \times 6 series \times 40 W) is developed here, and other coefficient and parameters are described in Table 2.

2.2 VSC’s Dynamic Relation for Grid PLL

A three-phase DC-AC conversion is obtained by IGBT-based voltage source converter (VSC) for bidirectional operation of PV microgrid. This is obtained by pulse width modulation (PWM)-based technique. The proposed VSC-based DG integration is obtained in terms of the active and reactive power ($P - Q: P_1 + jQ_1$) regulation at PCC (bus 1, Fig. 1). The control dynamics is directly derived from instantaneous active and reactive power components, on the contrary of conventional instantaneous direct and quadrature-axis PCC current components ($I_d + jI_q$). This PLL operation between VSC terminal to PCC is expressed by reduced *abc-dq* conversion-based unmodelled PLL [15].

From Fig. 1 the VSC to PCC dynamics in *abc* frame can be expressed as:

$$(V_{i,abc} - V_{1,abc}) = L_1 \frac{dI_{i,abc}}{dt} + R_1 I_{i,abc} \tag{2}$$

where $V_{i,abc} \rightarrow$ AC side voltage of VSC; $V_{1,abc} \rightarrow$ PCC voltage; and $I_{i,abc} \rightarrow$ *abc* frame instantaneous current from VSC to PCC. The direct *P-Q*-based VSC dynamics can be expressed as:

$$\begin{bmatrix} \dot{P}_1 \\ \dot{Q}_1 \end{bmatrix} = \begin{bmatrix} -R_1/L_1 & -\omega \\ \omega & -R_1/L_1 \end{bmatrix} \begin{bmatrix} P_1 \\ Q_1 \end{bmatrix} + \begin{bmatrix} 1/L_1 & 0 \\ 0 & 1/L_1 \end{bmatrix} \begin{bmatrix} U_q \\ U_p \end{bmatrix} \tag{3}$$

where \dot{P}_1 and $\dot{Q}_1 \rightarrow$ active-reactive power differential relationships, respectively; $\omega \rightarrow$ grid operational frequency; and U_q and $U_p \rightarrow$ control inputs of P - Q dynamics. These control inputs can be expressed in terms of dq axis voltage parameters as:

$$U_q = V_{id}V_{1d} + V_{iq}V_{1q} - (V_{1d}^2 + V_{1q}^2) \quad (4)$$

$$U_p = [V_{id}V_{1q} - V_{iq}V_{1d}] \quad (5)$$

where $V_{id} + jV_{iq} \rightarrow dq$ axis voltage at VSC, $V_{1d} + jV_{1q} \rightarrow dq$ axis voltage at PCC. The PWM-based pulse generation is possible to achieve by reference modulating signal calculation of these VSC voltage parameters as:

$$V_{id} = \frac{V_{MPP}}{L_1}(m_{VSC} \cos \phi) \quad (6.a)$$

$$V_{iq} = \frac{V_{MPP}}{L_1}(m_{VSC} \sin \phi) \quad (6.b)$$

where $V_{MPP} \rightarrow$ PV system-based MPPT voltage, $m_{VSC} \rightarrow$ modulation index for PWM, and $\phi \rightarrow$ firing angel of IGBT. This VSC is targeted for proposed PV-based DG integration to PCC via FL-PI-based feedback path (IDGC) as depicted in next section.

3 Proposed FL-PI-Based IDGC

The IDGC or feedback path for PWM-based VSC-PLL is obtained with PI-based second-order closed-loop operation. The PI control is obtained here with conventional structure, and then the gain parameters are updated with respect to feedback error or dynamic error. These dynamic errors are obtained from VSC dynamic architecture as depicted in Eq. (2), where a multi-variable formulation is considered. The feedback path is comprised with individual proportional ($K_{p,P1}$ for P_1 dynamics and $K_{p,Q1}$ for Q_1 dynamics) and integral ($K_{i,P1}$ for P_1 dynamics and $K_{i,Q1}$ for Q_1 dynamics) gains as:

$$\begin{aligned} U_q^K &= U_q^{K-1} + \left[K_{p,P1} + \frac{K_{i,P1}}{s} \right] (P_1^* - P_1^K) \\ U_p^K &= U_p^{K-1} + \left[K_{p,Q1} + \frac{K_{i,Q1}}{s} \right] (Q_1^* - Q_1^K) \end{aligned} \quad (7)$$

here superscript $K \rightarrow$ iteration instant, $(P_1^* - P_1^K) \rightarrow P_1$ dynamic error, and $(Q_1^* - Q_1^K) \rightarrow Q_1$ dynamic error. Now this control inputs' calculation in Eq. (7) is limited when state matrix in Eq. (3) is within grid limit. But when the ω in Eq. (3)

varies drastically with operational contingencies, these K_p and K_i gains are not able to provide desired stability limit. Thus, adaptive gain parameter estimation according to FL rules is depicted here. The error and changes in error ($\partial(P_1^* - P_1^K)/T_s$) and ($\partial(Q_1^* - Q_1^K)/T_s$) are considered for proposed FL-based adaptive gain estimation. The calculation is obtained in bilinear method (z-domain) where Laplace domain representation of Eq. (7) is obtained as:

$$\begin{aligned}
 U_q^s &= \left[K_{p,P1} + \frac{K_{i,P1}}{s} \right] (Er_1^s) \\
 U_p^s &= \left[K_{p,Q1} + \frac{K_{i,Q1}}{s} \right] (Er_2^s)
 \end{aligned}
 \tag{8}$$

where $s \rightarrow$ Laplace complex variable, Er_1 and $Er_2 \rightarrow P_1$, and Q_1 dynamics' error (Er). The s to z -domain transform is obtained by transfiguration formulation:

$$\begin{aligned}
 U_q^z &= (K_{p,P1} - K_{i,P1}(T_s)/2 - K_{i,P1}(T_s)/(1 - z^{-1})) \\
 U_p^z &= (K_{p,Q1} - K_{i,Q1}(T_s)/2 - K_{i,Q1}(T_s)/(1 - z^{-1}))
 \end{aligned}
 \tag{9}$$

By assuming:

$$\begin{aligned}
 \tilde{K}_p &= K_p - \frac{K_i T_s}{2} \\
 \tilde{K}_i &= K_i T_s
 \end{aligned}
 \tag{10}$$

and by taking inverse z -domain (time domain), the control inputs can be derived as:

$$\begin{aligned}
 U_q(K \times T_s) &= U_q(K \times T_s - T_s) + T_s \times \Delta U_q(K \times T_s) \\
 U_p(K \times T_s) &= U_p(K \times T_s - T_s) + T_s \times \Delta U_p(K \times T_s)
 \end{aligned}
 \tag{11}$$

where

$$\begin{aligned}
 \Delta U_q(K \times T_s) &= K_{p,P1} \times \partial Er_1(K \times T_s) + K_{i,P1} \times Er_1(K \times T_s) \\
 \Delta U_p(K \times T_s) &= K_{p,Q1} \times \partial Er_2(K \times T_s) + K_{i,Q1} \times Er_2(K \times T_s)
 \end{aligned}
 \tag{12}$$

here $\Delta U_q(K \times T_s)$ and $\Delta U_p(K \times T_s) \rightarrow$ incremental controller coefficients, $\partial Er_1(K \times T_s)$ and $\partial Er_2(K \times T_s) \rightarrow$ rate of change of error for P_1 and Q_1 dynamics, respectively.

The PI gains (i.e. proportional: $K_{p,P1}$ and $K_{p,Q1}$; and integral: $K_{i,P1}$ and $K_{i,Q1}$) are selected adaptively according to grid instability region (i.e. dynamic errors: Er_1 and Er_2). The role of FL is to select the optimal feedback (PI control based) path gains selection under different operational contingencies, to provide improved stability margin with adaptive functionality. The optimal selection is further introduced with error minimized gains by virtue of WC-based optimization problem.

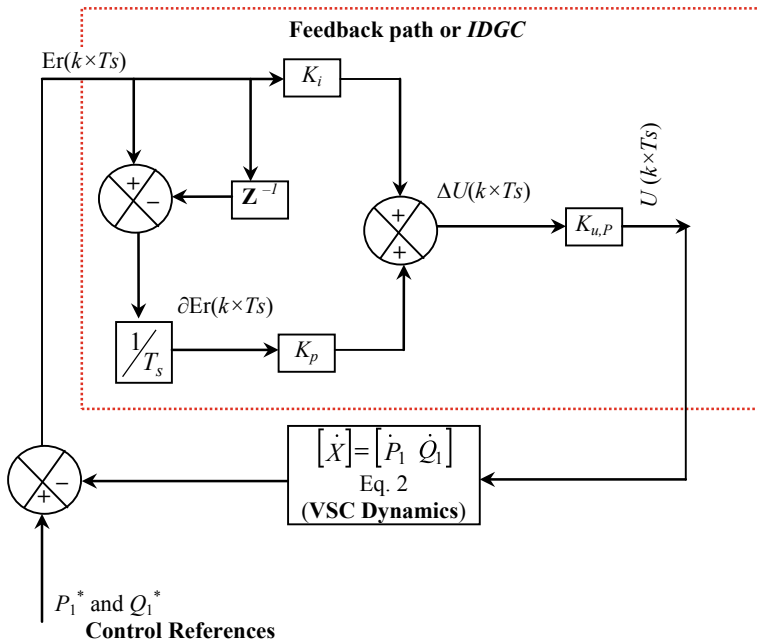


Fig. 2 Proposed VSC feedback controller for PV microgrid operation

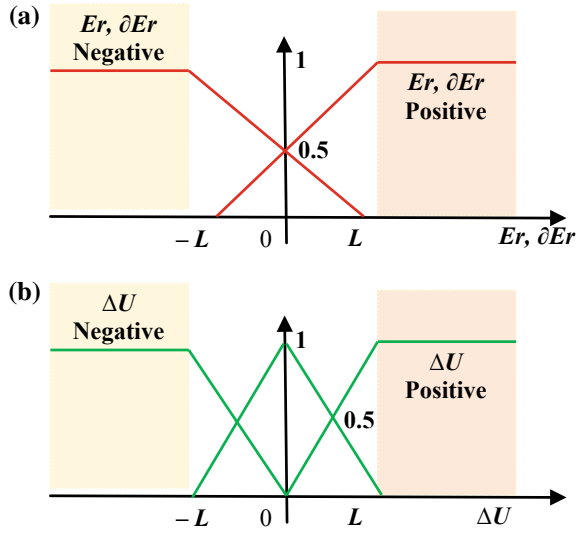
3.1 FL Architecture

Fuzzification, FRs, and *Defuzzification* processes are the constructing element for FL architecture. The VSC-PLL by this FL-PI-based IDGC for PV-based DG to microgrid is depicted in Fig. 2.

3.1.1 Fuzzification

The VSC dynamic system errors are considered for fuzzification of K_p and K_i gains prior to system stability limits. The input (*IP*) and output (*OP*) membership functions are designed according to VSC-PCC dynamic stability limits (Fig. 3). The dynamic error (Er_1 and Er_2) and rate of change in error (∂Er_1 and ∂Er_2) are considered for present FL *IP* membership design, where control inputs (ΔU_q and ΔU_p for P_1 and Q_1 dynamics, respectively) are targeted as *OP* membership. The FL membership constant L is considered >0 . This L is needed to be optimized further to achieve optimal FL-PI operation under uncertainties (partial shading, islanding, etc.).

Fig. 3 Membership functions for FL-PI gains: *IP* and *OP* membership function



3.1.2 Fuzzy Rule Base

By using the *IP* and *OP* memberships (Fig. 3), the following fuzzy rules (FRs) are developed for PI gain adaptiveness:

- Rule1.** IF $Er(kT_S) = Er_{NEG}$ AND $\partial Er(kT_S) = \partial Er_{NEG}$, THEN $\Delta U(kT_S) = \Delta U_{NEG}$.
- Rule2.** IF $Er(kT_S) = Er_{NEG}$ AND $\partial Er(kT_S) = \partial Er_{POS}$, THEN $\Delta U(kT_S) = \Delta U_{ZER}$.
- Rule3.** IF $Er(kT_S) = Er_{POS}$ AND $\partial Er(kT_S) = \partial Er_{NEG}$, THEN $\Delta U(kT_S) = \Delta U_{ZER}$.
- Rule4.** IF $Er(kT_S) = Er_{POS}$ AND $\partial Er(kT_S) = \partial Er_{POS}$, THEN $\Delta U(kT_S) = \Delta U_{POS}$.

The rules are based on the side of membership functions where subscript POS → positive side, NEG → negative side, and ZER → zero output. The IF AND THEN-based operation is effective as AND is providing minimum tolerance to the FRs. These four rules are considered for PI gains decision.

3.1.3 Defuzzification

The centroid relationship is implemented for defuzzification of incremental FL control. The *IP* and *OP* memberships are further decomposed into 20 IO combinations as depicted in [16]. Finally, the gains for PI ($K_{gain}: K_p, K_i$) is calculated as:

$$K_{gain} = \frac{\sum \text{value of IP membership} \times \text{corresponding OP membership}}{\sum \text{value of IP membership}} \quad (13)$$

These IO combinations are depicted as FRs in Fig. 4. For present consideration, the error (Er_1 and $Er_2 \rightarrow$ Fig. 3a) and rate of change in error (∂Er_1 and $\partial Er_2 \rightarrow$ Fig. 3a) are positioned in horizontal and vertical axes, respectively. These two membership functions overlapped and create a third-dimensional representation [16] over two-dimensional membership maps. The upside region of Er is representing $[0 \text{ to } L]$ region where the downside is showing $[0 \text{ to } -L]$ region, in two-dimensional plane. The left side and right side of ∂Er are showing $[0 \text{ to } -L]$ and $[0 \text{ to } L]$ planes of two-dimensional error mapping. The third-dimensional membership functions for K_p and K_i gains are obtained from rule-based R1 to R20 as in Fig. 4. The selection of IF-THEN rules is implemented as:

$$Er = Er_{NEG} \text{ AND } \partial Er = \partial Er_{NEG} \\ \text{THEN min}(Er, \partial Er) \tag{14}$$

For the region IO1 and IO2, the rule R1 can be implemented as:

- Step 1.** Select the input (Er and ∂Er) memberships (as in Eq. 14).
- Step 2.** Obtain the corresponding output (K_p and K_i) memberships.

The Er and ∂Er are obtained from two-dimensional limits as:

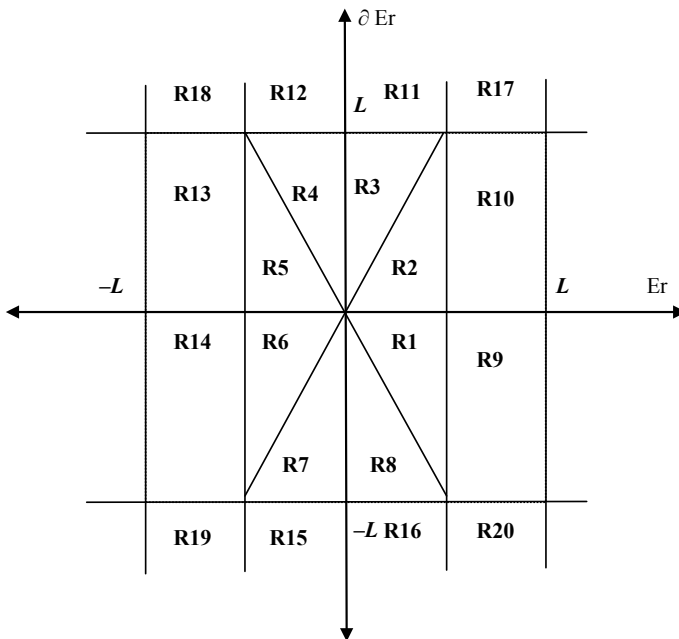


Fig. 4 Rule base by combining Er and ∂Er as IP and K_p and K_i as OP membership functions

$$\begin{aligned} Er_{NEG} &= \frac{-Er(K \times T_s) + L}{2L} \\ Er_{POS} &= \frac{Er(K \times T_s) + L}{2L} \end{aligned} \tag{15.a}$$

and

$$\begin{aligned} \partial Er_{NEG} &= \frac{-\partial Er(K \times T_s) + L}{2L} \\ \partial Er_{POS} &= \frac{\partial Er(K \times T_s) + L}{2L} \end{aligned} \tag{15.b}$$

The final K_{gain} values can be obtained from defuzzification formulation as in Eq. (13).

4 Proposed Modified WC-Based Optimization

The water flow is the basic idea behind this nature-inspired algorithm where evaporation, transpiration, condensation, precipitation, and runoff take place to reach a raindrop to sea (optimal point) [17]. Raindrop population is created initially. These are equivalent to *PI gains* ($K_{p,P1}$, $K_{p,Q1}$ and $K_{i,P1}$, $K_{i,Q1}$). To minimize the $Er(kT_s)$, the cost function for proposed optimization problem is derived as:

$$f(\phi) = \min \left(\sum_{k=1}^{N_{Tot}} \sqrt{(Er_1(kT_s))^2 + (Er_2(kT_s))^2} \right) \tag{16}$$

where N_{Tot} = total iteration intervals. The raindrop population is defined as: $[Rd]_{B \times C} = [rd_1^K, rd_2^K, \dots, rd_C^K]$. The number of rivers is: Rv streaming towards sea (S_E). The number of streams (Str) can be obtained as:

$$Str_{k=1 \text{ to } S_E} = \text{round} \left(\left| \frac{CG^k}{\sum CG^k} \right| \times Str \right), CG^k = f(\phi)^k - f(\phi)^{S_E+1} \tag{17}$$

Here river is CG . With each generation (k), the Str changes their flow and approaches towards optimal point S_E . The flow position is estimated adaptively by introducing chaos signal (Chao) as:

$$k_{str}^i(t+1) = k_{str}^i(t) + \text{Chao}(t) \times (K_{S_E}(t) - K_{str}(t)) \tag{18}$$

($i=1$ to S_E)

To make the flow adaptive towards optimal solution (S_E), the evaporation process is influenced by chaotic mapping as:

$$\left\| k_{S_E} - k_{R_V}^i \right\| < \text{Chao}(t)$$

$$\text{or} \left\| k_{S_E} - K_{Str}^j \right\| < \text{Chao}(t) \text{ or } \text{Chao}(t) < 0.1 \quad (19)$$

Finally, when the process reaches to total generation, the optimal solution is obtained for Eq. (16).

5 Result Analysis

The performance of the proposed modified WC-based FL-PI controller for PV-VSC-based DG integration (Fig. 1) is evaluated in MATLAB environment. Here, initially a small-signal study is presented under SISO consideration of VSC dynamics (Eq. 2) with proposed feedback path (Fig. 2). The Bode plot (Fig. 5a) and Nyquist diagram (Fig. 5b) are evidenced against that study. Here, the proposed controller is showing superiority over conventional FL-PI and PI in terms of improved stability margin (i.e. damping ratio: 0.76, 0.43, and 0.06, respectively; with poles: $-0.24 \pm j0.73$, $-0.09 \pm j0.31$, and $-0.01 \pm j0.08$, respectively).

The control response is further evaluated in terms of PCC response (i.e. frequency: Fig. 6b, voltage: Fig. 6c, and active power: Fig. 6d). The PV system (Fig. 1) is subjected to partial shading condition (different irradiancies 1000 W/m^2 , 700 W/m^2 and 200 W/m^2 for different PV panels: Sect. 2.1, Fig. 6a) at time $t = 7 \text{ s}$. The dynamic oscillations of PCC parameters are recorded for proposed WC-based FL-PI (15 cycles), conventional FL-PI (38 cycles), and conventional PI (67 cycles) as

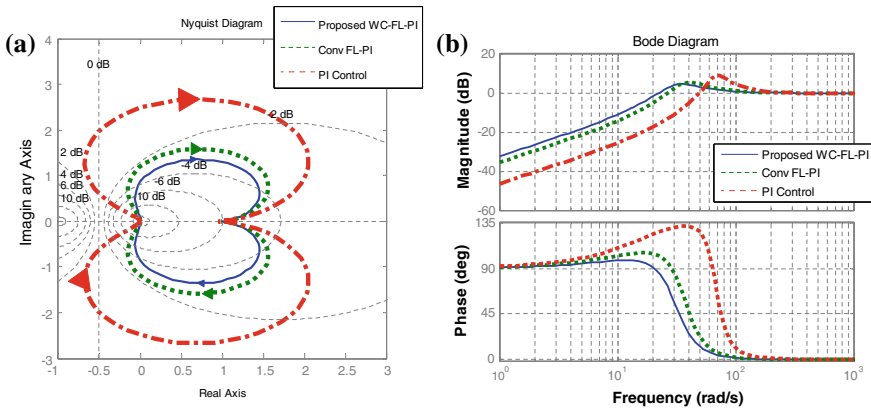


Fig. 5 Small signal stability analysis for PI, FL-PI, and proposed WC-based FL-PI controller

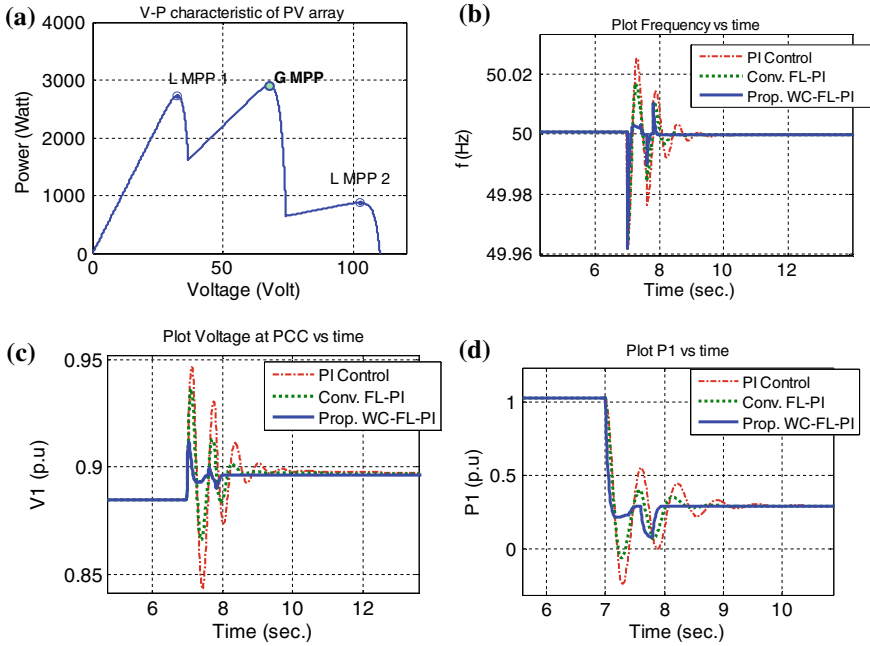


Fig. 6 Performance evaluation of proposed WC-based FL-PI under partial shading condition: **a** PV output under shading, PCC measured parameters: **b** grid frequency, **c** voltage, **d** active power

depicted in Fig. 6b–d. The proposed IDGC is evidenced superior under operational uncertainty as compared with conventional controllers.

6 Conclusion

The paper proposes a new modified water cycle (WC)-based optimized fuzzy logic (FL)-PI controller for photovoltaic (PV)-based grid integration. This distributed generation (DG) operation is implemented as single-stage conversion via voltage source converter (VSC). As the microgrid operational contingencies (faults, load switching, etc.) are able to pose uncertainty for VSC dynamics-based IDGC-PWM, linear PI controllers have limited stability margin. To operate the PI controller in an adaptive way, FL-based rules (system stability) are obtained where controllers' error and change in error are considered for IP membership, and control input to VSC dynamics is considered as OP membership. The new instantaneous active-reactive power (P-Q) dynamics are further operated in an optimal way where the PI gains are optimized under system stability limit by modified (chaos) WC algorithm. The performance of the proposed IDGC is evidenced superior over conventional FL-PI and PI in terms of small-signal stability and dynamic oscillations. The performance study is presented in MATLAB environment.

References

1. Katiraei F, Agüero JR (2011) Solar PV integration challenges. *IEEE Power Energy Mag* 9(3):62–71
2. Khushalani S, Solanki JM, Schulz NN (2007) Development of three-phase unbalanced power flow using PV and PQ models for distributed generation and study of the impact of DG models. *IEEE Trans Power Syst* 22(3):1019–1025
3. Dhar S, Dash PK (2016) A new backstepping finite time sliding mode control of grid connected PV system using multivariable dynamic VSC model. *Int J Electr Power Energy Syst* 82:314–330
4. Barik SK, Dash PK, Dhar S (2015) Finite-time sliding mode power control of grid-connected three-phase photovoltaic array. *Aust J Electr Electron Eng* 12(4):301–311
5. Kumar S, Verma AK, Hussain I, Singh B, Jain C (2017) Better control for a solar energy system: using improved enhanced phase-locked loop-based control under variable solar intensity. *IEEE Ind Appl Mag* 23(2):24–36
6. Rezkallah M, Hamadi A, Chandra A, Singh B (2015) Real-time HIL implementation of sliding mode control for standalone system based on PV array without using dumpload. *IEEE Trans Sustain Energy* 6(4):1389–1398
7. Zhu Y, Fei J (2018) Disturbance observer based fuzzy sliding mode control of PV grid connected inverter. *IEEE Access* 6:21202–21211
8. Dhar S, Dash PK (2016) Harmonic profile injection-based hybrid active islanding detection technique for PV-VSC-based microgrid system. *IEEE Trans Sustain Energy* 7(4):1473–1481
9. Sankar RS, Kumar SV, Mohan Rao G (2018) Adaptive fuzzy PI current control of grid interact PV inverter. *Int J Electr Comput Eng* (2088–8708) 8(1)
10. Sukumar S, Marsadek M, Ramasamy A, Mokhlis H, Mekhilef S (2017) A fuzzy-based PI controller for power management of a grid-connected PV-SOFC hybrid system. *Energies* 10(11):1720
11. Sefa I, Altin N, Ozdemir S, Kaplan O (2015) Fuzzy PI controlled inverter for grid interactive renewable energy systems. *IET Renew Power Gener* 9(7):729–738
12. Tang K-Sg, Man KF, Chen G, Kwong S (2001) An optimal fuzzy PID controller. *IEEE Trans Ind Electron* 48(4):757–765
13. Dhar S, Sridhar R, Mathew G (2013) Implementation of PV cell based standalone solar power system employing incremental conductance MPPT algorithm. In: 2013 international conference on circuits, power and computing technologies (ICCPCT). IEEE, pp 356–361
14. Chowdhury S, Taylor GA, Chowdhury SP, Saha AK, Song YH (2007) Modelling, simulation and performance analysis of a PV array in an embedded environment. In: 2007 42nd international universities power engineering conference. IEEE, pp 781–785
15. Dhar S, Dash PK (2016) Adaptive backstepping sliding mode control of a grid interactive PV-VSC system with LCL filter. *Sustain Energy Grids Netw* 6:109–124
16. Abedini M, Mahmodi E, Mousavi M, Chaharmahali I (2019) A novel Fuzzy PI controller for improving autonomous network by considering uncertainty. *Sustain Energy Grids Netw* 18:100200
17. Eskandar H, Sadollah A, Bahreininejad A, Hamdi M (2012) Water cycle algorithm—a novel metaheuristic optimization method for solving constrained engineering optimization problems. *Comput Struct* 110:151–166

Voltage Stabilization in a Single-Phase SEIG System with Electronic Load Controller



Subhendu Khatua, Abhijeet Choudhury, Swagat Pati, Sanjeeb Kumar Kar and Renu Sharma

Abstract In this modernizing and developing world, consumers are demanding fresh, high-quality power. However, in distant locations or mountainous regions, it is not feasible for the utility grid to offer clean energy as it involves lengthy transmission, power shading and failures which is a primary reason for a large voltage drop. In an attempt to mitigate all these problems, isolated framework is introduced in this paper, comprising of a single-phase self-excited induction generator, an electronic load controller and a capacitor bank, which have been used for its self-excitation function. Self-excited induction generators operate in the saturation region. This creates poor voltage regulation at the load terminal, with the aim of alleviating this problem, and the electronic load controller is connected in parallel across the load. The electronic load controller comprises an unrestrained bridge rectifier, a chopper circuit and a dump resistive load. It works in a smart manner, i.e., the complete power at the end of the customer and the dump load is always retained at a steady value, and to resolve this issue, a control protocol is disclosed in this paper.

Keywords Voltage regulation · Single-phase SEIG · Electronic load controller · Main winding · Starting winding

S. Khatua · A. Choudhury (✉) · S. Pati · S. K. Kar · R. Sharma
Department of Electrical Engineering, Institute of Technical Education and Research, Siksha 'O' Anusandhan (Deemed to Be University), Bhubaneswar, Odisha, India
e-mail: abhijeet9966@gmail.com

S. Khatua
e-mail: subhendukhatua29@gmail.com

S. Pati
e-mail: swagatiter@gmail.com

S. K. Kar
e-mail: sanjeebkar@soa.ac.in

R. Sharma
e-mail: renusharma@soa.ac.in

© Springer Nature Singapore Pte Ltd. 2020
R. Sharma et al. (eds.), *Innovation in Electrical Power Engineering, Communication, and Computing Technology*, Lecture Notes in Electrical Engineering 630,
https://doi.org/10.1007/978-981-15-2305-2_51

1 Introduction

In this modern era of growth, electrical power grids have grown into an extremely convoluted and collectively useful system that is geographically distributed and closely linked to the other systems. In an attempt to get purge of power shading and enhance stability as well as the reliability and efficiency of the power system, isolated systems are introduced. Due to astonishing benefits like a combination of renewable energy system, fewer losses and short line length, isolated systems are recommended. Renewable energy sources such as solar, wind and micro-hydro can be used to produce clean energy. Natural energy is first transformed into mechanical energy, i.e., by the revolution of the prime mover which, in turn, is utilized to produce electricity through the utilization of generators in the wind and hydro systems. In distant, far-flung regions and mountainous regions, where the majority of the population relies on single-phase supplies, decentralized systems using local renewable energy make significance. Self-excited induction generators [1] are appropriate for aforementioned applications as they are inexpensive, robust, safe, brushless and user-friendly. In this research paper, the proposed system is taken into consideration to an autonomous isolated system which comprises a single-phase self-excited induction generator (SEIG) which is a source to provender resistive lighting. In an isolated system, the induction machine must be self-excited due to limitation of non-availability of the reactive power supply [2]. However, it can be accomplished by linking the motor magnetizing impedance to a capacitance linked in parallel to create an LC resonant circuit. The benefit of the SEIG system is, low maintenance, simple operating processes, it is self-protective against the faults occurring in short-circuit by reducing the excitation due to drop of voltage, its ability to generate power at variable speeds and its excellent dynamic response. The detailed mathematical modeling of single-phase SEIG system is given in [3]. The power generated by SEIG is fed to the load. It is a matter of concern and attention that as “SEIG” operates in the saturation region, the change in load produces substantial deviations in voltage and frequency in the system, respectively, i.e., the voltage and frequency regulation of such system is poor [4–6]. An electronic load controller (ELC) [7] is executed for the maintenance of continuous voltage over the load terminals in the rated allowable limits.

2 System Configuration and Operation

In this work, two induction motors are taken. One acts as a prime mover as a substitute for hydro turbine and other acts as a generator. As it is an isolated system, the machine should be capable of self-excitation as there will be no availability of external power source. So self-excitation capacitors are connected in parallel with the motor magnetizing impedance. Charged capacitors are connected across the auxiliary winding, i.e., starting winding of the single-phase induction motor [1, 2, 4, 5]. When prime mover rotates and generator achieves the critical speed, then the

charging capacitors are switched into the circuit which circulates the magnetizing current into the starting winding of the induction motor. The circulating current in the starting winding produces a flux in the air gap. When the rotor cuts the flux, EMF is induced in the rotor. As the rotor terminals are short-circuited, current flows in the rotor due to the rotor-induced emf. The rotor current produces the rotor flux which is rotating in nature. The rotor flux cuts the auxiliary and main winding conductors, which as a result strengthens the auxiliary winding flux which results in increased rotor emf and rotor flux, thus increasing the main winding voltage. This cumulative process goes on till the core of the machine saturates. When saturation sets in, the voltage becomes constant across the main winding.

Capacitors can also be connected across the running winding to provide further reactive power support during loading conditions [3, 8, 9]. If reactive power generated by the starting winding capacitor holds sufficient during loading conditions, then the requirement of capacitors across running winding is not mandatory.

The single-phase load [4] is connected across the output terminals of a generator. As the SEIG operates in saturation region, it is very much prone to voltage fluctuation. A slight change in load current results in a change in output voltage and frequency. Mostly loads are time varying in nature. So it becomes very difficult to maintain the voltage at a constant value for an SEIG with varying load as stated in [10]. Any deviation in the load side affects the voltage. Again the load should get rated voltage irrespective of the load terminals. Hence a control device needs to be implemented for maintaining the rated voltage across the load terminals. The control device used here is an electric load controller. The block diagram of whole system with electronic load controller is given below in Fig. 1.

The ELC basically comprises a full wave rectifier, capacitor, a control switch and a dump load resistor [6, 7, 11–15]. The operating principle of the ELC is based on the concept of variable load consumption so as to keep the voltage constant and maintaining the total power P_T supplied by the machine at a constant value. The ELC

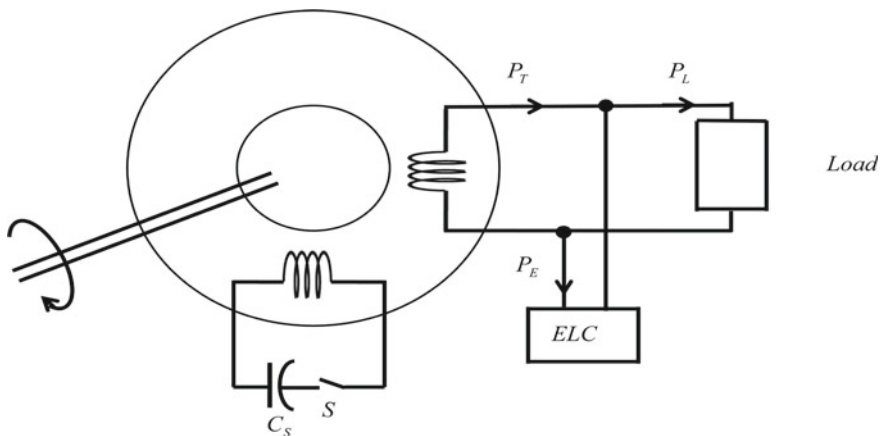


Fig. 1 System diagram with power flow

is designed such that it can handle the maximum power generated by the machine. During light load condition, the surplus power is consumed by the ELC. As the load increases, the ELC reduces its power consumption such that the load voltage remains constant.

3 Proposed Work

The proposed system in this paper comprises three important parts, namely SEIG system, electronic load controller and load design as shown in Figs. 2, 3 and 4, respectively. The SEIG system comprises two induction machines, in which one machine acts as a prime mover and other as generator. The configurations of motor are described in Tables 1 and 2.

The voltage buildup in an SEIG system depends on the speed of the rotor rotation and capacitance value. Hence the prime mover is selected such that it would drive the generator at or above its synchronous speed. By different tests, it is seen that the prime mover at 1960 rpm corresponds to 34% slip. SEIG can generate voltage at variable speeds, but the voltage buildup and power generation are not considerable as voltage regulation is very poor. So as to avoid the above issue, a 2-pole 0.5 HP motor is used as a prime mover to drive a 4-pole 0.25 HP induction machine (generator). A controlling mechanism is designed to maintain rated voltage across the load terminals irrespective of load variations which were maintained by the electronic load controller (ELC). The design of the ELC consists of an uncontrolled full wave rectifier with an

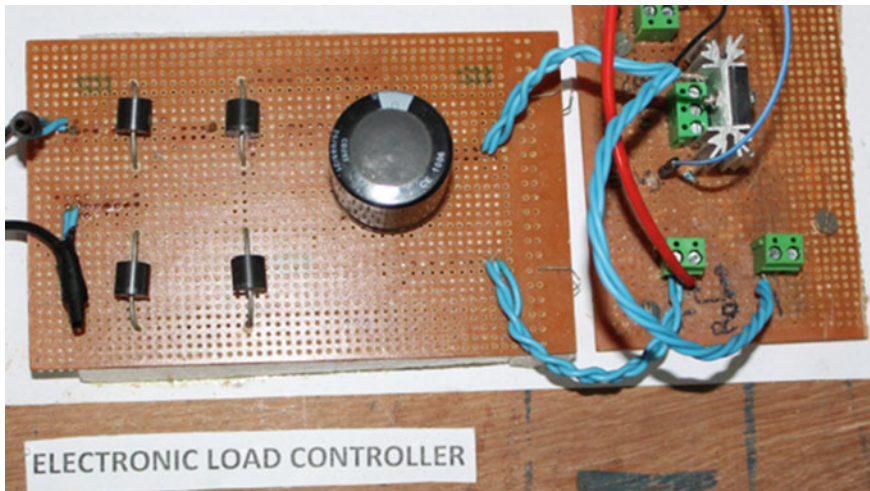


Fig. 2 Hardware depiction of ELC

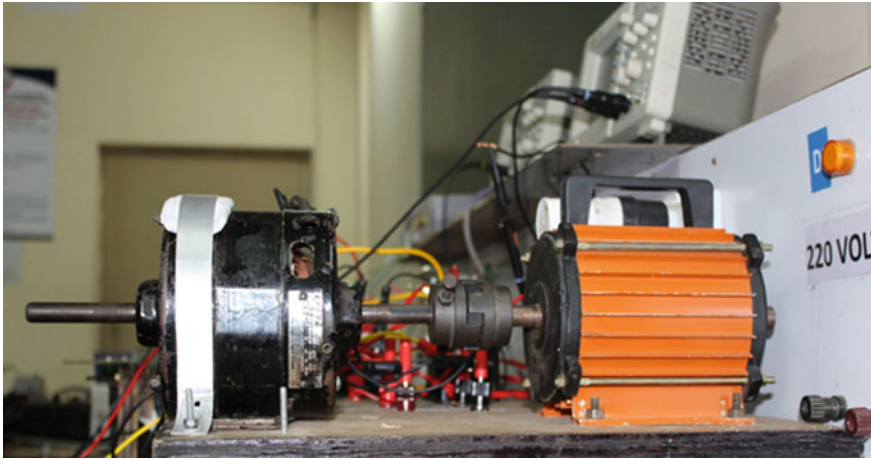


Fig. 3 Hardware depiction of SEIG system



Fig. 4 Hardware depiction of resistive load

insulated gate bipolar transistor (IGBT) along with a dump load connected in series. The duty cycle of the switch is controlled by using an opto-coupler (MCT2E), which is controlled in such a way that the voltage across the terminals remains constant irrespective of load variations.

Table 1 Specification of 2-pole induction machine

Voltage	230 V
Poles	2 Poles
Phase	1 Φ
Speed	2800 RPM
Current	2.7 A
Hp	0.5 HP

Table 2 Configuration of 4-pole induction machine

Voltage	230 V
Poles	4 Poles
Phase	1 Φ
Speed	1480 RPM
Current	0.8 A
Hp	0.25 HP

4 Results Analysis and Discussion

The evaluation findings from the proposed system and its analysis are discussed in this chapter. The voltage was found out to be 200 V using 5 μ F in the auxiliary part.

The capacitance values for excitation were defined by trial and error method, and the best values were obtained as shown in Table 3.

In this subsection, the performance of the SEIG load system is evaluated when the system is in open loop. The generator was run at no load at 1960 rpm, and charged capacitors are switched to the auxiliary circuit of the generator. After switching the capacitor, the no-load voltage developed was found to be 520 V. As the ELC was turned on, the no-load voltage was reduced and was found to be 240 V. An increase in the load led to severe voltage fluctuations. As a load of 100, 60 W is connected, the voltage further dips to 188 V and as the load was disconnected, the voltage was same as 520 V which is not acceptable for a healthy system (Fig. 5).

Table 3 Sample values of capacitance used

S. No.	Capacitor across auxiliary winding (μ F)	Capacitor across main winding (μ F)	Voltage at full load (V)	Power (W)
1	10	5	228	44
2	12.5	5	188	48
3	15	5	195	48
4	5	–	200	92
5	5	–	220	88

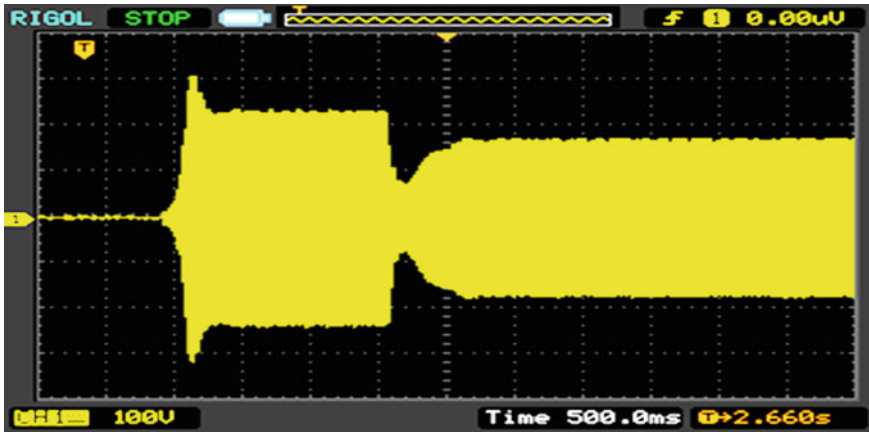


Fig. 5 Result of switching the ELC on throughout no-load condition

As discussed in the previous section, higher the load change more intense is the voltage fluctuation which is undesirable for any optimum system. This fluctuation is due to the fact that the power generated by the machine cannot be handled properly. So as to maintain a constant voltage generation by the machine, the generator current needs to be maintained constant. Here, an ELC is connected in parallel with the load. The purpose of the controller is to consume power so that the generator current remains constant throughout the operation process. The filter inductor restricts the ELC current to reduce suddenly creating a slight sluggish response. As the load toward the ELC is increased, the duty ratio is increased and the ELC current is also increased. With different watts usage, it was observed the voltage fluctuation was drastically improved as compared to the previous subsection (Fig. 6).

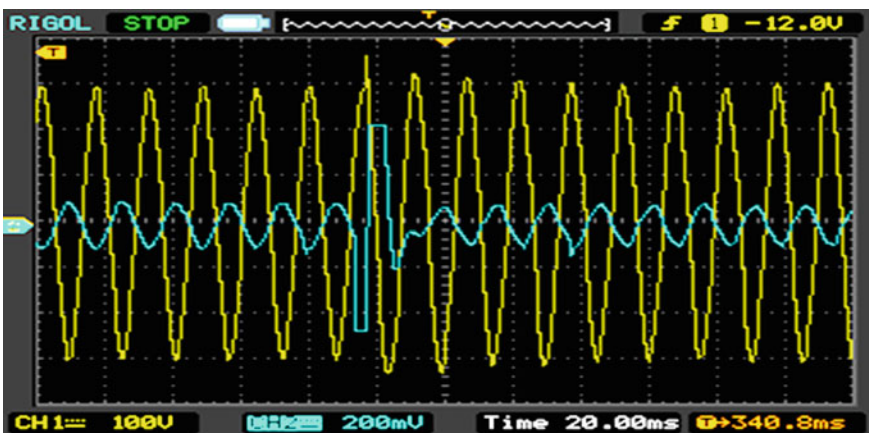


Fig. 6 Total generator current remains constant

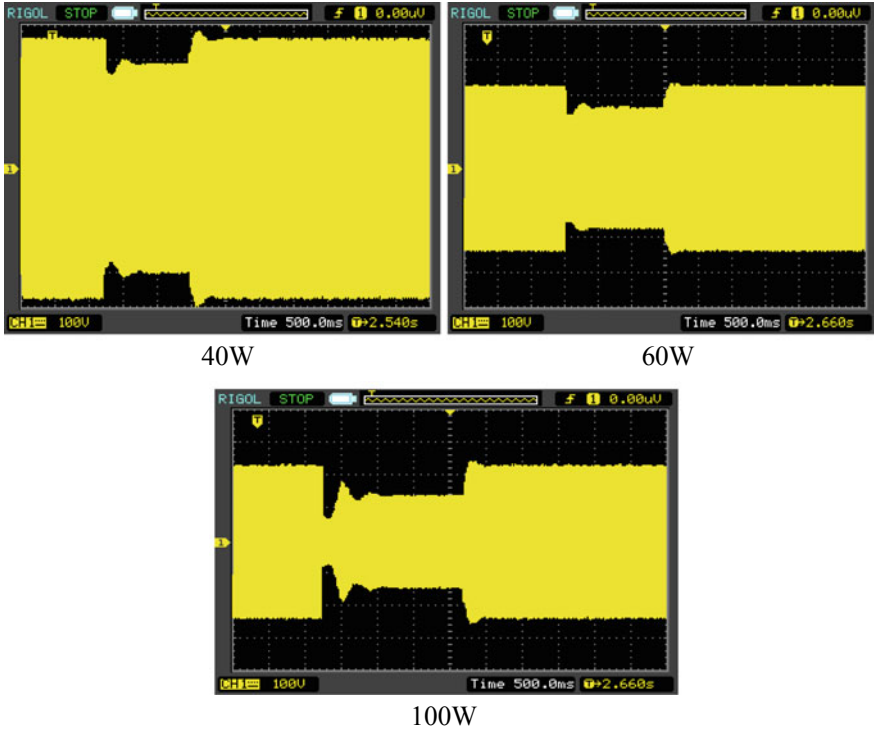


Fig. 7 Comparison of loads (40, 60, 100 W) without ELC

The comparison of various loads with ELC and without ELC is also presented in this paper, refer to Figs. 7 and 8.

5 Conclusion

In no-load configuration, the SEIG system produced 520 V under no load which dips into 200 V at full load of 92 W. The proposed system demonstrated a “150”% of voltage regulation from no load to full load, which is highly unacceptable for any power systems. In order for reduction in voltage regulation, an electronic load controller had been designed and implemented that would be able to the regulate power generated by SEIG remains constant irrespective of load variation. The ELC has been designed for 100 W of power and has an integrated PI module which controls the duty cycle of the switch such that the voltage at the load terminals remains constant. The voltage regulation of the system with the use of ELC reduced

5. Murthy SS, Singh B, Sandeep V (2011) A novel and comprehensive performance analysis of a single-phase two-winding self-excited induction generator. *IEEE Trans Energy Convers* 27(1):117–127
6. Singh B, Murthy SS, Gupta S (2005) An electronic voltage and frequency controller for single-phase self-excited induction generators for pico hydro applications. In: 2005 international conference on power electronics and drives systems, vol 1. IEEE
7. Singh B, Kasal GK (2008) Solid state voltage and frequency controller for a stand alone wind power generating system. *IEEE Trans Power Electron* 23(3):1170–1177
8. Chan TF (1993) Capacitance requirements of self-excited induction generators. *IEEE Trans Energy Convers* 8(2):304–311
9. Wang L, Su J-Y (1999) Dynamic performances of an isolated self-excited induction generator under various loading conditions. *IEEE Trans Energy Convers* 14(1):93–100
10. Bonert R, Rajakaruna S (1998) Self-excited induction generator with excellent voltage and frequency control. *IEE Proc—Gener Transm Distrib* 145(1):33–39
11. Singh B et al (1988) A single-phase self-excited induction generator for lighting loads in remote areas. *Int J Electr Eng Educ* 25(3):269–275
12. Singh B, Murthy SS, Gupta S (2006) A voltage and frequency controller for self-excited induction generators. *Electric Power Components and Systems* 34(2):141–157
13. Murthy SS, Malik OP, Tandon AK (1982) Analysis of self-excited induction generators. In: IEE proceedings C (generation, transmission and distribution), vol 129, no 6. IET Digital Library
14. Kalla UK, Singh B, Sreenivasa Murthy S (2016) Modified electronic load controller for constant frequency operation with voltage regulation of small hydro-driven single-phase SEIG. *IEEE Trans Ind Appl* 52(4):2789–2800
15. Singh B, Murthy SS, Gupta S (2006) A voltage and frequency controller for self-excited induction generators. *Electr Power Compon Syst* 34(2):141–157

EV Battery Charging with Input Power Factor Correction Using a Buck–Boost Converter



Prateek Kumar Sahoo, Sagar Kumar Champati, Ashish Pattanaik
and Tapas Kumar Mohapatra

Abstract Some of the devices that are used in industrial, commercial and residential applications need DC supply for their proper functioning and operation. The devices that are used for conversion of AC supply to DC are basically behaved as non-linear loads and thus have non-linear input characteristics, which results in production of non-sinusoidal line current. Also, current comprising of frequency components at multiples of line frequency is observed which lead to line harmonics. Due to the increasing demand of these devices, the line current harmonics pose a major problem by degrading the power factor of the system thus affecting the performance of the devices. Hence, there is a need to reduce the line current harmonics, so as to improve the input power factor (IPF) of the system. This has led to designing of IPF correction circuits using new buck–boost converter topology. In this article, the authors used this circuit particularly for electric vehicle (EV) battery charging from AC supply. A passive power factor correction circuit with new buck–boost converter (BBC) is implemented for improving the IPF. Hysteresis current control (HCC) technique and PID controllers are used for both voltage regulation and IPF correction.

Keywords Buck–boost converter (BBC) · Input power factor (IPF) · Hysteresis current control (HCC) · EV

P. K. Sahoo · S. K. Champati · A. Pattanaik · T. K. Mohapatra (✉)
Institute of Technical Education and Research, SOA Deemed to be University, Bhubaneswar
751030, India
e-mail: tapasmohapatra@soa.ac.in

P. K. Sahoo
e-mail: prateekkumarmsd7@gmail.com

S. K. Champati
e-mail: sagar.champati007@gmail.com

A. Pattanaik
e-mail: ashish.pattanaik3@gmail.com

© Springer Nature Singapore Pte Ltd. 2020
R. Sharma et al. (eds.), *Innovation in Electrical Power Engineering, Communication, and Computing Technology*, Lecture Notes in Electrical Engineering 630,
https://doi.org/10.1007/978-981-15-2305-2_52

1 Introduction

The automotive industry is forced to think of electric vehicles (EVs) due to extreme use of fossil fuel and air pollution. Currently, modeling and charging an EV battery is a good area of research. The switch mode power supply is well known to be the cornerstone of power conversion technology. For charging the battery, an effective and easy DC–DC converter is necessary. For their battery charging cycle, most of the EV uses buck–boost converters. Buck and boost converters are simple and efficient but cannot provide high-voltage gain. Some new topologies with different gain and voltage range variations are proposed [1–4]. Here, the authors are trying to use an efficient BBC [5] for the charging of EV battery which has a gain of $D^2/(1 - D^2)$. This BBC also provides a positive output voltage which is basically not obtained by BBCs. With increase in the use of semiconductor devices and electronic loads, greater stress is placed on the correction of the IPF [6–9] and on the decrease of total harmonic distortion (THD) present in the AC power supply input. In order to enhance the quality of input power, scientists have been more interested in designing fresh power converter topologies and control techniques. Here, the authors are also trying to use the robust current control technique, i.e., HCC [10] with PID controller to adjust the voltage output to the required value and enhance the IPF. The input power factor becomes poor due to non-sinusoidal input current and the phase angle between the fundamental component of source current and voltage. The HCC technique is used to generate the pulse for BBC to regulate the output voltage as well as to improve the power factor by reducing the phase difference between supply voltage and current and also improve the current nature.

2 Control Strategies

For input power factor correction, there are various control strategies available, such as

1. Peak current control
2. Average current control
3. Hysteresis control
4. Borderline control
5. Discontinuous PWM control.

In this project, we have tried to improve the power factor using a buck–boost converter, so we need to control the output voltage as well as improve the power factor. So, we adopted a control strategy including both PID control and hysteresis control to control output voltage and improve input power factor, respectively.

2.1 Output Voltage Control

In this control technique, the output voltage of the DC/DC converter is controlled with the help of a PID controller. The output voltage is controlled to provide a required DC voltage as per the user’s demand. First, the output voltage is evaluated and the necessary output voltage is compared and the error is supplied to the PID controller. The PID controller output is then provided to the hysteresis control module as an input.

2.2 Hysteresis Control

In this control technique, with respect to upper and lower boundary limits, two reference currents are generated. Narrow hysteresis band is preferred for input current with fewer ripples. The hysteresis band and the pulse generation technique are shown in Figs. 1 and 2.

Fig. 1 Hysteresis band

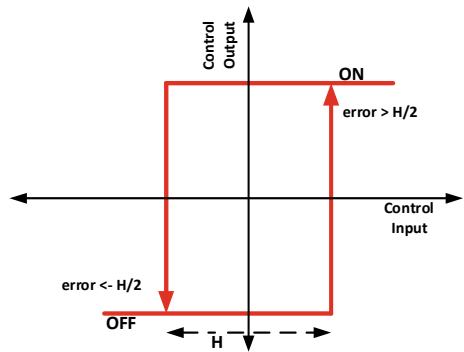
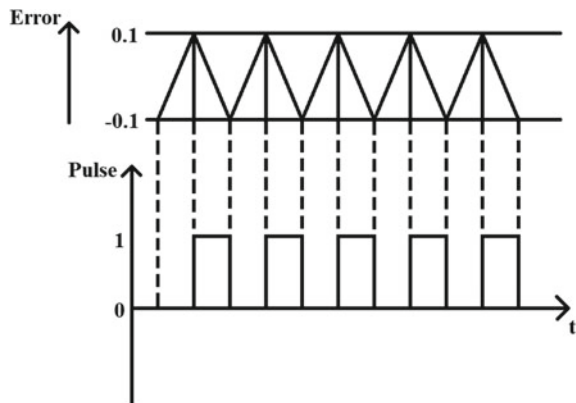


Fig. 2 Pulse generation technique using hysteresis band



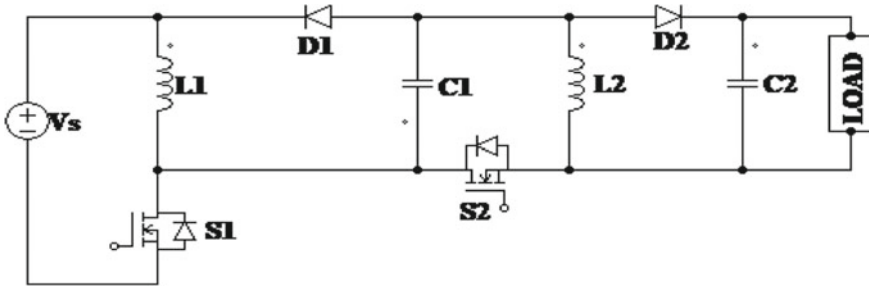


Fig. 3 Schematic diagram of new buck–boost converter

The rectified voltage is measured and multiplied with the output of the PID controller and the product is compared with the inductor current, which gives rise to an error, which when passed through a hysteresis band, produces a variable frequency pulse. This pulse is fed to the switching devices that drive the circuit. The frequency of the pulse depends on the hysteresis band that is set by the user. This control technique enables the converter to work in continuous conduction mode (CCM).

3 Topology of Buck–Boost Converter

A buck–boost converter is an electronic circuit that converts an input of direct current (DC) from a certain voltage level to either higher or lower voltage level. It is a type of power converter. The application of buck–boost converter ranges from very low power utilities (small batteries) to very high power utilities (high-voltage power transmission).

The buck–boost converter used, as shown in Fig. 3, is a cascade connection of two simple buck and boost converters. It contains two power switches (S_1 and S_2), two diodes (D_1 and D_2), two inductors (L_1 and L_2), two capacitors (C_1 and C_2) and a load R . Two active switches in the converter, Switch₁ (S_1) and Switch₂ (S_2), are switched ON and OFF at a time and both the diodes are also operating simultaneously. The buck–boost converter used in this project provides the required output voltage for a higher range of input voltage variations as compared to conventional buck–boost converter.

4 Modes of Operation of Buck–Boost Converter

See Figs. 4 and 5.

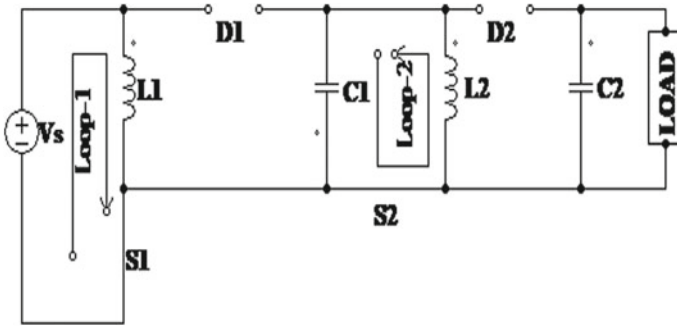


Fig. 4 Schematic diagram of buck–boost converter when both the switches are closed

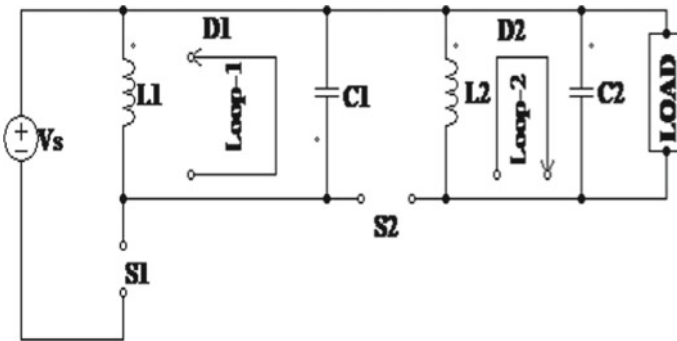


Fig. 5 Schematic diagram of buck–boost converter when both the switches are open

4.1 Mode-1 (Both Switches Are ON) ($0 < T < DT$)

When both the switches are ON (act as short circuit), the diodes are reverse biased (act as open circuit) and current will flow through the path ‘ $V_S \rightarrow L_1 \rightarrow \text{Switch}_1 \rightarrow V_S$ ’ and ‘ $C_1 \rightarrow \text{Switch}_2 \rightarrow L_2 \rightarrow C_1$.’ The schematic of this mode is shown in Fig. 4. Here, D signifies the duty ratio.

The dynamic equations for this mode are given below.

$$V_{L1} = V_S \tag{1}$$

$$V_{L2} = V_{C1} \tag{2}$$

$$\frac{di_{L1}}{dt} = \frac{V_s}{L_1} \quad (3)$$

$$\frac{dV_{C1}}{dt} = \frac{i_{L2}}{C_1} \quad (4)$$

$$\frac{di_{L2}}{dt} = \frac{V_{C1}}{L_2} \quad (5)$$

$$\frac{dV_{C2}}{dt} = \frac{-V_{C2}}{RC_2} \quad (6)$$

where V_{L1} and V_{L2} are the voltage drops of both the inductors. V_{C1} and V_{C2} are the voltage drops of both the capacitors. i_{L1} and i_{L2} are the currents through both the inductors. V_s is the DC supply of the converter.

4.2 Mode-2 (Both Switches Are OFF) ($0 < T < (1 - D)T$)

When both the switches are OFF (act as open circuit), the diodes are forward biased (act as short circuit) and current will flow through the path ' $L_1 \rightarrow C_1 \rightarrow D_1 \rightarrow L_1$ ' and ' $L_2 \rightarrow D_2 \rightarrow C_2$ & Load $\rightarrow L_2$.' The schematic of this mode is shown in Fig. 5

The dynamic equations for this mode are given below.

$$V_{L1} = -V_{C1} \quad (7)$$

$$V_{L2} = -V_{C2} \quad (8)$$

$$\frac{di_{L1}}{dt} = \frac{-V_{C1}}{L_1} \quad (9)$$

$$\frac{dV_c}{dt} = \frac{-i_{L1}}{C_1} \quad (10)$$

$$\frac{di_{L2}}{dt} = \frac{-V_0}{L_2} \quad (11)$$

$$\frac{dV_{C2}}{dt} = \frac{i_{L2}}{C_2} - \frac{V_{C2}}{RC_2} \quad (12)$$

Using the equation from Eqs. (1) to (12), the average state space matrix of the given DC–DC converter can be explained as:

$$\begin{bmatrix} \frac{di_{L1}}{dt} \\ \frac{di_{L2}}{dt} \\ \frac{dv_{C1}}{dt} \\ \frac{dv_{C2}}{dt} \end{bmatrix} = \begin{bmatrix} 0 & 0 & \frac{-(1-D)}{L_1} & 0 \\ 0 & 0 & \frac{D}{L_2} & \frac{-(1-D)}{L_2} \\ \frac{-(1-D)}{C_1} & \frac{D}{C_1} & 0 & 0 \\ 0 & \frac{1-D}{C_2} & 0 & \frac{-1}{RC_2} \end{bmatrix} \begin{bmatrix} i_{L1} \\ i_{L2} \\ v_{C1} \\ v_{C2} \end{bmatrix} + \begin{bmatrix} \frac{D}{L_1} \\ 0 \\ 0 \\ 0 \end{bmatrix} V_s$$

$$V_0 = [0 \ 0 \ 0 \ 0 \ 1] \begin{bmatrix} i_{L1} \\ i_{L2} \\ v_{C1} \\ v_{C2} \end{bmatrix} + [0]V_s$$

From the above equations, we can derive a relation between input and output voltage of the buck–boost converter. Equation (13) shows the relation between the input and output

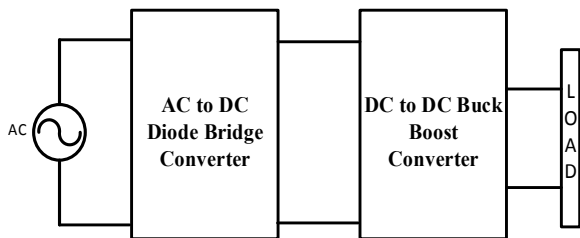
$$V_0 = V_s \left(\frac{D}{1-D} \right)^2 \tag{13}$$

From this equation, it is clearly observed that gain is the square of $\frac{D}{1-D}$. That means high-voltage gain can be obtained with a small change in duty ratio.

5 Power Factor Correction Circuit Using Buck–Boost Converter

When we give AC supply directly to the rectifier, we got a very bad power factor. So we have corrected the IPF bypassing the AC supply to the LC filter and then the filtered AC is given to the rectifier and the buck–boost converter subsequently. The basic blocks of AC to DC converters are shown in Fig. 6.

Fig. 6 AC to DC converter with buck–boost converter



6 Simulation and Results

The parameters, along with their corresponding specifications, used in the PFC charger circuit, are specified in Table 1. The specified parameters are used for the simulation of the PFC charger circuit for resistive load and battery load.

Initially, the charger circuit was implemented for resistive load without power factor correction, i.e., LC filter. In that condition, we obtained the required output voltage and current; however, the charger was drawing a huge amount of current from the AC source, thereby decreasing the efficiency and the IPF, which can be seen in Table 2. The corresponding block diagram is shown in Fig. 7 which is implemented in MATLAB/Simulink and the output voltage and input voltage and current waveforms are shown in Figs. 8 and 9. The IPF varied from 0.63 to 0.82 with the variation in

Table 1 Parameters and their specifications used in the PFC charger

Parameters	Specifications
Minimum input voltage (RMS)	24 V
Maximum input voltage (RMS)	40 V
Diode (in rectifier)	6A4
Diode (in DC–DC converter)	10A04
MOSFET	IRF540
Filter inductor	25 mH
Filter capacitor	220 μ F
Inductor (in DC–DC converter)	2 \times 10 mH
Coupling capacitor	47 μ F
Output capacitor	2 \times 6800 μ F

Table 2 Results obtained from the simulation of the PFC charger circuit

$(V_{in})_{rms}$ (V)	Without PFC				With PFC			
	$(I_{in})_{rms}$	V_{out} (V)	I_{out} (A)	Power factor	$(I_{in})_{rms}$	V_{out} (V)	I_{out} (A)	Power factor
24	4.24	14	3	0.63	2.43	13.7	3	0.9
26	4.18	14	3	0.66	2.37	13.7	3	0.94
28	4.10	14	3	0.71	2.32	13.9	3	0.96
29	4.07	14	3	0.72	2.26	14	3	0.97
30	4.03	14	3	0.74	1.98	14	3	0.99
32	3.81	14	3	0.73	1.98	14	3	0.97
34	3.63	14	3	0.75	1.98	14	3	0.94
36	3.60	14	3	0.78	1.98	14	3	0.90
38	3.53	14	3	0.80	1.98	14	3	0.86
40	3.46	14	3	0.82	1.98	14	3	0.84

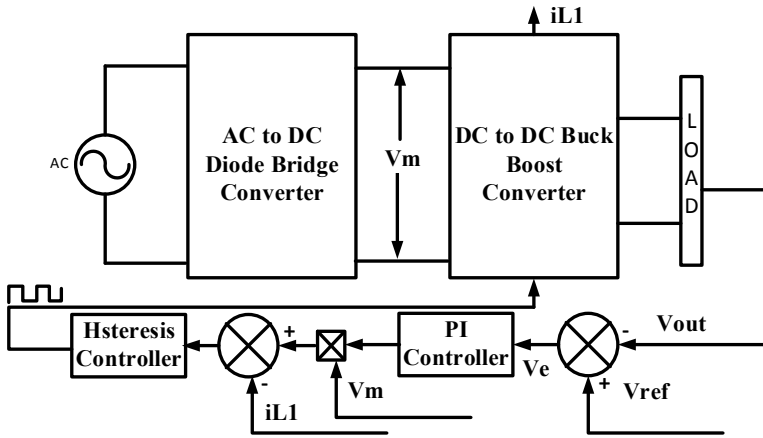


Fig. 7 Buck–boost converter without PFC

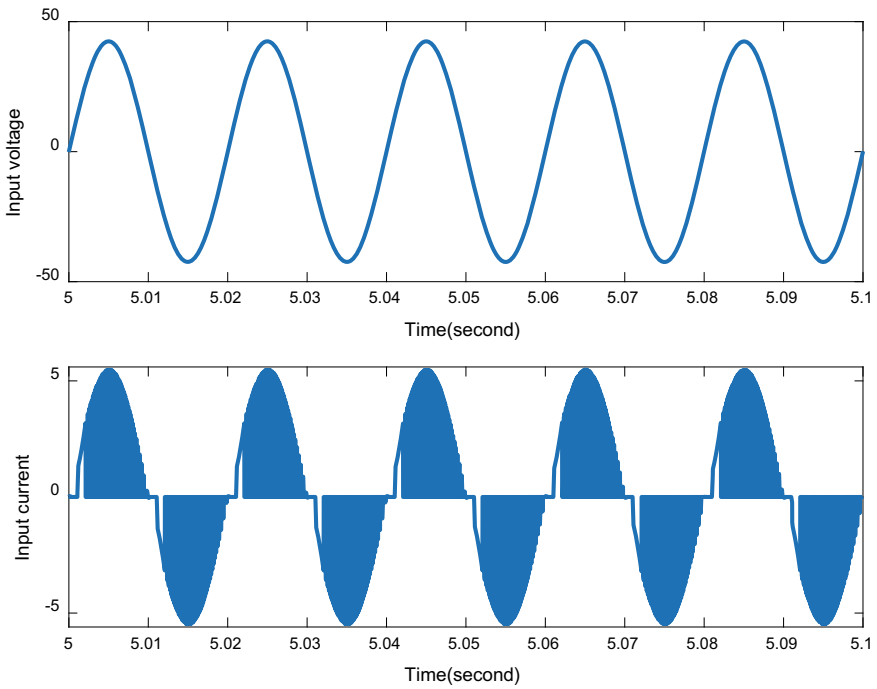


Fig. 8 Waveform of input voltage and current without PFC

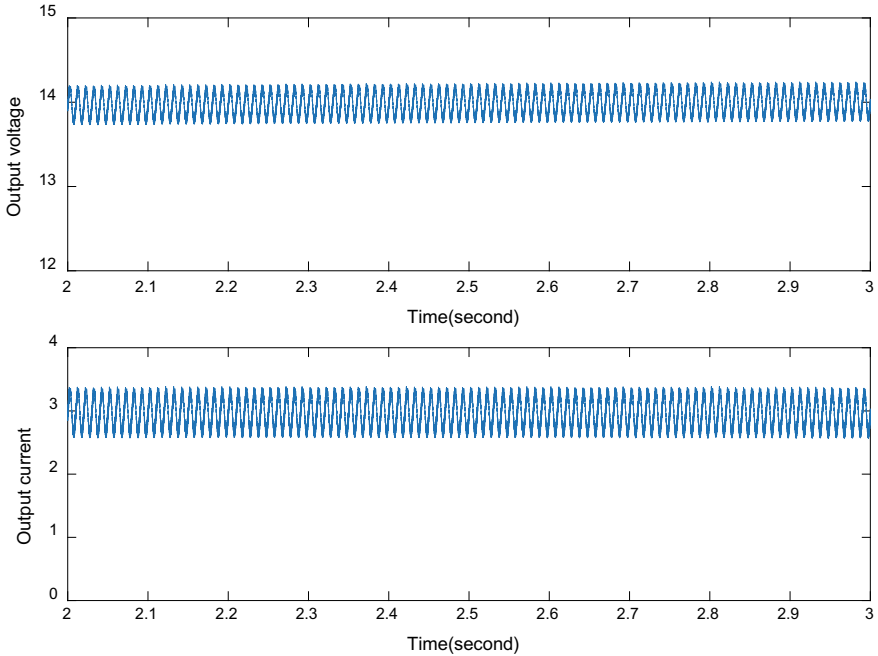


Fig. 9 Waveform of output voltage and current without PFC

the AC input voltage. After connecting the LC filter and proper controller, it can be observed in Table 2 that the input current drawn from the AC supply has reduced to almost half of that in previous condition, which increases the efficiency of the charger. Also, the IPF remains higher than 0.94 for a variation of input AC voltage from 26 to 34 V, with the highest IPF being 0.99 for an input AC voltage of 30 V, as highlighted in Table 2. The corresponding block diagram which is implemented in MATLAB/Simulink is shown in Fig. 10, and the output voltage and input voltage and current waveforms are shown in Figs. 11 and 12.

7 Conclusion

In electric vehicle, the extensive use of battery charges has given more consideration to the correction of the power factor (PFC) and the harmonic reduction of distortion in the input current from the AC power supply. A range of techniques for PFC, i.e., buck converters, boost converters and buck–boost converters, are used to solve the problems power quality. This paper suggests a buck–boost converter to use hysteresis control to enhance the power factor and thus decrease the THD, along with a power factor correction control. Simulation of the converter with and without PFC controller was conducted in MATLAB/Simulink. This resulted in the correction of the input

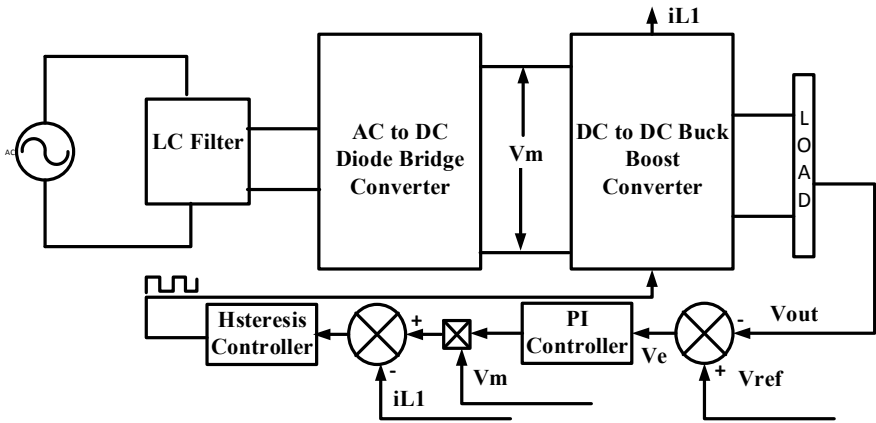


Fig. 10 Buck-boost converter with PFC

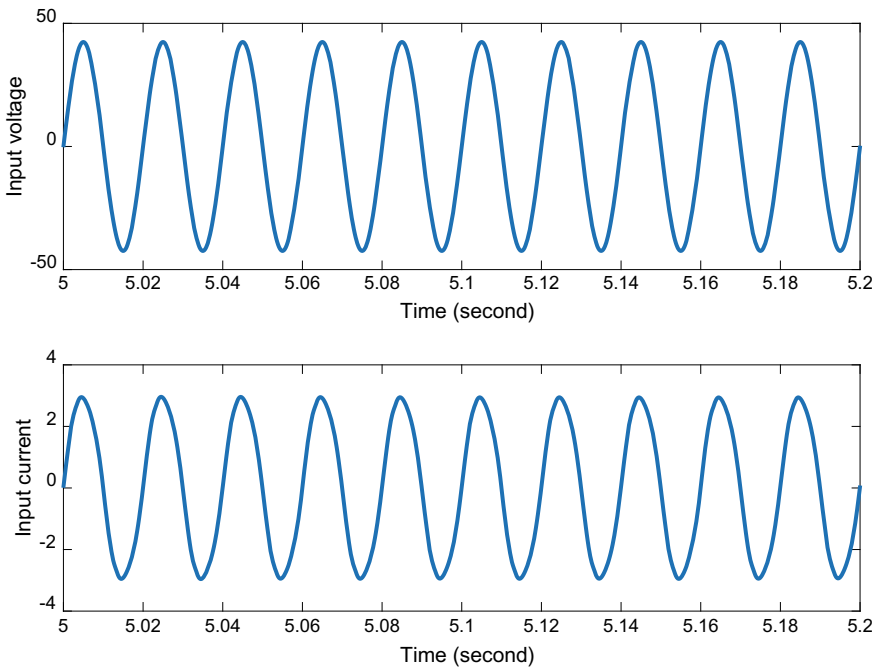


Fig. 11 Waveform of input voltage and current with PFC

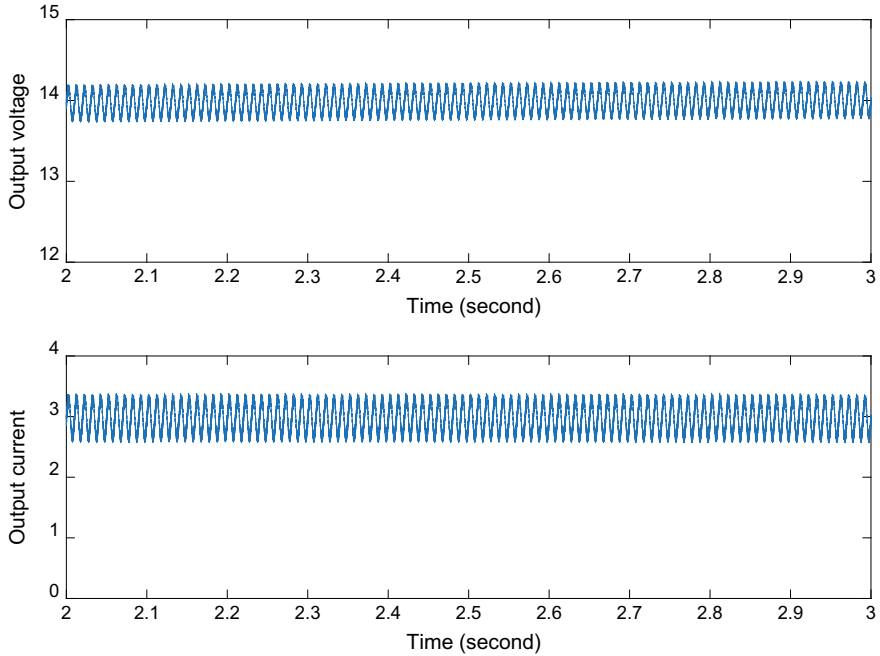


Fig. 12 Waveform of output voltage and current with PFC

power factor and the regulation of the output voltage using this controller. From the simulations, we observe and conclude that the designed circuit can provide the desired output, i.e., 14 V DC for an input variation from 30 to 40 V AC with an acceptable power factor of 0.99.

References

1. Miao S, Wang F, Ma X (2016) A new transformer less Buck-Boost converter with positive output voltage. *IEEE Trans Ind Electron* 63(5)
2. He Y, Luo FL (2005) Analysis of Luo converters with voltage-lift circuit. *Proc Inst Elect Eng Electr Power Appl* 152(5):1239–1252
3. Maksimovic D, Cuk S (1991) Switching converters with wide DC conversion range. *IEEE Trans Power Electron* 6(1):151–157
4. Luo FL, Ye H (2004) Positive output cascade boost converters. *Proc Inst Elect Eng Electr Power Appl* 151(5):590–606
5. Mohapatra TK, Dey AK, Mohapatra KK, Sahu B (2019) A novel non-isolated positive output voltage buck-boost converter. *World J Eng* 16(1):201–211
6. Hingorani NG, Gyugi L (2000) Understanding FACTS, concepts and technology of flexible AC transmission systems
7. Erickson RW, Maksimovic D (2011) *Fundamentals of power electronics*. Kluwer, Norwell, MA, USA

8. Singh B, Singh BN, Chandra A, Al-Haddad A, Pandey A, Kothari DP (2003) A review of single phase improved power quality AC DC converters. *IEEE Trans Ind Electron* 50(5):962–981
9. Ekemezie PN (2010) Design of A power factor correction AC-DC converter. *IEEE Conference Publications*. Accessed 10 March 2010
10. Kazmierkowski MP, Malesani L (1998) Current control techniques for three-phase voltage-source PWM converters: a survey. *IEEE Trans Ind Electron* 45(5):691–703

IoT Based Real-Time Water Quality Monitoring and Classification



Sujaya Das Gupta, M. S. Zambare, N. M. Kulkarni and A. D. Shaligram

Abstract Rivers are the major freshwater sources. Good health and well-being require clean and good quality water. Recent time has witnessed severe degradation of water quality owing to heavy industrialization, agriculture, and anthropogenic activities. Such high levels of pollution can be health threatening. Hence water quality monitoring plays a vital role in assessing the water quality conditions of water resources; report the spatial and temporal variations in the conditions, identifying the cause and location of water pollution. This research work focuses on developing wireless sensor nodes capable of real-time analyses of the various physicochemical characteristics of any water resource. The work may offer a small leap towards providing safe water by updating the authorities through a web-based portal and mobile phone platforms regarding the contamination status so that preventive measures can be devised in time.

Keywords Real-time water quality monitoring · Internet of things (IoT) · Mula river

1 Introduction

Water pollution has a significant impact on the human and ecosystem's health. One of the major uses of water is drinking. Other uses are namely, domestic purposes, agriculture, industries, recreation, and transportation. Approximately, 70% of our

S. Das Gupta (✉) · M. S. Zambare · N. M. Kulkarni
Department of Electronic Science, Fergusson College, Pune, India
e-mail: Sujaya_dasgupta@rediffmail.com

M. S. Zambare
e-mail: drmsz29@gmail.com

N. M. Kulkarni
e-mail: nmkulkarni123@gmail.com

A. D. Shaligram
Department of Electronic Science, Savitribai Phule Pune University, Pune, India
e-mail: adshaligram@gmail.com

© Springer Nature Singapore Pte Ltd. 2020
R. Sharma et al. (eds.), *Innovation in Electrical Power Engineering, Communication, and Computing Technology*, Lecture Notes in Electrical Engineering 630,
https://doi.org/10.1007/978-981-15-2305-2_53

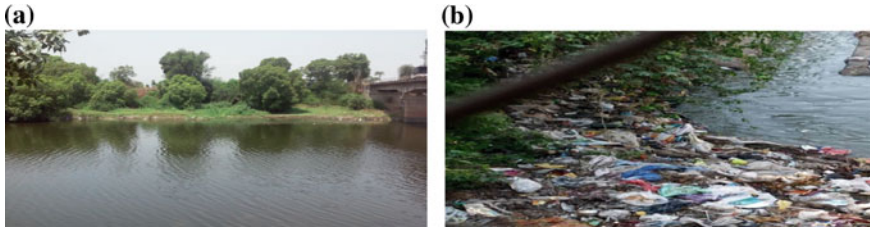


Fig. 1 a Mula river at Lavale, Pune b pollution at the bank of Mula river at Lavale, Pune

body is composed of water and approximately an average of 2–3 litres of water every day is required by every human being for drinking. With increasing populations, there has been a heavy demand for good quality water. Biodiversity is evident in the coastal regions due to the presence of migratory birds, coral reefs, mangrove forests, etc. Such places promote tourism of any state and providing various livelihood opportunities like fishing, recreational activities, transportation, etc. Pollution in these coastal areas has a long term effect on aquatic life. Hence regular water quality monitoring plays a vital role in reporting and assessing the quality conditions of water resources; identifying the cause and location of water pollution and also initiates a step towards reducing pollution by creating awareness.

Traditional water quality testing methods rely on random water sample collection at various locations and analyzing them in the laboratories which involve manual work and a long time. Moreover, most of the available online water quality systems commercially available in the market are very expensive. Therefore, this research work aims to develop an Internet of things (IoT) based wireless sensor nodes for water quality monitoring. Such a platform can measure the various characteristics quality parameters, store, process and wirelessly transmit data to a remote cloud server indicating the pollution status of water resources. The knowledge of the quality of water can be used to identify its suitability for various uses like drinking, irrigation, domestic uses, recreation, etc. As a case study, we have monitored the basic water parameters at the upstream and downstream locations of River Mula to study the pollution effect. Mula River in Pune city, Maharashtra is one of the major sources of drinking water supply in the city. Mula river originates in the Western Ghats of Maharashtra is dammed at Mulshi. The rivers through its journey into the city get highly polluted caused by industrial effluents, domestic sewage flows, agriculture wastes and due to other anthropogenic activities (Fig. 1b).

2 Earlier Work

According to a 2018 report by Central Pollution Control Board, Maharashtra state has the highest number of 53 polluted rivers. Out of 672 water bodies in Maharashtra, 566 rivers like Mithi, Mula, Mutha, Ulhas from Mumbai and Pune had bad water quality

and were found to be most polluted [1]. A recent report by the MPCB has revealed that the major river stretches in Pune city like Bhima, Pavana, Mula, and Mutha is faced with the problem of severe pollution [2]. The Environment Status Report (ESR) of 2017–2018 states that “There has been a consistent rise in Biological Oxygen Demand (BOD) and Chemical Oxygen Demand (COD) of Mula river leading to organic matter and chemical matter contamination respectively” [3]. Several researchers supported the fact that the quality of river Mula before it entered Pune city was well within the acceptable limits but subsequently deteriorated on its progress into the city [4–6]. A report by Maharashtra Pollution control board indicates bad water quality index of Mula River at downstream locations like Aundh Bridge and Harrison Bridge; Mula-Mutha River at Sangam bridge and Mundhawa Bridge [7]. Research works in developing an IoT based wireless monitoring systems to measure physical and chemical water quality parameters [8] and deployment of wireless sensor networks distributed over a large area for river and lake water quality monitoring with wireless data transfer to a remote server for analysis have been reported earlier [9].

3 System Architecture of Basic Wireless Sensor Node

The proposed wireless sensor node for water quality monitoring comprises of the sensors and their respective signal conditioning units; data logger for data acquisition and storage, processing and operations; and wireless transmission unit as seen in Fig. 2. The detailed description of each block and sensor specifications were described by the authors in their earlier research publications [10].

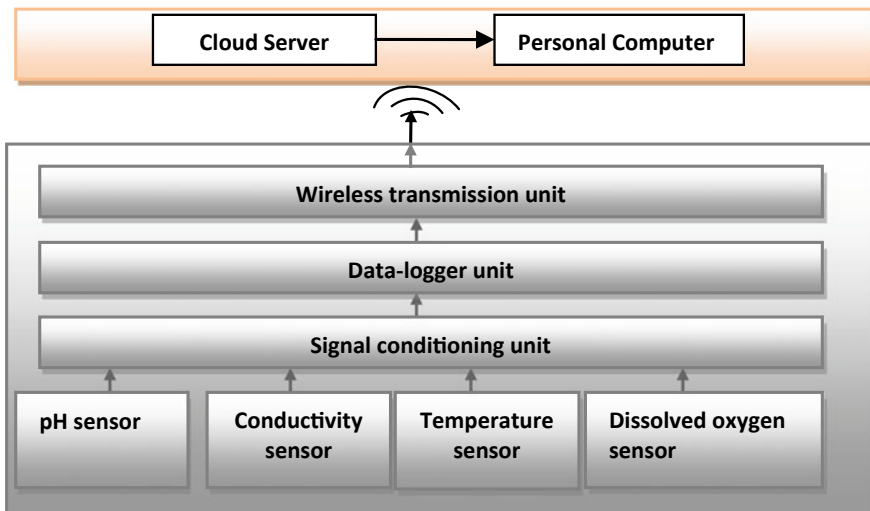


Fig. 2 Architecture of basic sensor node

Table 1 Measured water quality parameters

S. No.	Make and model	Description	Range	Sensor output	Output voltage change of measuring circuit
1	MicroSet	Temperature sensor, type: Pt-100 simplex-3 wire	0–100 °C	100–138.4 Ω	10 mV/°C
2	MicroSet MS CD 04	Electrical conductivity sensor MOC of electrodes: glass/platinum, cell constant: $K = 1.0$	0–10,000 $\mu\text{S}/\text{cm}$	0–5 V	66 mV/10 $\mu\text{S}/\text{cm}$
3	MicroSet MS pH 02	pH sensor, body: CPVC max temp: 0–80 °C bar junction: four ceramic ref: Ag/AgCl process	0–14	–414.4 mV to +414.4 mV (59.2 mV/pH change)	200 mV/pH
4	MicroSet MS DO 714	Maintenance free dissolved oxygen temp. range: 0–40 °C, ATC: Pt-100	0–20 mg/l	0–55 mV	75 V/mg/l

Table 1 displays different sensors with the specifications used in this project and their respective output voltage per unit change displayed by the designed measuring circuit. The sensors were scanned with a sampling time of 10 s. The major blocks of the data logger are: an 8-bit microcontroller (Atmega 328) used as the main controller for analog to digital conversion, computing and operations; onboard memory and interfacing circuit for transmission of wireless data. The input voltage range of the data logger unit was set to a range of 0–5 V. The acquired real-time sensors' data were processed and stored by the data logger and further transmitted to the “ThingSpeak” cloud server using a SIM 800C based GSM modem. New channels for recording and displaying the plot of water quality field data was created in the cloud server.

4 Result and Discussion

Real-time measurements of various upstream and downstream locations of the Mula river in the summer season were made using the developed wireless sensor nodes. The experimental in situ setup established for the real-time measurement of the river quality parameters at three different locations and their obtained real-time plots on the “ThingSpeak” cloud application is indicated by Figs. 3, 4, 5. The in situ results so obtained are displayed in Table 2. Figure 6 shows the designed MATLAB graphical user interface(GUI) to display real-time data plots.

4.1 Upstream of Mula River

Location 1: Mulshi Agro-Tourism

(a)



(b)



Fig. 3 a In situ sensor node deployment at location 1, b continuous plots at “ThingSpeak” cloud application

Location 2: Lavale Village

(a)



(b)



Fig. 4 a In situ sensor node deployment at location 2, b continuous plots at “ThingSpeak” cloud application

4.2 Downstream of Mula River

Location 3: COEP Boat Club

(a)



(b)

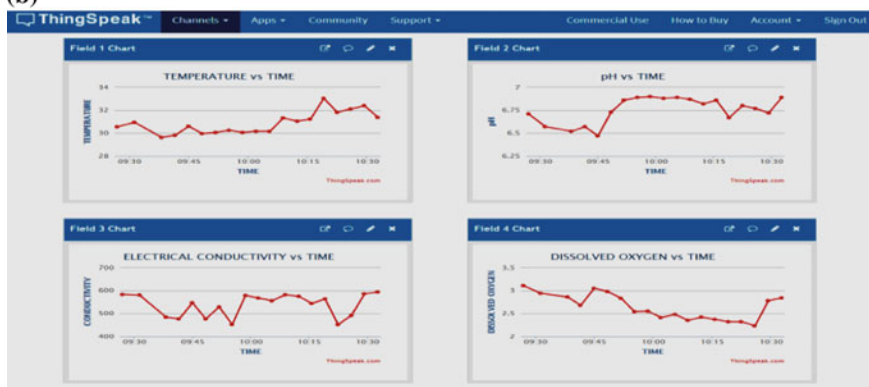


Fig. 5 a In situ sensor node deployment at location 3, b continuous plots at “ThingSpeak” cloud application

Table 2 Measured water quality parameters

S. No.	Mula river locations	Date	Quality parameters			
			Temperature (°C)	pH	Electrical conductivity	Dissolved oxygen
1	Mulshi agro-tourism	22/5/2019	28.45–29.6	7.3–8.03	70–79.42	3.23–3.77
2	Lavale village	21/5/2019	30.30–33.28	6.95–7.39	135–144.46	2.83–3.26
3	COEP boat club	17/5/2019	29.60–33.04	6.47–6.89	451.02–593.8	3.11–2.84

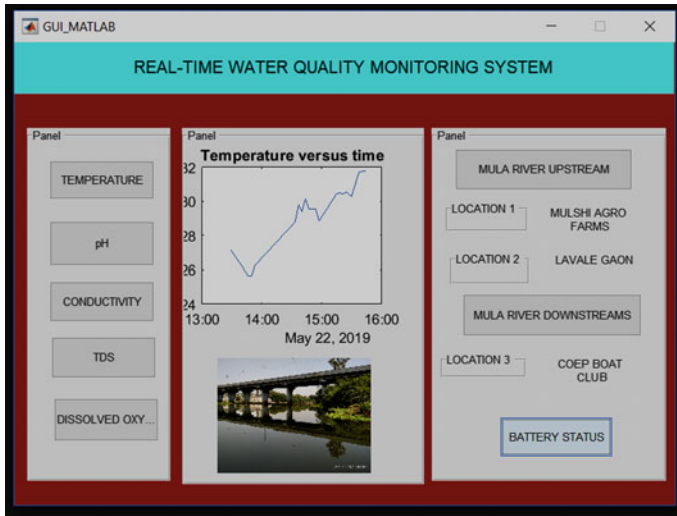


Fig. 6 MATLAB GUI

4.3 Water Quality Index and Classification

The water quality index calculations have been discussed in detail by the authors in the earlier research publications [11]. The calculations were made based on the water quality standards recommended by the Indian Council of Medical Research (ICMR) and the Bureau of Indian Standards(BIS). Weighted Arithmetic Index Method was used for the calculation of the water quality index (WQI) [12]. Table 3 indicates the standard categorization of water resources according to the value of WQI [13].

Water quality field data uploaded in the cloud server can be accessed by the centralized controller and saved in a database for further analysis and classification. Using MATLAB software, the calculation of water quality indices based on the data imported from the database was made. **Classification Learner** application of MATLAB was used to classify the water resources into various categories aforementioned, based on their water quality index values. This application applied supervised machine learning with several classifiers to train models for data classification. The classification models available were decision trees, discriminant analysis, support

Table 3 WQI and water quality status [13]

S. No	WQI	Description	Categories
1	0–25	Excellent	A
2	26–50	Good	B
3	51–75	Poor	C
4	76–100	Very poor	D
5	>100	Heavily polluted	E



Fig. 7 Trained model and confusion matrix

vector machines, logistic regression, support vector machines, and ensemble classification. To train a model, a set of known data and the responses to the data was fed to the application. The automated training was performed to select the best available classification model. A fine tree trained model was created with 98.4% accuracy and the classifier algorithm required 87 iterations to train the model with the training time of 8.7 s as shown in Fig. 7. Once training was done, the model could classify the new unknown water quality data of different locations under the current study, into the standard categories (as Table 3). Locations 1 and 2 based on their WQI were categorized into C class indicating poor quality whereas location 3 was categorized into E class indicating heavily polluted.

5 Conclusion and Future Scope

The water quality index of the Mula river at the upstream locations in Mulshi and Lavale were found to be in the poor category due to the effluents from the factories near the selected locations and agricultural run-offs into the river. As the river progresses into the city, i.e., the downstream locations of river Mula were found to be in the heavily polluted category and can be attributed to the disposal of municipal wastes like plastics, heavy metals, rubbers, etc., industrial effluents, other anthropogenic activities into the river. In other words, upstream of the river is less polluted than the downstream. The developed system could measure and record the basic quality parameters of the water resource under investigation with good accuracy and further could wirelessly transfer data to a remote cloud server. Wireless sensor nodes were battery-operated, rechargeable with a PV module. This research work allows real-time reporting of quality of water resources thereby, can bring to the notice of the concerned authorities and stakeholders about the pollution levels. This could further be assistance to devise early solutions under critical conditions. In the future, the work can be extended by monitoring other water quality physicochemical parameters and also attention can be focused on miniaturizing the developed sensor nodes.

Acknowledgements We are thankful to the management of the Mulshi Agro Tourism and Boat club at the College of Engineering Pune (COEP) for granting permission to pursue our research on their premises.

References

1. ENVIS Centre on Control of Pollution Water, Air, and Noise. http://www.cpcbenvis.nic.in/water_pollution_main.html
2. Maharashtra Pollution Control Board (2019) Water quality index summary of 206 stations in Maharashtra. E-bulletin of water quality national water monitoring programme (NWMP)
3. Environmental Current Status Report. https://pmc.gov.in/sites/default/files/reports_dpr/Draft%20ESR%202017-18.pdf
4. Vinaya V, Mane T (2007) Studies on water pollution of Mula, Mutha and Pawana rivers in summer season in the Pune city region. *Nature Environ Pollut Technol* 6(3):499–506 (Technoscience Publications)
5. Pali S, Sonali K, Sagar C, Sourabh K (2015) Physicochemical analysis Of Mula Mutha river pune. *Civil Eng Urb Plan Int J (CIVIJ)* 2(2):37–46 (AIRCC Publishing Corporation, Tamilnadu)
6. Jadhav SD, Jadhav MS (2017) Analysis of water quality using physico-chemical parameters of Mula-Mutha river, Pune (Maharashtra). *Int J Trend Sci Res Develop (IJTSRD)* 1(6):250–256 (Amreli, India)
7. Water Quality Status of Maharashtra. http://www.mpcb.gov.in/ereports/pdf/Water_Quality_Maharashtra_2017_18_report_07022019.pdf
8. Manoharan S, Sathiyaraj G, Thiruvankadkrishnan K, Vetriselvan V, Kishor P (2019) Water quality analyzer using IoT. *Int J Innov Technol Explor Eng (IJITEE)* 8(8):34–37 (Blue Eyes Intelligence Engineering and Sciences Publication (BEIESP), Bhopal)
9. Taufik S, Hilman A, Rian P, Irfan A, Aris M (2017) Portable and online water quality monitoring system using wireless sensor network. In: 2nd international conference on automation, cognitive science, optics, micro-electro-mechanical system, and information technology (ICACOMIT), IEEE Digital Xplore, Indonesia, pp 34–40
10. Dasgupta S, Zambare MS, Kulkarni N, Shaligram A (2019) Real-time water quality monitoring system analysis of Pashan lake, Maharashtra, India. *Int J Eng Adv Technol (IJEAT)* 8(6):2331–2335 (Blue Eyes Intelligence Eng. and Sci. Publ. (BEIESP), Bhopal)
11. Dasgupta S, Zambare MS, Kulkarni N, Shaligram A (2019) Real-time water quality monitoring system for rivers. *Acta Technica Napocensis. Electronica-Telecomunicatii* 60(2):17–22 (Mediamera Science Publisher, Romania)
12. Yogendra K, Puttaiah ET (2008) Determination of water quality index and suitability of an urban water body in Shimoga town, Karnataka. In: *Proceedings of Taal 2007: the 12th world lake conference*, pp 342–346
13. Chatterjee PR, Raziuddin M (2002) Studies on the water quality of a water body at Asansol town, West Bengal. *Nature Environ Pollut Technol* 1(2):181–189 (Technoscience Publications)

Motion Control of an IPMSM Drive System Using Sliding Mode Controller



A. K. Naik, A. K. Panda, Sanjeeb Kumar Kar and M. Sahoo

Abstract The conventional PI controller is most commonly used in vector control of ac motor drive system. However, this conventional control technique is found to be incapable of achieving the necessary regulation, dynamic response, and stability requirement which makes it unsuitable for nonlinear load, any kind of parametric variation and external disturbances. This paper presents sliding mode control (SMC) technique for controlling the speed of PMSM drive which provides high tracking performances to PMSM drive in steady-state as well as transient condition. Both the conventional PI controller and sliding mode controller have been analyzed for IPMSM drive system in the steady-state and transient state with constant and step load and speed variation. To investigate the dynamic performance of motor using both the strategy of speed controller, i.e., PI and sliding mode controller are designed and tested by the help of MATLAB-Simulink environment.

Keywords IPMSM · Sliding mode control (SMC) · Field oriented control

Nomenclature

B	Friction coefficient
i_a, i_b, i_c	3- ϕ input current
I_q, I_d	Stator current component of q and d -axis
J	Motor inertia
L_q and L_d	Self-inductance of stator q and d -axis
P	Number of pole
R_s	Resistance of stator

A. K. Naik (✉) · S. K. Kar · M. Sahoo
Department of Electrical Engineering, Institute of Technical Education and Research, Siksha O Anusandhan (Deemed to be University), Bhubaneswar, India
e-mail: amiyanaik@soa.ac.in

A. K. Panda
Department of Electrical Engineering, National Institute of Technology, Rourkela, India

© Springer Nature Singapore Pte Ltd. 2020
R. Sharma et al. (eds.), *Innovation in Electrical Power Engineering, Communication, and Computing Technology*, Lecture Notes in Electrical Engineering 630,
https://doi.org/10.1007/978-981-15-2305-2_54

T_e	Torque developed by the motor
T_L	Load Torque
V_q, V_d	Stator voltage component of q and d -axis
λ_q, λ_d	Stator flux linkage component of q and d -axis
λ_f	Main field flux
θ_r	Position of rotor
ω_m	Speed of rotor in rad/sec (mechanical)
ω_{rated}	Motor rated speed in rad/sec

1 Introduction

In motion control field the most conventional and well-known machines are dc shunt motors and induction motors. But limitations like low torque-speed characteristics, narrow speed range, frequent maintenance requirement, etc. introduce efficient and high power density based PMSM drive system which is not only capable of overcoming all those limitations but also has the ability to run with very high-speed IPM based motor drive system. However Being a practical system it also suffers from some disadvantages like unmodelled dynamics, parameter variation, friction force, load disturbances (Fluctuation in torque-speed characteristics), etc. Earlier the most conventional approach to avoid such problems was linear control method due to its simple implementation however it was extremely hard to confine these unsettling influences [1–3]. In this way, numerous nonlinear control strategies have been received to improve the control exhibitions in frameworks with various unsettling influences and vulnerabilities.

To maintain Faster dynamic response along with smooth torque-speed characteristics advance version of current controllers has been introduced such as modified hysteresis current controller [4] and adaptive hysteresis current controller [5, 6] which eliminate all limitations present in traditional current controllers and makes the system more efficient both in transient and steady-state. For perfect tracking of speed in any condition, nonlinear methods like Sliding Mode control, robust control, adaptive control, etc. are being adopted instead of PI controllers. Among those Sliding mode control is outstanding because of its unvarying characteristics to definite inward parameter variation and outside unsettling influences that can ensure impeccable ideal tracking inspite of parameters or model vulnerabilities and in this manner enhance the dynamic execution of the system and gives great precision situating under transient as well as steady-state condition [7, 8].

The vigor of SMC must be ensured by the assurance of huge control gains, However, the huge gains normally lead to chattering phenomena, that can energize high-frequency elements. Along these lines, a few methodologies have been suggested to tackle chattering, for example, higher order sliding mode control strategy, integral sliding mode and reaching law control techniques. The reaching law technique manages these reaching processes, as chattering is occurred due to the non-perfect

coming to at the edge of the reaching stage [9–11]. In [11], author displayed a number of reaching laws that can control chattering by regulating gains or building the irregular gain a variable of sliding mode surface.

This paper presents the field-oriented control of a PMSM system. The speed below base speed has been controlled in constant torque region. Adoption of field-oriented technique will deliver the basic motion control stage by giving autonomous control of flux and torque components. Hysteresis current controller has been used here for efficient control of speed and for fastens the response. Sliding mode control has adopted here to provide perfect tracking performance under both steady and transient states. With this close-loop control has been used to reduce steady-state error. Mathematical modeling has been done to analyze the behavior under the condition of transient and steady-state. The projected control proposal is modeled, examined and compared with conventional PI controller using MATLAB-Simulink software.

2 Dynamic Modeling of IPMSM

A dynamic mathematical modeling is essential to realize the algorithm of vector control for autonomous control of torque and flux of the system. Therefore, the d - q model of IPMSM is derived on the rotor reference with some assumptions such as negligible saturation, exclusive of damper winding, sinusoidal induced emf, negligible eddy current, hysteresis losses, etc.

The voltage equations for d and q -axis stator components are given in Eqs. (1) and (2).

$$V_d = R_s i_d - \omega_r \lambda_q + \frac{d\lambda_d}{dt} \quad (1)$$

$$V_q = R_s i_q + \omega_r \lambda_d + \frac{d\lambda_q}{dt} \quad (2)$$

$$\lambda_d = L_d i_d + \lambda_f \quad (3)$$

$$\lambda_q = L_q i_q \quad (4)$$

Putting the flux linkages equation given in (3) and (4) in Eqs. (1) and (2), the Eqs. (5) and (6) are obtained.

$$V_d = R_s i_d - \omega_r L_q i_q + \frac{d}{dt} (L_d i_d + \lambda_f) \quad (5)$$

$$V_q = R_s i_q + \omega_r (L_d i_d + \lambda_f) + \frac{d}{dt} (L_q i_q) \quad (6)$$

The developed electromagnetic torque of motor is given by Eq. (7)

$$T_e = \frac{3}{2} \left(\frac{P}{2} \right) (\lambda_d i_q - \lambda_q i_d) \quad (7)$$

The mechanical torque balance equation is given by Eq. (8)

$$T_e = T_L + B\omega_m + J \frac{d\omega_m}{dt} \quad (8)$$

Solving Eq. (8) to obtain the rotor speed produced mechanically can be expressed as given in Eq. (9).

$$\omega_m = \int \left(\frac{T_e - T_L - B\omega_m}{J} \right) dt \quad (9)$$

Equation (10) shows the electrical speed of rotor.

$$\omega_r = \omega_m \left(\frac{P}{2} \right) \quad (10)$$

3 Vector Control Strategy for IPMSM Drive System

A vector control technique is typically a decoupled or independent control strategy where the 3- ϕ input stator currents are alluded to a virtual field having orthogonal 2- ϕ components. Among two components, one part demonstrates the flux and the other one depicts the torque of the machine and can be controlled independently like dc machine.

Using the mathematical model, the vector control of PMSM is inferred.

Taking into consideration the input as 3- ϕ stator currents are given in Eqs. (11)–(13)

$$i_a = I_m \sin(\omega_r t + \delta) \quad (11)$$

$$i_b = I_m \sin\left(\omega_r t + \delta - \frac{2\pi}{3}\right) \quad (12)$$

$$i_c = I_m \sin\left(\omega_r t + \delta + \frac{2\pi}{3}\right) \quad (13)$$

where δ = angle between the rotor field and stator mmf.

To control the aforementioned input 3- ϕ stator current independently, it must be converted to d and q -axis segment of stator current utilizing park's transformation as given in Eq. (14).

$$i_{qdo} = T_{abc \rightarrow qdo} \cdot i_{abc} \tag{14}$$

where

$$T_{abc \rightarrow qdo} = \frac{2}{3} \begin{pmatrix} \cos\theta_r & \cos(\theta_r - 120) & \cos(\theta_r + 120) \\ \sin\theta_r & \sin(\theta_r - 120) & \sin(\theta_r + 120) \\ 0.5 & 0.5 & 0.5 \end{pmatrix} \tag{15}$$

After substituting Eqs. (15) in (14), we get Eq. (16).

$$\begin{bmatrix} i_q \\ i_d \end{bmatrix} = I_m \begin{bmatrix} \sin\delta \\ \cos\delta \end{bmatrix} \tag{16}$$

Two diverse control plans are given from vector control from the knowledge of instantaneous orientation of rotor position or field excitation for treating the IPMSM as a dc motor.

- (a) Constant torque control method (beneath rated speed).
- (b) Field weakening control method (above base speed).

In this work constant torque control technique has been adopted, where the most extreme plausible torque is required at each time similar to separately excited dc motor. This can be accomplished by proper maintaining q -axis component of stator current as:

$$i_q = I_m$$

This is realized by choosing the δ to be 90° . Consequently $i_d = 0$

Hence the electromagnetic torque is given in Eq. (7) be able to express as Eqs. (17) and (18):

$$T_e = \left(\frac{3}{2}\right) \left(\frac{P}{2}\right) \lambda_f i_q \tag{17}$$

So

$$T_e = k_t i_q \tag{18}$$

where

$$k_t = \left(\frac{3}{2}\right) \left(\frac{P}{2}\right) \lambda_f$$

Now the performance of IPMSM can be experienced as a dc motor.

The schematic diagram of vector control strategy for IPMSM drive is obtained from the above discussion and equations which is given in Fig. 1.

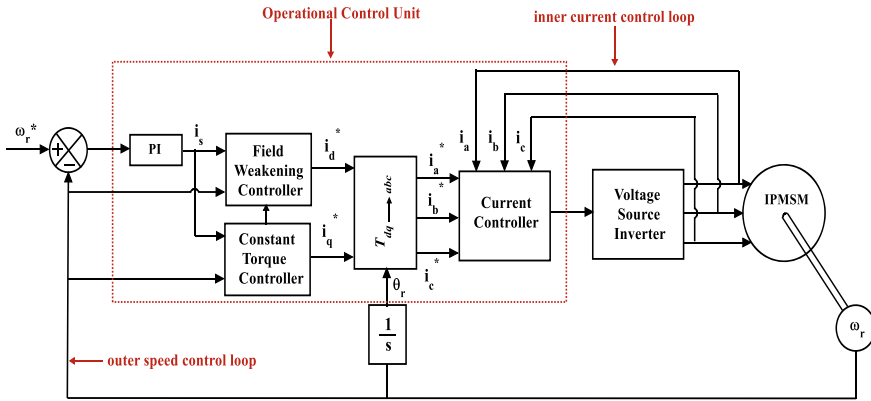


Fig. 1 Schematic diagram of vector control of IPMSM

3.1 Current Control Technique

The performance of the projected PMSM drive system normally relies upon the attributes of kind of current control methods that we utilize for controlling the current of Voltage Source Inverter (VSI). Hence, this is how current control of VSI is an additional vital subject when we consider the betterment of performance of motion control drive applications. In this proposed model, the inner loop of the system is being designed of hysteresis current controller which work is to produce the fully controlled gate signals for regulating the inverter output which in spite control output torque of PMSM.

Among various PWM techniques, hysteresis band current control PWM technique is quite popular because of easy execution. It is a kind of control methodology in which controller tries to maintain the current within a certain specified zone (normally referred to as hysteresis band) as shown in Fig. 2.

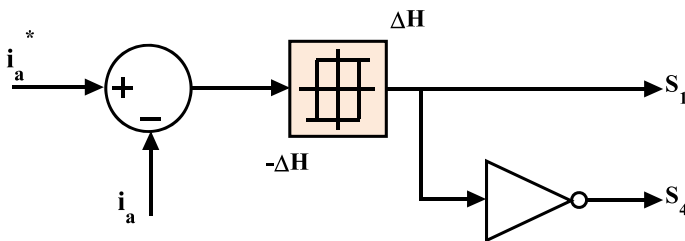


Fig. 2 Hysteresis control

3.2 Speed Control Technique

The layout of speed controller normally plays a vital role when it comes upon to confer desired transient and steady-state characteristics in any motion control platform. Its main purpose is to gain a signal referring to the demanded speed. Here Sliding mode controller has been used as a speed tracking controller for analyzing its behavior. With this, a comparative study has also been done with traditional PI controller.

3.2.1 Sliding Mode Controller

The control objective of sliding mode control is to drive the real rotor speed ω_e to pursue the ideal instructed speed ω_{ref} . The difference between the reference and actual speed can be written as $e = \omega_{ref} - \omega_e$, which symbolizes the sliding surface S . Since the speed regulating loop of the IPMSM is genuinely a first-order system, the SMC layout is conventional in its determination, and depends on the stability concept given by Lyapunov.

Now in order to ensure perfect tracking performance, sliding mode control pertains to three important conditions, i.e., hitting condition, existence condition, and stability conditions.

i. Hitting condition:

Hitting condition is to ensure despite the initial position the controlled trajectory of the system will consistently be coordinated towards sliding surface that appeared in Fig. 3.

$$s \frac{ds}{dt} < 0 \quad (\text{For } t > 0 \text{ and that } |s| \geq \delta)$$

This has been derived from Lyapunov second theorem of stability.

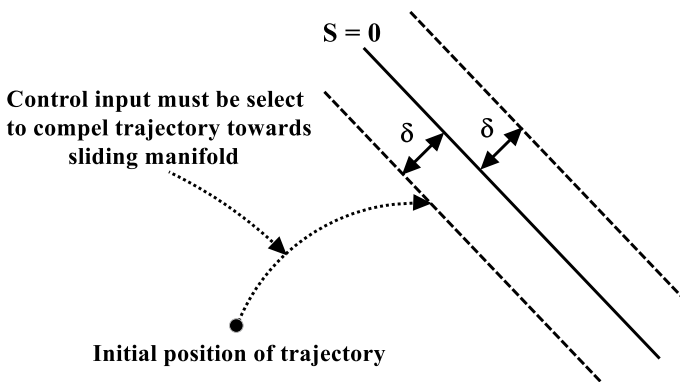


Fig. 3 Trajectory S converging to the sliding manifold

Where the Lyapunov candidate is given in Eq. (19)

$$V = \frac{1}{2}s^2 \tag{19}$$

ii. Existence condition:-

It ensures that once the trajectory enters the sliding manifold it will always remain in that zone.

It can be estimated by the condition as given in Eq. (20).

$$\lim_{s \rightarrow 0} s \frac{ds}{dt} < 0, 0 < |s| < \delta \tag{20}$$

And can be written as Eq. (21)

$$\lim_{s \rightarrow 0^+} \frac{ds}{dt} < 0 \text{ and } \lim_{s \rightarrow 0^-} \frac{ds}{dt} > 0 \tag{21}$$

The controller can now be designed as given in Eq. (22),

$$\begin{aligned} \dot{S} &= \dot{\omega}_{ref} - \dot{\omega}_e \\ &= \dot{\omega}_{ref} + \frac{B\omega}{J} - \left(\frac{T_e - T_L}{J} \right) \\ &= \dot{\omega}_{ref} + \frac{B\omega}{J} + \frac{T_L}{J} - \frac{3P}{2J}(\lambda_d i_q - \lambda_q i_d) \end{aligned} \tag{22}$$

Hence we define the reference q -axis current i_q^* with the following form.

So, the reference $i_q (= i_q^*)$ can now be expressed as given Eq. (23),

$$i_q^* = (\lambda_d)^{-1}(\lambda_q i_d) + \left(\frac{3P\lambda_d}{2J} \right)^{-1} \left(\dot{\omega}_{ref} + \frac{B\omega}{J} + \frac{T_L}{J} + k \text{sign}(s) \right) \tag{23}$$

where

$$\text{sgn}(s) = \begin{cases} 1, & s > 0 \\ 0, & s = 0 \\ -1, & s < 0 \end{cases}$$

Here the value of k would be determined from Routh Hurwitz criterion of stability.

iii. Stability condition

This condition assures that the followed path of the system and sliding mode operation will remain on a stable point. It can be obtained by ensuring Eigenvalue of Jacobian of the system has negative real parts which have been derived from Routh Hurwitz criterion of stability.

4 Matlab Results

This part of the paper demonstrates the behavior of a IPMSM drive system through the MATLAB results. For comparative studies, both PI and SMC methods are being separately designed and shown in the speed controller loop. Along with that hysteresis current controller has been modeled with the inner loop of the system. Table 1 shows all the parameters of motor which are being utilized in modeling of both MATLAB/SMULINK Environment and also in real-time experimental prototype. 200 rad/sec has been taken as Reference speed for the performance studies.

4.1 Steady-State Result at Constant Speed and at No Load

In this study, the IPMSM drive system is allowed to run at no load at its reference speed 200 rad/sec.

4.1.1 For PI Outer Loop Speed Controller

Figure 4 describes the electrical speed of the motor. It is being noticed that around at 20 ms the controller track the desired speed.

Table 1 IPMSM Drive parameters

Parameters	Nominal values
Rated voltage (V_{LL})	220 V
Output power (P_{out})	900 W
No. of poles (P)	4
Rated speed (ω_m)	1700 rpm
Stator resistance (R_S)	4.3 Ω
PM flux linkage (λ_f)	0.272 Wb
d -axis inductance (L_d)	27 mH
q -axis inductance (L_q)	67 mH
Rated current (I_S)	3 A
Maximum current (I_{SMAX})	$2I_{Srated}$
Input voltage of inverter (V_{dc})	300 V
Motor inertia (J)	0.000179 kg m ²
Damping coefficient (B)	0.05 N-m/rad/s

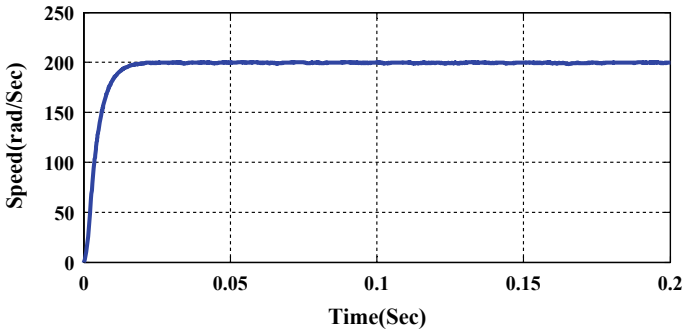


Fig. 4 Rotor speed response for PI controller

4.1.2 For SMC Outer Loop Speed Controller

In this section dynamic response of the IPMSM drive system is studied using SMC as the speed controller. For comparative performance analysis, same operating conditions as that of PI controller are considered. Here also, it is observed that actual rotor speed tracks the commanded speed linearly almost at 20 ms as appeared in Fig. 5.

4.2 Transient Results with Step Speed Change at No Load

In this study, the drive system is run at no load and the reference speed is suddenly reduced from 200 rad/sec to 150 rad/sec at 0.1 s.

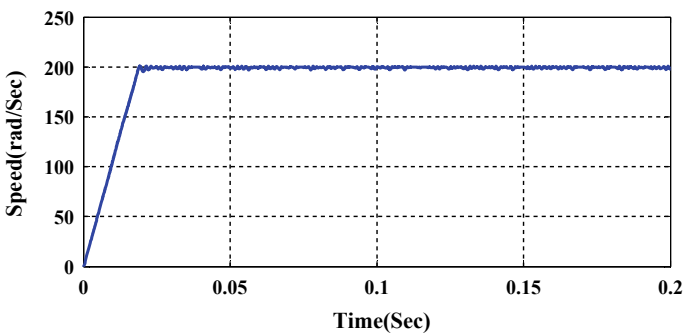


Fig. 5 Rotor speed response for SMC

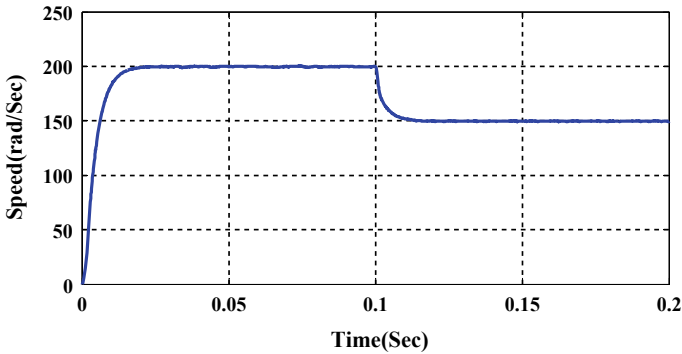


Fig. 6 Rotor speed response for PI controller

4.2.1 For PI Outer Loop Speed Controller

As seen in Fig. 6 the motor achieves the new steady-state speed at about 0.12 s, i.e., within 0.02 s.

4.2.2 For SMC Outer Loop Speed Controller

Here the motor is achieving its new steady-state speed somehow less than 0.02 s which is shown in Fig. 7. Also, the change is linear and very smooth for which the transient period will not put any pressure on the motor. So, SMC lay down minimum effort to arrive at the steady-state linearly, regardless of system parameter uncertainty.

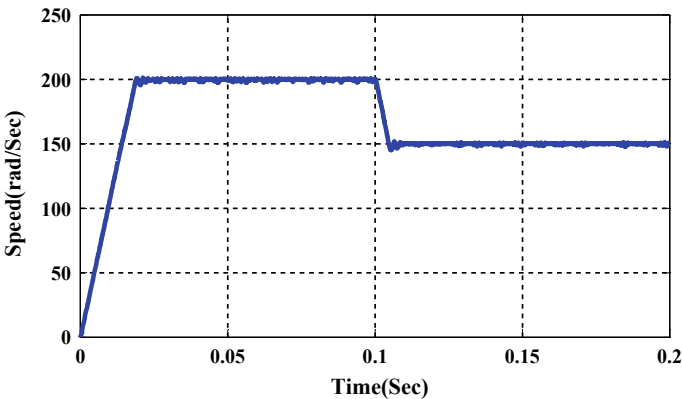


Fig. 7 Rotor speed response for SMC

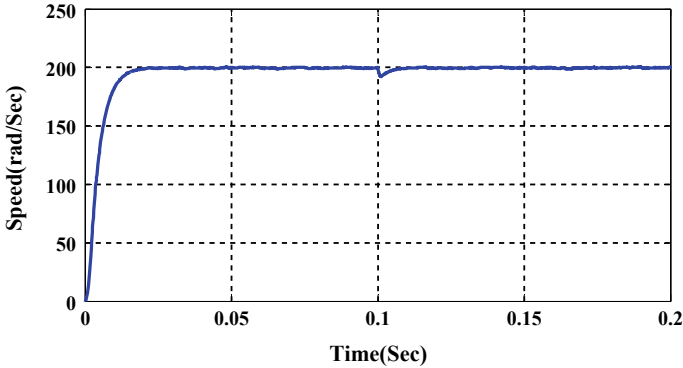


Fig. 8 Rotor speed response for PI controller

4.3 Transient Results with Constant Speed at Step Load Torque

The transient response can also be analyzed of IPMSM drive system by changing the load. Therefore, in this section the applied load torque T_L is increased from 0 to 1 N-m at time $t = 0.1$ s.

4.3.1 For PI Outer Loop Speed Controller

As speed of IPMSM drive is independent of load torque, speed of the machine remains constant at 200 rpm/sec as shown in Fig. 8. Figure 8 clearly depicts that small hops are observed for a small duration due to sudden change in torque.

4.3.2 For SMC Outer Loop Speed Controller

In this Fig. 9 we can observe that IPMSM drive system with SMC controller is capable of eliminating hops that were created due to sudden change in torque 0.1 s. From Fig. 9, it can be concluded that SMC is also insensitive to load variation.

5 Conclusions

In this paper, a sliding mode controller is designed for speed control of IPMSM. So as to affirm the quality of the SMC controller, a performance correlation with a traditional PI controller is additionally given. The feasibility of both the controllers are realized in MATLAB-Simulink environment. Comparative execution examination

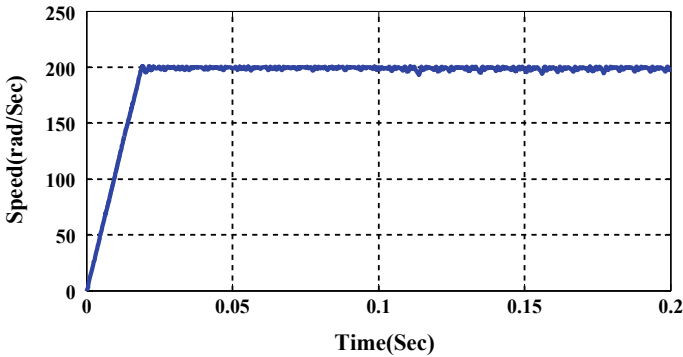


Fig. 9 Rotor speed response for SMC

is done under different working conditions which uncover that SMC sets aside less effort to arrive at the steady-state linearly, in spite of system parameter uncertainty and disturbance in load torque. Therefore, for modern acknowledgment SMCs are favored in drive applications in presence of nonlinearities and system uncertainty.

References

1. Jahns TM, Kliman GB, Neumann TW (1986) Interior permanent-magnet synchronous motors for adjustable-speed drives. *IEEE Trans Ind Appl IA-22*:738–46
2. Su YX, Zheng CH, Duan BY (2005) Automatic disturbances rejection controller for precise motion control of permanent-magnet synchronous motors. *IEEE Trans Ind Electron* 52(3):814–823
3. Li S, Liu Z (2009) Adaptive speed control for permanent-magnet synchronous motor system with variations of load inertia. *IEEE Trans Ind Electron* 56(8):3050–3059
4. Naik AK, Mishra R (2014) A performance analysis scheme by the help of modified hysteresis current controller for PMSM drive. *Int J Recent Trends Eng Technol* 11:386–395
5. Naik AK, Panda AK, Kar SK (2016) Improving the dynamic response during field weakening control of IPMSM drive system using adaptive hysteresis current control technique. *Int J Emerg Electric Power Syst* 17:235–249
6. Naik AK, Panda AK, Kar SK (2018) realisation of adaptive hysteresis current controller for performance improvement of vector control based IPMSM drive system. *Int J Emerg Electr Power Syst* 19(6):1–20
7. Fnaiech MA, Betin F, Capolino G-A, Fnaiech F (2010) Fuzzy logic and sliding-mode controls applied to six-phase induction machine with open phases. *IEEE Trans Ind Electron* 57(1):354–364
8. Chen CS (2010) Tsk-type self-organizing recurrent-neural-fuzzy control of linear micro stepping motor drives. *IEEE Trans Power Electron* 25(9):2253–2265
9. Li THS, Chen CY, Lim KC (2010) Combination of fuzzy logic control and back propagation neural networks for the autonomous driving control of car-like mobile robot systems. In: *Proceedings of SICE annual conference, Taipei*, pp 2071–2076
10. Castillo-Toledo B, Di Gennaro S, Loukianov AG, Rivera J (2008) Hybrid control of induction motors via sampled closed representations. *IEEE Trans Ind Electron* 55(10):3758–3771
11. Wang L, Chai T, Zhai L (2009) Neural-network-based terminal slidingmode control of robotic manipulators including actuator dynamics. *IEEE Trans Ind Electron* 56(9):3296–3304

Performance of Second-Order Generalized Integrator Based Adaptive Filter Under Adverse Grid Conditions



Banishree Misra, Arkadip Majumdar and Sudhananda Pal

Abstract It is a major challenge for the grid-connected power electronic converter circuits to get synchronized with the utility grid when the grid voltage is highly unbalanced and polluted with harmonics. In this situation designing a phase lock loop (PLL) is a challenge to estimate the phase, frequency, and amplitude of the utility voltage. Phase lock loop (PLLs) is a closed-loop synchronization structure where the error signal is generated from the difference of estimated phases and the reference phase values. This paper presents a filtering technique based on adaptive filter called second-order generalized integrator (SOGI). Under transient fault condition when the three-phase grid signal is highly polluted with harmonics and sudden frequency change or voltage dip occurs, it is a critical task to extract the fundamental component of the grid signal. Here for the extraction of the fundamental component from the polluted signal, two adaptive filters using SOGI can be implemented on the stationary $\alpha\beta$ reference frame. To analyze the disturbance rejection capability of the SOGI filter different distortions have been introduced in the three-phase grid signal and the robustness is estimated on the basis of its transient response and harmonic analysis. The simulation results will validate the excellent performance of the filter.

Keywords Adaptive filter · Synchronous reference frame phase locked loop · Robust second order generalized integrator · Dynamic response · Harmonics · Voltage sag

B. Misra (✉) · A. Majumdar · S. Pal
School of Electrical Engineering, KIIT (Deemed to Be University), Bhubaneswar 751024, India
e-mail: bmisrafel@kiit.ac.in

A. Majumdar
e-mail: arkadip18.am@gmail.com

S. Pal
e-mail: sudhanandapal472@gmail.com

© Springer Nature Singapore Pte Ltd. 2020
R. Sharma et al. (eds.), *Innovation in Electrical Power Engineering, Communication, and Computing Technology*, Lecture Notes in Electrical Engineering 630,
https://doi.org/10.1007/978-981-15-2305-2_55

1 Introduction

Maintaining power quality at the point of integration of the grid with the distributed energy sources, i.e., at (PCC) is a major challenge in the recent developments [1–4]. This is mainly due to the presence of power electronic inverters at the integration point of the grid and the distributed energy sources. In this situation, the major task is the precise estimation of the frequency, phase angle, and magnitude of the grid voltage for generation of the reference commands for the grid-connected converters. So the priority is to properly synchronize the grid with the power electronic converter (PEC) to maintain the continuity of grid service even under transient grid faults and adverse grid conditions.

Here the phase-locked loops (PLL) design plays the major role for proper synchronization of PECs with the grid-voltage. Amongst different phase-locked loops (PLL) schemes, synchronous reference frame (SRF) based PLL is the most popular one under healthy condition of operation of the grid.

But once the grid voltage becomes unbalanced and distorted with sudden voltage sag or higher order harmonics and a phase change then SRF-PLL is not able to estimate the phase angle and frequency properly. So, nowadays, the PLLs designed on basis of adaptive resonant filters are gaining popularity because of their robust response to any kind of grid disturbances [5–7]. This paper describes the extraction of the fundamental positive sequence component of the grid voltage, from a signal disturbed with voltage sag or higher order harmonics or a sudden phase change by using adaptive filtering technique based on second-order generalized integrator (SOGI) quadratic signal generator (QSG) in the continuous time-domain [8–10].

This research work is explained as follows. Section 2 provides a structural and operational detail of the second-order generalized integrator (SOGI) in the continuous time-domain. Its dependency on various design parameters was discussed. Section 3 presents the performance analysis of the filter when the grid signal is polluted with harmonics. The results were shown in MATLAB/SIMULINK. In Sect. 4 test cases for different disturbances in the grid signal was analyzed to justify the robustness of the adaptive filter. The results are shown in different reference frames. The harmonic analysis of the extracted fundamental signal was examined. In Sect. 5, the performance of the filter was concluded.

2 Design of Phase Lock Loop Based on Second Order Generalized Integrator

Phase lock loops are the most approved synchronization structures when the utility grid is highly distorted. The basic structural blocks of the phase lock loop are a phase detector (PD), a loop filter (LF), and a voltage-controlled oscillator (VCO) [11] as shown in Fig. 1.

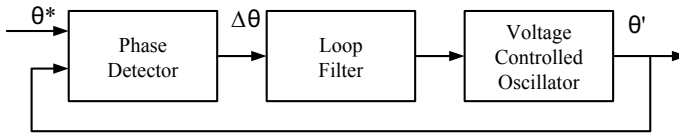


Fig. 1 Structural blocks of the phase lock loop (PLL)

The synchronization structure based on SOGI adaptive filter in the synchronous reference frame is provided in Fig. 2 [12, 13]. Generation of the two in-quadrature signals v'_1 and qv'_1 are shown in Fig. 3. The signal v'_1 has the same magnitude and phase as that of the fundamental input signal v_1 .

Various output to input responses of a SOGI filter is developed for a single sinusoidal grid signal [14, 15]. The transfer function of output to error can be found in (1) as

$$SOGI_{r1}(S) = \frac{v'_1(S)}{k_2 \in'_v(S)} = \frac{k_2 \hat{\omega} S}{S^2 + \hat{\omega}^2} \tag{1}$$

For the SOGI filter, the output to input transfer function will act like a band pass filter given in (2) as

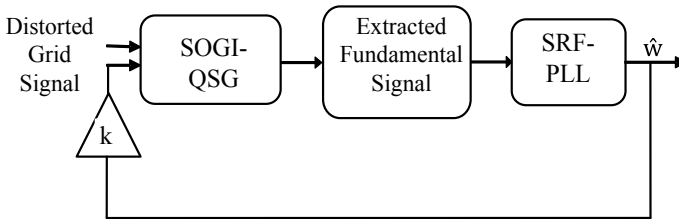


Fig. 2 Synchronization structure based on SOGI-QSG and SRF-PLL

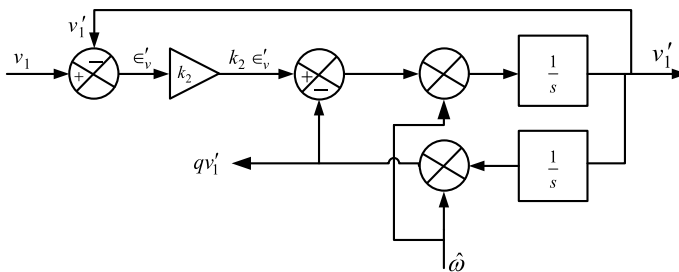


Fig. 3 Internal components of SOGI filter and QSG

$$\text{SOGI}_{bp1}(S) = \frac{v_1'(S)}{v_1(S)} = \frac{k_2 \hat{\omega} S}{S^2 + k_2 \hat{\omega} S + \hat{\omega}^2} \quad (2)$$

Error signal to input signal transfer function behaves like a second order notch filter. This filter is having a zero gain at the centre frequency. The transfer function is represented in (3) as

$$\text{SOGI}_{nf1}(S) = \frac{k_2 \epsilon_v^1(S)}{v_1(S)} = \frac{S^2 + \hat{\omega}^2}{S^2 + k_2 \hat{\omega} S + \hat{\omega}^2} \quad (3)$$

The damping factor (ζ_1), time constant (τ) and settling time (T_s) of SOGI based bandpass filter for separation of positive and negative sequence components [16, 17] can be estimated using (4):

$$\begin{aligned} &\text{Damping factor, time constant, settling time,} \\ \zeta_1 = \frac{k_2}{2} \quad \tau = \frac{2}{k_2 \hat{\omega}} \quad T_s = \frac{9.2}{k_2 \hat{\omega}} \end{aligned} \quad (4)$$

From the equations discussed above, it can be summarized that both the damping factor and the settling time of the extracted fundamental signal are dependent on the gain value. So a proper trade-off must be decided while deciding the value of damping factor and gain value. As seen the T_s is inversely proportional to product of gain and frequency [15]. So, it is evident that in SOGI filter bandwidth depends only upon the gain (k_2) and it is independent of the center frequency $\hat{\omega}$, which makes it suitable for variable-frequency applications.

3 Performance Analysis of SOGI-QSG-Phase-Lock-Loop

In this section, the performance of the SOGI-QSG filter is analyzed from the derived transfer functions and their frequency response is evaluated in MATLAB/SIMULINK environment. The assumed grid signal is distorted with fifth and seventh order harmonics as shown in Fig. 4. Using the SOGI-QSG filter the fundamental component of the grid signal is extracted from the harmonically polluted signal.

From the fundamental three-phase balanced sinusoidal signal extracted from distorted grid signal as shown in Fig. 5 it can be concluded that the settling time of the filter is within one to two cycles of the supply voltage which shows its quick response to grid disturbance (polluted with harmonics). The THD of the calculated fundamental component as presented in Fig. 6, is 1.2% and it is well within the IEEE limit. The frequency response of different transfer functions of the SOGI filter for several gain values are presented in Figs. 7, 8, 9 respectively. As seen in Fig. 7, SOGI based

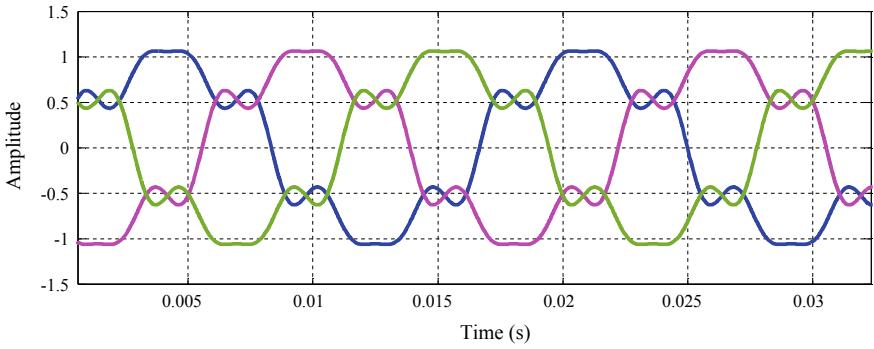


Fig. 4 Distorted grid signal (three phase) with 5th and 7th order harmonic

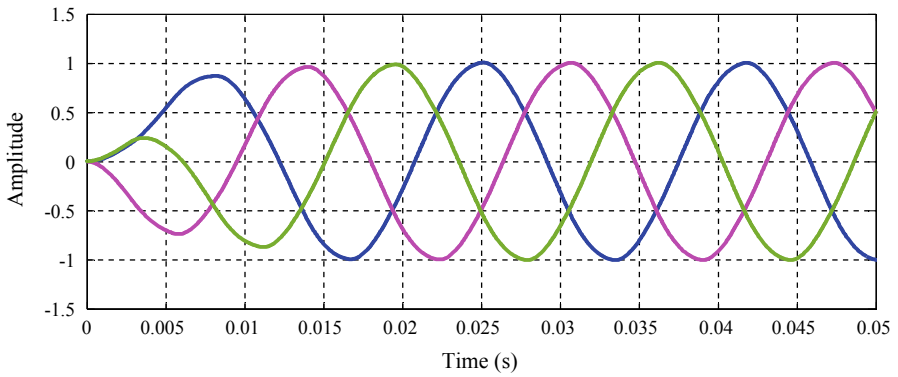


Fig. 5 Fundamental three phase balanced sinusoidal signal extracted from distorted grid signal using SOGI based adaptive filter

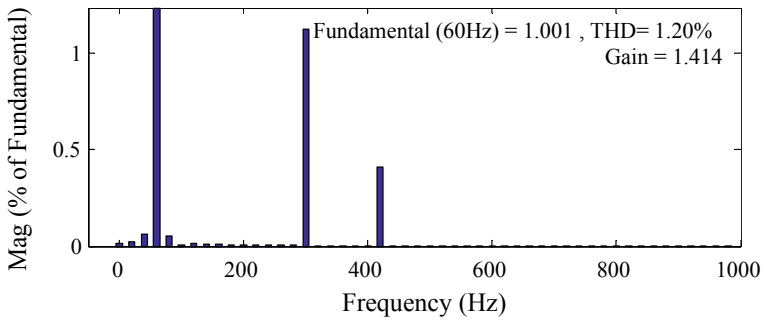


Fig. 6 Harmonic analysis of the extracted fundamental component with SOGI technique

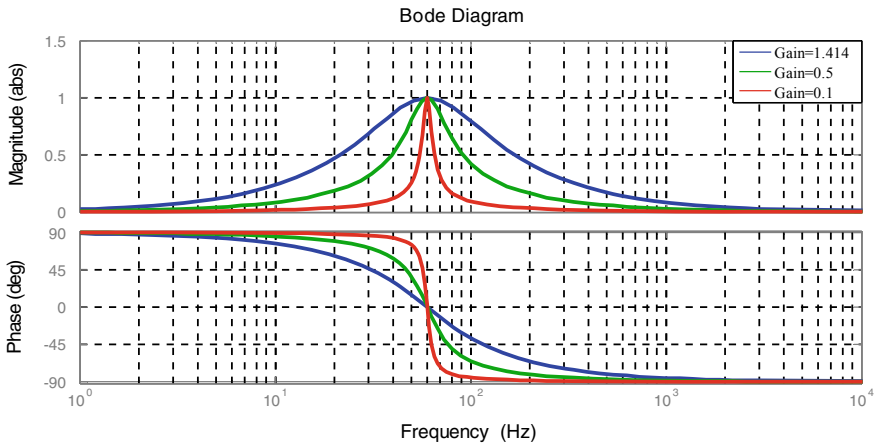


Fig. 7 Bode plots (bandpass filter) of SOGI (in phase signal)

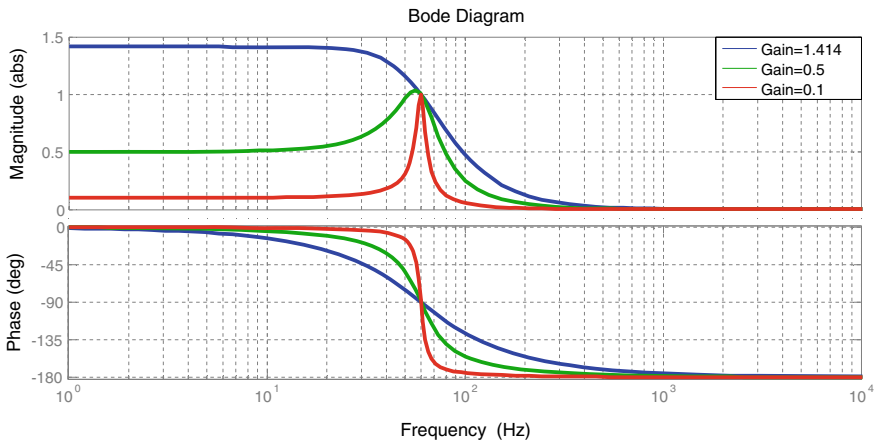


Fig. 8 Bode plot (band pass filter) of SOGI (quadrature signal)

adaptive filter achieves stability in a comparatively wider frequency band centred around the resonance frequency. The width of the band depends on the value of gain k_2 . A higher value of k_2 results in a wider band whereas a lower value of k_2 results a very narrow band. So it can be concluded that lower gain value will decrease the band pass which will result in heavy filtering but slow dynamic response. A proper trade-off between gain value and dynamic stability of the system has to be decided to justify the robustness of the adaptive SOGI filter.

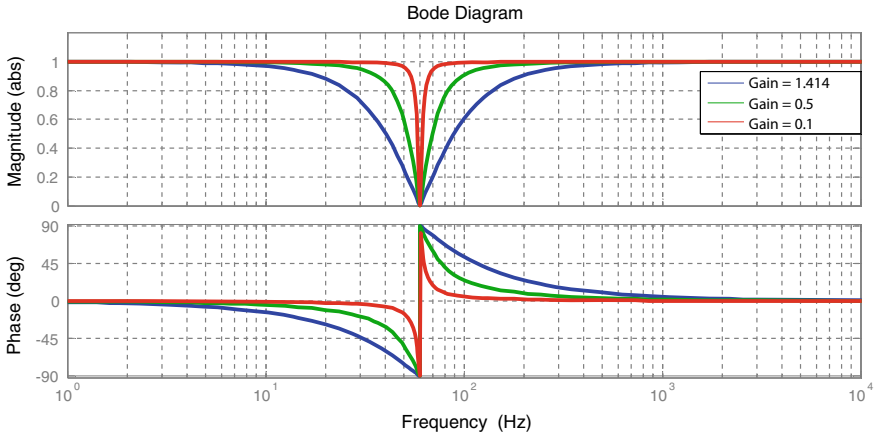


Fig. 9 Bode plot of error to input (adaptive notch filter) transfer function of SOGI filter

4 Performance Analysis of Robust SOGI-QSG-Phase-Lock-Loop from Simulation Result

The robustness of the SOGI-QSG filter is evaluated for different test conditions in MATLAB/SIMULINK environment considering a distorted and polluted grid signal. Several disturbances are applied at different steps for a particular duration. Different types of disturbances in the grid voltage considered here are balanced voltage sag, the introduction of fifth and seventh order harmonics and sudden change in supply frequency. The normal grid voltage assumed is having a balanced voltage of amplitude 1 p.u and frequency of 60 Hz. A sudden balanced three-phase voltage sag of 0.6 p.u occurs at 0.05 s and continues up to 0.1 s. Again balanced voltage amplitude of 1 p.u continues for 0.05 s. After a time-lapse of 0.15 s, 5th harmonic component of magnitude 0.2 p.u & 7th harmonic component of magnitude 0.143 p.u with a balanced voltage sag of 0.6 p.u fundamental voltage component was introduced for 0.05 s. Again balanced voltage amplitude of 1 p.u is maintained for 0.05 s. Again a sudden frequency change (from 60 to 65 Hz) along with balanced voltage sag of 0.6 p.u occurs at 0.25 s and continues up to 0.3 s. Finally, the balanced voltage amplitude of 1 p.u is maintained from 0.3 to 0.35 s. For all the above-mentioned test conditions the robustness of the SOGI-QSG filter was studied to evaluate the system stability.

Figure 10 shows the grid voltage distorted with voltage sag, harmonics and sudden frequency change. After the implementation of the SOGI-QSG filter between the distorted grid signal and the SRF-PLL, the response was studied. In the case of usual SRF-PLL technique, the grid voltage is transformed from the stationary reference frame (abc) to the synchronously rotating reference frame (dq) by means of Park's transformation. The output d -signal of SRF-PLL with filters is dc value and its

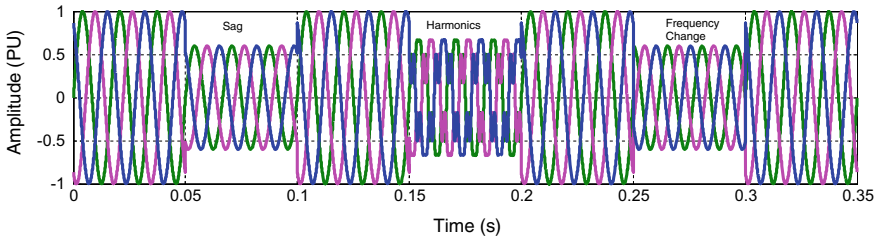


Fig. 10 Grid voltage distorted with voltage sag, harmonics and frequency change

magnitude equal to amplitude of positive sequence signal and the output q -signal is zero which confirms that no negative sequence and harmonics are injected as an input to SRF-PLL. For all three cases of disturbance, the settling time is provided in Table 1.

The results of the extracted signal in all three reference frames are as shown in Figs. 11, 12 and 13 and the phase angle and magnitude of the extracted signal is according to the requirement. The extracted d -component of voltage (v_d) will provide the magnitude of the voltage and it is shown in Fig. 13. For a gain value of 1.414 the filter performance is quite good and it can be verified from Table 1. The THD

Table 1 Response time and THD analysis of extracted signals

Value of K_2	Case study (step change in)	Total harmonic distortion (THD) (%)	Settling time (s) (after step change)
1.414	Three phase voltage sag	0.09	0.005
1.414	Voltage sag with harmonics (fifth and seventh)	2.0	0.005
1.414	Voltage sag and frequency change	0.16	0.017

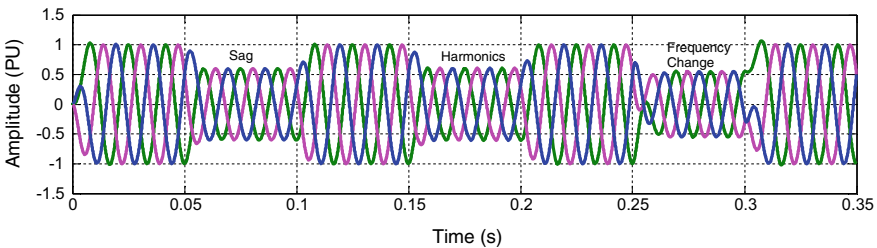


Fig. 11 Robust response of SOGI-QSG filter to voltage sag, harmonics and frequency change in abc -reference frame

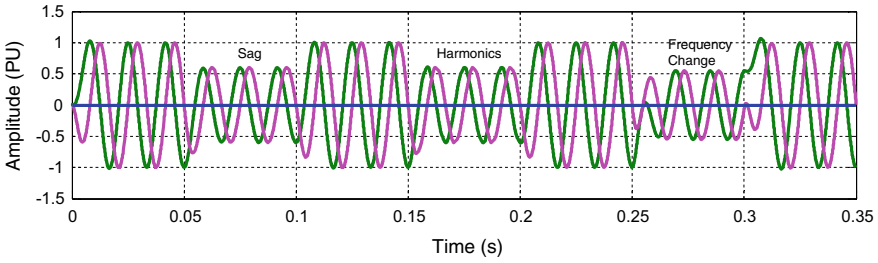


Fig. 12 Robust response of SOGI-QSG filter to voltage sag, harmonics and frequency change in $\alpha\beta$ -reference frame

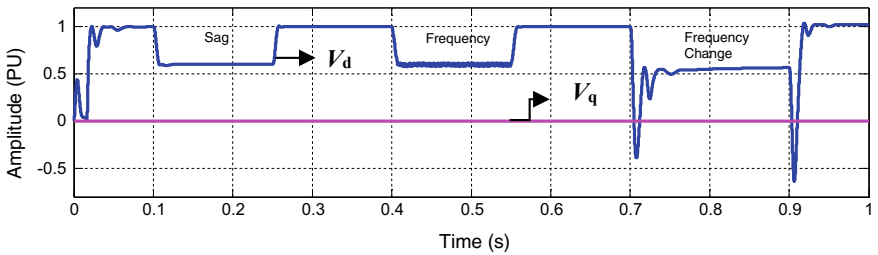


Fig. 13 Robust response of SOGI-QSG filter to voltage sag, harmonics and frequency change in dq -reference frame

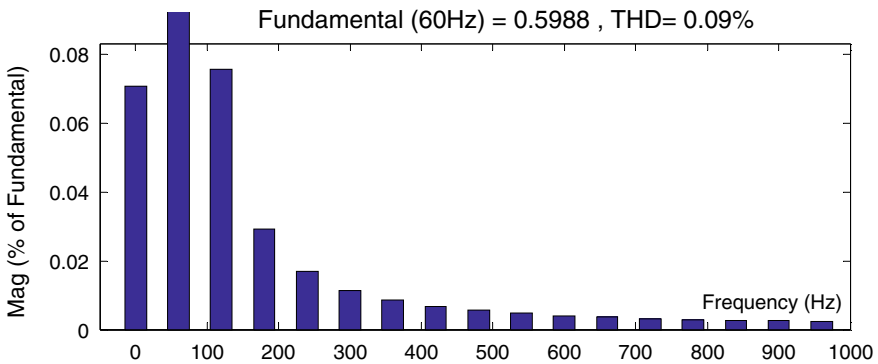


Fig. 14 Estimation of THD of extracted signal (three-phase voltage sag)

content in the extracted signal in all the three distorted conditions are within IEEE limit and the dynamic response time is also very fast. The total harmonic analysis of extracted signal for the case of sag, harmonics and frequency change are shown in Figs. 14, 15 and 16.

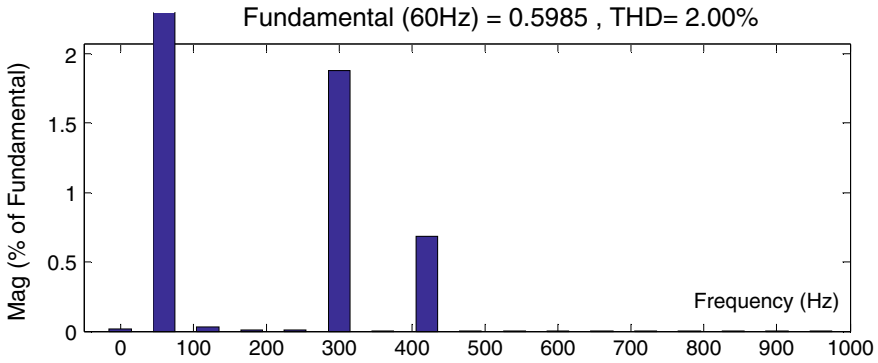


Fig. 15 Estimation of THD of extracted signal (sag with harmonics)

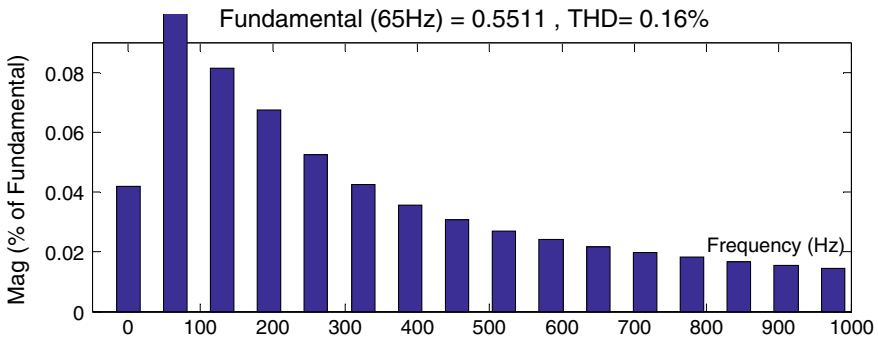


Fig. 16 Estimation of THD of extracted signal (sag with frequency change)

5 Conclusion

In this paper, the robustness of second-order adaptive filter with generalized integrator (SOGI) based phase lock loop was discussed. The effectiveness of the filter was examined by extracting a fundamental signal from a polluted signal containing 5th and 7th order harmonics. To study its disturbance rejection capability and dynamic response, different transient disturbances were considered. The distortions in the grid signal considered are balanced voltage sag, appearance of harmonics and sudden change in frequency. The response of SOGI-QSG filter to all the disturbances was well studied based on their settling time response, and presence of total harmonic distortion. The role of gain value and damping factor on the system response was analyzed from the frequency response of the SOGI-QSG filter. The ability of this adaptive filter to operate in variable frequency environment makes it most suitable for advanced synchronization structures.

References

1. Rodríguez P, Luna A, Muñoz-Aguilar R, Etxeberria-Otadui I, Teodorescu R, Blaabjerg F (2012) A Stationary reference frame grid synchronization system for three-phase grid-connected power converters under adverse grid conditions. *IEEE Trans Power Electron* 27:99–112
2. Kaura V, Blasko V (1997) Operation of a phase locked loop system under distorted utility conditions. *IEEE Trans Ind Appl* 33:58–63
3. Ciobotaru M, Teodorescu R, Blaabjerg F (2006) A new single-phase PLL structure based on second order generalized integrator. In: 37th IEEE PESC/IEEE power electronics specialists conference, pp 1–6
4. Nayak B, Misra B, Mohapatra A (2018) A proposed reference current signal generation technique for shunt active power filter. *J Eng Sci Technol* 13:1834–1849
5. Misra B, Nayak B (2018) Modified second order adaptive filter for grid synchronization and reference signal generation. *Int J Renew Energy Res* 8:428–437
6. Chung S-K (2000) A phase tracking system for three phase utility interface inverters. *IEEE Trans Power Electron* 15:431–438
7. Rodriguez F, Bueno E, Aredes M, Rolim L, Neves F, Cavalcanti M (2008) Discrete-time implementation of second order generalized integrators for grid converters. In: Proceedings of IEEE 34th annual conference of industrial electronics, pp 176–181
8. Rodriguez P, Luna A, Candela I, Mujal R, Teodorescu R, Blaabjerg F (2011) Multiresonant frequency-locked loop for grid synchronization of power converters under distorted grid conditions. *IEEE Trans Ind Electron* 58:127–138
9. Blaabjerg F, Teodorescu R, Liserre M, Timbus A (2006) Overview of control and grid synchronization for distributed power generation systems. *IEEE Trans Ind Electron* 53(5):1398–1409
10. Gardner F (2005) *Phaselock techniques*. Wiley-Interscience, Hoboken
11. Jaalam N, Rahim N, Bakar A, Tan C, Haidar A (2016) A comprehensive review of synchronization methods for grid-connected converters of renewable energy source. *Renew Sustain Energy Rev* 59:1471–1481
12. Wang Y, Li Y (2013) Three-phase cascaded delayed signal cancellation PLL for fast selective harmonic detection. *IEEE Trans Ind Electron* 60(4):1452–1463
13. Karimi-Ghartemani M, Irvani M (2004) A method for synchronization of power electronic converters in polluted and variable-frequency environments. *IEEE Trans Power Syst* 19(3):1263–1270
14. Widrow B (1975) Adaptive noise cancelling: principle and applications. *Proc IEEE* 63(12):1692–1716
15. Teodorescu R, Liserre M, Rodriguez P (2011) *Grid converters for photovoltaic and wind power system*. IEEE, Wiley
16. Misra B, Nayak B (2017) Performance analysis of robust second order adaptive filters for power quality improvement in a polluted grid. In: 2nd international conferences for convergence of technology (I2CT), pp 808–813
17. Misra B, Nayak B (2017) Second order generalized integrator based synchronization technique for polluted grid conditions. In: 2nd international conferences for convergence of technology (I2CT), pp 1080–1084

Stability Improvement in Power System Integrated with WECS Using Dolphin Echolocation Optimized Hybrid PID Plus FLC-Based PSS



Prakash K. Ray, Shiba R. Paital, Lalit Kumar, Bhola Jha, Sanjay Gairola and Manoj Kumar Panda

Abstract This paper focuses on the stability study of power system integrated with wind energy conversion system (WECS) under various operating conditions. Being a stochastic variation in the input wind speed, WECS affects the stability of the power system. Hence, a hybrid proportional-integral-derivative plus fuzzy logic controller (hPID plus FLC)-based power system stabilizer (PSS) is adopted for improving the stability in single machine infinite bus (SMIB) power system under different operating conditions. The parameters of the proposed hPID plus FLC are optimized using dolphin echolocation optimization (DEO) technique. Several investigations are carried out for assessing the superiority of the proposed technique. It is evident from the graphical as well as the quantitative comparative results using integral of time multiplied absolute error (ITAE), maximum overshoot and the settling time that the proposed DEO tuned hPID plus FLC gives much better performance over GWO and PSO tuned hPID plus FLC controllers.

Keywords Dolphin echolocation · PID controller · Hybrid PID plus FLC controller · PSS · SMIB · Transient stability · WECS

P. K. Ray (✉)

Department of Electrical Engineering, CET Bhubaneswar, Bhubaneswar, India
e-mail: pkrayiii@gmail.com

S. R. Paital

Department of Electrical Engineering, IIIT Bhubaneswar, Bhubaneswar, India
e-mail: shiba.paital@gmail.com

L. Kumar · B. Jha · S. Gairola · M. K. Panda

Department of Electrical Engineering, GBPIET, Pauri Garhwal, India
e-mail: lalitnbd@gmail.com

B. Jha

e-mail: bholajhaeee@gmail.com

S. Gairola

e-mail: sanjaygairola@gmail.com

M. K. Panda

e-mail: pandagbpec@gmail.com

© Springer Nature Singapore Pte Ltd. 2020

R. Sharma et al. (eds.), *Innovation in Electrical Power Engineering, Communication, and Computing Technology*, Lecture Notes in Electrical Engineering 630,
https://doi.org/10.1007/978-981-15-2305-2_56

1 Introduction

Power systems can be termed as multivariable, complex and nonlinear systems which constitute of several generators, transformers, transmission lines and various protective devices. Disturbances due to faults, load switching, line outages, etc. are common which give rise to the growth of low-frequency oscillations (LFOs) in the power system. LFOs are small in magnitude (0.2–3 Hz) and can affect power system stability, reliability and also power transfer capability. This happens due to a mismatch between generation and demand of power [1]. In the literature, efforts are made especially on damping out LFOs through PSSs. It basically senses the variation of speed of generator, process it and produces the required excitation signal via automatic voltage regulator (AVR) loop for producing a rotor torque for damping out electromechanical oscillations [2, 3]. But, its performance degrades with continuous load perturbation, severe disturbances and re-tuning of parameters with respect to varying operating conditions. Therefore, optimum selection of PSS parameters is necessary. Several approaches like proportional-integral-derivative (PID) control, pole placement technique, adaptive control, self-tuning regulators along with some robust control techniques like sliding mode control, linear matrix inequality (LMI), H-infinity control, H2/H-infinity, etc. [4, 5] are proposed previously to improve the stability. Also soft computing approaches like genetic algorithm (GA), simulated annealing (SA), particle swarm optimization (PSO), BAT search algorithm, backtracking search algorithm, cuckoo search optimization (CSO), firefly algorithm, etc. are applied in literatures for optimizing parameters of PSS [6–8]. But oscillations still persists in the power system. In order to overcome the limitations, adaptive control approach such as fuzzy logic control (FLC) is adopted for designing the PSS [9, 10]. Furthermore, growth in wind power technology is increasing day by day. But penetration of WECS generates stability issues and must be taken care of. The stochastic variation in the output of WECS introduces uncertainties and affects power system stability especially small signal stability. Many efforts have made in past literatures for stability improvement in renewable energy integrated power system [11, 12]. In this paper, a hybrid FLC-based PID-PSS controller is proposed in this study for improvement of stability in SMIB power system under various operating conditions. The performance of the proposed controller is improved based on the optimum selection of its gain parameters using DEO and PSO. The simulations are done in MATLAB/Simulink software. It is evident from the simulation results that the proposed DEO optimized hPID plus FLC-PSS gives much better performance over GWO and PSO optimized hPID plus FLC-PSS.

2 Power System Modelling

2.1 Single Machine Infinite Bus (SMIB) System

The schematic representation of SMIB system considered for stability analysis was presented in Fig. 1. The nonlinear equations describing the system dynamics derived by neglecting resistances are presented below [1]:

$$\dot{\delta} = \omega_0(\omega - 1) \tag{1}$$

$$\dot{\omega} = (P_m - P_e - D\Delta\omega) / M \tag{2}$$

$$\dot{E}_{fd} = [-E_{fd} + K_a(V_{ref} - V_t)] / T_a \tag{3}$$

$$\dot{E}'_q = (-E_q + E_{fd}) / T'_{do} \tag{4}$$

$$T_e = v_q i_q + v_d i_d \tag{5}$$

The linearized system equations of the considered system can be derived by linearizing the differential equations about an operating point are as follows [2]:

$$\Delta\dot{\delta} = \omega_0\Delta\omega \tag{6}$$

$$\Delta\dot{\omega} = (-\Delta P_e - D\Delta\omega) / M \tag{7}$$

$$\Delta\dot{E}'_q = (-\Delta E_q + \Delta E_{fd}) / T'_{do} \tag{8}$$

$$\Delta\dot{E}_{fd} = -(1/T_a)\Delta E_{fd} - (K_a/T_a)\Delta V \tag{9}$$

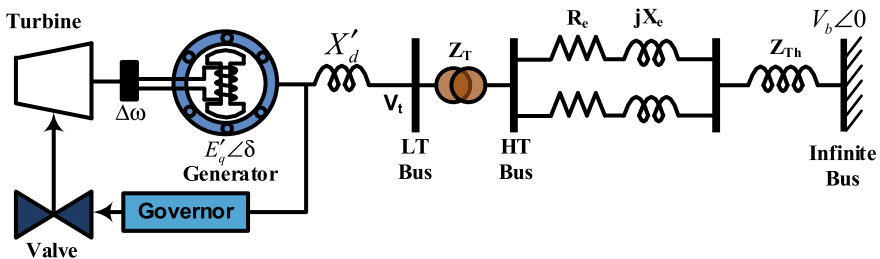


Fig. 1 Configuration of SMIB power system

In state space, the above system expressions can be represented by assuming A , B as system and input matrix can be obtained as follows:

$$\dot{X} = f(X, U) \quad (10)$$

$$\dot{X} = AX + BU \quad (11)$$

$$\begin{bmatrix} \Delta \dot{\delta} \\ \Delta \dot{\omega} \\ \Delta \dot{E}'_q \\ \Delta \dot{E}'_{fd} \end{bmatrix} = \begin{bmatrix} 0 & \omega_0 & 0 & 0 \\ -\frac{K_1}{M} & 0 & -\frac{K_2}{M} & 0 \\ -\frac{K_4}{T_f} & 0 & -\frac{K_3}{T_f} & -\frac{1}{T'_{do}} \\ -\frac{K_a K_5}{T_a} & 0 & -\frac{K_a K_6}{T_a} & -\frac{1}{T_a} \end{bmatrix} \begin{bmatrix} \Delta \delta \\ \Delta \omega \\ \Delta E_q \\ \Delta E_{fd} \end{bmatrix} + \begin{bmatrix} 0 & 0 \\ \frac{1}{M} & 0 \\ 0 & 0 \\ 0 & \frac{K_a}{T_a} \end{bmatrix} \begin{bmatrix} \Delta T_m \\ \Delta V_{ref} \end{bmatrix} \quad (12)$$

where X and U are the corresponding vectors of state variable and input variable. δ represents the rotor angle whereas ω , ω_0 and $\Delta\omega$ represent rotor speed, base speed and change in speed of the generator. P_m and P_e mechanical and electrical power. D and M are damping coefficient and inertia constant. E'_{fd} and E'_q represent field and internal voltage of the generator whereas E_q is the q -axis voltage. T'_{do} represents open circuit field time constant whereas T_e represents electrical torque. v_d , i_d and v_q , i_q are the corresponding voltages and currents of d - and q -axis. K_a and T_a represent gain and time constant of excitation system. V_{ref} , V_t represents reference and terminal voltage. $K_1 - K_6$ represents the constants of the Phillips-Heffron model which interrelates rotor speed and voltage of the machine.

2.2 Conventional Power System Stabilizer

The function of PSS is to supply the required amount of torque to the exciter circuit of the synchronous machine for damping low-frequency oscillations. It is composed of a stabilizer gain (K_{PSS}) is considered for determining required damping to the PSS, a washout filter (T_w) which acts like a high pass filter, limiters for preventing over excitation of the exciter, lead-lag dynamic compensators (T_1 , T_2 , T_3 , T_4) for compensating lag between output and torque of PSS. The deviation in speed ($\Delta\omega$) sensed and supplied as input to PSS whereas its output is the correcting voltage signal $U(s)$. The mathematical modelling of the PSS is given by [4]:

$$U(s) = K_{PSS} \left(\frac{sT_w}{1 + sT_w} \right) \left(\frac{1 + sT_1}{1 + sT_2} \right) \left(\frac{1 + sT_3}{1 + sT_4} \right) \Delta\omega(s) \quad (13)$$

2.3 Modelling of Wind Energy Conversion System

Wind energy conversion system (WECS) is used for converting kinetic energy of wind into electrical energy. The output of WECS primarily relies on the wind speed (V_W) which is a combination of base wind speed (V_{WB}), gust wind speed (V_{WG}), ramp wind speed (V_{WR}) and noise wind speed (V_{WN}).

Mathematically, wind speed is computed as follows [10]:

$$V_W = V_{WB} + V_{WG} + V_{WR} + V_{WN} \quad (14)$$

The output power of WECS (P_w) is expressed by the following mathematical expression:

$$P_w = \frac{1}{2} C_p(\lambda) \rho A v_w^3 \quad (15)$$

where C_p denotes power coefficient, λ , ρ , A represent tip speed ratio, air density and swept area. The transfer function of WECS formulated by neglecting the nonlinearities is given below:

$$G_{WECS}(s) = \frac{K_{WECS}}{1 + sT_{WECS}} \quad (16)$$

where K_{WECS} and T_{WECS} represent gain and time constant of the WECS.

3 Structure of Proposed Controllers

3.1 Proportional-Integral-Derivative Controller

PID controllers are the most popular feedback controllers because of its simplest design and less parameters. The output of the PID controller depends on its gains such as proportional gain (K_P), integral gain (K_I) and derivative gain (K_D). A washout filter having washout gain (K_W) was also included with the PID controller for eliminating the unwanted signals. In this paper, washout gain (K_W) is considered as 10 s [4].

The mathematical modelling of PID controller can be computed as follows;

$$H(s) = \frac{sT_W}{1 + sT_W} \left(K_P + \frac{K_I}{s} + sT_D \right) \quad (17)$$

PID being a linear controller is unable to handle uncertainties. Hence to overcome this demerit, fuzzy logic system is combined with PID controller which can be used as a stabilizer. Fuzzy logic controller has simplest structure and it can handle

nonlinearities efficiently without a mathematical model. It can adjust its parameters as per the operating conditions [5].

3.2 Hybrid PID Plus FLC Controller

Hybrid PID plus FLC controller is a modification of PID controller which combines the effect of fuzzy logic controller for its control action [13]. The schematic diagram of excitation system and the proposed hPID plus FLC scheme were presented in Fig. 2a–b. The FLC follows its basic procedures such as fuzzifier, decision-making, rule base and defuzzifier. In this paper, a Sugeno type fuzzy inference mechanism was used, and for an economic point of view, triangular type membership functions at interval $[-1, 1]$ are considered. In this paper, 25 rules with 05 linguistic variables such as EN, MN, ZE, MP and EP which represent excess negative (EN), medium negative (MN), zero (ZE), medium positive (MP) and excess positive (EP) are considered. In this paper, a triangular MFs are adopted due to its ability of handling uncertainties and imprecise information in a logically correct manner. The rule base of the presented scheme was presented in Table 1. The fuzzy membership function is shown in Fig. 1c, respectively. In the above figure, $\Delta\omega$ and $p(\Delta\omega)$ represent change in rotor speed and its derivative, T_W is the washout time constant, K_P , K_I and K_D are the corresponding gains of the PID controller. K'_p , K'_I and K'_D are the auxiliary gains generated from

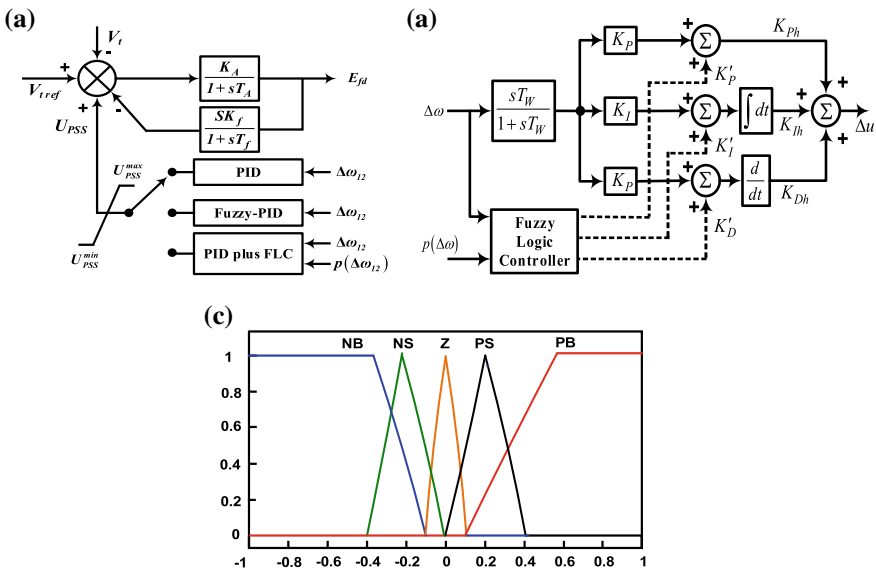


Fig. 2 Schematic diagram of **a** excitation system **b** proposed hybrid PID plus FLC controller **c** membership function

Table 1 Rule base

$\Delta\omega$	$p(\Delta\omega)$				
	EN	MN	ZE	MP	EP
EN	ZE	MN	EP	EP	EP
MN	MP	ZE	MP	EP	EP
ZE	EN	MN	ZE	MP	EP
MP	EN	EN	MN	ZE	EN
EP	EN	EN	EN	EP	ZE

the fuzzy logic controller. The gains of PID controller and the auxiliary gains from the fuzzy logic controller were further updated as follows [13].

$$K_{Ph} = K_P + K'_P; K_{Ih} = K_I + K'_I; K_{Dh} = K_D + K'_D \tag{18}$$

4 Objective Function

Hybrid PID plus FLC controller is designed for minimizing low-frequency oscillations in the power system followed by a disturbance for transient stability enhancement. Generally, these oscillations are produced due to speed of rotor, rotor angle and tie-line power. Therefore, minimizing any of these quantities could be chosen as the objective. In this paper, ITAE of speed deviation ($\Delta\omega$) is selected as the objective function. The objective function of the proposed control scheme can be formulated as follows [4];

$$J = \int_0^{t_{sim}} |\Delta\omega| \cdot t \cdot dt \tag{19}$$

Minimize J

Subject to

$$K_P^{max} \leq K_P \leq K_P^{min}; K_I^{max} \leq K_I \leq K_I^{min}; K_D^{max} \leq K_D \leq K_D^{min} \tag{20}$$

where max and min represent maximum and minimum values of the constants, ' t_{sim} ' is the simulation time, $\Delta\omega_L$ and $\Delta\omega_I$ represent local and inter-area modes of oscillations.

5 Dolphin Echolocation Optimization Technique

Dolphin echolocation optimization is a newly developed nature-inspired metaheuristic technique proposed by Karveh and Farhoudi [14]. It mimics the foraging strategy of bottlenose dolphins. While echolocating, dolphin produces random sound signals for identifying the prey through the high-frequency bounced echoes. High-frequency sound waves are emitted by dolphins and get bounced back as echoes after being striking the prey. The varying strength of echoes and the gap of time help for predicting the distance and direction. The intensity of producing clicks increases with the closeness on object of interest. They use a kind of voice called sonar for locating its target. Initially, search for their prey starts randomly. Once the prey is detected, then dolphin increases their clicks for concentrate near the discovered position of prey.

The process of dolphin echolocation optimization algorithm is explained below [14]:

1. Initialize the position of dolphins.
2. Calculate the predefined probability (PP) of dolphins using the following expression:

$$PP(\text{Loop}_i) = PP_1 + (1 - PP_1) \frac{\text{Loop}_i^{\text{Power}} - 1}{(\text{Loops Number})^{\text{Power}} - 1} \quad (21)$$

3. Obtain the fitness value of each location and replace if the current fitness value is better than the previous one.
4. Allocate the best location with others as per the distribution.
5. Obtain the accumulative fitness (AF) by summing all assigned fitness values and add minimal value ε to the accumulative fitness matrix.
6. Calculate the magnitude of ε as per the following expression:

$$AF = AF + \varepsilon \quad (22)$$

7. Obtain the best location and set AF value to zero.
8. Obtain the probability of AF (P_{ij}) by the following expression:

$$P_{ij} = AF_{ij} / \sum_{i=1}^{\text{Max}A_j} AF_{ij} \quad (23)$$

where AF_{ij} is the accumulative fitness of i th alternative at j th dimension; $\text{Max}A_j$ represent maximum alternative value.

9. Assign percentage of PP of loop to obtain the best location and pass the values to calculate P_{ij} .
10. Repeat the echolocation process until the stopping criteria is met.

6 Simulation Results and Discussions

In this section, simulation results are presented for the stability analysis in SMIB system integrated with WECS with design of robust DEO optimized hPID plus FLC-PSS, GWO and PSO optimized hPID plus FLC-PSS. The linearized model of a SMIB power system which is taken in the current stability analysis is being developed using MATLAB/Simulink. The accumulative fitness and probability curve representing the variation in the gain values of hPID plus FLC controller optimized by DEO technique for the dynamic behaviour of the system were presented in Fig. 3a–b. Different components of the power system with the respective parameters are being included in the Appendix section. Different gain values of the PID controller optimized by DEO and PSO technique were presented in Table 2.

Three case studies considered for the stability analyses are given below:

- Case 1: Fixed wind power generation with variable power generation
 - (i) $P_{WECS} = 0.4$ p.u. and $P_g = 1$ p.u. (ii) $P_{WECS} = 0.4$ p.u. and $P_g = 0.4$ p.u.
- Case 2: Variable wind power generation with variable power generation
 - (i) $P_{WECS} = 0.2$ p.u. and $P_g = 0.8$ p.u. (ii) $P_{WECS} = 0.6$ p.u. and $P_g = 0.5$ p.u.
- Case 3: Random variation in wind speed.

The simulated results for the three aforementioned case studies are shown in Figs. 4, 5, 6, 7 and 8, respectively, which shows active power deviation and speed deviation for different operating conditions. It is analysed from the figures that due to a change in operating conditions, system responses deviated from their nominal value. But, due to a quick action of the proposed hPID plus FLC-based PSS, the responses settle down, and oscillation is minimized to stay within the specified limit. From the comparative results, it is observed that the DEO optimized hPID plus FLC-PSS shows much better performance with lesser settling time and peak overshoot

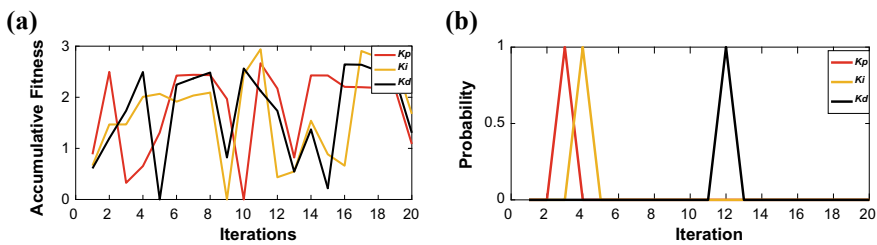


Fig. 3 a Accumulative fitness b probability curve

Table 2 Optimal gain values

Techniques	K_p	K_i	K_d
DEO technique	3.88	5.44	0.44
GWO technique	3.56	2.57	0.62
PSO technique	2.24	6.35	4.98

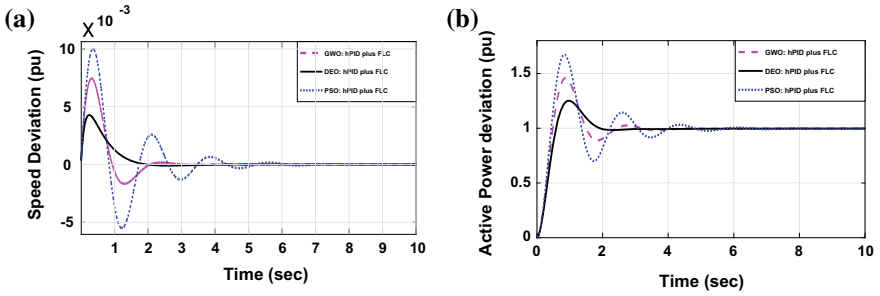


Fig. 4 a Speed and active power deviation for case-I, condition-I

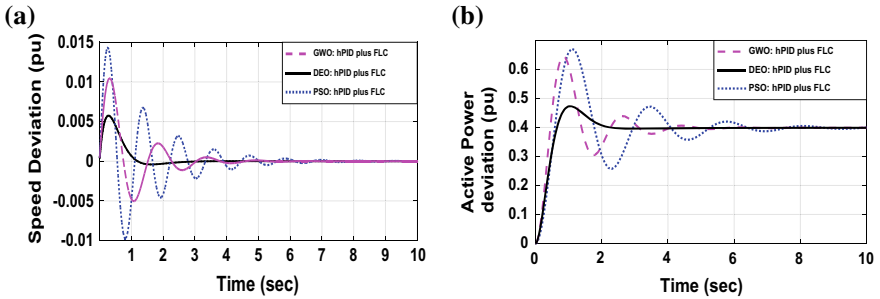


Fig. 5 a Speed and active power deviation for case-I, condition-II

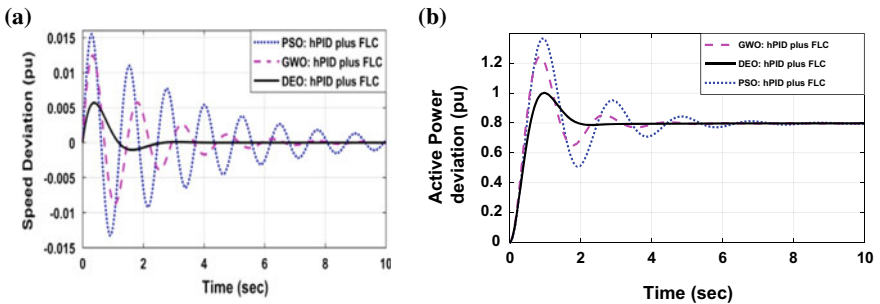


Fig. 6 a Speed and active power deviation for case-II, condition-I

as compared to the GWO and PSO optimized hPID plus FLC-PSS controller. Of course, this is being achieved by an effective reactive power management so that the reactive power generated by the system matches with that of the load demand.

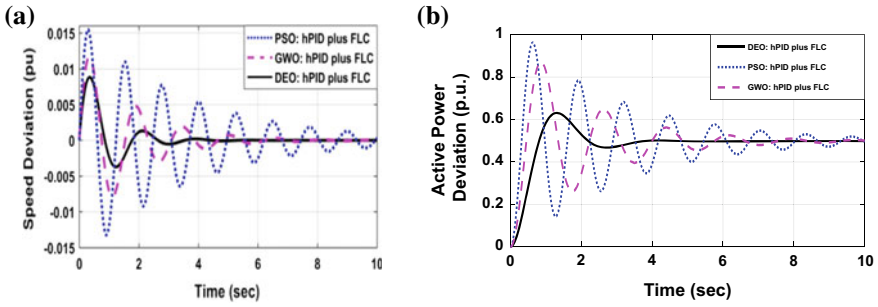


Fig. 7 a Speed and active power deviation for case-II, condition-II

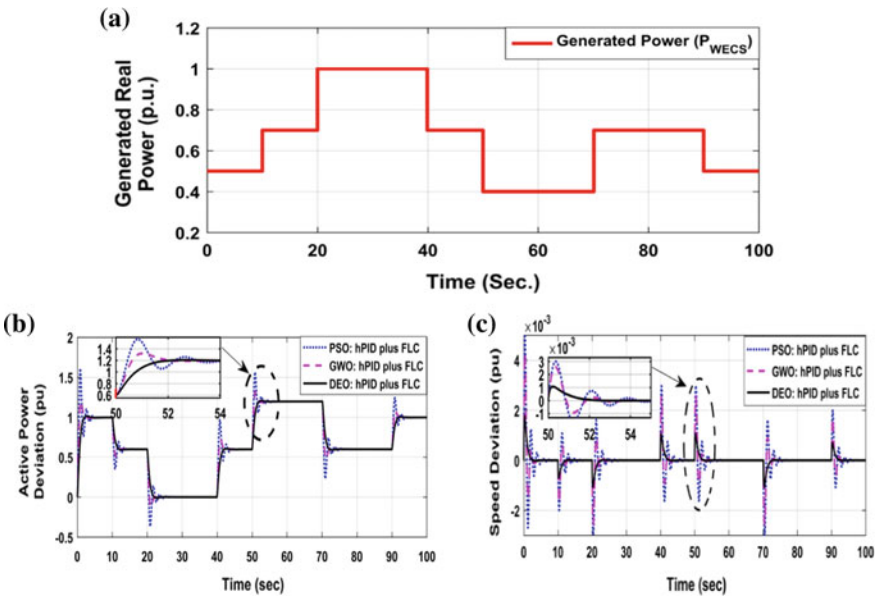


Fig. 8 a Generated active power b active power deviation c speed deviation for case-III

7 Conclusion

The stability study in SMIB power system integrated with WECS is presented in this paper under varying operating scenarios. Variation in wind power generation and random wind speed are taken as the input disturbance to study the robustness of the proposed DEO optimized hPID plus FLC-PSS, GWO optimized hPID plus FLC-PSS and PSO optimized hPID plus FLC-PSS for enhancement in small signal stability. It is observed that the proposed controller stabilizes the low-frequency oscillations quickly with reduced settling time and peak overshoot as compared to that of the others at different operating conditions.

Appendix

Single machine infinite bus power system: $M = 2H = 0.8$ MJ/MVA; $D = 0$; $T'_{do} = 5.21$; $X_d = 1.9$; $X_q = 1.6$; $x'_d = 0.48$; $K_a = 100$; $T_a = 0.01$ s; $\omega_b = 3.14$; $f = 60$ Hz; $K_1 = 0.9439$; $K_2 = 1.2240$, $K_3 = 0.3600$; $K_4 = 0.0626$; $K_5 = 0.4670$; $K_6 = 0.9565$.

Conventional power system stabilizer: $K_{PSS} = 50$, $T_w = 10$ s, $T_1 = 1.99$, $T_2 = 0.025$ s, $T_3 = 0.81$, $T_4 = 0.004$.

References

1. Kundur P (1994) Power system stability and control. McGraw-Hill
2. Grigsby LL (2016) Power system stability and control. CRC Press
3. Paital SR, Ray PK, Mohanty A (2018) Comprehensive review on enhancement of stability in multimachine power system with conventional and distributed generations. IET Renew Power Gener 12(16):1854–1863
4. Ray PK, Paital SR, Mohanty A, Panigrahi TK, Kumar M, Dubey H (2020) Swarm and bacterial foraging based optimal power system stabilizer for stability improvement. In: 2016 IEEE region 10 conference (TENCON), IEEE, pp 1916–1920
5. Ray PK, Paital SR, Mohanty A, Eddy FY, Gooi HB (2018) A robust power system stabilizer for enhancement of stability in power system using adaptive fuzzy sliding mode control. Appl Soft Comput 73:471–481
6. Singh M, Patel RN, Neema DD (2019) Robust tuning of excitation controller for stability enhancement using multi-objective metaheuristic Firefly algorithm. Swarm Evolut Comput 44:136–147
7. Chitara D, Niazi KR, Swarnkar A, Gupta N (2018) Cuckoo search optimization algorithm for designing of a multimachine power system stabilizer. IEEE Trans Ind Appl 54(4):3056–3065
8. Sambariya DK, Gupta R, Prasad R (2016) Design of optimal input–output scaling factors based fuzzy PSS using bat algorithm. Eng Sci Technol Int J 19(2):991–1002
9. Ghoshal SP, Chatterjee A, Mukherjee V (2009) Bio-inspired fuzzy logic based tuning of power system stabilizer. Expert Syst Appl 36(5):9281–9292
10. Lee DJ, Wang L (2008) Small-signal stability analysis of an autonomous hybrid renewable energy power generation/energy storage system part I: Time-domain simulations. IEEE Trans Energy Convers 23(1):311–320
11. Bian XY, Huang XX, Wong KC, Lo KL, Fu Y, Xuan SH (2014) Improvement on probabilistic small-signal stability of power system with large-scale wind farm integration. Int J Electr Power Energy Syst 61:482–488
12. Supriyadi AC, Takano H, Murata J, Goda T (2014) Adaptive robust PSS to enhance stabilization of interconnected power systems with high renewable energy penetration. Renew Energy 63:767–774
13. Wang L, Truong DN (2013) Stability enhancement of DFIG-based offshore wind farm fed to a multi-machine system using a STATCOM. IEEE Trans Power Syst 28(3):2882–2889
14. Kaveh A, Farhoudi N (2013) A new optimization method: dolphin echolocation. Adv Eng Softw 59:53–70

Economic Operation of Diesel Generator in an Isolated Hybrid System with Pumped Hydro Storage



Subrat Bhol, Nakul Charan Sahu and AmarBijay Nanda

Abstract Hybrid energy system is generally a combination of renewable energy sources like photovoltaic, wind energy and micro-hydro generator. It is integrated with a diesel generator to solve power supply problems in remote places which are far from the grid. Hybrid system is also an economical solution for remote places where grid power availability is limited. The PV and wind energy sources are highly nature dependant and cannot meet the load demand for all times of a day. That is why it requires designing and developing a device to store energy and to meet the peak load demand. In this paper, micro-hydro pumped storage/generator plant has been considered to store the excess energy and also to generate whenever required. A diesel generator has been integrated with hybrid sources to meet the peak load demand. The saliency of this paper is to develop an operational methodology for the nonconventional sources to meet the load demand and to minimize the cost of power generation. A computer programme has been developed to achieve the minimum operational cost of diesel generator.

Keywords Hybrid energy system · Load demand · Pumped hydro storage

1 Introduction

In present days, renewable energy sources like solar, wind, tidal, etc., have been more popular and cost-effective. These sources purely depend on the climatic conditions throughout the day. The solar energy is highly prominent in mid-hours of the day and inactive in the night. Similarly, wind power also varies throughout the day. Due

S. Bhol · N. C. Sahu (✉) · A. Nanda

Department of Electrical Engineering, Institute of Technical Education and Research, Siksha 'O' Anusandhan (Deemed to be University), Bhubaneswar 751030, Odisha, India

e-mail: nakulsahu@soa.ac.in

S. Bhol

e-mail: subrat93eee@gmail.com

A. Nanda

e-mail: amarnanda@soa.ac.in

© Springer Nature Singapore Pte Ltd. 2020

R. Sharma et al. (eds.), *Innovation in Electrical Power Engineering, Communication, and Computing Technology*, Lecture Notes in Electrical Engineering 630,

https://doi.org/10.1007/978-981-15-2305-2_57

to the randomness of renewable energy, it has become difficult to manage the load demand accurately [1, 2]. Hybrid energy systems play a vital role towards meeting the requirement of electricity demand and make the system economically viable. Sometimes, these requirements are not available due to the remote location and weak grid supply. The load demand is practically varying in nature which depends basically on consumer. The complicity of the system increases due to the anecdotal nature of the source and load. The hybrid system comprising of solar photovoltaic (PV), wind turbine (WT) and pumped hydro storage (PHS) offers a convenient solution to the time-varying nature of the solar source as well as load demand and properly utilizes the supplementary renewable resources [3–6].

Energy storage systems are one of the important components of hybrid energy systems because of the fluctuation of renewable resources. Pumped hydro storage (PHS) is the most widely used energy storage system which is free from pollutant emissions during the conversion of electricity. Considering the different renewable energy sources used nowadays hydroelectric power is one of the most sought-after sources of clean energy amongst energy storage system. Several researchers have been focused on the joint operation of renewable energy sources (RES) and pumped hydro storage (PHS) plant on optimal sizing, operational and economical studies [7–9].

In the remote area where the grid power is not available, diesel generators are the main source of electrical energy. But it is not cost-effective and produces pollutant. Diesel generator (DG) is used to balance the energy deficiency during peak load hours. DG can be integrated with other renewable sources in the stand-alone system to increase reliability, availability of power supply and economic operation [10–12].

In this paper, attention has been given on the economic consideration of an isolated system. An analytical approach has applied to PV-WT-PHS integrated with DG. A mathematical model has been developed for economical scheduling in a stand-alone system to minimize the operating cost of diesel generator [13]. These models are simulated in MATLAB. The layout of the proposed system is given in Fig. 1.

The proposed hybrid system consists of a PV-WT-PHS and DG as shown in Fig. 1. Load requirements primarily supplied from PV and WT generators which are purely nature dependent. When there is surplus of power from above two sources, pumping operation is carried out to raise the water from lower reservoir and to store in upper reservoir. When the load demand is not satisfied, the water from upper reservoir is utilized to generate electricity by turbine generator set. During peak hours of the load, the DG is operated to balance the load requirement. The flow chart illustrates the sequence of operation of the proposed hybrid system as shown in Fig. 2.

1.1 Photovoltaic (PV) System

The performance of the photovoltaic (PV) system mostly depends upon the solar radiation and area of the solar panel. The solar irradiance strikes on the solar plates and converts solar energy to electrical energy [14], which is expressed in the Eq. (1) given below.

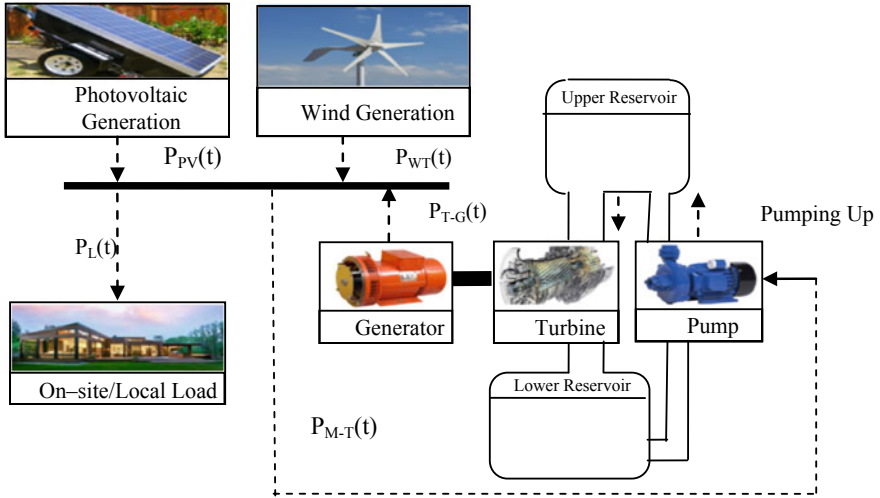


Fig. 1 Layout of the proposed system under study

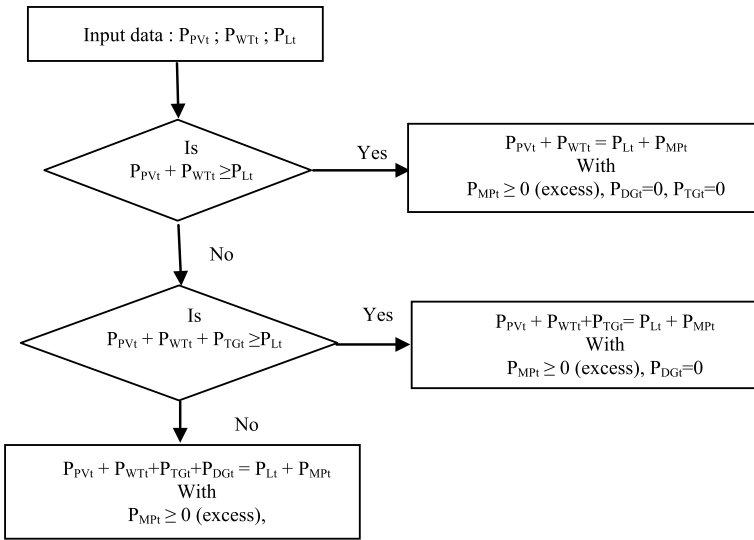


Fig. 2 Sequential operation of proposed hybrid system

$$E_{PV} = A \times \eta_m \times \eta_{pc} \times I \tag{1}$$

A is area of solar panel (m^2)
 η_m is efficiency
 η_{pc} is power conditioning efficiency
 I is hourly irradiation (kWh/m^2).

1.2 Wind Energy System

The wind velocity is converted to electrical energy by a wind turbine (WT). The power generated by the wind turbine (P_{WT}) [15] is given in the Eqs. (2) and (3).

$$P_{WT} = \frac{1}{2} \times \rho_a \times A \times V^3 \times C_{pw} \times \eta_{WT} \quad (2)$$

$$E_{WT} = P_{WT} \times t \quad (3)$$

where ρ_a is the density of air (kg/m^3)

η_{WT} is the joint efficiency of both wind turbine and generator

A is swept area of the wind turbine.

C_{pw} is performance coefficient of wind turbine

V is the wind speed velocity.

1.3 Diesel Generator (DG)

A diesel generator is normally an electrical generator where diesel engine acts as a prime mover. The diesel is the only source of input for extracting power from a DG. It is normally operated at its rated output. The fuel cost is a nonlinear quadratic equation [6] as given in the Eq. (4) below.

$$c_f \sum_{t=1}^T a P_{DG(t)}^2 + b P_{DG(t)} + c \quad (4)$$

where a, b, c are the fuel cost coefficients, C_f is the price of one litre of diesel, and $P_{DG(t)}$ is the output power of DG.

1.4 Pumped Hydro Storage Generation System

The pumped hydro storage generation system consists of

- (i) Motor pump set
- (ii) Turbine generator set.

PHS plants comprise an upper reservoir (UR) and a lower reservoir (LR). During light load conditions, surplus energy is utilized by pumping the water from lower reservoir to upper reservoir. During higher load conditions, this stored water from the UR is released through turbine generator into LR to produce electricity.

1.4.1 Motor Pump Set

The electrical energy utilized by the motor pump set (E_{mp}) for pumping water from LR to UR is given by Eq. (5) as described below.

$$E_{mp} = \frac{\rho \times g \times h \times Q_{mp}}{\eta_{m-p}} \quad (5)$$

ρ is density of water (1000 kg/m³)

Q_{m-p} is the rate of flow of water (m³/s)

g is the acceleration due to gravity (9.8 m/s²)

η_{m-p} is the overall pumping efficiency

h is the net pumping head (m).

1.4.2 Turbine Generator Set

The turbine generator operates when the load demand is more than the renewable power available in that instant. It utilizes the stored water in the upper reservoir to generate electrical energy in the principle of hydropower generation.

Energy generated (E_{T-G}) by the turbine generator can be described as in Eq. (6).

$$E_{T-G} = \rho \times g \times h \times Q_{T-G} \times \eta_{T-G} \quad (6)$$

η_{T-G} is turbine generator efficiency and Q_{T-G} is volumetric flow rate of water (m³/s).

1.5 Reservoir Volume

The net volume of water in the reservoir can be used to generate power when PV and wind are not sufficient to meet the load demand. The potential energy in the reservoir is given as in Eq. (7).

$$E_R = \rho \times V \times g \times h \quad (7)$$

E_R is the potential energy in KWh

V is the volume of the reservoir (m³).

2 Proposed Methodology

In the present work, minimization of daily operational cost is done by the proposed method for the hybrid power system. The hybrid system is analysed in three different cases, and the operational cost of diesel generator is compared.

The describing function for minimization of fuel cost of diesel generation can be expressed as given below in Eq. (8).

$$\min c_f \sum_{t=1}^T aP_{DG(t)}^2 + bP_{DG(t)} + c \quad (8)$$

2.1 Constraints

The present work involves the following operational constraints.

Equality constraint: At any time during operation, sum of power generated by different sources must meet the load demand that can be expressed as in Eq. (9).

$$P_{load(t)} = P_{PV(t)} + P_{WT(t)} + P_{TG(t)} - P_{MP(t)} + P_{DG(t)} \quad (9)$$

Limit constraints: All the recourses must operate between their upper and lower limits of respective power sources as described in Eqs. (10)–(15).

$$0 \leq P_{PV(t)} \leq P_{PV(t)}^{\max} \quad (1 \leq t \leq T) \quad (10)$$

$$0 \leq P_{WT(t)} \leq P_{WT(t)}^{\max} \quad (1 \leq t \leq T) \quad (11)$$

$$0 \leq P_{DG(t)} \leq P_{DG}^{\max} \quad (1 \leq t \leq T) \quad (12)$$

$$0 \leq P_{MP(t)} \leq P_{MP}^{\max} \quad (1 \leq t \leq T) \quad (13)$$

$$0 \leq P_{TG(t)} \leq P_{TG}^{\max} \quad (1 \leq t \leq T) \quad (14)$$

$$V_R^{\min} \leq V_{R(t)} \leq V_R^{\max} \quad (15)$$

The reservoir volume changes can be described by the Eq. (16).

$$V_{R(t)} = V_{R(0)} \times (1 - \delta) + t_s \times \left(\eta_{MP} \times \sum_{i=1}^t P_{MP(i)} - \frac{\sum_{i=1}^t P_{TG(i)}}{\eta_{TG}} \right) \quad (16)$$

where $V_{R(t)}$ is the volume of the reservoir at any instant of operation
 δ is the leakage and evaporation loss factor
 $P_{MP(t)}$, $P_{TG(t)}$ are pumping and generating power PHS system.

3 Case Study

For the present analysis, three different cases have been considered. Resources data are obtained from energy survey carried out in rural communities in South Africa [6]. Both summer and winter data are presented for study in these three different cases. Table 1 shows the simulation parameters for study. The components of hybrid system are designed looking into the peak load demand and variation of wind velocity, irradiations throughout the day. The pumped hydro storage units are also designed to utilize the wind power accordingly.

3.1 Case-1: Only DG Is Operated

The load profile of summer and winter days is shown in Fig. 3a and b, respectively. The DG operating in the same way as per the load changes in a day. During winter, the load demand is generally higher than summer because of the harvesting and heating equipments used by the consumers. The cost variation is similar pattern as in the load demand as shown in Fig. 4a and b. As the DG supplies power to load alone, the cost of operation is high. The total operating cost is shown in Table 2.

Table 1 Simulation parameters

Parameters	Ratings	Parameters	Ratings
Sampling time (t)	1 h	Wind rated power	1 kW
PHS generation capacity	4.8 kW	DG rated power	8 kW
PHS pumping capacity	5.6 kW	Diesel fuel price	1.42\$/l
PHS overall efficiency	0.67	a	0.2411
PHS volume limit	0–100%	b	0.0814
PV rated power	4 kW	c	0.4332

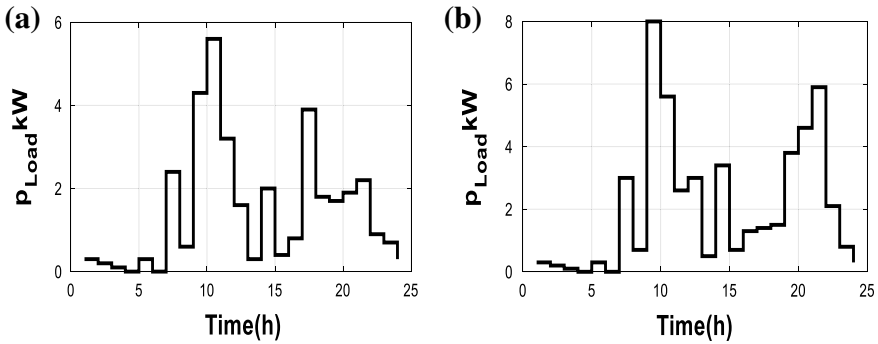


Fig. 3 a Daily load profile in summer b daily load profile in winter

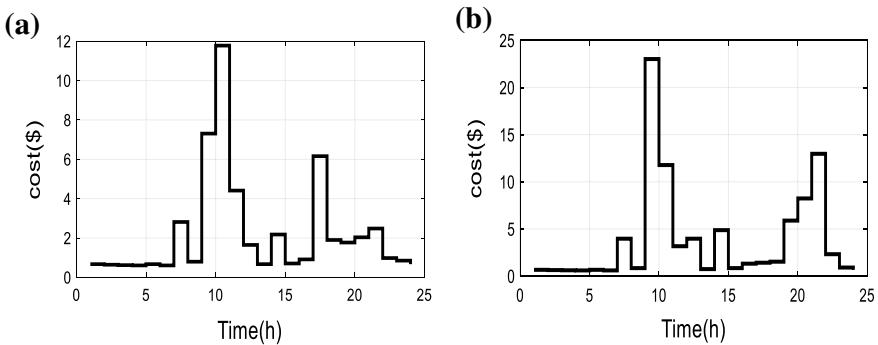


Fig. 4 a DG cost operating alone in summer b DG cost operating alone in winter

Table 2 DG operating cost in different cases in a day

Cases	Power (summer) kW	Power (winter) kW	Cost (summer) \$	Cost (winter) \$
Only DG	38.49	65.96	53.89	92.34
DG + PV + WT	19.9	53.67	27.89	75.14
Hybrid system	10.73	21.82	15.03	30.55

3.2 Case-2: DG Operating with PV and WT Without PHS

In this case, the load demand is supplied from PV and WT without any storage. DG is operated only when these sources are not able to meet the load demand. The power is supplied to a dump load during excess power generation from the renewable sources to maintain power balance and system stability. The output power from PV and WT are shown in Fig. 5a, b, c, d respectively. The wind speed in the winter days is higher than the summer. The wind speed measured is maximum during evening hours of

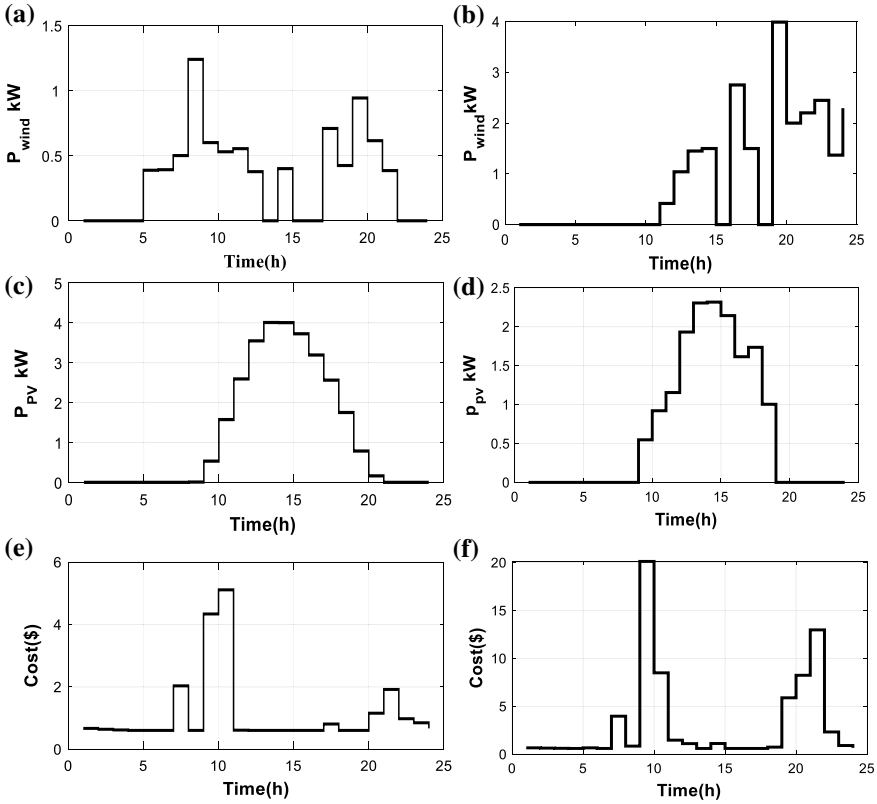


Fig. 5 a Wind power generation in summer b wind power generation in winter c PV power generation in summer d PV power generation in winter e DG operating cost without PHS in summer f DG operating cost without PHS in winter

the day and minimum during morning hours in winter but in summer it is consistent throughout the day and drops with fall of night. The costs of operation of DG in this situation are shown in Fig. 5e and f. The total cost falls in the participation of PV and WT.

3.3 Case-3: Hybrid System-DG Operating with PV, WT with PHS

In this case, pumped hydro storage plant is operated during excesses or deficiency of power, generated from PV and WT to meet the load demand. Both pumping and generation are restricted at the same time. Figure 6a and b shows the pumping and generation of power in summer and winter through the 24 h of operation. It can be observed that during pumping operation, no power is generated by turbine

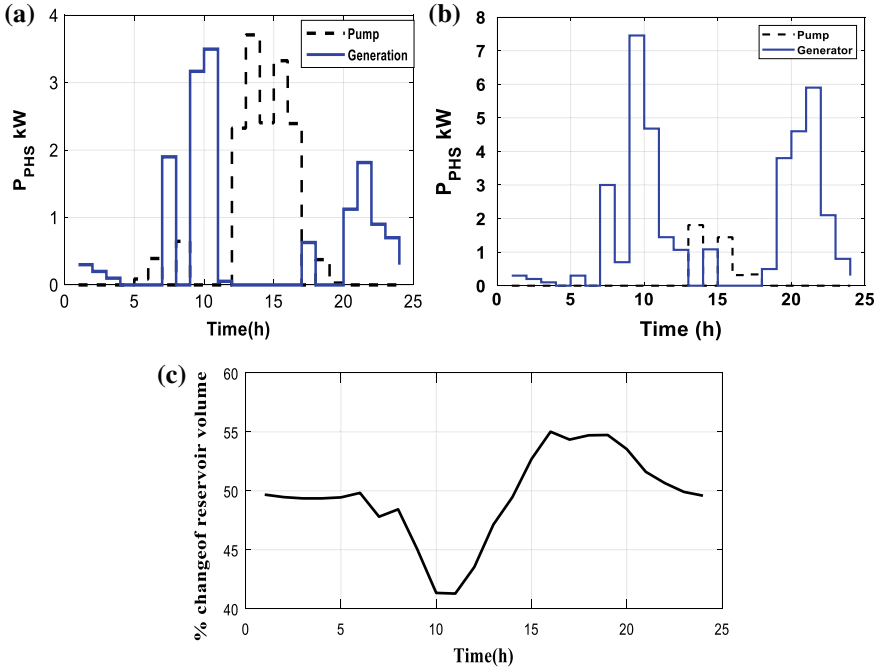


Fig. 6 a Pumping and generating power in summer b pumping and generating power in winter c % change of volume in reservoir

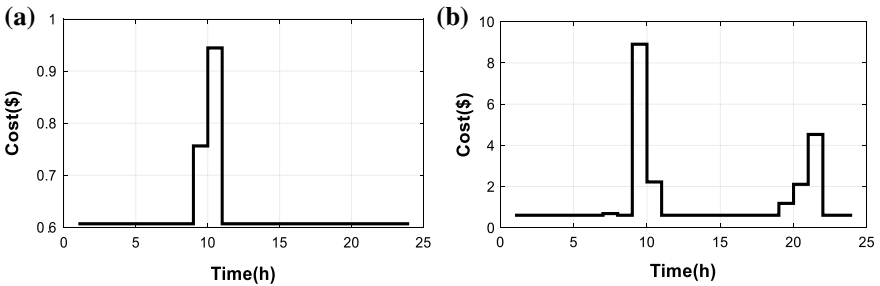


Fig. 7 a DG cost during summer b DG cost during winter

generator. The pumping and generating is so adjusted that the volume of the reservoir is maintained after end of each day for recycling of power generation as shown Fig. 6c. The volume of upper and lower reservoir can be filled to its maximum capacity. Looking into PHS operation, the volume of upper reservoir is started with 50% of its maximum capacity. Table 2 shows the summary of operating cost of DG under different cases. The cost variation of DG is shown in Fig. 7a and b. It can be observed that in hybrid system, the participation of PHS reduces the cost of operation of DG.

4 Conclusion

In the present work, a simulated model was developed to analyse the variations in operational cost of DG in the different case studies. For the present analysis, the three different sources have been considered. The renewable sources like PV and WT help in reducing of operational cost of DG. But without any storage devices, its effectiveness gets reduced by a great extent as seen in the result where renewable power generated was dumped in absences of load demand. The use of pumped hydro storage plant improves the economy of system. The volume of the reservoir is restored to starting position after the end of operation in each to make the system cyclical. The present work will help the researchers for proper management of renewable sources under various environments.

References

1. Al-Falahi MDA, Jayasinghe SDG, Enshaei H (2017) A review on recent size optimization methodologies for standalone solar and wind hybrid renewable energy system. *Energy Convers Manag* 143:252–274
2. Bilal BO et al (2010) Optimal design of a hybrid solar-wind-battery system using the minimization of the annualized cost system and the minimization of the loss of power supply probability (LPSP). *Renew Energy* 35(10):2388–2390
3. Rehman S, Al-Hadhrami LM, Alam MM (2015) Pumped hydro energy storage system: a technological review. *Renew Sustain Energy Rev* 44:586–598
4. Lv Y, Yu X, Yue T (2018) Study on the optimal scheduling of a hybrid wind-solar-pumped storage power generation system. In: 2018 IEEE 3rd advanced information technology, electronic and automation control conference (IAEAC), IEEE
5. Rathore A, Patidar NP (2019) Reliability assessment using probabilistic modelling of pumped storage hydro plant with PV-wind based standalone microgrid. *Int J Electric Power Energy Syst* 106:17–32
6. Kusakana K (2016) Optimal scheduling for distributed hybrid system with pumped hydro storage. *Energy Convers Manag* 111:253–260
7. Zhang Q et al (2017) Research on scheduling optimisation for an integrated system of wind-photovoltaic-hydro-pumped storage. *J Eng* 2017(13):1210–1214
8. Salimath G, Singh NK, Badge SS (2017) Coordination and performance analysis of pumped hydro storage system integrated with solar, wind hybrid system. In: 2017 international conference on energy, communication, data analytics and soft computing (ICECDS), IEEE
9. Jamii J, Abbas D, Mimouni MF (2016) Scheduling optimization of wind power generation with pumped storage hydro plant. In: 2016 17th international conference on sciences and techniques of automatic control and computer engineering (STA). IEEE, 2016
10. Maleki A, Askarzadeh A (2014) Optimal sizing of a PV/wind/diesel system with battery storage for electrification to an off-grid remote region: a case study of Rafsanjan, Iran. *Sustain Energy Technol Assess* 7:147–153
11. Bonanno F et al (1999) Transient analysis of integrated diesel-wind-photovoltaic generation systems. *IEEE Trans Energy Convers* 14(2):232–238
12. Kapambwe E (2012) Economic feasibility photovoltaic/diesel/battery hybrid power systems to replace stand-alone diesel generators in off-grid remote areas of Zambia
13. Kusakana K (2015) Optimal scheduled power flow for distributed photovoltaic/wind/diesel generators with battery storage system. *IET Renew Power Gener* 9(8):916–924

14. Kusakana K, Vermaak HJ (2014) Hybrid diesel generator/renewable energy system performance modeling. *Renew Energy* 67:97–102
15. Vermaak HJ, Kanzumba K (2014) Design of a photovoltaic-wind charging station for small electric Tuk–tuk in DR Congo. *Renew Energy* 67:40–45

SHO Algorithm-Based Fuzzy-Aided PID Controller for AGC Study



S. Sahoo, N. K. Jena, D. P. Das, Binod Kumar Sahu
and Manoj Kumar Debnath

Abstract This paper articulates automatic generation control (AGC) of a three-area multi-unit power system by proposing a fuzzy-aided PID controller incorporated with filter (FPIDF). An inexhaustible photovoltaic (PV) source is injected in the first area of the recommended conventional power system. The challenges arise due to the PV source; a sturdy secondary controller is quintessential. An optimal FPIDF controller is designed by applying a new algorithm named as selfish herd optimization algorithm. To demonstrate the validity of the proposed controller, the transient response evaluated by FPIDF is compared with the PID controller. Further, the robustness is examined by forcing a random step load in area-1.

Keywords AGC · Fuzzy-based PID controller with filter (FPIDF) · Selfish herd optimization (SHO)

Nomenclature

B	Frequency bias constant
R	Regulation constant
K_{ps}	Control area gain
T_{ps}	Control area time constant
T_g	Governor time constant
T_t	Turbine time constant
K_r	Reheat gain
T_r	Reheat time constant
T_{ij}	Synchronization coefficient torque
K_{pv}	Solar system gain
T_{pv}	Solar system time constant
T_{GH}	Hydro governor time constant

S. Sahoo · N. K. Jena · D. P. Das · B. K. Sahu (✉) · M. K. Debnath
Department of Electrical Engineering, ITER, SOA Deemed to be University, Bhubaneswar, India
e-mail: binoditer@gmail.com

T_{RH} Hydro reheat time constant
 T_w Water turbine time constant

1 Introduction

Due to the constant increase in power demand, the modern power system turns out to be increasingly intricate and nonlinear with increment in size. To provide a reliable and quality power supply by such complex system becomes a challenging issue for power system personnel. Quality of power system refers to maintain the voltage and frequency at a desirable level. Frequency deviation is due to the mismatch between power generation and load demand. Since consumer power demand varies frequently, the area control error (ACE) which is caused due to frequency and tie-line power deviation increases. The prime function of AGC is to reduce the ACE. Hence, intelligent control strategies are to be introduced into the conventional AGC system which can enhance the stability of the power system by reducing the area control error (ACE) and thereby keeping the frequency and tie-line power within a permissible limit.

Many researchers over the last few decades have proposed different intelligent control techniques to solve the AGC problems in a power system apart from the classical I/PI controllers [1, 2]. Pradhan et al. [3] employed firefly algorithm for the tuning of PID controller used for the AGC of two equal area non-reheat thermal system. Hasanein and El-Fergany [4] suggested SOS-optimized PID controller for a two-area reheat thermal system. Sahu et al. [5] proposed PID controller tuned by TLBO for AGC of two-area reheat-type thermal system. Guha et al. [6] used quasi-oppositional SOS (QOSOS) to optimize the conventional PID controller for LFC of a two-area thermal system with GDB and GRC. A cascaded PD-PID controller is used by Debnath et al. [7] for AGC of a two-area multi-source power system. Mishra et al. [8] considered a three equal area thermal system for the application of IDD controller with filter in AGC. IDDF controller for both ALFC and AVR of a multi-source three-area power system is proposed by Rajbongshi and Saikia [9]. Acharyalu et al. [10] studied PID controller with filter optimized by MFO technique for a multi-source three-area power system.

The conventional PID controller may not guarantee to give an improved dynamic response having parameter uncertainties, nonlinearities. Hence, fuzzy logic-based controllers are chosen as the secondary controller for AGC problem on any realistic system which can provide better frequency and voltage regulation. Kashyap et al. [11] applied fuzzy PID controller for a two-area hydropower system. Lal et al. [12] suggested GWO-based fuzzy PID controller for frequency regulation of two-area hydro-thermal system with GRC and TCPS. TLBO-tuned fuzzy PID controller is proposed by Sahu et al. [13]. Fuzzy-based PID controller with filter is demonstrated

by Arya [14] for a two-area hydro-thermal system with CES in each area. SOS-based fuzzy PID controller is applied by Nayak et al. [15] for frequency control in a three-area thermal system consisting of GRC.

The above study reflects that the fuzzy-aided controller handles the system performance efficiently under the presence of parameter uncertainties and nonlinearities. But the selection of input and output scaling parameters along with rule formulation is an obscure job. So the rule formulation is still a challenge to the researchers. In this paper, design of FPIDF is carried out with evaluating the input and output scaling parameters by the help of SHO technique to study the AGC in the presided system.

Objective of the paper

- i. The design of FPIDF as secondary controller employed in a three-area power system.
- ii. Assessment of the dynamic response produced in the presence of PV source.
- iii. Performance of the system with FPIDF controller is validated by comparing the response with PID controller.
- iv. Robustness of FPIDF controller is examined by subjecting a highly perturbed step load in area-1.

2 System Under Study

In this paper, to justify the supremacy of proposed controller a three unequal area power system is taken for the investigation of AGC. The system is modelled in MATLAB/SIMULINK environment of version 2016b. In each area, two different sources are used. Area-1 consists of solar thermal (STPP) unit and hydro unit whereas thermal and hydro units are present in area-2. In area-3, the same thermal system is connected with gas unit. The system parameters are taken from Ref. [10]. For the analysis of LFC 1%, step load perturbation is introduced in area-1 of Fig. 1.

3 Controller Structure and Objective Function

To maintain the frequency and tie-line power of the system at a desirable level, different controllers are used which works to reduce the area control error (ACE). Here, in this paper, fuzzy logic-based PID controller with filter is demonstrated for better transient response and is compared with the response of PID controller. The block diagram of the proposed controller is shown in Fig. 2a. Similar type of controllers but of different scaling factors are used in each area of the system under consideration. The area control error (ACE) and its derivative are the two input signals to the FLC, and its output(y) is multiplied with PIDF controller in the second stage to get FPIDF controller. FLC consists of four stages: fuzzification, rule base, fuzzy inference system and defuzzification. In this FLC, five membership

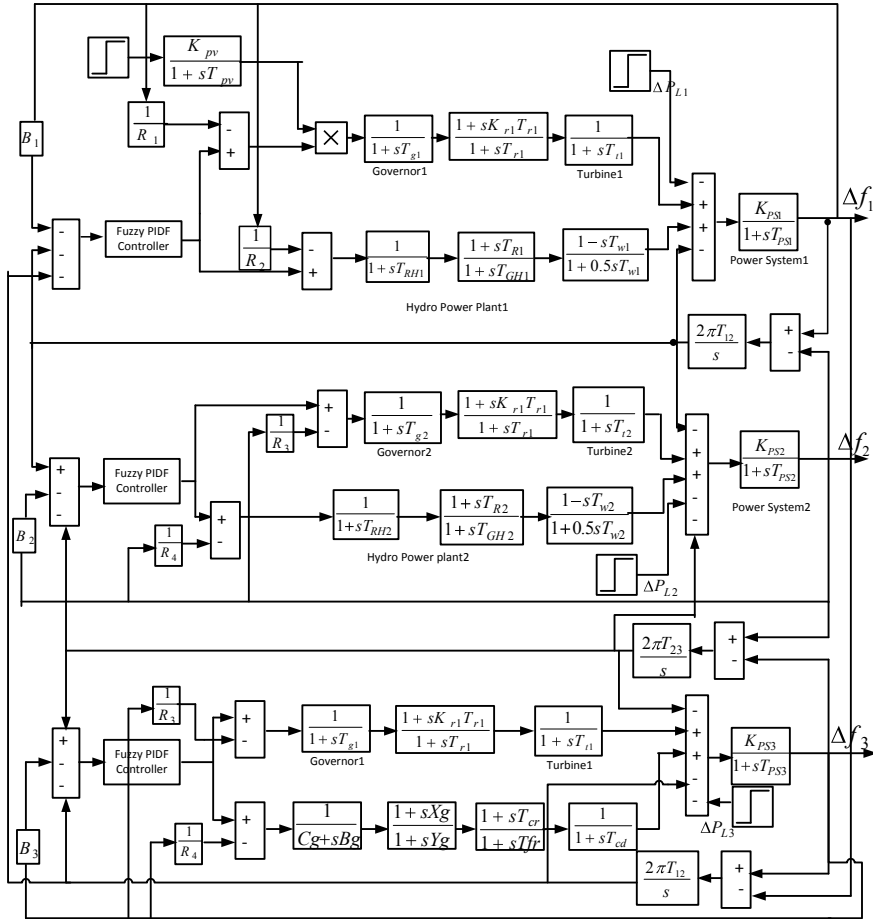


Fig. 1 Proposed three-area interconnected power system

functions (MFs), three triangular and two trapezoidal with five linguistic variables: NB (Negative Big), NS (Negative Small), ZE (Zero), PS (Positive Small), and PB (Positive Big) are implemented for both input and output variables and shown in Fig. 2b. Fuzzy rule base is given in Table 1.

Along with the controller structure, the selection of controller parameter is also very important for reducing the ACE. Therefore, different optimization techniques are used to obtain the controller gain parameters. For the design of any optimization technique, objective function or fitness function is necessary. Various kinds of objective functions may be used such as integral square error (ISE), integral time square error (ITSE), integral absolute error (IAE), integral time absolute error (ITAE), etc. In this article, ITAE expressed in Eq. (1) is considered as the cost function of the system to design the proposed controller.

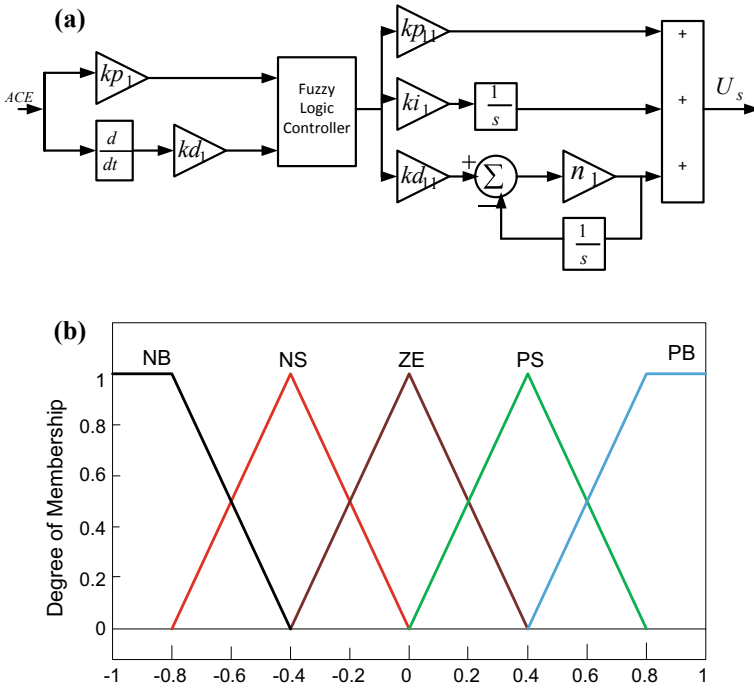


Fig. 2 a FPIDF controller structure. b Membership function structure for both the inputs and output of fuzzy logic system

Table 1 Rule base for fuzzy logic system

ACE	ΔACE				
	NB	NS	ZE	PS	PB
NB	NB	NB	NS	NS	ZE
NS	NB	NS	NS	ZE	PS
ZE	NS	NS	ZE	PS	PS
PS	NS	ZE	PS	PS	PB
PB	ZE	PS	PS	PB	PB

$$J = ITAE = \int_0^t [|\Delta f_1| + |\Delta f_2| + |\Delta f_3| + |\Delta ptie_{12}| + |\Delta ptie_{23}| + |\Delta ptie_{31}|] t dt \tag{1}$$

where Δf_1 , Δf_2 and Δf_3 are the system frequency deviations of area 1, 2 and 3, respectively, and $\Delta ptie_{ij}$ is change in tie-line power between area ‘i’ and ‘j’.

4 Selfish Herd Optimization (SHO) Algorithm

SHO is a swarm optimization-based algorithm that mimics the selfish herd theory which is developed by Fausto et al. [16]. According to this theory, a group of animals are divided into two kinds of search agents, such as prey and predator. Each element in a prey group changes their position to survive from the predators. The element having higher survival value is at the safest position and vice versa. Each element in the predator group changes their position to attack and kill the prey. Predator can kill the prey or herd if the herd is within its domain of danger and survival value of the predator is more than that of prey. The flow chart of SHO algorithm is given in Fig. 3.

5 Simulation Results and Discussion

In this paper, for the analysis of AGC of a three unequal area power system having renewable sources is considered. The MATLAB/SIMULINK (2016b) environment is used for the simulation of the system shown in Fig. 1. To study the dynamic response of the above system, PID and FPIDF controllers are employed and SHO algorithm is used for the tuning of controller gains.

5.1 Case-1: Transient Analysis of Presided System

The study is carried out by injecting a step load change of 0.01 pu in area-1 at $t = 0$ s. The transient performance of frequency and tie-line power excursion in each of three areas is shown in Fig. 4. The transient performance indices are expressed in terms of undershoot, overshoot and settling time which are given in Table 1. From Fig. 4 and Table 2, it is evident that the proposed controller yields better dynamic performance in terms of all the transient indices.

5.2 Case-2: Robustness Analysis

The practicability of the suggested controller is established by varying the load randomly. The random load is inserted in area-1. The random load, the change in frequency in area-1 and change in tie-line power between area-1 and area-2 are shown in Fig. 5. From the response, it is clear that the dynamic stability of the system is also maintained by randomly varying the load.

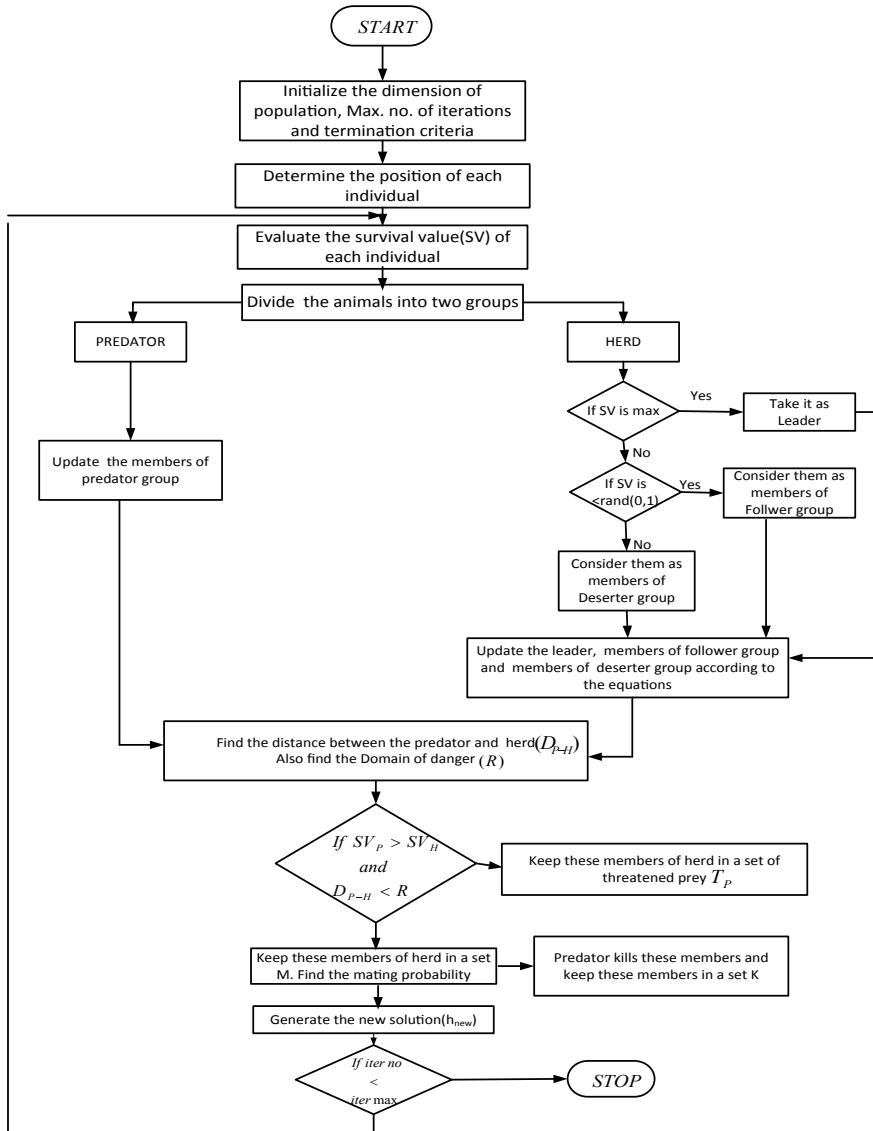


Fig. 3 Flow chart of SHO

6 Conclusion

In this article, a metaheuristic optimization technique, selfish herd optimization (SHO), is used to find the accurate values of gain parameters of the different controllers for AGC of a three-area power system. In the investigated system, renewable

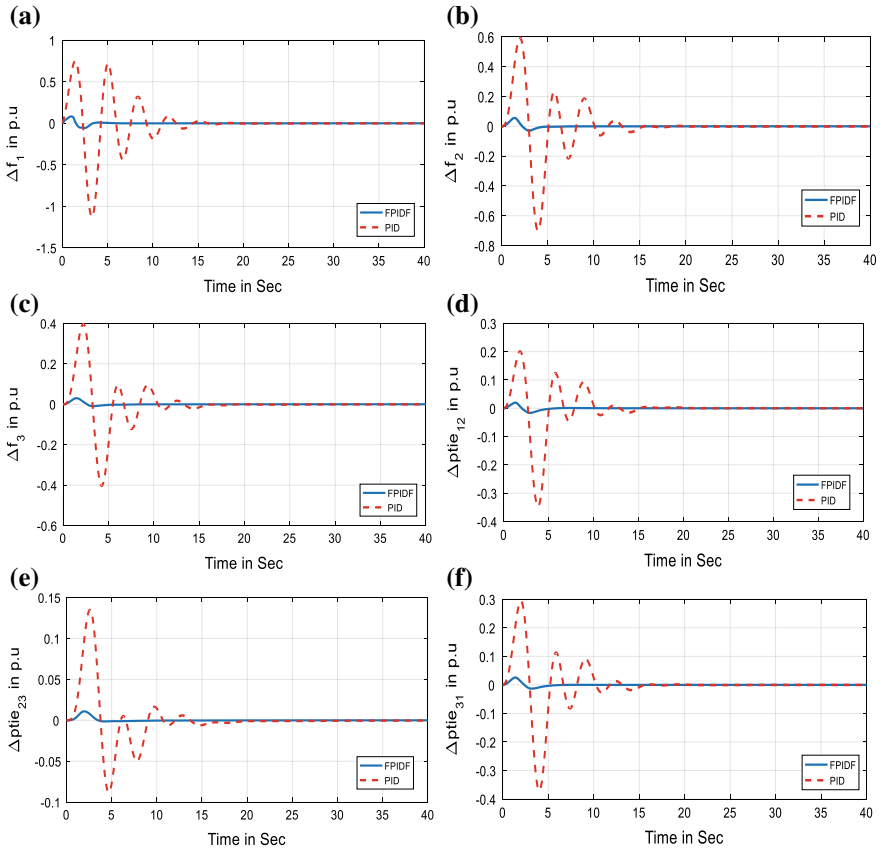
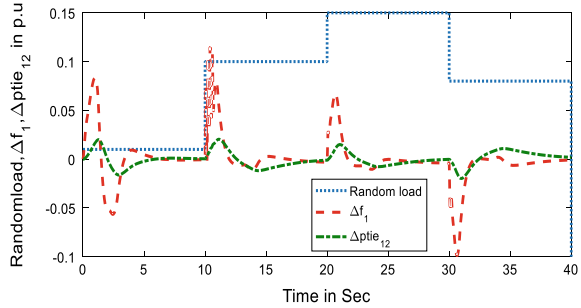


Fig. 4 Transient response curve of area frequencies and tie-line powers **a** frequency deviation in area-1, **b** frequency deviation in area-2, **c** frequency deviation in area-3, **d** tie-line power deviation between area-1 and area-2, **e** tie-line power deviation between area-2 and area-3, **f** tie-line power deviation between area-3 and area-1

Table 2 Transient parameters

	PID			FPIDF		
	U_{sh}	O_{sh}	t_s	U_{sh}	O_{sh}	t_s
Δf_1	-1.1276	0.7482	21.5129	-0.0566	0.0832	5.7004
Δf_2	-0.7004	0.5952	19.6625	-0.0294	0.0562	6.4072
Δf_3	-0.4040	0.3972	18.4777	-0.0096	0.0302	6.7815
Δp_{tie12}	-0.3468	0.2014	19.8704	-0.0162	0.0200	5.0712
Δp_{tie23}	-0.0878	0.1350	18.8934	-0.0014	0.0110	3.1737
Δp_{tie31}	-0.3703	0.2936	15.3178	-0.0131	0.0260	5.4465

Fig. 5 Random load and its effect on the transient response



energy sources are incorporated to meet the increasing load demand without pollution. The transient response curve shows that SHO-tuned FPIDF controller gives better performance than the conventional PID controller in terms of undershoot, overshoot and settling time.

Appendix

$K_{ps1} = K_{ps2} = K_{ps3} = 100 \text{ Hz/puMW}$, $T_{ps1} = T_{ps2} = T_{ps3} = 20 \text{ s}$, $T_{G1} = T_{G2} = T_{G3} = 0.08 \text{ s}$, $T_{T1} = T_{T2} = T_{T3} = 0.3 \text{ s}$, $R_1 = 2 \text{ Hz/puMW}$, $R_2 = 2.4 \text{ Hz/puMW}$, $R_3 = R_5 = R_6 = R_1$, $B_1 = B_2 = B_3 = 0.425 \text{ puMW/Hz}$, $T_{12} = T_{23} = T_{31} = 0.0707 \text{ puMW/rad}$

$T_{RH} = 48.7 \text{ s}$, $T_{R1} = T_{R2} = 5 \text{ s}$, $T_{GH} = 0.513 \text{ s}$, $T_w = 1 \text{ s}$, $k_{r1} = k_{r2} = k_{r3} = 1$, $T_{r1} = T_{r2} = T_{r3} = 5 \text{ s}$

$K_{PV} = 1$, $T_{PV} = 1.8 \text{ s}$, $X_g = 0.6$, $Y_g = 1$, $B_g = 0.05$, $C_g = 1$, $T_{fr} = 0.23$, $T_{cr} = 0.01$, $T_{cd} = 0.2$.

References

1. Kundur P (2009) Power system stability and control, eighth reprint. Tata McGraw Hill, New Delhi
2. Elgerd OI, Fosha CE (1970) Optimum megawatt-frequency control of multi-area electric energy systems. IEEE Trans Power App Syst 89(4)
3. Padhan S, Sahu RK, Panda S (2014) Application of firefly algorithm for load frequency control of multi-area interconnected power system. Electr Power Compon Syst 42(13):1419–1430
4. Hasanien HM, El-Fergany AA (2016) Symbiotic organisms search algorithm for automatic generation control of interconnected power systems including wind farms. IET Gener Transm Distrib 11(7):1692–1700
5. Sahu RK, Gorripotu TS, Panda S (2016) Automatic generation control of multi-area power systems with diverse energy sources using teaching learning based optimization algorithm. Eng Sci Technol Int J 19(1):113–134
6. Guha D, Roy P, Banerjee S (2017) Quasi-oppositional symbiotic organism search algorithm applied to load frequency control. Swarm and Evol Comput 33:46–67

7. Debnath MK, Jena T, Mallick RK (2016) Novel PD-PID cascaded controller for automatic generation control of a multi-area interconnected power system optimized by grey wolf optimization (GWO). In: IEEE 1st international conference on power electronics, intelligent control and energy systems (ICPEICES), July. IEEE, pp 1–6
8. Mishra DK, Panigrahi TK, Ray PK, Mohanty A (2017) Application of integral double derivative with filter for load frequency control in multi area power system. In: *IEEE Calcutta conference (CALCON)*, December. IEEE, pp 220–225
9. Rajbongshian R, Saikia LC (2017) Combined control of voltage and frequency of multi-area multisource system incorporating solar thermal power plant using LSA optimised classical controllers. *IET Gener Transm Distrib* 11(10):2489–2498
10. Acharyulu BV, Mohanty B, Hota PK (2019) Comparative performance analysis of PID controller with filter for automatic generation control with moth-flame optimization algorithm. In: *Applications of artificial intelligence techniques in engineering*. Springer, Singapore, pp 509–518
11. Kashyap R, Sankeswari SS, Patil BA (2013) Load Frequency Control using fuzzy PI controller generation of interconnected hydropower system. *Int J Emerg Technol Adv Eng* 3(9):655–659
12. Lal DK, Barisal AK, Tripathy M (2016) Grey wolf optimizer algorithm based fuzzy PID controller for AGC of multi-area power system with TCPS. *Procedia Comput Sci* 92:99–105
13. Sahu BK, Pati S, Mohanty PK, Panda S (2015) Teaching–learning based optimization algorithm based fuzzy-PID controller for automatic generation control of multi-area power system. *Appl Soft Comput* 27:240–249
14. Arya Y (2019) AGC of PV-thermal and hydro-thermal power systems using CES and a new multi-stage FPIDF-(1 + PI) controller. *Renew Energy* 134:796–806
15. Nayak PC, Prusty UC, Prusty RC, Barisal AK (2018) Application of SOS in fuzzy based PID controller for AGC of multi-area power system. In: *Technologies for smart-city energy security and power (ICSESP)*, March 2018. IEEE, pp 1–6
16. Fausto F, Cuevas E, Valdivia A, González A (2017) A global optimization algorithm inspired in the behavior of selfish herds. *Biosystems* 160:39–55